Springer Series in Materials Science 304

Elke Meissner
Rainer Niewa *Editors*

Ammonothermal Synthesis and Crystal Growth of Nitrides

Chemistry and Technology

Springer

Springer Series in Materials Science

Volume 304

The Springer Series in Materials Science covers the complete spectrum of materials research and technology, including fundamental principles, physical properties, materials theory and design. Recognizing the increasing importance of materials science in future device technologies, the book titles in this series reflect the state-of-the-art in understanding and controlling the structure and properties of all important classes of materials.

More information about this series at http://www.springer.com/series/856

Elke Meissner · Rainer Niewa
Editors

Ammonothermal Synthesis and Crystal Growth of Nitrides

Chemistry and Technology

Springer

Editors
Elke Meissner
Fraunhofer Institute for Integrated Systems and Device Technology
Erlangen, Germany

Rainer Niewa
Institute of Inorganic Chemistry
University of Stuttgart
Stuttgart, Germany

ISSN 0933-033X ISSN 2196-2812 (electronic)
Springer Series in Materials Science
ISBN 978-3-030-56304-2 ISBN 978-3-030-56305-9 (eBook)
https://doi.org/10.1007/978-3-030-56305-9

This Springer imprint is published by the registered company Springer Nature Switzerland AG
The registered company address is: Gewerbestrasse 11, 6330 Cham, Switzerland

Foreword

Gallium nitride (GaN) is a direct wide bandgap semiconductor of great and still growing technological importance. In particular, light-emitting diodes (LEDs) based on GaN induced breakthrough changes in general lighting techniques, which was awarded by the Nobel Prize in physics in 2014.

As a rule, semiconductor devices [including microprocessors (Si), telecommunication lasers (GaAs)] require perfect single-crystalline substrates as basis for epitaxy and processing for a final product. For Si or GaAs, the bulk crystals of high quality and large size are grown by Czochralski or Bridgman method from stoichiometric melts cooled down for single-crystal growth. For GaN, such stoichiometric melt cannot be obtained due to the presence of nitrogen in the GaN crystal, which leads to decomposition of the nitride at high temperatures and formation of N_2 gas and liquid gallium. GaN is therefore unstable against its constituents containing molecular nitrogen lowering the free energy of the Ga + N_2 system. To increase the free energy of the constituents and thus to make GaN thermodynamically stable, sufficiently high pressure of N_2 gas is necessary at high temperature. For example, at 1500 °C, the equilibrium pressure of N_2 is as high as 1.0 GPa. The temperature of 1500 °C seems nominally high; however, it is still significantly lower than the one expected for melting of GaN. The melting temperature of GaN most probably and significantly exceeds 2500 K, and the pressure necessary for melting is higher than 6.0 GPa. A direct confirmation of such a high melting temperature is extremely low solubility of nitrogen in gallium. For example, at 1500 °C (and corresponding N_2 pressure of 1.0 GPa) this solubility is not higher than 0.5 at. %.

Consequently, the equilibrium method of GaN crystallization from a solution in liquid gallium, although it allowed obtaining structurally perfect crystals, proved to be ineffective for use in industry.

Therefore, the super-efficient GaN LEDs were constructed on foreign substrates, mismatched to GaN, which necessarily meant a high number of defects in the active structure of the device.

Due to its physical properties and the resulting figures of merit, GaN is also considered the best material for high-frequency and high-power electronics where silicon has reached its physical limits. However, to take full advantage of GaN's physical potential, monocrystalline GaN substrates with high structural quality are necessary.

In the opinion of many scientists and engineers, the future of GaN will belong to optoelectronic and electronic devices based on GaN-on-GaN technology. It means that epitaxial structures of light-emitting diodes (LEDs), laser diodes (LDs), and all kinds of transistors (of vertical and lateral architecture) will be built on native GaN wafers.

Unfortunately, the lack of native substrates of high structural quality and appropriate size as well as required electrical properties still limits the development and progress of the mentioned technology. As mentioned, the most known GaN-based devices, LEDs, are built on foreign sapphire substrates. In the case of nitride-based electronic devices, high-electron-mobility transistors (HEMTs) are constructed today mainly on silicon carbide and silicon substrates. Some devices have already been commercialized. A long and bumpy road is, however, ahead of the industry in order to achieve a full commercial success, comparable to that of LEDs. Still, the structural quality of the mentioned electronic devices is insufficient to obtain their maximum operation level. On the other hand, vertical electronic devices based on GaN (e.g., metal-oxide semiconductor field-effect transistor; MOSFET) are at the beginning of their road to commercialization.

There is no doubt that GaN substrates are needed to explore full potential of GaN in electronics. For the last three decades, crystallization of bulk gallium nitride (GaN) and fabrication of native substrates has been one of the main goals of the "application oriented nitride community" as the expected technical potential is very high. On the other hand, nitride materials and components appear in many fields other than electronic as well. However, as it was already mentioned, crystallizing GaN is quite a challenging task. For fundamental reasons, it is impossible to grow GaN crystals from the melt. This compound should be grown by other techniques requiring lower pressure and temperature. Crystallization from gas phase, solution, or any combination thereof must be included. Three main methods are applied for obtaining GaN: sodium flux, ammonothermal, and halide vapor phase epitaxy (HVPE). The first two methods represent crystallization from solution, the third one from gas phase. HVPE is the most advanced technique strongly developed by the industry. Today, GaN crystals of the highest structural quality can be obtained by the ammonothermal method. Ammonothermally grown GaN crystals and wafers demonstrate low threading dislocation density, not higher than 5×10^4 cm^{-2}, and they are crystallographically flat. The bowing radius of (0001) crystallographic planes for 2-inch wafer can exceed 30 m. Moreover, the technology is scalable because, like for hydrothermal technology of quartz, a number of seeds can be placed in the growth zone of the reactor, and thus, a number of crystals can be grown simultaneously, in one process. This makes ammonothermal crystal growth technology and especially GaN crystal growth worth a further effort and development.

The approach based on the ammonothermal synthesis and crystallization of GaN started in Poland at the Faculty of Physics of the University of Warsaw in the middle of 1990s. The pioneer of this method was Dr. Robert Dwilinski. Based on some very encouraging results of ammonothermal synthesis of GaN, Dwilinski and his colleagues with a help of the Japanese company Nichia Chemical Industries (today Nichia Corporation) created Ammono SA in 1999. For first 12 years, Ammono developed very fast demonstrating 1-inch and 2-inch GaN wafers of the highest structural quality. One-inch wafers were sold in small quantities. In 2012, Glencross Company Limited (GHL) became a financial investor of Ammono. In 2015, due to a disagreement between shareholders, insolvency of the company was declared. Since then a court-appointed liquidator has run Ammono until 2019. On January 8, 2019, the Institute of High Pressure Physics of the Polish Academy of Sciences (IHPP PAS) acquired Ammono, and the company became a part of the institute. The acquiring was conducted in the best interest of the nitride semiconductor science and technology. A significant development of ammonothermal GaN crystallization technology is observed, again (see Fig. 1). Crystals are grown with a twice higher rate and without deteriorating their amazing structural quality during the growth. This is mostly due to successful elimination of detrimental influence of lateral growth sectors being source of stress in the resulting bulk crystals. Commercial activity is maintained in the form of the institute's pilot line. Currently, 2-inch wafers are sold as a regular product of the line.

At present, there are several companies and research institutes working on ammonothermal growth of GaN, such as SixPoint Materials Inc. (USA), Mitsubishi Chemical Corp. (Japan), Kyocera (formerly Soraa, Inc., USA/Japan), University of California Santa Barbara (USA), Lehigh University (USA), Tohoku University (Japan), and Nagoya University (Japan). However, these researchers usually address no other compounds as the technological potential is primarily focused on. Ammonothermal GaN synthesis and the fundamental understanding of the crystallization processes are intensively studied in Germany by the research group FOR1600 created by Friedrich Alexander at University of Erlangen, the Ludwig-Maximilian University in Munich, and the University in Stuttgart. The

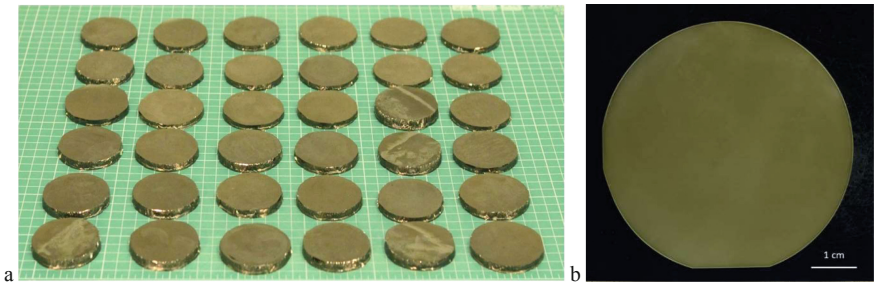

Fig. 1 **a** Ammonothermal "as grown" GaN crystals from one crystal growth process; grid 1 mm; **b** 2-inch ammonothermal GaN substrate in polarized light. IHPP PAS, 2020

researchers in Germany also explored a wider spectrum of compounds that would be best available through the ammonothermal synthesis. This demonstrates not only the recently expected potential for this method through the example of GaN crystal growth, but also the open future capabilities for production of new nitride materials.

We are convinced that the book "Ammonothermal Synthesis and Crystal Growth of Nitrides—Chemistry and Technology" is published at the right time, when the bulk GaN crystallization takes on new meaning for the upcoming breakthrough GaN applications. The book shows recent progress in understanding the ammonothermal processes, so crucial for efficient growth of perfect GaN crystals. It leads us from a general information on the synthesis and crystal growth of nitrides, through technology and chemistry of ammonothermal processes to the future aspects and challenges.

It is highly probable that the ammonothermal method will also show its strength in thermodynamically challenging cases such as InN or ternary compounds, e.g., solid solutions $In_xGa_{1-x}N$. Quite the same is true for crystallization of hard to access novel ternary and higher nitrides based on silicon or germanium. Many of the achievements of the co-authors of this book can be considered as convincing proof of concept of such a forecast. Obtaining bulk InN crystals would be of fundamental importance, whereas $In_xGa_{1-x}N$ substrates would be groundbreaking for further development of optoelectronics based on nitride semiconductors. Other nitrides have huge potential as hard, semiconducting, ion-conducting, or optical materials, to name only few.

Outstanding scientists and technologists, leaders in the field of ammonothermal synthesis and crystallization, present their new visions. The book is extremely important not only for our technical and scientific nitride community but also for young people, students, and PhD students, who want to work on new semiconductors.

Michał Bockowski
Institute of High Pressure Physics
Polish Academy of Sciences
Warsaw, Poland

Izabella Grzegory
Institute of High Pressure Physics
Polish Academy of Sciences
Warsaw, Poland

Preface

The development of new materials to solve urgent future problems is one of the greatest challenges of the twenty-first century, and materials research is a key technology for almost any scientific, technological and economic progress. New materials are the basis for new products, which directly influence our daily life and the whole society, by solving technological and environmental problems. Nearly, 70% of all innovations depend directly or indirectly on material innovations. Alternative synthesis methods for materials with desired intrinsic properties are the basis for such developments of more efficient and sustainable technologies.

Especially nitrides are a class of materials, which already have enabled tremendous innovations like the blue light-emitting diodes (LED), high-electron mobility transistors, UVC light devices, blue and green semiconductor lasers and much more. The three scientists who invented the blue LED based on GaN even received the Nobel Prize in 2014 due to the enormous impact they created for the societies worldwide.

As an emerging technology for exploration and preparation of such new nitride-based materials, ammonothermal synthesis is an innovative and powerful method carried out in supercritical ammonia. The application of this technique can range from the synthesis of fully new compounds, over the fabrication of micro-crystalline materials up to the growth of larger volume crystals. However, many fundamental questions remain unsolved and immanent to the nature of the ammonothermal process, and it is hard to solve such questions for a closed system under extreme conditions.

In Germany, groups with diverse backgrounds in crystal growth, chemistry, materials science and engineering from the Friedrich-Alexander-University Erlangen-Nuremberg, the Ludwig-Maximilian University Munich and the University of Stuttgart joint there forces in the research group FOR1600, funded by the German Science Foundation, DFG, starting from 2010. Researchers in FOR1600 since then have intensively studied the fundamentals of ammonothermal synthesis. The topics comprised studies of synthesis of so far unknown binary and ternary nitride compounds, corrosion of autoclave and liner materials under ammonothermal conditions, the development of sophisticated in situ observation

tools, new technical solutions, studies of solubility of compounds in supercritical ammonia, the chemistry of intermediates and the crystal growth of GaN. A large number of publications emerged from this intensive and focussed collaboration, many of which are unique and first findings. This book is a comprehensive and dense compilation of results from this collaboration. It may serve as a compendium for students, researchers, engineers and any other interested readers to discover the enormous potential of this so far to our opinion underestimated and underdeveloped synthesis method.

The Editors are very grateful that a number of renowned and internationally very recognized researchers, collaboration partners and close colleges of the members of FOR1600, added their valuable contributions to this compendium and such contribute to an even broader and well-balanced picture about ammonothermal synthesis. However, a large number of open questions still remain for challenging explorations, and we dearly hope that this book can draw further attention to this field and trigger future research. The Editors, also in the name of the further members of FOR1600, would like to thank the German Science Foundation for long-standing continuous research funding.

Erlangen, Germany — Elke Meissner
Stuttgart, Germany — Rainer Niewa

Contents

Contributors

Quanxi Bao Institute of Multidisciplinary Research for Advanced Materials, Tohoku University, Sendai, Japan;
Crystal Business Promotion Office, The Japan Steel Works, Ltd., Muroran, Japan

Hasan Baser Institute of Chemical Reaction Engineering, University of Erlangen-Nuremberg, Erlangen, Germany

Shigefusa F. Chichibu Institute of Multidisciplinary Research for Advanced Materials, Tohoku University, Sendai, Japan

Niklas Cordes Chair of Inorganic Solid-State Chemistry, Department of Chemistry, University of Munich (LMU), Munich, Germany

Jaime A. Freitas Jr. Naval Research Laboratory, Washington, DC, USA

Benjamin Hertweck Hugo Kern und Liebers GmbH & Co KG, Schramberg, Germany

Tohru Ishiguro Institute of Multidisciplinary Research for Advanced Materials, Tohoku University, Sendai, Japan

Dietmar Jockel Chair for Electron Devices, University of Erlangen-Nuremberg, Erlangen, Germany

Anna-Carina Luise Kimmel Chair of Process Machinery and Systems Engineering, Friedrich-Alexander-University of Erlangen Nuremberg (FAU), Erlangen, Germany

Martina Koch Chair for Electron Devices, University of Erlangen-Nuremberg, Erlangen, Germany

Mathias Mallmann Chair of Inorganic Solid-State Chemistry, Department of Chemistry, University of Munich (LMU), Munich, Germany

Elke Meissner Chair for Electron Devices, University of Erlangen-Nuremberg, Erlangen, Germany;
Fraunhofer Institute for Integrated Systems and Device Technology, Erlangen, Germany

Rainer Niewa Institute of Inorganic Chemistry, University of Stuttgart, Stuttgart, Germany

Siddha Pimputkar Materials Science and Engineering Department, Lehigh University, Bethlehem, PA, USA

Makoto Saito Institute of Multidisciplinary Research for Advanced Materials, Tohoku University, Sendai, Japan;
Mitsubishi Chemical Corp, Tokyo, Japan

Saskia Schimmel Institute Materials for Electronics and Energy Technology (I-MEET), Friedrich-Alexander-University Erlangen-Nuremberg (FAU), Erlangen, Germany;
Institute of Materials and Systems for Sustainability (IMaSS), Nagoya University, Nagoya, Japan

Eberhard Schlücker Chair of Process Machinery and Systems Engineering (IPAT), Friedrich-Alexander-University, Erlangen-Nuremberg, Germany

Wolfgang Schnick Chair of Inorganic Solid-State Chemistry, Department of Chemistry, University of Munich (LMU), Munich, Germany

Wilhelm Schwieger Institute of Chemical Reaction Engineering, University of Erlangen-Nuremberg, Erlangen, Germany

Thomas G. Steigerwald Chair of Process Machinery and Systems Engineering, Friedrich-Alexander-University of Erlangen Nuremberg (FAU), Erlangen, Germany;
SiCrystal GmbH, Nuremberg, Germany

Daisuke Tomida Institute of Multidisciplinary Research for Advanced Materials, Tohoku University, Sendai, Japan

Peter Wellmann Institute Materials for Electronics and Energy Technology (I-MEET), Friedrich-Alexander-University Erlangen-Nuremberg (FAU), Erlangen, Germany

Tanakorn Wonglakhon Lehrstuhl für Theoretische Chemie/Computer Chemie Centrum, Friedrich-Alexander Universität Erlangen-Nürnberg, Erlangen, Germany

Dirk Zahn Lehrstuhl für Theoretische Chemie/Computer Chemie Centrum, Friedrich-Alexander Universität Erlangen-Nürnberg, Erlangen, Germany

Marcin Zając Institute of High Pressure Physics, Polish Academy of Sciences, Warsaw, Poland

Part I
General Importance for the Synthesis and Crystal Growth of Nitrides

Chapter 1
Significance of Ammonothermal Synthesis for Nitride Materials

Rainer Niewa

Abstract This chapter is intended to introduce the ammonothermal synthesis as an alternative technique to other methods for nitride materials production. Properties of liquid and supercritical ammonia with focus on use as a solvent for nitride synthesis and crystal growth are discussed and compared to those of water. Finally, inherent drawbacks of the use of fluidic ammonia arising from its chemical properties are considered.

The overwhelming majority of functional materials, both traditionally in use and more novel and innovative ones, are based on oxides. These are most often thermodynamically stable and can be synthesized simply by high-temperature treatment, often in air. Nitrides, as one important more specialized materials class, in contrast are typically thermodynamically less stable than oxides, thus require inert handling during synthesis. Figure 1.1 gathers formation enthalpies of some selected binary nitrides. As a general trend one can observe rather high negative enthalpies of formation for the more ionic salt-like binary nitrides highlighted with yellow background as well as for the more covalent main-group element nitrides emphasized with blue background. The formation enthalpy of InN already tends to a small negative value and is overcompensated by the unfavorable entropy of formation, thus results rather metastable. More metal-like interstitial transition metal nitrides depicted with green background show a decreasing stability with increasing group number, and even positive values for several late-transition metal nitrides [1].

R. Niewa (✉)
Institute of Inorganic Chemistry, University of Stuttgart, Pfaffenwaldring 55, 70569 Stuttgart, Germany
e-mail: rainer.niewa@iac.uni-stuttgart.de

E. Meissner and R. Niewa (eds.), *Ammonothermal Synthesis and Crystal Growth of Nitrides*, Springer Series in Materials Science 304,
https://doi.org/10.1007/978-3-030-56305-9_1

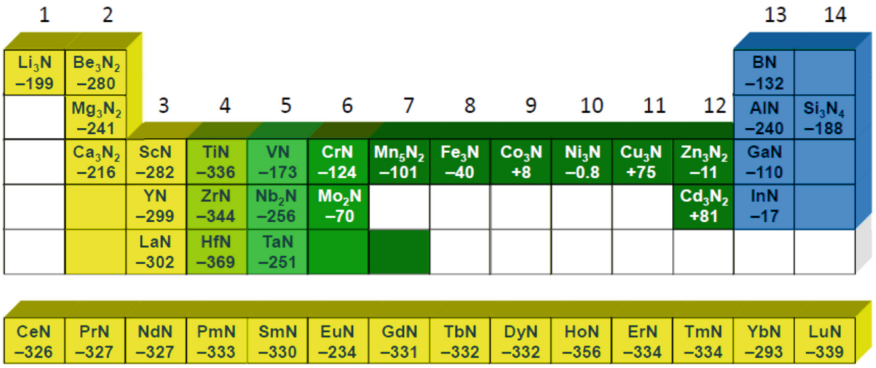

Fig. 1.1 Enthalpies of formation [kJ/mol] of some selected binary nitrides within the periodic table of the elements (modified according to [1])

1.1 Classical Nitride Synthesis

The progress of existing synthesis techniques as well as the development of new and innovative methods is one central subject to gain access to novel functional nitride materials. Already, there are a variety of techniques available to synthesize nitrides, like direct nitridation of metals, metallic alloys or hydrides in nitrogen atmosphere, carbothermal reduction or metathesis reactions of oxides, sulfides or halides with gaseous ammonia, typically at elevated temperatures. General challenges in synthesis, different from the majority oxide materials, concern the significantly lower thermal and thermodynamic stability of basically all corresponding nitrides and the necessary activation energy of molecular nitrogen. The second point often prevents the direct reaction of elements or precursors with elemental nitrogen. Although many elements react with molecular nitrogen to form nitrides, frequently only low-level nitrogen containing product phases are obtained or complete reaction is difficult to achieve. A good example in this respect is the interaction of elemental gallium with nitrogen. At lower temperatures no reaction can be observed, while high temperatures require high nitrogen pressures to prevent decomposition of the desired GaN. Congruent melting of gallium nitride demands a nitrogen pressure of 6 GPa resulting in a melting point of about 2200 °C [2]. Therefore, reactions of elements with the more reactive ammonia as nitrogen source or metathesis reactions of precursor compounds like metal halides with gaseous ammonia, normally referred to as ammonolysis reactions, are often preferred, since they provide faster and more complete reactions for products with even typically higher nitrogen content [1]. As a drawback, unintended contamination with hydrogen or even formation of different compounds like amides, imides, hydrides or else must be considered [3]. Furthermore, the higher stability of virtually all oxides compared with nitrides makes it difficult to remove any oxide impurities in a post-treatment of a product nitride.

Particularly for crystal growth of binary or multinary nitrides, either application of very high temperatures [1, 4] or the use of a liquid phase to aid crystal growth

processes must be taken into account. The liquid phase may act as nitrogen source, as demonstrated for synthesis in molten alkali metal amides [5, 6] or in lithium nitride melt [7, 8]. Alternatively, it may enhance the nitride formation by functioning as solvent or via enhancing the kinetics by surface modification and mediation [9, 10]. In the latter case, the typical liquid phases are molten metals, which do not form a stable binary nitride, but may be constituent of the nitride product. If the target product nitride material is prone to decomposition under nitrogen evolution, liquid solvents or fluxes and high nitrogen partial pressures assist the nitride crystal growth significantly [10]. Consequently, ammonia at elevated pressures directly must come into mind as one fluidic medium of choice for nitride synthesis and crystal growth [3, 11].

1.2 Fluidic Ammonia as Reaction Medium and Solvent

Given the success of solvothermal synthesis in general and hydrothermal synthesis in particular, for both crystal growth of various hard to access materials as well as materials synthesis with different morphologies and metastable forms, there is plenty of room for further developments in the comparably less explored ammonothermal synthesis. In this respect, the ammonothermal synthesis represents a highly promising and scalable technique combining rather moderate temperatures with pressurized ammonia as reaction medium or solvent [11, 12]. For the closely related hydrothermal synthesis particularly the industrial crystal growth of quartz comes into mind, recently in many aspects adapted for ammonothermal GaN crystal growth. Although declining in importance, a further successful hydrothermal materials synthesis on an industrial scale is carried out for CrO_2 for use in magnetic tape emulsions via decomposition of higher chromium oxides [13]. The oxygen partial pressure developing during this process is discussed to stabilize the rather unusual oxidation state of chromium in the desired product material [12]. Additionally, hydrothermal synthesis proved superior in zeolite preparation, where a vast plethora of different silica polymorphs and alumosilicates in various morphologies can be reproducibly synthesized upon changes of process parameters like concentrations, pressure and temperature with addition of different mineralizers and templates. Water in this respect is probably the most similar fluid to ammonia due to several properties compared below [14]. However, many further prototropic solvents as (water free) hydrofluoric acid, hydrochloric acid, sulfuric acid or else may be used for various material synthesis applications, depending on the target compounds. Additionally, solvents showing transfer of ions other than protons in equilibria in oxido-, fluorido- or chloridotropic solvents, to name only the most common ones, or basically non-polar solvents like carbon dioxide, methane or benzene have been successfully applied in solvothermal synthesis.

As water is especially appropriate to grow oxygen-based materials like oxides, hydroxides or hydrates thereof, ammonia is best suited for synthesis of nitrogen-based

Table 1.1 Comparison of selected properties of water and ammonia [19, 65, 66]

	Water	Ammonia
T_{melt} (°C)	0	−77.7
T_{boil} (°C)	100	−33.4
$T_{crit.}$ (°C)	374.5	132.1
$p_{crit.}$ (bar)	221	113
Autoprotolysis	$2\ H_2O \rightleftarrows H_3O^+ + OH^-$	$2\ NH_3 \rightleftarrows NH_4^+ + NH_2^-$
Acids	H_3O^+	NH_4^+
Bases	OH^-	NH_2^-
Ionic product (mol^2/L^2)	10^{-14} (at 25 °C)	10^{-32} (at −34 °C)
pK_B	15.7	4.75
Permitivity ε_r	78.3 (at 25 °C)	16.9 (at 25 °C)
Polarizablity α ($Å^3$)	1.5	2.1
Proton affinity (eV)	7.9	9.2

materials as nitrides, imides, amides or ammoniates [11]. In this respect, the critical pressure and temperature to reach a supercritical state of ammonia are somewhat lower than those of water (see Table 1.1 and Fig. 1.2). Ammonia presents a similar autoprotolysis equilibrium, however, with a more than 15 orders of magnitude lower ionic product at its boiling point under atmospheric pressure (−34 °C) than water at room temperature. Therefore, any ammonobase or ammonoacid will provide much lower concentrations of ammonium or amide ions as compared to the respective species in similar water-based systems of alike concentrations. However, the ionic

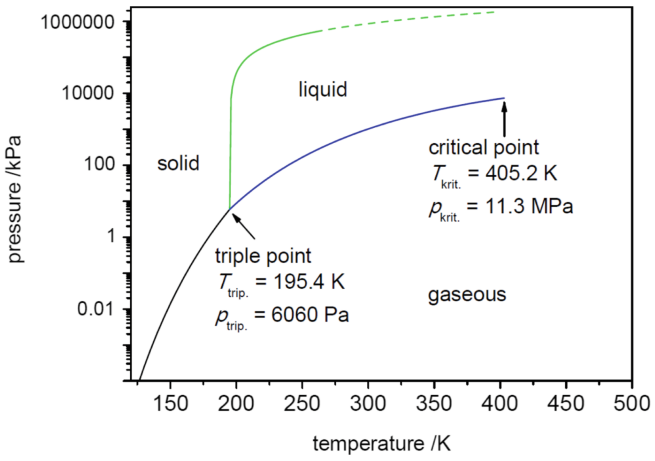

Fig. 1.2 Schematic pressure-temperature phase diagram of ammonia with emphasis on the fluideous states (according to data from [65]). The dashed line is extrapolated. Note the logarithmic pressure-scale of the ordinate

products, respectively the pH- or pK_A-values, of water and ammonia are subject to significant changes upon variation of temperature and pressure: As might be expected from its endothermal nature, the degree of autoprotolysis in water increases with rising temperature until approaching the critical temperature of about 375 °C. This effect is even more pronounced for higher pressures. Above the critical temperature, the ionic product again drops even well below the order of magnitude of pure water at room temperature [15]. Ammonia in contrast, according to molecular dynamics simulations under isochoric conditions shows an increasing pK_A, thus increasing autoprotolysis, up to at least a temperature of 500 °C well above the critical temperature, however, with values residing well below those observed for water and with changes clearly less pronounced [16]. Ammonia as a solvent additionally shows an about four-times lower permittivity (dielectric constant) around room temperature, meaning a lower potential to dissolve ionic compounds than water, due to lower solvation energy (c.f. the born equation). Like for water [12, 17], the permittivity of ammonia drops with increasing temperature, although less dramatically [16] (about 50% from room temperature to 500 °C, while ε_r for water drops well below 10% in this temperature interval). Related, the tendency to association of ions, this means formation of ion pairs and larger associates, particularly also of amide ions, in ammonia is much higher than in water. For water this ion association has been impressively demonstrated, for example by a UV/vis-spectroscopic study of $K_2[Cr_2O_7]$ in aqueous solution of KOH. The concentration of $HCrO_4^-$ ionic species rises with temperature until the critical point of the solvent, when it dramatically decreases and the formation of ion pairs $\{K^+[CrO_4]^{2-}\}$ becomes favorable. Eventually, this results in further ion association and finally precipitation of $K_2[Cr_2O_7]$ at around 420 °C [18]. On the other hand, ammonia provides a higher polarizability compared to water, resulting in a higher potential to dissolve non-polar solutes at room temperature; in other words, more covalent compounds can be better dissolved by ammonia than by water. Ammonia has a larger proton affinity than water (energy release upon proton attachment within the gas phase), thus it is the stronger base, reflected in the lower pk_B value [19]. Due to these properties, ammonia is ideally suited as solvent for nitrides and thus for crystal growth of nitride-based materials, if a suitable high solubility can be achieved by adding mineralizers, which typically modify the autoprotolysis reaction to achieve formation of soluble intermediates. Furthermore, it can also be used as solvent for synthesis of many further, often water-sensible compounds like, for example, oxide nitrides, hydrides, sulfides, hydrogen sulfides, hydroxides, pure metals and intermetallic compounds, and related [e.g., 3, 11, 20–29]. Even if the solubility of a target material in ammonia is vanishing low it may still be used as fluxing agent with high nitridation potential, meaning that, for example, metals may be effectively nitrided, de facto without significant dissolution of the metal, any intermediate or the product metal nitride, for instance in pure supercritical ammonia. In summary, a number of binary nitrides have already been synthesized in supercritical ammonia up to date, the current state is gathered in Fig. 1.3 [11, 30]. Next to the group three nitrides AlN, GaN, and InN, crystal growth of binary nitrides was most successful for two different manganese nitrides, namely η-Mn_3N_2, and θ-Mn_6N_{5+x} [31, 32], an iron nitride (γ′-Fe_4N [33–35]), copper nitride (Cu_3N [36]) and few rare-earth metal nitrides (LaN,

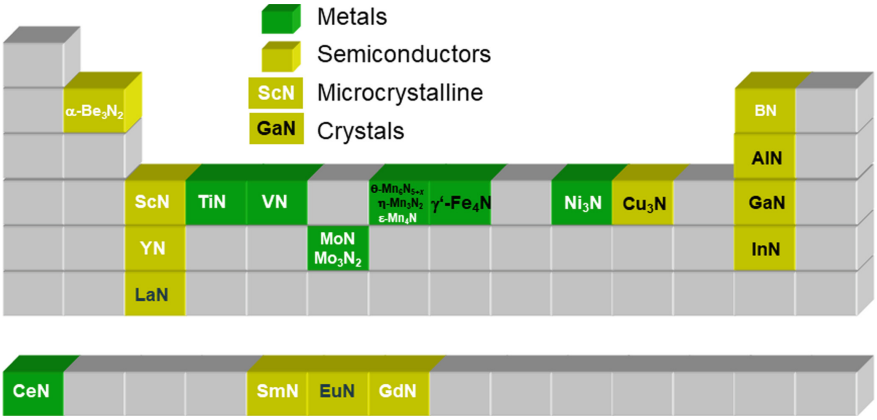

Fig. 1.3 Binary nitrides synthesized under ammonothermal conditions throughout the periodic table of the elements (shown with focus on the stable metallic elements up to group 14). Compositions in white letters were obtained as microcrystalline powders only, while crystal growth succeeded in case of compositions in black letters (for references compare main text body)

EuN [3, 37, 38]). Furthermore, a number of various binary transition and rare-earth metal nitrides was obtained in microcrystalline form [30, 39–44]. Directing further research efforts to ammonothermal nitride synthesis and crystal growth, optimizing process conditions, mineralizer systems and starting precursors designed for the specific product nitride, clearly has highest potential for further developments in this broad field. Early ternary nitrides from ammonothermal synthesis cover few nitridotantalates, -silicates and -phosphates [45–49]. The huge synthetic potential was recently indicated with the production of some carbodiimides [50, 51] and several multinary nitrides from ammonothermal conditions [52–64]. Most promising current examples like rare-earth and alkaline-earth metal transition metal oxide nitrides as, for example, $LaTaN_2O$ for thermoelectric and water splitting applications, oxonitridosilicates and related materials for use in superior lightning applications or new piezoelectrics with potential applications in piezoacoustic devices will be focused on in Chap. 2.

1.3 Drawbacks of Ammonothermal Technique

General drawbacks of application of ammonia under high temperatures and pressures concern its corrosive behavior and the equilibrium to decomposition into hydrogen and nitrogen next to environmental, health and security considerations, to name only few most obvious ones. Ammonia solutions act corrosive on the autoclave material in several ways, which may equally harm the autoclave or liner materials and introduce impurities into the solution and thus into the products. Both solutions containing ammonoacidic and ammonobasic mineralizers are prone to produce

nitrides within the metal surface of the metallic material of the autoclaves [67, 68]. Although some protective aid against further corrosion by formed metal nitride layers was postulated [3], the further progress of corrosion due to different corrosive mechanisms is evident. In ammonobasic solutions rather blistering of nitride-based layers occurs, while in ammonoacidic solutions pitting corrosion dominates. Additionally, dissolved metals may agglomerate within the autoclave wall or other metallic installations [69] and even lead to destruction of the pressure vessel. A more detailed view of these processes will be discussed in Chap. 3. Dissolved autoclave material components due to corrosion may be incorporated into the desired product as impurities with strong impact on the materials properties. Furthermore, the decomposition of ammonia at elevated temperatures adds elemental hydrogen to the fluid phase, possibly also produced by further chemical processes like reaction of ammonia with the chosen mineralizer or precursor thereof, metallic feedstock or metallic autoclave wall, which may provoke hydrogen embrittlement. In addition, a significant degree of decomposition directly reduces the amount of ammonia acting as solvent for the desired nitride product, respectively for the dissolved intermediates. In this way, the decomposition of ammonia may lead to non-static conditions for feedstock dissolution and crystal growth [70].

Key points for a successful development of the ammonothermal synthesis for future application in nitride-based materials synthesis are thus progress in high-pressure equipment development including reduction of corrosion, extension of accessible process parameters pressure and temperature, and knowledge-based optimization of mineralizer systems and feedstock precursor material customized for the desired product.

References

1. P. Höhn, R. Niewa, Nitrides of non-main group elements, in *Handbook of Solid State Chemistry*, vol. 1, Materials and Structure of Solids, ed. by R. Dronskowski, S. Kikkawa, A. Stein (Wiley-VCH, Weinheim, Germany, 2017), p. 251.
2. W. Utsumi, H. Saitoh, H. Kaneko, T. Watanuki, K. Aoki, O. Shimomura, Congruent melting of gallium nitride at 6 GPa and its application to single crystal growth. Nat. Mater. **2**, 735–738 (2003)
3. H. Jacobs, D. Schmidt, High-pressure ammonolysis in solid-state chemistry. Curr. Top. Mater. Sci. **8**, 387–427 (1982)
4. M. Zeuner, S. Pagano, W. Schnick, Nitridosilicates and oxonitridosilicates: from ceramic materials to structural and functional diversity. Angew. Chem. Int. Ed. **50**, 7754–7775 (2011)
5. H. Jacobs, E. von Pinkiowski, Synthese ternärer Nitride von Alkalimetallen: Verbindungen mit Tantal, $M\mathrm{TaN_2}$ mit M = Na, K, Rb und Cs. J. Less-Common Met. **146**, 147–160 (1989)
6. A. Miura, Low-temperature synthesis and rational design of nitrides and oxynitrides for functional material development. J. Ceram. Soc. Jpn. **125**, 552–558 (2017)
7. S. Broll, W. Jeitschko, The ternary rare-earth chromium nitrides $\mathrm{Ce_2CrN_3}$ and $\mathrm{Ln_3Cr_{10-x}N_{11}}$ with Ln = La, Ce, Pr. Z. Naturforsch. B **50**, 905–912 (1995)
8. M. Pathak, D. Stoiber, M. Bobnar, A. Ovchinnikov, A. Ormeci, R. Niewa, P. Höhn, Synthesis, characterization and chemical bonding analysis of the lithium alkaline-earth metal gallide nitrides $\mathrm{Li_2(Ca_3N)_2[Ga_4]}$ and $\mathrm{Li_2(Sr_3N)_2[Ga_4]}$. Z. Allg. Anorg. Chem. **643**, 1557–1563 (2017)

9. A. Simon, Group 1 and 2 suboxides and subnitrides—metals with atomic size holes and tunnels. Coord. Chem. Rev. **163**, 253–270 (1997)
10. R. Niewa, H. Jacobs, Group V and VI alkali nitridometalates: a growing class of compounds with structures related to silicate chemistry. Chem. Rev. **96**, 2053–2062 (1996)
11. T.M.M. Richter, R. Niewa, Chemistry of ammonothermal synthesis. Inorganics **2**, 29–78 (2014)
12. A. Rabenau, The role of hydrothermal synthesis in preparative chemistry. Angew. Chem. Int. Ed. **24**, 1026–1040 (1985)
13. G. Anger, J. Halstenberg, K. Hochgeschwender, C. Scherhag, U. Korallus, H. Knopf, P. Schmidt, M. Ohlinger, Chromium compounds, in *Ullmann's Encyclopedia of Industrial Chemistry*, vol. 9 (Wiley-VCH, Weinheim, Germany, 2000), pp. 157–191
14. E.C. Franklin, C.A. Kraus, Some properties of liquid ammonia. Am. Chem. J. **21**, 8–14 (1899)
15. A.V. Bandura, S.N. Lvov, The ionization constant of water over wide ranges of temperature and density. J. Phys. Chem. Ref. Data **35**, 15–30 (2006)
16. D. Zahn, A molecular simulation study of the auto-protolysis of ammonia as a function of temperature. Chem. Phys. Let. **682**, 55–59 (2017)
17. T.M. Seward, Metal complex formation in aqueous solutions at elevated temperatures and pressures. Phys. Chem. Earth **13–14**, 113–132 (1982)
18. J.B. Chlistunov, K.P. Johnston, UV/vis spectroscopic determination of the dissociation constant of bichromate from 160 to 400 nm. J. Phys. Chem. B **102**, 3993–4003 (1998)
19. A. Holleman, N. Wiberg, E. Wiberg, *Lehrbuch der Anorganischen Chemie*, 102nd edn. (de Gruyter, Berlin, Germany, 2007)
20. P. Böttcher, U. Kretschmann, Darstellung und Kristallstruktur von Dirubidiumpentatellurid, Rb_2Te_5. J. Less-Common Met. **95**, 81–91 (1983)
21. A.P. Purdy, Ammonothermal crystal growth of sulfide materials. Chem. Mater. **10**, 692–694 (1998)
22. H. Jacobs, J. Kockelkorn, T. Tacke, Hydroxide des Natriums, Kaliums und Rubidiums: Einkristallzüchtung und röntgenographische Strukturbestimmung an der bei Raumtemperatur stabilen Modifikation. Z. Anorg. Allg. Chem. **531**, 119–124 (1985)
23. A.P. Purdy, S. Case, C. George, Ammonothermal crystal growth of germanium and its alloys: synthesis of a hollow metallic crystal. Cryst. Growth Des. **3**, 121–124 (2003)
24. P. Böttcher, J. Getzschmann, R. Keller, Zur Kenntnis der Dialkalimetalldichalkogenide β-Na_2S_2, K_2S_2, α-Rb_2S_2, β-Rb_2S_2, K_2Se_2, Rb_2Se_2, α-K_2Te_2 und Rb_2Te_2. Z. Anorg. Allg. Chem. **619**, 476–488 (1993)
25. D.M. Young, G.L. Schimek, J.W. Kolis, Synthesis and characterization of $[Yb(NH_3)_8][Cu(S_4)_2] \cdot NH_3$, $[Yb(NH_3)_8][Ag(S_4)_2] \cdot 2\ NH_3$, and $[La(NH_3)_9][Cu(S_4)_2]$ in supercritical ammonia: metal sulfide salts of the first homoleptic lanthanide ammine complexes. Inorg. Chem. **33**, 7620–7625 (1996)
26. G.L. Schimek, G.W. Drake, J.W. Kolis, Crystal structure of calcium heptaammine hexasulfide, $Ca(NH_3)_7S_6$. Acta Chem. Scand. **53**, 145–148 (1999)
27. M. Monz, H. Jacobs, Kaliumamidotrioxogermanate(IV)—Wasserstoff-Brückenbindungen in $K_3GeO_3NH_2$ und $K_3GeO_3NH_2 \cdot KNH_2$. Z. Anorg. Allg. Chem. **621**, 137–142 (1995)
28. T.J. Hennig, H. Jacobs, Strukturchemische Verwandtschaft von Kaliumhexahydroxoscandat(III), $K_3[Sc(OH)_3]$ mit den isotypen Hydroxometallaten $Rb_3[Sc(OH)_3]$, $K_3[Cr(OH)_3]$ und $Rb_3[Cr(OH)_3]$. Z. Anorg. Allg. Chem. **616**, 71–78 (1992)
29. H. Jacobs, J. Bock, Kaliumhexahydroxochromat(III), $K_3[Cr(OH)_6]$: Beispiel eines neuen Syntheseweges für Metallhydroxide und Hydroxometallate. Z. Anorg. Allg. Chem. **546**, 33–41 (1987)
30. S. Pimputkar, T.F. Malkowski, S. Griffiths, A. Espenlaub, S. Suihkonen, J.S. Speck, S. Nakamura, Stability of materials in supercritical ammonia solutions. J. Supercrit. Fluids **110**, 193–229 (2016)
31. G. Kreiner, H. Jacobs, Magnetische Struktur von η-Mn_3N_2. J. Alloys Compd. **183**, 345–362 (1992)
32. H. Jacobs, C. Stüve, Hochdrucksynthese der η-Phase im System Mn-N: Mn_3N_2. J. Less-Common Met. **96**, 323–329 (1984)

33. H. Jacobs, D. Rechenbach, U. Zachwieja, Structure determination of γ′-Fe_4N and ε-Fe_3N. J. Alloys Compd. **227**, 10–17 (1995)
34. H. Jacobs, D. Rechenbach, U. Zachwieja, Untersuchungen zur Struktur und zum Zerfall von Eisennitriden—γ′-Fe_4N und ε-Fe_3N. Härterei Techn. Mitt. **50**, 205–213 (1995)
35. H. Jacobs, J. Bock, Einkristallzüchtung von γ′-Fe_4N in überkritischem Ammoniak. J. Less-Common Met. **134**, 215–220 (1987)
36. U. Zachwieja, H. Jacobs, Ammonothermalsynthese von Kupfernitrid, Cu_3N. J. Less-Common Met. **161**, 175–184 (1990)
37. H. Jacobs, U. Fink, Untersuchung des Systems Kalium/Europium/Ammoniak. Z. Anorg. Allg. Chem. **438**, 151–159 (1978)
38. H. Jacobs, H. Scholze, Untersuchung des Systems Na/La/NH_3. Z. Anorg. Allg. Chem. **427**, 8–16 (1976)
39. R. Juza, H. Jacobs, Ammonothermal synthesis of magnesium and beryllium amides. Angew. Chem. Int. Ed. **5**, 247 (1966)
40. A. Stuhr, H. Jacobs, R. Juza, Amide des Yttriums. Z. Anorg. Allg. Chem. **395**, 291–300 (1973)
41. B. Harbrecht, H. Jacobs, Hochdrucksynthese von Caesiumamidazid, $Cs_2(NH_2)N_3$ aus Caesiummetall und Ammoniak. Z. Anorg. Allg. Chem. **500**, 181–187 (1983)
42. M. Zając, J. Gosk, E. Grzanka, S. Stelmakh, M. Palczewska, A. Wysmołek, K. Korona, M. Kamińska, A. Twardowski, Ammonothermal synthesis of GaN doped with transition metal ions (Mn, Fe, Cr). J. Alloys Compd. **456**, 324–338 (2008)
43. SixPoint Materials, www.spmaterials.com. Accessed 30 Oct 2017
44. R. Dwiliński, R. Doradziński, J. Garczyński, L. Sierzputowski, M. Palczewska, A. Wysmolek, M. Kamińska, MRS Internet J. Nitride Semicond. Res. **3**, e25 (1998)
45. H. Jacobs, H. Mengis, Preparation and crystal structure of a sodium silicon nitride, $NaSi_2N_3$. Eur. J. Solid State Inorg. Chem. **30**, 45–53 (1993)
46. Th Brokamp, H. Jacobs, Synthese und Kristallstruktur eines gemischtvalenten Lithium-Tantalnitrids $Li_2Ta_3N_5$. J. Alloys Compd. **176**, 47–60 (1991)
47. H. Jacobs, R. Nymwegen, Darstellung und Kristallstruktur eines Kaliumnitridophosphats, $K_3P_6N_{11}$. Z. Anorg. Allg. Chem. **623**, 429–433 (1997)
48. E. von Pinkowski, Darstellung und Charakterisierung von Alkalimetalltantalnitriden und Untersuchungen am System Natriumamid/Natriumazid. Doctoral Thesis (Universität Dortmund, 1988)
49. J. Häusler, W. Schnick, Ammonothermal synthesis of nitrides: recent developments and future perspectives. Chem. Eur. J. **24**, 11864–11879 (2018)
50. M. Mallmann, J. Häusler, N. Cordes, W. Schnick, Ammonothermal synthesis of alkali-alkaline earth metal and alkali-rare earth metal carbodiimides: $K_{5-x}M_x(CN_2)_{2+x}(HCN_2)_{1-x}$ (M = Sr, Eu) and $Na_{4.32}Sr_{0.68}(CN_2)_{2.68}(HCN_2)_{0.32}$. Z. Anorg. Allg. Chem. **643**, 1956–1961 (2017)
51. S. Zhang, D.A. Zherebtsov, F.J. DiSalvo, R. Niewa, $Na_5[CN_2]_2[CN]$, $(Li, Na)_5[CN_2]_2[CN]$, and $K_2[CN_2]$: carbodiimides from high-pressure synthesis. Z. Anorg. Allg. Chem. **638**, 2111–2116 (2012)
52. J. Li, T. Watanabe, H. Wada, T. Setoyama, M. Yoshimura, Low-temperature crystallization of Eu-doped red-emitting $CaAlSiN_3$ from alloy-derived ammonometallates. Chem. Mater. **19**, 3592–3594 (2007)
53. Y. Maruyama, T. Watanabe, Low-temperature synthesis of $CaAlSiN_3$:Ce^{3+} using the ammonothermal method. J. Ceram. Soc. Jpn. **124**, 66–69 (2016)
54. T. Watanabe, K. Nonaka, J. Li, K. Kishida, M. Yoshimura, Low temperature ammonothermal synthesis of europium-doped $SrAlSiN_3$ for a nitride red phosphor. J. Ceram. Soc. Jpn. **120**, 500–502 (2012)
55. K. Nonaka, K. Kishida, C. Izawa, T. Watanabe, Low temperature ammonothermal synthesis of europium-doped $SrAlSiN_3$: effect of mineralizers. J. Ceram. Soc. Jpn. **122**, 17–20 (2014)
56. Y. Maruyama, Y. Yanase, T. Watanabe, Ammonothermal synthesis of charge-compensated $SrAlSiN_3$:Ce^{3+} phosphor. J. Ceram. Soc. Jpn. **125**, 399–401 (2017)
57. J. Häusler, L. Neudert, M. Mallmann, R. Niklaus, A.-C.L. Kimmel, N.S.A. Alt, E. Schluecker, O. Oeckler, W. Schnick, Ammonothermal synthesis of novel nitrides: case study on $CaGaSiN_3$. Chem. Eur. J. **23**, 2583–2590 (2017)

58. T. Toshima, K. Kishida, Y. Maruyama, T. Watanabe, Low-temperature synthesis of $BaTaO_2N$ by an ammonothermal method. J. Ceram. Soc. Jpn. **125**, 643–647 (2017)
59. C. Izawa, T. Kobayashi, K. Kishida, T. Watanabe, Ammonothermal synthesis and photocatalytic activity of lower valence cation-doped $LaNbON_2$. Adv. Mater. Sci. Eng. 465720 (2014)
60. T. Watanabe, K. Tajima, J. Li, N. Matsushita, M. Yoshimura, Low-temperature ammonothermal synthesis of $LaTaON_2$. Chem. Lett. **40**, 1101–1102 (2011)
61. N. Cordes, W. Schnick, Ammonothermal synthesis of crystalline oxonitride perovskites $LnTaON_2$ (Ln = La, Ce, Pr, Nd, Sm, Gd). Chem. Eur. J. **23**, 11410–11415 (2017)
62. J. Häusler, S. Schimmel, P. Wellmann, W. Schnick, Ammonothermal synthesis of earth-abundant nitride semiconductors $ZnSiN_2$ and $ZnGeN_2$ and dissolution monitoring by in situ X-ray imaging. Chem. Eur. J. **23**, 12275–12282 (2017)
63. J. Häusler, R. Niklaus, J. Minár, W. Schnick, Ammonothermal synthesis and optical properties of ternary nitride semiconductors Mg-IV-N_2, Mn-IV-N_2 and Li-IV_2-N_3 (IV = Si, Ge). Chem. Eur. J. **24**, 1686–1693 (2018)
64. J. Häusler, L. Eisenburger, O. Oeckler, W. Schnick, Ammonothermal synthesis and crystal structure of the nitridogermanate $Ca_{1-x}Li_xAl_{1-x}Ge_{1+x}N_3$ ($x \approx 0.2$). Eur. J. Inorg. Chem. 759–764 (2018)
65. H.W. Xiang, Vapor pressures, critical parameters, boiling points, and triple points of ammonia and trideuteroammonia. J. Phys. Chem. Ref. Data **33**, 1005–1011 (2004)
66. S. Rondinini, P. Longhi, P.R. Mussini, T. Mussini, Autoprotolysis constants in nonaqueous solvents and aqueous organic solvent mixtures. Pure Appl. Chem. **59**, 1693–1702 (1987)
67. B. Hertweck, T.G. Steigerwald, N.S.A. Alt, E. Schluecker, Corrosive degeneration of autoclaves for the ammonothermal synthesis: experimental approach and first results. Chem. Eng. Technol. **37**, 1903–1906 (2014)
68. B. Hertweck, T.G. Steigerwald, N.S.A. Alt, E. Schuecker, Different corrosion behavior of autoclaves made of nickel base alloy 718 in ammonobasic and ammonoacidic environment. J. Supercrit. Fluids **95**, 158–166 (2014)
69. S. Griffiths, S. Pimputkar, J.S. Speck, S. Nakamura, On the solubility of gallium nitride in supercritical ammonia-sodium solutions. J. Cryst. Growth **456**, 5–14 (2016)
70. T.G. Steigerwald, J. Balouschek, B. Hertweck, A.-C.L. Kimmel, N.S.A. Alt, E. Schluecker, In situ investigation of decomposing ammonia and ammonobasic solutions under supercritical conditions via UV/vis and Raman Spectroscopy. J. Supercrit. Fluids **134**, 96–105 (2018)

Chapter 2
The Potential of Nitride Materials

Mathias Mallmann, Niklas Cordes, and Wolfgang Schnick

Abstract The following chapter provides an overview of the most important application fields of nitride and oxonitride materials and outlines briefly their structural features as well as their materials properties. (Oxo)nitrides are employed in a variety of important technological areas such as structural ceramics, heat conductors, semiconductor technology, solid-state lighting, water splitting and solid-state battery materials. Their significance for daily life as well as possible advancement of (oxo)nitride materials with respect to these applications is examined.

A world without innovative electronic technology developments such as computers, smartphones, wireless communication, autonomous driving or solid-state lighting is unimaginable. These technologies have already and will further enrich human's life. Therefore, in industry there is a broad interest in these business branches, involving the issue of high energy and resource consumption due to the production and development of novel technologies. For this reason, one of the most important tasks is the quest for new materials that allows us to retain or even improve our living standards, but with better energy efficiency and environmental acceptability. In many cases, nitride materials have great potential for remedying or alleviating these problems.

Nitride materials such as silicon nitride exhibit high chemical, thermal and mechanical stability. This is due to the strength of the bonds between the involved elements (provided by low electronegativity difference of the elements resulting in a covalent character of the bonds) and the presence of highly crosslinked structures in nitrides. While oxygen in silicates is able to connect a maximum of two Si tetrahedra centers, nitrogen can even link up to four Si together, resulting in highly crosslinked structures [1]. Furthermore, nitrogen atoms in nitridosilicates are capable to connect neighboring tetrahedra both via common corners and edges. Contrary, in oxosilicates almost exclusively corner sharing tetrahedra have been found. However, considering

M. Mallmann · N. Cordes · W. Schnick (✉)
Chair of Inorganic Solid-State Chemistry, Department of Chemistry, University of Munich (LMU), Butenandtstr. 5-13, 81377 Munich, Germany
e-mail: wolfgang.schnick@uni-muenchen.de

E. Meissner and R. Niewa (eds.), *Ammonothermal Synthesis and Crystal Growth of Nitrides*, Springer Series in Materials Science 304,
https://doi.org/10.1007/978-3-030-56305-9_2

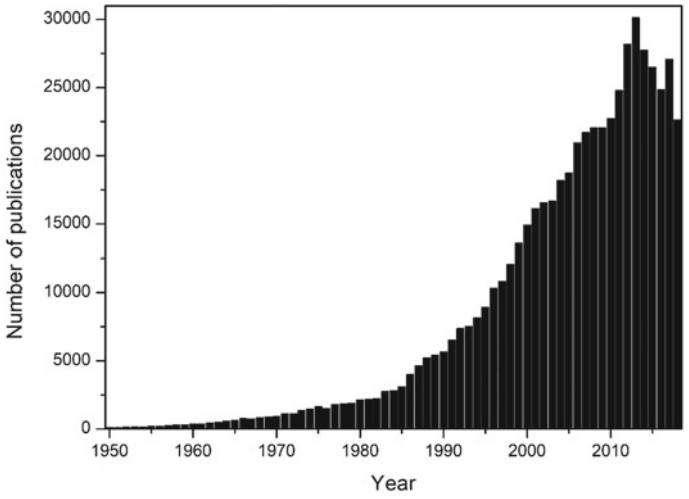

Fig. 2.1 Development of the number of publications per year including the keywords "nitride" or "nitrides" from 1950 to 2018 [3]

thermal stability, other criteria such as the binding energy of possible decomposition products must be included as well. N_2 as a possible decomposition product of nitrides has an extremely high bond energy (941 kJ mol^{-1}). Therefore, the thermal decomposition of nitride materials occurs typically at lower temperatures compared to corresponding oxides (bond energy of O_2: 499 kJ mol^{-1}) [2]. Furthermore, the bond energies of nitrogen to other elements are generally lower than oxygen-element bonds. This raises the problem of possible side reactions (oxides as by-products) during synthesis of nitrides, which can be overcome by severe exclusion of oxygen and water and employment of inert gas technique during synthesis.

Nonetheless, the high structural diversity as well as their chemical, thermal and mechanical stability, makes this materials class interesting for various application fields. The multitude of applications led to an extensive exploration of these substances, resulting in a rapid increase in the number of publications on nitrides since 1950 (see Fig. 2.1). The following chapter summarizes the chemical and physical properties of nitrides and gives an overview of the related applications and the predicted potential of nitride materials.

2.1 Ceramic Materials

The above mentioned high covalence and bond strength in nitrides make them interesting for high performance ceramics. Especially, Si_3N_4 is an important nonoxidic ceramic material, with high temperature applications (e.g. aerospace engineering for gas turbines, crucibles) because of their exceptional chemical, physical and

mechanical properties. Such ceramics tend to have a low density and combine several important properties. These include a high decomposition temperature (about 1500 °C), high mechanical stability, low friction coefficients, good thermal shock properties, as well as good resistance to oxidation and corrosive environments [4]. Additional doping with oxides results in elimination of the sensitivity against mechanical damages like fractures. These explorations eventually led to the group of SiAlONs. The latter are solid solutions of Si_3N_4 and Al_2O_3 with general formula $Si_{6-n}Al_nO_nN_{8-n}$. The mixed phases result in an improvement of mechanical strength. For example, sintered α-SiAlON has a Vickers hardness of about 21–22 GPa [5]. One of the hardest materials is cubic boron-nitride (c-BN). It is considered the third hardest material following diamond and c-BC_2N [6], and is used as an abrasive or cutting material for steel. The advantage over diamond lies in the higher thermodynamic stability, resulting in no side reactions with steel even at high temperatures. In contrast, the hexagonal form (h-BN) has a very low hardness (similar to graphite) and is therefore used as a lubricant. The advantage over graphite lies, as with many other nitrides, in the very high thermal stability, making h-BN interesting as a high-temperature lubricant. Jansen et al. demonstrated, that amorphous ceramics based on Si, B, N and C show unique properties. Amorphous compounds like $Si_3B_3N_7$ or $SiBN_3C$ were synthesized by polymerization of trichlorosilylaminodichloroborane (TADB) in ammonia or methylamine and subsequent pyrolysis [7, 8]. Adjustment of the viscosity of the polymer solution (by adjusting the degree of cross-linking), influences the type and shape of the ceramics (coatings, fibers or individual components). These compounds exhibit outstanding properties. $Si_3B_3N_7$ for example has a 150 °C higher decomposition temperature than crystalline Si_3N_4 or Si_3N_4/BN-composites. $SiBN_3C$ shows an even better thermal stability. Furthermore, they show high stability against oxidation [7].

2.2 Thermal Conducting Nitrides

Furthermore, thermally conductive materials are also of great importance for industrial application. These materials are mainly used as heat sinks in electronic components, such as in electronic circuits or similar devices. Thermal conduction is mediated by propagation and collisions of phonons. Already in 1973, Slack postulated that especially sphalerite and wurtzite type compounds show high thermal conductivities [9]. Such materials exhibit values greater than 100 W m^{-1} K^{-1}. Especially, AlN is interesting for this application field, because it shows a relatively high thermal conductivity. The thermal conductivity of pure AlN at room temperature is 319 W m^{-1} K^{-1} and has a maximum conductivity of $\kappa = 2300$ W m^{-1} K^{-1} at 52 K [10]. Particularly the value at room temperature is in the same region as that of pure copper. In addition, thermal conductivity studies were also carried out on Grimm-Sommerfeld analogous $MgSiN_2$ (wurtzite superstructure). It has been shown that this compound is thermally conductive as well, but with lower efficiency than AlN [11]. More recently, it has been reported that silicon nitride (Si_3N_4) ceramics have high

thermal conductivity as well. Together with the high chemical and thermal stability of nitrides and the high fracture toughness compared to other ceramics, these results make Si_3N_4 interesting as promising substrate materials for next-generation power devices [12].

2.3 Semiconducting Materials

One of the most important technological discoveries has been the development of semiconductors based on silicon. The scope of applications for such semiconducting materials is very large, for instance solar energy conversion, data handling, signal processing or transistors to name a few. Besides elemental semiconductors (e.g. Si or Ge), Grimm-Sommerfeld analogous compounds like SiC, III-V pnictides (GaAs, GaN and InP) or II-VI chalkogenides (ZnO, CdTe or ZnS) are of particular interest as well. Especially, III-V nitrides are one of the most important semiconductors, because they paved the way to optoelectronic devices like light emitting diodes (LEDs) or short wavelength diode lasers [13]. This group of nitrides, including aluminum nitride (AlN), gallium nitride (GaN), indium nitride (InN) and solid solutions thereof (Al,Ga,In)N covers a bandgap range from around 0.7–6.2 eV. Additionally, the high chemical and thermal resistance of these materials is essential for applications in electronic devices. One of the most promising characteristics of these nitrides is the fact that they can enable light emission from the ultraviolet to the infrared region in LEDs. In combination with the later mentioned luminescent materials, the development of highly efficient pc-LEDs led to environmentally friendly alternatives for commonly inefficient light sources like incandescent or halogen lamps [14]. According to a report from the United States Energy resort, the energy consumption of lighting can be reduced by 75% until 2035 due to solid-state lighting, which is equal to the energy consumption of 45 million U.S. homes. Thereby, from 2015 to 2035, 630 billion US-dollars energy costs can be avoided, indicating the importance of solid-state lighting and thereby the importance of GaN based semiconductors [15].

Compared to silicon, GaN exhibits a wide bandgap, high electron mobility and large critical breakdown electric field, improving the power performance with higher efficiency in electrical systems such as field-effect transistors [16]. The use of such devices would increase the efficiency and therefore decrease the overall energy consumption. Further applications for III-N semiconductors include laser diodes or photovoltaic devices [14, 17].

First-principle calculations as well as practical measurements showed, that in addition to group 13 nitrides especially ternary zinc nitrides, for example Grimm-Sommerfeld analogous compounds $ZnSiN_2$, $ZnGeN_2$ and $ZnSnN_2$, are of particular interest as possible next-generation semiconductors due to their promising semiconducting properties including good bandgap tunability, high carrier mobility and small carrier effective masses [18]. Besides, these nitrides as well as their solid solutions show similar lattice parameters and cover almost the same bandgap range compared to the already discussed group 13 nitrides [19]. Especially, the similarity in lattice

constants as well as their structural analogy (superstructures of hexagonal GaN) can enable the formation of hybrid structures or epitaxial growth on group 13 nitrides. One of the great advantages of these compounds is the high abundance of the constituting elements (e.g. Zn, Si) compared to Ga or In [20]. In particular, indium is one of the rarest elements of the earth (reserves ~15,000 tonnes) and, similar to gallium, only occurs as a byproduct by the production of copper, aluminum, lead or zinc [21, 22]. Such semiconducting materials can be synthesized under ammonothermal conditions and will be discussed in detail in Chap. 12.

2.4 Optical Materials

As mentioned above, solid-state lighting has the potential to reduce 75% of light energy consumption until 2030. In addition to the development of doped GaN-wafers, especially research and advancement of phosphors is important for the design of phosphor converted (pc)-LEDs, promoting a revolution in the lighting industry. Depending on the choice of the used LED (ultraviolet or blue), appropriate phosphors are needed to convert the emitted radiation into white light. By additive color mixing of the underlying LED with the used phosphors, white light can be generated. Figure 2.2 shows the schematic structure of a two pc-LED.

These luminescent materials have to fulfill some important requirements, namely an efficient absorption of the UV or blue light emitted by the primary LED, a good conversion efficiency, small thermal quenching and high chemical and thermal stability. Especially, (oxo)nitridosilicates, (oxo)nitridoalumosilicates and nitridoaluminates, doped with activators such as Eu^{2+} or Ce^{3+} ions, do accomplish these requirements and have therefore proven to be excellent luminescent materials. The

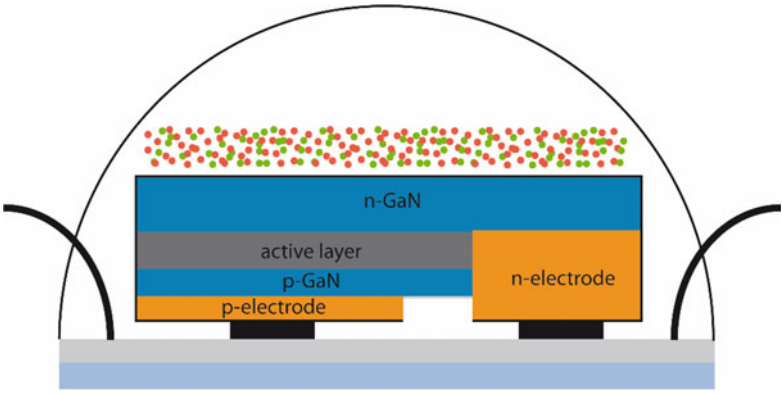

Fig. 2.2 Schematic design of a two pc-LED composed of a GaN-wafer with green and red luminophors on top of it

high structural diversity of these compounds as well as the composition and the dopant, makes it possible to cover the entire visible range of the emission spectrum (from blue to red). The excitation of the luminescent material by UV or blue light leads to absorption of energy, which is transported to the activator. This results in the parity allowed relaxation of electrons from an excited state to the ground state (Ce^{3+}: $5d^1 \rightarrow 4f^1$, Eu^{2+}: $4f^6 5d^1 \rightarrow 4f^7$), causing light emission. As d-orbitals of the activator interact with ligand orbitals, the luminescence properties are strongly influenced by the surrounding of the activator. Accordingly, the emission of luminescent materials covers the whole visible range, depending on crystal field splitting and nephelauxetic effect. Due to their high formal charge and covalent bonds nitride ligands in nitridosilicates and nitridoaluminates can exhibit a very strong nephelauxetic effect towards Eu^{2+} or Ce^{3+} which can even allow for luminescence in the deep red and infrared region of the spectrum. One of the most famous representatives of luminescent materials are the Eu^{2+}-doped alkaline-earth compounds of the 2-5-8-family with general formula $M_2Si_5N_8$ with M = Ca, Sr and Ba with strong emission maxima between 590 and 630 nm. In addition to their remarkable optical properties, they offer the opportunity to affect the emission wavelength by change of the chemical composition of solid solutions, making them interesting for application in high performance pc-LEDs. Further prominent luminescent LED materials are $MSi_2O_2N_2$ (M = Ca, Sr, Ba) with emission maxima from 498 to 560 nm, $MAlSiN_3$ (M = Ca and Sr) with emission maxima at 650 and 610 nm and $Sr[LiAl_3N_4]:Eu^{2+}$ ($\lambda_{max} \approx 650$ nm) [11, 23, 24]. In $MSi_2N_2O_2$ as well as in $MAlSiN_3$ the emission wavelength can be shifted by solid solutions. The ammonothermal process can also be used for the syntheses of phosphors and will be discussed in detail in Chap. 12.

Another possible field of application of nitridosilicates, such as the above mentioned $M_2Si_5N_8$, is the development for their use as non-linear optical materials (NLO). The latter are used in optical signal processing as well as telecommunication [11]. Again, the great advantage of nitrides is their high stability and a noticeable accumulation of non-centrosymmetric space groups in the case of nitridosilicates (highly condensed tetrahedral networks exhibit a disproportionately high amount of non-centrosymmetric space groups), which are required for NLO materials. However, the major challenge in this area still lies in the growth of large single crystals of these compounds.

2.5 Ion Conductors

In addition to the conversion of energy as used in LED technology, the storage of energy is an important topic of modern research as well. Especially, in the case of solid electrolytes, nitride materials have a great potential to achieve improvements in this application sector.

Due to their high efficiency and high-energy-density storage, lithium ion batteries are good candidates for a broad field of energy storage applications, for example in automotive industry or in portable electrical storage applications. Already in

2014, approximately 41% of the annual lithium production was used for lithium ion batteries [25]. Commonly, lithium ion batteries are composed of an anode, a cathode and a liquid electrolyte. The C|$LiPF_6$|$LiCoO_2$ cell for example consists of graphite as anode, $LiPF_6$ as liquid electrolyte (dissolved in ethylene carbonate) and $LiCoO_2$ as cathode [26]. A significant disadvantage of such batteries with liquid electrolytes is the safety problem, resulting from overloading or low discharging. This leads to lithium metal deposition in dendritic form at the cathode, causing a short-circuit [27]. This problem has already led to some accidents as well as product recalls. In 2006, millions of Sony laptops were recalled due to this battery issue [28]. Or even more recently in 2016, Samsung mobile phones caught fire due to battery overheating [29]. One possibility to solve these problems is the replacement of liquid electrolytes by non-flammable ones. Especially, solid ceramic electrolytes are expected to be well-suited materials. Because of their high mechanical, electrochemical and thermal stability as well as the nonappearance of leakage, they lead to an increased safety compared to liquid electrolytes [30].

Some of the most promising solid-state electrolytes are perovskites (e.g. $La_{0.5}Li_{0.5}TiO_3$), garnets (e.g. $Li_7La_3Zr_2O_{12}$), NASICON-type $Li_{1.3}Al_{0.3}Ti_{1.7}(PO_4)_3$ or $Li_{10}GeP_2S_{12}$ (LGPS) [31]. They show ionic conductivities ranging from 10^{-2} to 10^{-6} Ω^{-1} cm^{-1} at room temperature and activation energies E_a between 0.3 and 0.6 eV [27]. One disadvantage of such compounds is their low stability against Li metal. Most of them are thermodynamically unstable against lithium metal and are reduced. LGPS for example reacts with Li and forms germanium or intermetallic lithium-germanium-compounds, causing an interface formation between Li and electrolyte. The kinetics of such interphases are essential for the performance of rechargeable batteries. In the case of LGPS the interface still growth after decomposition, making the use of LGPS in batteries with direct contact to Li metal difficult. In contrast, nitride materials are mostly stable against Li or build kinetically stable solid electrolyte interphases (SEIs) [32]. Such SEIs should have an acceptable ionic conductivity and preferably no electronic conductivity to prevent the growth of the interface. Amorphous "LiPON" (with composition $Li_{2.88}PO_{3.73}N_{0.14}$) for example, which is already used in thin-film solid-state batteries with $LiCoO_2$ as cathode and Li as anode material, is unstable in contact with lithium metal, but forms a stable SEI consisting of binary and ternary Li-compounds like Li_3PO_4, Li_3N, Li_3P and Li_2O. This formed SEI protects the electrolyte from further decomposition. Due to this protection, such "LiPON" based batteries achieve a life time of over 10,000 cycles [31]. In contrast to the previously mentioned solid electrolytes, however, "LiPON" shows a relatively low conductivity (2×10^{-6} Ω^{-1} cm^{-1}), making high-energy applications not profitable. Therefore, the research for new nitride-type solid electrolyte materials or the research for possible protective layers between anode and electrolyte is of essential importance. Ideally, the SEI should only consist of highly conductive materials such as Li_3N or Li_3P, since poorly conductive SEIs (e.g. Li_2O or Li_2S) can negatively affect the overall performance of the battery. For example, lithium nitridophosphates would build an SEI only consisting of Li_3P and Li_3N in contact with lithium metal. Additionally, lithium nitridosilicates show similar behavior. For more precise statements regarding the stability of the individual compounds against

lithium metal, however, individual experiments would be required. The ionic conductivity of lithium nitridophosphates (e.g. $LiPN_2$, Li_7PN_4, $Li_{10}P_4N_{10}$, $Li_{18}P_6N_{16}$) and lithium nitridosilicates (e.g. $LiSi_2N_3$, Li_2SiN_2, Li_5SiN_3, Li_8SiN_4, $Li_{18}Si_3N_{10}$) ranges from 10^{-4} to 10^{-8} Ω^{-1} cm^{-1} and activation energies E_a between 40 and 64 kJ mol^{-1} [33–36]. In comparison with the above mentioned ionic conductors, the conductivity of these compounds are relatively small. However, it should be noted that most of the measurements were made on cold-pressed and non-optimized samples. For example, NASICON-type compounds like $LiTi_2(PO_4)_3$ also showed low conductivity, which could be highly improved by sintering and substitution with Al or Ge. Thus, a partial substitution of Li^+ by higher charged cations like Ca^{2+} in the presented nitrides would create vacancies, leading to an increase in conductivity, due to easier Li^+ movement. Furthermore, annealing of the pellets results in relaxed grain boundaries, further leading to an increase of conductivity and a decrease of activation energy as well.

2.6 Nitride Superconductors

Nitride materials, such as NbN or TiN, were investigated as the first compound superconductors. These materials crystalize in the NaCl structure type and have critical temperatures up to $T_c = 16$ K [37]. Later, $La_3Ni_2B_2N_3$ was synthesized with superconductivity at temperatures around 12–13 K. The crystal structure consists of three rocksalt type LaN layers alternating with Ni_2B_2 layers and is related to superconductive $LuNi_2B_2C$ [38]. Superconductivity was also found in electron-doped layered metal nitride halides with general formula MNX (M = Ti, Zr, Hf; X = Cl, Br, I) [39–41]. There are two kinds of layered polymorphs of these compounds (α- and β-form). Both polymorphs are constructed of MN-layers which are separated by halogen-layers. Upon doping small amounts of electrons, by intercalation of alkali, alkaline earth or rare earth elements between the layers, the band insulators become superconducting nitrides. For example the co-intercalated lithium and tetrahydrofuran (THF) compound $Li_{0.48}(THF)_yHfNCl$ is a superconductor with a high T_c ($T_c = 25.5$ K) [40]. These compounds exhibit higher critical temperatures than the corresponding 3D nitrides (TiN, ZrN, HfN) [41].

2.7 Carbon Nitrides

The chemistry of carbon nitride type materials is based on two building blocks triazine (1,3,5-triazine, C_3N_3) and heptazine (1,3,4,6,7,9,9b-heptaazaphenalene, C_6N_7). The most prominent molecule resulting from this precursor is melamine (triaminotriazine), which has been named by Justus Liebig [42]. Such molecules (melamine, melem, melam or melon) can be formed by condensation of precursors like cyanamide or ammonium dicyanamide. Nowadays, the chemistry of carbon

nitrides is more about the applications in electrocatalysis, photoelectrode applications, batteries, fuel and solar cells, light emitting devices, supercapacitors and sensors. A challenge in the context of energy is an alternative from fossil fuels. Carbon nitrides, which are semiconducting materials composed of earth abundant elements can convert water with sunlight to hydrogen. This so called photocatalytic water splitting method provides clean and sustainable energy for mankind. Furthermore, the binary sp^3-hybridized carbon nitride, C_3N_4 was predicted to show extreme incompressibility and superhardness and was claimed in literature as a theoretical material which is "harder than diamond" [43, 44].

2.8 Oxonitride Perovskites

By exchanging oxygen with nitrogen in the anionic network of the perovskite structure, a vast spectrum of new compounds is accessible. Oxonitrides combine the advantages of metal oxides and nitrides. In general, oxides have wide bandgaps and are therefore often colorless compounds and nitrides are very stable compounds with interesting electronic characteristics.

The combination leads to an even higher stability in comparison to pure nitrides and simultaneously reduces the bandgaps compared to oxides leading to useful electronic and optical properties. The general formula of oxonitride perovskites is $ABO_{2-x}N_{1+x}$ with A = Ca, Sr, Ba or rare earth elements, and B = Nb, Ta, Ti and other transition metals. These materials were first synthesized by Marchand et al. [45] and later industrial applications were predicted [46]. Nowadays, oxonitrides with perovskite structure are well known for various kinds of applications due to the flexibility of their crystal structure towards substitution. Thereby, suitable modifications are possible.

Oxide perovskites are normally insulators with an optical absorption within the visible spectral range. By introducing nitrogen into the lattice as a non-metal with lower electronegativity, the bandgap decreases about 1 eV. This changes the color of these compounds which can cover the entire visible range of the spectrum from yellow to orange, red, ochre and black. Good examples are $CaTaO_2N$ and $LaTaON_2$ and their solid solutions ($Ca_{1-x}La_xTaO_{2-x}N_{1+x}$) in which color tuning is possible from yellow ($x = 0$) to red ($x = 1$) [46]. Their characteristics like high chemical and physical stability makes them promising candidates for inorganic pigments as colorants for papers, thermoplastics, rubbers, ceramics and enamels. In addition to their stability in air, water or diluted acids at room temperature, the fact that they do not contain toxic elements like Cd, Pb or Cr is a huge advantage for the application as inorganic pigments [47].

The reduced bandgaps (around 2 eV) of oxonitride perovskites offers another promising application area of this material class. Kasahara and co-workers showed that oxonitride perovskites like $LaTiO_2N$ can be used as photocatalysts for the evolution of H_2 and O_2 from water under irradiation with visible light (420 nm $< \lambda <$ 600 nm) like sunlight. $LaTiO_2N$ reduces H^+ to H_2 and oxidizes H_2O to O_2 in the

presence of an electron donor (methanol) or acceptor (Ag^+) [48]. The big advantage compared to other photocatalysts is the above mentioned stability of perovskites [49]. Other oxonitride perovskites like $CaTaO_2N$, $SrTaO_2N$, $BaTaO_2N$, $LaTaON_2$ and $BaNbO_2N$ are suitable for both water oxidation and reduction under visible light. The tantalum oxonitrides are able to evolve H_2 from water but are not active in O_2 production. $CaNbO_2N$ has the highest activity for both H_2 and O_2 of the niobium oxonitride perovskites [50]. The difference between oxonitrides of different compositions most likely result from the energy positions of the valence and the conduction bands. The potential of the top of the valence band must be lower than the one of the H_2O/O_2 redox pair for the evolution of oxygen. Whereas for the hydrogen evolution, the bottom of the conduction band must be higher in energy than H_2/H^+. Because of this, the energy position has to be suitable for the water splitting reaction and not only the size of the bandgap itself [49].

In terms of the potential of oxonitride perovskites, synthesis of these compounds plays a crucial role. Oxonitride perovskites are commonly synthesized in flowing ammonia (ammonolysis). Newly developed synthesis methods are thin film deposition by reactive sputtering [51], heteroepitaxial growth [52], the fabrication of a nanowire photoanode [53], and the ammonothermal approach [54]. These new synthetic methods lead to varying morphologies of the compounds resulting in different application fields. For instance, the ammonothermal approach is useful to obtain high crystallinity and well-shaped crystals of oxonitride perovskite (see Chap. 12). Further research has to be done in order to achieve a better understanding on the intrinsic properties which lead to new applications of oxonitride perovskites.

By combining transition metals like Nb^{5+} with mixed valence states and magnetic rare earths, like Eu^{2+}, colossal magnetoresistance can be achieved in $EuNbO_2N$ and $EuWO_2N$ at low temperatures [55]. By manipulating the O/N content within $EuWO_{1+x}N_{2-x}$ films or monoliths, it can be used to create spintronic or nonlinear resistive devices operating at low temperatures [56]. As the oxidation state of both metals (Eu, W) can be tuned by varying the O/N ratio, this reveals a remarkable electronic flexibility by enabling hole- and electron-doped regimes to be accessed. Furthermore, these materials are of fundamental interest and practical importance for new memory and sensor technology.

The oxonitride perovskites have a great potential for various applications. Especially, for environmental reasons, this field is a highly fascinating class of compounds. The structural challenges and their physical properties offer the possibility of applications as pigments, dielectrics, photocatalysts and magnetic materials. To conclude, it can be noted that the partial substitution of O by N in the perovskite structure leads to surprising new physical and chemical properties. Further research in terms of new synthetic approaches needs to be done in order to achieve possible single crystals which are desired for measurements of physical properties.

References

1. W. Schnick, H. Huppertz, Nitridosilicates—a significant extension of silicate chemistry. Chem. Eur. J. **3**, 679 (1997)
2. W. Schnick, Festkörperchemie mit Nichtmetallnitriden. Angew. Chem. **105**, 846 (1993); W. Schnick, Solid-state chemistry with nonmetal nitrides. Angew. Chem. Int. Ed. Engl. **32**, 806 (1993)
3. Publication numbers are given as results according to keywords search ("nitride, nitrides") on the SciFinder database (2018), https://scifinder.cas.org. Accessed 22 Nov 2018
4. A. Ziegler, J.C. Idrobo, M.K. Cinibulk, C. Kisielowski, N.D. Browning, R.O. Ritchie, Interface structure and atomic bonding characteristics in silicon nitride ceramics. Science **306**, 1768 (2004)
5. L.-O. Nordberg, Z. Shen, M. Nygren, T. Ekström, On the extension of the α-SiAlON solid solution range and anisotropic grain growth in Sm-doped α-SiAlON ceramics. J. Eur. Ceram. Soc. **17**, 575 (1997)
6. V.L. Solozhenko, D. Andrault, G. Fiquet, M. Mezouar, D.C. Rubie, Synthesis of superhard cubic BC_2N. Appl. Phys. Lett. **78**, 1385 (2001)
7. H.P. Baldus, M. Jansen, Moderne Hochleistungskeramiken—amorphe anorganische Netzwerke aus molekularen Vorläufern. Angew. Chem. **109**, 338 (1997); H.P. Baldus, M. Jansen, Novel high-performance ceramics—amorphous inorganic networks from molecular precursors. Angew. Chem. Int. Ed. **36**, 328 (1997)
8. M. Jansen, J.C. Schön, L.V. Wüllen, Der Weg zur Struktur amorpher Festkörper—eine Studie am Beispiel der Keramik $Si_3B_3N_7$. Angew. Chem. **118**, 4350 (2006); M. Jansen, J.C. Schön, L. van Wüllen, The route to the structure determination of amorphous solids: a case study of the ceramic $Si_3B_3N_7$. Angew. Chem. Int. Ed. **45**, 4244 (2006)
9. G.A. Slack, Nonmetallic crystals with high thermal conductivity. J. Phys. Chem. Solids **34**, 321 (1973)
10. G.A. Slack, R.A. Tanzilli, R.O. Pohl, J.W. Vandersande, The intrinsic thermal conductivity of AIN. J. Phys. Chem. Solids **48**, 641 (1987)
11. M. Zeuner, S. Pagano, W. Schnick, Nitridosilicate und Oxonitridosilicate: von keramischen Materialien zu struktureller und funktioneller Diversität. Angew. Chem. **123**, 7898 (2011); M. Zeuner, S. Pagano, W. Schnick, Nitridosilicates and oxonitridosilicates: from ceramic materials to structural and functional diversity. Angew. Chem. Int. Ed. **50**, 7754 (2011)
12. Y. Zhou, H. Hyuga, D. Kusano, Y.-I. Yoshizawa, T. Ohji, K. Hirao, Development of high-thermal-conductivity silicon nitride ceramics. J. Asian Ceram. Soc. **3**, 221 (2015)
13. F.A. Ponce, D.P. Bour, Nitride-based semiconductors for blue and green light-emitting devices. Nature **386**, 351 (1997)
14. S.P. DenBaars, D. Feezell, K. Kelchner, S. Pimputkar, C.-C. Pan, C.-C. Yen, S. Tanaka, Y. Zhao, N. Pfaff, R. Farrell, M. Iza, S. Keller, U. Mishra, J.S. Speck, S. Nakamura, Development of gallium-nitride-based light-emitting diodes (LEDs) and laser diodes for energy-efficient lighting and displays. Acta Mater. **61**, 945 (2013)
15. DOE SSL Program, *Energy Savings Forecast of Solid-State Lighting in General Illumination Applications* (US Department of Energy, Navigant Consulting, Inc., 2016) (2018), https://energy.gov/sites/prod/files/2016/09/f33/energysavingsforecast16_2.pdf. Accessed 29 Jan 2018
16. D. Ehrentraut, E. Meissner, M. Bockowski, *Technology of Gallium Nitride Crystal Growth* (Springer, Berlin, 2010), p. 3
17. A. Zakutayev, Design of nitride semiconductors for solar energy conversion. J. Mater. Chem. A **4**, 6742 (2016)
18. Y. Hinuma, T. Hatakeyama, Y. Kumagai, L.A. Burton, H. Sato, Y. Muraba, S. Iimura, H. Hiramatsu, I. Tanaka, H. Hosono, F. Oba, Discovery of earth-abundant nitride semiconductors by computational screening and high-pressure synthesis. Nat. Commun. **7**, 11962 (2016)
19. P.C. Quayle, K. He, J. Shan, K. Kash, Synthesis, lattice structure, and band gap of $ZnSnN_2$. MRS Commun. **3**, 135 (2013)

20. J. Häusler, S. Schimmel, P. Wellmann, W. Schnick, Ammonothermal synthesis of earth-abundant nitride semiconductors $ZnSiN_2$ and $ZnGeN_2$ and dissolution monitoring by in situ X-ray imaging. Chem. Eur. J. **23**, 12275 (2017)
21. D.R. Wilburn, *Byproduct Metals and Rare-Earth Elements Used in the Production of Light-Emitting Diodes—Overview of Principal Sources of Supply and Material Requirements for Selected Markets* (U.S. Geological Survey Scientific Investigations Report, 2012) (2018), https://pubs.usgs.gov/sir/2012/5215/. Accessed 14 June 2018
22. M. Lokanc, R. Eggert, M. Redlinger, *The Availability of Indium: The Present, Medium Term, and Long Term* (National Renewable Energy Laboratory, 2015) (2018), https://www.nrel.gov/docs/fy16osti/62409.pdf. Accessed 14 June 2018
23. M. Mikami, H. Watanabe, K. Uheda, S. Shimooka, Y. Shimomura, T. Kurushima, N. Kijima, New phosphors for white LEDs: material design concepts. Mater. Sci. Eng. **1**, 012002 (2009)
24. P. Pust, V. Weiler, C. Hecht, A. Tücks, A.S. Wochnik, A.-K. Henß, D. Wiechert, C. Scheu, P.J. Schmidt, W. Schnick, Narrow-band red-emitting $Sr[LiAl_3N_4]:Eu^{2+}$ as a next-generation LED-phosphor material. Nat. Mater. **13**, 891 (2014)
25. V. Zepf, J. Simmons, A. Reller, M. Ashfield, C. Rennie, *Materials Critical to the Energy Industry. An Introduction*, 2nd edn. (BP p.l.c, London, 2014), pp. 38–40
26. A. Vezzini, Elektrofahrzeuge. Mobilität und erneuerbare Energie. Phys. Unserer Zeit. **41**, 36 (2010)
27. Y. Wang, W.D. Richards, S.P. Ong, L.J. Miara, J.C. Kim, Y. Mo, G. Ceder, Design principles for solid-state lithium superionic conductors. Nat. Mater. **14**, 1026 (2015)
28. *Battery Recall Could Cost $400 Million for Dell and Sony—Business—International Herald Tribune* (The New York Times, 2006)
29. *Galaxy Note 7 Fires Caused by Battery and Design Flaws, Samsung Says* (The New York Times, 2017)
30. B.V. Lotsch, J. Maier, Relevance of solid electrolytes for lithium-based batteries: a realistic view. J. Electroceram. **38**, 128 (2017)
31. Y. Zhu, X. He, Y. Mo, Strategies based on nitride materials chemistry to stabilize Li metal anode. Adv. Sci. **4**, 1600517 (2017)
32. S. Wenzel, T. Leichtweiss, D. Krüger, J. Sann, J. Janek, Interphase formation on lithium solid electrolytes—an in situ approach to study interfacial reactions by photoelectron spectroscopy. Solid State Ionics **278**, 98 (2015)
33. W. Schnick, J. Luecke, Lithium ion conductivity of $LiPN_2$ and Li_7PN_4. Solid State Ionics **38**, 271 (1990)
34. E.-M. Bertschler, C. Dietrich, T. Leichtweiß, J. Janek, W. Schnick, Li^+ Ion conductors with adamantane-type nitridophosphate anions β-$Li_{10}P_4N_{10}$ and $Li_{13}P_4N_{10}X_3$ with X = Cl. Br. Chem. Eur. J. **24**, 196 (2018)
35. E.-M. Bertschler, C. Dietrich, J. Janek, W. Schnick, $Li_{18}P_6N_{16}$—a lithium nitridophosphate with unprecedented tricyclic $[P_6N_{16}]^{18-}$ Ions. Chem. Eur. J. **23**, 2185 (2017)
36. H. Yamane, S. Kikkawa, M. Koizumi, Preparation of lithium silicon nitrides and their lithium ion conductivity. Solid State Ionics **25**, 183 (1987)
37. B.T. Matthias, J.K. Hulm, A search for new superconducting compounds. Phys. Rev. **87**, 799 (1952)
38. R.J. Cava, H.W. Zandbergen, B. Batlogg, H. Eisaki, H. Takagi, J.J. Krajewski, W.F. Peck Jr., E.M. Gyorgy, S. Uchida, Superconductivity in lanthanum nickel boro-nitride. Nature **372**, 245 (1994)
39. S. Yamanaka, H. Kawaji, K.I. Hotehama, M. Ohashi, A new layer-structured nitride superconductor. Lithium-intercalated β-zirconium nitride chloride, Li_xZrNCl. Adv. Mater. **8**, 771 (1996)
40. S. Yamanaka, K.-I. Hotehama, H. Kawaji, Superconductivity at 25.5 K in electron-doped layered hafnium nitride. Nature **392**, 580 (1998)
41. Y. Kasahara, K. Kuroki, S. Yamanaka, Y. Taguchi, Unconventional superconductivity in electron-doped layered metal nitride halides MNX (M = Ti, Zr, Hf; X = Cl, Br, I). Phys. C **514**, 354 (2015)

42. J.V. Liebig, Ueber einige Stickstoff-Verbindungen. Ann. Pharm. **10**, 1 (1834)
43. F.K. Kessler, Y. Zheng, D. Schwarz, C. Merschjann, W. Schnick, X. Wang, M.J. Bojdys, Functional carbon nitride materials—design strategies for electrochemical devices. Nat. Rev. Mater. **2**, 17030 (2017)
44. E. Wirnhier, B. Mesch Maria, J. Senker, W. Schnick, Formation and Characterization of Melam, Melam Hydrate, and a Melam–Melem Adduct. Chem. Eur. J. **19**, 2041 (2012)
45. R. Marchand, F. Pors, Y. Laurent, Preparation and characterization of new oxynitrides with a perovskite structure. Rev. Int. Hautes Temp. Refract. **23**, 11 (1986)
46. M. Jansen, H.P. Letschert, Inorganic yellow-red pigments without toxic metals. Nature **404**, 980 (2000)
47. R. Aguiar, D. Logvinovich, A. Weidenkaff, A. Rachel, A. Reller, S.G. Ebbinghaus, The vast colour spectrum of ternary metal oxynitride pigments. Dyes Pigm. **76**, 70 (2008)
48. A. Kasahara, K. Nukumizu, G. Hitoki, T. Takata, J.N. Kondo, M. Hara, H. Kobayashi, K. Domen, Photoreactions on $LaTiO_2N$ under visible light irradiation. J. Phys. Chem. A **106**, 6750 (2002)
49. S.G. Ebbinghaus, H.-P. Abicht, R. Dronskowski, T. Müller, A. Reller, A. Weidenkaff, Perovskite-related oxynitrides—recent developments in synthesis, characterisation and investigations of physical properties. Prog. Solid State Chem. **37**, 173 (2009)
50. A. Fuertes, Metal oxynitrides as emerging materials with photocatalytic and electronic properties. Mater. Horiz. **2**, 453 (2015)
51. C. Le Paven-Thivet, L. Le Gendre, J. Le Castrec, F. Cheviré, F. Tessier, J. Pinel, Oxynitride perovskite $LaTiO_xN_y$ thin films deposited by reactive sputtering. Prog. Solid State Chem. **35**, 299 (2007)
52. D. Oka, Y. Hirose, T. Fukumura, T. Hasegawa, Heteroepitaxial growth of perovskite $CaTaO_2N$ thin films by nitrogen plasma-assisted pulsed laser deposition. Cryst. Growth Des. **14**, 87 (2014)
53. M. Davi, F. Schrader, T. Scholz, Z. Ma, A. Rokicinska, R. Dronskowski, P. Kustrowski, A. Slabon, $SrTaO_2N$ nanowire photoanode modified with a ferrihydrite hole-storage layer for photoelectrochemical water oxidation. ACS Appl. Nano Mater. **1**, 869 (2018)
54. N. Cordes, W. Schnick, Ammonothermal synthesis of crystalline oxonitride perovskites $LnTaON_2$ (Ln = La, Ce, Pr, Nd, Sm, Gd). Chem. Eur. J. **23**, 11410 (2017)
55. A.B. Jorge, J. Oró-Solé, A.M. Bea, N. Mufti, T.T.M. Palstra, J.A. Rodgers, J.P. Attfield, A. Fuertes, Large coupled magnetoresponses in $EuNbO_2N$. J. Am. Chem. Soc. **130**, 12572 (2008)
56. A. Kusmartseva, M. Yang, J. Oró-Solé, A.M. Bea, A. Fuertes, J.P. Attfield, Large magnetoresistances and non-ohmic conductivity in $EuWO_{1+x}N_{2-x}$. Appl. Phys. Lett. **95**, 022110 (2009)

Chapter 3
Technological Challenges of Autoclave Design for Ammonothermal Syntheses

Eberhard Schlücker and Anna-Carina Luise Kimmel

Abstract The challenges of ammonothermal reactor design are manifold. High-pressure and temperature require the use of high-performance alloys with sufficient strength at elevated temperature and excellent creep resistance: highly alloyed Ni-base and Co-base alloys and a Mo-base alloy have been in use in ammonothermal reactor design. Furthermore, the dimensioning rules have to be strictly followed to minimize stress concentration. Repeated loading cycles and degradation over time have to be considered. Finally yet importantly, good handling of the equipment not only minimizes the workload but also reduces the risk of crucial operating errors. The chapter *Technological challenges of autoclave design* discusses design options for high-pressure at high-temperature equipment with regard to their mechanic and thermal stability. Materials suitable for ammonothermal pressure vessels will be reviewed and some basic safety advice is given at the end of this chapter.

3.1 High-Pressure Autoclave Design

The development of high-pressure vessels and components requires a very disciplined approach. On the one hand, the applicable dimensioning rules (e.g. the ASME *Boiler and Pressure Vessel code* [1] in the US or the *Pressure Equipment Directive* [2] in the EU) must be consistently implemented. On the other hand, high-performance materials with high strength, ductility and creep resistance have to be selected. In addition, the design, e.g. the wall thickness of the autoclave, is based on the selected materials. Therefore, the choice of suitable materials is the first priority.

E. Schlücker (✉) · A.-C. L. Kimmel
Chair of Process Machinery and Systems Engineering, Friedrich-Alexander-University of Erlangen Nuremberg (FAU), Erlangen, Germany
e-mail: sl@ipat.uni-erlangen.de

A.-C. L. Kimmel
e-mail: annacarina.kimmel@gmail.com

E. Meissner and R. Niewa (eds.), *Ammonothermal Synthesis and Crystal Growth of Nitrides*, Springer Series in Materials Science 304,
https://doi.org/10.1007/978-3-030-56305-9_3

3.1.1 Selection of High-Performance Alloys for Ammonothermal Autoclave Design

In principle, materials for high-pressure application should possess a yield strength of at least 500 N/mm^2 and must me sufficiently ductile. According to the *Pressure Equipment Directive* of the EU they must have an elongation at break of at least 14% and an impact strength of at least 27 J at the lowest process temperature or at 20 °C max [2]. As surfaces, although ground, are not free of small recesses and micro cracks, it is beneficial that the notch effect emanating from such geometric elements (see also Sect. 3.1.3) is mitigated by a high elasticity of the material. Deformation energy is consumed during fracture of a ductile material, which means that usually, fracture occurs only after a strong deformation of the alloy. The higher the notched bar impact strength, the tougher the material will be during fracture and the longer the fracture phase. It is therefore possible to react to an incipient fracture, in most cases.

High-pressure materials such as duplex steel 1.4452 in Fig. 3.1a no longer have a pronounced yield strength limit. Instead, the so-called 0.2% yield strength ($R_{p0.2}$) is used as a yield strength substitute. This means that a load that leaves a remaining elongation of 0.2% is considered to be the yield strength. If one thinks of high-pressure components and especially of seals (see below), it is also important that the compressive strength is always greater and also permits higher elongations. This can also be understood as an indication that compressive stresses should be aimed at whenever possible.

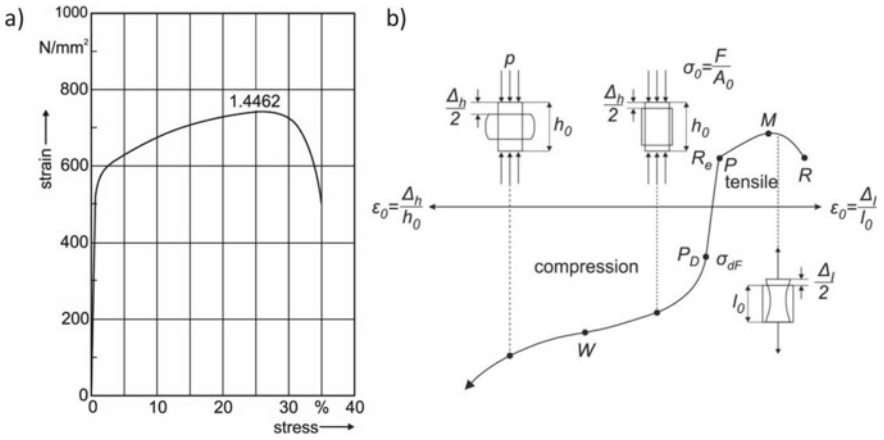

Fig. 3.1 **a** Stress strain curve of a duplex steel 1.4462 (measured at institute of process machinery and systems engineering), as well as **b** exemplary tensile and compressive stress curve

Table 3.1 Materials suitable for high-pressure applications with their yield strength, ultimate tensile strength, rupture elongation and notch bar impact work at room temperature [3, 4]

ISO No.	Notation	Yield strength maximum [N/mm^2]	Ultimate tensile strength [N/mm^2]	Rupture elongation [%]	Notch bar impact work min. [J]
1.4542	X5CrNiCuNb16-5	1000	1270	10–14	15
1.6580	30CrNiMo8	1250	1450	9–11	30
1.4922	X20CrMoV12-1	490	830	16	41
1.7709	21CrMoV57	440	780	16	69
1.8523	39CrMoV9	1080	1420	8	27
1.6956	33NiCrMo14 5	1030	1470	8	20
2.4668	8NiCrMo55-21-3 IN718, Alloy 718	1100	1375	25	68

Table 3.1 shows a number of selected high-pressure alloys with yield strength, tensile strength, elongation at break and impact strength data. This shows that the elongation at break and the notched bar impact strength decrease with increasing yield strength and tensile strength. The higher the pressure, the higher the strength of the alloy to be selected. This, however, reveals the dilemma that ductility is lost with increasing yield strength. The only possibility is therefore to work on the quality and design of the high-pressure component to rule out all possible notch effects. This often only means absolutely straight container bores without any step or notch and fine ground surfaces.

As it can be seen in Table 3.1, basically, the higher the tensile strength, the lower the rupture elongation and notch bar impact work. The mechanical behavior of each alloy results from a complex interplay between the composition, manufacturing process, heat treatment and the resulting microstructure of the alloy. Several strengthening mechanisms are exploited when developing high-strength alloys: dislocation hardening, grain boundary strengthening, solid solution hardening or particle hardening [5]. With regard to the application in ammonothermal processes always the high process temperature has to be considered. In general, with increasing temperature the tensile strength and yield strength decrease, with elongation at break and impact strength generally increasing. According to [6], alloys suitable for high-temperature applications have to maintain their mechanical properties and withstand loading at elevated temperature, close to their melting point ($T > 0.4\ T_{\mathrm{melt}}$). Additional they possess high creep resistance (maintaining their mechanical properties over time) high yield stress/ultimate tensile strength, fracture toughness. To withstand severe operating environments a high oxidation and corrosion resistance is desirable. This means that the mechanical data must always be obtained for the desired operation temperature. Yet, the increase in temperature and its effects on the mechanical properties also offer opportunities. If an alloy with unsatisfactory elongation at break at room temperature is selected, it could be suitable at higher temperatures. In this case, it must not be subjected to maximum stress at room temperature.

At the described process conditions of ammonothermal syntheses (p = 100–300 MPa, T = 300–800 °C) only particle-hardened alloys are conceivable as materials that permit sufficient strength [5]. Carbide and solid solution hardening as strength mechanisms in austenitic iron-based alloys achieve sufficient mechanical properties up to temperatures of $T_{\text{maxFe-Basis}} \approx 500$ °C [6]. However, for even higher process temperatures, precipitation hardened superalloys (e.g. Ni-base superalloys) have the biggest potential in the high-pressure/high-temperature autoclave design. The extensive use of Ni-base superalloys, among others in aerospace or power plant technology, resulted in a highly developed microstructure, manufacturing process and corrosion resistance [6–9]. Therefore and depending on the desired pressure/temperature ranges or synthesis route, state of the art materials for ammonothermal pressure vessels are among others René 41 [10, 11], Alloy 625 (Inconel®Alloy 625; 2.4856) [12, 13], Alloy 718 (Inconel®Alloy 718; 2.4668) [14], and Alloy 282 (Haynes®282®Alloy) [15]. Excellent strength at elevated temperatures because of precipitation hardening was the primary selection criterion for those alloys. Sufficient corrosion and oxidation resistance at high temperature is given, but not necessarily under ammonothermal conditions, see Chap. 11.

Another class of suitable superalloys are precipitation hardened Co-base superalloys of the system Co–Al–W. The development of the precipitation of an ordered Co_3(Al, W) phase (γ') in a Co solid solution matrix, similar to the Ni_3Al γ' phase in Ni-base superalloys [16], together with improved oxidation resistance and mechanical properties due to additional alloying [17–20], promises a wide range of high-pressure/high-temperature applications. The higher melting point of Co, compared to Ni, and resulting higher liquidus and solidus temperatures of the alloy help to expand the possible temperature window of ammonothermal synthesis to higher temperature (T > 600 °C). The raise to even higher temperature and pressure have been shown beneficial in ammonothermal synthesis for new synthesis routes, especially when developing new compounds [15]. Potential alloys of this class for ammonothermal applications have already been developed [19] and optimized [21–23], however, they are not commercially available yet.

The Mo-base Ti-Zr-Mo alloy TZM is another alternative in ammonothermal reactor design that has been recently tested successfully [24], especially due to its good resistance in ammonoacidic environment (see Chap. 11). Mo possesses excellent high-temperature strength and creep resistance, a high melting point, a low coefficient of thermal expansion and high thermal conductivity [25]. However, some disadvantages have to be considered: the unsatisfactory oxidation resistance at temperatures above 500 °C requires protective coatings or an oxygen free containment during heating. Additionally the high ductile to brittle transition temperature (DBTT) of 100–150 °C challenges handling and manufacturing of autoclaves [25, 26].

Figure 3.2 shows a *Larson-Miller* Plot for some exemplary Ni-base, Co-base alloys suitable for or already in use in ammonothermal reactor design. The creep resistance of Alloy 718 and Alloy 282 is similarly high. The one of CoWAlloy2 even higher.

Figure 3.3 depicts the yield strength over temperature for selected alloys. Possible working areas for autoclaves made of those alloys are indicated. The drop in

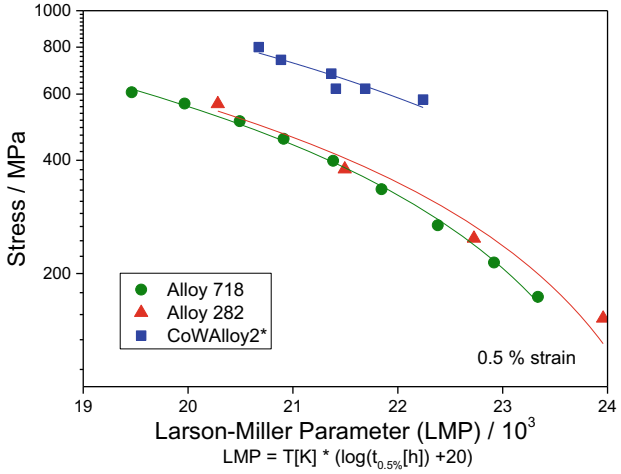

Fig. 3.2 *Larson-Miller* plot for 0.5% creep strain of Alloy 718 [27], Alloy 282 ([28], data for 100 h and 0.5% creep strain) and CoWAlloy2 (*compression creep strain), data reprinted with permission from [29]

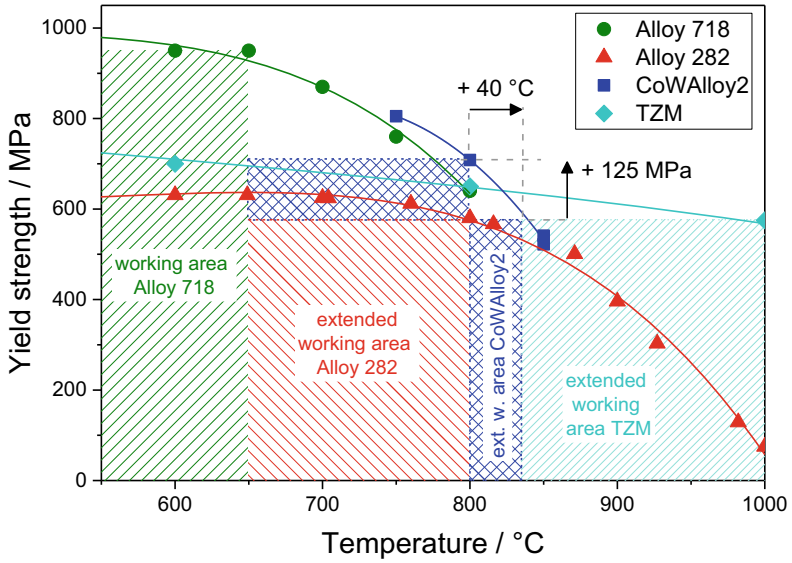

Fig. 3.3 Yield strength over temperature for selected high-performance alloys in ammonothermal autoclave design, with possible working areas for autoclaves made of those alloys. Alloy 718 (solution annealed and age hardened [33], green-striped area), Alloy 282 (solution annealed and age hardened sheet [28, 34], red-striped), CoWAlloy2 [21], blue-checkered area] and TZM (stress relieved sheet [30], light-blue-fine-striped area). Data reprinted and modified with permission according to [29]

yield strength at a certain temperature is mostly due to irreversible changes in the microstructure and loosening of the strengthening mechanisms and therefore represents the maximum operating temperature. With about 1000 MPa Alloy 718 possesses the highest yield strength of the presented alloys, but its use is limited to a temperature of about 600–650 °C. The microstructure of Alloy 282 is stable up to about 800 °C, however the maximum yield strength is significantly lower (about 600 MPa) than the one of Alloy 718. The use of the Co-base alloy CoWAlloy2 expands the possible working area of Alloy 282 to ether higher temperature (about 850 °C) or to a 125 MPa higher yield strength at the same $T_{\max}$ of 800 °C. In oxygen free environment TZM is supposed to be stable in ammonia gas up to 1000 °C and shows high yield strength at this temperature of about 600 MPa [30], which would expand the possible temperature range of ammonothermal growth of another 250 °C. Pressure vessels made of TZM have been used among others at internal pressures and temperatures of up to 100 MPa/1200 °C [31] or 150 MPa/1025 °C [32]. Yet, in ammono-thermal environment, autoclaves made of TZM have only been tested up to >100 MPa/650 °C so far [24].

As materials used for internal setups inside the autoclave are not exposed to tensile stresses they will be only discussed regarding their chemical stability in Chap. 11.

3.1.2 Dimensioning an Autoclave

The core elements of high pressure vessels are usually straight pipe sections. Depending on the pressure, these are calculated using either the boiler formula (3.1) or formulae (3.2)–(3.4).

$$s_0 = \frac{d_a \cdot p}{2 \cdot \nu \cdot \frac{K}{S}} [\text{mm}]; \quad s = s_0 + c_1 + c_2 \tag{3.1}$$

where: s: wall thickness [mm]; s_0: theoretical wall thickness [mm], d_a: tube outer diameter [mm], p: maximum internal pressure [N/mm^2], ν: Poisson's ratio [−], K: Material value [N/mm^2], S: safety factor, c_1: Add on for wall thickness correction, c_2: Add on for corrosion and wear.

This equation assumes that the stress is constant over the wall thickness and also considers only one stress component. This assumption applies up to a wall thickness ratio of $u = 1.2$.

$$u = \frac{r_o}{r_i} = 1.2 \tag{3.2}$$

For wall thickness ratio $u > 1.2$, all three stress components must be considered and the following equations apply [35]:

$$\sigma_t = \frac{P_{\text{in}} \cdot \left[\left(\frac{r_2}{r}\right)^2 + 1\right]}{\left(\frac{r_2}{r_1}\right)^2 - 1}; \quad \sigma_r = \frac{P_{\text{in}} \cdot \left[\left(\frac{r_2}{r}\right)^2 - 1\right]}{\left(\frac{r_2}{r_1}\right)^2 - 1}; \quad \sigma_z^{\text{closed ends}} = \frac{P_{\text{in}}}{\left(\frac{r_2}{r_1}\right)^2 - 1} \tag{3.3}$$

Figure 3.4 shows the exemplary course of the three stress components (σ_ϕ: tangential stress; σ_r: radial stress; σ_z: axial stress). The tangential stress is always the greatest stress in a straight tube and the radial stress always begins with $\sigma_r = p_{\text{in}}$. The comparative stress is usually similar to the tangential stress with a slightly lower starting value at the inner diameter.

Since three stress components are difficult to work with, several equilibrium stress theories have been developed in the past. The theory best suited to high-pressure technology is that of *von Mises*, who developed Formula [36]:

$$\sigma_e = \sqrt{0.5 \cdot \left[(\sigma_\varphi - \sigma_z)^2 + (\sigma_z - \sigma_r)^2 + (\sigma_r - \sigma_\varphi)^2\right]} \tag{3.4}$$

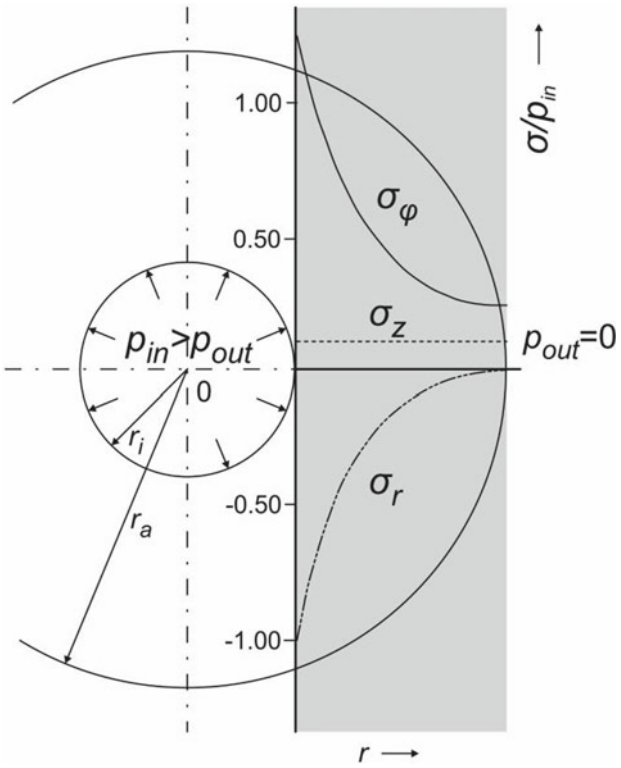

Fig. 3.4 Stress distribution in a thick walled tube: tangential, axial and radial stress with respect to the internal pressure p_{in} over the radius

3.1.3 *Influence of Notch Factor and Dynamic Load*

As already described above, well designed and manufactured high-pressure components are very smooth and free of notches and corners, to minimize the notch effect of the surface structures. However not every cross-section transition, deflection or bore can be avoided. The bore in the test component in Fig. 3.5 represents such a location; the notch effect here values about three.

This means that the stress at the corner of the bore intersection is about three times higher than in the undisturbed area of the main bore. However, the sharpness of the intersection edge is also decisive for the notch factor. If the edge is rounded off, the notch factor decreases noticeably. In addition, a material with high elongation at break at the notch point can react with greater plasticizing. This can mean that for constructions that cannot do without notches, a material that is more less solid but has more elongation at break may be better suited.

Additionally dynamic load reduces the material strength significantly. Under high dynamic loading (beginning at about 10^7 load cycles), the permissible stress falls below half the yield strength of the material. The suitability of a material for dynamic high pressure can be seen from the Wöhler curve. This curve is available for many materials.

Figure 3.6 shows the results of dynamic testing with the component shown in Fig. 3.5 made of four different alloys. The components were tested up to failure in bending-rotation test, pulsating tensile test and with pulsating pressure of about 300 MPa (*v. Mises*).

It shows very clearly that material 1.4404 with a yield strength of approx. 250 N/mm^2 and an elongation at break of 45% withstands about the same internal pressure (*v. Mises*) as material 1.4462 (Fig. 3.1a) with a yield strength of approx. 500 N/mm^2 and an elongation at break of 25%.

The ammonothermal method usually does not generate a dynamic load as it was applied to the example in Figs. 3.5 and 3.6, especially not during research scale. The few load cycles of an ammonothermal autoclave and its accessories (max. a few hundred loads) can be regarded as static loads. Nevertheless, this topic should not be omitted when heading to industrial scale or during special operation processes, for example when filling the autoclave with oscillating positive displacement pumps.

This all leads to the five basic rules we have to consider during design or use of a high-pressure-vessel:

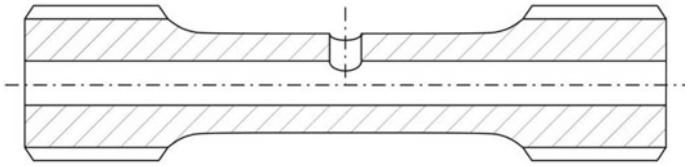

Fig. 3.5 Component for dynamic high-pressure testing with transverse bore for testing the notch effect

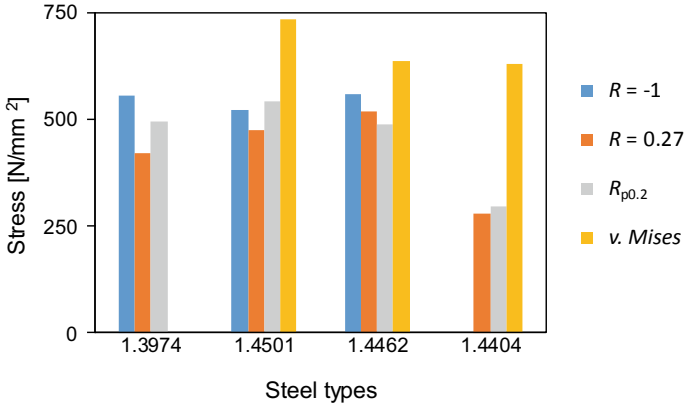

Fig. 3.6 Results from a fatigue test of four materials: $R = -1$: Bending-rotation test, $R = 0.27$: Pulsating tensile test, $Rp_{0.2}$: yield strength, *v. Mises*: comparative stress generated with high-pressure component test with specimens according to Fig. 3.5

(1) Select the material with the best properties for the application.
(2) Consider all elastically and plastically developed deformations of the pressure-loaded and temperature-exposed parts.
(3) Let the pressure help to seal the autoclave! To get a perfect and tight seal, the material at the detail of seal should plasticize. This smoothens the roughness of the surfaces.
(4) Avoid every sharp or even every edge in the pressure loaded area because these details will produce notch factors up to a value of three, resulting in a stress three times higher than in the area around.
(5) Surface quality is essential, as surface imperfections on a rough surface represent a high number of small notches that may lead to breakdown of the autoclave. Therefore a coarseness value of about $R_a = 0.8$ µm is recommended.

3.1.4 Safety Factor

Each component is never loaded up to its yield point. There is always a safety distance. This should cover imponderables such as wall thickness fluctuations or corrosion. Simple components such as beams have a safety factor of $S = 2 - 3$, lifts up to $S = 10$ (typical for passenger transport). High-pressure components, on the other hand, have precisely manufactured components and tested materials. Therefore, the required minimum safety factor is about $S = 1.5$ [37].

3.1.5 Sealing Options for the Autoclave Closure

High-pressure seals have a special requirement for tightness, because even a microscopically small channel in a seal, which can result, for example, from unsatisfactory production (machining roughness), already shows a pressure-driven leakage, which can quickly increase, supported by rinsing effects. Absolute precision during machining of the components is therefore required to reach maximum tightness. However, this is only possible if the surface roughness is either levelled or perfectly filled and plasticized at the sealing points. Since this must pass through on both sides of the seal, seals and high-pressure vessels are often made of similarly solid materials. This means that seals at high pressure are usually made of steel or comparable metallic materials. Figure 3.7 shows two examples of plasticization in the sealing area.

With the compression ring seal (Fig. 3.7a), when nut 1 is tightened, the ring 2 is pressed and the compression ring along the cone in the base body (6) is pressed into the pipe surface. Both contact surfaces plasticize and "interlock" so that the cutting ring can no longer be separated from the tube. This also plasticizes the cone. Thus, this screw connection is perfectly tight. The limitation in pressure is about 64 MPa. The reason for this is that the sealing effect is generated screw in the nut.

Sealing lenses (Fig. 3.7b, c), on the other hand, are pressed together by the flanges and flange screws in such a way that plasticization occurs. To support this process, the lens is rounded, while the counterface at the pipe end is conical. At the beginning of the pressing process there is a line contact. If the force is then further increased, the contact is first elastically pressed into a contact surface (ring). If the yield point is exceeded, the most heavily loaded area near the first contact plasticizes. The maximum of pressure reached with this design is 360 MPa, but it depends directly on the material used. If a high strength material would also have the chance plasticize, also higher pressure would be possible.

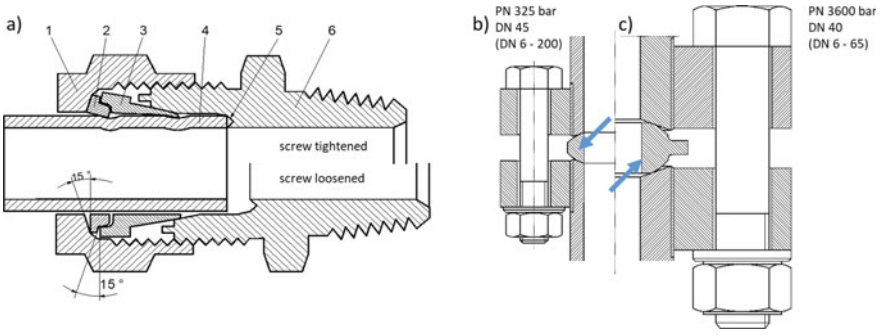

Fig. 3.7 High-pressure seals: **a** Compression fitting (1 union nut, 2 pressure ring, 3 separating ring, 4 pipe, 5 stop for pipe, 6 body), suitable up to 64 MPa, **b**, **c** lens seals for 32,5 up to 360 MPa (DN 40/45), lens indicated by blue arrows

These two types of seals show that plasticization is basically required and also possible. Based on the text above, we can state that also the seals for the ammonothermal process should have the ability to plasticize, but then the pressure of 300 MPa would not be a big problem anymore.

A basic rule for high pressure seals is that the pressure should help with sealing. The first idea for the sealing of pressure vessels was the *Bridgeman* seal (Fig. 3.8a). Here the pressure helps to seal by compress a stack of rings, whereby the middle one is the softest ring and therefore produces the greatest radial expansion and thus represents the core seal. The outer rings only serve to avoid the extrusion of the inner ring. Such a design can also be realized with five rings. Unfortunately, this seal has a serious disadvantage: the inner ring should plasticizes and due that clamps so tightly that it can only be dismantled by destroying the seal. This is not acceptable for the ammonothermal process. The search was therefore for a seal that could be easily dismantled and, and tightened with the help of pressure. The result was the C-ring (Fig. 3.8b, c) [38]. If the pressure penetrates into the C, this expands and creates sealing pressures at the two contact points. However, the C-ring has to be preloaded to achieve sealing at lower pressure. High pressure reinforces the sealing effect by bending the C towards the supporting groove. In the pressure and temperature ranges of the ammonothermal process, however, this ring also reaches its limits. It will be pressed into the edge volume. Therefore, the ring must be perfectly fitted into the locating groove without contact edges (Fig. 3.8c), otherwise fatigue fractures may occur. However, each new loading of a container generates a certain repositioning of the seal, which means a relative movement of the seal under high load. This requires a material with good emergency running properties. The choice fell again on a soft material like copper, silver or gold.

Figure 3.9 shows a finite element method (FEM) calculation result of the C-ring arrangement. As it can be seen, the C-ring generates a stress increase in the supporting area.

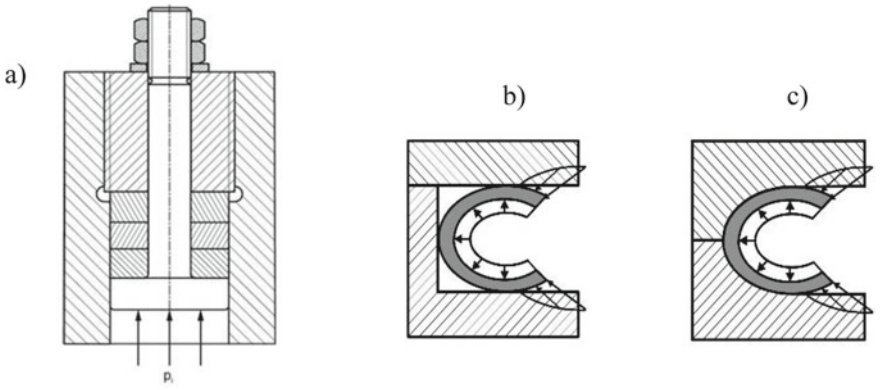

Fig. 3.8 High-pressure seals **a** vessel with a *Bridgeman* seal with 3 rings, **b** C-ring seal (not in a perfect groove), **c** C-ring in a perfect groove [38]

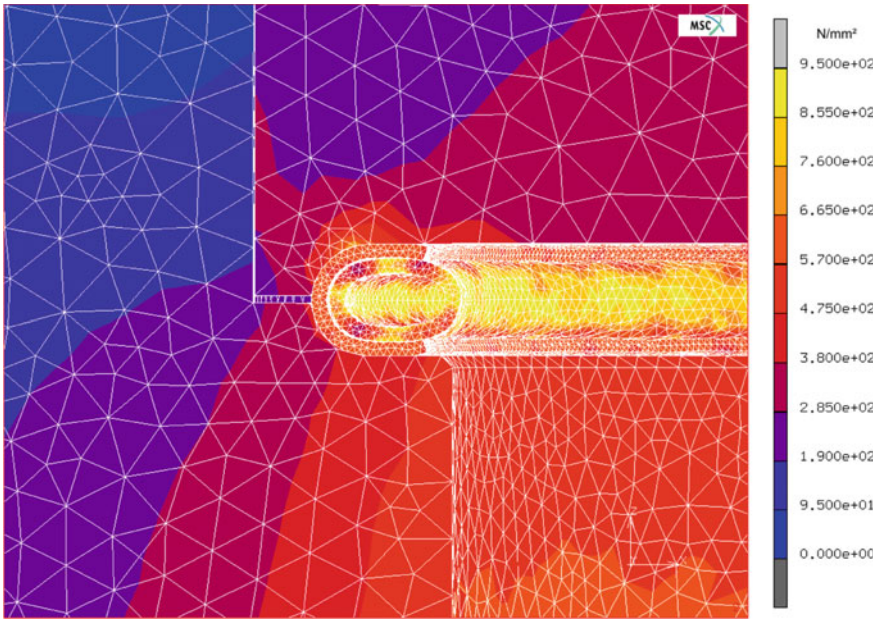

Fig. 3.9 FEM-simulation of the C-ring seal. Ring is completely under compression stress, reprinted with permission from [38]

3.1.6 Closure Types

There are several concepts for the closure of high-pressure containers. However, the higher the pressure, the lesser suitable are concepts with clamps, bolts or joints etc., and it is only a matter of the three concepts shown in Fig. 3.10, each of which uses threads in different variants.

Figure 3.10a shows a concept with flanges. A thread is cut onto the high-pressure pipe and a flange is screwed onto it. The mating flange represents the container cover, which also holds the seal. It is important that the gasket is pressed without rotation, i.e. only linearly. Figure 3.10b shows a concept with a central screw and is therefore very compact. This concept follows the rule that the forces should not be allowed to walk under high pressure. Unfortunately, the seal is pressed under the rotation of the central screw. In variant three in Fig. 3.10c, threads are cut into the vessel wall. Thus the screw flange from Fig. 3.10a is omitted, but the threads require a thicker wall, but together with the bore they represent a notch which generates a certain notch factor and causes a distortion of the stress situation. When the vessels are big, then the advantage is the small effort for material. In this concern, the ends of the vessel will be widened to a bigger diameter with a conical changeover, that the screw bores are not harmful anymore. Another chance if a *Bridgeman* seal is used, and the sealing point in the vessel is below the ends of the bores. The selection of the optimal variant for the ammonothermal process is driven by the rather small container sizes, the high

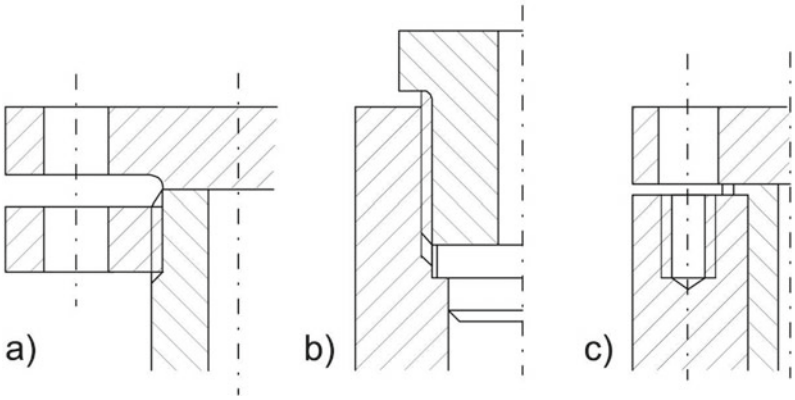

Fig. 3.10 Vessel closures for high-pressure: **a** Flange variant. **b** Variant with internal screw. **c** Thread in pipe wall

pressure and the expensive container materials. Variant Fig. 3.10b is suitable for even higher pressures and larger vessels, whereby the seal is pressed (in the case of the C-ring) under the rotary motion of the threaded piece. This creates a shear stress on the seal surface and can lead to premature wear which already begins during assembly, whereas variant Fig. 3.10c is rarely used (especially for very big vessels), since the notch effect of the threaded holes requires considerably thicker wall thicknesses than with Fig. 3.10a. The result is that the thread is notched and the thread is not pressed.

Up to this point, the technical design of the pressure vessels above was carried out only based on mechanical properties and without special consideration of temperature. In ammonothermal applications, however, temperatures reach up to 800 °C. Consequently, and in addition to the selection of high-performance alloys with sufficient strength at the operation temperature (see Sect. 3.1.1), thermal expansion of the components has to be considered. This applies in particular when different material types are used and a big mismatch in the coefficient of thermal expansion occurs.

Finally, the chemicals used inside the designed pressure vessels and their impact on the used materials have to be taken into account. Corrosion and stability of materials under ammonothermal conditions will be discussed in detail in Chap. 11.

3.2 System and Safety

Even after conscientious design and manufacturing of the autoclave, failure of the process equipment cannot be ruled out completely. Corrosiveness of new compounds or reaction mixtures and their behavior at hardly explored process conditions cannot always be predicted precisely. Additionally, unexpected high rates of ammonia decomposition, e.g. due to catalytic effects of metallic reaction compounds, could lead to a prohibited pressure increase and failure of the autoclave. Therefore, a number

of safety measures have to be taken to prevent damage to people and equipment during operation. Table 3.2 sums up potential risks when operating high-pressure vessels together with measures to rule them out, following and supplemented according to the *EU Pressure Equipment Directive* [2].

During operation, the monitoring of the process parameters is crucial: pressure and temperature of the autoclave should be followed at all times, with a safety shutdown at exceeding pressure/temperature. Bursting discs are a cheap addition to an automatic shutdown, but thermal and corrosion influences on the bursting disc have to be taken into account. Containment vessels with suction ensure, that in case of leakage during operation no operating staff gets harmed. Periodical review of the material quality of the pressure vessel, the additional process equipment and the working space together with regular training of staff help to prevent such failures in the early stages of failure. Figure 3.11 shows an ammonothermal autoclave with some basic safety equipment, such as inlet/outlet valve, pressure sensor and bursting disc.

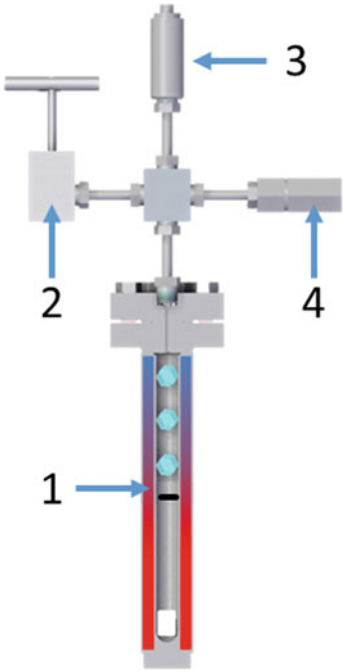

Fig. 3.11 Autoclave for ammonothermal crystal growth (1) with inlet/outlet-valve (2), pressure sensor (3) and bursting disc (4)

Table 3.2 Potential risks and their causes when operating high-pressure vessels

Potential risk	Caused by	Protection measures	Monitoring possibilities
Mechanical failure	• Pressure • Temperature • Operating mode • External loads • External fire	• Application of suitable materials • Conscientious design and construction • Review through approved authorities	• Continuous monitoring of pressure and temperature during operation • Periodical review of material quality of pressure vessel (measuring thickness, roughness, surface quality, …) • Regular review of additional process equipment (valves, thermocouples, pressure transducers…) • Regular review of working space
Corrosion erosion	• Corrosive or erosive reaction solution • Operation mode	• Application of stable materials • Use of corrosion and erosion protection	
External fire		Fire protection	
Leakage or opening at operating pressure or temperature	• Failure of interlock, mechanical failure of pressure vessel, • Operating error	• Use of reliable interlocks • Use of containment vessels • Regular training of staff	

Some protection measures and monitoring possibilities are given, oriented and supplemented according to the *EU Pressure Equipment Directive* [2]

3.3 Summary

The development and construction of high-pressure/high-temperature autoclaves for ammonothermal synthesis is subject to compliance with regulations (e.g. the ASME *Boiler and Pressure Vessel code* [1] in the US or the *Pressure Equipment Directive* [2] in the EU) and the effect of a number of influencing parameters. An essential prerequisite is the correct selection of materials, which have high strength, high fracture toughness, an elongation at break greater than 14% and at the same time have a high chemical resistance. For these reasons, only highly developed materials for example Ni-base, Co-base, or Mo-base superalloys are used.

Another important aspect are the seals. In the case of ammonothermal process parameters, those can only be manufactured from metallic materials and must therefore be plasticized in order to achieve a reliable and safe sealing. There are various types of seals for high pressure such as *Bridgeman* seal, sealing lenses or the C-ring seal. The C-ring seal shows good potential for high pressure and temperature as it is ideally supported by pressure, easy to exchange and can be combined well with all types of closure systems. Additionally protective coatings can be easily applied.

When handling high pressure/high temperature equipment, which may also contain hazardous substances, it is essential to develop a safety philosophy and strategy. Only when these have been worked out, should the ammonothermal process be put into operation.

References

1. The American Society Mechanical Engineers, *ASME Boiler and Pressure Vessel Code* (USA, 2019)
2. European Parliament, Council of 15 May 2014, *Pressure Equipment Directive* (European Union, 2014)
3. C. Wegst, *Stahlschlüssel*, 25th edn. (Verlag Stahlschlüssel, Marbach, 2019)
4. E. Roos, K. Maile, M. Seidenfuß, *Werkstoffkunde für Ingenieure*, 6th edn. (Springer Vieweg, Berlin, 2017)
5. R. Bürgel, H.J. Maier, T. Niendorf, *Handbuch Hochtemperatur-Werkstofftechnik* (Vieweg+Teubner, 2011)
6. R.C. Reed, *The Superalloys Fundamentals and Applications* (Cambridge University Press, 2006)
7. I.A. Choudhury, M.A. El-Baradie, Machinability of nickel-base super alloys: a general review. J. Mater. Process. Technol. **300**, 278–284 (1998)
8. C. Slama, M. Abdellaoui, Structural characterization of the aged Inconel 718. J. Alloys Compd. **306**, 277–284 (2000)
9. T. Chen, H. John, J. Xu, Q. Lu, J. Hawk, X. Liu, Influence of surface modifications on pitting corrosion behavior of nickel-base alloy 718. Part 1: effect of machine hammer peening. Corros. Sci. **77**, 230–245 (2013)
10. K. Yoshida, K. Aoki, T. Fukuda, High-temperature acidic ammonothermal method for GaN crystal growth. J. Cryst. Growth **393**, 93–97 (2014)
11. S. Pimputkar, S. Kawabata, J.S. Speck, S. Nakamura, Surface morphology study of basic ammonothermal GaN grown on non-polar GaN seed crystals of varying surface orientations from m-plane to a-plane. J. Cryst. Growth **368**, 67–71 (2013)

12. S. Pimputkar, T.F. Malkowski, S. Griffiths, A. Espenlaub, S. Suihkonen, J.S. Speck, S. Nakamura, Stability of materials in supercritical ammonia solutions. J. Supercrit. Fluids **110**, 193–229 (2016)
13. D. Tomida, K. Kuroda, N. Hoshino, K. Suzuki, Y. Kagamitani, T. Ishiguro, T. Fukuda, C. Yokoyama, Solubility of GaN in supercritical ammonia with ammonium chloride as a mineralizer. J. Cryst. Growth **312**, 3161–3164 (2010)
14. N.S.A. Alt, E. Meissner, E. Schlücker, L. Frey, In situ monitoring technologies for ammonthermal reactors. Phys. Status Solidi **9**, 436–439 (2012)
15. J. Häusler, L. Neudert, M. Mallmann, R. Niklaus, A.C.L. Kimmel, N.S.A. Alt, E. Schlücker, O. Oeckler, W. Schnick, Ammonothermal synthesis of novel nitrides: case study on $CaGaSiN_3$. Chem. A Eur. J. **23**, 2583–2590 (2017)
16. J. Sato, T. Omori, K. Oikawa, I. Ohnuma, R. Kainuma, K. Ishida, Cobalt-base high-temperature alloys. Science **312**, 90–91 (2006)
17. T.M. Pollock, J. Dibbern, M. Tsunekane, J. Zhu, A. Suzuki, New Co-based γ-γ' high-temperature alloys. J. Miner. **62**, 58–63 (2010)
18. A. Bauer, S. Neumeier, F. Pyczak, M. Göken, Microstructure and creep strength of different γ/γ'-strengthened Co-base superalloy variants. Scr. Mater. **63**, 1197–1200 (2010)
19. S. Neumeier, L.P. Freund, M. Göken, Novel wrought γ/γ' cobalt base superalloys with high strength and improved oxidation resistance. Scr. Mater. **109**, 104–107 (2015)
20. H.-Y. Yan, V.A. Vorontsov, D. Dye, Effect of alloying on the oxidation behaviour of Co–Al–W superalloys. Corros. Sci. **83**, 382–395 (2014)
21. L.P. Freund, S. Giese, D. Schwimmer, H.W. Höppel, S. Neumeier, M. Göken, High temperature properties and fatigue strength of novel wrought γ/γ' Co-base superalloys. J. Mater. Res. **32**, 4475–4482 (2017)
22. M. Kolb, L.P. Freund, F. Fischer, I. Povstugar, S.K. Makineni, B. Gault, D. Raabe, J. Müller, E. Spiecker, S. Neumeier, M. Göken, On the grain boundary strengthening effect of boron in γ/γ' Cobalt-base superalloys. Acta Mater. **145**, 247–254 (2018)
23. L.P. Freund, A. Stark, F. Pyczak, N. Schell, M. Göken, S. Neumeier, The grain boundary pinning effect of the μ phase in an advanced polycrystalline γ/γ' Co-base superalloy. J. Alloys Compd. **753**, 333–342 (2018)
24. T.F. Malkowski, S. Pimputkar, J.S. Speck, S.P. DenBaars, S. Nakamura, Acidic ammonothermal growth of gallium nitride in a liner-free molybdenum alloy autoclave. J. Cryst. Growth **456**, 21–26 (2016)
25. B.V. Cockeram, The mechanical properties and fracture mechanisms of wrought low carbon arc cast (LCAC), molybdenum-0.5pct titanium-0.1pct zirconium (TZM), and oxide dispersion strengthened (ODS) molybdenum flat products. Mater. Sci. Eng. A **418**, 120–136 (2006)
26. B.V. Cockeram, Measuring the fracture toughness of molybdenum-0.5 pct titanium-0.1 pct zirconium and oxide dispersion-strengthened molybdenum alloys using standard and subsized bend specimens. Metall. Mater. Trans. A Phys. Metall. Mater. Sci. **33**, 3685–3707 (2002)
27. K. Löhnert, *Dissertation: Einfluss der thermomechanischen Vorbehandlung auf die Eigenschaften der Nickelbasissuperlegierung A718Plus* (Friedrich-Alexander-Universität Erlangen-Nürnberg, 2011)
28. Haynes® International Inc, *Haynes®282®Alloy, Datasheet* (2006)
29. A.-C.L. Kimmel, T.F. Malkowski, S. Griffiths, T.G. Steigerwald, L.P. Freund, S. Neumeier, M. Göken, J.S. Speck, E. Schluecker, High-temperature corrosion of Inconel®Alloy 718, Haynes®282®Alloy and CoWAlloy1&2 in supercritical ammonia/ammonium chloride solution. J. Cryst. Growth **498**, 289–300 (2018)
30. Plansee, *Molybdenum* (2017). https://www.plansee.com/en/materials/molybdenum.html. Accessed 25 October 2017
31. D.W. Williams, Externally heated cold-seal pressure vessels for use to 1200° C at 1000 bars. Mineral. Mag. J. Mineral. Soc. **35**, 1003–1012 (1966)
32. A. Lindoo, J.F. Larsen, K.V. Cashman, A.L. Dunn, O.K. Neill, An experimental study of permeability development as a function of crystal-free melt viscosity. Earth Planet. Sci. Lett. **435**, 45–54 (2016)

33. VDM-Metals, *VDM Alloy 718, Datasheet* (2016)
34. Haynes® International Inc., *HAYNES® 282® alloy, Datasheet* (2017)
35. H. Buchter, *Apparate und Armaturen der chemischen Hochdrucktechnik, Konstruktion, Berechnung und Herstellung* (Springer, Berlin, 1967)
36. L. Issler, H. Ruoß, P. Häfele, *Festigkeitslehre-Grundlagen*, 2nd edn. (Springer, Berlin, 2006)
37. Holzmann, Meyer, Schumpich, H. Altenbach, *Technische Mechanik 3: Festigkeitslehre*, 11th edn. (Teubner, Stuttgart, 2014)
38. N.S.A. Alt, *Dissertation: Entwicklung spezieller Hochdruckapparate und Methoden zur Durchführung von in-situ Messungen beim ammonothermalen Prozess* (Friedrich-Alexander-Universität Erlangen-Nürnberg, 2010)

Part II
Technology of Ammonothermal Synthesis

Chapter 4
Technical Solutions for In Situ Monitoring of Ammonothermal Processes

Eberhard Schlücker

Abstract Due to the thick-walled autoclaves, the ammonothermal system has long been regarded as a black box and the crystal quality was only improved through systematic, time-consuming experiments [1]. One of the main goals therefore was to bring "light into the dark" with new window design for the extreme process parameters of larger than 650 °C and simultaneously 300 MPa.

4.1 Dimensioning Sight Glasses

The material selection for the viewing windows depends first on the spectral transmission range. If suitable materials are found for the expected wavelengths, the suitability must be examined with regard to their mechanical strength properties. The bending strength R_b, compressive strength R_d and Poisson's ratio μ are particularly important for this. Last but not least, the chemical resistance of the material to the fluid used must be tested. The most important properties of various window materials for high-pressure technology are shown in Table 4.1 Depending on the material quality and the manufacturing process, there may be minor deviations from the stated values.

Based on this table it is not difficult to select the best material. The first choice is sapphire glass! It has a high mechanical stability, a high thermal stability and also a good chemical resistance, but has, typical for such glass, brittle properties. When brittle parts should be clamped in-between metal parts, we should accept only compression stress and avoid any tensile stress. And even when optical monitoring goals should be fulfilled, the optic properties should stay in a good quality, which means no remarkable bendings. Figure 4.1 shows three types of clamped sight glasses.

In the design of the counterforce or squeezer type (a), the sealing force must be applied via an external force. This means that the sealing force is at its greatest at the

E. Schlücker (✉)
Chair of Process Machinery and Systems Engineering, Friedrich-Alexander-University of Erlangen Nuremberg (FAU), Erlangen, Germany
e-mail: sl@ipat.uni-erlangen.de

E. Meissner and R. Niewa (eds.), *Ammonothermal Synthesis and Crystal Growth of Nitrides*, Springer Series in Materials Science 304,
https://doi.org/10.1007/978-3-030-56305-9_4

Table 4.1 Strength and transmission properties of different window glasses [2]

Properties	Borosilicate glass	Quartz glass	Sapphire glass
Bending strength R_b (N/mm^2)	160	80–100	420
Compression strength R_d (N/mm^2)	100–140	1250	2000
Poisson number μ (–)	0.2	0.170	0.25–0.30
Transmission range (nm)	350–2500	180–2500	170–5500

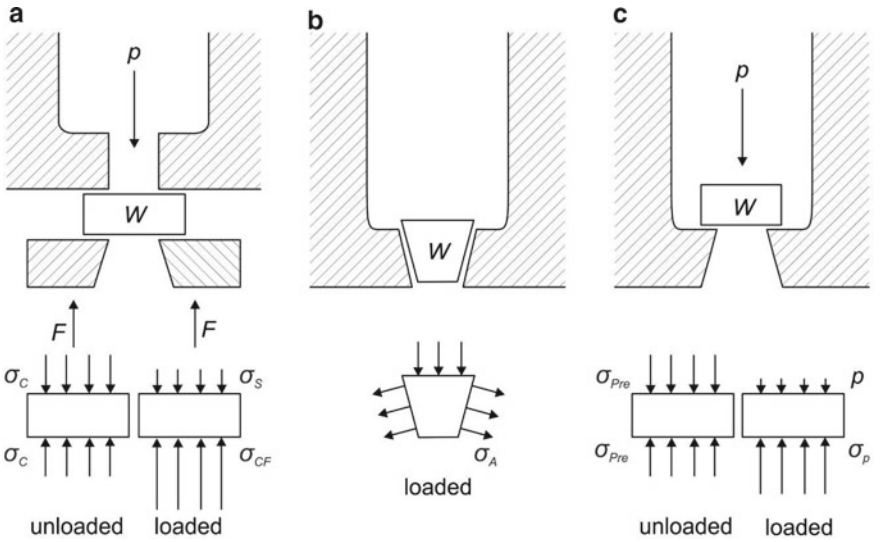

Fig. 4.1 Variants of sight glass clamping: **a** counterforce type, **b** amagat type and **c** poulter type [2], real design see Fig. 4.5: σ_C = clamping stress; σ_S = minimal sealing stress; σ_{CF} = counter force stress; σ_A = amagat stress, should be equal to σ_C; σ_{pre} = preload stress; σ_P = poulter stress (smaller than σ_{CF})

upper side in the unpressurized state. The reason for this is that the internal pressure relieves this point again and it must still be tight. At the same time, it should be noted when designing that the force at the clamping surface is particularly high in a pressurized case, as the preload force and the compressive force add up at this point. For these reasons, this type is more suitable for viewing windows with small clear widths.

The Amagat type places very high demands on the parallelism of the conical sealing surfaces. Even with the ideal shape of the window, inhomogeneity's occur in the contact pressure. This effect is further intensified by the different thermal expansion of the materials and the deformation of the container when the internal pressure is applied. All in all, many window materials are not particularly suitable for use in this type, as this inhomogeneous stress distribution quickly causes the compressive strength of the window material to be exceeded, resulting in breakage.

Due to the larger contact surface, however, better results are obtained when using Poulter-type viewing windows. These are therefore used in most applications [2].

4.2 Dimensioning a Poulter Type Window

For the design of cylindrical viewing windows, various calculation equations for the window thickness T_F can be found in the literature. Equations (4.1) and (4.2) are taken from the calculation bases of a sapphire glass manufacturer, (4.3) and (4.4) are taken from the literature [3]. The basic material parameter here is the bending strength R_b of the glass.

$$T_F = d_{Fi} \cdot K \cdot \sqrt{p} \tag{4.1}$$

$$K = \sqrt{\frac{3}{32} \cdot (3 + \mu) \cdot \frac{S}{R_b}} \tag{4.2}$$

$$T_F = \frac{p \cdot S \cdot d_{Fi}}{4 \cdot R_b} \tag{4.3}$$

$$T_F = \sqrt{\frac{1.1 \cdot p \cdot d_{Fi}^2 \cdot S}{4 \cdot R_b}} \tag{4.4}$$

The basic dimensions for calculating the thickness of the viewing window are shown in Fig. 4.2.

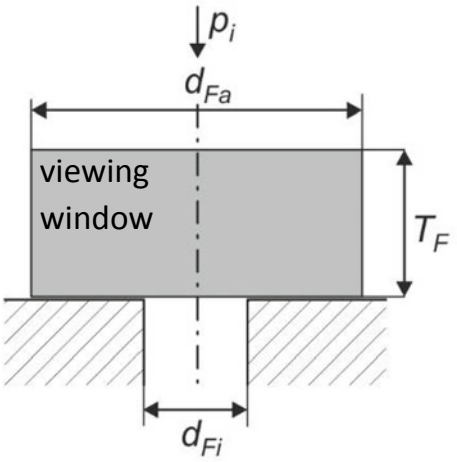

Fig. 4.2 Dimensions of the viewing window for window thickness calculation viewing window

$$p_{\text{seal}} = p_i \cdot \frac{D^2}{D^2 - d^2} \tag{4.5}$$

A safety factor $S = 5$ is usually used to calculate the window thickness [4]. The diameter of the window d_{Fa} results from the required overpressure on the sealing surface. It can also be calculated according to the equation for a gasket according to the unsupported area principle (see 4.5). An overpressure of at least 15% should be achieved on the sealing surface, which corresponds to a diameter ratio d_{Fa} to d_{Fi} of 2.77:1. If a lower ratio is selected, the overpressure at the sealing surface increases. The minimum outer diameter d_{Fa} should not be less than the value determined according to (4.6). The overpressure in the sealing surface is then about 41.4% [2].

$$d_{\text{Fa}} = \sqrt{2} \cdot d_{\text{Fi}}. \tag{4.6}$$

4.3 Construction of Inspection Windows

In the design and manufacture of high-pressure inspection windows, particular importance is to be given to manufacturing tolerances and surface quality. There must be no sharp edges on the contact surfaces between glass and metal. Instead, radii must be provided at the edges. The sealing surfaces must be parallel, absolutely flat and provided with an optical polish. This is the only way to achieve an optimum distribution of forces and a functioning seal. The metallic sealing surface must be manufactured in such a way that the glass protrudes slightly so that it is not pressed into the sealing surface and stress peaks form. If necessary, a coating of the metallic sealing surface with a soft metal is required in order to compensate for low roughness depths of the glass and metal surface by plastifying it. Particularly with low-viscosity media such as gases and supercritical fluids, the slightest unevenness is sufficient to cause leaks. In addition, attention should be paid to the parallelism of the window surfaces, the orientation along the crystallographic axis and the crystal quality of the window material. The edges of the window should at least have a small bevel, as it is difficult to produce defined radii.

In order to achieve an efficient seal, the window glass must be pre-stressed. This is the only way to ensure an initial seal at a low process pressure. When mounting and applying the prestress, however, the sealing surfaces must not be twisted against each other (i.e. no rotating cover attachment), as otherwise unevenness and scratches can occur which lead to stress peaks in the glass and consequently to breakage [2].

A problem is that under the compression of steel and glass can easily generate the compressive stress necessary for sealing, but the glass bends slightly under compressive stress and the pressure loading, which would already result in a notch effect from

the upper steel surface. For this reason, we need a sealing material that is capable of smoothing such effects. This material should plasticize much better than steel and of course glass. Also it should be able to follow smalls deflection due pressure loadings but should still have enough strength to be not extruded completely. Copper, silver or gold are materials with which good experiences have been made. The greatest success, however, was the use of a very thin layer of gold on both steel surfaces. The layer was thick enough to perfectly cover the coarseness and also to avoid notch effects.

4.4 Dimensions of an Inspecting Window

Due to its excellent mechanical properties, sapphire is suitable for use under the required operating conditions. At the same time, the transmission range is larger than that of borosilicate and quartz glass, allowing more flexible use. However, the determination of strength values at elevated temperatures is problematic, as these are usually only given for room temperature in the literature and by the manufacturers. Furthermore, several different formulas are available for design. For this reason, the dimensions of sapphire glass are determined conservatively by determining the corresponding extreme value. Figure 4.3 shows the values for bending strength as a function of temperature. The diagram shows the determined values for two different specimens (round disc and rectangular plate) with orientation along the crystallographic *c*- and *a*-axis. For reasons of conservative design, the smallest value from the diagram is selected for the bending strength. The temperature-dependent representation of the compressive strength is shown in Fig. 4.3.

At a temperature of 650 °C, the data can be used to determine the minimum value of the bending strength of sapphire to 317 N/mm^2 along the *c*-axis and to 414 N/mm^2 along the *a*-axis. The clear width of the window should be 6 mm, since endoscopes and detectors are available for this diameter. Since the glass deflects during operation at the unsupported point of the window in the area of the hole in the window holder, a

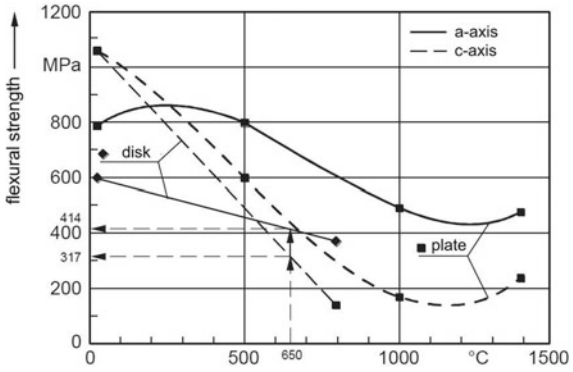

Fig. 4.3 Flexural strength of sapphire as a function of temperature [8]

Table 4.2 Result of the calculation the thickness of an inspection window

Orientation sapphire *a*-axis		*a*-axis	*c*-axis
Window thickness according to Bieg	Equations (4.1), (4.2)	7.21	8.24
Window thickness according to Robertson	Equation (4.3)	6.48	8.46
Window thickness according to Whyman	Equation (4.4)	6.8	7.78
Surcharge for the bevel		1	1
Thickness including the champfer		8.21	9.46

small radius must be provided at the edge. Thus the sapphire does not press on a sharp edge. This results in a slightly larger unsupported diameter of 6.5 mm, which is used for the calculation. The Poisson's ratio is given as 0.29 in the literature. As mentioned, a safety factor of $S = 5$ is used. For the calculation pressure of 330 MPa, the window thickness is calculated according to the (4.4)–(4.5) according to Table 4.2. Due to the conservative design, the minimum window thickness results from the maximum of the three determined values plus a chamfer of 1 mm. Thus the minimum window thickness along the *a*-axis is 8.21 mm, along the *c*-axis 9.46 mm. As a result, a thickness of 10 mm was selected.

The minimum outside diameter is calculated according to (4.5) to 9.19 mm and should not exceed 18 mm. For the final determination of the outer diameter, the surface pressure between glass and metal must still be checked on the basis of the occurring stress and the compressive strength. This can be determined by interpolation according to Fig. 4.4.

The compressive strength of sapphire along the c-axis decreases sharply with temperature, so that at 650 °C only a value of 412 N/mm^2 is determined. Along the crystallographic *a*-axis, a significantly lower decrease can be observed, resulting in a significantly higher compressive strength of 1662 N/mm^2.

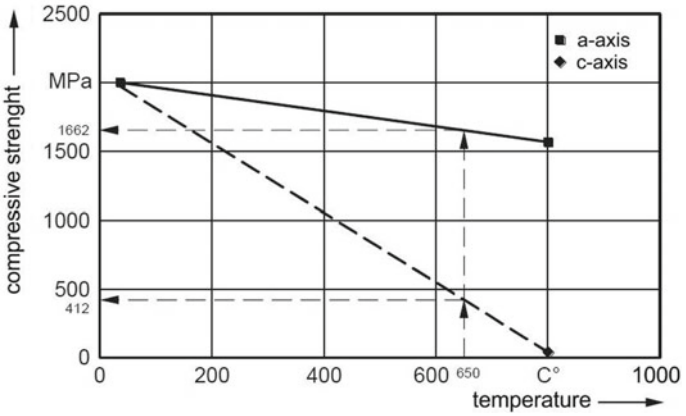

Fig. 4.4 Compression strength of Sapphire depending on temperature

Table 4.3 Specifications for a sapphire sight glass

Outer diameter d_{Fa}	12 mm
Thickness of the window h_F	10 mm
Bevel	1 mm × 45° und 0.1 mm × 45°
Orientation	*a*-axis along the cylindrical axis
Surface quality	S/D 40/20
Flatness	1 Lambda
Quality	Stress free tempered
State	Sapphire grade 1

A comparison of the pressure acting on the sealing surface with the strength shows that sapphire in the *c*-direction at 650 °C does not have sufficient strength. If necessary, sufficient strength is given with a safety of 1.4 at 600 °C and an outer diameter of 18 mm. Since this low safety level is unsuitable for a brittle material such as sapphire, the axis of the sapphire glass must be oriented along the *a*-axis. With an outer diameter of 12 mm, the safety against overloading at design conditions above 3.5 is provided. This results in the specification of the viewing window according to Table 4.3.

In addition, it is of great importance that the viewing window is tempered without tension after machining.

4.5 Construction of the Window Unit

As already described, the window unit is based on the Bridgman sealing stamp. This is additionally provided with a hole and a shoulder with an external thread, in order to apply the necessary pretension via a window holder for the construction of an initial seal between glass and metal. Figure 4.5 shows a sectional drawing of the window unit (a) and a detailed section in the area of the sealing surface (b).

An important criterion in the production of the individual components of the window unit is that they are aligned completely parallel to each other, otherwise uneven force application and glass breakage will occur. The sealing surface on the metal stamp must have an absolutely flat, smoothly polished surface, otherwise no sealing of gases and supercritical fluids is possible. In addition, there is a thin galvanically applied gold layer on the surface. This significantly improves the sealing by plastically compensating for the slightest unevenness.

For the reasons already mentioned (see Chap. 3), the window unit must be mounted without twisting, otherwise the surfaces in the area of the seal may be damaged. For this purpose, the glass is pressed onto the metal stamp with a hydraulic ram and only then is the window holder firmly screwed into place. After the hydraulic plunger has been released, a pre-tensioning force is maintained which guarantees a seal at

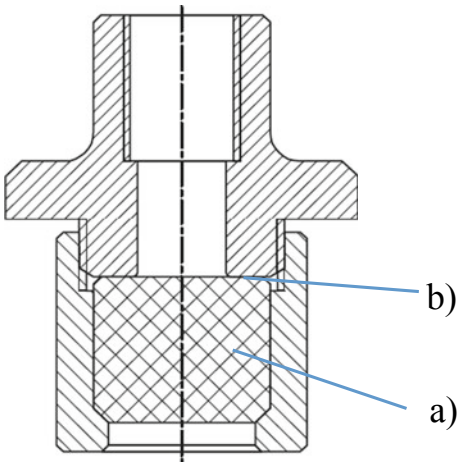

Fig. 4.5 Cross section drawing of the window unit: **a** glass part, **b** sealing surface

the beginning. This does not have to be very large, as the seal is self-sealing during operation (Figs. 4.6 and 4.7).

Finally, the assembled viewing cell is shown in a sectional view in Fig. 4.8. Inside the sighting cell a metallic crucible is visible in which the solid educts can be placed. A light beam is stylized in red.

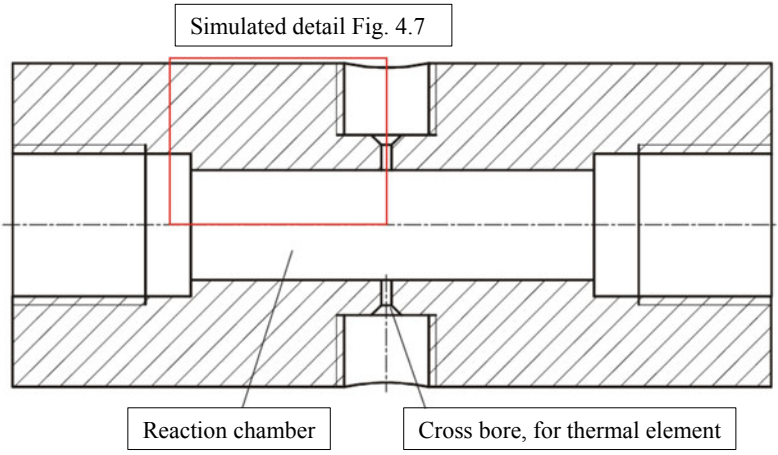

Fig. 4.6 Autoclave core part

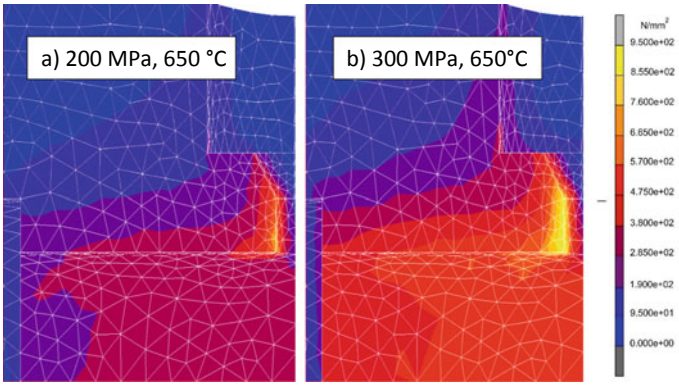

Fig. 4.7 Result of an FEM-Simulation; van Mises equilibrium stress 200 MPa (**a**) and 300 MPa (**b**) and a heating temperature of 650 °C in a detail (**a**) of the glass window

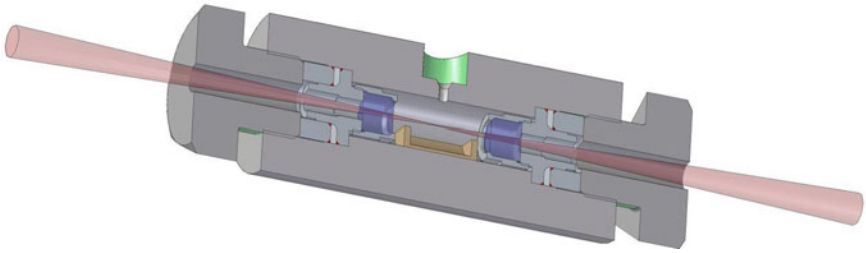

Fig. 4.8 Autoclave with glass Windows to be used up to 300 MPa and 650 °C simultaneously [1]

4.6 UV-VIS Spectroscopy

With the help of spectroscopic measurements on the autoclave in Fig. 4.8, the general feasibility of spectroscopic investigations in the ultraviolet (UV) and visible to near-infrared range is to be demonstrated. In these experiments, a deuterium lamp (Heraeus Noblelight DO 520) was used, since the emission of conventional halogen lamps in the UV range is not sufficient. This is positioned directly in front of the viewing cell. To detect the transmitted light, a glass fiber probe is installed on the opposite side, which transmits the received light to the UV-Vis spectrometer (Avantes Avaspec 2048-2) for analysis. The determined spectra are constantly updated and displayed on the screen. The data is stored by manual activation in the software. The stored spectra were evaluated with the help of signal acquisition software. By comparing the determined spectra, changes in the system can be evaluated depending on the process variables pressure and temperature.

For the investigations the starting materials are presented and then heat is supplied to the system via heating sleeves. In order to keep the experiments comparable, identical boundary conditions have been selected. Within the scope of these investigations, an ammonothermal system consisting of ammonia, the mineraliser ammonium chloride and gallium nitride was investigated. So-called counts are used as units of measurement for the measurements carried out. This term refers to the number of photons detected per wavelength after the light passes through the sight cell. The increase in pressure and temperature is achieved solely by adding heat to the closed system.

Starting from the ambient temperature, there are hardly any changes in the wavelength spectrum at the beginning, so that the black curve for 285 °C in Fig. 4.9 can be regarded as representative of the recorded spectra up to this temperature. At the same time, these data serve as a basis for comparison with other measurements. From a temperature of about 300 °C a continuous decrease of the measured light intensity can be observed. The reduction takes place relatively quickly in the low wavelength range (UV and blue) and to a greater extent relative to the other ranges. The behaviour is therefore analogous to that of video-optical investigations. The assumption that absorption takes place in the low wavelength range is confirmed. However, the reduction of the light intensity occurs much earlier than optically determined (observation). The decrease of the intensity of the detected, transmitted light decreases further with increasing temperature, until at a temperature in the range of 400–410 °C hardly any light is emitted through the sight cell.

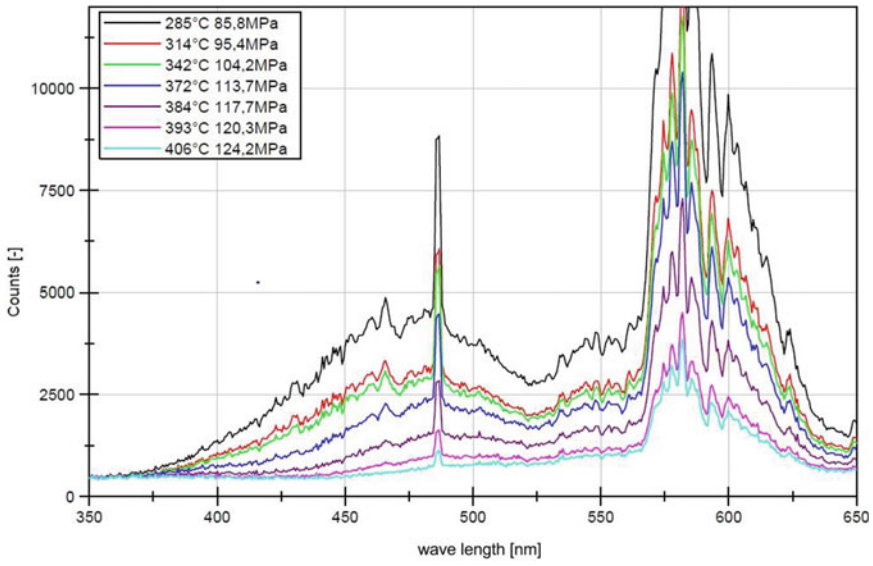

Fig. 4.9 Change of spectrum of light intensity (counts vs. wavelength in [nm]) with simultaneous change of temperature and pressure in the autoclave from 285 °C to 406 °C and 85.8 MPa to 124.2 MPa [1]

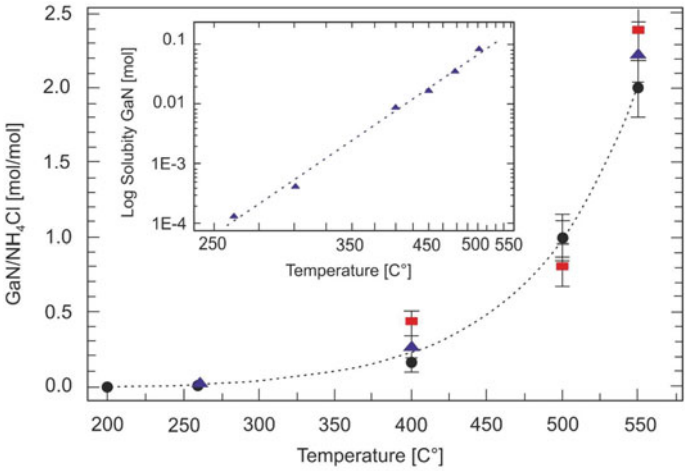

Fig. 4.10 Progression of the solubility of an NH_4Cl/GaN mixture in ammonia, solubility of GaN is shown for three different molar ratios of GaN and NH4Cl: 0.0127 (red square), 0.032 (black up-pointing triangle), and 0.127 (black square). The exponential fit is made to the latter curve. The inset shows the Arrhenius plot drawn for the molar ratio of 0.032 [9]

With a further temperature increase, the minimum light transmission is finally reached at a temperature of approx. 540 °C. This is the minimum temperature at which the light can pass through the light source.

Figure 4.9 shows, as the first result, clear influences of the parameter change on the spectrum signal. The measured radiation reduction also shows a similarity to the solubility behaviour of GaN in a supercritical ammonia solution containing NH_4Cl, as can be seen Fig. 4.10 in the solution course of the NH_4Cl/GaN mixtures. From 300 °C the solubility increases there. It can therefore be concluded that an intermediate formation is responsible, which subsequently changes at higher temperatures and becomes more permeable at higher wavelengths!

Through further test series, with an additional use of UV/Vis-spectroscopy, the decomposition of sodium azide and subsequent formation of sodium amide above 300 °C was observed. This showed that at first only the decomposition of the azide takes place and the formation of amide is either slower or results from a further increase in temperature. During the decomposition of sodium azide, no increase in absorption in the long wavelength range was observed in the UV/Vis-spectra. However, the experiments to detect intermediates of GaN and sodium amide have not been successful so far. As also shown in preliminary tests of in liquid ammonia, $[Ga(NH_2)_4]^-$, with the characteristic peak at 500 cm^{-1} in the fingerprint range, is one of the alkali-based species with very low Raman activity. Due to this and the very low mass loss of only one weight percent of the precursor crystals, it is probable that the detection limit has not been reached yet. Further alkali compounds promise a higher potential, e.g. cesium amide has proven to be a promising candidate. The cesium amide synthesized was heated under ammonia atmosphere in the optical

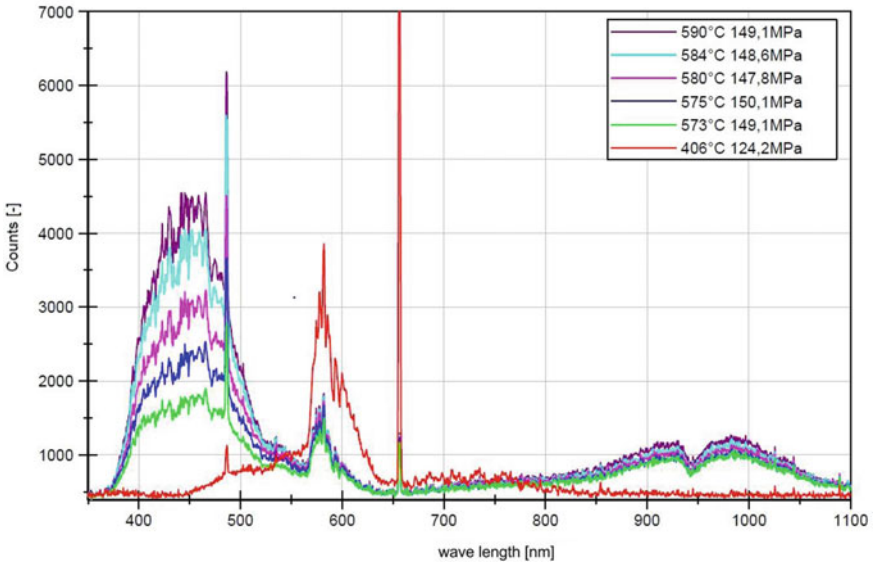

Fig. 4.11 Change of spectrum of light intensity (counts vs. wavelength in nm) with simultaneous change of temperature and pressure in the autoclave from 406 °C to 590 °C and 124.2 MPa to 149.1 MPa [1]

cell. The imaging procedures have shown the presence of a second insoluble liquid phase up to approx. 400 °C, which only disappears when temperature rises further and is accompanied by a subsequent color shift from yellowish to reddish-brown up to approx. 550 °C. However, the evaluation of the spectra is still under evaluation (Fig. 4.11).

4.7 Raman Spectrocopy

Pimputkar et al. [5] were able to estimate the influence on the decomposition of ammonia under ammonothermal conditions using a modelling approach. These predictions were checked experimentally via Raman spectroscopy, by comparing the characteristic peaks of NH_3 at 3300 cm^{-1}, N_2 at 2330 cm^{-1} and H_2 at 4153 cm^{-1}. Using a system of pump, compressor and storage tanks, mixtures of pure ammonia and nitrogen with mole fractions between $x_{NH_3} = 0.25$ to 0.75 were set and analyzed. To exclude the influence of the fluctuating absolute intensity of the laser power and to compare measurements at different pressures, the intensity ratio $R(NH_3)$ was introduced, in which the area integrals under the respective peaks are related to each other. The dependencies between intensity ratio and mixture showed that the ammonia-nitrogen composition can be investigated during ammonothermal synthesis. This allows further experiments to study the decomposition of ammonia and mixtures of

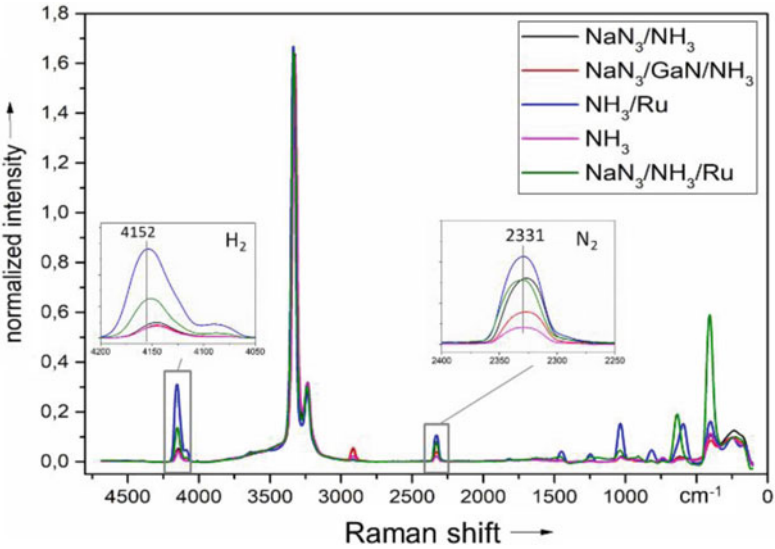

Fig. 4.12 Raman spectra of ammonia and ammonothermal mixtures after 100 h at process conditions of: ultimate temperature: 530–550 °C, ultimate pressure: 110–230 MPa

ammonia and nitrogen at temperatures above 400 °C. Figure 4.12 shows the influence of ruthenium catalysts, mineralizers (here NaN_3) and gallium nitride on ammonia decomposition after 100 h at ultimate process conditions. The catalytic limitation of decomposition was discussed, as the signal intensity was increased by the addition of highly active catalysts. In comparison with [2] this leads to the assumption of a kinetic limitation of the ammonia decomposition in our setup.

Such information, generated with Raman Spectroscopy and the transparent autoclave, is important not only for ammonothermal synthesis, but also for other chemical processes. Thus, ammonia offers the possibility of acting as an energy storage through the three bound hydrogen atoms [5], which makes it necessary to expand the known data on the decomposition kinetics towards higher temperatures.

Figure 4.13 shows Raman spectra of an experiment with pure ammonia, which is used as an example for ammonia decomposition. For this test, a low density of only 8.69 mol/l was chosen. Although higher densities are used in ammonothermal crystal growth, the pressure and thus also the density, as shown in Fig. 4.13, have a great influence on the equilibrium position of the decomposition reaction of NH_3. The concentration of NH_3 is described by:

$$x_{NH_3} = \frac{n_{NH_3}}{n_{NH_3} + n_{N_2} + n_{H_2}} \tag{4.7}$$

In this example at pressures of about 70.0 MPa and a temperature of 563 °C accordingly to experimental data of [6] and the calculated values of [5] the concentration at equilibrium should roughly be between 0.3 and 0.4. In order to make the spectra

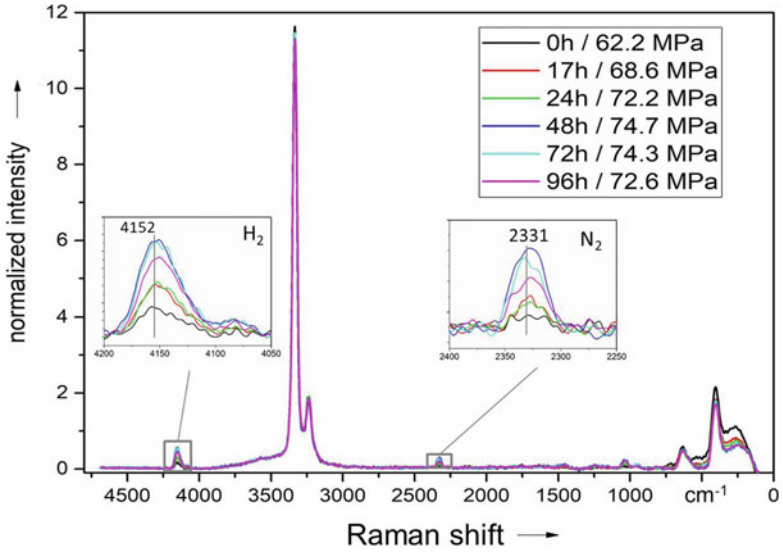

Fig. 4.13 Raman spectra of ammonia; filling density $\rho_{NH3} = 8.69$ mol/l; $T_{max} = 563$ °C; $P_{max} = 74.7$ MPa; duration 96 h Measuring parameters: $P_{Laser} = 2000$ mW; integration time 100 ms; 1 measurement; normalized to NH_3 signal [10]

more comparable with those of other experiments, the spectra were normalized to the ammonia signal. Figure 4.13 shows spectra recorded after reaching maximum temperature of 563 °C. The peaks of ammonia, nitrogen and hydrogen are localized at the expected wavenumber, but the peaks of hydrogen and nitrogen have a low signal to noise ratio, due to short integration time. The ratio according (4.1) and (4.2) are presented in Table 4.3. The first measurement at 563 °C shows a very low N_2 signal at 2331 cm^{-1} and only a very weakly formed H_2 peak at 4154 cm^{-1}. After 24 h the peaks develop stronger, reaching their maximum value after 48 h. The spectra recorded after 48 h and 72 h are quite similar, indicating that the decomposition will succumb at this time. This observation of the decomposition of NH_3 is also described by an increase in pressure from 62.2 to 74.7 MPa.

$$R\left(\frac{N_2}{H_2}\right) = \frac{I_{N_2}}{I_{H_2}} \sim \frac{N_{N_2}}{N_{H_2}} \tag{4.8}$$

where R is the proportionality of the Raman intensity I to the number of molecules N_2. Furthermore, the intensity ratio $R(NH_3)$ according to the mole fraction of ammonia is described in (4.9):

$$R_{NH_3} = \frac{I_{NH_3}}{I_{N_2} + I_{H_2} + I_{NH_3}} \tag{4.9}$$

These examples show that Raman spectroscopy in combination with the window technique for ammonothermal crystallization processes offers many possibilities for new insights.

4.8 Monitoring with X-rays

Another possibility of in situ monitoring is the use of X-rays for the analysis of the absorption contrast of different materials and the resulting observation of the size development of crystals. Chapter 10 deals with the measurement results in detail, so that only the technological requirements are discussed here.

In contrast to the UV-VIS and Raman investigations, the material B_4N is used here as a glass substitute due to the good transferability of X-rays. Thus, volume changes of the crystals can be observed very well. Figure 4.14 shows an example of the stepwise resolution of a GaN crystal. The kinetics determined in this way are important both for the definition of the resolution kinetics and for crystal growth. The investigations were performed in the presence of both ammonobasic and ammonoacid mineralizers (NaN_3, NH_4F and NH_4Cl).

A dissolution process with ammonium fluoride is shown in Fig. 4.15. Experiments with different orientation of the crystal in the autoclave were carried out using the

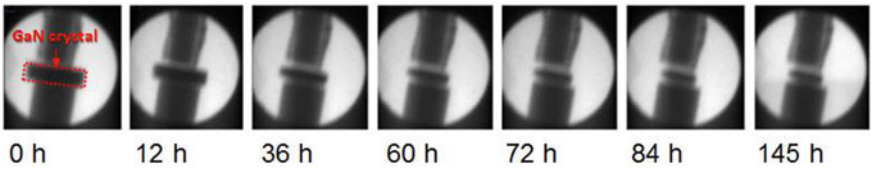

Fig. 4.14 Series of X-rays with an ammonium acidic autoclave content with indication of the current test time [3]

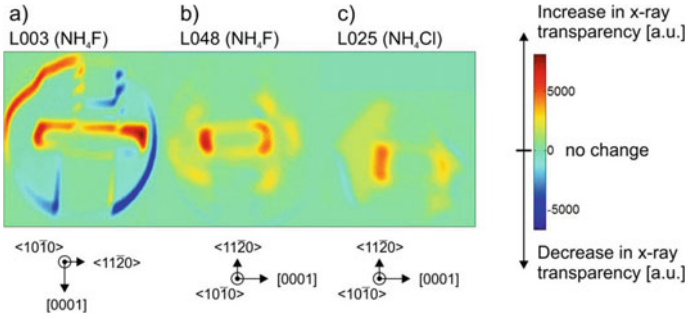

Fig. 4.15 Differential images of the ammonosaur experiments **a** L003, **b** L048 and **c** L025 to visualize the anisotropic resolution of the GaN single crystals (according to [2])

autoclave in Fig. 4.1c with rotatable execution. This shows that a preferred resolution of one side always occurs, so that a dominant effect of convective mass transport on the anisotropy of the etching attack seems unlikely [11, 12].

4.9 Ultra Sonic Monitoring

Another monitoring method that has already been tested is the ultrasonic method, which was used for the first time in this form for [7] and has been proven to work. The idea is based on the fact that each continuum has its own sound velocity. This is a function of compressibility and density (4.10).

$$c_{\text{free}} = \frac{\delta p}{\delta p} \tag{4.10}$$

where is: c_{free} = speed of sound in a free environment or in parts, δp = pressure amplitude, $\delta \rho$ = density amplitude.

But please be careful, (4.10) only applies to the speed of sound, for example in free water or in building components. The speed of sound in fluids is reduced by the elasticity of, for example, pipes or other fluid-bearing components. It is therefore essential that it be measured using simple test equipment. This can be done, for example, by using a closed pipe filled with the correct pressure and at the correct temperature. If structure-borne sound sensors are placed on both end faces and one of the end faces is hit with a small hammer, the transit time of the sound can be measured with the two structure-borne sound sensors. Since we know the running length, the speed is then easy to calculate. The same can be done with hardware components. But then a very high sampling frequency in the range of 100 kHz is necessary.

If an ultrasonic wave is passing through a component and hits a phase boundary at the end, at least part of the wave is reflected and the other part flows over the phase boundary into the following phase. Since we know the speed of sound, we can determine the length of the component from the travel time of the sound wave to the phase boundary and back. If the part of the wave that continued to flow is reflected at another phase boundary, a part of it will flow back and you can see again how thick the second layer was by the running time, the length and the speed of sound. In the same way, the signal can be evaluated in relation to the transmitter at the other side.

For the ammonthermal synthesis, the autoclave shown in Fig. 4.16 on the left was set up (comparable to the autoclave for the ultrasonic viscosity measurement in Chap. 8). The special feature is that two ceramic components are used here as transmitter (1) and receiver (2) (Fig. 4.16). The figure on the right shows the unfiltered and filtered signal. In the filtered signal, the peaks represent the arrival times of the ultrasound at the sensor.

Figure 4.17a shows the change in the speed of sound as a crystal grows, while Fig. 4.17b shows that the method works well. The NIST-data are hit perfectly.

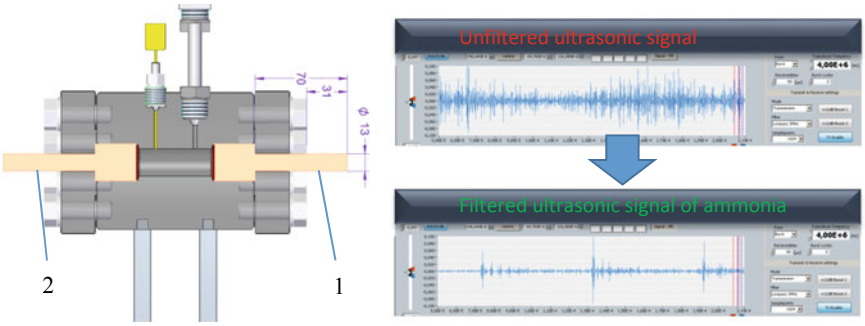

Fig. 4.16 Left: Autoclave for monitoring the autoclave contents with ultrasound: 1 sound input, 2 sound output. Right: The unfiltered and filtered ultrasonic signal

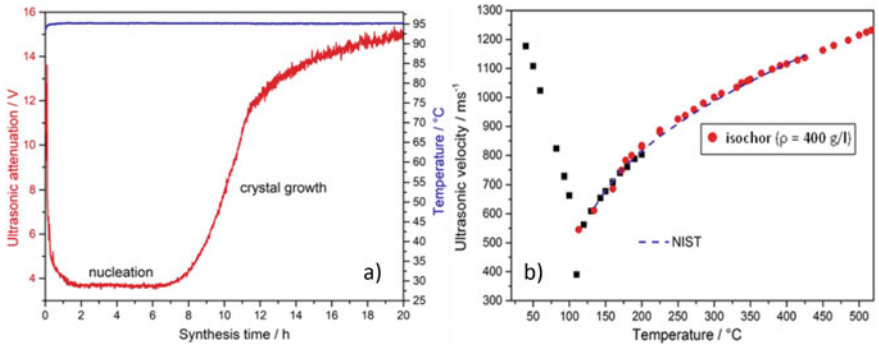

Fig. 4.17 Results out of the test with the autoclave in Fig. 4.16: **a** attenuation of ultrasonic signal: crystal growth in hydrothermal synthesis can be monitored. **b** Ultrasonic measurement established for HP-HT-Applications by use of delay lines based on (NIST data)

In addition, it should be noted that with this method, in a special experiment it was possible to detect that not only gas was in the autoclave but also a layer of liquid. No other monitoring method presented in this chapter was able to do this.

4.10 Summary

For a comprehensive understanding of the procedures in an ammonothermal process, it is essential to look inside the autoclave, respectively to make it "transparent". Alt [1] achieved the first step towards this goal already in 2012 by demonstrating that windows are possible for the critical parameters of the ammonothermal process and that UV-VIS and Raman spectroscopy are extremely useful for obtaining data. In addition, the X-ray method and the ultrasound technique were used. Thus, an

ammonothermal autoclave can now be described as transparent and with the methods presented here it is possible to obtain high-quality results in a comprehensive manner.

References

1. N.S.A. Alt, E. Meissner, E. Schlücker, L. Frey, In situ monitoring technologies for ammonothermal reactors. Phys. Status Solidi **9**, 436–439 (2012)
2. W.F. Sherman, A.A. Stadtmuller, *Experimental Techniques in High-Pressure Research* (Wiley, 1987). ISBN 0-471-10313-6
3. R. Whyman, *Laboratory Methods in Vibrational Spectroscopy*, ed. by H. A. Willis, J. H. van der Maas, R. G. J. Miller, Wiley (1987)
4. DIN 7080:2005-05, Deutsches Institut für Normung e.V. (2005)
5. S. Pimputkar, S. Nakamura, Decomposition of supercritical ammonia and modeling of supercritical ammonia–nitrogen–hydrogen solutions with applicability toward ammonothermal conditions. Supercrit. Fluids **107**, 17–30 (2016)
6. A.T. Larson, The ammonia equilibrium at high pressures. J. Am. Chem. Soc. **46**, 367–372 (1924)
7. H. Baser, W. Schwieger, D. Freitag, T. Steigerwald, E. Schlücker, Solubility studies of sodium azide in liquid ammonia by in situ ultrasonic velocity measurement. Chem. Eng. Technol. **6**, 1101–1106 (2017)
8. MolTech, *Main properties of sapphire* (MolTech GmbH). http://www.mt-berlin.com/frames_cryst/crystals_frameset1.htm (2009)
9. D. Ehrentraut, Y. Kagamitani, C. Yokoyama, T. Fukuda, Physico-chemical features of the acid ammonothermal growth of GaN. J. Cryst. Growth **310**, 891–895 (2008)
10. T. Steigerwald, J. Balouschek, B. Hertweck, A.C. Kimmel, N.S.A. Alt, E. Schluecker, In situ investigation of decomposing ammonia and ammonobasic solutions under supercritical conditions via UV/vis and Raman Spectroscopy. J. Supercrit. Fluids **134**, 96–105 (2018)
11. S. Schimmel, P. Duchstein, T. Steigerwald, A.C. Kimmel, E. Schlücker, D. Zahn, R. Niewa, P. Wellmann, In situ X-ray monitoring of transport and chemistry of Ga-containing intermediates under ammonothermal growth conditions of GaN. J. Cryst. Growth **498**, 214–223 (2018)
12. S. Schimmel, M. Koch, P. Macher, A.C. Kimmel, T. Steigerwald, N. Alt, E. Schlücker, P. Wellmann, Solubility and dissolution kinetics of GaN in supercritical ammonia in presence of ammonoacidic and ammonobasic mineralizers. J. Cryst. Growth **479**, 59–66 (2017)

Chapter 5
Innovative Techniques for Fast Growth and Fabrication of High Purity GaN Single Crystals

Daisuke Tomida, Makoto Saito, Quanxi Bao, Tohru Ishiguro, and Shigefusa F. Chichibu

Abstract The ammonothermal method involves an upper and lower temperature difference that is provided in an autoclave by a baffle plate, and GaN, which is dissolved in supercritical ammonia in the raw material dissolution region and deposited on a seed crystal in the crystal growth region. Because dissolution and deposition can be continuously performed in an autoclave, this is a suitable method for producing large crystals. The growth of bulk GaN single crystals by the ammonothermal method is currently under development and there remain many indeterminate factors. This chapter describes the technological developments to achieve a high-speed growth and high quality of grown crystals.

5.1 Introduction

In the field of power electronics, the development of high-energy devices with low energy loss is one of the ways to reduce the total energy consumption. In addition, high-speed wireless communication systems that transmit large amounts of information are expected to support the future information society by advancing network technology. To realize such a system, a power transistor capable of switching at high frequency is required. Power electronics using GaN may enable the fabrication of high frequency, high-power devices over Si based devices. To make such a device practical for use, a large diameter, high quality and low cost GaN wafer sliced from a large bulk single crystal is required. The ammonothermal method, which is a type of solvothermal method, is one of the most promising methods to make GaN

D. Tomida (✉) · M. Saito · Q. Bao · T. Ishiguro · S. F. Chichibu
Institute of Multidisciplinary Research for Advanced Materials, Tohoku University, Sendai, Japan
e-mail: tomida@imass.nagoya-u.ac.jp

M. Saito
Mitsubishi Chemical Corp, Tokyo, Japan

Q. Bao
Crystal Business Promotion Office, The Japan Steel Works, Ltd., Muroran, Japan

E. Meissner and R. Niewa (eds.), *Ammonothermal Synthesis and Crystal Growth of Nitrides*, Springer Series in Materials Science 304,
https://doi.org/10.1007/978-3-030-56305-9_5

single crystals. Using the pioneering work reported by Dwiliński et al. [1], research aimed at the fabrication of large diameter and high quality GaN single crystals is proceeding. This chapter outlines the ammonothermal method and describes the present condition of the high quality GaN single crystal growth technology using the acidic ammonothermal method.

5.2 Ammonothermal Method

The GaN crystal growth apparatus used in the ammonothermal method is shown in Fig. 5.1 [2]. The ammonothermal method is a method in which an upper and lower temperature difference is provided in an autoclave via a baffle plate and GaN dissolved in supercritical ammonia in a raw material dissolution region, is deposited on a seed crystal in a crystal growth region. Because dissolution and deposition can be continuously performed in an autoclave, this is a suitable method for producing large crystals. In a similar method, there is a good track record for commercial growth of quartz crystals by the hydrothermal method, and it is a method expected to mass produce GaN single crystal. For mass production, the production cost of the GaN

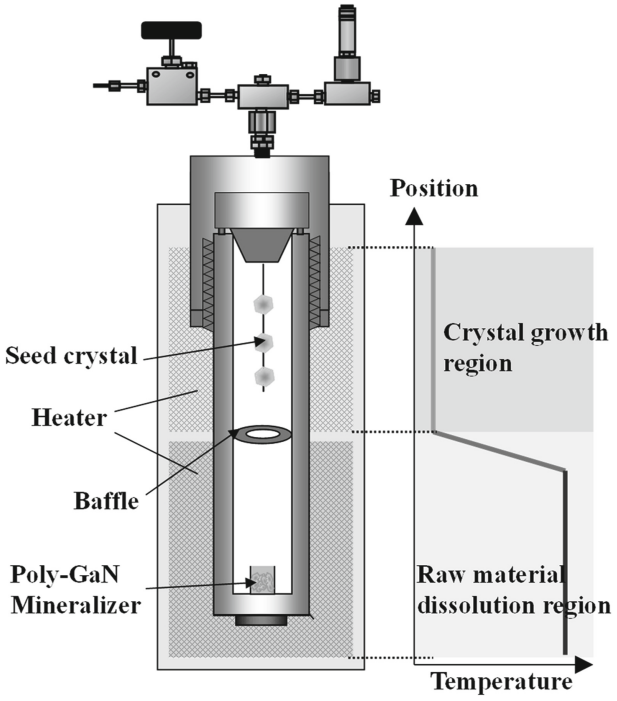

Fig. 5.1 Schematic illustration of the experimental apparatus for growth of GaN crystals [2]

Table 5.1 Main mineralizers used in the ammonothermal method

Acidic mineralizer	NH_4F, NH_4Cl, NH_4Br, NH_4I
Neutral mineralizer	NaI, KI
Basic mineralizer	KNH_2, $NaNH_2$, $LiNH_2$

single crystal is important, and the crystal growth rate becomes important to lower the production cost.

For this method, it is necessary for GaN to be dissolved in supercritical ammonia; however, GaN is hardly dissolvable in supercritical ammonia. Therefore, a mineralizer that promotes dissolution is added. Table 5.1 shows the main mineralizers used in the ammonothermal method. Mineralizers include acidic mineralizers such as ammonium chloride, neutral mineralizers such as sodium iodide, and basic mineralizers such as potassium amide. When dissolving in ammonia, mineralizers that produce ammonium ions are called acidic, those that produce amide ions are basic, and those that produce neither ammonium ions nor amide ions are called neutral. Because a neutral mineralizer has a low solubility promoting effect, the crystal growth can be roughly classified as using an acidic mineralizer or a basic mineralizer.

The basic ammonothermal method has been reported to produce GaN crystals having a diameter of 2 in., which exhibit a low dislocation density and little warpage [3]. However, in the case of the basic ammonothermal method, because a high pressure (200–500 MPa) is required to fabricate high quality crystals, it is difficult for scale-up to an autoclave and it is difficult to mass-produce crystals. Additionally, because the solution is basic, an autoclave is corroded so that the transition metal contained in the base material of the autoclave dissolves into the supercritical ammonia and becomes mixed into the grown crystal. As for the corrosion resistance of metals under ammonothermal conditions, a detailed investigation has been performed by Pimputkar et al. [4] In growing a bulk crystal of ZnO, a platinum inner cylinder is used to prevent contamination of transition metals arising from corrosion of the autoclave [5]. However, in the basic ammonothermal method, because the growth solution reacts with platinum, corrosion protection of the autoclave using platinum cannot be performed. However, in the case of the acidic ammonothermal method, because the inside of the autoclave can be lined with platinum, contamination of the transition metal into the crystal owing to corrosion of the autoclave can be prevented. In addition, it is possible to grow crystals under comparatively moderate growth pressures of 100–150 MPa, which are conditions that are suitable for industrialization.

The main growth parameters of the ammonothermal method are the growth temperature, the growth pressure and the mineralizer concentration, but the crystal growth rate and crystal quality also change depending on the type of mineralizer and the opening ratio of the baffle plate.

5.3 Temperature Inside the Autoclave

The growth temperature is one of the important growth parameters. To control the crystal growth rate, it is necessary to properly control the temperatures in the raw material dissolution region and in the crystal growth region. However, because the temperature controlled by the thermocouple contacted with the outer wall of the autoclave is different from the temperature inside the autoclave, and the temperatures of the upper and lower heaters are different, a natural convection is generated inside the autoclave, and so it becomes necessary to accurately determine the temperature inside the autoclave. In addition, because the temperature distribution inside the autoclave varies with the opening ratio and shape of the baffle plate, it is important to accurately understand the natural convection and the internal temperature distribution.

Table 5.2 shows the results of the internal temperature measurement using Ni-Cr superalloy lined with platinum with the inner diameter φ of 20 mm [6] when the lower heater temperature was fixed at 570 °C. The lower area temperature inside the autoclave was 50–100 °C lower than the set temperature, while the upper area temperature inside the autoclave was 20–50 °C higher than the set temperature. Hence, there was a large temperature difference both in the upper area and in the lower area inside the autoclave compared with the set temperature. Therefore, it is important to determine the actual temperature inside the autoclave by an internal temperature measurement or convection simulation.

Mineralizer concentration is also an important growth parameter. When an acidic mineralizer is used, the solubility linearly increases with an increase of the mineralizer concentration. Therefore, the amount of raw material transported from the raw material dissolution region to the crystal growth region also increases by increasing the mineralizer concentration. When the raw material conveying speed is too high, crystals are deposited on the inner walls rather than on the seed crystal, and needle-like crystals are deposited. When the raw material conveying speed is slow, the crystal growth rate naturally slows down. The raw material transport speed is influenced not only by the mineralizer concentration but also by the temperature difference between the raw material dissolution region and the crystal growing region, as well as the shape of the baffle plate. However, because the raw material transport speed is not systematized at present, it is not possible to calculate the raw material transport speed from the growth condition.

Table 5.2 Heater set temperature and actual measurements of the internal temperature

	Set temperature of upper part heater [°C]	Set temperature of lower part heater [°C]	Temperature of crystal growth region [°C]	Temperature of raw material dissolution region [°C]
Case 1	330	570	350	467
Case 2	400	570	383	485
Case 3	430	570	398	496
Case 4	470	570	421	517

5.4 High Speed Crystal Growth Technique

As mentioned above, GaN hardly dissolves in supercritical ammonia. Therefore, it is necessary to add a mineralizer to promote dissolution, but this selection greatly affects crystal growth. In the acidic ammonothermal method, crystal growth was initially performed using NH_4Cl as a mineralizer. This is because the use of the NH_4Cl mineralizer has the advantage that the GaN dissolves at a relatively low temperature and the crystals after dissolution and deposition have a hexagonal shape [7]. However, it the crystal growth rate was remarkably slow, with a rate of 5 μm/day or less [8, 9]. The solubility curve shown in Fig. 5.2 reveals that when NH_4Cl was used as a mineralizer, it dissolved at a relatively low temperature, but the temperature dependence of the solubility was moderate [10]. However, the slope of the solubility curve in the case of NH_4I as a mineralizer was larger than that obtained with the NH_4Cl mineralizer although almost no GaN was dissolved at 400 °C in the case of using NH_4I as a mineralizer [11]. Therefore, an autoclave that could withstand high pressures at a higher temperature than before was developed, and by growing crystals on the high temperature side using NH_4I as a mineralizer, a crystal growth rate of more than 100 μm/day has been achieved [2]. Hence, the crystal growth rate could be dramatically increased (Fig. 5.3).

When ammonium iodide is used as a mineralizer, because the temperature dependence of the solubility is steep, unless the temperature difference and mineralizer concentration are properly controlled, needle-like crystals, as shown in Fig. 5.3, can be deposited on the inner wall of the autoclave. Therefore, it is necessary to carefully decide on the experimental conditions.

Figure 5.4 shows GaN crystals grown using each of the acidic mineralizers [12]. The dotted line represents the shape of the original hydride vapor phase epitaxy

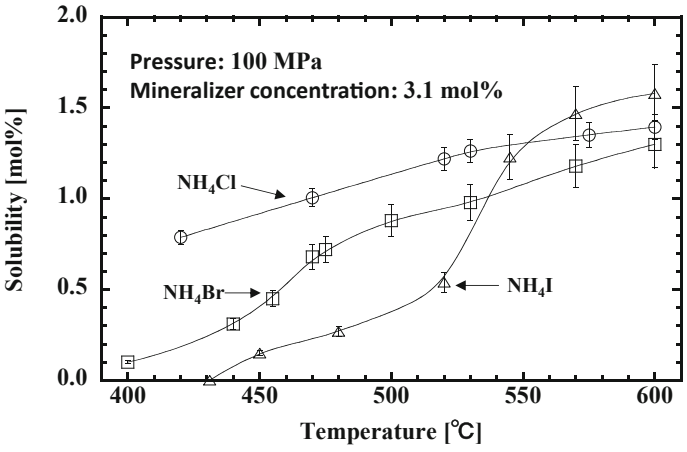

Fig. 5.2 Comparison of temperature dependence of GaN solubility in supercritical ammonia arising from the difference in halogen species of the acidic mineralizer [10, 11]

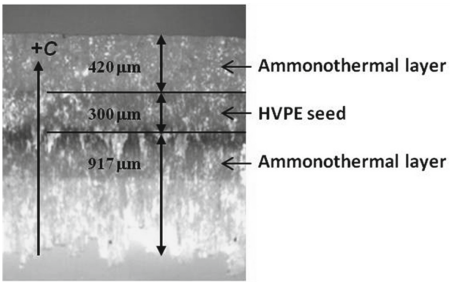

Fig. 5.3 Photomicrograph of GaN crystals grown at 558 °C for 4 days using NH_4I mineralizer [2]

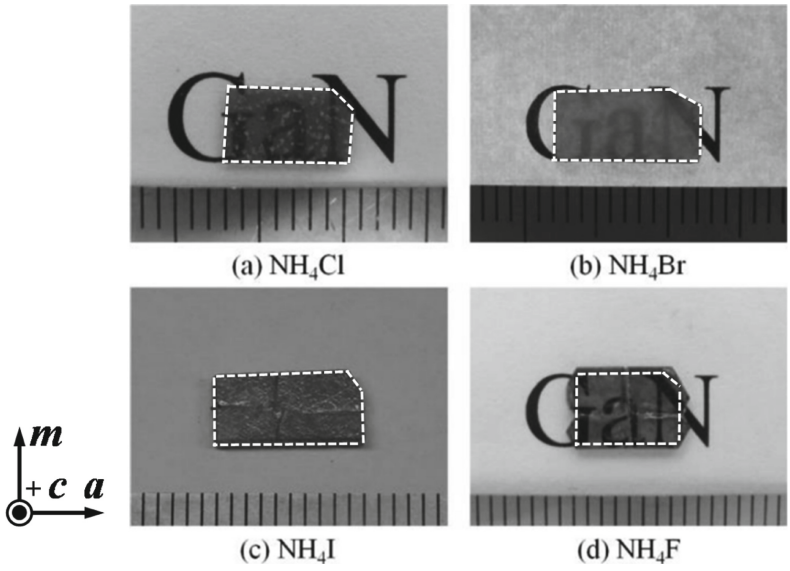

Fig. 5.4 GaN crystals grown using each acidic mineralizer [12]

(HVPE) seed. Crystal growth occurred only in the polar direction (*c*-plane) when NH_4Cl, NH_4Br and NH_4I were used as the mineralizer. However, when NH_4F was used, the crystal grew in nonpolar directions (*a*-plane, *m*-plane) in addition to the *c*-plane. For the acidic mineralizers, only NH_4F caused growth to the *a*-plane and *m*-plane, but the reason for this has not yet been elucidated.

Figure 5.5 shows the relationship between the growth rate of the GaN crystal and the pressure for each acidic mineralizer used [12]. A crystal growth rate that exceeded that obtained with the NH_4I mineralizer was obtained when the NH_4F mineralizer was used, and high-speed growth in the *m*-plane as well as the *c*-plane was achieved. The pressure is an important factor of the crystal growth rate, and the crystal growth rate increases with an increase in pressure no matter which mineralizer is used.

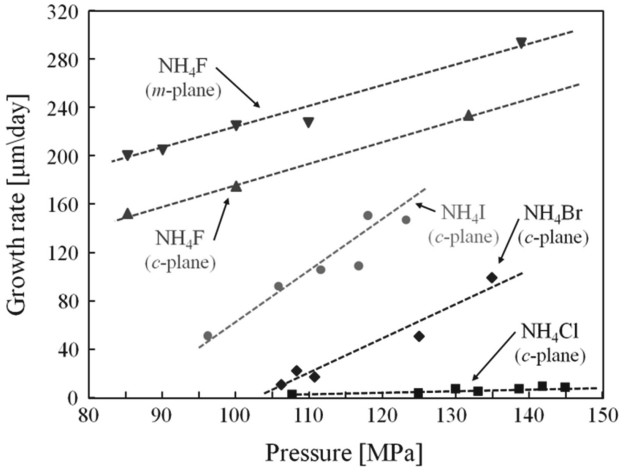

Fig. 5.5 Relationship between GaN crystal growth rate and pressure for each acidic mineralizer used [12]

Seed crystals are important to fabricate GaN single crystals with no distortion and low dislocation density. By using crystals resulting from spontaneous nucleation as a seed crystal, there is a possibility that GaN single crystals with no distortion/low dislocation density can be fabricated. In the acidic ammonothermal method using NH_4F as a mineralizer, high quality spontaneous nucleation crystals have been successfully obtained, as shown in Fig. 5.6 [13].

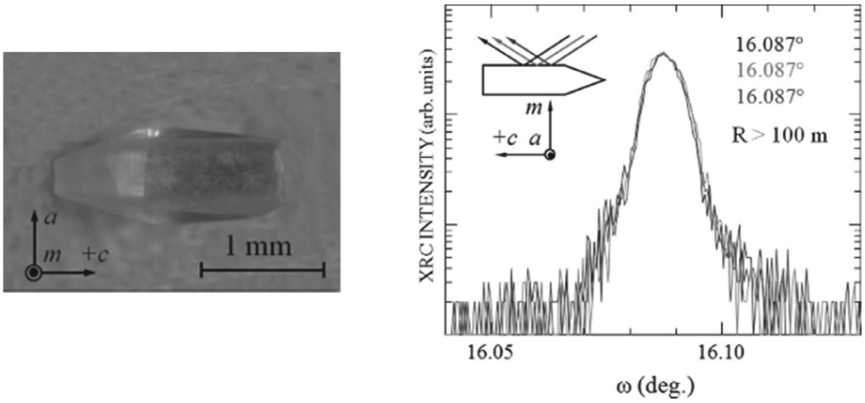

Fig. 5.6 Spontaneous nucleation GaN crystals and XRC measurement results obtained by the acidic ammonothermal method using NH_4F as a mineralizer [13]

5.5 Technique Towards High Purity GaN Crystals

A high purity GaN single crystal substrate is indispensable to realize a high current/high voltage GaN vertical power device. To fabricate a high purity GaN crystal, the uptake of Fe, Ni, Cr and other transition metals, and O into the crystals must be avoided. Here, we will introduce techniques to reduce oxygen uptake into the crystal.

The main source of oxygen contamination in a crystal is moisture contained at trace amounts in ammonia used as a solvent and extremely small amounts of moisture contained in hygroscopic ammonium halide. Conventionally, NH_4Cl powder has mainly been used as a mineralizer in the acidic ammonothermal method. However, powdered NH_4Cl is hygroscopic and is considered to be a source of oxygen contamination. Therefore, a mineralizer gas phase synthesis (GPS) method that synthesizes NH_4Cl by reacting HCl and NH_3 in an autoclave was developed [14]. Figure 5.7 shows a comparison of the experimental procedures for the conventional method and the GPS method. In the conventional method, polycrystalline GaN as a raw material, NH_4Cl powder as a mineralizer and HVPE-GaN as seed crystal are charged, and then the autoclave is sealed. Thereafter, after vacuum degassing at room temperature, the autoclave is cooled with a methanol/dry ice bath and filled with NH_3. However, in the GPS method, polycrystalline GaN as a raw material and HVPE-GaN as a seed crystal are charged and the autoclave is sealed. Thereafter, the autoclave is heated to 200 °C and vacuum degassed. In the case of the conventional method, because NH_4Cl sublimates, vacuum degassing cannot be performed while heating. However, in the GPS method, because the mineralizer is not introduced at the time of closing the autoclave, it is possible to perform vacuum degassing while heating. As a result, it is possible to remove the extremely small amounts of moisture adhering to the inner wall of the autoclave and the raw material. Thereafter, the autoclave is cooled with a methanol/dry ice bath, filled with NH_3, and HCl gas is introduced. HCl gas reacts immediately with ammonia in the autoclave to produce NH_4Cl, which is dissolved in ammonia.

Figure 5.8 shows the secondary ion mass spectrometry (SIMS) measurement results of GaN crystals grown using powdered NH_4Cl as the mineralizer and GaN crystals grown using NH_4Cl synthesized by the GPS method as the mineralizer. By fabrication with the GPS method, a reduction of O in the GaN grown crystal by a factor of approximately 3 was achieved compared with that observed with the GaN crystals grown using powdered NH_4Cl, so this method was shown to be effective.

As another method, it is conceivable that oxygen in the autoclave could be immobilized by adding a metal with which it is easy to form a metal oxide, thereby preventing the contamination of oxygen into the crystal. Therefore, crystal growth was carried out by adding Al, Si, Ca and Ti, which form oxides that are more stable than gallium oxide, as oxygen gettering agents [15]. The appearance of the grown crystal is shown in Fig. 5.9. Transparent crystals were obtained only when Al was added. Figure 5.10

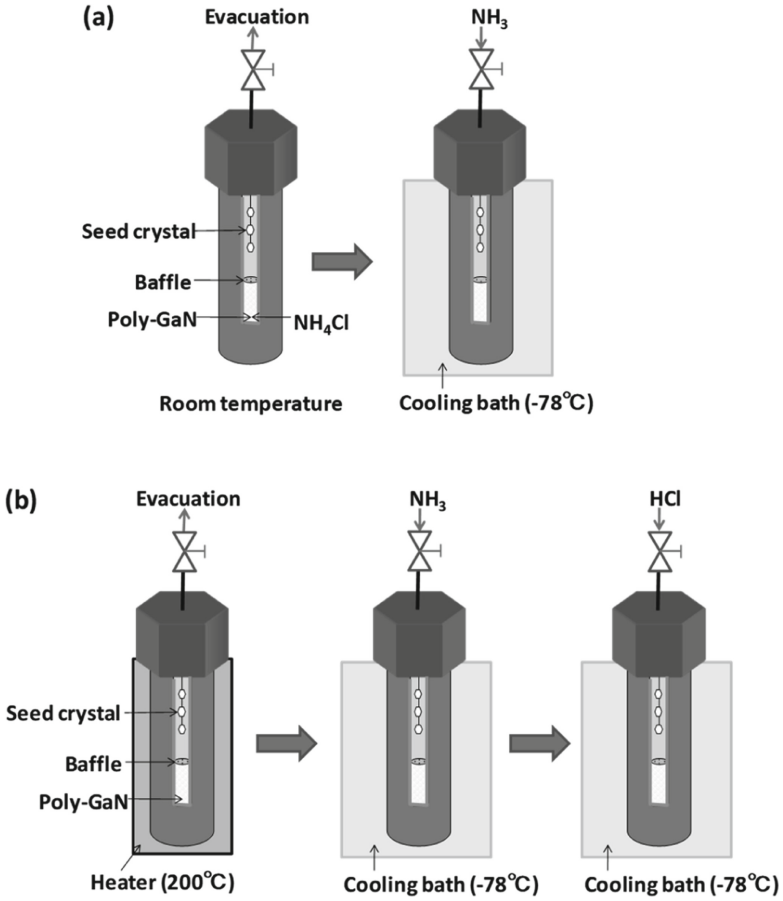

Fig. 5.7 Experimental procedures of the ammonothermal method using NH_4Cl as a mineralizer. **a** Conventional method and **b** GPS method [14]

shows the photoluminescence (PL) measurement results of crystals grown by adding Al and crystals grown without adding Al. In the crystal grown without adding Al, the spectrum was broad, which indicates that the impurity concentration was high. However, the spectrum of the crystal grown by adding Al had separated peaks, which suggests that the oxygen concentration in the crystal was low. From these results, adding Al is effective for fabricating high purity GaN crystals.

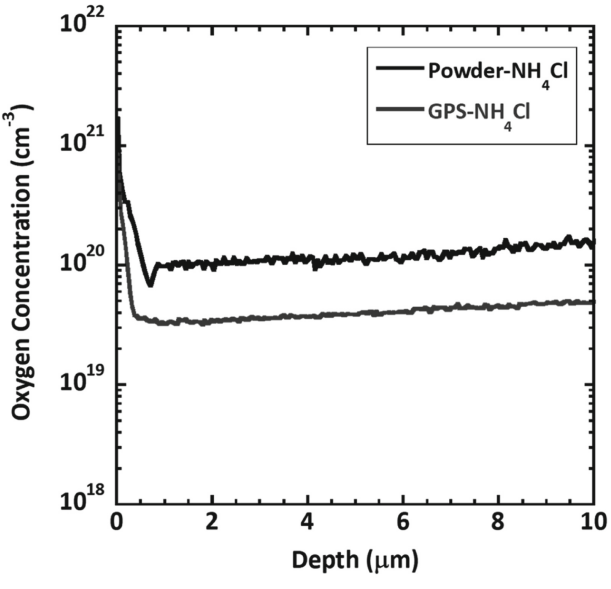

Fig. 5.8 Comparison of oxygen concentrations contained in GaN crystals grown by the conventional method and GPS method [14]

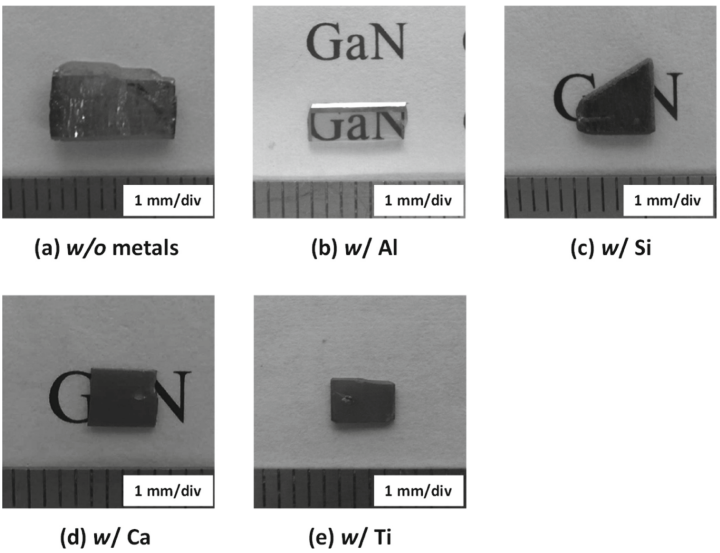

Fig. 5.9 GaN crystals grown at 615 °C using NH_4F as a mineralizer. **a** No metal addition. **b** Al addition. **c** Si addition. **d** Ca addition and **e** Ti addition [15]

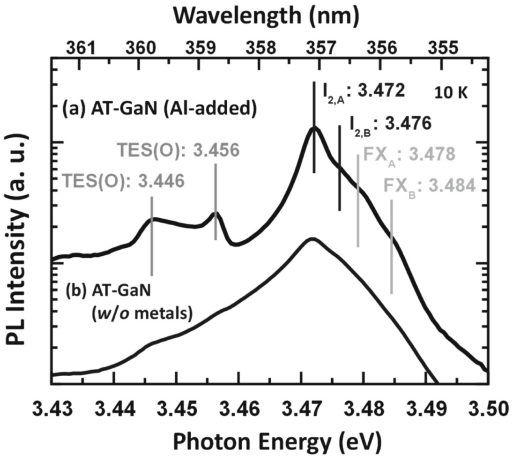

Fig. 5.10 PL spectra of GaN crystals (**a**) grown by adding Al and GaN crystals and (**b**) grown without adding Al [15]

5.6 Summary

GaN crystal fabrication using the ammonothermal method is in the developmental stage. In terms of increasing the growth rate, great progress has been achieved in recent years. As a future task, it is necessary to further reduce the concentration of the transition metal contained in the grown crystal and the development of techniques to solve this problem is under way.

References

1. R. Dwiliński, J.M. Baranowski, M. Kamińska, R. Doradziński, J. Garczyński, L.P. Sierzputowski, Acta Phys. Pol. A **90**, 763 (1996)
2. D. Tomida, Y. Kagamitani, Q. Bao, K. Hazu, H. Sawayama, S.F. Chichibu, C. Yokoyama, T. Fukuda, T. Ishiguro, J. Cryst. Growth **353**, 59 (2012)
3. R. Dwiliński, R. Doradziński, J. Garczyński, L. Sierzputowski, R. Kucharski, M. Zając, M. Rudziński, R. Kudrawiec, W. Strupiński, J. Misiewicz, Phys. Status Solidi A **208**, 1489 (2011)
4. S. Pimputkar, T.F. Malkowski, S. Griffiths, A. Espenlaub, S. Suihkonen, J.S. Speck, S. Nakamura, J. Supercrit. Fluids **110**, 193 (2016)
5. E. Ohshima, H. Ogino, I. Niikura, K. Maeda, M. Sato, M. Ito, T. Fukuda, J. Cryst. Growth **260**, 166 (2004)
6. Y. Masuda, A. Suzuki, T. Ishiguro, C. Yokoyama, J. Therm. Sci. Technol. **7**, 379 (2012)
7. D. Ehrentraut, N. Hoshino, Y. Kagamitani, A. Yoshikawa, T. Fukuda, H. Itoh, S. Kawabata, J. Mater. Chem. **17**, 886 (2007)
8. A. Yoshikawa, E. Ohshima, T. Fukuda, H. Tsuji, K. Oshima, J. Cryst. Growth **260**, 67 (2004)
9. Y. Kagamitani, D. Ehrentraut, A. Yoshikawa, N. Hoshino, T. Fukuda, S. Kawabata, K. Inaba, Jpn. J. Appl. Phys. **45**, 4018 (2006)
10. D. Tomida, K. Kuroda, N. Hoshino, K. Suzuki, Y. Kagamitani, T. Ishiguro, T. Fukuda, C. Yokoyama, J. Cryst. Growth **312**, 3161 (2010)
11. D. Tomida, T. Kuribayashi, K. Suzuki, Y. Kagamitani, T. Ishiguro, T. Fukuda, C. Yokoyama, J. Cryst. Growth **325**, 52 (2011)

12. Q. Bao, M. Saito, K. Hazu, K. Furusawa, Y. Kagamitani, R. Kayano, D. Tomida, K. Qiao, T. Ishiguro, C. Yokoyama, S.F. Chichibu, Cryst. Growth Des. **13**, 4158 (2013)
13. Q. Bao, M. Saito, K. Hazu, Y. Kagamitani, K. Kurimoto, D. Tomida, K. Qiao, T. Ishiguro, C. Yokoyama, S.F. Chichibu, J. Cryst. Growth **404**, 168 (2014)
14. D. Tomida, S.F. Chichibu, Y. Kagamitani, Q. Bao, K. Hazu, R. Simura, K. Sugiyama, C. Yokoyama, T. Ishiguro, T. Fukuda, J. Cryst. Growth **348**, 80 (2012)
15. D. Tomida, Q. Bao, M. Saito, K. Kurimoto, F. Sato, T. Ishiguro, S.F. Chichibu, Appl. Phys. Express **11**, 091002 (2018)

Chapter 6
A New Perspective on Growth of GaN from the Basic Ammonothermal Regime

Elke Meissner, Dietmar Jockel, Martina Koch, and Rainer Niewa

Abstract Although the crystal growth of GaN under ammonothermal conditions is being performed for quite some years now, the physical processes going on in the autoclave are still debated. Insight in the autoclave by in situ techniques is difficult and numerical simulations are based on physical models where the experimental prove is eventually vague. This chapter reports a period of experimental work leading to a new vision of the basic ammonothermal process. We shortly summarize the 3D thermal- and transport model and a first chemical model. Subsequently, we propose an alternative picture for the ammonobasic crystal growth of GaN, which not only leads to consequences with regard to required pressures and temperatures but also to a potential new growth process. The proposed hypothesis and empirical model involves the presence of a liquid phase in the autoclave in form of an amidogallate complex.

6.1 Introduction

Nowadays the importance of semiconductor crystal growth is still unbroken. The growth of large crystal bodies enables the production of semiconductor wafers for the fabrication of electronic devices. However, the semiconductor materials are very different with regard to the crystal growth techniques which could be applied for the growth of volume crystals. Amongst the new compound semiconductors with wide

E. Meissner (✉) · D. Jockel · M. Koch
Chair for Electron Devices, University of Erlangen-Nuremberg, Cauerstr. 6,
91058 Erlangen, Germany
e-mail: elke.meissner@iisb.fraunhofer.de

E. Meissner
Fraunhofer Institute for Integrated Systems and Device Technology, Schottystr. 10,
91058 Erlangen, Germany

R. Niewa
Institute of Inorganic Chemistry, University of Stuttgart, Pfaffenwaldring 55,
70569 Stuttgart, Germany

E. Meissner and R. Niewa (eds.), *Ammonothermal Synthesis and Crystal Growth of Nitrides*, Springer Series in Materials Science 304,
https://doi.org/10.1007/978-3-030-56305-9_6

band gaps and in front of the developing markets, it is not much disproportionate to say, the GaN is the second most important semiconductor after silicon [1, 2].

In ammonothermal crystal growth, evidently the problem is, that many essential observations which would be needed to explain the ongoing processes cannot be made in situ due to the pressurized growth system. So the understanding of transport processes inside the autoclave is very limited and explanations often vague. In this chapter we describe a different view on the existing understanding of an ammonobasic growth regime, based on our own experimental observations during the last years. Even though some of the conclusions may have speculative aspects, there is enough experimental evidence for a new vision.

The ammonothermal crystal growth is usually considered a solution growth process. The GaN shall be solved in the supercritical ammonia at a given thermodynamic pair of temperature and pressure. However, a solution growth process and the resulting growth rates depend on the amount of material that can be dissolved in the solvent. The solubility of GaN in pure supercritical ammonia is not very high, respectively nearly zero. Therefore, the so called mineralizers are added to the system, which should help to solve enough GaN through the formation of an intermediate species. The intermediate can be transported to the place of crystallization at the location of the seeds where the GaN crystalizes. So the action of the mineralizers is at least twofold. Many different mineralizers were used in the past years which all act differently depending on the chemical environment they create. Also the habit and even the structure of the GaN crystals can change from hexagonal to cubic in relation to the mineralizer as described in e.g. [3, 4] and references therein. In this chapter we concentrate on the basic ammonothermal regime. However, some consideration will also be valid for acidic ammonothermal processes.

Not much is known about the nature of the intermediates. The newest findings are described in Chap. 13. The mineralizers in the ammonobasic system shall form a complex which must be transported from the source (the place of dissolution of the GaN feedstock) to the seeds (place of crystallization) in the autoclave. In the ammonobasic regime the complex is likely a tetraamidogallate ion. Solid alkali metal compounds comprising this complex ion were described by some authors [5–7]. However, a full description of the growth process of GaN inside the autoclave, including the chemical reactions, is very difficult due to the limited options for direct observation.

In a former study by the first author's group, published by Erlekampf et al. [8] and Seebeck et al. [9] we reported the study of the temperature fields and related convection patterns, established in the autoclave, in order to facilitate the transportation of the complex through the system and suggested a first transportation model based on the formulation of two basic transport channels. The model is simply assuming the following two general processes (A) and (B):

$$\text{(A)}\ \mathrm{GaN_{feedstock}} + \text{mineralizer} \rightarrow \text{complex}$$
$$\text{(B)}\ \text{complex} \rightarrow \mathrm{GaN_{seed}} + \text{mineralizer}$$

In the process (A) the GaN feedstock will be dissolved by the aid of the mineralizer and the Ga-containing complex is formed, which transports Ga to the seed crystals. There the crystal growth can happen by the process (B), which is the formation of GaN from the complex in the presence of the ammonia. In turn, the mineralizer is released from the complex and reformed. Through that "backward channel" the mineralizer must be transported back to the feedstock region in order to start the process of dissolution again, which means that, a constant transportation action is required in order to continuously drive the system forward. From the first, this description is independent on the type of growth environment and the applied orientation of the temperature field. However, the directions of mass and heat transport will depend on the choice of the mineralizers. The basic idea is to always have the hotter zone at the bottom of the autoclave in order to profit from convection, due to natural buoyancy, no matter what the chemical processes inside the autoclave are. For the ammonobasic regime this results in a geometry where the seeds are placed at the bottom of the autoclave and the feedstock at the top, which is also described in the literature from groups working in the ammonobasic regime e.g. [10–13]. As this configuration emerges from the fact that a retrograde solubility for GaN was described for the usage of typical ammonbasic mineralizers, like the alkali metal amides $LiNH_2$, $NaNH_2$ or KNH_2 creating the NH_2^- ions in the solution, one of the biggest benefits could be, that unwanted impurities in the grown crystals may have an opposite transport direction in case of an own regular solubility. Thus, such impurities would be less incorporated into the crystals, as crystallization under retrograde solubility will not happen at the place of low temperature like in classically crystal growth, but instead at the higher temperature zone of the growth setup. So the impurities should be transported away from the surface of the growing crystal. On the other hand the transport direction of the "backward channel" (B), where the mineralizer releases from the complex after formation of the GaN and should be transported back to the feedstock region at the top of the autoclave for solving new material, would be opposite gravity. This functions trough the up-flow, induced by the implementation of the thermal field and relative positions of feedstock and seed as described before. On the other hand the complex must be transported "downwards" with the gravitation vector but against natural buoyancy. So how the transport of chemical species is really established may be quite complex in the ammonobasic crystal growth of GaN as also solubilities of many mineralizers are thought to be retrograde. In turn this means that a compound with a retrograde solubility can be probably transported back to the zone of dissolution, but solubility would decrease at the same time.

The first considerations that we made for a chemical model, based on the numerical simulations performed by Erlekampf et al. [8] and Seebeck et al. [9], will be discussed later in this chapter. The chemical model we propose is however preliminary and describes fundamental principles based on existing observations, but would of cause benefit from more data and further studies of crystal growth rates for different configurations and places in the autoclave related to the temperature, convection, concentration fields, type of mineralizers and pressure conditions during the growth process. Wang et al. [14] published an empirical vision about mass transport and

the ongoing processes in the autoclave but did not perform numerical simulation or attempt to further quantify.

The knowledge of the nature of the dissolved complex is very important, not only for the inclusion of the chemical species in the numerical model, but also for the considerations with regard to the growth kinetic of the crystals. Additionally, not only the growth rates of crystals would be interesting, but also the observation of growth instabilities, growth habits or facet morphology which contains information about the growth kinetic or rate limiting steps. A small number of papers describe the growth habit of the crystals e.g. for the different mineralizers used in the growth process [14–20]. The growth rates and shapes of the crystals, are of cause important and contain information about the growth process. From classical theory of solution growth the presence of solvents can change the shape of the grown crystals. The fundamentals of the related PCB (Periodic Bond Chain) theory can be found at Hartmann and Perdock [21] or its revisits [22, 23]. Many observations stem from the solution growth of KH_2PO_4 (KDP) crystals e.g. [24–26] or other e.g. [27] and references therein, which could be easily observed in situ during the growth process in the applied environment. The knowledge about the nature of all transported species in the basic ammonothermal process and the involved intermediate complex would be essential for the description of surface energies budgets. On the other hand there are many impurities underway in an ammonothermal autoclave, due to the corrosive action of the supercritical ammonia together with the mineralizers at high pressure and temperature. These impurities may additionally change the expected equilibrium shape or growth rates of the crystal if they are collected on a growing surface, modify the boundary layer or local supersaturation, which may also result in growth instability. This cannot be taken into account easily in theoretical considerations. So, in this sense the final shape of the crystal grown from an ammonothermal process is hardly predictable and difficult to judge and it is likely not possible to distinguish between the individual contributions.

Growth rates documented in literature are manifold resulting from different ammonobasic and acidic processes using various mineralizers, liner materials and different impurity contents in the process. Usually, growth rates between 20 and 100 μm per day were achieved for the basic ammonothermal process [28]. The special growth technique for ammonoacid growth, developed by Ehrentraut et al., resulted in about 5–100 times higher growth rates than conventionally observed [29], which may be obvious from the higher solution temperatures and pressures possible in their system. Due to the ammonoacid condition the dissolution takes place at higher temperatures and crystallization happens at lower temperatures. Ehrentraut et al. reported about 30–40 μm/h growth rate which could be routinely established and is the highest growth velocity reported so far. Interestingly the authors find this possible for all crystallographic directions. So basically for ammonoacidic technique an establishment of a stronger driving force for crystallization is present, obviously due to higher possible supersaturation. The observation of growth rates in general can be taken as a measure for the limitations of the growth process and growth kinetics involved.

Usually the growing crystal in an ammonothermal reactor cannot be directly observed. Special analytical setups are necessary for operando observations in the autoclave, like described and elaborated in other chapters of this book. Beside the in situ measurements, the only way to better understand and describe the growth process is the observation of shape and growth rates of crystals in relation to the position in the autoclave for a given growth process and the correlation of such data with a model understanding of heat and mass transport. Ideally combined with a chemical model, involving the transportation of the chemical species in the flow fields, this could give a full picture about the ongoing processes and how to control them.

This chapter on the one hand reports the results of a research project spanning from in situ temperature measurements, development of a 2D and 3D model describing temperature fields and convection transport as well as the development of a first chemical model, which can be further advanced and adjusted to different process conditions of ammonothermal growth processes. On the other hand the focus of this chapter will be the description of an alternative picture of the basic ammonothermal growth process. This view results from the observations made during the course of the project and involves a liquid phase of intermediates in the autoclave, which was not considered before as present compound during the growth run. This may promote and advance further discussion and understanding of the results from crystal growth in supercritical ammonia in general and offers new options for the design of a growth process for GaN.

6.2 Experimental Details

The experiments described in this chapter were performed in autoclaves suitable for ammonobasic conditions and made out of Inconel alloy 718. Due to the processing in the ammonobasic regime the inner wall of the autoclave was not coated with a liner, since corrosion is minimized in ammonobasic milieu. A detailed study on the corrosion of autoclave material can be found in Chap. 11 of this book. The autoclave has a range of safe usage from room pressure up to 300 MPa and a temperature range up to 600 °C under pressure. The experimental conditions of the experiments performed during this study made use of the full span of possible conditions. The inner setup differed slightly as a result of the design of individual experiments e.g. with regard to the relative positioning of feedstock and seeds. The inner setup was also fabricated out of Inconel parts. Two versions of an autoclave with upper and lower flange or with only a top flange were used. Additionally, a flange with five feed troughs for thermocouples (TCs) was available for the in situ temperature measurements that were performed in order to validate the numerically calculated 2D temperature distribution in the autoclave. This “temperature-measurement-flange” could be used with the double flange autoclave. As the filling and pressurization could be still realized from the top in that case, the TC-flange would be placed as bottom flange. For the experiments either of the autoclaves was placed in a three zone or two zone

furnace, which also offered the possibility of an air gap or local cooling in the middle of the setup for the eventual creation of a thermal knife or implementation of local steep temperature gradient. The components were chosen to offer maximum flexibility for the complete setup. The heater cassettes can be opened as half shells such that the autoclave can be placed inside together with a fitting insulation for the best possible stability and most accurate control of the temperature fields around the autoclave body. Figure 6.1 shows as an example the autoclave with the upper and lower flange in front of the two zone furnace for illustration of the setup and at the right hand side the temperature measurement flange with mounted thermocouples, type K with Inconel mantle.

The filling with ammonia was performed by condensation of the cold ammonia into the autoclave. The filling degree is calculated for $T = -33$ °C, the amount of ammonia condensated into the autoclave was measured by weighting and at a later point by direct monitoring of the filling height by ultrasound measurements through the outer wall of the autoclave. This type of determination of degree of filling is considered precise and is described detailed by Baser and Schwieger in Chap. 7 of this book. The autoclave was loaded with the feedstock, seeds and mineralizers under inert gas condition inside a glove box and afterwards attached to the high pressure system for pump and purge cycles with N_2 and subsequent ammonia filling. As seeds and feedstock material we used trimmed GaN crystal pieces made by hydride vapor phase epitaxy (HVPE) and broken pieces of bulk GaN crystals. The mineralizer was

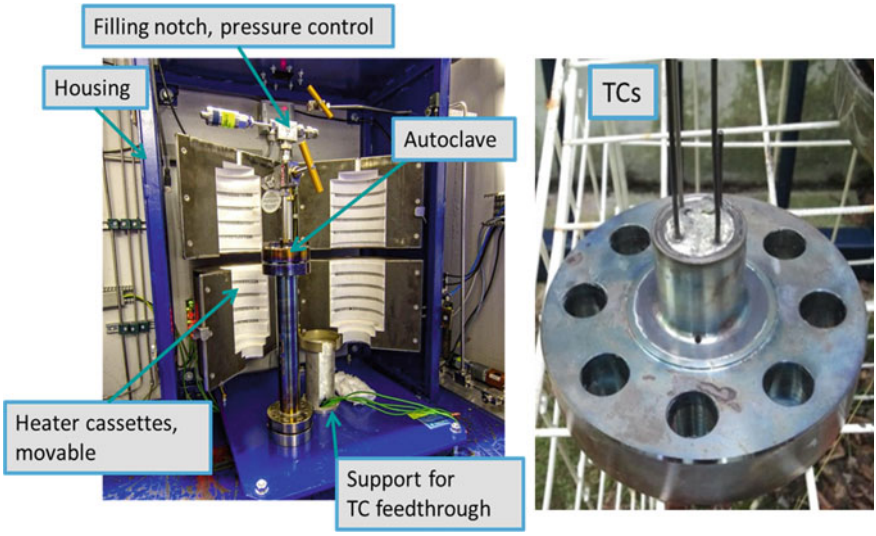

Fig. 6.1 Left picture: image of the opened 2-zone furnace setup. The autoclave with the two flanges is placed on the support-foot in the center during the experiments. The picture shows the support foot for the temperature measurement flange which would be the bottom flange. Right picture: image of the temperature measurement flange with the thermocouples (TCs) reaching to the inside volume of the autoclave after mounting

weighted and brought into the autoclave in form of a powder compacted inside a small net-cup. At a later point in the study, the mineralizer was placed underneath the seeds, for the purpose that will be described later in the chapter. As mineralizer we used KNH_2, $NaNH_2$ or KN_3 in different concentrations. As this refers to an ammonobasic regime, a retrograde solubility is expected. More details will be mentioned at the individual experiments described in the results section since the setup for some experiments changed after the target of the runs. All materials loaded into the autoclave were weighted. At the end of the processes the autoclave was cooled down and depressurized. After opening, the interior was washed with water and alcohol in order to dissolve the residual mineralizer and capture the grown crystals and residual feedstock for determination of weight, size and mass balance. The total mass balance will not be further used later on, as the value is quite inaccurate due to deposition not only on the seeds but also elsewhere in the autoclave. In case any liquid phase separated from the water/alcohol mixture (which we used for solving the residuals in the autoclave after opening), it was collected as well, as will be described later in the chapter. The source material as well as the crystalline material which was deposited was investigated by different microscopic means. The layer thickness of the newly grown GaN was measured by microscopy from the cross section of the seeds. This values were also used to determine the growth rates. The geometry and weight change were used to determine the amount of etching and deposited material. The shaped seeds (regular and kinetic seeds) were investigated by microscopy with respect to the crystal faces that developed.

For the description of the temperature field and the development of a 3D model of the thermal and convective fields in the autoclave, as well as the development of a first chemical model of an ammonothermal process, we used combinations of numerical 2D simulations and 3D simulations in order to reveal non axisymmetric effects. The details for the numerical simulations can be read elsewhere [8, 9]. The numerical description of the thermal field and flow pattern were not only utilized for the understanding of the mass and heat transport but also for the design of the inner components like the baffle plate and their action with regard to transportation of the intermediate species from the feedstock to the seed region. Calculations were done for an autoclave aspect ratio of 1:20, which is very common.

6.3 Results and Discussion

6.3.1 Calculation and Validation of the Temperature Fields

First we studied the temperature distribution in the autoclave as this is essential for the crystal growth and the design of the furnace-heater-system and insulation. The temperature fields were calculated by numerical simulation and directly measured using a special flange with through feds for 3–5 thermocouples, resistive enough to the corrosive environment. The results of the direct temperature measurements

validated the numerical calculations and confirmed first of all the correctness of the 2D temperature distribution model. The details were earlier reported [8, 30]. The calculated 2D temperature field was taken as a boundary condition for the 3D model to calculate the convection pattern and mass transport. For the calculation of the transport of species the respective molar weights of involved species were taken to calculate solutal buoyancy. As species involved in the process we considered the GaN, a gallium carrying complex as intermediate and the mineralizer. The results of the calculations were described in detail in our former publications [8, 9]. The findings showed e.g. that the geometry of the inner autoclave parts is essential for the steering of the mass flow which is kind of intuitive. However, it also turned out that the convection pattern is neither independent on time nor axis symmetric and cannot be described accurate enough with a 2D axis symmetric calculation only, which does represent the vast majority of the published data [31–34]. In [9] we showed the action of the shaping and positioning of the baffle plate, placed e.g. in the center of the autoclave, which can result in a drastic enhancement of mass transport along the axis of the autoclave. Such action is particularly important in the case of the ammonobasic regime where the transport can be expected to be low because it is contrary to natural convention. It could be also shown by the 3D approach that there are significant fluctuations of the temperature and flow velocity which are highest close the baffle plate. The dissolution of the feedstock may be mainly governed by diffusion, so strong fluctuations at the dissolution zone around the GaN source block are clearly favorable as the mixing and steering of the solution would be enhanced. On the other hand, inside the crystallization zone, where the crystals should have a most controlled environment with stable temperature field and transport rates, such fluctuations would be unfortunate and could dramatically deteriorate the quality of the growing crystals. This would be especially critical for bigger scale autoclaves in an industrial environment, when many seed crystals are placed inside an autoclave at the same time.

For transport of the species we additionally considered the contribution of solutal buoyancy. Which is not the case in the existing publications on numerical simulation of ammonothermal process. The results of our calculations were reported in [8, 9]. With the chemical model we formulated it was possible to calculate local time averaged concentration profile of the involved chemical species, which showed that the mineralizer can collect at places in the autoclave under certain circumstances and by that could not contribute to the growth process any more. We moreover found that the solutal buoyancy makes a significant contribution to mass transport, in quantity comparable to thermal induced transport. It could be concluded that the transport of species cannot be described good enough only based on the convection patterns. The work demonstrated the importance of a suitable transportation model for the chemical species involved in the growth process. The first chemical model we suggested, could—in further developed state of cause—allow to calculate true concentration patterns for a chosen setup and geometry of inner autoclave parts like e.g. baffle plates. This would be particularly important for larger industrial scale autoclaves. However, in any case all the numerical models were calculated for the case of a full supercritical system. No other phases than the solid and later dissolved

GaN, the crystallized GaN in solid form and the mineralizer with the intermediates dissolved in the supercritical ammonia were taken into account so far.

6.3.2 Crystal Growth Experiments

In all processes performed it was generally difficult to run the experiments for a long time as the tightness of the sealings evolved more and more critical with the total duration of a run. This was also due to the fact the experiments were often performed at the technical specification limits of the components and quite a number of runs failed to run until the end. However, some of the growth runs experienced a spontaneous pressure drop due to the breakage of the rupture disc. Experiments with unexpected spontaneous pressure drop were of cause unfortunate as not running to plan, but turned out to be very informative. In all of such respective processes the growth rates of the material crystallized on the seeds was found to greatly exceed the growth rates of the experiments which run to the end as planned at constant pressure. This was from the first glance unexpected and counterintuitive, also with regard to the numerical calculations and the transport possibilities as well as to the existing literature. The later experiments were such designed that the explanation of those observations could be formulated, which lead to a different understanding of the basic ammonothermal process for the deposition of GaN, compared to the existing literature. This chapter reports the interpretation of the results achieved during the study and as a result a corresponding model of growth of GaN from an ammonobasic process involving a liquid phase. To our knowledge there is no publication describing the ammonothermal crystal growth of GaN including the action and the formation of a liquid intermediate. The formation of liquid compounds with ammonobasic mineralizers KNH_2, $RbNH_2$ and $CsNH_2$ was described by some authors Zhang et al. [35], Molinie et al. [36], Wang and Callahan et al. [37]. Whether such compound eventually exists in its liquid form under the experimental conditions of the ammonthermal growth experiments was so far unknown.

Figure 6.2 shows on the left side the principle setup of the experiments and on the right hand side a graph of experiments performed. The resulting materials crystallization is indicated first of all simply as happened (deposit, red symbols in the figure) or not happened (no deposit, black symbols in the figure). In the experiments, qualitatively spoken, a deposition of GaN was measured or not at the place of the seeds at the bottom of the autoclave. Deposition or not was identified as a positive or negative weight change or by a visual and microscopic inspection. The plotted temperature data refers to the temperature at the bottom of the autoclave as measured by thermocouples at that place. The pressure is given as the maximum pressure that was achieved or maintained during an experiment. Three experiments are special marked with a blue rim. The three marked red squares with the blue rim represent growth runs that had a remarkable deposition, although the experiment experienced a sudden drastic pressure drop during the run time and then proceeded regular for the rest of the process time at a lower pressure. We would have expected that those

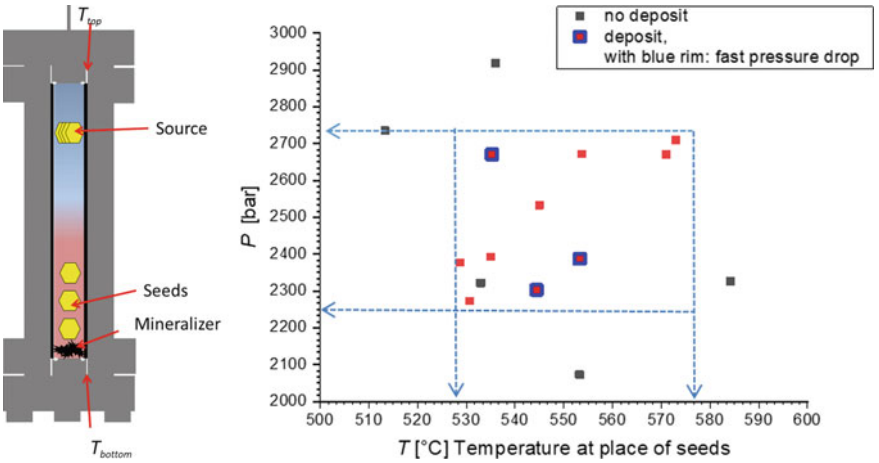

Fig. 6.2 Schematic drawing of the experimental setup (left) and experimental results in terms of positive (red symbols) or no deposition (black symbols) of GaN on the seeds. Three experiments are marked where deposition took place although the experiment experienced a fast pressure drop (red symbols with blue rim). Dashed lines represent the boundary conditions were growth on the seed was possible

experiments would lead to no deposition, which was not the case. On the other hand, these experiments turned out to be important for the total interpretation of results.

Of cause in this diagram, we ignore for the moment the solubility, the quantitative amount of mineralizer (KNH_2 in this cases) other than simply the fact "enough mineralizer", and an existing temperature gradient between the source zone and the place of crystal growth. However, involving these parameters may result in the same factum, whereby the influence of the pressure as a parameter in the crystallization of GaN on a seed is so far unclear. From that diagram, a GaN deposition could be achieved for the following boundary criteria:

$$\sim 2250\,\text{bar} < p \sim 2730\,\text{bar}$$

and

$$\sim 530\,^{\circ}\text{C} < T \sim 575\,^{\circ}\text{C}$$

The interesting results appear, if the data is analyzed for any individual experiment and simple fundamental assumptions. From this point of view, a crystallization can only happen if a supersaturation exists such that the system is slightly pushed out of equilibrium and simply more deposition than dissolution happens. So, a most simple postulate would be that at those experiments where a deposition of GaN was found, a high enough supersaturation was achieved on the surface of the seeds. From theoretical consideration one would expect that the dissolution of the GaN from the feedstock and the transport of the Ga-containing complex to the place of crystallization should be first of all a function of temperature and transportation in the

autoclave. For the ammonobasic case one would expect that the dissolution of GaN and formation of transported intermediate is higher at lower temperatures as a result from the retrograde solubility with potassium amide mineralizer. Supersaturation could occur if enough GaN was dissolved at the source zone and mass transport in the autoclave towards the seed region was high enough. These conditions were obviously fulfilled for the boundary criteria given above.

After the first chemical model we proposed, a supersaturation can be created if the complex was formed at the source zone and the transported intermediate species in the autoclave has a high enough concentration at the growth zone. Then, if the GaN crystalizes the mineralizer will be released, transported back and dissolves again the source material. So, as a consequence the area in Fig. 6.2 where the GaN could be crystallized, can be considered as kind of a stability field of the existing intermediate phase for the respective experimental conditions. Without the intermediate phase above a critical concentration no crystallization would happen. The only black point falling into that field represents an experiment that was accidentally stopped, shortly after the autoclave reached the experimental conditions. As a result there was either not enough time for the formation or the transportation of the complex and in consequence the concentration of the intermediate at the surface of the seed was not high enough, to create a supersaturation and finally no deposition of GaN took place. Otherwise, for a longer run time (as originally anticipated) the formation of GaN on the seed would have to be expected. Thus, we consider that particular experiment as belonging to the set of "red" points.

One can conclude that the intermediate phase would not exist much above a threshold pressure of roughly 2730 bar and not below 2250 bar, respectively, not much below a temperature of approximately 530 °C and no more above 575 °C; or at least not in the form that was effective for the crystallization of the GaN with KNH_2 mineralizer in the given set of experiments. Figure 6.3 shows the collected data together with a line through the red data points at or below which the crystallization of GaN should be expected. The line is meant as eye guide and does so far not represent a fit of a physical model to the data points. However, it indicates a nonlinear relation between the pressure and temperature condition for the formation of the complex.

There is some scatter of the experimental data laying close around that line. Due to the complexity of the experimental situation, we did not calculate numerical error bars, but visualize the uncertainty region by the gray shaded area. As below that line, GaN crystallization can be expected until the lower threshold values are reached, we consider it as the boundary curve for the stability field of the intermediate complex. Of cause, a much larger number of experiments would be necessary, in order to truly verify an equilibrium curve for the stability field of the particular intermediate involved in the case of the applied KNH_2 mineralizer.

Now, the experiments with the blue-rimmed red symbols will be discussed (#1–#3 in Fig. 6.3). As in that growth runs the deposition of GaN on the seeds was observed, we count them to lay inside the existence field of the intermediate, at some point in time during the course of growth run, although, they came to lay outside the grey shaded area, with respect to the experimental conditions. Obviously, it happened

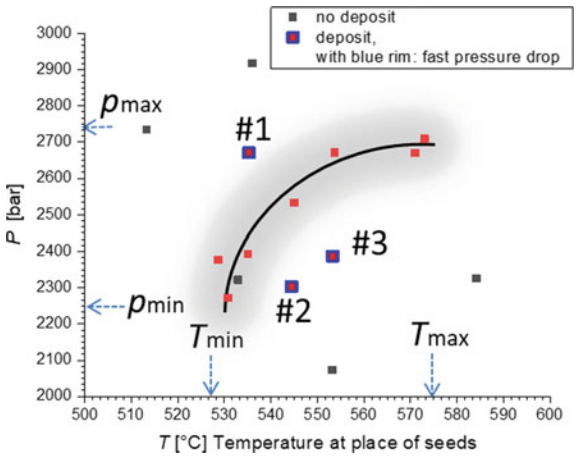

Fig. 6.3 Estimated boundary line for the stability region of the intermediate complex involved in the experiments. Below T_{min} and P_{min} and above T_{max} and P_{max} a deposition of GaN is not expected. The line is an eye guide and does not represent a physical model. The gray area visualizes the scatter interval

to have enough supersaturation around the seed to create a GaN deposition, especially for #1 which was initially far above the boundary curve, close to T_{max}. These experiments are marked and have to be discussed differently as they experienced a sudden pressure drop shortly after the start of the run time. However, a remarkable deposition of a thick layer of GaN was found on the surface of the seeds. The growth of that material could not be the same "regular" growth as in the experiments marked with the red squares in Figs. 6.2 and 6.3. It could as well not have occurred due to supersaturation based on the temperature and transport gradient established between the source and the growth zone, nor could it have occurred directly from the supercritical phase, as this was released from the autoclave due to the pressure drop after sudden leakage. A fast growth directly from the supercritical phase as a result of a solubility limit excess would have resulted likely in a kind of mass crystallization of many polycrystals, which was not observed. Instead the GaN deposit occurred in form of a thick epitaxial layer on the seeds. The growth happening in this experiment can be understood, if the pressure drop would cause the intermediate complex to dissociate, fall under the stability limit in terms of pressure and release the gallium. This means in a consequence, that the complex transporting the Ga may dissociate with temperature rise, but is stabilized by the pressure. In this case the temperature was nearly constant and dropped only minor (measured by the bottom thermocouple) and could not likely cause the dissociation of the complex. Instead, because the pressure was decreasing rapidly due to the unplanned pressure loss, the complex could decompose, which caused the growth of a crystalline GaN layer. If a lower total pressure or a huge pressure gradient would be taken into account the respective data point may fall into the grey area. The #2 and #3 experiments are below the boundary curve but inside the temperature window where we usually observe a

GaN growth on the seeds. Although they experienced an accidental pressure loss, which would cause additional dissociation of the complex, the GaN deposition was expected. So the pressure drop brought them out of the planned p, T condition and the stability field of the complex, but the fast pressure drop decomposed the complex additionally and growth rate was higher than usual. Both of the points #2 and #3 would rather move to lower temperatures if the pressure release would cause a slight temperature drop and by that may fall as well into the grey zone or get closer to it.

As a conclusion it can be stated, that the growth of GaN in the ammonobasic regime with KNH_2 mineralizer occurs if the system is hold between p_{max} and p_{min} and T_{max} and T_{min}. According to the chemical model, suggested before, the transported complex must be dissociated in order to release the Ga for the formation of GaN. This can be achieved by either $p = \text{const.}$ and $T \neq \text{const.}$ within the given p and T boundaries (red points in the diagram) or for $p \neq \text{const.}$ and $T = \text{const.}$ (the pressure drop experiment). This implies that the intermediate compound in the potassium containing ammonobasic regime is stable within that p and T boundaries. The corresponding intermediate is thought to be a tetraamidogallate ion or condensation products thereof [38]. As below $p_{min} \cong 2250$ bar and $T_{min} \cong 530$ °C no growth occurred, the complex could obviously not be formed, whereas above $p_{max} \cong 2730$ bar it may no more exist. Alternatively, the complex exists but is stabilized by the pressure and cannot be dissociated enough to release the gallium. The temperatures beyond $T_{max} \cong 575$ °C may lead to a thermal decomposition of the complex irrespective of the pressure, as the curve sketched above implies a "flattening" rather than a continuous rise, which would be in accordance to fundamental thermodynamics as the Gibbs free energy depends on T and p differently.

The following diagrams show how much of the GaN source material was dissolved as a function of temperature or pressure for the application of KNH_2 as a mineralizer. From this plots there is no clear correlation with either of the parameters p or T. However, it looks more like a peak function, which was put to the graph for illustration; it does not represent the fit of a physical model. If it can be assumed that the formation of the gallate is a prerequisite for the mass dissolution of GaN at the source zone, this should more or less correspond to the stability field of the complex as describe before. The difference to the curves discussed above is that Fig. 6.4 shows the situation at the source zone, whereas Figs. 6.2 and 6.3 are monitoring the situation at the seed position. In terms of pressure dependence the threshold of slightly above 2000 bar is also visible which corresponds to the described stability field of the complex discussed above. With view to temperature the picture is a little different as the lowest temperature at the crystallization zone where growth on the seed was observed was approximately 530 °C and with higher temperature the growth increased, which indicates a retrograde temperature behavior of solubility of the Ga carrying species in the supercritical NH_3 between 530 °C and T_{max}. This is not unexpected as described before in the literature. The mass dissolution of GaN measured at the source zone is highest around 400 °C.

The combined action of pressure and temperature on the dissolution of the GaN feedstock is depicted in Fig. 6.5. The role of the pressure value is not completely clear. A certain pressure above 2000 bar is obviously necessary to enable the formation or

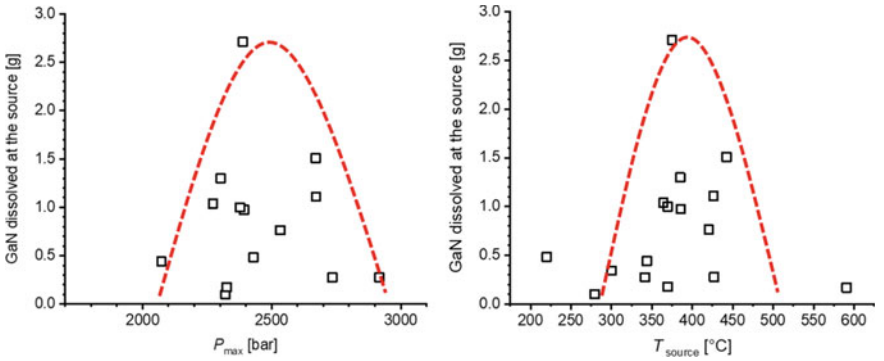

Fig. 6.4 Mass dissolution GaN at the source zone as a function of temperature at the source and pressure. The dashed lines are meant as eye guide and do not represent the fit line of a physical model

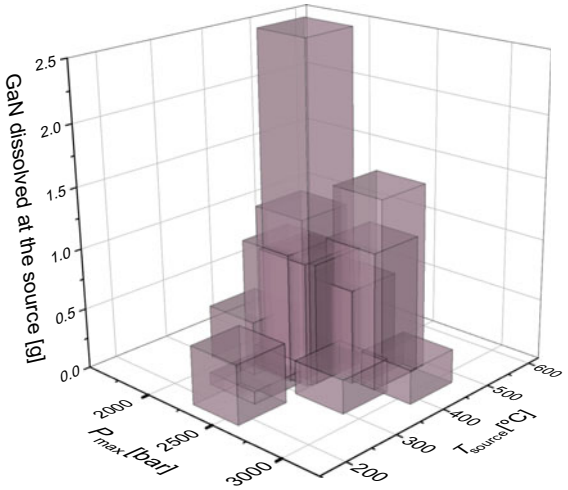

Fig. 6.5 Mass dissolution of the GaN feedstock at the place of the source in the upper part of the autoclave as a function of P and T. The plot contains all data observed, the initial concentration of mineralizer in neglected for the moment

stabilization of the complex, which dissolves the feedstock material, but the optimum condition may be a narrow space in p and T.

Figure 6.6 makes this minimum pressure threshold obvious. The graph shows the maximum measured thickness of the GaN layer which crystallized on the seed surface, plotted against the time that the system was held above 2000 bar. There is clearly a continuous increase of the deposited layer thickness with the run time above 2000 bar, which means that a stable transport and supersaturation was established and continuous growth could occur.

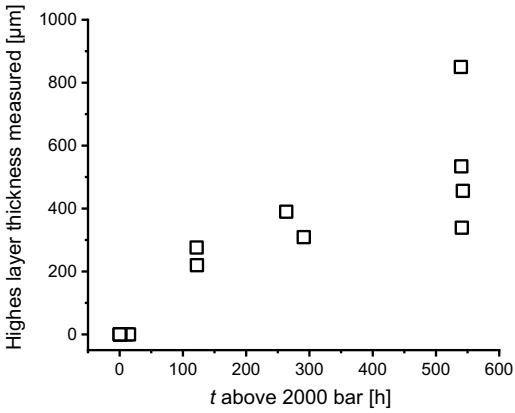

Fig. 6.6 Deposited layer thickness in relation to the process time above 2000 bar

The thickest deposited layer usually occurs on the *c*-face of the seed, which hangs on a wire in the crystallization zone at the bottom of the autoclave. Of cause there is also deposition and development of crystal facets at other sides of the seed, but the amount is small compared to the *c*-face growth and hard to measure correctly, so it was neglected for the graph. In turn the question remains if all the GaN material which was dissolved at the source zone could be transported to the bottom of the autoclave and crystallized. For this contemplation we use again the data from the growth runs with a significant run time above 2000 bar and correlate the amount of grown material with the mass dissolution of GaN at the source. This includes some error as the deposition is taken as a one dimensional value and the dissolution involves the whole surface area. However, as the dissolution can be seen as the inverse growth the same argument is valid as said before. The dissolution on the side faces will be small compared to that on the *c*-face. The following graph depicts the relation between the mass dissolution at the source and the deposited material on the seed (Fig. 6.7).The relation can be taken linear for the first, which proves that at least the majority of the material dissolved at the source is transported to the crystallization zone. The fact that there is not a perfect correlation with a slope of one may result from the assumptions and inaccuracies involved in this view, including the possibility that material was deposited elsewhere in the autoclave and the fact that a solution must saturate before deposition can start. Obviously, there is anyway quite a larger number of points where a significant dissolution of material was observed but no deposition of GaN on the seeds was found. This could be even a negative value of deposition, which means that the seed was rather dissolved. The kinetic of the formation of the teraamidogallate complex is not much known under this conditions and the potassium complex is not well described in literature. Niewa et al. report the formation of complexes with Cs and other anions at much lower temperatures e. g. 350 °C [38]. Pure $K[Ga(NH_2)_4]$ as a hypothetical intermediate should be a solid compound or a liquid which is unknown with this composition so

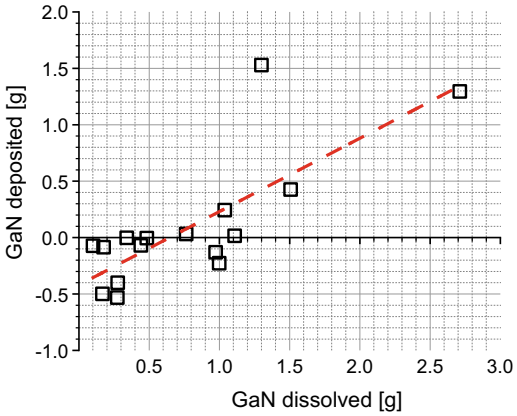

Fig. 6.7 Relation between the deposited GaN on the seed surface and the amount of mass dissolution of the GaN feedstock

far. However, the $[Ga(NH_2)_4]^-$ ion should be present in dilute form even at lower temperatures as was derived from solution NMR experiments [38]. This ion can be transported as an intermediate and dissolve the feedstock. The solution at the bottom of the autoclave may initially not be saturated and no deposition would take place. A saturation or supersaturating could be created if a more condensed species would be formed, which may happen through the action of the pressure and could explains why a minimum overpressure of at least 2000 bar would be required to create deposition at all. On the other hand the action of the pressure is not completely clear here, as from an equilibrium point of view, the pressure might not be necessary to condensate the isolated species if the concentrations are just high enough. Moreover, any solid intermediate could be eventually molten at the experimental temperatures involved. This could mean that the respective potassium-complex is formed by prominently dissolving feedstock and seeds because a supersaturation situation at the seeds cannot be created. This would be the case if either transport of that complex could not be established or concentration was even all over the autoclave. If, on the other hand a melt or liquid phase of the intermediate compound is formed as the temperature rises, it would likely take up different amounts of ammonia in relation to a given p and T condition. It can be imagined that a condensation reaction and formation of an imide compound takes place, involving various amounts of ammonia, gallium and amide ions, which would explain the involvement of an activation volume for the condensation reaction and would require a pressure activation of that process (p_{min}):

$$2\left[Ga(NH_2)_4\right]^- \rightarrow \left[(NH_2)_3Ga(NH)Ga(NH_2)_3\right]^{2-} + NH_3$$

What is really going on in the closed autoclave will still remain to be debated at the point in time, as the pressure dependence of the formation and the kinetic of the formation reaction of the potassium tetraamidogallate complex and related compounds is

unknown and was not investigated so far. Moreover, the findings described above may imply at least a two stage process which was not preconceived up to now. Otherwise this could explain why in some experiments the dissolved amount of GaN feedstock can be high even though no deposition took place.

The mass dissolution of GaN observed at the source zone could be interpreted as the dissolution of GaN taking place as a result of the formation reaction of the complex. Thus, the amount of dissolved feedstock or the dissolution rate would be mirroring the formation kinetic of the complex respectively a reaction rate of the KNH_2 and NH_3 with GaN to form the complex. This depends strongly on the total concentration of the mineralizer added to the system and probably whether it's added in form of the amide or azide. The later would, from the view of a crystal grower, mainly influence the distribution of mineralizer in the autoclave. The place and the way it is supplied to the autoclave plays a role. From experiments with sodium as a mineralizer we suspected that in case of the amide as the form of the mineralizer it was difficult to obtain a good enough dissolution of the feedstock. So the experiments with the amide were unsuccessful to a large extend. It can however not be ruled out that the amount of mineralizer was eventually too small. So far it was not possible to perform repeatable and reliable enough experiments to clarify such dependencies as the distribution of the mineralizer inside the autoclave is hard to be controlled systematically. The important difference is, that the azide compared to the amide will decompose spontaneously associated with a very short pressure peak event. This "explosion event" likely distributes the mineralizer everywhere in the autoclave including the zone of crystal growth where the seeds are located. In turn, this means that the complex can form readily everywhere in the autoclave where the Ga is available and thus dissolves the GaN at any place whether feedstock or seeds. A steady growth condition with a stable established heat and mass transport due to convection and solutal buoyancy can start only after that.

6.3.3 Presence of a Liquid Phase in Ammonobasic Crystal Growth of GaN

The out sticking difference of the experiments #2 and #3 in the above diagram 6.3 is the fact that the amount of GaN crystallized on the lowest positioned seed at the bottom of the autoclave was the highest compared to any other experiment.

In case of the KN_3 mineralizer experiments, three seeds were placed in the bottom zone of the autoclave during the growth runs. Below there is only the mineralizer as a powder. When the experiment is heated up under pressure, a sudden pressure peak occurred, which we attribute to the spontaneous decomposition of the KN_3, whereby we suspect that the mineralizer does not remain at its original position but distributes widely in the autoclave, for a while at least. After the system reaches above the minimum pressure and temperature threshold values the formation of the complex starts everywhere in the autoclave and the GaN at the source zone will

be dissolved and transported to the growth zone, as described by the numerical models developed during the study. However, we expected that the growth of the GaN occurs differently on the 3 seeds as they are placed along the vertical axis of the autoclave which is the direction of the temperature gradient. The temperature gradient established between the source and the growth zone was about 3 K/cm, which would mean that the maximal temperature difference between the uppermost and lowest seed position would be roughly 10 K. From the findings described before in this chapter we now would conclude that this is very likely too small to see a difference between the growth on the three seeds. Anyway, the uppermost seed and the lowest could develop different due to the convection field and the related transport of the complex. The mixing at the lowest possible seed position could be expected to be most difficult and the lowest seed will have the lowest deposition rate of GaN. In fact to the majority we found a more or less comparable amount of GaN which was grown on all three seeds positioned in the autoclave. However, we found a big difference in the amount of deposited material in the case of the experiments with the accidental pressure drop. There the lowest seed had a twice as high deposited layer of GaN compared to the upper seeds, which was unexpected.

When we opened the autoclave and deglazed the residuals with water and alcohol we found a second oily liquid phase at the bottom of the glass which we used for collecting the residuals. Figure 6.8 shows a picture of the liquid captured after the opening of the autoclave.

The chemical analysis showed that a high concentration of Ga is contained in that brownish to light yellow liquid phase after reaction with the water/alcohol mixture. Liquid complexes with K, Rb and Cs were earlier described in absence of water as amido-imidogallates [37, 38]. To the best of our knowledge in none of the publications concerning the basic ammonothermal growth there was ever a description about the existence of a liquid phase as a possible liquid amidogallate complex and its involvement or possible role in the crystal growth process. However, this could help to explain the much higher growth rates for the lower placed seed, if one imagines

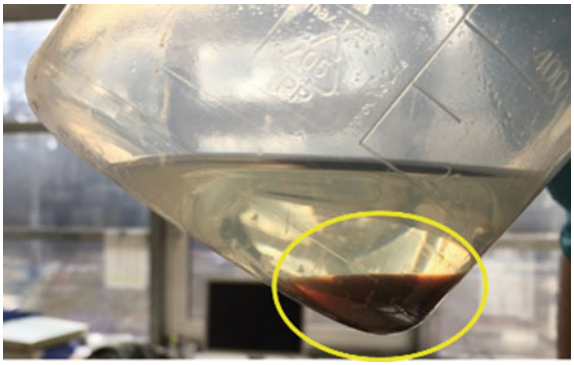

Fig. 6.8 Example of the "oily" liquid phase captured after the opening of the autoclave and washing with water and alcohol. The brownish liquid contains a high concentration of Ga

it was emerged in a Ga containing liquid during the process. In the case of a sharp pressure gradient due to depressurization, either intentionally or unintentionally (as a result of leakage), this liquid could decompose and release the Ga and forms GaN on the surface of the seeds with a high growth rate, as supersatuaration can be expected to be very high in such situation. From the observations described before, it seems that the pressure is essential to stabilize the complex at higher temperatures. If a seed is immersed in the liquid phase, which forms after the heat up and pressure rise of the system to the wanted experimental conditions, a pressure gradient or pressure release will cause a fast thermal decomposition of the complex. So if a controlled thermal decomposition would be established the GaN would grow from a liquid/solution rather than from the supercritical condition, by classically reducing the solvent.

This conclusion in fact opens a wide range of options which could be tried out. One of which would be the growth from such a gallate-complex liquid without the necessity of technically harsh ammonothermal conditions. Moreover, this finding probably is also helpful to explain why the growth rates reported in literature are widely varying. The liquid phase may have been present or not or as small portion only, depending e.g. on the absolute amount of mineralizer or the positioning of the seed, but was anyway never taken into account. The picture of the chemical model and the species transport will also change accordingly. However the presence of the liquid during the process is suspected to depend also on parameters like e.g. the concentration of the mineralizer, the positioning, the pressure and temperature conditions as described before in this chapter. It would be important to clarify the existence field of potential liquid complexes experimentally and explicitly generate them in the crystal growth experiments. Based on our findings and as a hypothesis we propose exemplarily a new model of the ammonobasic crystal growth process, which will be described in the next paragraph.

6.3.4 Two Models of Ammonobasic Crystal Growth of GaN Involving a Liquid Phase

The following considerations made from a theoretical point of view, may show that the existence of a Ga-containing liquid could modify the process design and process flow of the crystal growth process fundamentally. We could envision at least two different scenarios involving the above described findings and the usage of the mineralizer either in the form of (A) the amide or (B) the azide.

In either case the GaN source material, together with the mineralizer, would form the amidogallate complex, which is necessary in order to carry the Ga. The basic difference would be that the azide will decompose spontaneously during the heating up of the autoclave, whereas the amide will either solve in the ammonia or melt and form a liquid, which localizes itself at the bottom of the autoclave if no counter measure is taken.

If one imagines an amide melt as a molten bath at the bottom of the autoclave the following processes can be considered: the amide dissolves in the supercritical ammonia until the solubility limit is reached. The same applies for the ammonia which can solve in the amide liquid. The formation of the amidogallate complex is possible where the amide anions will get into contact with the gallium. So, if the mineralizer is in form of a melt at the bottom of the set-up and the GaN source is at the top in the colder temperature zone, the amide has to reach to the top and solve the Ga from the GaN source material. However, the amount of amide created and transported to the top zone can be limited by the interface reaction between the melt and the ammonia and if the solubility limit is reached nothing will dissolve anymore. The transported amide will solve the GaN from the source and form the amidogallate complex. As the complex (as a species) is heavy compared to the other species around and in conjunction with the natural convection, the result will be the transportation and mixing of the system and the amidogallate complex can reach the GaN seeds placed at the bottom of the set-up. It is hard to imagine that the solution can be strongly supersaturated with this case and growth rates will be low. At the same time, if the amount of melt at the bottom of the autoclave is large enough, the seeds could have been accidentally immersed in the liquid. This would result first in rather a dissolution of the seeds exposed to the melt, unless the amide melt is saturated with Ga, or the complex had formed at the interface to the ammonia. However, not much more GaN will grow as was dissolved before. Further growth by additional complex transported from the top part will likely be diffusion limited and limited by the interface kinetic at the melt-ammonia interface. This was visible from some of our experiments where we would have expected the growth of GaN with respect to the p and T conditions, but in fact found a negative growth rate. Moreover, the dissolution of GaN seeds at the bottom was much higher than the amount of GaN dissolved from the source GaN blocks. This could be explained with the existence of a melt and the processes described above. If taken into account that the amide is thought to have retrograde solubility in ammonia this scenario could be even worse. The same would apply if the amount of mineralizer would be too small, such that a melt residue cannot be formed. Proper supersaturation can then hardly be expected.

If one discusses the rate limiting steps, the concentration of the complex could be determined by the kinetic of the formation reaction of the complex at the surface of the amide melt or the decomposition pressure of the amide under temperature and pressure, which is unknown to our knowledge. In a case where the mineralizer would not be applied in excess, such that an amide liquid can be imagined, the picture of low growth rates remains the same. This would even not change much, if the mineralizer would be put in the top part around the GaN source at the beginning instead of beneath the seeds. If the amide melt would be stable under the applied pressure it could drop down from the source basket to form the melt bath or if put in a closed container the melt would stay there and the same surface reactions would be rate limiting, adding the step that the complex would have to diffuse out of the container. In this way the picture probably does more represent the actual vision of the ammonbasic process including the reported growth rates, which are typically low. To the above considerations one could expect that a huge amount of back etching from the seed

surface should be involved in the case (A). This is in principle to the majority of aspects positive, but must be compensated before a positive growth rate is achieved, which is unpleasant in front of low growth rates. Unfortunately, back etching was not studied fundamentally for the ammonothermal crystal growth and no systematic publications exist. In fact, this also adds uncertainties to observed growth rates. It is hard to discuss this detailed to its full extend, as the data in the literature is very diverse, the governing parameters are many and the materials data like solubility of different amides in NH_3 under pressure and temperature is not known. In the following Fig. 6.9 we sketched the proposed case (A) with the usage of e.g. K-amide as mineralizer, placed at the bottom of the autoclave. The amount of amide in powder form is not pictured in true scale to the amount of liquid expected, this was chosen for better visualization. It is more likely, that the amount of powder would be more than the height of the meniscus of the corresponding melt. The Ga entering the amide liquid is drawn as a halo around the seed crystal pictogram, indicating the existence of a concentration gradient of Ga. In fact such a gradient around a dissolving GaN crystal was observed in an in situ x-ray imaging experiment by Schimmel et al. [39] (and see also Chap. 10 of this book) and would contribute another little confirmation of the here proposed semi empirical model. In the figure the amidogallate complex is given as $[Ga(NH_2)_4]^-$.

In contrast to the case (A) the usage of the azide, case (B), will lead early in the process to an explosive decomposition of the mineralizer with fast distribution all over the volume of the reaction vessel. The amide ions will be formed everywhere

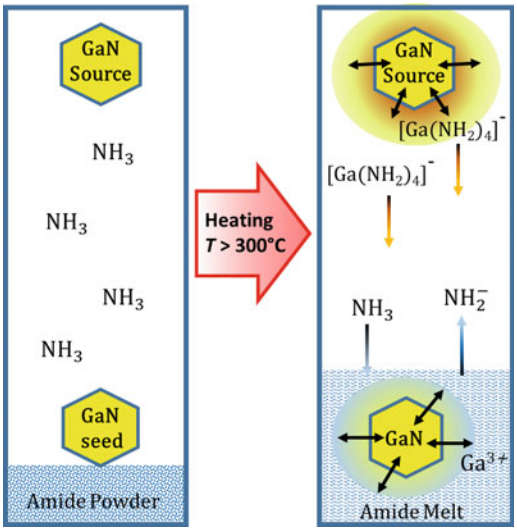

Fig. 6.9 Schematic drawing of the case (A) where the mineralizer is put at the bottom of the autoclave in form of an amide powder. In the second step the amide forms a melt situated at the bottom of the autoclave which can surround the seeds. The situation of a seed possibly placed above the melt surface is not drawn here. Other details are given in the text

in the autoclave and find access to the GaN source immediately. At that point in the process no liquid phase is involved so far, but the amidogallate complex can form readily. The formation reaction would be limited by the available interface area to a Ga containing source compound, which is the surface of the GaN source blocks. If the process condition with respect to p and T are such that the experiment falls into the stability field of the complex, which may exist in form of a liquid as discussed before, that can segregate to the bottom of the autoclave and could or could not immerse the seeds. The fundamental difference would be, that in the case (A) the liquid phase would be an amide and in case (B) the liquid phase would be the amidogallate complex. The amidogallate is now already saturated with Ga such that the GaN seed crystals see no driving force to dissolve. Consequently, back etching should not be a big issue here. As the bottom is the hotter zone, the complex can thermally dissociate and release the Ga. As the GaN seed surfaces offers the energetic sink, a GaN layer will grow with probably no or only few back etching that could have appeared in case (A) before. The free amide ions can be transported back to the source and bring about additional Ga and the complex compound forms again. The latter case can probably exhibit higher growth rates compared to case (A) if performed under optimized conditions or in a different way as will be discussed later. The case (B) is sketched in the following Fig. 6.10.

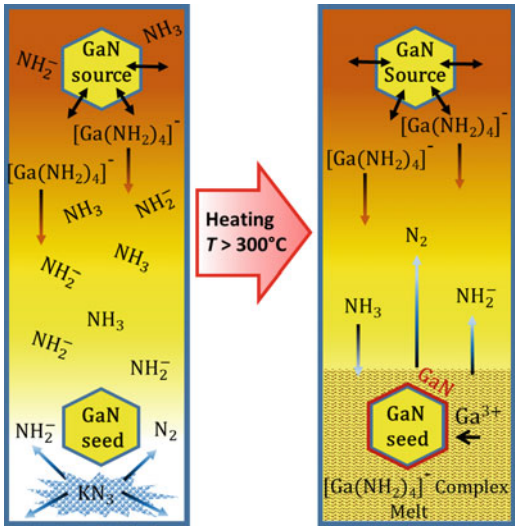

Fig. 6.10 Schematic drawing of the case (B) where the mineralizer is put at the bottom of the autoclave in form of an azide powder. After explosive azide decomposition the amidogallate complex will form readily everywhere in the volume. In the second step a melt formed by the amidogallate may exist at the bottom of the autoclave which could also surround the seeds. This melt is already saturated with Ga and GaN can grow onto the surface of the seeds easily. The condition of a seed possibly placed above the melt surface is not drawn here. Other details are given in the text

Table 6.1 Summary of the major differences and consequences between case (A) and case (B) or the application of an amide or azide mineralizer respectively

	Case A	Case B
Mineralizer-type	Amide	Azide
Limiting step for the formation of the complex	Solubility of amide mineralizer in supercritical ammonia	Surface area of the GaN source blocks
	Solution kinetic via the melt surface	Kinetic of the formation reaction
	Formation reaction at the surface of the melt	Thermal decomposition of the complex melt
Expected growth rate	Low	High
Expected supersaturation	Low	High
Expected backetching	High	Low
Dissolution rate at source	Low	High

Also in the case (B) the mineralizer could be as well placed around the GaN source blocks, which may change the amount of GaN readily solved. However, it would not change the principal picture discussed with case (B).

In the following Table 6.1 the major differences between the two cases are compiled, showing what consequences would be expectable due to the choice of an alkali amide or azide as a mineralizer.

6.3.5 New Perspective for the Growth of GaN from Amidogallate Liquids

In fact considering all the findings discussed here, the consequence for the crystal growth may be various and potentially groundbreaking, including a complete novel perspective for the design of the ammonothermal growth in a basic regime. Even though the picture drawn here contains speculative aspects, which need of cause additional prove, there is enough experimental basis also in conjunction with parallel findings from the other researchers reporting their studies in this book, to make this a valid hypotheses. The most jolting finding is unambiguously the existence of an amidogallate complex in a liquid form during the growth process, which offers a different perspective and options. It promotes a suggestion for a complete new growth process based on the thermal decomposition of the liquid amidogallate. The fundament is, that this liquid is already saturated with nitrogen and gallium ions with respect to the wanted compound (GaN) that should be crystallized. Hertrampf et al. [38] discussed the condensation reaction of the dissolved intermediates towards GaN and the action of access ammonia which obviously stabilizes the complex intermediate ions. This condensation would function even at temperatures as low as

room temperature. This implies also, that the assumption made in the model of case (B) as discussed above, that the GaN had crystallized from the amide complex liquid is very valid. Principally, the alkali metal amidogallate complexes, at least K-, Rb-, and Cs-amidogallates, could be synthesized individually as a liquids or amorphous solids. All show a significant vapour pressure and release ammonia if not kept sealed or under respective gas atmosphere, which means that the compounds can be stable in form of a liquid if kept under overpressure. As the vapour pressure likely increases if the compound is heated, the necessary required overpressure may rise to higher values. In turn this implies that the amidogallate complex could exist in liquid form under a high pressure like applied in the ammonothermal crystal growth regime and suggested by our before described experiments.

In consequence this would offer the opportunity to directly load the complex as solid or liquid into the autoclave and place the GaN seeds directly inside the liquid. The reaction vessel should then be filled with liquid ammonia to some excess. The liquid can be considered as a presaturated solvent. As for the crystallization the system has to be heated, the vessel will become pressurized. The fundamental principle of crystallizing the GaN out of the liquid, due to subsequent decomposition or reduction of the solvent would be a very classical way of crystal growth. The technique of flux evaporation has various advantage including the possibility of isothermal growth, provided the fact that the vapor pressure of the flux is high enough, which is indeed the case. Usually the evaporation is established by thermal decomposition of the solvent. Under the given circumstances with the amidogallate complexes, the decomposition of the flux could also be established by controlled lowering of the system pressure at constant temperature.

From the experimental observations made in our study we can conclude that lowering the pressure at constant temperature would effectively decompose the complex and release the GaN. However, controlling crystal growth by slow depressurization is quite difficult. So as an alternative the thermal decomposition at constant pressure can be taken as another option. Temperature control can be established quite easily and is uncritical even up to higher temperatures if the total applied pressure is low or medium high. This means by direct usage of the amide complex-liquid under excess ammonia and subsequent slow thermal decomposition, a GaN crystal growth could be established. The striking advantage could be, that such a process may need an overpressure and some temperature but by no means such harsh conditions, like the actual used ammonothermal temperature and pressure values. In turn for such a process one would not have to deal with retrograde solubility and would be undoubtedly easier to control and observe. Prerequisite would be to finally study the stability field of amidogallat complexes and related melts in a p, T diagram in more detail.

Figure 6.11 shows the picture of a crystal grown on a rounded seed at the very bottom of the autoclave likely surrounded by the K-amidogallate liquid. The seed was a piece of GaN grinded round as a cylinder and no crystal direction was offered prominently for further growth. We called this the “kinetic seeds” This is a classical experiment. The crystal can develop freely the respective equilibrium shape for the given condition.

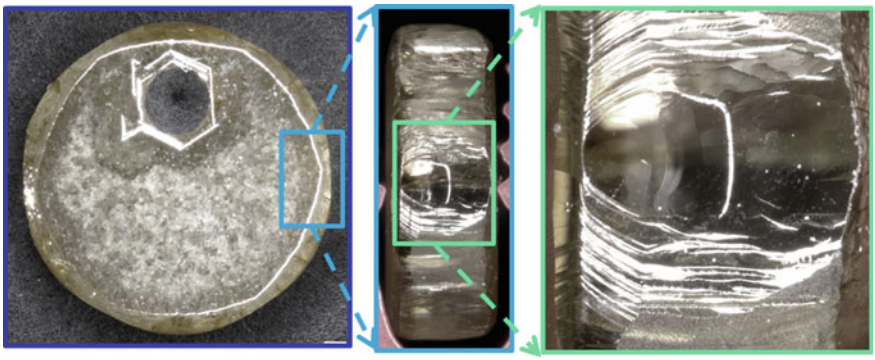

Fig. 6.11 Picture of the growth on the surface of a so called "kinetic seed" which was a piece of round grinded, cylinder shaped GaN

The hole in the seed was made for hanging the seed in a wire. It is visible that the pure cylinder shape changed and developed a natural facetted hexagonal crystal habit. The faces are mirror like flat and show stepped edges. It seems that the supersaturation was almost evenly distributed around the seed, thus growth could occur in any direction and the growth rate seems to be equal in any direction of the hexagonal prism. The basal plane directions (along the *c*-axis) grew fastest, at both *c*-directions evenly. As a conclusion the seeds must have been within a condition of metastable supersaturation, the so called Ostwald Miers regime. This observation is consequent if imagined that the seed came to lay inside the amidogallate liquid at the bottom of the autoclave and grew from the liquid.

6.4 Conclusions

The study of the basic ammonothermal regime reported here resulted in a better understanding of the ongoing processes in the autoclave. The first chemical model proposed and the later observation of a liquid phase after the opening of the autoclave in conjunction with the findings described by other colleagues here in this book not only lead to explanations for the experiments performed and discussed in this chapter, but also to a new hypothesis about the understanding of the basic ammonothermal crystal growth process in a different way. The dependencies of parameters are however manifold e.g. the type and amount of mineralizer, the place where it's being put in the autoclave, the places of the seeds, p and T, etc., which could help to explain e.g. the different growth rates or solubilities reported in literature. More studies concentrating on the intermediate species are necessary in order to achieve a full picture of the processes going on during basic ammonothermal crystal growth.

Even though some of the discussion contains speculative aspects the hypothesis made is justified.

This in turn made it possible to suggest a novel solvent evaporation growth process based on an alkali metal amidogallate liquid where crystal seed could be dipped into the amidogallate melt and the GaN could grow by thermal decomposition of the complex. Such a process would be a novelty and was never demonstrated for nitride crystal growth although different solution growth methods were tried. However, it is subject to further work to prove that suggestion and try it out experimentally.

References

1. G. Meneghesso, M. Meneghini, E. Zanoni, Gallium Nitride-enabled High Frequency and High Efficiency Power Conversion (Springer International Publishing, 2018)
2. H. Amano et al., The 2018 GaN power electronics roadmap, 1. Manufacturing challenges of GaN-on-Si HEMTs in a 200 mm CMOS fab. J. Phys. D: Appl. Phys. **51**, 163001 (2018)
3. D. Ehrentraut, N. Hoshino, Y. Kagamitani, A. Yoshikawa, T. Fukuda, H. Itoh, S. Kawabata, Temperature effect of ammonium halogenides as mineralizers on the phase stability of gallium nitride synthezised under ammonothermal conditions. J. Mater. Chem. **17**, 886–893 (2007)
4. D. Ehrentraut, M. Bockowski, E. Meissner, Technology of Gallium Nitride Crystal Growth (Springer, Berlin, New York, 2010)
5. A. Tenten, Amide und Nitride von Nickel, Palladium und Platin sowie von Aluminium, Gallium und Indium. Doctoral Dissertation, Universität Dortmund (1991)
6. R. Guarino, J. Rouxel, L'amidogallate de potassium $KGa(NH_2)_4$ et l'imidogallate $KGa(NH)_2$. L'obtention de l'amidure de gallium $Ga(NH_2)_3$. Bull. Soc. Chim. Fr. **7**, 2284–2287 (1969)
7. S. Zhang, Intermediates During the Formation of GaN under Ammonothermal Conditions. Doctoral Dissertation, Universität Stuttgart (2014)
8. J. Erlekampf, J. Seebeck, P. Savva, E. Meissner, J. Friedrich, N.S. Alt, E. Schlücker, L. Frey, Numerical time-dependent 3D simulation of flow pattern and heat distribution in an ammonothermal system with various baffle shapes. J. Crystal Growth **403**, 96–104 (2014)
9. J. Seebeck, P. Savva, J. Erlekampf, E. Meissner, J. Friedrich, L. Frey, Species transport by natural convection of supercritical ammonia, in Turbulence, Heat and Mass Transfer, 8, Begell House, Inc. (2015)
10. R. Dwilinski, R. Doradziński et al., Bulk ammonothermal GaN. J. Crystal Growth **311**, 3015–3018 (2009)
11. R. Kudrawiec et al., Nonpolar GaN substrates grown by ammonothermal method. Appl. Phys. Lett. **93**, 061910 (2008)
12. T. Hashimoto, M. Saito et al., Seeded growth of GaN by the basic ammonthermal method. J. Cryst. Growth **305**, 311–316 (2007)
13. M. Saito, D.S. Kamber, Plane dependent growth of GaN in supercritical basic ammonia. Appl. Phys. Express **1**, 121103 (2008)
14. B. Wang, M.J. Callahan, K.D. Rakes, L.O. Bouthillette, S.-Q. Wang, D.F. Bliss, J.W. Kolis, Ammonothermal growth of GaN crystals in alkaline solutions. J. Cryst. Growth **287**, 376–380 (2006)
15. T. Hashimoto, F. Wu, J.S. Speck, S. Nakamura, Growth of bulk GaN crystals by the basic ammonothermal method. Jpn. J. Appl. Phys. **2**, 889–891 (2007)
16. D. Bliss, B. Wang, M. Suscavage et al., Ammonothermal GaN: morphology and properties. J. Cryst. Growth **312**, 1069–1073 (2010)
17. D. Tomida, Y. Kagamitani, Q. Bao, K. Hazu, H. Sawayama, S.F. Chichibu, C. Yokoyama, T. Fukuda, T. Ishiguro, Enhanced growth rate for ammonothermal gallium nitride crystal growth using ammonium iodide mineralizer. J. Cryst. Growth **353**, 59–62 (2012)

18. R. Kucharski, M. Zając, R. Doradziński, M. Rudziński, R. Kudrawiec, R. Dwiliński, Non-polar and semi-polar ammonothermal GaN substrates. Semicond. Sci. Technol. **27**, 024007 (2012)
19. G.G.C. Arízaga, G.S. Herrera, A.M. Fischer, O.E.C. López, Influence of reaction conditions on the growth of GaN rods in an ammono-CVD reactor. J. Cryst. Growth **319**, 19–24 (2011)
20. T. Li, G. Ren et al., Growth behavior of ammonothermal GaN crystals grown on non-polar and semi-polar HVPE GaN seeds. Cryst. Eng. Comm. **21**, 4874–4879 (2019)
21. P. Hartman, W.G. Perdock, On the relations between structure and morphology of crystals. I, Acta Crystallogr. **8**, 49–52 (1955)
22. R.F.P. Grimbergen, H. Meekes, P. Bennema, C.S. Strom, L.J.P. Vogels, On the prediction of crystal morphology. I. The Hartman-Perdok theory revisited. Acta Crystallogr. A **54**, 491–500 (1998)
23. P. Bennema, H. Meekes, S.X.M. Boerrigter, H.M. Cuppen, M.A. Deij, J. van Eupen, P. Verwer, E. Vlieg, Crystal growth and morphology: new developments in an integrated Hartman−Perdok connected net roughening transition theory, supported by computer simulations. Cryst. Growth & Design **4**, 905–913 (2004)
24. L.N. Rashkovich, G.T. Moldazhanova, Growth kinetics and bipyramid-face morphology of KDP crystals, in Growth of Crystals, vol. 20, ed. by E.I. Givargizov, A.M. Melnikova (Springer, Boston, MA, 1996)
25. M. Rak, N.N. Eremin, T.A. Eremina et al., On the mechanism of impurity influence on growth kinetics and surface morphology of KDP crystals-I. J. Cryst. Growth **273**, 577–585 (2005)
26. T.A. Eremina, V.A. Kuznetsov, N.N. Eremin, T.M. Okhrimenko, N.G. Furmanova, E.P. Efremova, M. Rak, On the mechanism of impurity influence on growth kinetics and surface morphology of KDP crystals-II. J. Cryst. Growth **273**, 586–593 (2005)
27. F. Abbona, D. Aquilano, Morphology of crystals grown from solutions, in Springer Handbook of Crystal Growth (Springer, Berlin, Heidelberg, 2010). ISBN 978-3-540-74182-4
28. S. Pimputkar, S. Kawabata, J.S. Speck, S. Nakamura, Improved growth rates and purity of basic ammonothermal GaN. J. Cryst. Growth **403**, 7–17 (2014)
29. D. Ehrentraut, R. T. Pakalapati, D. S. Kamber, W. Jiang, D. W. Pocius, B. C. Downey, M. McLaurin, M. P. D'Evelyn, High quality, low cost ammonothermal bulk GaN substrates. Jpn. J. Appl. Phys. **52**, 08JA01 (2013)
30. N.S.A. Alt, E. Meissner, E. Schluecker, In situ monitoring technologies for ammonothermal reactors. Phys. Status Solidi C **9**, 436–439 (2012)
31. Q.-S. Chen, V. Prasad, W.R. Hu, Modeling of ammonothermal growth of nitrides. J. Cryst. Growth **258**, 181–187 (2003)
32. Y. Masuda, A. Suzuki,T. Ishiguro, Y. Chiaki, Numerical simulation of heat and fluid flow in ammonothermal GaN bulk crystal growth process. Jpn. J. Appl. Phys. **52**, 08JA05 (2013)
33. Y.-N. Jiang, Q.-S. Chen, V. Prasad, Numerical simulation of ammonothermal growth processes of GaN crystals. J. Cryst. Growth **318**, 411–414 (2011)
34. S. Pendurtia, Q.-S. Chen, V. Prasad, Modeling ammonothermal growth of GaN single crystals: the role of transport. J. Cryst. Growth **296**, 150–158 (2006)
35. S. Zhang, N.S.A. Alt, E. Schlücker, R. Niewa, Novel alkali metal amidogallates as intermediates in ammonothermal GaN crystal growth. J. Cryst. Growth **403**, 22–28 (2014)
36. P. Molinie, R. Brec, J. Rouxel, P. Herpin, Structures des amidoaluminates alcalins $MAl(NH_2)_4$ (M = Na, K, Cs). Structure de l' amidogallate de sodium $NaGa(NH_2)_4$. Acta Crystallogr. B **29**, 925–934 (1973)
37. B. Wang, M.J. Callahan, Transport growth of GaN crystals by the ammonothermal technique using various nutrients. J. Cryst. Growth **291**, 455–460 (2006)
38. J. Hertrampf, E. Schlücker, D. Gudat, R. Niewa, Dissolved intermediates in ammonothermal crystal growth: stepwise condensation of $[Ga(NH_2)_4]^-$ toward GaN. Cryst. Growth Des. **17**, 4855–4863 (2017)
39. S. Schimmel, M. Lindner, T.G. Steigerwald, B. Hertweck, T.M.M. Richter, U. Künecke, N.S.A. Alt, R. Niewa, E. Schlücker, P. Wellmann, Determination of GaN solubility in supercritical ammonia with NH_4F and NH_4Cl mineralizer by in situ x-ray imaging of crystal dissolution. J. Cryst. Growth **418**, 64–69 (2015)

Chapter 7
Ultrasound Measurement as a Tool for in Situ Determination of Filling Degree Under Extreme Conditions

Wilhelm Schwieger and Hasan Baser

Abstract Ammonothermal syntheses require high pressures and temperatures to realize the supercritical conditions. For this a special autoclave technology is required, which places special demands on both the material and the geometrical design. Characteristics are thick walls, high weight, opaque, narrow interior. Therefore the exact determination of initial weights and in particular filling degrees of liquids, which are liquid only under pressure, becomes difficult. In this section, we are going to compare three methods (i) pumping time measurement, (ii) determination by weighing and (iii) ultrasound for adjusting and/or determining the ammonia filling degree of ammonia in an autoclave are presented and the advantages and disadvantages of the individual methods are compared. In addition it is important to have the Ammonia amount very precise to describe the all the concentrations in the autoclave, even under the ammothermal conditions.

7.1 Introduction

Ammonia is used as a solvent in ammonothermal syntheses and is a colorless gas with a characteristic pungent odor. Ammonia boils at −33.3 °C under atmospheric pressure. Ammonia gas condenses to a colorless liquid during cooling and compression. The density and vapor pressure are 0.60 g/cm^3 and 8 bar respectively at ambient temperature (25 °C).

For an exact adjustment of the concentrations e.g. of used mineralizers in ammonia, the ammonia filling in the autoclave should be well controlled and reproducible. In addition, the filling level of the ammonia plays a safety-related role. The pressure of the supercritical ammonia at a given temperature shows a dependence on the filling degree. The maximum permissible pressure of 3000 bar (for Inconel 718) at 400 °C is reached with a filling level of 70%. The filling level should not exceed

W. Schwieger · H. Baser (✉)
Institute of Chemical Reaction Engineering, University of Erlangen-Nuremberg, Egerlandstraße 3, Erlangen 91058, Germany
e-mail: hasan.baser@fau.de

E. Meissner and R. Niewa (eds.), *Ammonothermal Synthesis and Crystal Growth of Nitrides*, Springer Series in Materials Science 304,
https://doi.org/10.1007/978-3-030-56305-9_7

58% if a temperature of 600 °C is reached in the autoclave [1]. Exceeding the filling level could lead to structural breakdown of the autoclave at the above temperatures.

Fill level sensors reliably detect the levels of liquids in containers or tanks. Critical process conditions, such as emptying a hydraulic tank or unintentional overfilling of a container, are also monitored with level sensors. A number of proven measuring methods are available for this purpose, such as ultrasound, non-contact and guided radar, capacitive electrode and conductivity sensor [2, 3]. In all of these methods, the probes or electrodes must be inserted into the vessel through an opening in the lid, which introduces further challenges in terms of leak tightness in the ammonothermal system. The high-pressure autoclaves are very solidly built so that they can withstand the extreme test conditions of up to 3000 bar. Thus, none of these in-line methods can be used to determine or adjust the ammonia level in an ammonothermal autoclave.

7.2 Ammonia Filling Process

For use, ammonia is taken from the bottle in gaseous form. Different approaches are used to fill the alloy autoclave with ammonia: condensation of ammonia in a cooled autoclave and filling the autoclave with ammonia by high-pressure pumps. The condensation of ammonia in the autoclaves is historically carried out by the by means of a tensieudiometer, a device for the simultaneous measurement of pressure and volume [4]. The autoclave, which is already filled with the solid reactants, is connected to the tensieudiometer and cooled to below the boiling point of ammonia ($T \leq 239.79$ K, ambient pressure) and ammonia condenses into the autoclave. By measuring the volume and pressure, the desired amount of ammonia can be filled into the autoclave. In order to cool the autoclave, the autoclave body is usually placed in a cooling bath made of acetone or ethanol and dry ice [1].

In the second method, the gaseous ammonia is liquefied by means of a high-pressure diaphragm pump. A cryostat has been placed between the gas cylinder and the pump, in which ammonia is cooled down to −15 °C and thus quickly liquefied in the pump. The flow rate can be adjusted by varying the pump capacity. In this constellation, the liquid ammonia flows into the autoclave. The ammonia flow is controlled by pneumatic valves between individual parts.

In our experiments, the second filling method was used, since only with this method is it possible to adjust the filling degree of the ammonia even at higher temperatures. The filling process was carried out in the following way. In the first step before the filling process, the plant lines and the autoclave are evacuated. This is done up to 80 mbar $< P <$ 100 mbar by means of a diaphragm pump. A turbo molecular pump then generates a vacuum of up to 4×10^{-7} mbar. The autoclave is then flushed with nitrogen. After repeated evacuation and rinsing of the autoclave, all moisture and oxygen is removed from the autoclave.

After the evacuation process, the ammonia pump is switched on and gaseous ammonia is liquefied in the pipes up to the autoclave valve. As long as there is still gaseous ammonia in the pipes, the pressure remains at 8 bar (at 25 °C). The fact that

the pipes are filled with liquid ammonia can be seen from the fact that the pressure rises above 10 bar. Ammonia was still compressed up to a pressure of 50 bar. After reaching 50 bar, the autoclave valve is opened and the liquid ammonia flows into the autoclave. The approximate duration of the filling process to reach a volume of 54 ml ammonia is approx. 5:30 min.

The filling process is terminated by switching off the ammonia pump. The autoclave manual valve is closed. Ammonia in the pipes is drained and the pipes are flushed with nitrogen. The autoclave can then be disconnected from the filling station and placed in the ovens to start the experiment.

7.3 Possibilities for Setting and Determining the Filling Degree

For the adjustment of the ammonia filling quantity, we had three methods at our service: (i) Control over the switch-on time of the ammonia pump, (ii) determination of the ammonia quantity gravimetrically by weighing the autoclave before and after filling and (iii) ultrasonic method. Here these methods are explained in detail with the advantages and disadvantages. The experimental feasibility and simplicity of the three filling methods are compared.

7.3.1 Filling the Autoclave over the Switch-On Time of the Ammonia Pump

The target value of the filling degree for the solubility measurements (see Chap. 9) of GaN was set at 55 vol.%. This corresponds to a volume of about 53.22 ml and a weight of about 33 g of liquid ammonia. The ammonia filling quantity was first tried to be adjusted via the switch-on time of the ammonia pump. In order to achieve a reproducible filling, the output of the ammonia pump was set so that approx. 10 ml of liquid ammonia per minute is pumped. In order to check the amount of ammonia filled by the pump, a series of measurements of the filling processes was carried out. The switch-on time of the pump was measured for each measurement. The amount of ammonia filled was determined from the difference between the autoclave weight before and after filling. Experience has shown that filling with a time measurement is very inaccurate and leads to large fluctuations of the filling level (Table 7.1).

Table 7.1 Results of the control of the constant flow rate of the ammonia pump

Measurement	Pumping time (min)	NH_3 (g)	NH_3 (g/min)	NH_3 (ml/min)
1	6	38	6.33	9.31
2	6	41	6.83	10.05
3	6.33	40	6.32	9.29
4	6.5	35	5.38	7.92
5	6.5	40	6.15	9.05
6	6.75	37	5.48	8.06
7	7	40	5.71	8.40
8	7.5	41	5.47	8.04
Mean value ($\bar{x}$)			**5.96**	**8.77**
Absolute deviation (Δx)			**0.49**	**0.72**
Relative deviation ($\Delta x/\bar{x}$)			**0.08**	**0.08**
Relative deviation (%)			**8.25**	**8.25**

7.3.2 Filling by Weighing of the Autoclave Before and After the Ammonia Filling

Another way of determining the amount of ammonia in an autoclave is to weigh the autoclave before and after filling. For this, the autoclave is separated from the filling station after filling and the amount of ammonia filled is determined by weighing it. If the ammonia filling quantity determined by weighing the autoclave is too high, the autoclave must be connected to the filling station and excess ammonia must be release into the scrubber via the pipes. The process of releasing and weighing must be repeated several times until the desired amount of ammonia remains in the autoclave. This also applies to autoclaves with little filling. In this case, the autoclave must be refilled at the filling station. The whole process turns out very demanding, since the massively built ammonothermal autoclaves weigh more than 10 kg.

7.3.3 Level Measurement by Means of Ultrasound Measurement

In the solubility experiments, the ultrasound was used to determine the NH_3 level in the autoclave. Ultrasound is a sound wave whose frequency range lies above the human hearing range.

The frequency range starts at 20 kHz. The range between 20 kHz and 10 MHz is technically relevant. With this technology, ultrasonic sensors emit sound waves that move in matter. The speed of sound in the matter depends on the properties of the substance.

An ultrasonic sensor using the pulse-echo method was used to check and monitor the ammonia filling level. In this method, short acoustic pulses are emitted by an ultrasonic transducer via the autoclave wall into the autoclave. The time of flight (TOFL) of ultrasonic waves for transmission through the autoclave wall and inside the autoclave are measured. At the interfaces between the different media with different densities, the transmitted wave is reflected back to the sensor, which functions both as transmitter and receiver. These reflections are called echoes (Fig. 7.1). In this way, characteristic echoes with different time of flight are generated with several contiguous media (sensor, autoclave wall, ammonia). The echoes 1–6 in Fig. 7.1 result from multiple reflections on the autoclave wall.

The additional signals I and II in Fig. 7.1 indicate the presence of ammonia in the autoclave. For the other liquids, only the position of the additional signal shifts according to the velocity of sound in the liquid present on the time scale. Thus, when ethanol or water is added to the autoclave, they appear at 52 µs for ethanol (1135 m/s) instead of 46 µs for ammonia (1315 m/s) and at 43 µs for water (1500 m/s) (Fig. 7.2, blue: signal of the empty autoclave, red: signal when the autoclave is filled with liquid).

The ultrasonic sensor is placed on the outside of the autoclave wall at a height determined from a calibration curve (Fig. 7.4). Figure 7.3 shows a schematic and photographic illustration of how the ultrasonic sensor is attached to an autoclave wall. For a good coupling of the sound waves, glycerine is introduced into the air gap between probe and autoclave. During the filling process, the pulse-echo signal is observed through the autoclave walls by means of the ultrasonic program.

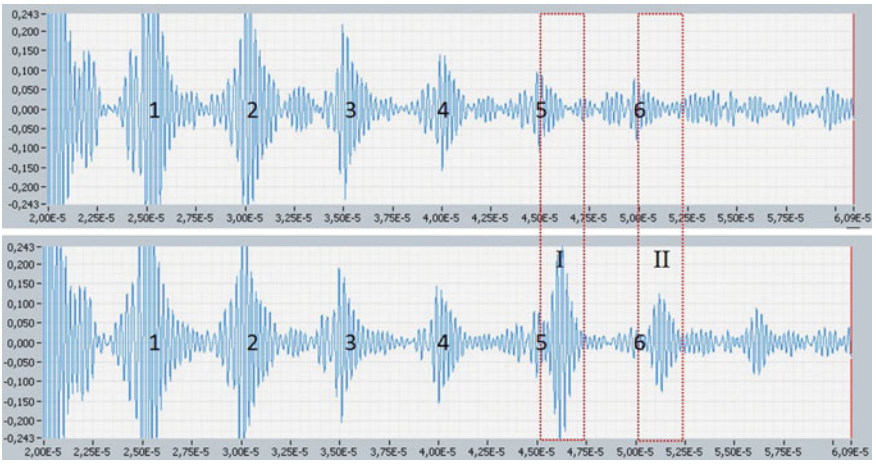

Fig. 7.1 The echoes resulting from the propagation of ultrasonic waves through the empty autoclave (top) and the autoclave filled with ammonia (bottom). The echoes 1 to 6 result from multiple reflections on the autoclave wall. The additional echoes I and II occur when the autoclave is filled with ammonia

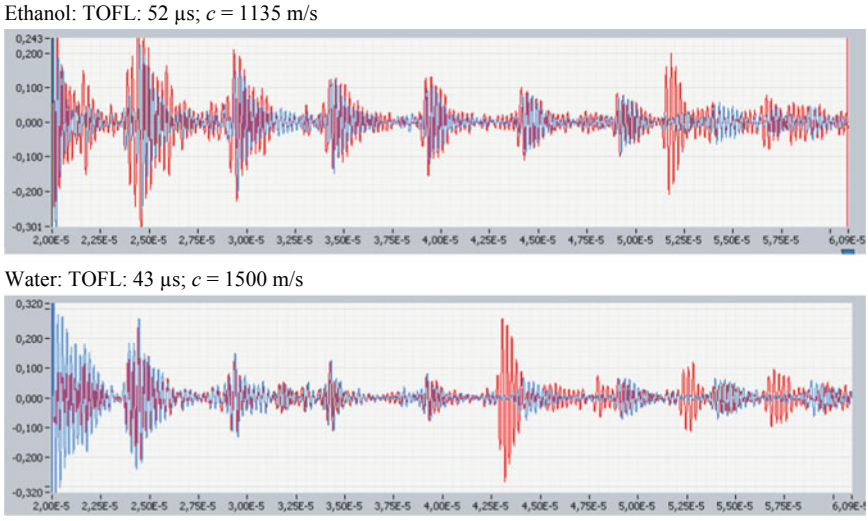

Fig. 7.2 Signal from an empty (blue) and liquid-filled autoclave (red)

Fig. 7.3 Placement of the ultrasonic sensor and adjustment of the filling level

As long as the filling level of ammonia is lower than the probe height, the upper signal from Fig. 7.1 is observed on the computer screen. It merely represents the repeated reflection of the ultrasonic signal on the autoclave wall.

As soon as the filling level of ammonia correlates with the ultrasonic sensor height, an additional signal is generated at a running time of 46 and 51 µs. This additional signal corresponds to the ammonia signal and is clearly visible in the lower part of Fig. 7.1.

In order to find out at what height the sensor must be placed on the autoclave so that the target volume in the autoclave can be measured, the sensor height was calibrated with the filling volume. For this purpose, different quantities of water (20–90 ml) were added to the autoclave and the corresponding height was determined by moving the sensor, where the signal showed the presence of the filled water (Fig. 7.4).

The advantage of the ultrasound method is that it is not only possible to determine the filling quantity of a filled autoclave, but also the ammonia quantity can be precisely adjusted by controlled release and monitoring of the ultrasound signal.

In order to check the accuracy of the ammonia filling level set by ultrasonic, the pressure/time dependence on pure ammonia was investigated at a filling level of 55%. The filled autoclave was heated in the oven to 400 °C (oven ramp 5 °C/min) and the pressure curve was recorded for 24 h. After the test, the decomposition gases (H_2 and N_2) were discharged at the filling station and the ammonia filling level was adjusted by means of ultrasound and the experiment was repeated at 50 °C increased temperature. The experiment was carried out at a temperature interval of $T = 400$–550 °C (increased by 50 °C each). The recorded pressure curves for the different temperatures are shown in Fig. 7.5. The in situ temperature measurements have shown that the set target temperatures in the autoclave are reached after 4 h. The pressures when the target temperatures were reached were read from the pressure curve and compared with those in the NIST database (Fig. 7.6). In the heating phase up to the hour $t = 4$ h, the steep pressure rise due to the temperature increase can be seen. The characteristic break point after approx. 1.5 h, which corresponds to the phase change of ammonia, is also clearly visible. In the isothermal phase from $t = 4$ h the final temperature is reached and the pressure increases with a slight gradient. The reason for this is the decomposition of ammonia to hydrogen and nitrogen.

The decomposition rate of ammonia depends on the temperature. The higher the temperature, the steeper the curve, i.e. the faster the ammonia decomposition takes place. Ammonia decomposition also takes place during the heating phase. Therefore, the pressures read off at 4 h are higher than they should be (additional pressures of

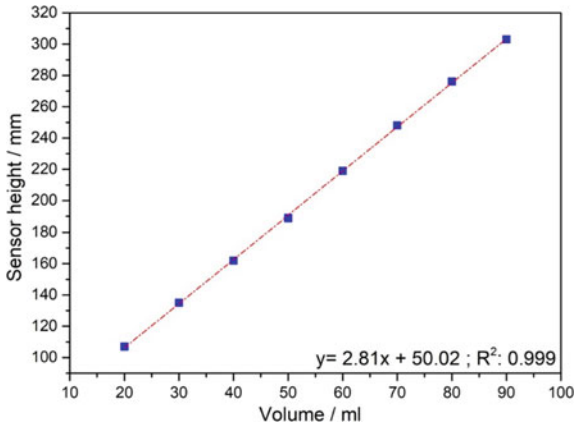

Fig. 7.4 Calibration curve to determine the dependency of the sensor height on the filling volume

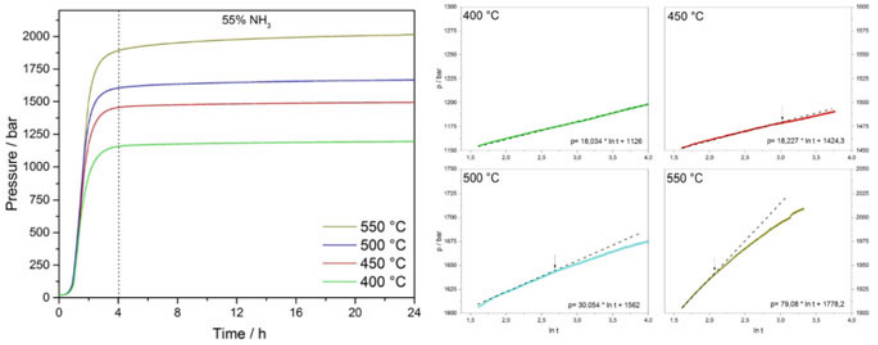

Fig. 7.5 Pressure progress of ammonia at different temperatures (left) and the linearized decomposition curve p versus ln(t) (right) (ammonia filling degree: 55%)

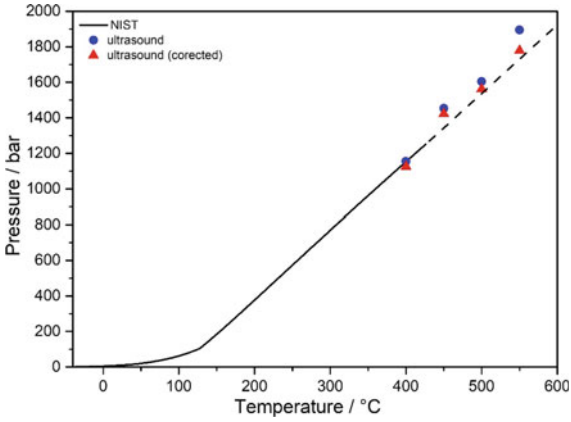

Fig. 7.6 Comparison of the pressure values at different temperatures (blue circle: row values, red triangle: corrected values) with those of calculated with NIST database

the resulting gases N_2 and H_2 in the heating phase) and must be corrected under consideration of the ammonia decomposition. This was done by extrapolating the linearized decomposition curve. The representation of (p) versus ln(t) allows better recognition of the linear pressure increase in the isothermal phase due to ammonia decomposition. The negative deviations from the linear curve at temperatures of 500 and 550 °C are due to the diffusion of the hydrogen from the autoclave.

If the corrected pressures are compared with those from the NIST database, a good agreement can be seen. This means that the ammonia fill levels have been correctly adjusted using the ultrasonic method.

7.3.4 Mathematical Error Analysis of the Three Filling Methods

In addition to the comparison of the experimental feasibility and simplicity, the absolute and relative deviations from the arithmetic mean value that occurred during filling were calculated mathematically and compared with each other. The arithmetic mean ($\bar{x}$) of a set of observed data is defined as being equal to the sum of the numerical values of each and every observation divided by the total number of observations:

$$\text{Mean value} = \bar{x} = \frac{1}{N}\sum_{i=1}^{N} x_i \tag{7.1}$$

The absolute deviation (Δx) is defined as a scale of the dispersion of the measured values around the mean value with the sum of the deviation squares:

$$\text{Absolute deviation} = \Delta x = \sqrt{\frac{1}{N-1}\sum_{i=1}^{N}(x_i - \bar{x})^2} \tag{7.2}$$

The absolute deviation (Δx) is a positive value that becomes zero when all measured values match. It provides an estimate of the deviation from the true value, which is generally not known. Therefore, the deviation from the mean value $\bar{x}$ is used.

Pumping Time
The absolute deviation calculated in Table 7.1 can be used to determine the deviation for different filling volumes, which results from the irregular pump performance of the ammonia pump. These can be found in Table 7.2 for the later comparison with those of the other filling methods.

Weighing
An important problem of the method is the inaccuracy of weighing. With such weights, many scales have an inaccuracy of ±1 g. Since the autoclave is weighed twice, the absolute inaccuracy is doubled to ±2 g. In the following Table 7.3, the resulting error analysis was calculated for fill levels of 30–60% by weight.

Ultrasonic Measurement
When filling by means of ultrasonic measurement, the sensor height must be adjusted correctly. Errors can occur when reading the height (±1 mm) from the meter rod (Table 7.4).

The calculated values of absolute and relative errors by the different filling methods are compared in Table 7.5. In Fig. 7.7, the absolute errors that occur when three methods are used for filling are shown graphically. For the absolute error, the ultrasonic and weighing methods show a constant progression as a function of the

Table 7.2 Calculation of errors by the filling with time measurement for the different filling volumes of the autoclave

Filling degree %	30%	40%	50%	60%
	V_{NH3} (ml)	V_{NH3} (ml)	V_{NH3} (ml)	V_{NH3} (ml)
1	27.22	36.24	45.34	54.44
2	25.23	33.59	42.02	50.46
3	27.28	36.32	45.44	54.57
4	32.02	42.63	53.33	64.04
5	28.02	37.30	46.66	56.03
6	31.45	41.87	52.39	62.90
7	30.17	40.17	50.25	60.34
8	31.54	41.99	52.53	63.07
Mean value ($\bar{x}$)	**29.12**	**38.76**	**48.50**	**58.23**
Absolute deviation (Δx)	**2.35**	**3.13**	**3.91**	**4.70**
Relative deviation ($\Delta x/\bar{x}$)	**0.08**	**0.08**	**0.08**	**0.08**
Relative deviation (%)	**8.07**	**8.07**	**8.07**	**8.07**

Table 7.3 Calculation of errors by the filling by weighing

	Before filling	After filling	Amount	Volume	
Error size	±1 g	±1 g	±2 g	±2.94 ml	
Filling degree	Amount of NH_3 (g)	Volume of NH_3 (ml)	Absolute (ml)	Relative	%
30	19.79	29.1	±2.94	0.10	10.10
40	26.38	38.8	±2.94	0.08	7.58
50	32.98	48.5	±2.94	0.06	6.06
60	39.58	58.2	±2.94	0.05	5.05

Table 7.4 Calculation of errors by the filling with ultrasonic measurement

		Height adjustment	Volume		
Error size		±1 mm	±0.76 ml		
Filling degree	Amount of NH_3	Volume of NH_3	Absolute (ml)	Relative	%
30	19.79	29.1	± 0.76	0.03	2.61
40	26.38	38.8	± 0.76	0.02	1.96
50	32.98	48.5	± 0.76	0.02	1.57
60	39.58	58.2	± 0.76	0.01	1.31

filling degree, whereas the lowest absolute errors are observed when filling with ultrasonic measurement (±0.75 ml). Filling by time measurement shows a dependence with the filling degree. The more the autoclave is filled, the greater is the absolute

Table 7.5 Comparison of errors by the different filling methods

		Time measurement		Weighing		Ultrasonic	
Filling degree %	V_{NH3} (ml)	Absolute (ml)	%	Absolute (ml)	%	Absolute (ml)	%
30	29.1	±2.35	8.07	±2.94	10.10	±0.76	2.61
40	38.8	±3.13	8.07	±2.94	7.58	±0.76	1.96
50	48.5	±3.91	8.07	±2.94	6.06	±0.76	1.57
60	58.2	±4.70	8.07	±2.94	5.05	±0.76	1.31

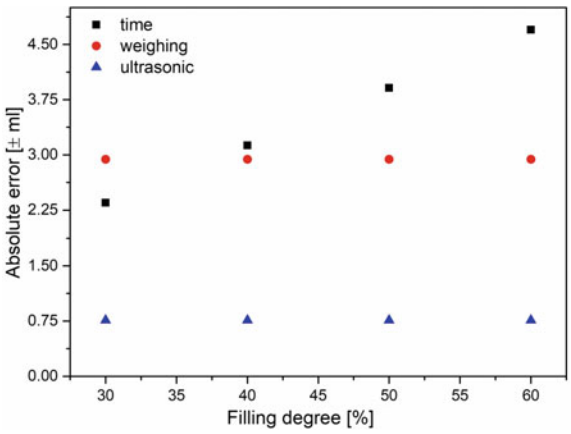

Fig. 7.7 Comparison of the absolute errors in the different filling methods

error. Figure 7.8 shows the relative errors calculated from the absolute errors for the three methods. Here too, it can be seen that the smallest error is made when filling with ultrasonic measurement.

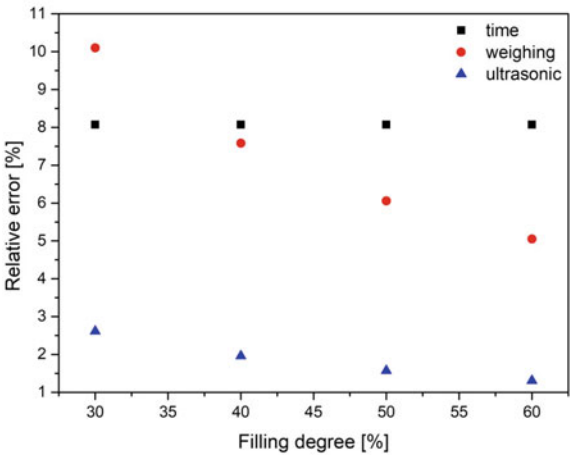

Fig. 7.8 Comparison of the relative errors in the different filling methods

7.4 Conclusion

Various techniques may give information on the filling degree of nontransparent autoclaves. For thick-walled heavy ammonothermal reactors determination of filling degrees via weight changes or pumping time measurements may lead to highly erroneous results. However, the filling height can be directly determined via ultrasound measurements and the filling level calculated via knowledge of autoclave interior shape and dimensions. Thus, this technique appears superior to other alternatives and is proposed as future standard method due to its simple experimental set-up after being once developed and established, and according to its high accuracy.

References

1. T.M.M. Richter, R. Niewa, Chemistry of ammonothermal synthesis. Inorganics **2**, 29–78 (2014)
2. G.J. Roy, *Notes on Instrumentation and Control* (Elsevier, London, 1994), pp. 20–26
3. D.R. Gillum, in *Industrial Pressure, Level, and Density Measurement* (New York, 1985)
4. G.F. Hüttig, Apparat zur gleichzeitigen Druck- und Raummessung von Gasen. Z. Anorg. Allg. Chem. **114**, 161 (1920)

Chapter 8
Direct Determination of Viscosity of Supercritical Solutions

Thomas G. Steigerwald and Eberhard Schlücker

Abstract The following chapter is mainly aimed at simulators and crystal growers, as viscosity has an influence on the flow behaviour in the reactor and the diffusion coefficient in the crystal's vicinity. So, the chapter gives an overview of influencing factors to viscosity in ammonothermal media, which are the pressure and temperature as well as the concentration of used mineralizers. Therefore, different possible viscometers are described and discussed in detail for its potential use in ammonothermal media. Hereby two promising options are presented in detail: a modified rolling ball viscometer as well as an adaptation of the ultrasonic pulse-echo method for viscosity measurement for ammonothermal systems. While the last is mostly based on literature research and only some general prove of principle are carried out, the first one is fully described and analysed during operation. This means for the adaptation of this principle four critical aspects have to be overcome. As a result, the viscosity of ammonia in the range above 400 °C up to 600 °C at maximum pressure of 252 MPa is shown. Additionally, some measurements of ammonia-ammonium-fluoride-mixtures are compared with pure ammonia, whereas the viscosity is about 1.4 times lager with ammonium fluoride then without.

8.1 Introduction

The entire understanding of the processes in the autoclaves also includes the flow currents and requires also for this aspect a full understanding of them. The reason for this is that free convection generally prevails in the autoclaves for ammonothermal

T. G. Steigerwald · E. Schlücker
Chair of Process Machinery and Systems Engineering, Friedrich-Alexander-University of Erlangen Nuremberg (FAU), Erlangen, Germany
e-mail: sl@ipat.uni-erlangen.de

T. G. Steigerwald (✉)
SiCrystal GmbH, Thurn-und-Taxis-Straße 20, 90411 Nuremberg, Germany
e-mail: thomas-steigerwald@gmx.de

E. Meissner and R. Niewa (eds.), *Ammonothermal Synthesis and Crystal Growth of Nitrides*, Springer Series in Materials Science 304,
https://doi.org/10.1007/978-3-030-56305-9_8

synthesis [1–3]. This is the predominant mechanism for the transport from the solution zone to the crystallization zone. Due to the Lamé viscosity constants from the Navier-Stokes equation the viscosity therefore has a considerable influence on the mass transport and because of this it is essential for the flows in the autoclaves. Additionally, temperatures and their distribution are also necessary, as these have a lasting influence on viscosity. This is also of particular importance because many substance combinations that can be used and their influence on the viscosity of the basic material, such as ammonia, are not yet to be found in any literature up to 650 °C.

A complicating factor is that the ammonothermal parameters lead to supercritical material states. With such states of substances, the viscosities are generally similar to those of gases. Consequently, the viscometer must have an integrating property and be able to collect the data e.g. on a movement path due to its structure. In addition, it is of elementary importance for the usability of the results, such as for flow simulation, that all processes in the reactor can be mapped. This means that either the viscometer represents an autoclave or that the components for the measuring method can be integrated into an autoclave without disturbing its function. Only then when it is possible to determine exact viscosity data for each operating state or aggregate state of the materials and to combine these with the temperature data, is it possible to optimally design and control the crystallization processes with the aid of flow simulation methods (CFD). *Chen* et al. currently work in the field of simulation of the ammonothermal processes [2]. They described at first the model of a modified Peng-Robinson-Equation-of-state (EOS) in order to extrapolate the values of pure ammonia to ammonothermal conditions given in literature up to 426.9 °C [3]. However, the problem of the influence of the reactants like different mineralizers to viscosity is still not solved, and some additional special effects, which are also important for the design of a viscometer should be taken into account.

One additional important effect was monitored by *Ehrentraut* et al. They showed that the solubility of the mineralizers changes in the temperature range between 570 and 680 K [4]. This effect was also observed by Alt et al. with the use UV/VIS-spectroscopy [5]. This means that the ammonothermal is in an unsteady state in this temperature range, which may lead to the remarkable errors. To avoid such influences it is not enough using the fluid properties of pure ammonia. The arising errors would be large. As a result, processes can be simulated more realistic when all factors are known.

Viscosity plays also a decisive role in the successful crystallization of nitrides. The growth can be limited by the viscosity via the diffusion coefficient from the Einstein-Stokes equation and the diffusion in the boundary layer of the crystal. Thus, the viscosity influences the maximum stable growth rate at which the crystals can be formed without impurities. Mathematically, this is described by the Schmidt number, by what the viscosity is included [6].

As a conclusion criterion, the measurement of viscosity can be an indicator of the progress or termination of the reaction, since the viscosity changes with successful crystallization. For all observations of viscosity in ammonothermal systems, pure substance data of ammonia have been used so far, since the influence of mineralizers on viscosity is not yet known [2, 3, 7–10].

8.2 Viscometer for Use in or for Ammonothermal Processes

The viscosity measurement under real ammonothermal conditions requires constructions that can serve as autoclaves, are similar to reactors, or can be integrated into autoclaves. If one starts from the substances that are in ammonothermal autoclaves, these are largely only gaseous or supercritical substances. This means, one needs a viscometer which is able to measure gas viscosities and those of supercritical states. Due to this requirement, some classic viscometer types are already excluded from the group of possible methods.

The types of known viscometers can be divided in four different main groups: capillary viscometers, oscillatory systems (e.g. vibration and ultrasonic viscometer), rotational viscometer or concentric cylinder rheometers and falling body/rolling ball viscometers. A review of some high-pressure applications is given by *Kulisiewicz* [11]. With a special focus to the ammonothermal application the implementation of vibration and especially the ultra sonic types offer a chance to be a part of the design of autoclaves and the falling ball types is ideal to be built in a high pressure/high temperature design similar to s special shaped Autoclave. Below the different main groups are discussed and examples for 600 °C and 300 MPa are shown.

8.2.1 Capillary Viscometer

Capillary viscometers are only applicable on flowing media [12]. It is based on pressure equalisation between an upper and a lower tank with lower pressure. This is conceivable, but one would need exact pressure transducers (there is no such thing for the target temperature) and a good knowledge about the capillary diameter changed by thermal expansion. Unfortunately, however, the capillary should be very thin and therefore have to be calibrated somehow. Due this especially at low viscosities, like supercritical fluids are, large inaccuracies appear, why very large and long spiral capillaries are used [13] (see Fig. 8.1) to integrate the influences acting to the capillary over a long distance. For ammonothermal conditions, a flowing apparatus, like this, is hardly feasible and capillaries will soon be jammed, due to the danger of crystallization. Additionally the heat extension is a very sensitive parameter because

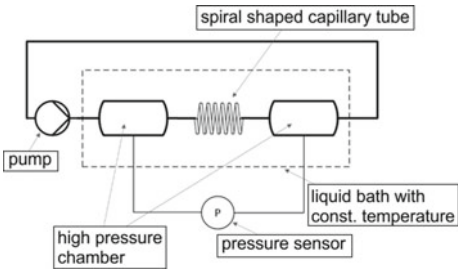

Fig. 8.1 Capillary viscometer based on Kawashima [13]

based on Hagen-Poiseuille-Law the capillary radius influences the capillary flow with the power of four. When not an absolute equal temperature exists along the complete capillary length, the resulting value can be a large error. Consequently, an application of the capillary viscometers is not suitable for the ammonothermal process parameters.

8.2.2 Rotational Viscometer

Rotational viscometer or cylinder rheometers do have application flexibility but are mainly used for ex situ measurement because of difficulties with sealing and also the functionality needed. Nevertheless pressures up to 900 MPa at 120 °C where realized by *Galvin* et al. [14] and Semjonow published an apparatus for 300 °C and 220 MPa [15]. At least *R. J. Murphy* patented a method which should work up to 371 °C and 138 MPa [16], but nothing was found about the feasibility. Summarizing, the maximum temperature needed for the ammonothermal process are not reached by these types. This has also to do with the heat extension but also with the supercritical fluid properties. It is a really difficult task to heat up such a device absolutely equal and without any temperature difference. But if the clearance wideness is not small enough for a laminar flow (can be jammed also) and also not constant over the whole shear area, the measurement quality is not sufficient. Due to these properties, the rotational viscometer will hardly be practicable for ammonothermal processes. In addition, the typical installation space and the required rotary feed-through in the high-pressure range are difficult to achieve. Due this the variant of the Money Viscometer or Process Viscometer is therefore also excluded.

8.2.3 Oscillatory Viscometers

Oscillatory systems—like vibrating strings or sticks—are widely used in high-pressure applications and high temperature can be handled quite well, too. The resistances against the movement of the vibrating elements are measured, which are then easily translated into viscosity values. Nevertheless, the strong dependence of the medium used (supercritical fluids viscosity is very small and gaseous fluids will show a Joule-Thomson effect), its corrosiveness (only a small corrosion effect will change the vibration frequency or the measurement properties) and the high frequency dependence associated are disadvantageous for the determination of viscosity [17]. It cannot be estimated how solutes affect the viscosity and the vibrating parts (i.e. string) work like a cooling device where crystallization may occur. For first measurements of the viscosity this method is less useful, but it is recommended for future experiments.

The same also applies to the quartz viscometer (oscillating quartz), which can only withstand an operating temperature of up to approx. 250 °C. In principle it would

be suitable, because it measures the oscillation change by the fluid. This could work for gas. For vibration viscometers, a round rod or wire is immersed in a liquid and vibrated transversally or longitudinally. This measuring principle then allows several methods to be used to determine the viscosity. First, the required power can be used to maintain a certain vibration, and second, the change in the vibration frequency can be measured by the medium. The time for the subside of an applied oscillation can also be used to determine the viscosity. In this case, the viscosity of the logarithmic decrease of the oscillation is calculated according to the Stokes principle, whereby the decay current at free oscillation is not included.

Nevertheless, vibration viscometers represent an extremely efficient system for viscosity measurement, since viscosity can also be measured by highly viscous fluids and suspensions as well as from strong bases and acids. In addition, the vibration viscometers require very little maintenance as there are no weak parts. However, there are also some disadvantages with vibration viscometers. Especially the flow behaviour must be known in advance in order to be able to carry out viscosity measurements [18]. Nevertheless, the vibration viscometers can still be adapted for such processes by means of simple modifications. One possibility has been presented by *Fitzgerald* et al.: This viscometer consists of an energy converter with a retractable tip, an electromagnetic winding coil and voltage source and a control unit. The voltage source measures the required current and the control unit ensures constant oscillation. The sensor tip is placed in a flexible container and is excited to torsion oscillate at a constant amplitude. The viscosity is measured by the resistance of the liquid to the oscillating motion of the sensor [19]. According to the patent, these are then suitable for high pressures and temperatures, but also this vibration viscometer measures the viscosity outside of operation. A possibility of direct in situ determination of viscosity was developed by *Bradfield*. The viscosity is determined by a mechanical oscillation at 300 °C and 50 MPa. In this case, the Curie temperature of the sensors must be above that of the iron, which is why the cable is coated with quartz or glass. A high accuracy of the determination of the natural frequency and the viscosity is made possible by the possibility of a high coupling of the components [20]. However, the direct contact of the sensors with the medium to be measured disqualifies this system for use in ammonothermal systems. On the one hand because the maximum Curie temperature of known materials is 460 °C and on the other hand because, as already shown in [21] quartz or other possible sheath materials are not resistant in ammonobasic environments.

8.2.4 Ultra Sonic Viscometer

Ultrasonic technology is suitable for measurement in autoclaves. The frequency is introduced into a cylindrical component which transmits the oscillation on the other side and also receives a reflection and can in turn transmit it to the rear side for registration of the measurement result. The cylindrical components can be made of durable materials such as ceramics or also high-strength metallic materials and sealed

and clamped with high-pressure technical elements (see Chap. 3). Such a measuring principle measures the entire space up to the reflection point and back. This means that the measurement result is an average value for the entire space. The measured variable here is the change in the vibration parameters. While the compressibility of the fluid influences the speed of sound, the viscosity has a damping effect. Such a system has not yet been implemented. However, the basics for this have been developed within the framework of this project. The status of the work is presented.

8.2.5 Falling and Rolling Ball Viscometer

The overview of the measuring methods is completed with the falling or rolling body viscometer which is relatively simple: A sphere falls through a long bore that is not much larger. The measure is the drop duration, which depends on the spatial conditions and friction conditions in the diameter along the drop distance. The construction (pipe, can be considered as an autoclave) and the resulting better planning of the thermal expansion already speak for a use. However, the use for gases and supercritical fluids is not published anywhere. The reason is that the drop time differences are very small. For this reason, a variant must be developed from this, the ball roller viscometer. The advantage of this design is that both the lubricating property, the bow wave during rolling and the flow resistance contribute to the material specific slowing down of the rolling ball. However, a detailed calibration is necessary for this.

Thus only the ultrasonic version remains from the entire group, in exceptional cases the vibration viscometer and the rolling ball viscometer. These were elaborated within the framework of the project and are presented below according to the status achieved.

8.3 Influence of Pressure and Temperature on the Viscosity of Pure Ammonia

Viscosity is a measure of the internal friction of a fluid and can be observed whenever a medium flows. There is an impulse exchange between the particles of the fluid and the fluid particles with the wall and thus forces occur between the individual molecules and the wall. These forces lead to flow friction and internal friction. It is a characteristic quantity in fluid mechanics. Viscosity is therefore also described as the toughness or flow resistance of a fluid. In the ammonothermal process, not only the pressure and temperature but also the substances dissolved in the ammonia, such as mineralizers, influence its viscosity. The common occurrence of the various factors make it difficult to make predictions about the viscosity. In the following,

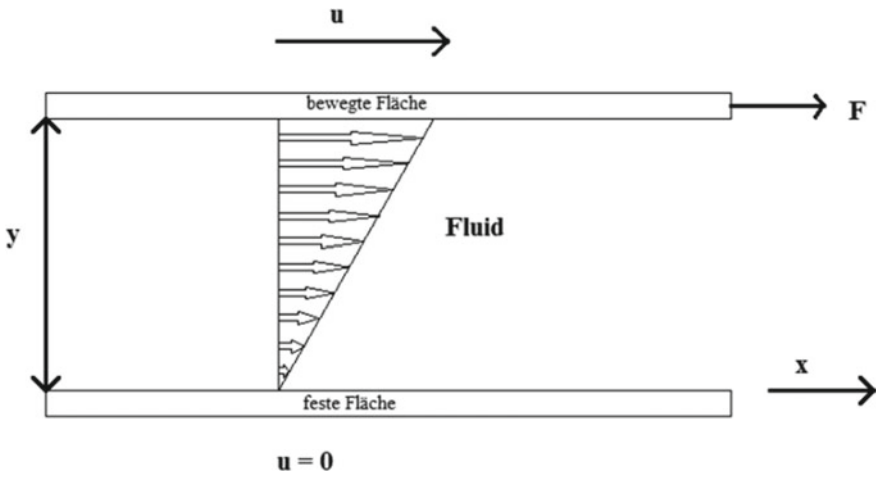

Fig. 8.2 Shear test

the physical definition of viscosity η is given and various influencing factors are discussed.

Figure 8.2 shows the so-called shear test. A fluid is located between a stationary plate (bottom) and a moving plate (top). The speed with which the upper plate moves is u, the distance between the plates is y. The force F required to move the upper plate is proportional to the velocity u, the area A of the plates and vice versa proportional to the distance y between the plates.

$$F \sim \frac{u \cdot A}{y} \tag{8.1}$$

If (8.1) is divided by A, the shear stress τ is obtained on the left side and the shear velocity in (8.2) is obtained on the right side.

$$\frac{u}{y} = \frac{\mathrm{d}u}{\mathrm{d}y} := \text{Shear Velocity} \tag{8.2}$$

The proportionality constant between shear stress and shear velocity is called dynamic viscosity η. Thus, according to [22], (8.3) is obtained, which at constant dynamic viscosity is referred to as the flow law for Newtonian fluids.

$$\tau = \frac{F}{A} = \eta \cdot \frac{\mathrm{d}u}{\mathrm{d}y}; \text{ with } \eta = \text{const. (Newtonian Fluid)} \tag{8.3}$$

Figure 8.3 shows for some Newtonian (A) and some non-Newtonian fluids (B, C, D) the shear stress τ over the shear velocity du/dy. For Newtonian fluids the dynamic viscosity is constant, i.e. the shear stress increases linearly with the shear rate.

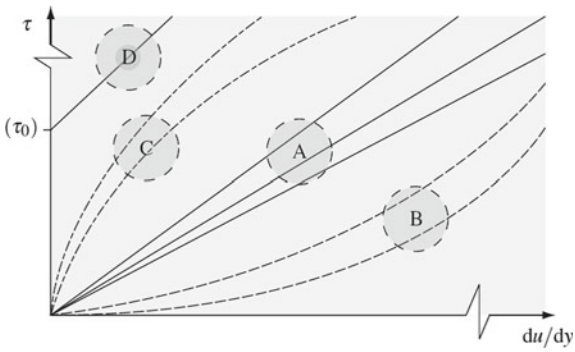

Fig. 8.3 Basic course of the Newtonian law of flow and non-Newtonian fluids: A Newtonsch, B and C Non-Newtonsch, D Thixotropic

Most technically relevant fluids such as water, air and oils have Newtonian properties. Fluids with longer molecular chains, such as polymer melts, often behave non-Newtonian [23]. In the ammonothermal process, the ammonia used is supercritical, which is why linear viscous flow behaviour is assumed a priori in this respect, but this must be checked in the experiments. Since supercritical fluids are rather assigned to the gaseous state from the point of view of their flow behaviour, the model of kinetic gas theory for the description of the fluid properties of gases is considered from the beginning in order to be able to better classify the expected measurement results. Various properties of gases can be derived from kinetic gas theory. For example, the viscosity of gases increases with increasing temperature, since the mean free path length between the gas molecules becomes smaller [24]. According to kinetic gas theory, the viscosity of ideal gases is independent of their density [25]. However, this prerequisite will not be fulfilled in the investigated areas of ammonothermal synthesis, since ammonia no longer behaves ideally at high pressures and is therefore regarded as a real gas. The viscosity can then be described approximately with the semi-empirical approximation according to *Sutherland* (8.4) [26].

$$\eta = \frac{a(\theta)^{\frac{3}{2}}}{b + \theta} \tag{8.4}$$

where a and b are material parameters that can be determined from two viscosities at two different temperatures and θ is the reduced temperature, i.e. the desired temperature divided by the critical temperature of the material. However, *Sutherland's* approximation does not take the behaviour under high pressure into account. Descriptions of substance mixtures are also difficult, so that as a rule only an order of magnitude of the viscosity of a mixture can be calculated [26].

8.4 Influence of Salts on Viscosity

Since there have been no investigations on the behaviour of the viscosity of ammonia under the influence of dissolved substances up to now, the viscosity change of aqueous solutions has to be dealt with here for the most part. Based on the already mentioned physical analogies between water and ammonia, however, conclusions can be drawn and the general description of the viscosity behaviour of solutions can be explained.

However, it is difficult to predict the viscosity behaviour of solutions and there are no general laws. Different solutions can have fundamentally different behaviors. For some aqueous electrolyte solutions, such as solutions of NaCl or LiCl and H_2O, the viscosity increases monotonously with concentration. For solutions of KCl or KBr in H_2O, the viscosity initially increases slightly at low concentrations, then falls to a minimum and increases again monotonously at higher concentrations, similar to a solution of NaCl and H_2O [27]. In 1929 *Jones* and *Dole* [28] investigated the viscosity behaviour of aqueous solutions and described them by the empirical (8.5):

$$\varphi = 1 + A \cdot \sqrt{c} + Bc \tag{8.5}$$

Thereby φ is the fluidity, the reciprocal value of the dynamic viscosity and c the concentration of the substance in the solution. A can calculate fairly accurately for each temperature from the dielectric constant, the viscosity of the solvent, the valence and the molar limiting conductivities of the ions, where B depends on the interactions between the ions and the solvent, but remains an empirical constant [29]. There A is negative, while B can either be positive, meaning the salt increases the fluidity and decreases the viscosity, or negative, meaning the salt increases the viscosity. In the first case the authors give the range of validity of the equation up to a concentration of 1 mol/l, in the second case the equation is only valid up to a concentration of 0.2 mol/l [28]. 1 mol/l means one mole of dissolved substance in one litre of solvent. This form of the Jones-Dole (8.6) is still used today to describe the viscosity of aqueous and non-aqueous solutions. Even if it was later extended by other authors by another constant D too (8.6):

$$\frac{\eta}{\eta_0} - 1 = A \cdot \sqrt{c} + Bc + Dc^2 \tag{8.6}$$

Thereby instead of the fluidity φ the relative viscosity η/η_0 is in the equation. The additional term with the constant D should better describe the influences of aqueous solutions with increased salt concentration. According to [30], the error in increasing the concentration from 0.1 to 0.4 mol/l can thus be reduced from 10% in (8.5) to 3% in (8.6).

Deviating behavior can also be shown by solutions of several components. *Motin* investigated the behaviour of aqueous solutions of sodium chloride and ammonium chloride with and without the addition of urea and came to the conclusion that ammonium chloride in an aqueous solution reduces the viscosity slightly, while ammonium chloride in solution with 5 mol/kg urea increases the viscosity [31].

Saeed et al. show that ammonium chloride in aqueous solutions strengthens the structure, i.e. increases the viscosity while in a 10% ethanol water solution it reduces the viscosity or weakens the structure of water [32]. This means that ammonium chloride in an aqueous solution has a positive B coefficient in (8.5) or (8.6), while ammonium chloride in a 10% ethanol-water mixture has a negative B coefficient. The viscosity behaviour of solutions is therefore complex and it is difficult to make general predictions for solutions. Not to mention that these considerations have only been studied for aqueous solutions. The investigations in ammonothermal synthesis are therefore dependent on determining the viscosity of the solutions used in situ.

8.5 Ultrasonic Viscometer

The conception of the ultrasonic viscometer presupposes how it is to be built. As preliminary work, solubility tests of sodium azide in liquid ammonia by in situ ultrasonic velocity measurement are used. These show the general feasibility of ultrasonic measurements in ammonothermal systems at elevated temperature and pressure and thus serve to design the viscometer. These were carried out together with Baser et al. and published in [33]. Here the general function of the ultrasonic viscometers is described first and already published adaptations to more extreme process conditions are examined more closely. Based on this, a possible design will be developed.

8.5.1 Functionality of an Ultrasonic or Vibration Viscometer and Possible Adaptations to Extreme Process Conditions

Ultrasonic viscometers work according to the pulse-echo method or the ultrasonic through beam method. Both methods are similar in construction, so that it is not a priori clear which method is better suited for ammonothermal synthesis. A brief overview of the two is intended to provide clarity on this point.

The through-sound method is realized with two sensors, which are connected to an ultrasonic device. The ultrasonic waves are emitted by one sensor and received by the other, the sensors have to be placed exactly opposite each other. This prevents the formation of a dead zone and allows measurements to be taken close to the surface. The pulse-echo method requires a sensor that emits the sound waves and captures reflected waves. The pulse-echo method is more widespread because the viscosity and density of the medium can be easily determined. For this purpose, a base on which the ultrasonic sensor (also known as transducer) is mounted is immersed in the fluid to be measured.

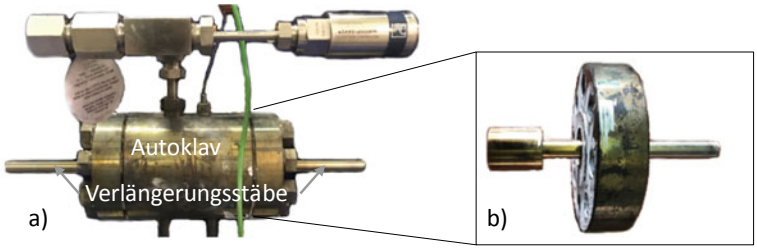

Fig. 8.4 **a** Autoclave for ultrasonic measurements to determine the solubility of different substances in ammonia at max. 600 °C and max. 300 MPa. **b** Free cut of the cover and the current extension base

The advantage here is the large variation possibility of the base, which can also be adapted to the respective medium. This means that the ultrasonic viscometers can also be adapted for use in processes. The Cohen-Tenoudji high-temperature ultrasonic viscometer was one of the first adaptations of its kind [34]. This viscometer allows the viscosity measurement of polymer mixtures and epoxy dressings at temperatures up to 170 °C. The reflected ultrasonic wave is measured via a piezoelectric element. In addition, the wave is doubly reflected by two buffers to be used. This method can also be used to adjust the flow properties and optimize the process. Nevertheless, the strong dependence on the medium used and the associated strong frequency dependence are disadvantageous for determining the viscosity. Although the maximum operating temperature in [34] is significantly lower than that required for ammonothermal synthesis, it is clear in this paper how even higher temperatures can be achieved: by cooling (active or passive) the sensitive sensors of the ultrasonic measurement are protected. These findings resulted in a base made of autoclave material as shown in Fig. 8.4b. Thus, the basic prerequisites for an application are given, since the resistance is given at least for the duration of an experiment and also the limitation of the Curie temperature can be overcome. The exact theoretical backgrounds of the ultrasonic pulse echo is described in the following chapter.

8.5.2 Theoretical Model of Ultrasonic Viscosity Measurement for Ammonothermal Systems

The preliminary work in [33] should lead to a new cell in which the viscosities of polytropic states with different compositions can be measured quickly. For this purpose, the previous ultrasonic measurements are briefly summarized, their limitations described and the possible extension described in more detail. The currently used measurement setup is shown in Fig. 8.4a, where the main points are the autoclave and the extension sockets for the ultrasonic transducers. This adaptation of the measurement setup from [33] is due to the necessary heating up to 625 °C. The temperature of the ultrasonic transducers is also shown. In addition, the measurement

signal can now be filtered out more easily from interference noise by means of planar surfaces. The structure is designed to determine the solubility of different substances in supercritical ammonia, since this simple measurement is ideal for the experimental suitability test of adaptation to high temperatures and simultaneously provides important measured values for ammonothermal synthesis. The current bases are shown in Fig. 8.4b. The extension base is guided through a cover flange and pressed into the autoclave with the thickening. The extension sockets are made of one piece and contain the sealing punch with 28.4 mm diameter including sealing geometry, as well as the extension with 13 mm diameter, which protrudes far enough from the heating sleeves with 120 mm length. For a more detailed description of the structure, please refer to Fig. 8.7, as further adjustments can be made to the extension base and the periphery is easier to see in the sectional view.

Up to now, the ultrasonic pulse-echo method has been the preferred measurement method. Here, the change point in the velocity of sound in ammonia-mineralizer mixtures is defined as the solubility limit of the mineralizer in ammonia, since at a constant temperature the ultrasonic velocity has a direct proportionality to the concentration [35]. The velocity of sound c in fluids is described by (8.7).

$$c = \sqrt{\frac{\mathrm{K}}{\rho}} = \sqrt{\frac{1}{\kappa \cdot \rho}} \tag{8.7}$$

In most fluids, sound waves can only propagate as longitudinal waves (Longitudinalwellen), i.e. as pressure waves in which the displacement of the medium occurs in the same direction as the running direction of the wave. The speed of sound c is then a function of the density ρ and the adiabatic compression module K or the compressibility $\kappa = 1/K$. This Boyle-Mariotte law is described in (8.8) by the infinitesimal pressure change (∂p), which is necessary to cause an infinitesimal volume change (∂V) at a certain volume V.

$$\kappa = -\frac{\partial V / V}{\partial p} \tag{8.8}$$

The adiabatic compression modulus for real gases is an intensive and intrinsic state variable. The fact that this model also applies to supercritical fluids was shown by the measurements of Natarajan [36] who examined different kerosene mixtures up to 400 °C and 30 MPa at the critical point [32] and whose results could be confirmed with the measurements shown here.

Preliminary investigations have shown that this method has a general applicability. However, in order to calculate the viscosity from the sound signals, it requires a suitable measurement setup that ensures accessibility for the input of the measurement signal. *Sheen* et al. have already shown an example of this in their work [37]. In the present case, this is the reflection coefficient R at the phase boundary between fluid and autoclave material, which is defined in (8.9) at perpendicular sound incidence. The ratio of the sound pressure of the reflected wave pr to the sound pressure of the

incident wave pe is measured.

$$R = \frac{Z_F - Z_A}{Z_F + Z_A} = \frac{p_r}{p_e} \tag{8.9}$$

As can also be seen in (8.10), the degree of reflectance is equal to the ratio of the difference and the sum of the sound impedance of the fluid Z_F and the autoclave material Z_A, respectively. These are generally determined by the product of the density and the sound velocity c of the respective medium i (8.15).

$$Z_i = \rho_i \cdot c_i \tag{8.10}$$

With a known flow velocity and the velocity of sound in the fluid c_F, only the density can be determined from this measurement according to (8.11) at first.

$$\rho_F = \frac{Z_A(1 - |R|)}{c_F(1 + |R|)} \tag{8.11}$$

The degree of reflection is used as an amount, since this is in principle an imaginary number. If the damping properties of the autoclave material and the fluid are neglected, however, they are considered to be real. In order to measure both the velocity of sound in the fluid and the degree of reflection simultaneously, the ultrasonic transducer requires a base with several paragraphs (see Fig. 8.7). Then three large reflections are expected when emitting longitudinal waves, corresponding to the reflections on the surface of the shoulder, on the pedestal in contact with the fluid and on the wall on the opposite side. The typical measurement signal to be expected is shown in Fig. 8.5 in simplified form.

The amplitude ratio of the first two reflections gives the degree of reflection according to (8.14), while for non-dispersive media the velocity of sound in the fluid

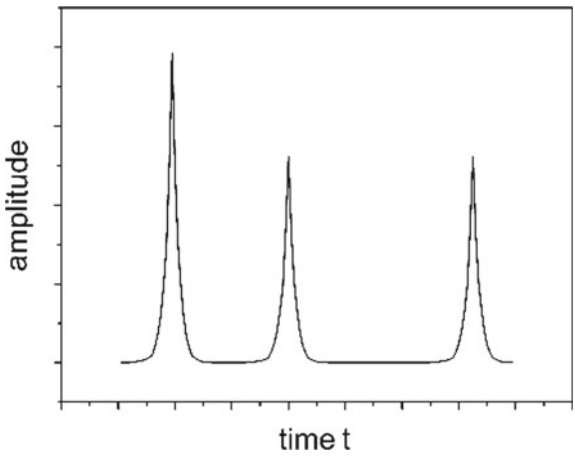

Fig. 8.5 Typical, highly simplified sketch of an expected measurement signal of a longitudinal wave from the ultrasonic pulse-echo method

can be determined from the transit time between the second and third reflections. Since the density of the autoclave material used and the speed of sound in the autoclave material are known, the fluid density is directly determined from measurements with longitudinal waves.

To measure viscosity, a shear force must be applied to the fluid, as in the thought experiment in Fig. 8.5. As mentioned at the beginning, shear waves (also called transverse waves) cannot propagate in most fluids. However, when voltage waves are transmitted, the viscous resistance triggers a movement in the fluid. So the pressure wave has to overcome the combined inertia of the solid and the additional inertia of the liquid. The net effect is a reduction in the wave velocity. *Roth* and *Rich* have shown that this speed reduction correlates in a first approximation with $\sqrt{(\rho \cdot \eta)}$ [38]. For the measurement, the shear wave reflectance is determined by analogy with (8.14), where the shear impedances replace the sound impedances. For a propagation direction of the wave normal to the base area, the shear impedance of fluids deviating from (8.12) is calculated as follows, where again the Newtonian fluid is assumed and ω is the radial frequency of the shear wave.

$$Z_{F,s} = \sqrt{\frac{\omega}{4} \cdot \rho \cdot \eta} \tag{8.12}$$

The shear impedance of the autoclave material is further determined according to (8.13), whereby the compression modulus K in (8.7) is replaced by the shear modulus $G_{A,23}$ of the base material, to calculate the speed of sound. This results in:

$$Z_{A,s} = \sqrt{\rho_A \cdot G_{A,23}} \tag{8.13}$$

These two terms for the shear impedance can then be used in (8.14) instead of the sound impedance. This results in an expression for the product of density and viscosity that can be calculated from the measurements of the reflectivities of the shear waves.

$$\sqrt{\rho \cdot \eta} = \sqrt{\frac{4 \cdot \rho_A \cdot G_{A,23}}{\omega}} \cdot \frac{(1 - |R|)}{(1 + |R|)} \tag{8.14}$$

An exact consideration of the shear impedances, where the wave is not normal to the base surface and the reflectance has to be calculated with imaginary part, because the fluid behaves non-Newtonian, can be found in the work of *Shah* et al. [39] or the early works of *Sheen* and *Raptis* [40]. Figure 8.6 again shows a typical measurement signal to be expected from the experiments with a shear wave. In comparison with Fig. 8.5, the absence of a third peak is noticeable, since no waves are transmitted by the fluid. The reflection factor from which the density-viscosity product is derived is calculated from the amplitude ratio of the two existing reflections.

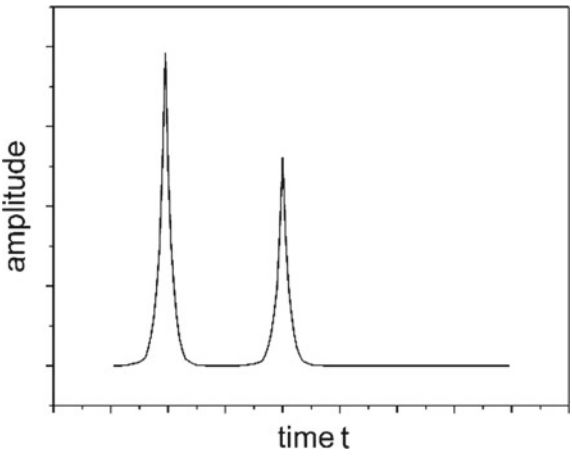

Fig. 8.6 Typical, highly simplified sketch of an expected measurement signal of a shear wave from the ultrasonic pulse-echo method

Equation 8.14 shows that the material used for the base has a large influence on the accuracy of the measuring apparatus. A good overview for current, also non-commercially established high-temperature transducers can be found in [41]. But also the different geometries of the sockets and the structure are the subject of research again and again. *Kim* and *Bau* have used two torsion wave sensors with different cross-sections respectively one consisting of a waveguide with two different sections with different cross-sections. In both cases, there must be a circular cavity and a rectangular cross-section. You estimate an accuracy of 0.5% for the density of fluids greater than 1000 kg/m^3 and an accuracy of one percent for the density shear viscosity product greater than 100 kg^2/(m^4 s). This gives the assumption, that precision can be further improved [42].

Sheen et al. for example, use two opposite polished sockets that dip into the fluid and stand at a certain angle to each other to increase the accuracy of the measurement system [43]. Since the sound impedance of liquids with viscosities of up to 0.5 mPas could already be measured, this measurement method has a great potential for use in ammonothermal synthesis. The accuracy depends mainly on the exciter frequency [44] and can be used without additional cooling of piezoelectric materials up to 460 °C [45], respectively temperatures up to 1500 °C can be measured by cooling measures [46]. The concluding statement refers to the great advantage of this measuring method, that also non-Newtonian fluids can be investigated [47], which has so far only been determined as an assumption.

8.5.3 *Adaptation of the Ultrasonic Pulse-Echo Method for Viscosity Measurement for Ammonothermal Systems*

At the end of this chapter, the finished concept for the adaptation of the ultrasonic pulse-echo method for viscosity measurement for ammonothermal systems is presented. The basic structure of the ultrasonic viscometer and the corresponding signal processing scheme is based on the work of *Sheen* and *Raptis* [37]. In the preparatory work [33] only transducers for the measurement of the longitudinal waves were used so far, whereby according to (8.16) only the density is accessible. Figure 8.4b also shows that the existing edge results from the seal geometry and is therefore not explicitly considered for the measurement. These two points are adapted in the basic design. Figure 8.7 shows this construction, which consists of two extension bases that are attached to the sight cell.

The bases are directly opposite to each other in the simplest construction, so that they can be used directly. Although it is possible to manufacture angled autoclaves, initial measurements should show whether the accuracy obtained here justifies the enormously increased manufacturing effort. The exact geometries of the bases have not yet been determined and should be part of future research. A possible design uses a staggered surface to provide the required reference reflection. In order to determine the viscosity at the same time, a sensor for the shear waves must also be attached. For an effective use of space, the transducers operated in pulse-echo mode are installed opposite each other.

The scheme for determining viscosity is shown in Fig. 8.8 for the analysis of ultrasonic waves, an inspection system with various components is required, on the one hand a waveform generator for excitation of the transducer, a low-noise, adjustable amplifier part and digital signal processing. The ultrasonic signal is generated by the

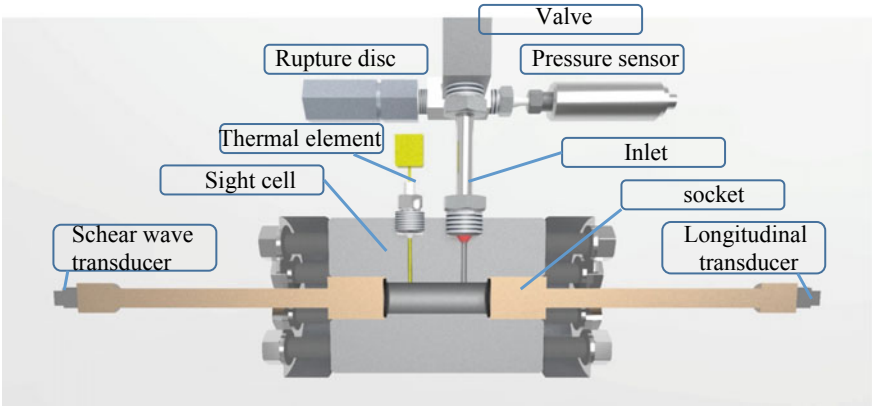

Fig. 8.7 High-pressure cell with schematically drawn elements for the ultrasonic pulse-echo measurement method (brown)

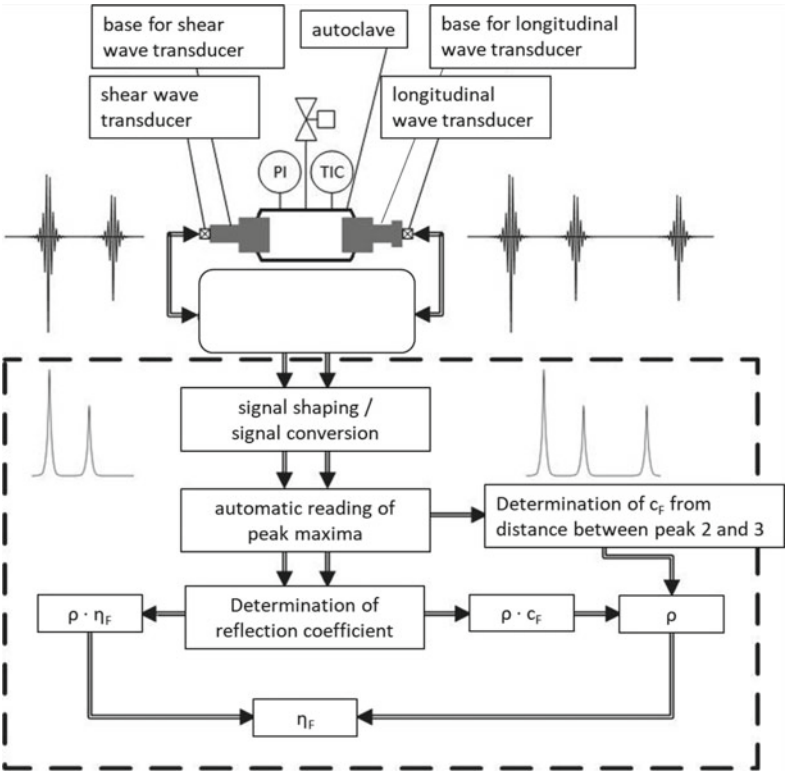

Fig. 8.8 Signal processing scheme ultrasonic pulse echo

waveform generator, introduced into the autoclave via the extension base, reflected at the respective opposite base and detected again by the waveform generator. The signal processing and signal conversion into defined peaks as well as the further steps up to the determination of the viscosity can be carried out automatically at the PC. On the one hand, the density of the fluid is determined from the longitudinal wave measurement according to Fig. 8.7 and the product of density and viscosity is determined from the shear wave measurement according to Fig. 8.8. The exact sequence is described in detail in the previous chapter. Finally, the viscosity is calculated from these two measurements.

The concept of the ultrasonic pulse-echo method for viscosity measurement has thus been largely elaborated. At this point, no statements on accuracy are made, since the base geometries will have a major influence on it and this will be part of subsequent research.

After it has been proven that a measurement is possible despite high temperatures, the authors are of the opinion that the ultrasonic pulse echo method for viscosity measurement is a very promising measurement method. This is mainly based on the

possibility to investigate two phase mixtures or even three phase mixtures if undissolved solids are present. The presence of a second liquid phase was not known at the beginning of the design phase. Annular discolorations on the autoclave bottom also indicate two phases within the ammonothermal system in experiments with other basic mineralizers, so that it can be concluded that this applies to all basic mineralizers. This is an exclusion criterion for most other viscosity measurement methods, including the ball roll viscometer. Also, the apparatus effort is reduced compared to the ball roll viscometer, since the complex tilting device and the accompanying uncoupling of the periphery from the filling station can be dispensed with.

8.6 Structure of a Rolling ball Viscometer for Ammonothermal Synthesis

In this chapter a system of a rolling ball viscometer shall be designed on the basis of a first theoretical consideration and in the following the gained knowledge shall be considered in the design and manufacturing. For detailed information the feasibility studies on this topic are recommended [48].

8.6.1 Theoretical Reflections

The physical basis of the falling body viscometers is the law of Stokes to determine the viscosity of the measuring media. This law is described by an equilibrium of forces that can be set up for each falling body in a medium as follows.

$$F_g = F_a \cdot F_r \tag{8.15}$$

F_g stands for the force of gravity, F_a for the buoyancy force and F_r for the resistance force. The three forces can be calculated for a sphere (the most common falling body), when the constant falling velocity u_{rel} is reached, according to the following formulas. Where g is the acceleration due to gravity, r is the radius of the falling body and ρ_K and ρ_{f} the density of the falling body K or the fluid f.

$$F_g = \frac{4}{3}\pi \cdot r^3 \cdot \rho_K \cdot g \tag{8.16}$$

$$F_a = \frac{4}{3}\pi \cdot r^3 \cdot \rho_f \cdot g \tag{8.17}$$

$$F_r = \frac{\rho_f}{2}\pi \cdot r^2 \cdot u_{\text{rel}}^2 \cdot c_D(\text{Re}) \tag{8.18}$$

The resistance coefficient $c_D(\mathrm{Re})$ depends on the Reynolds number Re and can be simplified for laminar flows with 24/Re. Viewed from the sphere, the radius of the sphere is thus included in the Reynolds number as the characteristic length and the velocity of fall as the flow velocity. The resistance force then includes the viscosity and is calculated as in the laminar range:

$$F_r = 6\pi \cdot r \cdot u_{\mathrm{rel}} \cdot \eta \tag{8.19}$$

The laminar process conditions are therefore essential for the measurements, since at a higher Reynolds number in Stokes' resistance law the viscosity is neglected, and the rolling time depends only on the density. Therefore, (8.20) introduces the criterion for laminar flow where the sensitivity is still sufficiently accurate.

$$\frac{f}{f_{\mathrm{cr}}} = \frac{\mathrm{Re}_{\mathrm{cr}}}{\mathrm{Re}} \geq 0.25 \tag{8.20}$$

With the resistance factor f, the Reynolds number Re, as well as f_{cr} and $\mathrm{Re}_{\mathrm{cr}}$ the resistance factor respectively the Reynolds number at critical speed. This criterion is then always checked in the test. By using the explicit expressions of the forces in (8.21) and the resolution of the equilibrium of forces according to the dynamic viscosity, the working equation for the viscosity determination of falling-body viscometers is obtained.

$$\eta = \frac{2r^2 \cdot g}{9 \cdot u_{\mathrm{rel}}} \cdot \left(\rho_K - \rho_f\right) \tag{8.21}$$

As already mentioned, the above equations for the falling body ball were established, but other falling bodies such as cones can also be used. However, only the sphere is suitable for viscosity measurements in ammonothermal synthesis. It is the simplest design of the falling body viscometer, since an even pressure distribution on the ball as well as an even expansion of the falling body is achieved by the thermal conditions. The best known variant of the falling sphere viscometer is the Höppler version. Since fundamental problems have already been solved here, the viscometer for ammonothermal media is based on this. The Höppler viscometer is shown in Fig. 8.9. The first thing to notice is that the downpipe is mounted at an angle on a tripod. On the one hand, this prevents an undesired rolling movement of the ball in free fall and on the other hand, it prolongs the rolling time of the ball, which makes it easier to achieve laminar flow. The measuring device is also equipped with a tempering jacket which allows viscosity measurements at different temperatures. In addition, three measuring marks 0, 1 and 2 for determining the drop time and an immersion heater are attached.

For the determination of viscosity, the instrument constant K is determined using various fluids of known density and viscosity. All geometric factors of the test setup, such as the measuring section, angle of inclination and radius of the sphere as well as the influence of the wall, flow into this instrument constant. Equation (8.26) is

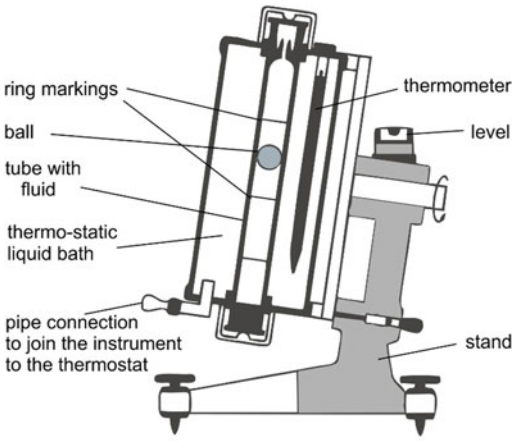

Fig. 8.9 Höppler-viskometer, simplified

thus greatly simplified and in (8.27) only the drop time t remains as the measured variable. This time is optically determined in the Höppler viscometer for fluids with a known density between measuring marks 1 and 2. The viscosity of the measuring medium can then be calculated from the density differences of the sphere and the measuring liquid, the required drop time t and the constant k.

The viscosity of the measuring medium can then be calculated from the density differences of the sphere and the measuring liquid, the required drop time t and the constant K. The viscosity of the measuring medium can then be calculated from the density differences of the sphere and the measuring liquid.

$$\eta = k \cdot t \cdot \left(\rho_K - \rho_f\right) \tag{8.22}$$

According to (8.22) the viscosity, with known device constant, depends only on the density of the liquid, the density of the ball and the rolling time. By repeated measurements with different ball densities the viscosity is accessible for unknown liquid densities. This is suitable for everyday use in many applications, but when used with ammonothermal media there are some significant limitations. The simple construction of the viscometer is the greatest advantage for a successful adaptation to the measurement of ammonothermal media, but the following four points listed in Table 8.1 have to be overcome in contrast to commercially available equipment.

For this purpose, the previous adaptations of rolling ball viscometers at the suitable locations will be examined more closely.

Table 8.1 Critical aspects for the design of a rolling ball viscometer for the ammonothermal process

1.	The measuring principle must be adapted to the high pressures and temperatures up to 650 °C
2.	The ball in the system must be brought back to the starting point so that the measurement can take place continuously
3.	The filling with the normally gaseous ammonia and the other educts must be realized as well as the temperature and the pressure must be monitored
4.	Finally, timekeeping must be optimally implemented. Optical methods should be avoided as far as possible, since a radial access would be required here, which would increase production costs and material requirements enormously

8.6.2 Preliminary Tests for the Design of the Rolling Ball Viscometer

In preliminary tests, the first point to be considered is point four in Table 8.1, in order to allow a rough design of the plant, since timing has a significant influence on the overall apparatus. It should be noted that it has already been shown here that a rolling ball viscometer with magnets for ammonothermal synthesis cannot be designed. Since these results can nevertheless be helpful elsewhere, they are briefly summarized here. Subsequently, the preliminary tests with structure-borne sound sensors are described in more detail and the general conclusions for the design of the rolling ball viscometer made of Inconel 718® are drawn.

As mentioned at the beginning, magnets cannot be used to detect the rolling time nor to return the falling body to its initial position after the test, although it is possible to influence a magnetic material in a high-pressure container made of Inconel 718® by means of magnets. The difficulty lies in finding suitable permanent magnets or electromagnets, as the maximum operating temperature determined was 450 °C in combination with commercially available permanent magnets and an electromagnet. The possible detection of rolling balls by means of a Hall sensor was also checked and classified as unsuitable, since a distance of at least 15 cm must be bridged for the detection. At a smaller distance, the existing temperature is too high for the sensors or the wall thickness of the reactor is too thick. Finally, it was found that magnetic lifting of objects causes considerable problems even when the reactor is at an angle. Thus, a movable bearing of the reactor is indispensable for the continuous use of a falling-ball viscometer, as otherwise the ball cannot be returned to its initial position. In addition, another method of rolling time detection needs to be investigated. One possibility is to use structure-borne sound sensors and an adapted reactor geometry to detect the rolling times of balls. For the ball, materials must be selected which have the lowest possible density so that a maximum rolling time of the balls can be achieved in the process. Furthermore, the materials used must be able to withstand the aggressive process conditions. Highly resistant steel or titanium compounds as well as ceramics such as silicon nitride are therefore the first choice.

In the test for the suitability of structure-borne sound sensors for time measurement with rolling ball viscometers in ammonothermal synthesis, the following preliminary test 4 examined whether there is a position dependency for the detection of a rolling ball in structure-borne sound sensors. Subsequently, two single-axis structure-borne sound sensors and a three-axis structure-borne sound sensor were examined to measure the sound pressure when the ball hit the pipe end. Furthermore, it is checked whether the starting point of the measurement can be detected by structure-borne sound sensors. The sensors should record an increase in sound pressure when a rolling ball passes through. In order to determine the position dependence of structure-borne sound sensors, spheres with 8, 10 and 12 mm were allowed to roll in a tube inclined by 45° and closed at the lower end, while the position of a single-axis sensor and a three-axis sensor was varied. The structure-borne sound sensors were connected to amplifiers and to a computer. To determine the position dependence, the sensors were then placed in three different positions, at the top, bottom and middle of the pipe, and the sound pressures were recorded for each position. The tests were carried out under normal conditions with air as the medium. The test setup for this is shown in Fig. 8.10. Two single-axis sensors (2) were connected to the downpipe (1). The three-axis sensor (7) was then fitted centrally between the two other sensors at a distance (6) of 20 mm. The downpipe was turned at an angle of 45° to the table top and attached to it. To amplify the measuring signals, the sensors are connected to amplifiers (11) via cables (8). The balls (3–5) are inserted manually into the tube and the sound pressure is recorded over the length of the tube.

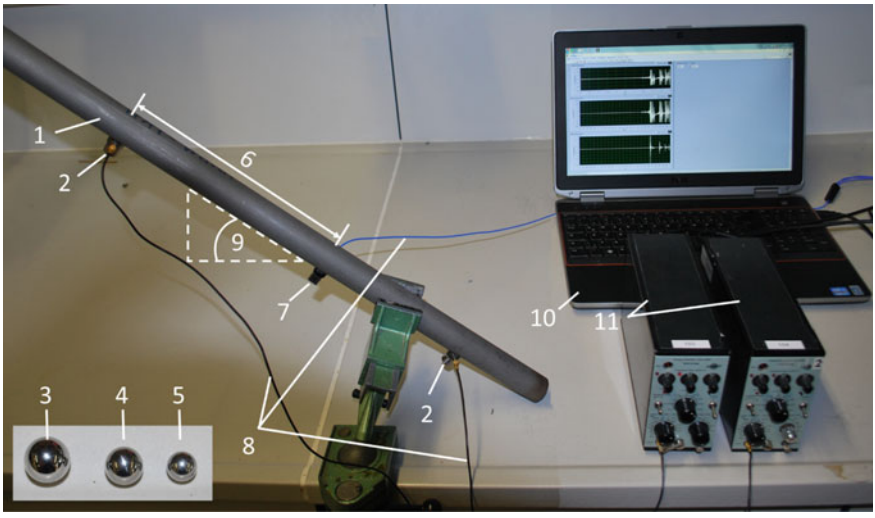

Fig. 8.10 Test rig for time keeping the rolling ball signal by structure born noise sensors: 1 Downpipe; 2: single-axis sensor, 3: ball 12 mm, 4: ball 10 mm, 5: ball 8 mm, 6: distance between the sensors, 7: 3 axis sensor, 8: amplifier cable, 9: tilt angle, 10: measurement computer, 11: amplifier

It turned out that generally no position dependence of the structure-borne sound sensors could be shown. As a result, a centrally positioned sensor can pick up the measuring signals (if available) over the entire downpipe. In addition, the general starting points of the measurements could also be clearly measured in these experiments by a percentage increase of the signal, as could the impact of the sphere on the closed end.

Through these preliminary tests, a promising concept is now being developed in which the further points from Table 8.1 must be fulfilled, as well as point four, which was mentioned in this chapter, are still being thought through in detail.

The test series for the detection of a rolling ball showed that the insertion of the ball into the downpipe via a rise in *x-axis* and *y-axis* direction could be clearly measured by the single-axis sensors with amplifiers. In addition, all three sensors were able to measure the impact of the ball on the tube end. However, the rolling of the ball was only recorded with a constant intensity. The total measuring time for a ball with 12 mm for these experiments was about 4 s, whereas the actual rolling time of the ball was only about 0.7 s.

For this reason, a notch is sawn into the centre of the downpipe to produce a perceptible acoustic signal when a ball passes through. This is to be recorded by the attached structure-borne sound sensors. The notch in the downpipe is at a distance of 400 mm from the pipe end. The total length of the downpipe is 800 mm. The test series on the suitability of a notch in the reactor for determining the drop time of a ball rolling past resulted in the graphs shown in Fig. 8.11. This clearly shows that the system works.

Based on these results, the runtime of the 8 mm Si_3N_4 ball in ammoniafluide, soluted in ammonia are:

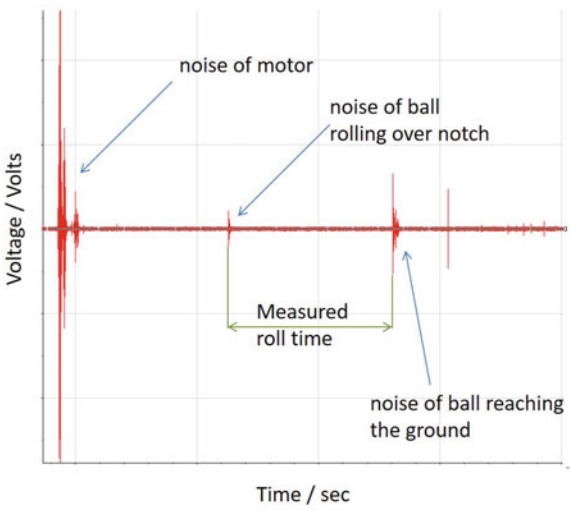

Fig. 8.11 Structure born noise signal from the rolling ball in the viscometer

T [°C] = 150 °C → rolling time t [s] = 1.3137 s
T [°C] = 200 °C → rolling time t [s] = 1.3466 s.

8.6.3 Adaptation of the Apparatus to High Pressures and Temperatures

From point one in Table 8.1 it follows inevitably that the measurement will take place in a thick-walled pipe made of Inconel 718®. The k-value must then be determined for each angle of inclination, each ratio of ball diameter to pipe diameter, different rolling distances in the pipe and different Reynolds numbers and since these values change with temperature and pressure, a very high calibration effort is required. A detailed discussion of the influencing factors can be found in the work of *Hubbard* and Brown [49]. If the criterion in (8.25) applies, the working equation for viscosity can be expressed with a variable C by:

$$\eta = \frac{C}{u} \cdot \left(\rho_K - \rho_f\right) \tag{8.23}$$

where this variable C is written as:

$$C = \frac{5\pi}{42} \cdot K \cdot g \cdot \sin\alpha \cdot (d(D+d) + \Delta[d(D+d)]) \tag{8.24}$$

With a new calibration constant K, the angle of inclination α, the sphere diameter d and the diameter of the autoclave D. Here, too, the constant K must be determined by experiments with fluids of known viscosity and density. However, this allows the influence of temperature and pressure on the diameter and the length changes to be taken into account, and the inclination angles adapted to the rolling time to be integrated, which ultimately significantly reduces the calibration measurements. If the mass of a closed system is constant, the density of the fluid at ambient temperature and pressure is calculated using the previously determined volumes of the autoclave. However, as the diameter and length of the autoclave increase with increasing temperature and pressure, the density decreases simultaneously due to the increase in volume. The change of the radius Δr_p at the internal pressure pi is calculated according to (8.30) with the inner and outer radius r_i and r_a of the autoclave, as well as the temperature-dependent modulus of elasticity $E(\vartheta)$ and the Poisson number μ of the autoclave material used [50].

$$\frac{\Delta d}{2} = \Delta r_p = \frac{p_i r_i}{E(\vartheta)} \cdot \left(\frac{r_a^2 + r_i^2}{r_a^2 - r_i^2} + \mu\right) \tag{8.25}$$

While the linear expansion of the autoclave or the shrinkage of the ball can be neglected due to the internal pressure, this is not the case with temperature changes and the internal pressure-related pipe expansion. The inner radius $r_i(\vartheta)$ and the

length $l(\vartheta)$ of the autoclave or the radius of the sphere r_ϑ at a given temperature are determined by (8.31) and (8.32).

$$r(\vartheta) = r_0 \cdot (1 + \alpha \cdot \Delta\vartheta) \tag{8.26}$$

$$l(\vartheta) = l_0 \cdot (1 + \alpha \cdot \Delta\vartheta) \tag{8.27}$$

where r_0 is the inner radius and l_0 the length at ambient temperature, $\Delta\vartheta$ the temperature change and α the coefficient of thermal expansion of the autoclave material or the ball material. It should be noted that the inner radius of the autoclave is increased by an increase in temperature and there is no expansion of the material towards the centre. The Inconel 718® alloy used is a superalloy with complex composition and heat treatment. Due to the many influencing factors, the thermal expansion coefficient of the autoclave material in the literature varies between 1.14×10^{-5} K^{-1} at 20 °C to 2.22×10^{-5} K^{-1} at 700 °C [51] and 1.75×10^{-5} K^{-1} at 400 °C [52] and 1.41×10^{-5} K^{-1} at 20 °C to 1.64×10^{-5} K^{-1} at 700 °C [53]. It is therefore unavoidable to know the exact coefficient of expansion for the material used. In the linear expansion $\Delta L/L_0$ is plotted over the temperature ϑ and the slope of the line represents the thermal expansion coefficient. For comparison, the coefficient of thermal expansion of silicon nitride (Si_3N_4 or SiN) is also plotted. SiN because it is one of the materials used for the sphere in the viscometer. A linearity over the entire temperature range is given for the materials used, so the coefficient of thermal expansion is regarded as constant for autoclaves and spheres (Fig. 8.12).

The absolute values are then read directly from the slope of the straight line. Thus, the coefficients of thermal expansion are dependent on the reciprocal temperature, in the unit (1/K), for: (a) Inconel 718® (α_{Inconel}) = 1.45×10^{-5} and (b) for silicon nitride ($\alpha_{Si_3N_4}$) = 3.49×10^{-6}.

These considerations show that the first point of Table 8.1 is achievable.

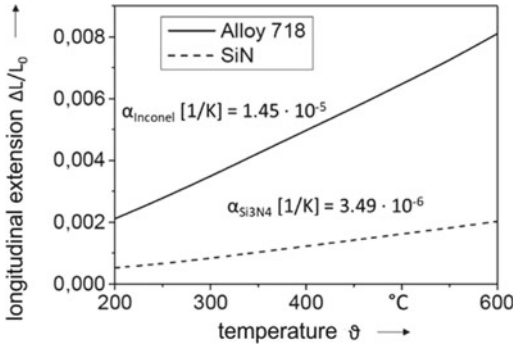

Fig. 8.12 Coefficient of thermal expansion of the alloy Inconel 718®, which is used for the manufacture of the autoclave and Si_3N_4 one of the materials used for the sphere

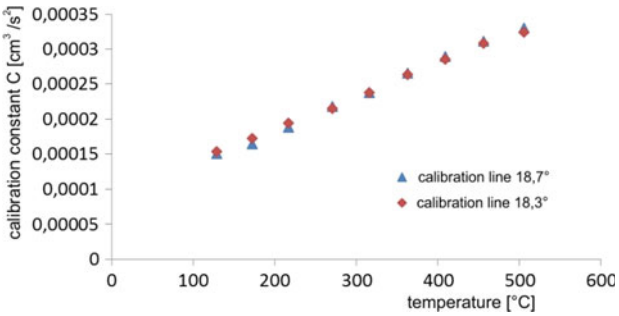

Fig. 8.13 Calibration values of the viscometer for the angles of 18.7° or 18.3° for a Si_3N_4 sphere with a diameter of 12 mm at temperatures between 129 and 505 °C and pressures between 11.3 and 27.8 MPa

8.6.4 Calibration of the Viscosiometer

Figure 8.13 shows the values for the calibration constants C at two different angles against the temperature. It can be observed that the values for the calibration constants increase linearly with pressure and temperature respectively and that the different values are close together. From this it can be concluded that the calibration constant deviates only slightly with a small change in angle (18.7–18.3°). Moreover, it can be confirmed that the results of the viscometer are reproducible.

The calibration constant can be described with (8.28).

$$C(T, 18, 6°) = 3.898 \times 10^{-7} \cdot T + 1.1049 \times 10^{-4} \tag{8.28}$$

8.6.5 Influence of the Mineraliser on Viscosity

First, the running times of the 7.938 mm Si_3N_4 ball were determined with pure ammonia. In Fig. 8.14 these are plotted against the temperature. It can be seen that the running times of the ball are between 1.8 and 2 s. They are therefore relatively short and show a relatively strong fluctuation (error band width maximum about 3%). Nevertheless, the trend of an increase at higher temperatures and pressures is again clearly visible. Thus, the results of the previous experiments are also confirmed here.

Calibration constants were determined from the ball running times of the Si_3N_4 ball in pure ammonia using (8.23) and literature values for viscosity and density [54], and the values of the viscosity of ammonia and ammonium fluoride were determined using the same equation. The values obtained are shown in Fig. 8.15.

This result shows, that the rolling ball viscometer deliver good viscosity data!

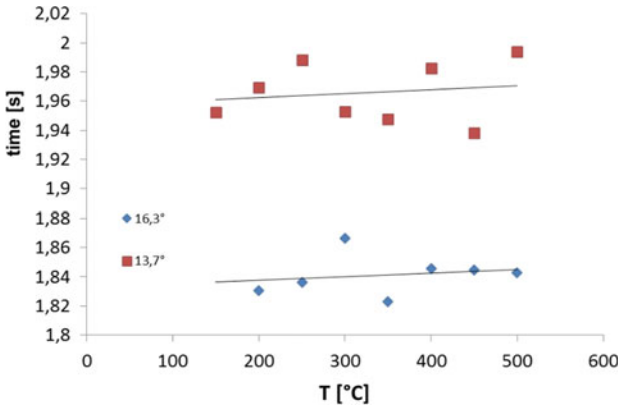

Fig. 8.14 Runtimes of the 7.938 mm Si_3N_4 ball without mineralizer

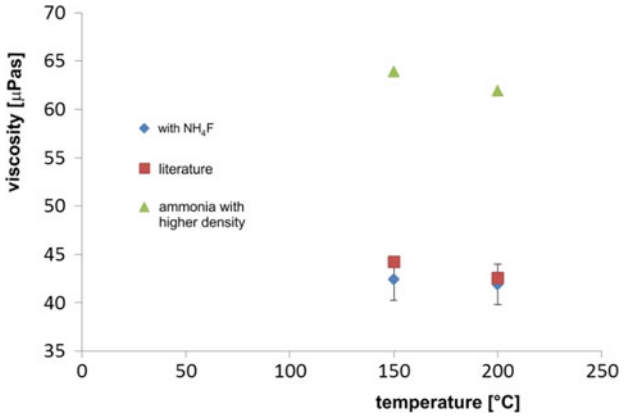

Fig. 8.15 Viscosities for pure ammonia and for ammonia with ammonium fluoride; comparison with literature values [54]

8.6.6 Continual Measurement by Tilting Apparatus

The second point in Table 8.1 sounds trivial at first, but is extremely difficult in high-pressure applications, as a glance at the literature shows. The apparatus [55] developed by Okamoto has an integrated return facility in the measuring tube so that the ball can be transported back to the starting point after the measurement. This possibility is electronically operated and is fixed at the lower end. The fall time is measured there within the apparatus via a relay circuit, which reacts to electrical changes when the free fall of the ball is completed. In addition, this mode of operation enables the ball to be developed from a wide variety of materials, which means that the weight can be extremely reduced and it was possible for the first time to accurately determine non-Newtonian media with a rolling ball viscometer. Through an opening

at the bottom of the apparatus, it is filled with the medium and emptied again through an opening at the upper end. The ball itself is released late by means of a plate ring and disc to ensure free fall through the medium. The fall time is measured by electronic changes, which can be registered by electromagnets. Continuous measurements are made possible by the built-in lift as well as the possibility of exchanging the measuring substance via a liquid inlet and outlet. This elaborate design demonstrates the general feasibility of ball roller viscometers even at higher pressures, but cannot be used due to elevated temperatures. At temperatures above 400 °C, which are usual in ammonothermal synthesis, both the plastic insulation materials for the sensors and the ferromagnetic properties of the magnets would fail due to exceeding the maximum operating temperature [56] (depending on the Curie temperature). Nishibata and Izuchi succeeded in continuous measurement at high pressures by means of a rotatably mounted apparatus [57]. A ball is used as a drop body, whereby the problem arises that the ball already begins to roll while the system is tilting. Nishibata and Izuchi solved this problem by using a magnetic holding coil, which briefly delays the rolling of the ball. Since a magnetic solution for the ammonothermal process is not possible, the premature rolling away of the ball is solved by a pocket at the autoclave ends with defined angles. However, this does not completely prevent premature loose rolling, which is why an additional section must be installed in the autoclave to achieve the constant rolling time. The considerations from Chap. 3 lead to the following autoclave design in Fig. 8.16. All parts from Inconel 718® were developed in the course of this work. A special problem was the deep hole drilling which requires a company specialized in precision.

A	Peripheric cover	E	C-Ring
B	Ball ($\phi = 12$ mm)	F	Ball pocket
C	High temperature structure born noise sensor	G	Thermal-Cover
D	Clearance (1.9 mm)	H	Thermal element

The autoclave consists of two halves connected by flanges and is closed by two different lids. A type K thermocouple welded into a sealing cone (H) is screwed

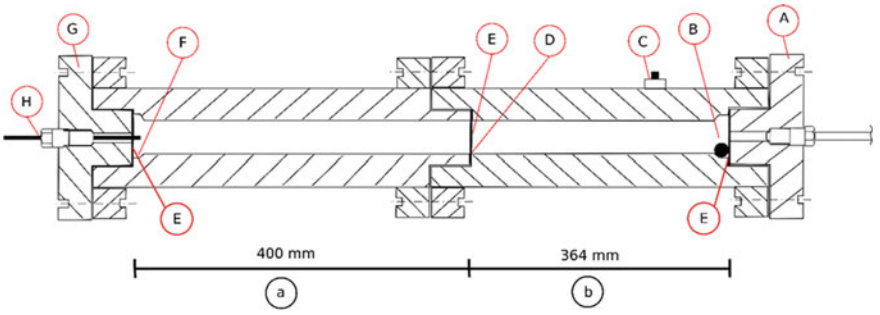

Fig. 8.16 Cross section drawing of the autoclave

into one lid (G) to enable in situ temperature determination. In the second cover (A) a tube section made of Inconel 718® is screwed in, which connects the autoclave with the periphery. The flange connections are sealed by silver-coated C-rings (E). The two autoclave halves are also connected by flanges and sealed with a C-ring (E), resulting in a 1.9 mm wide gap (D). The separation of the autoclave defines two measuring sections. Each measuring section begins at the connection of the two autoclave halves and ends at the respective autoclave cover. The long measuring section (a) has a length of 400 mm, the short measuring section (b) 364 mm.

The inner diameters at both ends of the autoclave are conically shaped so that the ball (B) only rolls off at a certain angle of inclination. This angle of inclination is critical and requires special attention. It must be ensured that the ball pockets (F) allow the ball to move at stationary speed when it reaches the measuring distance.

It must be ensured that the ball pockets (F) allow the ball to move at stationary speed when the measuring distance is reached. The speed of the ball is reduced when approaching the cover by the bow wave which pushes the ball in front of it. From this point of view, a free piece of pipe is the desired measuring section. The cross-sectional expansion of the ball pockets minimizes this damping of the ball speed. The entire rolling process is recorded with a special high-temperature structure-borne noise sensor (L) (Fig. 8.17).

The assembled autoclave from Fig. 8.16 is mounted on a frame (J) of a tiltable frame. With the help of adjustable wire ropes (I), the maximum angle of inclination of the frame, and thus of the autoclave, can be adjusted and limited. The inclination is detected by an inclination sensor (L). The frame is moved by the motor (P). The rotational movement of the motor is converted into an alternating tilting movement by a two-part drive linkage (N). The autoclave is heated by a three-part heating sleeve

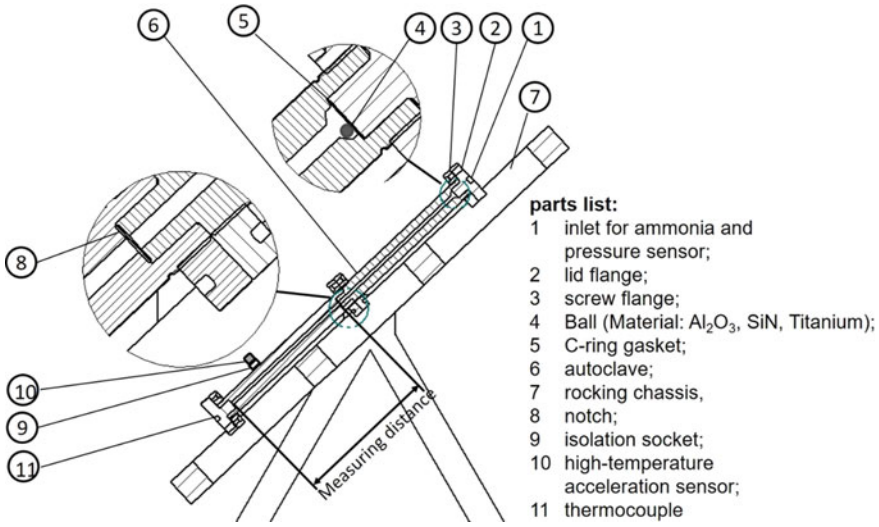

Fig. 8.17 Construction of the viscometer

set from Horst (not shown). Each of the heating sleeves has an output of 600 W. The data recording and control of the motor is done on the hardware side via a USB-6210 (multifunction I/O device) and on the software side via the graphical programming system.

8.6.7 Media-Supply

As described in Table 8.1 in the third point, ammonia is gaseous and toxic under normal conditions. For the filling of ammonothermal autoclaves it is therefore not trivial and a complex test setup with the combination of intensive cooling and the use of compressors is necessary. For this reason, all tests must be carried out in a closed system. Figure 8.18 shows the flow diagram of the plant used in this experiment, as it was already used by *Alt* [5] and adapted for this test setup.

Nitrogen and ammonia are extracted from a gas cylinder. The nitrogen is used to clean the system before and after tests and is connected to the system via several valves (V12, V13, V14). The NH_3 bottle is connected via the V1 valve to a cooling section which cools the ammonia to −15 °C so that it can be condensed out and conveyed in the liquid state. The cooling section is connected to the compressed air driven piston pump P1. The valves and pressure sensors V4 and V6 as well as

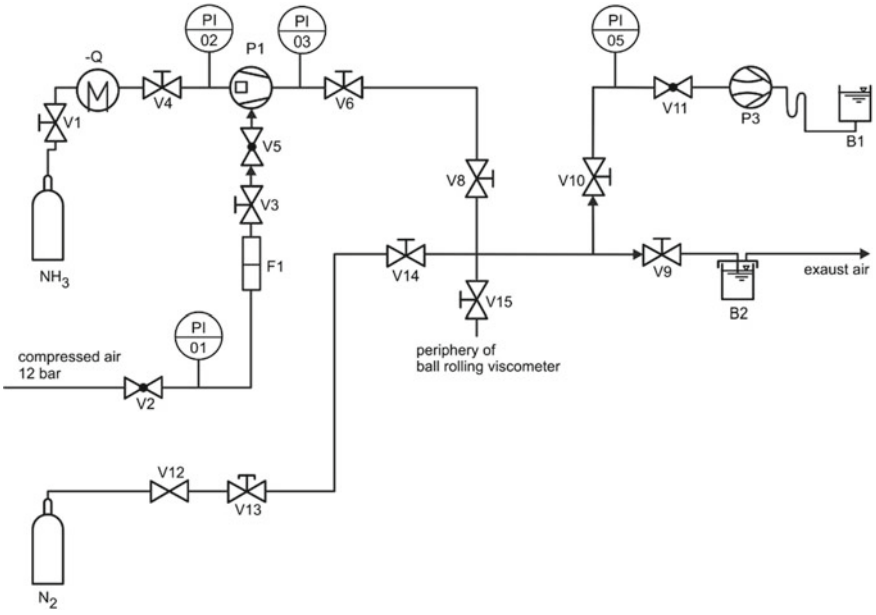

Fig. 8.18 Flow chart of the system

PI02 and PI03 can be used to adjust the inlet pressure of the pump and the delivery pressure of the pump. The V8 valve connects the pump and ammonia to the rest of the system. For calibration tests with carbon dioxide (Linde Ag, 5.3), the ammonia bottle is replaced and carbon dioxide is pumped in the same way. When changing these two media, care must be taken to ensure accurate rinsing, as otherwise urea can form which clog the apparatus and can only be removed by means of a complex water rinsing process. With the valve V9 the plant can be emptied of ammonia or other media and the plant can be vented. An absorber B9 is connected upstream of the exhaust air duct. Ammonia is washed out with this absorber and thus does not enter the exhaust air. The system is connected to a Venturi nozzle via valve V10. This is used to empty the system or the viscometer. The vacuum generated by the Venturi nozzle can be read off via the PI05 manometer. This depends on the vapour pressure of the water and is therefore at best 23 hPa at 20 °C, but in the test only 50 hPa is reached as standard. For the required purity, the autoclave is rinsed at least five times with N_2. The system is connected to the periphery of the rolling ball viscometer via the valve V15, see Fig. 8.19. The pipes and connecting pieces of the system are connected to each other by line seals.

A	Peripheric-Cover		
Q	Valve Type-4	R	Inconel 718®
S	Rupture Disc	T	Pressure Sensor
U	Flexible HP-hose	V	Filling Station

The central components of the peripherals, shown schematically in Fig. 8.19, are a typical high pressure valve. It has an always open connection (solid blue line) from the pressure sensor (T), the bursting disc (S) and to the peripheral cover (A) of the autoclave. Since the temperature in the periphery is considerably lower than in the autoclave, only the supply pipe (R) is made of Inconel 718®. A flexible pressure hose (U) is connected to the shut-off side of the valve (dotted blue line). This is then connected to the filling station (V).

In order to close the autoclave without the mineralizer and ball coming into contact, it is recommended to proceed as follows. The autoclave is inserted vertically in the

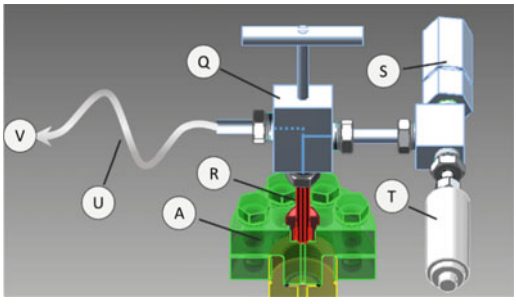

Fig. 8.19 Technical drawing of the system

specially developed opening station. The lower side of the autoclave is already closed with the thermocouple lid so that the mineralizer is filled from above and falls onto the lower side. Three thin wires are passed through the tube of the other cap, forming a kind of claw which encloses the ball, as shown in Fig. 8.18. Now the autoclave can be closed and carried to the viscometer frame. If the autoclave is stored horizontally, first carefully pull a wire out of the cover, so that the ball falls out of the claw. The other two wires are also removed. The autoclave can now be connected to the peripherals.

In order to close the autoclave without the mineralizer and ball coming into contact, it is recommended to proceed as follows. The autoclave is inserted vertically in the specially developed opening station. The lower side of the autoclave is already closed with the thermocouple lid so that the mineralizer is filled from above and falls onto the lower side. Three thin wires are passed through the tube of the other cap and form a kind of claw which encloses the ball, as shown in Fig. 8.20. Now the autoclave can be closed as usual and carried to the viscometer frame. If the autoclave is stored horizontally, first carefully pull a wire out of the cover, so that the ball falls out of the claw. The other two wires are also removed. The autoclave can now be connected to the peripherals as usual.

These solutions ensure a perfect supply of the media and the pressure and temperature can be recorded with sufficient accuracy. The exact sensors for pressure and temperature are explained in more detail in Sect. 8.6.8.

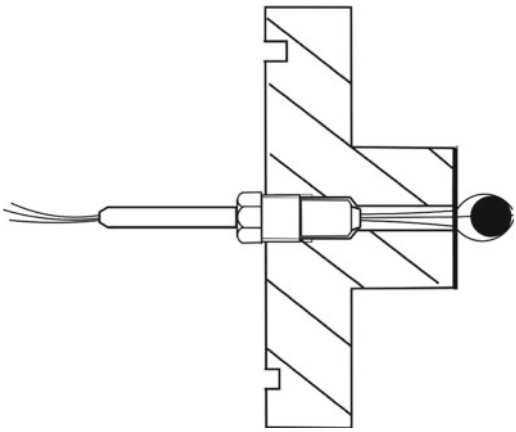

Fig. 8.20 Wire claw for closing the autoclave

8.6.8 Sensoric

8.6.8.1 Thermocouples

Two thermocouples are used for the temperature measurement as described above. These are based on the so-called Seebeck effect: If a conductor is in a temperature gradient, an electron flow is generated inside the conductor, which is caused by an electromotive force proportional to the temperature gradient. If one measures the voltage between the two free ends of the conductor, a voltage difference results which depends on the size of the temperature gradient as well as on the thermoelectric properties of the conductor. For different temperature profiles above the conductor, the same voltage is obtained if the temperatures at both ends match. In practice, this effect is used for temperature measurement by connecting two conductors with different thermoelectric properties at one end. This end is the measuring point. At the other end of the two wires, a voltage can be tapped which depends on the thermoelectric properties of the two conductors and on the temperature difference between the measuring point and the reference junction. With thermocouples only one temperature difference is measured, therefore a reference junction is needed to determine the absolute temperature of the measuring point. Type *K* thermocouples are used in this test. It consists of a nickel-chromium and a nickel-aluminium conductor and can be used at temperatures between −250 and 1100 °C, whereby the temperature may deviate a maximum of 0.75% from the nominal temperature [58, 59].

8.6.8.2 Pressure Sensor

The pressure sensor is based on the principle of strain gauge technology. When a strain gauge is deformed, its electrical resistance changes. By changing the resistance or the electrical signal, the force or pressure acting on the body can be determined. With the pressure transducer, pressures from 0 to 500 MPa can be measured with an accuracy of 0.3% [60, 61].

8.6.8.3 Data Acquisition

A USB multifunction I/O device (USB-6210) is used for data acquisition. It has 16 analog inputs (with 16 bit resolution and a sampling rate of 250 kS/s) and all measured values (pressure, temperature, structure-borne sound sensor and inclination sensor) can be read out from a central card, so that the time stamp is the same for all. The motor can also be controlled via the four digital inputs and outputs. Another advantage is the complete compatibility of the hardware component with a graphical development environment. This allows the measurements to be displayed visually during the tests. For the algorithms developed for data analysis, the extensive program blocks in the associated library are used.

8.6.8.4 Structure Born Noise Sensor

With a structure-borne sound sensor, the vibrations of the body can be converted into an electrical signal. The structure-borne sound sensor used here is an acceleration sensor. This consists of a measuring body with Inconel housing and is suitable for temperatures of up to 538 °C. The sensor is designed for use in the field of vibration measurement. A silver foil on the upper side of the housing, which becomes more permeable to air as the temperature rises, enables oxygen to be supplied to the crystal of the sensor element while maintaining the hermetic seal. The sensor is also mounted on an insulation base to reduce electromagnetic interference and ground loop disturbances.

8.6.8.5 Decline Sensor

The angle of inclination is an important influencing parameter on the viscosity values determined with a rolling ball viscometer. The dynamic viscosity is directly proportional to the rolling angle, as shown in (8.23). Due to the structure of the frame, the movement of the autoclave is quite dynamic. This, together with the large weight of the autoclave, causes inaccuracies in the angle adjustment. Therefore, it makes sense to determine the angle of inclination individually for each measurement. Since the inclination angle should be determined with the greatest possible accuracy and data acquisition with a computer is desirable, rotary encoders and inclination sensors as angle encoders are a closer selection. Most rotary encoders are designed for hollow shaft journals. Although there are also encoders that can be mounted in the middle of the shaft, these require a large shaft diameter. Since the shaft ends in a ball bearing on both sides, an encoder for hollow shaft journals is only possible by additional conversions of the frame. The shaft diameter of the measuring apparatus is too small for conventional rotary encoders which do not require a shaft journal. Inclination sensors are acceleration sensors which determine the inclination with respect to the earth's gravitational field. The measuring principle can, for example, be inductive or capacitive [62]. The inclination angle is determined in relation to the earth's axis, which is why an inclination sensor was selected due to the design of the frame. The sensor has a measuring accuracy of $\pm 0.06°$ in the measuring range of $\pm 90°$ [63]. A 0–10 V interface was selected, whereby the measured values can be read out directly via a graphics card.

8.7 Summary

The flow in the ammonothermal autoclaves is of essential importance for the crystallization process. Since the flow in the autoclaves can only be measured unsatisfactorily (e.g. laser Doppler anemometry does not reach the entire interior and is only accurate when flow is noticeable). Therefore, numerical simulation remains the most powerful tool. However, this requires precise knowledge of the viscosity. Therefore, it is necessary to have well-suited measuring methods for viscosity. From the variety of viscosity measuring techniques, only the ball roller viscometer as an external method and the ultrasonic method for direct measurement in an autoclave have emerged. The rolling ball viscometer requires its own design, which must also meet all the requirements of an autoclave. However, this still means a relatively long downpipe, which can then be used to provide good measured values. The ultrasonic method can be used directly at the autoclave, during the process and therefore provides data that can map the entire process sequence. In addition, a phase interface can also be detected. If liquid and gas are present in the autoclave, this can be detected. The measurement quality that can be achieved with this method is also good but requires more experience in carrying out the measurements.

Literature

1. H. Enayati, A.J. Chandy, M.J. Braun, N. Horning, 3D large eddy simulation (LES) calculations and experiments of natural convection in a laterally-heated cylindrical enclosure for crystal growth. Int. J. Therm. Sci. 1–21 (2017)
2. Q.S. Chen, S. Pendurti, V. Prasad, Effects of baffle design on fluid flow and heat transfer in ammonothermal growth of nitrides. J. Cryst. Growth 271–277 (2004)
3. J. Erlekampf, J. Seebeck, P. Savva, E. Meissner, J. Friedrich, N.S.A. Alt, E. Schlücker, L. Frey, Numerical time-dependent 3D simulation of flow pattern and heat distribution in an ammonothermal system with various baffle shapes. J. Cryst. Growth **403**, 96–104 (2014)
4. D. Ehrentraut, Y. Kagamitani, C. Yokoyama, T. Fukuda, Physico-chemical features of the acid ammonothermal growth of GaN. J. Cryst. Growth **310**, 891–895 (2008)
5. N. Alt, E. Meissner, E. Schlücker, L. Frey, In situ monitoring technologies for ammonthermal reactors. Phys. Status Solidi **9**, 436–439 (2012)
6. J. Kunes, Dimensionless Physical Quantities in Science and Engineering (Elsevier, London, Waltham, 2012)
7. T. Chen, H. John, J. Xu, Q. Lu, J. Hawk, X. Liu, Influence of surface modifications on pitting corrosion behavior of nickel-base alloy 718. Part 2: Effect of aging treatment. Corros. Sci. **78**, 151–161 (2014)
8. Q. Chen, Y. Jiang, J. Yan, M. Qin, Progress in modeling of fluid flows in crystal growth processes. Prog. Nat. Sci. **18**, 1465–1473 (2008)
9. Q.S. Chen, S. Pendurti, V. Prasad, Modeling of ammonothermal growth of gallium nitride single crystals. J. Mater. Sci. **41**, 1409–1414 (2006)
10. Y. Masuda, A. Suzuki, T. Ishiguro, C. Yokoyama, Numerical simulation of heat and fluid flow in ammonothermal gan bulk crystal growth process. Jpn. J. Appl. Phys. **52**, 08JA05 (2013)
11. L. Kulisiewicz, A. Delgado, High-pressure rheological measurement methods: a review. Appl. Rheol. **20**, 13018 (2010)
12. E. Kuss, Federbalg-Kapillar-Viskosimeter, Patent DE 3237 130 A1

13. S. Kawashima, Z. Shirahama, N. Hidekazu, Capillary type viscosimeter, US Patent US4932242A
14. G.D. Galvin, J.F. Hutton, B. Jones, Development of a high-pressure, high-shear-rate capillary viscometer. J. Nonnewton. Fluid Mech. **8**, 11–28 (1981)
15. V. Semjonow, Über ein Rotationsviskosimeter zur Messung der Druckabhängigkeit der Viskosität hochpolymerer Schmelzen. Rheol. Acta **2**, 138–143 (1962)
16. R.J. Murphy, Apparatus and method for measuring viscosity, US Patent US4571988A
17. S.-H. Sheen, H.-T. Chien, A.C. Paul Raptis, in Instrumentation for Fluid Particle Flow (Elsevier, 1999), pp. 162–211
18. T. Retsina, S.M. Richardson, W.A. Wakeham, The theory of a vibrating-rod viscometer. Appl. Sci. Res. **43**, 325–346 (1987)
19. J.V. Fitzgerald, F.J. Matusik, J.L. Batton, High Viscosity transducer for vibratory viscometer, US Patent US5317908A
20. G. Bradfield, Improvements in or relating to Viscometers, Patent GB910881A
21. S. Pimputkar, T.F. Malkowski, S. Griffiths, A. Espenlaub, S. Suihkonen, J.S. Speck, S. Nakamura, Stability of materials in supercritical ammonia solutions. J. Supercrit. Fluids **110**, 193–229 (2016)
22. J. Spurk, N. Aksel, Strömungslehre (Springer, Berlin, 2010)
23. H. Herwig, Strömungsmechanik: Einführung in die Physik von technischen Strömungen (Vieweg+Teubner Verlag/GWV Fachverlage GmbH, Wiesbaden, 2008)
24. J. Draxler, M. Siebenhofer, Verfahrenstechnik in Beispielen Problemstellungen, Lösungsansätze, Rechenwege (Springer, Wiesbaden, 2014)
25. VDI Gesellschaft Verfahrenstechnik und Chemieingenieurwesen, *VDI-Wärmeatlas*, 11th edn. (Springer, Heidelberg, 2013)
26. W. Sutherland, LII. The viscosity of gases and molecular force. Lond. Edinb. Dublin Philos. Mag. J. Sci. **36**, 507–531 (1893)
27. M.M. Lencka, A. Anderko, S.J. Sanders, R.D. Young, Modeling viscosity of multicomponent electrolyte solutions 1 (1998)
28. G. Jones, M. Dole, The viscosity of aqueous solutions of strong electrolytes with special reference to barium chloride. J. Am. Chem. Soc. **51**, 2950–2964 (1929)
29. H.D.B. Jenkins, Y. Marcus, Viscosity B-coefficients of ions in solution. Chem. Rev. **95**, 2695–2724 (1995)
30. D. Feakins, K.G. Lawrence, The relative viscosities of solutions of sodium and potassium chlorides and bromides in N-methylformamide at 25, 35, and 45°. J. Chem. Soc. A 212–219 (1966)
31. M.A. Motin, Temperature and concentration dependence of apparent molar volumes and viscosities of NaCl, NH_4Cl, $CuCl_2$, $CuSO_4$, and $MgSO_4$ in pure water and water + urea mixtures. J. Chem. Eng. Data **49**, 94–98 (2004)
32. R. Saeed, F. Uddin, S. Masood, N. Asif, Viscosities of ammonium salts in water and ethanol + water systems at different temperatures. J. Mol. Liq. **146**, 112–115 (2009)
33. H. Baser, W. Schwieger, D. Freitag, T.G. Steigerwald, E. Schluecker, Solubility studies of sodium azide in liquid ammonia by in situ ultrasonic velocity measurement. Chem. Eng. Technol. **40**, 1101–1106 (2017)
34. F. Cohen-Tenoudji, L.A. Ahlberg, B.R. Tittmann, W.J. Pardee, High temperature ultrasonic viscometer, US Patent US4779452A
35. S.J. Kleis, L.A. Sanchez, Dependence of speed of sound on salinity and temperature in concentrated NaCl solutions. Sol. Energy (1990)
36. S. Natarajan, T.W. Randolph, Ultrasonic velocity measurements in supercritical jet fuel, J. Supercrit. Fluids **10**, 65–70 (1997)
37. S.H. Sheen, H.-T. Chien, A.C. Raptis, in Review of Progress in Quantitative Nondestructive Evaluation, ed. by D.O. Thompson, D.E. Chimenti, vol. 14 (Plenum Press, New York, 1995), pp. 1151–1158
38. W. Roth, S.R. Rich, A new method for continuous viscosity measurement. General theory of the ultra-viscoson. J. Appl. Phys. **24**, 940 (1953)

39. V. Shah, K. Balasubramaniam, R.D. Costley, J. Singh, in Review of Progress in Quantitative Nondestructive Evaluation (Springer US, Boston, MA, 1996), pp. 2067–2071
40. S.-H. Sheen, A.C. Raptis, A Feasibility Study on Advanced Techniques for On-line Monitoring of Coal Slurry Viscosity. Argonne Natl. Lab. Tech. Memo. 87 (1987)
41. R. Kažys, A. Voleišis, B. Voleišienė, High temperature ultrasonic transducers: review. Ultragarsas "Ultrasound" **63**, 7–17 (2016)
42. J.O. Kim, H.H. Bau, Instrument for simultaneous measurement of density and viscosity. Rev. Sci. Instrum. **60**, 1111–1115 (1989)
43. S.H. Sheen, K.J. Reimann, W.P. Lawrence, A.C. Raptis, in *Ultrasonics Symposium Proceedings* (IEEE, 1988), pp. 537–541
44. H.J. Mcskimin, P. Andreatch, Measurement of dynamic shear impedance of low viscosity liquids at ultrasonic frequencies. J. Acoust. Soc. Am. **42**, 248–252 (1967)
45. S. Sherrit, X. Bao, Y. Bar-Cohen, Z. Chang, in Smart Structures and Materials 2004: Active Materials, ed. by D.C. Lagoudas (International Society for Optics and Photonics, 2004), p. 411
46. K. Balasubramaniam, V.V. Shah, R.D. Costley, G. Boudreaux, J.P. Singh, High temperature ultrasonic sensor for the simultaneous measurement of viscosity and temperature of melts. Rev. Sci. Instrum. **70**, 4618 (1999)
47. R.S. Moore, H.J. McSkimin, in *Physical Acoustics* (1970), pp. 167–242
48. T.G. Steigerwald, N.S.A. Alt, B. Hertweck, E. Schlücker, Feasibility of density and viscosity measurements under ammonothermal conditions. J. Cryst. Growth **403**, 59–65 (2014)
49. R.M. Hubbard, G.G. Brown, The rolling ball viscometer. Ind. Eng. Chem. Anal. Ed. **15**, 212–218 (1943)
50. H.H. Buchter, Apparate und Armaturen der Chemischen Hochdrucktechnik Konstruktion, Berechnung und Herstellung (Springer, Berlin, 2014)
51. Lamineries Matthey SA Inc., *Legierung 718*, 3 (2013)
52. D. Joshi, Dissertation: Finite element simulation of machining a Nickel-based superalloy—Inconel 718, Oklahoma State University (2000)
53. Metals VDM Inc., *VDM® Alloy 718, Datasheet* (2016)
54. E.W. Lemmon, M.O. McLinden, D.G. Friend, Thermophysical Properties of Fluid Systems, NIST Stand (National Institute of Standards and Technology, Gaithersburg, MD, 2017)
55. T. Okamoto, Falling Body Viscometer, US Patent 3512396
56. I. Fehrenkemper, Aluminium-Nickel-Kobalt (AlNiCo) (2018), https://www.fehrenkemper.de/produkte/rohmagnete/aluminium-nickel-kobalt-alnico/. Accessed 15 Dec 2019
57. K. Nishibata, M. Izuchi, A rolling ball viscometer for high pressure use. Phys. B + C **139**, 903–906 (1986)
58. TC Direct, TC Direct für Temperatur-Sensoren, -Messung und -Regelung (2019), https://www.tcdirect.de/Default.aspx?level=2&department_id=190/3. Accessed 23 Mar 2019
59. Deutsches Institut für Normung e. V, Thermoelemente - Teil 1: Thermospannungen und Grenzabweichungen (IEC 60584-1:2013); Deutsche Fassung EN 60584-1:2013 (Germany, 2013), p. 65
60. HBM Germany, Drucktransmitter|P 2VA1/P2VA2|Integrierter Verstärker| HBM (2019), https://www.hbm.com/de/2479/p2va1-p2va2-drucktransmitter/. Accessed 23 Mar 2019
61. E. Schrüfer, L.M. Reindl, B. Zagar, *Elektrische Messtechnik: Messung elektrischer und nichtelektrischer Größen* (Carl Hanser Verlag GmbH & Co. KG, München, 2018)
62. S. Hesse, G. Schnell, Sensoren für die Prozess- und Fabrikautomation, 7th edn. (Springer, Plauen, 2009)
63. Sensors GEMAC, *IS2BP090-U-CL* (2019), https://gemac-sensors.com/de/sensoren/neigungssensoren/is2bp090-u-cl/. Accessed 24 Mar 2019

Chapter 9
Determination of Solubility of GaN in Ammonobasic Systems

Wilhelm Schwieger and Hasan Baser

Abstract In this study, the solubility of GaN in the ammonobasic MNH$_2$–GaN–NH$_3$ (M = Na, K) systems in the temperature range of 350–550 °C was studied. The target value for the ammonia filling degree was 45% and 55% for mineralizers NaNH$_2$ and KNH$_2$, respectively. The mineralizer concentration was varied at all temperatures from 1 M to 3 M, in respect to the liquid ammonia. It has been found that the solubility of GaN with NaNH$_2$ as a mineralizer increases slightly with increasing temperature in the range 400–600 °C, but is generally very low. A dependence of solubility on mineralizer concentration was not observed. An increase in the ammonia filling degree from 45% to 55% only slightly increased the solubility of GaN. The use of KNH$_2$ as a mineralizer brought an enormous increase in the solubility of GaN. Here, 7 times higher solubilities than those for NaNH$_2$ were observed. A retrograde solubility behavior of GaN in the temperature range 400–550 °C was determined for KNH$_2$ as a mineralizer. In the range of 350–400 °C the solubility showed a positive temperature dependence. The maximum solubility was reached at 400 °C. The solubility of GaN at 400 °C was found three times higher than at 550 °C.

9.1 Introduction

The ammonothermal method is characterized as a system in which supercritical ammonia acts as solvent. Basically, a distinction can be made between three different types of systems: Ammonobasic, ammononeutral and ammonoacidic. Which environment is present depends on the starting products and the mineralizers used [1].

The ammonothermal crystal growth of GaN takes place in the metastable Ostwald-Miers area. In order to significantly increase the concentration of metastable products in the reaction with GaN, mineralizers are of enormous importance. Because GaN is

W. Schwieger · H. Baser (✉)
Institute of Chemical Reaction Engineering, University of Erlangen-Nuremberg, Egerlandstraße 3, 91058 Erlangen, Germany
e-mail: hasan.baser@fau.de

E. Meissner and R. Niewa (eds.), *Ammonothermal Synthesis and Crystal Growth of Nitrides*, Springer Series in Materials Science 304,
https://doi.org/10.1007/978-3-030-56305-9_9

poorly soluble in ammonia, the transition from NH_3 to the supercritical state does not change the solubility behavior of GaN. Only by adding a mineralizer the solubility of GaN in ammonia is made possible, in which the mineralizer forms compounds with GaN that are easily soluble in ammonia [1].

The advantages of the ammonothermal method are the lower defect densities of the crystals produced, the possibility of growing crystals with large diameters and outstanding structural properties, the controlled crystallization process, the simple scale-up of the method and the possibility of growing several crystals during a synthesis process. In the past, low growth rates were the biggest problem of the ammonothermal method [2–14]. Currently, research has already succeeded in increasing growth rates from 24–106 μm/d up to 300 μm/d and more.

The addition of mineralizers allows the solubility of GaN in ammonia. The mineralizers supply the system with different ions depending on the choice of mineralizer. In the ammonobasic environment, the mineralizers supply amide ions to the system; in the ammonoacidic system, however, NH_4^+ ions. When neutral mineralizers are selected, none of these ions are made available to the system in excess concentrations.

The added mineralizers form intermediates with GaN in the solution zone, which are highly soluble in ammonia. It is still necessary to determine which intermediates are actually formed [5]. In the ammonobasic environment, for example, the following process is conceivable when using the alkali amide KNH_2 as a mineralizer.

The basic mineralizer is getting in contact with the GaN in the solution zone. A metal amide compound such as $KGa(NH_2)_4$ [14], which is soluble in ammonia, is formed. The following reaction could take place (9.1):

$$KNH_2 + GaN + 2NH_3 \rightleftharpoons KGa(NH_2)_4 \tag{9.1}$$

After convective transport of the intermediate to the crystallization zone, it is deposited on the GaN seed crystal and crystallizes GaN. Typical process conditions are specified for the ammonothermal process with $T = 400$–600 °C and $P = 0.1$–0.3 GPa [4]. Furthermore, the choice of the mineralizer influences the position of the crystallization and solution zones. Under ammonobasic conditions, GaN has a retro grade solubility in ammonia, so that the solution zone is placed in the colder, upper zone. The seed crystals are therefore located in the lower, warmer area [13].

In ammonoacidic systems, both the positive and negative temperature dependence of the solubility of GaN in supercritical ammonia was observed. For NH_4X (X = Cl, Br, I) as mineralizer, GaN is more soluble in the warmer area, so that the crystallization zone is placed in the colder, upper part of the autoclave [8].

The basic mineralizers of the form MNH_2 are mainly mineralizers with M = K or Na. KN_3 and NaN_3 are also used as mineralizers. When azides are used in the system, additional pressure is created by the decomposition of azides to form amide at a certain temperature [4, 5, 8, 13]. The reactions in (9.2) and (9.3) take place:

$$2\,MN_3 \rightarrow 2\,M + 3\,N_2 \tag{9.2}$$

$$2\,M + 2\,NH_3 \rightarrow 2\,MNH_2 + H_2 \tag{9.3}$$

with $M = \mathrm{K}$ or Na.

Equations (9.2) and (9.3) show that the additional pressure in the system is caused by formation of N_2 and H_2. The resulting KNH_2 or $NaNH_2$ influences the system in the same way as the direct addition of the metal amides.

9.2 State of the Art

Basic mineralizers mainly include alkali metal amides such as lithium, sodium or potassium amide. Few data on the solubility experiments with the basic mineralizer $NaNH_2$ can be found in the literature. In contrast, KNH_2 has been studied more frequently because of the higher solibility in ammonia compared to $NaNH_2$ (66 g KNH_2/100 g NH_3, $T = -33$ °C [1]; 0.004 g $NaNH_2$/100 g NH_3; $T = 25$ °C [16, 17]). In Fig. 9.1 previously measured solubilities of GaN in ammonobasic system in the literature as a function of temperature are summarized.

Dwilinski et al. [12] have investigated the temperature dependence of GaN solubility in the KNH_2–NH_3 system at two different temperatures. The molar ratio of mineralizer to ammonia KNH_2/NH_3 was 0.07, which equals a concentration of 2.6 M KNH_2. Their results show a retrograde solubility of GaN in the ammonobasic system. Solubility at 400 °C is greater for any pressure than GaN solubility at 500 °C. Furthermore, the solubility of GaN for this system shows a clear pressure dependence. Solubility increases with pressure and strives for both temperatures above a pressure of approx. 300 MPa against solubility limits of approx. 3 mol% for 400 °C and 2 mol% for 500 °C. Whether the solubility decreases with increasing pressure is not mentioned in their publication.

Wang et al. [13] have studied the solubility of GaN in the KNH_2–NH_3 system. The dissolved amount of GaN was determined by weighing GaN before and after the

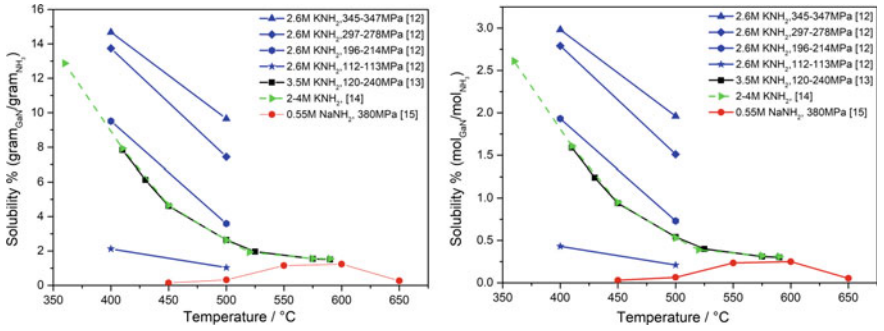

Fig. 9.1 Summarized previously measured solubilities of GaN in ammonobasic system in the literature as a function of temperature [12–15]

experiment. The experiments normally lasted one week. The pressure was changed in the interval of 1.2–2.4 kbar. The concentration of the mineralizer was 3.5 ± 0.5 M. Information about the ammonia filling level is not given. In Fig. 9.1 shows the already mentioned retrograde solubility of GaN in the ammonobasic system. Thus, the highest value for the GaN solubility is achieved at approx. 410 °C with 8% by weight (ammonia specific) and the lowest solubility at approx. 550 °C with approx. 1.5% by weight. Furthermore, it can be seen from the results that the ammonia-specific solubility of GaN at the same mineralizer concentration runs with increasing temperature against a limit value of 1.5% by weight.

Callahan et al. [14] have also conducted solubility studies on GaN in the ammonobasic system. Their investigations cover the temperature interval from 360 to 600 °C. They used 15 ml autoclaves with an inner diameter of 1 cm for their solubility experiments. The solubility experiments took 3–7 days. The pressure was not kept constant. The amide concentrations were chosen between 2 and 4 M. The amount of NH_3 in the system was between 0.65 and 0.85 mol. The quantities of GaN used varied between 5 and 10 g. Retrograde solubilities between ~13 wt% and 1.5 wt% GaN for approx. 360 °C and 590 °C could be achieved. In their publication, however, it is not mentioned which basic mineralizer has been specifically used. It is probable that KNH_2 has been used as a mineralizer here, judging by the results of Wang et al. [13], Dwilinski et al. [12] and Hashimoto et al. [15]. The results of Callahan et al. [14] seem to belong to the experiment series of Wang et al. [13], because many values lie graphically on the identical spot.

Another behavior shows the solubility of GaN when using $NaNH_2$ as a mineralizer. The solubility behavior of GaN in the $NaNH_2$–NH_3 system has been investigated by Hashimoto et al. [15]. The NH_3 filling degrees are given as 40, 34, 30, 24 and 19% at oven temperatures of 450, 500, 550, 600 and 650 °C. The pressure is indicated as constant at 830 MPa. The reaction time was 120 h. The concentration of $NaNH_2$ in the system was selected to 1.5 mol%. The maximum solubility of GaN for the system shown is 1.2% by weight at 600 °C. Up to ~560 °C the GaN solubility increases exponentially and reaches a value of approx. 1.19% by weight. Subsequently, a slow increase up to 600 °C takes place. After reaching the solubility maximum at 600 °C, the solubility of GaN is retrograde and steeply decreasing. Whether a limit value for solubility is reached after 650 °C remains unclear.

In summary, an exponentially retrograde solubility of GaN in the temperature range of 360– 590 °C is observed when KNH_2 using basic mineralizers. For $NaNH_2$ the solubility of GaN decreases in temperature range from 450 to 600 °C. At higher temperatures then 600 °C the solubility becomes retrograde. Furthermore, the conditions of the solubility experiments described in the literature are not sufficiently specified. Thus, often no information is given on the ammonia filling level. In addition, little data is available on $NaNH_2$ as a mineralizer (Table 9.1).

Table 9.1 Comparison of the solubility values in the literature as a function of temperature, pressure and concentration of the basic mineralizer

Lit.	Mineralizer	Pressure (Mpa)	Filling (%)	Temp. °C	Solubility [%] ($gGaN/gNH_3$)*	Solubility [%] ($molGaN/molNH_3$)*
[12]	2.60 M KNH_2	112 196 297 345 113 214 278 347	–	400 400 400 400 500 500 500 500	2.12 9.51 13.74 14.68 1.03 3.59 7.44 9.65	**0.43** **1.93** **2.79** **2.98** **0.21** **0.73** **1.51** **1.96**
[13]	3.50 M KNH_2	120 – 240	–	410 430 450 500 525 575 590	**7.84** **6.13** **4.61** **2.64** **1.96** **1.54** **1.50**	1.59 1.24 0.94 0.54 0.40 0.31 0.30
[14]	2–4 M Amide	–	~0.65 mol NH_3 in 15 ml autoclave	360 410 450 500 520 575 590	**12.87** **7.93** **4.66** **2.63** **1.93** **1.56** **1.54**	2.61 1.61 0.95 0.53 0.39 0.32 0.31
[15]	0.55 M $NaNH_2$	380 MPa	40 34 30 24 19	450 500 550 600 650	**0.14** **0.32** **1.15** **1.23** **0.26**	0.03 0.06 0.23 0.25 0.05

*The bold printed values are original values for the solubility of GaN from the literature. The values with standard letter are the recalculated values for comparability with each other

9.3 Results

9.3.1 Description of the Experiment Setup

In this study the influence of temperature on the solubility of GaN in the system MNH_2–GaN–NH_3 (M = Na or K) was investigated. The mineralizer concentration calculated on base of the liquid ammonia volume at the filling temperature was varied from 1 to 3 M. The amount of NH_3 was kept constant for the different temperatures with a target filling degree of 50% for $NaNH_2$ and 55% for KNH_2. The temperature was increased between 350 and 550 °C in 50 °C steps. Polycrystalline GaN single crystals produced by the HVPE method were used. The dissolved amount of GaN was determined gravimetrically. Furthermore, the pressure curve was recorded in situ.

This made it possible to check the tightness of the autoclave and thus to obtain meaningful results. In addition to checking the tightness, the analysis of the pressure curves is used to gain insights into the processes in the ammonobasic system.

The autoclave used in the solution experiments is shown in Fig. 9.2. This autoclave was made of a nickel-based alloy (Inconel-718) and was specially developed for ammonothermal experiments. It is designed for a maximum temperature of 600 °C and a maximum internal pressure of 300 MPa. The temperature and pressure curves are with welded or soldered thermocouples type K and pressure transmitters of type P2VA1 (HBM). Thermocouple and pressure transmitters are attached to the lid of the autoclave via a connecting tube.

During the tests, the corresponding quantity of mineralizer and GaN crystal weighed was placed in the autoclave and the autoclave is sealed. The sealed autoclave is first weighed to determine its weight in the absence of ammonia. A leak test is then carried out on the autoclave. For this purpose, nitrogen is introduced into the autoclave at the final pressure expected in the respective solubility test (approx. 150 to 200 MPa) and the pressure development in the autoclave is observed over a period of time. If the autoclave is tight, nitrogen is released and a vacuum of up to 4×10^{-7} mbar is generated in the autoclave using a turbomolecular pump. Liquid ammonia is now introduced into the degassed autoclave until the target volume is reached. The target volumes are adjusted by means of ultrasonic measurement. Now the filled autoclave is weighed again and the value compared with the reference weight without

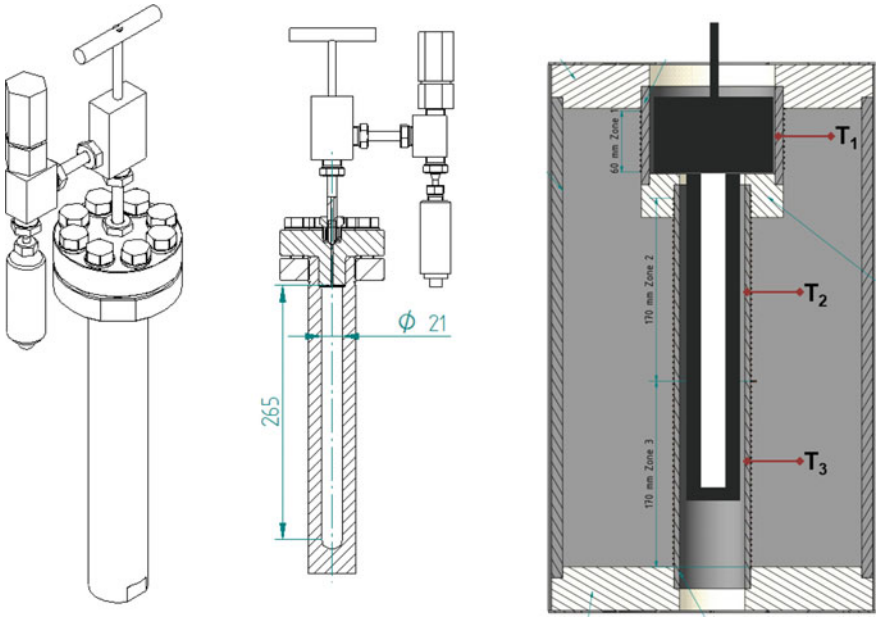

Fig. 9.2 Schematic representation of the autoclave and the tree zone oven used in the solubility experiments

ammonia. If the difference is 33 g (≙55% filling degree), the autoclave can be placed in the furnace. The furnaces used here have three separate heating zones (Fig. 9.2). In the first heating zone (zone 1) the lid and the flange are heated. In addition to insulation, the autoclave lid is covered with glass wool. The other lower zones serve to heat the autoclave body (zones 2 and 3). In the solubility tests, the temperature in all zones was set to the same value.

The duration of the solubility experiments was 120 h. After this time, the oven was switched off and the autoclave was left in the oven for another 20 h to cool down. The overpressure created by amide formation and ammonia decomposition is released from the autoclave. After opening the degassed autoclave, the basic mineralizer was removed from the autoclave by dissolution in a water-alcohol (isopropanol for KNH_2 and ethanol for $NaNH_2$) mixture with a mixing ratio of 1:5 ($V(H_2O)$ = 10 ml; V(alcohol) = 50 ml;). The water is diluted with alcohol because the reaction of the amide with pure water would be too vigorous. The GaN crystals are then removed from the autoclave and their mass is determined gravimetrically. The dissolved amount of GaN is determined by calculating the difference between m_{GaN} before and after the solubility experiment.

9.3.2 *Time and Temperature Dependency of the Pressure Buildup Under the Conditions of Ammonobasic Solubility Measurements*

Figure 9.3 shows that the system pressure develops similarly for all temperatures. The heating-up period extends from the start $t = 0$ h to $t = 4$ h. A linear increase in pressure can be seen in this period. After a heating-up period in which the pressure rises steadily, an isothermal state is reached ($t = 0$–120 h). The pressure increases with a very small gradient after reaching the target temperature. The maximum pressure

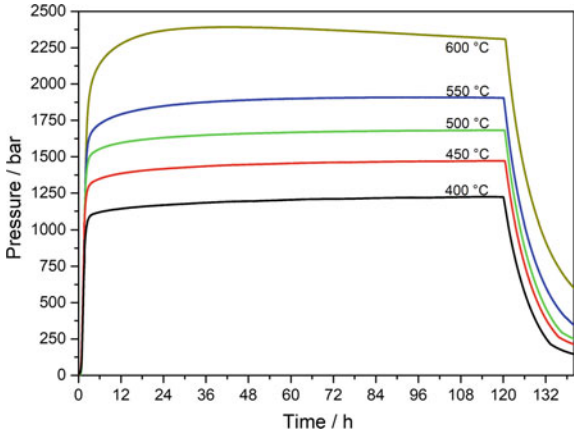

Fig. 9.3 In situ recorded pressure curves in the autoclave at different temperatures during the solubility studies of GaN with a concentration of 1 M of $NaNH_2$ as mineralizer and with an ammonia filling degree of 50%

reached causes a temperature dependence. The higher the temperature, the higher the system pressure. The maximum pressure value is reached for the temperatures of 400–550 °C at the end of the isothermal phase at $t = 120$ h. An exception can be observed at 600 °C. For this temperature, the maximum pressure is reached at approx. 36 h. After reaching the maximum value the pressure decreases slightly. This slight decrease in pressure is an indication of the beginning of hydrogen diffusion from the autoclave. In the subsequent cooling phase, the pressure continuously decreases.

Figure 9.4 shows the pressure jump resulting by the thermal decomposition of NaN_3 for the different amount of NaN_3. The pressure jump occurs abruptly within a few milliseconds. The resulting N_2 according (9.2) leads to a sudden increase in pressure.

The decomposition of NaN_3 also produces stoichiometric amounts of sodium, which reacts with ammonia to form sodium amide. The mathematically calculated pressure of the nitrogen formed in this equation is equal to the experimentally determined pressure difference during the pressure jump. As an example, the value of the pressure jump by thermal decomposition of 2 M NaN_3 is calculated as follows:

$$dp = \frac{n \times R \times T}{V} = \frac{0.142\,\text{mol} \times 0.083\left(\text{bar} \times \frac{1}{\text{mol}} \times K\right) \times 573.15\,K}{0.048l} = 141\,\text{bar}$$

dp: pressure jump
n: molar amount of formed nitrogen gas
R: ideal gas constant; T: decomposition temperature of sodium azide (573, 15 K)
V: free volume of the autoclave ($=V_{\text{autoclave}} - V_{\text{ammonia(liq.)}}$).

For all temperatures, the pressure continues to rise slowly with time after reaching the target temperature (t: 4 h). At the end of the stationary phase at $t = 120$ h the

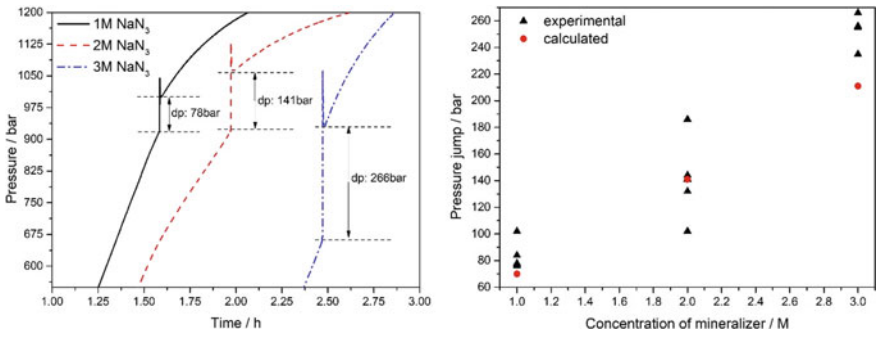

Fig. 9.4 **Left**: Representation of the pressure jump due to thermal decomposition of NaN_3 for different concentrations of NaN_3. The pressure jump takes place between 1.3 and 1.6 h, where the autoclave has an internal temperature of approx. 300 °C. For better recognition, the curves in the diagram were plotted with a time shift (2 M NaN_3: 30 min and 3 M NaN_3: 60 min), **Right**: Comparison of the calculated and experimental value of the pressure jump (plotted are all values for the solubility experiments described in Sect. 9.3.3)

maximum process pressure is reached. The reason for the increase of pressure at constant temperature is the decomposition of ammonia to hydrogen and nitrogen. For the process, temperature of 600 °C a different behavior can be seen after reaching the target temperature.

In Fig. 9.3, a maximum pressure of 600 °C is reached after approx. 40 h. The process temperature of 600 °C is reached after approx. 40 h. The maximum pressure of 600 °C is reached after approx. 40 h. The pressure then drops slowly to the end of the stationary phase. This indicates that a significant amount of hydrogen diffuses through the autoclave walls at a temperature of 600 °C for the present system.

9.3.3 *Solubility of GaN with $NaNH_2$ as Mineralizer*

The volumetric ammonia filling degree for each process temperature was 50%. The total volume of the autoclave used was 97 ml. Thus, the volume of ammonia for the intended filling degree $V_{\text{ammonia}} = V_{\text{autoclave}} \times 50\% = 48.5$ ml. Based on this volume of ammonia, the molar amounts of NaN_3 was 0.047, 0.095 and 0.142 mol for the concentration of $NaNH_2$ 1 M, 2 M and 3 M, respectively. $NaNH_2$ was produced in situ according to the equation by decomposition of NaN_3.

The experimentally determined solubility data (Fig. 9.5 and Table 9.2) can be concluded as follows. With an absolute dissolved amount of GaN of 0.008 g (lowest solubility, 1 M $NaNH_2$, 400 °C) to 0.134 g (highest solubility, 1 M $NaNH_2$, 600 °C), the dissolved amounts are very low in all experiments performed. These are too small to allow a meaningful crystal growth. Overall, the solubility increases with increasing temperature. However, the increase in solubility with temperature is small. A significant increase can only be observed at 600 °C. In the temperature range between 400 and 600 °C no retrograde solubility was observed, as reported by Hashimoto et al. [15]. An increase of the mineralizer quantity leads slightly to an

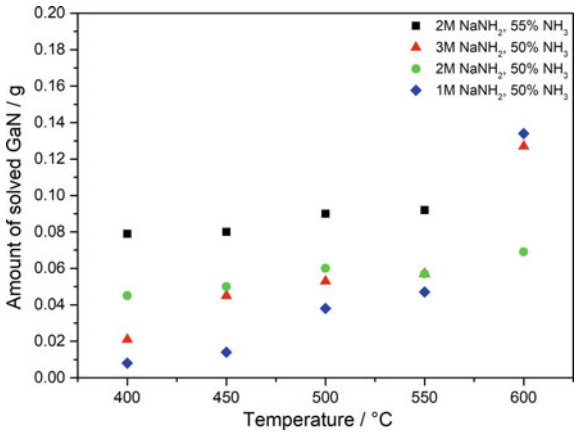

Fig. 9.5 The absolute dissolved amounts of GaN over the temperature at different mineralizer concentrations

Table 9.2 Results of the solubility experiments as a function of temperature for different $NaNH_2$ concentrations (ammonia filling degree 50%)

	$NaNH_2$: 1 M; 50% NH_3				
Temperature [°C]	400	450	500	550	600
Absolutely solved GaN [g]	0.008	0.014	0.038	0.047	0.134
Solubility related to ammonia % [m_{GaN}/m_{NH3}]	0.030	0.052	0.140	0.174	0.495
Solubility related to ammonia % [mol_{GaN}/mol_{NH3}]	0.006	0.011	0.029	0.035	0.101
	$NaNH_2$: 2 M; 50% NH_3				
Temperature [°C]	400	450	500	550	600
Absolutely solved GaN [g]	0.045	0.050	0.060	0.057	0.069
Solubility related to ammonia % [m_{GaN}/m_{NH3}]	0.034	0.038	0.045	0.043	0.052
Solubility related to ammonia % [mol_{GaN}/mol_{NH3}]	0.166	0.185	0.222	0.211	0.255
	$NaNH_2$: 3 M; 50% NH_3				
Temperature [°C]	400	450	500	550	600
Absolutely solved GaN [g]	0.021	0.045	0.053	0.057	0.127
Solubility related to ammonia % [m_{GaN}/m_{NH3}]	0.016	0.034	0.040	0.043	0.095
Solubility related to ammonia % [mol_{GaN}/mol_{NH3}]	0.078	0.166	0.196	0.211	0.469
	$NaNH_2$: 2 M; 55% NH_3				
Temperature [°C]	400	450	500	550	-
Absolutely solved GaN [g]	0.079	0.080	0.090	0.092	-
Solubility related to ammonia % [m_{GaN}/m_{NH3}]	0.048	0.049	0.055	0.056	-
Solubility related to ammonia % [mol_{GaN}/mol_{NH3}]	0.239	0.242	0.272	0.278	-

increase of the solubility of GaN. This means that $NaNH_2$ itself has a low solubility in supercritical ammonia and only a small part of the $NaNH_2$ used contributes to the dissolution of GaN. Only an increase of the ammonia amount (from 50 to 55%) seems to be more efficient to increase the solubility of GaN.

9.3.4 Solubility of GaN with KNH_2 as Mineralizer

The total volume of the autoclave used was 97 ml. The volumetric ammonia filling degree for each process temperature was 55%. Thus, the volume of ammonia for the intended filling degree $V_{ammonia} = V_{autoclave} \times 55\% = 53.35$ ml. Based on this volume

of ammonia, the molar amount of KN_3 was 0.0534 mol, 0.1067 and 0.1600 mol for the concentration of KNH_2 1 M, 2 M and 3 M, respectively. KNH_2 was produced by in situ decomposition of KN_3.

In the literature, different units of solubility are given. Therefore, the absolute solubilities determined in this work are also normalized in relation to the ammonia quantity in order to allow a comparison with the literature values. The results are summarized in Table 9.3.

A bell-shaped curve for the absolutely solubility of GaN with a maximum of approximately over 0.850 g for the KNH_2 concentration of 3 M at just over 400 °C can be seen (Fig. 9.6). After reaching the maximum, a retrograde solubility towards the higher temperatures is observed.

Table 9.3 Results of the solubility experiments as a function of temperature for different KNH_2 concentrations (ammonia filling degree 55%)

	KNH_2: 1 M				
Temperature [°C]	350	400	450	500	550
Absolutely solved GaN [g]	0.374	0.438	0.366	0.226	0.149
Solubility related to ammonia % [m_{GaN}/m_{NH3}]	1.13	1.32	1.11	0.68	0.45
Solubility related to ammonia % [mol_{GaN}/mol_{NH3}]	0.23	0.27	0.23	0.14	0.09
Solubility related to mineralizer % [$mol_{GaN}/mol_{Mineralizer}$]	8.37	9.81	8.19	5.06	3.34
	KNH_2: 2 M				
Temperature [°C]	350	400	450	500	550
Absolutely solved GaN [g]	0.519	0.705	0.601	0.512	0.415
Solubility related to ammonia % [m_{GaN}/m_{NH3}]	1.57	2.14	1.82	1.55	1.26
Solubility related to ammonia % [mol_{GaN}/mol_{NH3}]	0.32	0.43	0.37	0.32	0.26
Solubility related to mineralizer % [$mol_{GaN}/mol_{Mineralizer}$]	5.81	7.89	6.73	5.73	4.65
	KNH_2: 3 M				
Temperature [°C]	350	400	450	500	550
Absolutely solved GaN [g]	0.706	0.850	0.830	0.675	0.521
Solubility related to ammonia % [m_{GaN}/m_{NH3}]	2.14	2.58	2.52	2.05	1.58
Solubility related to ammonia % [mol_{GaN}/mol_{NH3}]	0.44	0.52	0.51	0.42	0.32
Solubility related to mineralizer % [$mol_{GaN}/mol_{Mineralizer}$]	5.27	6.34	6.20	5.04	3.89

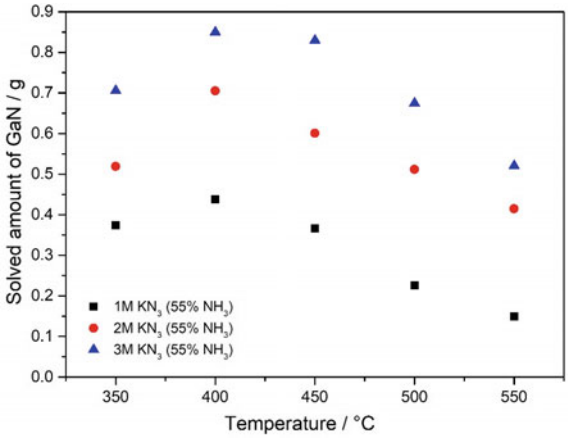

Fig. 9.6 The absolute dissolved amounts of GaN over the temperature at different mineralizer concentrations

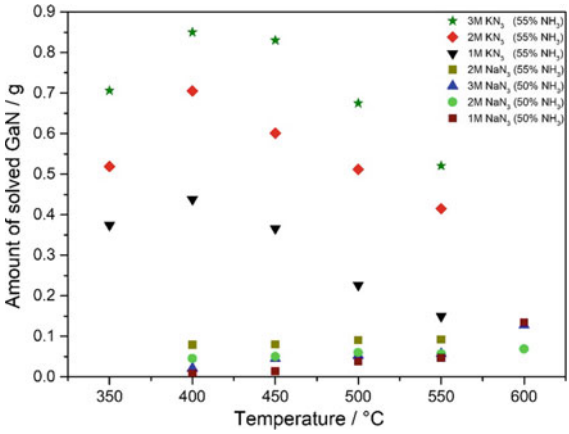

Fig. 9.7 Comparison of the solubilities of GaN in dependence of the temperature by the use of $NaNH_2$ and KNH_2 as mineralizer

This means that the solubility decreases with increasing temperature with a linear dependence between 450 and 550 °C. The experiment at 550 °C provides the lowest dissolved quantity of GaN in the temperature range examined.

In order to compare these results better with other experiments from the literature, it is common to normalize the solubility. The figures show the calculated relative solubilities in relation to the amount of ammonia (Fig. 9.8).

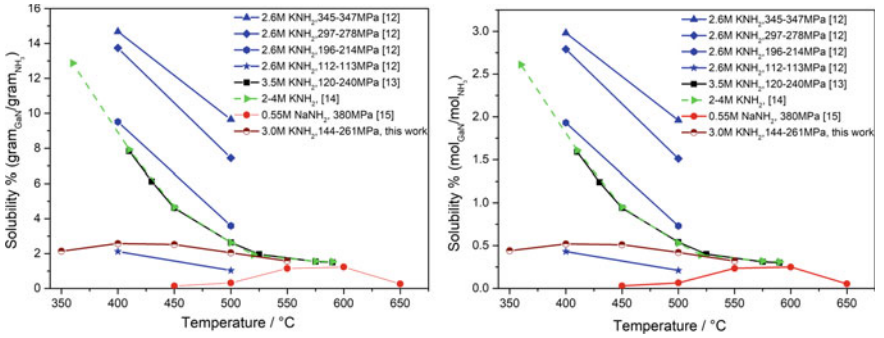

Fig. 9.8 Comparison of the results of this work with those from literature

9.4 Kinetic Investigation of the Solubility of GaN

The solubility experiments considered so far were all set at duration of 120 h, since it was assumed that the solution equilibrium had in any case adjusted after this time. However, in order to verify this fact once again and to investigate the temporal course of the solubility more closely, a further series of experiments was carried out.

Under otherwise constant conditions (T = 400 °C, filling degree = 55%, 3 M KNH_2) the duration was varied. The aim of the series is to check when the solution equilibrium is reached in the autoclave. For this purpose, the isothermal phase in the autoclave was extended until the dissolved amount of GaN no longer changed.

In Fig. 9.9 an exponentially increase in solubility over the time can be seen, whereby the dissolved amount seems to be almost constant from 144 h. Compared to the dissolved GaN quantity at 120 h (0.85 g), increase the solubility by a good 15% to 0.98 g after a time of 192 h. A state of equilibrium cannot therefore be assumed for a duration of 5 days. Wang et al. report test durations of one week or more. The

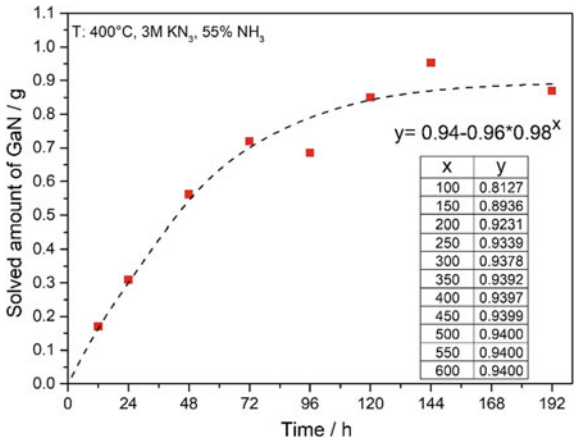

Fig. 9.9 The solubility of GaN over time at 400 °C by the use of 3 M KNH_2 as mineralizer with an ammonia filling degree of 55%

dissolved 0.98 g GaN correspond to a relative quantity of 0.0296 $gGaN/gNH_3$, which is still not nearly as high as the 0.08 achieved by Wang et al. [13].

If extremely long durations are inserted into the equation of the fit curve (equation in Fig. 9.9) in order to simulate a true equilibrium state, the values shown in Table in Fig. 9.9 are obtained. An equilibrium state of solubility with 0.94 g dissolved GaN is only reached after 450 h. In comparison to the 0.85 g dissolved after 120 h, the dissolved quantity can be increased again by approx. 10.5% with enough time. It must therefore be taken into consideration for the later application whether the additional GaN the additional expenditure on heating power and equipment wear is worth this.

9.5 Summary

In this work the solubility of GaN in the ammonobasic MNH_2–GaN–NH_3 system (M = Na or K) in the temperature range of 350–600 °C was investigated. Starting from 350 °C, the temperature was increased in 50 °C steps for each experiment. The degree of ammonia filling was 50 and 55% for $NaNH_2$ and KNH_2, respectively.

The development of solubility with temperature increase seems to be different for both mineralizers. In the case of $NaNH_2$ as a mineralizer, a normal solubility of GaN was considered. The solubility of GaN increases with increasing temperature. Here the solubility maximum of 0.134 g GaN was reached for 600 °C using 1 M $NaNH_2$ as mineralizer and a 50% NH_3 filling degree.

With the solubilities where KNH_2 was used as mineralizer, a retrograde solubility behavior of GaN in the temperature range of 400–550 °C was determined. In the range of 350–400 °C the solubility showed a positive temperature dependence. The maximum solubility was reached at 400 °C. The solubility of GaN at 400 °C was three times higher compared to 550 °C.

In contrast to literature, the retrograde dependence is not exponential, rather linear in the temperature range from 400 to 550 °C. In addition, the high solubility values documented in the literature could not be achieved in the course of the work (see Fig. 9.8).

Furthermore, the dependence of the dissolved amount of GaN on the mineralizer concentration was observed. The dissolved amount of GaN increases with the mineralizer concentration. The negative slope of the retrograde solubility is the same at different KNH_2 concentrations. Unlike $NaNH_2$, the solubility of GaN shows a dependence on the KNH_2 concentration used. The solubility of GaN at 2 M KNH_2 is slightly more than twice that of 1 M KNH_2 concentration. Increasing the mineralizer concentration to 3 M leads to a lower increase of GaN solubility. This non-linear relationship could be because the saturation concentration of KNH_2 in supercritical ammonia has been achieved here.

In comparison to the mineralizer $NaNH_2$, a significant increase of the dissolved amount of GaN could be achieved in the temperature range considered. For KNH_2,

the maximum solubility of GaN at 400 °C with 0.438 g dissolved GaN was reached in the present study.

For the growth experiments, KNH_2 is better suited as mineralizer compared to $NaNH_2$. It combines the milder process temperatures and thus lower pressures with higher solubilities of GaN in sc-NH_3. This allows more solid crystals to be produced and milder process conditions result in additional energy, cost and material savings.

9.6 Conclusion

The aim of this study was to generate the temperature-dependent solubility data of GaN in supercritical ammonia by using the basic mineralizers $NaNH_2$ and KNH_2 in order to determine the optimal process conditions for the growth of GaN single crystals.

The solubility values obtained in this work can only be compared to those obtained from literature to a limited extent, since not all process parameters are clearly stated in the literature. Above all, the literature does not specify the amount of ammonia for each of the solubility data. With the developed ultrasonic method, we were able to adjust the filling level exactly. The use of the three-zone oven enabled an isothermal temperature distribution in the autoclave. The pressure values were recorded in the course of the experiment and so the tightness of the autoclave could be checked. Nevertheless, a comparison of our results with those from the literature should be done here.

The temperature dependence of the solubility shows similar results in both mineralizers as in the literature. As expected, a retrograde solubility of the mineralizer KNH_2 was observed here as well. The solubilities are only compatible with those of the literature at temperatures around 550 °C. At the lower temperatures, there are large differences.

We found a maximum solubility at 400 °C for all KNH_2 concentrations in this work, which was not reported in the literature.

In the case of $NaNH_2$ as mineralizer, a normal course of solubility was observed. The solubility of the GaN was not dependent on the concentration of the mineralizer. Thus, it was indirectly confirmed that $NaNH_2$ dissolves very poorly in supercritical ammonia and contributes to the dissolution of GaN. Here, as in the literature, very small solubilities were obtained.

References

1. D. Ehrentraut, T. Fukuda, Ammonothermal crystal growth of gallium nitride—a brief discussion of critical issues. J. Cryst. Growth **312**, 2514–2518 (2010)
2. V. Avrutin, D.J. Silversmith, Y. Mori, F. Kawamura, Y. Kitaoka, H. Morkoc, Growth of bulk GaN and AlN: progress and challenges. Proc. IEEE **98**, 1302–1315 (2010)

3. S. Pendurti, Q.S. Chen, V. Prasad, Modeling ammonothermal growth of GaN single crystals: the role of transport. J. Cryst. Growth **296**, 150–158 (2006)
4. D. Ehrentraut, E. Meissner, M. Bockowski, Technology of Gallium Nitride Crystal Growth (Springer, Berlin, Heidelberg, 2010), p. 140f
5. T.M.M. Richter, R. Niewa, Chemistry of ammonothermal synthesis. Inorganics **2**, 29–78 (2014)
6. D. Ehrentraut, Y. Kagamitani, A. Yoshikawa, N. Hoshino, H. Itoh, S. Kawabata, K. Fujii, T. Yao, T. Fukuda, Ammonothermal synthesis of thick gallium nitride film employing acidic mineralizers. J. Mater. Sci. **43**, 2270–2275 (2008)
7. D. Ehrentraut, T. Fukuda, Acidic ammonothermal growth of bulk GaN crystals. Acta Crystallogr. A **64**, C19–C20 (2008)
8. D. Ehrentraut, T. Fukuda, The ammonothermal crystal growth of gallium nitride—a technique on the up rise. In: Proceedings of the IEEE (2010), p. 1319
9. D. Gogova, P.P. Petrov, M. Buegler, R. Wagner, C. Nenstiel, G. Callsen, M. Schmidbauer, R. Kucharski, M. Zajac, R. Dwilinski, M.R. Phillips, A. Hoffmann, R. Fornari, J. Appl. Phys. **113**, 203513 (2013)
10. T. Sochacki, M. Amiluski, B. Lucnik, M. Boćkowski, J. L. Weyher, G. Nowak, B. Sadovyi, G. Kamler, I. Grzegory, R. Kucharski, M. Zajac, R. Doradzinski, R. Dwilinski, HVPE-GaN growth on ammonothermal GaN crystals, in Proceedings of SPIE, Gallium Nitride Materials and Devices VIII, vol. 86250B (2013)
11. R. Dwiliński, R. Doradziński, J. Garczyński, L. Sierzputowski, R. Kucharski, M. Zając, M. Rudziński, R. Kudrawiec, W. Strupiński, J. Misiewicz, Ammonothermal GaN substrates: growth accomplishments and applications. Phys. Status Solidi A **208**, 1489–1493 (2011)
12. R. Dwiliński, R. Doradziński, J. Garczyński, L.P. Sierzputowski, A. Puchalski, Y. Kanbara, K. Yagi, H. Minakuchi, H. Hayashi, Excellent crystallinity of truly bulk ammonothermal GaN. J. Cryst. Growth **310**, 3911–3916 (2008)
13. B. Wang, M.J. Callahan, K.D. Rakes, L.O. Bouthillette, S.-Q. Wang, D.F. Bliss, J.W. Kolis, Ammonothermal growth of GaN crystals in alkaline solutions. J. Cryst. Growth **287**, 376–380 (2006)
14. M. Callahan, B.-G. Wang, K. Rakes, D. Bliss, L. Bouthillette, M. Suscavage, S.-Q. Wang, GaN single crystals grown on HVPE seeds in alkaline supercritical ammonia. J. Mater. Sci. **41**, 1399–1407 (2006)
15. T. Hashimoto, M. Saito, K. Fujito, F. Wu, J.S. Speck, S. Nakamura, Seeded growth of GaN by the basic ammonothermal method. J. Cryst. Growth **305**, 311–316 (2007)
16. H. Hunt, L. Boncyk, Liquid ammonia as a solvent. III. The solubility of inorganic salts at 25°. J. Amer. Chem. Soc. **55**, 3528–3530 (1933)
17. P.W. Schenk, H. Tulhoff, Das System Kaliumamid/Ammoniak. Angew. Chem. **74**, 943 (1962)

Chapter 10
In Situ Visualization of the Ammonothermal Crystallization Process by X-ray Technology

Saskia Schimmel and Peter Wellmann

Abstract X-ray based in situ monitoring techniques for ammonothermal processes are reviewed. Technological aspects are discussed, including general aspects of in situ X-ray visualization technology as well as the corrosion resistance of prospective materials for X-ray transparent windows under ammonothermal conditions (for more comprehensive information on corrosion resistance see Chap. 11). In situ X-ray visualization methods have proven to be extremely useful for gaining insights that are inaccessible through other methods to date. Results obtained by in situ X-ray imaging comprise information on solubility and dissolution kinetics as well as insights into the transport of solutes and local concentration changes of solutes. Moreover, phase changes of the fluid can be monitored and the technique has been adapted for solubility studies of novel materials that are unavailable as bulk materials to date. Findings of particular interest include a revision of solubility data for GaN, insights into face-selective and mineralizer-selective dissolution kinetics of GaN, and the visualization of Ga transport within the fluid upon dissolution of GaN. The observed extremely slow motion of Ga-containing species suggests a pronounced influence of solutes on the viscosity of the fluid, which has largely been treated as negligible due to the lack of data for the respective mixtures so far.

S. Schimmel · P. Wellmann (✉)
Institute Materials for Electronics and Energy Technology (I-MEET), Friedrich-Alexander-University Erlangen-Nuremberg (FAU), Martensstrasse 7, 91058 Erlangen, Germany
e-mail: peter.wellmann@fau.de

S. Schimmel
e-mail: sas.schimmel@imass.nagoya-u.ac.jp

S. Schimmel
Institute of Materials and Systems for Sustainability (IMaSS), Nagoya University, Nagoya 464-8601, Japan

E. Meissner and R. Niewa (eds.), *Ammonothermal Synthesis and Crystal Growth of Nitrides*, Springer Series in Materials Science 304,
https://doi.org/10.1007/978-3-030-56305-9_10

10.1 General Aspects of X-ray Based In Situ Monitoring Technologies

Two types of X-ray based methods for in situ investigation of the chemical and physical processes occurring during ammonothermal syntheses are addressed in this book. These comprise in situ monitoring techniques that utilize projection images and techniques that are based on recording diffraction signals. The former will be discussed in detail in this chapter, including a broad range of results obtained so far. With respect to the latter, only some fundamental aspects will briefly be mentioned within this chapter. Being a recent technical development, the technology for in situ X-ray diffraction measurements will be discussed primarily in Chap. 17.

A general aspect that needs to be considered for virtually all X-ray based in situ monitoring methods is the transmittance of the autoclave material for both the incident beam and the measurement signal exiting the autoclave. According to the well-known *Lambert-Beer* law, the initial intensity I_0 is attenuated upon radiographing an absorbing object, resulting in a remaining intensity I behind this object [1, 2]:

$$I = I_0 \cdot \exp\left(-\frac{\mu}{\rho}\left(\text{element}, E_{\text{photon}}\right) \cdot \rho \cdot d\right)$$

According to *Lambert-Beer* law, the remaining intensity I depends on the following properties of the radiographed object: its mass attenuation coefficient μ/ρ, its density ρ and its thickness d. The mass attenuation coefficient itself varies with the elemental composition of the radiographed material and with the energy of the X-ray photons E_{photon} [2, 3]. The product of the mass attenuation coefficient μ/ρ and the density ρ is often referred to as attenuation coefficient μ [1, 2], consequently, it can also be related to the concentration c and the molar mass M if the absorbing object is a solution:

$$\mu = \frac{\mu}{\rho}\left(\text{element}, E_{\text{photon}}\right) \cdot \rho = \frac{\mu}{\rho}\left(\text{element}, E_{\text{photon}}\right) \cdot c \cdot M$$

Besides its importance to the transmittance of autoclave materials, the absorption coefficient and its dependence on energy and atomic number is also relevant to the contrast of X-ray projection images. The Michelson contrast C_m is determined by the initial intensity I_0 and the transmitted intensity I as follows [4, 5]:

$$C_m = \frac{I_0 - I}{I_0 + I}$$

Depending on the X-ray energy range, different mechanisms of attenuation dominate the mass attenuation coefficient [2]. Its dependence on the atomic number originates from the contribution of the photoeffect to the overall attenuation coefficient $\mu \sim \rho \cdot Z^3 \cdot E^{-1}$ [6]. The photoeffect dominates the overall absorption at lower

energies [6]. Accordingly, lower X-ray energies (up to about 60 keV [2]) are advantageous for distinguishing different materials in the X-ray images. A direct consequence is that the contrast between a nitride material sample and the surrounding supercritical fluid benefits from the use of low to intermediate X-ray energies. However, there is a trade-off between the contrast and the transmitted intensity, which is relevant to the signal-to-noise ratio as well as to exposure times. The reason is that if lower energy X-rays are used, a larger fraction of the initial intensity I_0 is absorbed, resulting in a loss of overall intensity. Due to these aspects, the autoclave material which needs to be radiographed plays a decisive role for selecting an appropriate energy range for a particular application. At intermediate to high energies (from ~60 keV up to several hundred keV), the attenuation coefficient μ is increasingly dominated by the Compton effect whereas the photoeffect plays a diminishing role [2, 6]. The contribution of both the photoeffect and the Compton effect to the attenuation coefficient μ are proportional to the density ρ [6], consequently, higher X-ray energies are favorable for distinguishing density or concentration changes if they are not associated with a change in elemental composition.

An overview of relevant mass attenuation coefficients as well as exemplary X-ray spectra is given in Fig. 10.1. To represent metallic autoclave walls, nickel (Ni), chromium (Cr) and iron (Fe) are included, since they are the main components

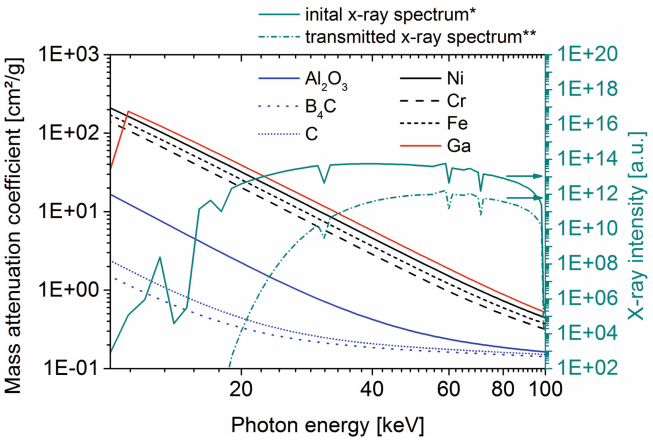

Fig. 10.1 Mass attenuation coefficients relevant to in situ X-ray monitoring of ammonothermal experiments and exemplary X-ray spectra representing typical, application-relevant cases. The materials comprise the main alloy components of Inconel 718 (Ni, Cr, Fe), Ga as a solute of interest and as the main absorbing constituent of GaN, and compounds with existing or potential application as autoclave window materials (Al_2O_3, B_4C and C). The X-ray spectra represent the simulated initial intensity using a tungsten anode X-ray source with 2.5 mm Al-equivalent filter and accounting for 500 mm radiographed path in air (*), and the resulting spectrum after additionally passing through 20 mm of Al_2O_3 (**). Note that the absorption of the sapphire windows is most pronounced in the low energy range, resulting in a modification in the shape of the spectrum (known as beam hardening). The data of the graph are based on [11] for mass attenuation coefficients and [12, 13] for the initial intensity distribution of the X-ray spectrum

of the nickel base alloy Inconel 718 which is frequently used as a material for ammonothermal autoclaves. It is evident from Fig. 10.1 that the mass attenuation coefficient of these elements is large compared to sapphire (Al_2O_3), boron carbide (B_4C) and carbon (C), which are given because of their existing or potential application for X-ray transparent autoclave windows. The mass attenuation coefficient of gallium nitride (GaN) is also shown. The fact that it even exceeds the absorption of the main alloy components indicates that Ga-containing materials are very well suited for studying ammonothermal reactions by means of in situ X-ray imaging. It is evident from comparing the mass attenuation coefficients of the metals to that of sapphire that sapphire windows already represent a huge improvement in comparison to the metal autoclave walls. However, it is also evident from Fig. 10.1 that materials composed of even lighter elements, such as B_4C and C, are very promising for further improvements of X-ray transparency, in particular in the lower energy range. To illustrate the transmittance of a pair of sapphire windows for a typical application case, Fig. 10.1 shows also a simulated X-ray spectrum of an X-ray source with tungsten (W) anode, which corresponds to the actual X-ray source that is used for ammonothermal in situ X-ray imaging [1, 7, 8]. Note that due to the dependence of the mass attenuation on photon energy, the attenuation caused by the sapphire windows is more pronounced for lower energies, resulting in a modification of the X-ray spectrum known as beam hardening.

Due to the high attenuation coefficient of the construction materials that pressure vessels are typically made of (e.g. the nickel base alloy Inconel 718, and generally most metals), in situ monitoring even by X-ray methods is only feasible if very high energies far above 100 keV are used. This has been demonstrated using a computed tomography (CT) setup operated at an acceleration voltage of 320 kV (note that this experiment greatly benefited from the large number of about 1000 single images for one reconstruction dataset, alongside with data acquisition in three dimensions) [4]. A major advantage of the use of such high energies is that it permits in situ monitoring of the entire inner volume of the autoclave. A drawback lies in the higher initial costs and efforts associated with setting up radiation protection for such high X-ray energies [4]. In addition, the above-mentioned advantage associated with low energies with respect to image contrast cannot be exploited. While the use of a high-energy CT setup is believed to make very interesting complementary results accessible, the development of ammonothermal autoclaves equipped with windows [9] made of much lighter elements compared to the autoclave alloys was of great importance for establishing in situ X-ray monitoring techniques. This has led to a variety of results obtained by 2D X-ray imaging using an optical cell equipped with sapphire or boron carbide windows [1, 7, 8, 10], which will be described and discussed in the subsequent sections of this chapter.

For in situ X-ray diffraction measurements, an additional constraint lies in the angular resolution, which generally decreases with increasing energy because the diffraction angles depend on the wavelength used. For this reason, autoclave windows with improved X-ray transmittance are of particular relevance for some in situ diffraction applications. Another aspect to consider is which and how many reflections need

to be accessible for the desired application. This is due to geometrical and mechanical limitations in the number, size and proximity of optical cell windows that can be integrated into one autoclave body [14].

The requirements for practical usage of autoclave windows are very challenging. The window material must resist the process conditions of ammonothermal syntheses such as high pressure and high temperature. In addition, supercritical ammonia combined with acidic or basic mineralizers represents a very corrosive environment for most construction materials (see Chap. 11). In this context, corrosion is not only an issue with respect to a potential influence on the measurement result through changes in the chemical composition of the fluid but also with respect to mechanical failure. The latter is particularly relevant if the corrosive attack leads to the formation of cracks, as pressurized components are naturally prone to stress-corrosion-cracking. While chemical stability and mechanical properties are essential for all construction materials for pressurized components, prospective materials for X-ray windows must have as low X-ray absorption as possible or at least tolerable for the specific application.

10.2 X-ray Transparent Materials for Autoclave Windows

Sapphire was the first material to be established as an autoclave window, initially for optical spectroscopy applications [9]. While sapphire provides good X-ray transparency for X-rays provided that the X-ray energy is sufficiently high, it is not necessarily the optimum material for all ammonothermal in situ X-ray monitoring techniques. X-ray applications do not require optical transparency, which broadens the range of potentially applicable materials. Therefore, it is reasonable to search for alternative materials if the use of low to intermediate X-ray energies is desired or if the application of choice requires a particularly good signal to noise ratio. As an early step when considering alternative materials, it is reasonable to estimate their transmittance for the actual application based on their mass attenuation coefficient, their density and the required thickness, which in turn depends on the mechanical properties of the material and on the desired maximum operating pressure. The result of such a calculation is shown in Fig. 10.2 for a number of materials that are potentially applicable as the bulk material of ammonothermal autoclave windows. As it can be seen from the graph in Fig. 10.2, the use of the carbon-based materials allows to maintain the transmittance of the established combination of sapphire windows with a tungsten anode while moving to much lower photon energies. Alternatively, the transmittance can be greatly improved if the photon energy is kept constant.

Based on the above considerations, a number of carbon modifications and carbon compounds have been investigated [15]. Boron carbide and vitreous carbon are particularly promising carbon-based materials for low photon energy applications, at least in terms of X-ray absorption. The same holds for diamond in terms of the material properties, however, the extremely limited availability of thick bulk diamond renders the application as bulk window material virtually impossible to date [15].

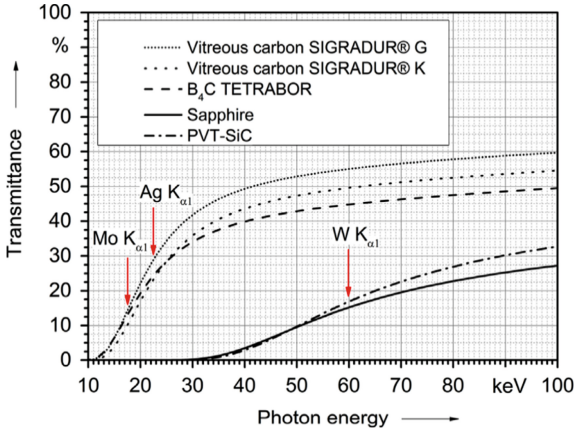

Fig. 10.2 Calculated transmission of window materials in an optical cell designed for ammonothermal experiments up to 300 MPa. The energies of the characteristic radiation of selected anode materials (molybdenum, silver and tungsten), which are particularly relevant to diffraction applications with monochromatic radiation, are also indicated. (Reproduced from [15])

However, its application as bulk window material may be feasible for specific applications if the maximum operating pressure is sufficiently low or if a reduced area of view is tolerable for the specific application. Furthermore, it may be possible to use diamond as a liner material in the window area by integrating it into the setup in the same way as it is described for other ceramic materials in [16]. While the lack of thick bulk material certainly narrows the application space for diamond as an ammonothermal X-ray window, its unrivalled chemical stability is unmeasurably advantageous given the fact that many other materials suffer from noticeable to catastrophic corrosive attack if exposed to ammonothermal reaction media.

10.3 Chemical and Mechanical Stability of Potential Window Materials for X-ray Applications

The chemical stability of potential bulk window materials for in situ X-ray monitoring applications was investigated, including the use of ammonobasic and ammonoacidic mineralizers [15]. Screening experiments were performed using a windowless Inconel 718 autoclave in which the samples were exposed to the respective reaction medium [15]. About 4.5 mmol mineralizer were used for both ammonobasic and ammonoacidic experiments [15]. An overview of the chemical stability of diamond, the two investigated variants of vitreous carbon (Sigradur G and Sigradur K), boron carbide and silicon carbide is found in Table 10.1.

Under ammonobasic conditions established by using NaN_3 mineralizer, boron carbide is an ideal material for X-ray window applications [15] which has been successfully applied in practice [14], however, it should be noted that this does not hold for KN_3 mineralizer [14]. This example clearly demonstrates that the chemical stability of materials under ammonothermal conditions is enormously mineralizer-specific [14]. Under ammonoacidic conditions, samples of B_4C tend to develop signs

Table 10.1 Overview of the chemical stability of potential X-ray window materials in presence of different mineralizers under ammonothermal process conditions. (Reproduced from [15])

	Diamond	Vitreous carbon (Sigradur G)	Vitreous carbon (Sigradur K)	Boron carbide	Silicon carbide
NH_4F	✓	o	o	x	o
NH_4Cl	✓	o	o	x	o
NaN_3	✓	o	x	✓	o

The symbols denote good to excellent chemical stability (✓), intermediate chemical stability (o) and insufficient chemical stability for most applications (x), respectively

of corrosive attack, especially at lower pressures [15]. In presence of ammonium fluoride, the chemical stability of boron carbide is better than in presence of ammonium chloride. In the standard screening experiments conducted without mechanical load on the sample, the corrosion damage often only became obvious through the analysis of cross-section samples [15]. However, the damage was found to be much more pronounced if the sample was simultaneously exposed to application-typical mechanical stress [15]. This was observed in test experiments with NH_4F that were conducted using an optical cell in which the sample material was applied as the window material [15]. In this case, a corrosion layer was found, consisting of B, C, O, F and traces of Si, Ca, Fe [15].

The two tested vitreous carbon variants show similar properties in terms of chemical stability [15]. However, the corrosion resistance of Sigradur G is generally better than that of Sigradur K [15]. In presence of sodium azide, both vitreous carbon variants were severely damaged by cracks penetrating the bulk of the material [15]. In addition, mass changes of the samples were observed, which are ascribed to dissolution and corrosion processes and the diffusion of foreign (heavier) elements (e.g. N, O) into the material [15]. Ammonoacidic conditions created by adding ammonium fluoride led to similar observations as the ammonobasic experiments with NaN_3 mineralizer, however, the corrosive attack was not as pronounced, and the cracks were only present at the surface and did not reach into the bulk of the material [15]. Sigradur G seems to be considerably more stable than Sigradur K and might be applicable in combination with ammonium fluoride [15], however, this has not yet been verified through test experiments with the material employed as an optical cell window under operating conditions.

Silicon carbide generally showed a rather good chemical stability [15], which is in accordance with an extensive study on the chemical stability of construction materials by Pimputkar et al. [17]. Under ammonobasic conditions, silicon carbide presented an excellent stability [15]. Using ammonium chloride as mineralizer, no loss of mass was detectable but signs of minor corrosive attack were observed [15]. In presence of ammonium fluoride, p-type silicon carbide was stable [15]. Deviating from that, the surface of n-type silicon carbide changed slightly during the experiment, also the mass of the sample decreased slightly [15].

Diamond did not show any detectable corrosive attack regardless of the mineralizer used, making it an ideal material for autoclave window applications in terms of chemical stability [15].

10.4 X-ray Imaging Technology for Ammonothermal Reactors

For in situ X-ray imaging, optical cells as originally developed for optical measurement techniques are used. For details of the optical cell construction, the reader is referred to Chap. 4. In the present chapter, however, specific details related to in situ X-ray imaging technology will be given.

Besides the optical cell, an X-ray tube with tungsten anode (Poskom PXP-20HF PLUS) and a CCD detector equipped with a scintillator (Dürr DR6.2) are main components of the setup [7]. A photograph of this setup is depicted in Fig. 10.3.

The optical cell itself is shown in greater detail in Fig. 10.4a. As it becomes obvious from the cross-section image, the area of view is smaller than the inner diameter of the autoclave. Therefore, an additional piece of equipment is needed to mount the nitride sample in the area of view, since it is usually very desirable to monitor the entire sample. This piece of equipment will be referred to as sample mount. Photographs of different variants of sample mounts are shown in Fig. 10.4b–d, whereas its location within the optical cell can be seen from Fig. 10.4a. The first two variants differ by coating, i.e. the variant in Fig. 10.4b is made of uncoated Inconel 718 and the variant in Fig. 10.4c is made of Inconel 718 coated with gold. By using uncoated Inconel 718 for ammonobasic experiments and gold-coated Inconel 718 for ammonoacidic experiments, the chemical stability in the respective environment is optimized [14]. The last variant of the sample mount, which is depicted in Fig. 10.4d, was tested aiming at improving the X-ray contrast between nitride crystal and sample mount

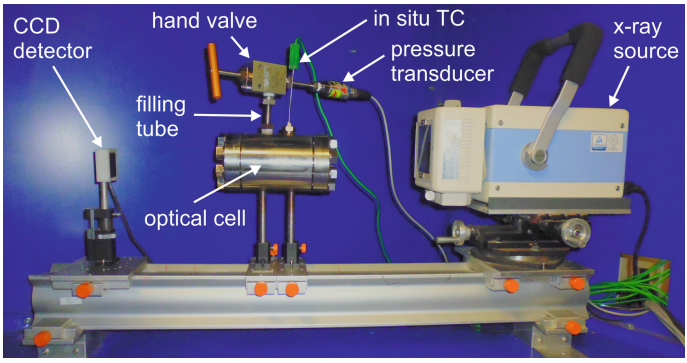

Fig. 10.3 Experimental setup for 2D in situ X-ray monitoring using an optical cell. (Reproduced from [14])

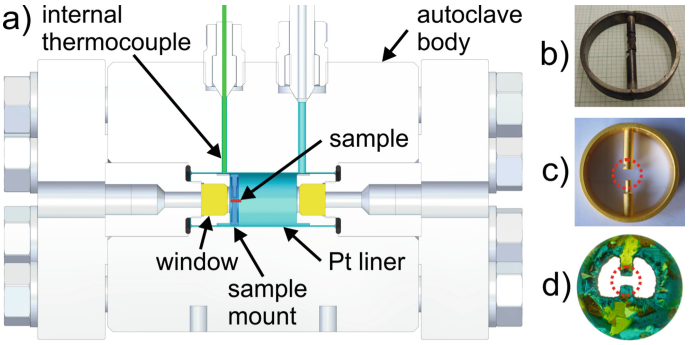

Fig. 10.4 Compact optical cell equipped with X-ray transparent windows. **a** Fully equipped autoclave body (in case of ammonobasic experiments, a liner-free optical cell is used) and variants of the sample mount, **b** Inconel 718 without coating (ammonobasic experiments), **c** Inconel 718 with gold coating (ammonoacidic experiments) and **d** polycrystalline SiC grown by physical vapor transport. In **c** and **d**, the area of view is indicated by a dotted circle in red color. (Adapted from [14])

(see Fig. 10.5 for an illustration of this aspect). Based on earlier investigations that suggest that ceramic silicon carbide is preferentially attacked at the grain boundaries of the sintered material [16], this sample mount was manufactured without the use of sintering additives. For this purpose, polycrystalline silicon carbide was grown directly into a negative form made of graphite by physical vapor transport (PVT) in analogy to [18]. As it is evident from Fig. 10.5 (compare a, b), the contrast between GaN samples and the sample mount could be tremendously improved compared to Inconel 718 sample mounts [14]. However, experiments with NH_4F mineralizer indicated that slight etching and a transport of silicon occurred, posing the question as to what extent corrosion products from the mount would affect the measurement results. For this reason, the experiments on GaN dissolution and crystallization

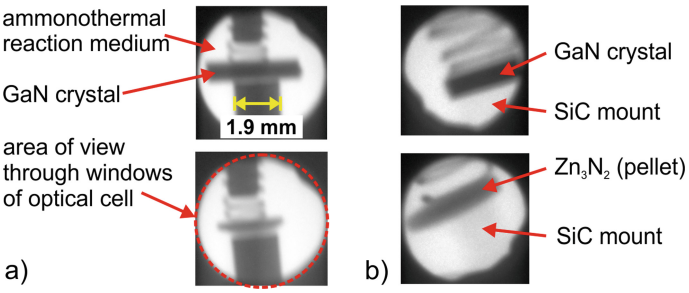

Fig. 10.5 Projection X-ray images obtained in situ during ammonothermal dissolution experiments using an optical cell and NH_4F mineralizer. **a** Dissolution of GaN with the GaN sample held in place by a gold-coated metal sample mount, **b** dissolution of a Zn_3N_2 pellet with a sample mount made from polycrystalline silicon carbide. Note the excellent contrast between sample and sample mount in the latter case. (Reproduced in modified form based on [14])

were continued using Inconel 718 based sample mounts. For investigations on Si-containing nitride compounds, however, contamination from the slight corrosion of the SiC sample mount should not have a noticeable effect on the chemical reactions investigated. Consequently, the novel type of sample mount is promising for experiments with Si-containing compounds.

Examples of in situ X-ray images obtained with optical cells as shown in Fig. 10.4 are shown in Fig. 10.5. The depicted examples comprise an experiment with GaN as sample material and metal sample mount (Fig. 10.5a) as well as an experiment with a Zn_3N_2 pellet sample and a sample mount made from PVT-SiC.

Regarding the lateral resolution, it is important to distinguish between the determination of absolute positions and the determination of changes such as the movement of phase boundaries. This is illustrated by data obtained from an experiment with minimal but measurable dissolution of GaN, which are shown in Fig. 10.6. Although the solid-fluid phase boundary occupies a relatively broad strip of about 500 µm due to the limited sharpness of the X-ray image (which is related to the divergence of the beam), displacements of the phase boundary as small as 15 µm can be detected [14]. This example also illustrates the use of profile lines for image evaluation (i.e. extracting a line of grayscale values from the image matrix). Besides

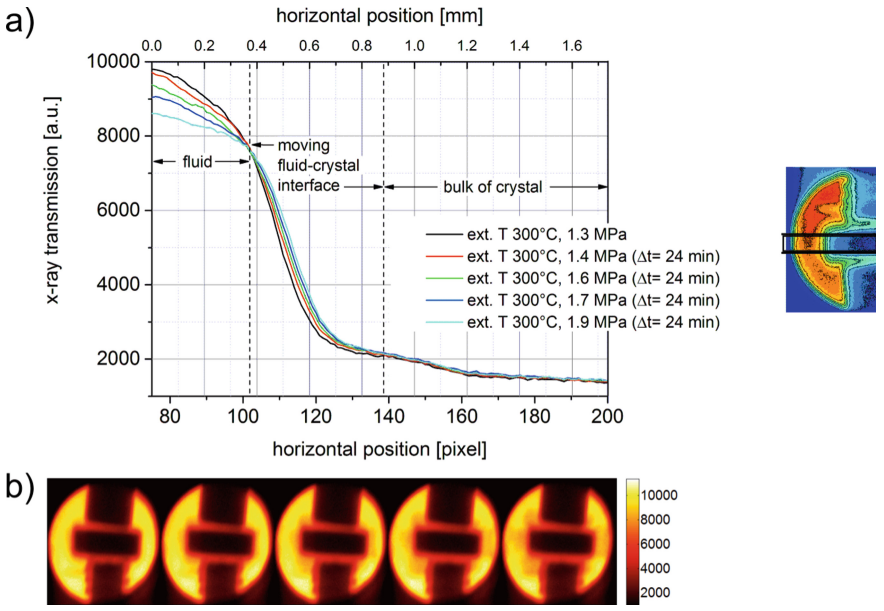

Fig. 10.6 Evaluation of phase boundary movement upon dissolution of GaN with NH_4F mineralizer utilizing averaging of the profile lines running through the section indicated in the color map figure in **a**. A set of original images is depicted in **b**. Note also that there are areas of increased X-ray absorption emerging from the crystal surface and drifting away from it, an observation that will be discussed in 10.5 information accessible through in situ X-ray imaging in subsection insights into the transport of Ga-containing species. (Reproduced from [1])

making changes more easily visible, the use of profile lines also allows to improve the signal to noise ratio if the respective case of application does not prevent averaging of a number of neighboring profile lines.

Besides analyzing the movement of objects and their edges, it is also feasible to extract additional information from quantitative analysis of the grayscale values and their change during the experiment. It is important to keep in mind that the change in grayscale values reflects all changes in X-ray absorption occurring along the path of rays (i.e. both the sample and the fluid behind and in front of it). Nevertheless, quantitative analysis of grayscale value changes is a viable tool to extract valuable additional information that is otherwise not quantitatively accessible. Due to the pronounced energy dependence of the mass attenuation coefficient, knowing the mean effective photon energy (or the wavelength distribution, i.e. the precise X-ray spectrum) is very important for quantitative evaluation of absorption changes. For this reason, the mean effective photon energy as well as the repeatability of the initial intensity were verified based on a model experiment that was conducted with pure nitrogen as a absorbing material of variable density [1]. While the experimental details can be found in greater detail in [1, 14], the most relevant results will be summarized here. Using two sapphire windows with a thickness of 10 mm each, the mean effective photon energy was experimentally determined to be 51.1 ± 2.1 keV [1]. The detection limit for Ga is estimated to be 0.13 mmol/ml [1]. This concentration corresponds to an attenuation coefficient μ of 0.116 ± 0.040 cm^{-1} [1]. Based on the known mean effective photon energy, the determined detection limit expressed as an attenuation coefficient and mass attenuation coefficients from NIST database [11], the detection limit for other materials of interest can be estimated [1].

10.5 Information Accessible Through In Situ X-ray Imaging

Based on monitoring the contours of the nitride sample crystal, a variety of related chemical-physical processes can be investigated by in situ X-ray imaging. One of the parameters of great interest for crystal growth is the solubility of the nitride as well as dissolution kinetics. In addition, the technique has also proven to yield intriguing insights into chemo-physical processes occurring in the fluid phase.

10.5.1 Solubility and Dissolution Kinetics

For determining the solubility through experimental observation of the saturation of the solution, it is necessary to first derive the changes of the crystal volume from the X-ray images. As the in situ X-ray images are 2D projection images, the third dimension needs to be accessed either through evaluating the changes in the

X-ray absorption or through feeding in additional information obtained in separate experiments as it will be described in the following. The latter is based on conducting separate experiments in which the crystal is mounted in different crystallographic orientations with respect to the path of rays to investigate face-specific dissolution kinetics. Knowledge on face-specific dissolution rates is essential for a well-grounded estimation of the third dimension of the crystal, which in turn is relevant to the determination of the remaining crystal volume. Exemplary data on face-specific dissolution kinetics for the dissolution of GaN using NaN_3 are shown in Figs. 10.7 and 10.8.

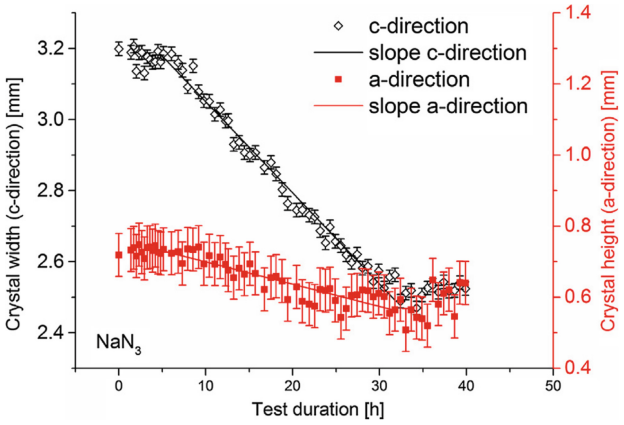

Fig. 10.7 Dissolution kinetics of the polar c-direction and the nonpolar a-direction of a GaN crystal upon ammonothermal dissolution using NaN_3 mineralizer. (Reproduced from [8])

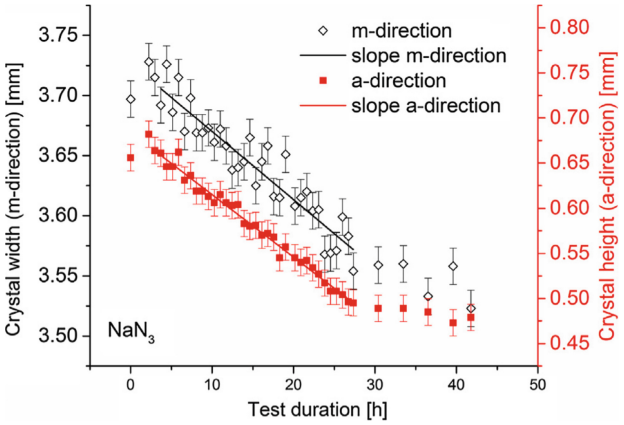

Fig. 10.8 Dissolution kinetics of the nonpolar m- and a-directions of a GaN crystal upon ammonothermal dissolution using NaN_3 mineralizer. (Reproduced from [8])

As it can be seen from the graphs in Figs. 10.7 and 10.8, the dissolution kinetics differ considerably between nonpolar and polar directions but are virtually identical for the two nonpolar directions [8]. Similar results have been obtained for the dissolution of GaN using NH_4F mineralizer [7]. Based on the virtually identical dissolution kinetics of the two nonpolar faces, the volume of the crystal can be estimated based on evaluating the two directly accessible dimensions in the projection image if the image contains contours in c-direction and one of the nonpolar directions [7, 8].

Examples for resulting plots of the remaining crystal volume over time are depicted in Fig. 10.9 for NaN_3 mineralizer and in Fig. 10.10 for NH_4F mineralizer, respectively. The graphs generally exhibit three subsequent phases of the experiment: temperature ramp-up (I) resulting in a proportionate increase in pressure as determined primarily by the fill level, a phase of constant temperature (II) and cool-down (III). The dissolution of the GaN crystal typically sets in during phase I, at pressure and temperature conditions depending on the mineralizer used [8]. Under ammonoacidic conditions, crystal dissolution was found to set in much more rapidly than under the investigated ammonobasic conditions [8]. It is not yet clear to what extent the observed sluggish reaction kinetics in case of the ammonobasic mineralizer NaN_3 originate from the kinetics of the conversion of NaN_3 to $NaNH_2$ [8].

Through experimental observation of the remaining crystal volume upon saturation of the solution, the solubility of GaN in ammonoacidic and ammonobasic reaction media has been investigated [7, 8]. The results substantiate that the existing, fragmentary and scattered literature data on GaN solubility in ammonothermal reaction media need to be revisited [7, 8]. Even though there is a lack of data obtained at well-comparable process parameters, the findings suggest the solubility is about an order of magnitude lower than reported in the older literature [7, 8]. This is in accordance with a recent study on GaN solubility in supercritical ammonia with sodium as mineralizer, which was conducted by Griffiths et al. using refined gravimetric

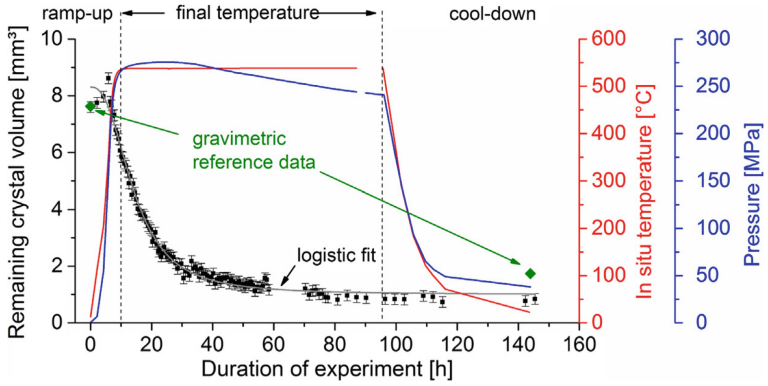

Fig. 10.9 Remaining crystal volume over time as determined from in situ X-ray images recorded during dissolution of GaN using 3 mol% NaN_3 mineralizer (corresponding to a molar concentration of 0.72 mmol/ml). The temperature measured in the fluid in proximity to the inner wall of the autoclave is also shown, as well as the resulting pressure. (Reproduced from [8])

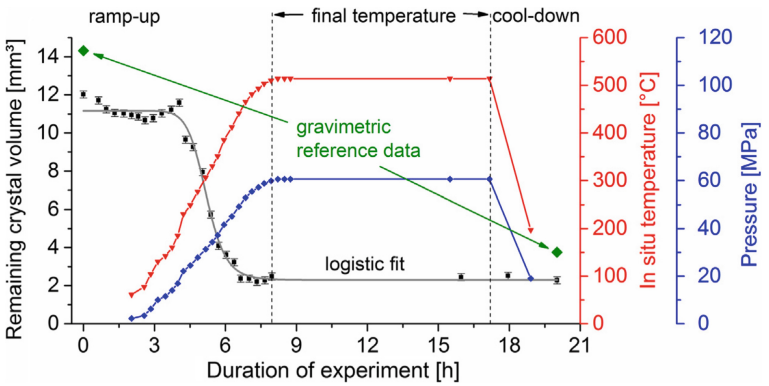

Fig. 10.10 Remaining crystal volume over time as determined from in situ X-ray images recorded during dissolution of GaN using 11 mol% NH_4F mineralizer (corresponding to a molar concentration of 0.76 mmol/ml). The temperature measured in the fluid in proximity to the inner wall of the autoclave is also shown, as well as the resulting pressure. (Reproduced from [8])

methods [19]. There are a couple of reasons that are believed to contribute to the discrepancy within literature data. One aspect is that small unintentionally present temperature gradients may have led to continuous transport and redisposition of GaN in conventional gravimetric experiments (i.e. it might be that not all GaN that was recorded as dissolved was actually in solution simultaneously) [7]. Another aspect is that the autoclave walls act as a Ga sink and source in subsequent experiments, which was first pointed out by Griffiths et al. [19]. Meanwhile, this has been confirmed based on investigations of sample mounts used for ammonobasic optical cell experiments with in situ X-ray imaging [8]. A second source of errors first reported by Griffith et al. is the existence of a Na-rich phase (likely consisting primarily of $NaNH_2$) at the bottom of the autoclave which also can absorb and release Ga [19]. This Na-rich phase may have an even more pronounced impact on the apparent solubility of GaN if the GaN samples are placed at the bottom of the autoclave. If the GaN samples are located at the bottom of the autoclave, this may result in a measurement of the solubility of GaN in a $NaNH_2$ melt, instead of a measurement of GaN solubility in supercritical ammonia with a $NaNH_2$ fraction no larger than its solubility limit in supercritical ammonia. On the contrary, both the study by Griffiths et al. [19] and the optical cell experiments with in situ X-ray monitoring employ standoffs to place the sample crystals away from the bottom of the autoclave. In the case of the in situ X-ray monitoring experiments, it is ascertained that the sample crystal was not immersed in a $NaNH_2$ melt. Firstly, the amount of mineralizer used could not fill up the entire volume below the bottom edge of the area of view. Secondly, the additional absorption of the melt would have been evident from the X-ray images and no respective observations have been made up to now.

10.5.2 Insights into the Transport of Ga-Containing Species

As already suspected based on the relatively high atomic number of gallium in [4], even the contribution of dissolved Ga-containing intermediates to the overall absorption of the fluid is measurable provided that their concentration is sufficiently high [1]. This is most easily demonstrated by dissolution experiments using NH_4F mineralizer since this mineralizer leads to a particularly rapid dissolution of GaN and the temporary buildup of local concentration inhomogeneities [1]. An example of such local inhomogeneities in fluid absorption is shown in Fig. 10.11. One characteristic of these fluid absorption inhomogeneities is their spherical shape with the dissolving crystal in their center (see 3rd subfigure within Fig. 10.11) [1]. Over time, the rings of high X-ray absorption move away from the crystal [1]. Together with the fact that the initial appearance of the inhomogeneities in X-ray absorption coincides with the onset of the dissolution of the GaN crystal, these two characteristics strongly suggest that the locally increased X-ray absorption originates from Ga-containing intermediates [1]. This is further underpinned by the observation that the fluid absorption homogenizes as the dissolution of the crystal slows down, and saturates as the crystal dissolution terminates [1].

In situ X-ray imaging is the first reported technique that is capable of accessing the transport of Ga-containing intermediates within an ammonothermal reaction medium experimentally [1]. Obtaining such experimental insights into mass transport under ammonothermal process conditions is expected to be particularly rewarding. An important aspect is that the properties of the actual fluid mixtures are largely unknown to date. Numerical simulations are usually based on the physical properties of pure ammonia [20–22], however, the addition of mineralizers is suspected to significantly alter fluid properties such as the viscosity [22] (see also Chap. 8). Based on the movement of the schlieren of intermediates observed by in situ X-ray imaging under ammonoacidic conditions employing NH_4F mineralizer, a diffusion coefficient for the Ga-containing species has been determined under the presumption of purely diffusion-based transport [1]. The obtained value of $1.76 \cdot 10^{-6}$ cm^2/s [1] is exceptionally low in comparison to other supercritical fluids as well as in comparison to liquids [23]. Molecular dynamics simulations qualitatively support the observation of a very low mobility of Ga-containing dissolved species and suggest that the

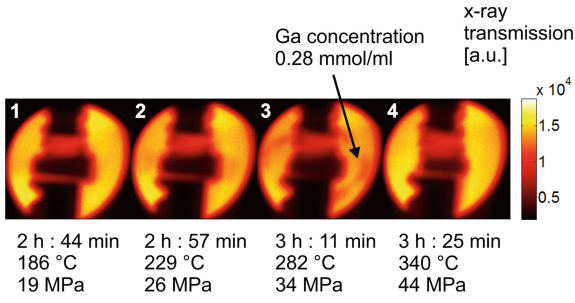

Fig. 10.11 Local changes of the X-ray absorption of the ammonothermal reaction medium surrounding the GaN crystal, as observed using the ammonoacidic mineralizer NH_4F. (Reproduced from [1])

exceptionally low diffusivity is caused, at least in part, by the formation of larger $[Ga_xF_y]^{3x-y}$ aggregates [1]. The simulation indicates that the formation of aggregates in turn originates from the relatively low polarity and density of ammonia under the investigated process conditions (720 K, 26.5 MPa) [1]. In addition, a second contribution to the low diffusivity by an increased viscosity of the fluid mixture containing solutes (as compared to the viscosity of pure ammonia) is likely [1]. This exemplary result demonstrates clearly that in situ X-ray transmission measurements can provide highly relevant insights into the properties of ammonothermal reaction media. Firstly, it indicates the feasibility of experimental insights into the properties of the fluid by in situ X-ray imaging. Secondly, it confirms the necessity to account for the impact of solutes and to determine these properties experimentally. Such properties have been largely inaccessible through experimental methods so far and are of crucial importance for obtaining meaningful results through numerical simulations (e.g. of mass transport within ammonothermal growth reactors).

The above-described observation of Ga-containing intermediates drifting away from the crystal without a distinguishable relation to the field of gravity suggests that the mass transport in the investigated optical cell experiments occurs primarily by diffusion. Convective mass transport being negligible in these experiments is expectable because the setup has been designed to provide a reaction chamber with nominally isothermal temperature conditions [1]. The absence of relevant temperature gradients is fostered by the short inner length of the autoclave in relation to the wall thickness as well as by its horizontal positioning in the setup [1]. Nevertheless, one might suspect thermal convection to occur during non-stationary phases of the experiment such as heat-up and cool-down. As the optical cell is routinely equipped with an internal thermocouple, this question can be clarified based on fluid temperature measurements [14]. As elaborated in more detail in [14], internal thermocouples reaching into the fluid have proven to be a viable tool for gaining insights into convective heat transfer in ammonothermal autoclaves, as well as into chemical reactions associated with enthalpy changes [14]. Convective heat transfer is typically associated with fluctuations in local fluid temperature. This is derived based on consistent experimental results which were obtained using a variety of autoclave geometries and heating systems, as described in detail in [14]. In addition, the observation of convection-related temperature fluctuations (and fluctuations in flow velocity) is in accordance with numerical simulations [20, 21, 24] on the fluid flow in ammonothermal growth setups designed to exhibit thermal gradients and thermal convection. In the compact, isothermally heated optical cell used for the 2D X-ray imaging experiments, however, such fluctuations of fluid temperature have been observed neither during the stationary period of the experiment nor during heat-up (which are the two phases of the experiment relevant to the in situ X-ray imaging results) [14]. Note that it has been confirmed that such fluctuations would be detectable in the particular case, as indicated by an observation obtained during cool-down [14]. Measureable fluctuations in temperature can be initiated by a sudden change of cooling rate, as demonstrated by removing the heating sleeve that otherwise insulates the autoclave during cool-down [14]. The respective temperature and pressure data are shown in Fig. 10.12. The absence of oscillatory features in the

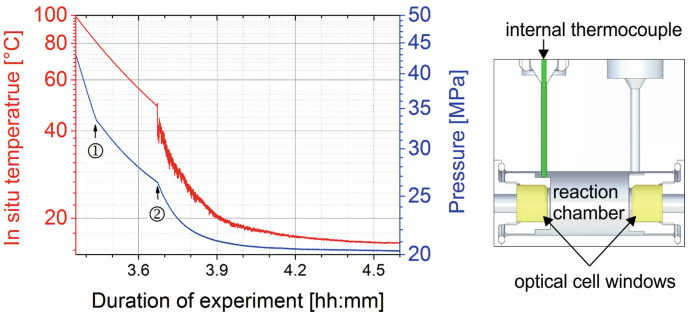

Fig. 10.12 Local fluid temperature and overall pressure measured during an optical cell experiment upon cool-down (dissolution experiment with Mg_2PN_3 pellet as nitride sample [25] and supercritical ammonia with NaN_3 mineralizer as solvent). **a** Overview with an inset depicting the location of the internal thermocouple (shown in green and reaching about 2 mm into the reaction chamber), **b** close-up of the time period starting with the sudden change in cooling rate initiated by removing the heating sleeve. (Adapted from [14])

pressure over time plot confirms that the measured temperature fluctuations are of local nature, i.e. a redistribution of heat within the reaction chamber occurs while the average temperature decreases in a steady way that reflects only the increase in cooling rate [14]. The results of in situ X-ray imaging and internal fluid temperature measurements thus are consistent with each other and in accordance with expectations based on general considerations as well as with numerical simulations of heat transfer and the aggregation of dissolved species, respectively.

10.5.3 Monitoring of Fluid Absorption for Solubility Studies on Microcrystalline Samples

Owing to the large variety of promising novel materials becoming accessible through the ammonothermal synthesis method [26], it is of particular interest to investigate the solubility of novel materials early in their development in order to facilitate the advance of their synthesis. For many materials the feasibility of addressing the question of their solubility by means of in situ X-ray imaging is beyond doubt in terms of their absorption coefficient. However, a challenge is associated with the unavailability of compact bulk material of sufficient size to mount it within the area of view and investigate its solubility in full analogy to the investigations on bulk GaN. While pressing microcrystalline powder samples into pellet shape allows to mount them the same way as their monocrystalline GaN counterparts, such samples tend to disintegrate mechanically during the experiment (see Fig. 10.13). Therefore, based on the remaining pellet size alone, it cannot be clarified whether all apparently vanished solid has been dissolved in a chemical sense or whether parts of the disintegrating solid just dropped out of view without being dissolved. To resolve this technical issue,

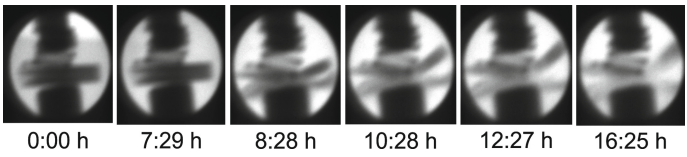

Fig. 10.13 X-ray images of a disintegrating and dissolving pellet of $ZnGeN_2$ prepared as a pellet to allow for mounting in the window area of the optical cell. Note also the visibility of the phase boundary between liquid and gaseous ammonia in the first image. (Reproduced from [10])

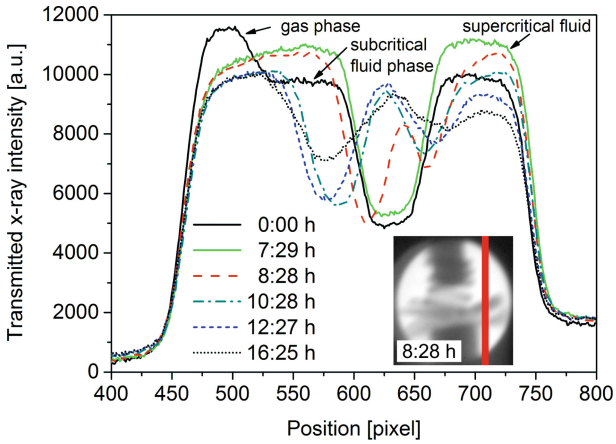

Fig. 10.14 Profile lines obtained from the images shown in Fig. 10.13 along the path indicated in the inset. Besides the absorption increase due to the presence of dissolved species, the phase change of the fluid upon heat-up is also visible. (Reproduced from [10])

the increase in fluid absorption associated with solutes can be utilized to confirm the presence of solutes within the fluid (see also the section Insights into the transport of Ga-containing species in this chapter). This method of evaluation has initially been established in the course of investigating the solubility of $ZnGeN_2$ [10].

For evaluating local changes of fluid absorption, it is often useful to extract profile lines from the X-ray images as shown in Fig. 10.14. Note that besides the absorption increase in the areas occupied by the fluid, the profile lines also reflect phase changes of the fluid upon heat-up.

10.6 Summary

The integration of optical cell technology and in situ X-ray visualization has proven to provide a variety of insights into physical and chemical processes occurring under

ammonothermal process conditions. Using this technique, the kinetics of the dissolution of GaN could be accessed experimentally for the first time. Besides revealing striking differences in the dissolution kinetics observable using different mineralizers, this also revealed that the solubility of GaN is about one order of magnitude lower than reported in most of the literature. In situ X-ray imaging also allows to investigate the face-selectivity of dissolution rates which are of interest with respect to the chemistry of intermediates as well as with respect to etch back during early stages of crystal growth experiments.

Beyond results derived from monitoring the size of the GaN sample crystal, processes in the solution can also be monitored. This comprises phase boundaries and phase transitions associated with density changes such as the transition to the supercritical state and the fill level if within the area of view. A particularly interesting feature of in situ X-ray imaging is its capability to detect local inhomogeneities of solute concentrations, provided that the solute contains sufficiently heavy elements such as gallium and its concentration is sufficiently high. In conjunction with the rapid dissolution of GaN observed with the ammonoacidic mineralizer NH_4F, the technique's capability of monitoring local concentration changes has led to intriguing results which imply that the impact of solutes on the fluid properties is extraordinarily large, at least under the investigated conditions. This has important implications for numerical simulations of fluid flow because such simulations typically are based on the properties of pure ammonia, which is due to the lack of data for the respective mixtures containing mineralizer and intermediates.

While the technique has originally been based on the use of sapphire windows as a previously established window material, investigations on the chemical stability of alternative window materials have been conducted. In particular, boron carbide has shown excellent compatibility with Na-based mineralizers, making it a material of choice to further improve the X-ray transmittance of the autoclave windows for selective applications. The most promising candidate material for X-ray transparent liner windows is diamond, given its uniquely universal chemical stability under all investigated ammonothermal conditions.

Acknowledgements Financial support by the German Research Foundation (DFG) under contract numbers WE2107/4 and WE2107/6-2 (FOR1600) is greatly acknowledged by the authors. In addition, the authors would like to thank Jonas Ihle for assistance with the preparation of the manuscript.

References

1. S. Schimmel et al., J. Cryst. Growth **498**, 214 (2018)
2. L. Spieß et al., *Moderne Röntgenbeugung* (Vieweg+Teubner, Wiesbaden, 2009)
3. B.L. Henke et al., At. Data Nucl. Data Tables **27** (1982)
4. S. Schimmel et al., Phys. Status Solidi Curr. Top. Solid State Phys. **11**, 1439 (2014)
5. H. Kukkonen et al., Vis. Res. **33**, 1431 (1993)
6. B.J. Heismann et al., J. Appl. Phys. **94**, 2073 (2003)
7. S. Schimmel et al., J. Cryst. Growth **418**, 64 (2015)
8. S. Schimmel et al., J. Cryst. Growth **479**, 59 (2017)
9. N.S.A. Alt et al., J. Cryst. Growth **350**, 2 (2012)
10. J. Häusler et al., Chem. A Eur. J. **23**, 12275 (2017)
11. M.J. Berger et al., *NIST Standard Reference Database 8* (National Institute of Standards and Technology, Gaithersburg, MD, 2010)
12. Simulation Using Siemens OEM Products X-ray toolbox. https://www.oem-xray-components.siemens.com/x-ray-spectra-simulation. Accessed 3 Feb 2017
13. J.M. Boone et al., Med. Phys. **24**, 1661 (1997)
14. S. Schimmel, *In Situ Visualisierung Des Ammonothermalen Kristallisationsprozesses Mittels Röntgenmesstechnik*, Dissertation, Friedrich-Alexander-Universität Erlangen-Nürnberg (SHAKER-Verlag, ISBN 978-3-8440-6613-5, 2019)
15. S. Schimmel et al., J. Cryst. Growth **456**, 33 (2016)
16. B. Hertweck et al., J. Supercrit. Fluids **99**, 76 (2015)
17. S. Pimputkar et al., J. Supercrit. Fluids **110**, 193 (2016)
18. M. Kaiser et al., IOP Conf. Ser. Mater. Sci. Eng. **56**, 012001 (2014)
19. S. Griffiths et al., J. Cryst. Growth **456**, 5 (2016)
20. I. Mirzaee et al., Numer. Heat Transf. Part A Appl. **70**, 460 (2016)
21. J. Erlekampf et al., J. Cryst. Growth **403**, 96 (2014)
22. T.G. Steigerwald et al., J. Cryst. Growth **403**, 59 (2014)
23. P.E. Savage et al., AIChE J. **41**, 1723 (1995)
24. Y.-N. Jiang et al., J. Cryst. Growth **318**, 411 (2011)
25. M. Mallmann et al., Chem. A Eur. J. **1** (2018)
26. J. Häusler et al., Chem. A Eur. J. **24**, 11864 (2018)

Chapter 11
Corrosive Degeneration of Process Equipment and Technical Solutions for Corrosion Protection Under Ammonothermal Conditions

Anna-Carina Luise Kimmel and Eberhard Schlücker

Abstract In addition to the high pressure and temperature, process equipment for ammonothermal syntheses has to withstand ammonothermal reaction media: an aggressive mixture of supercritical ammonia with basic or acidic additives. Severe corrosive attack of process equipment can occur under ammonothermal conditions but needs to be minimized for two reasons. Firstly, corrosive attack can lead to safety issues that must not be neglected. Secondly, corrosion products represent a major source of impurities, which represents a critical issue especially for the synthesis of semiconductors. Consequently, measures for minimizing corrosion are of utmost importance for the adequate design of ammonothermal equipment. In this chapter, materials suitable for ammonothermal applications, for pressure bearing parts as well as for internal setups and corrosion protection, and recent investigations on their corrosion behavior will be reviewed with suggestions for suitable applications and protection systems.

11.1 Stability of Autoclave Alloys Under Ammonothermal Conditions

Corrosion is one of the big challenges ammonothermal research has to overcome. Corrosive attack of the process equipment, e.g. autoclaves or internal setups, and the resulting corrosion products reduce crystal quality as well as safety. It was known from the beginning of ammonothermal research that especially ammonoacidic environments tend to attack autoclaves severely [1–4]. Also in ammonobasic environment, elements originating from dissolved autoclave materials have been found in

A.-C. L. Kimmel (✉) · E. Schlücker
Chair of Process Machinery and Systems Engineering, Friedrich-Alexander-University of Erlangen Nuremberg (FAU), Erlangen, Germany
e-mail: annacarina.kimmel@gmail.com

E. Schlücker
e-mail: sl@ipat.uni-erlangen.de

E. Meissner and R. Niewa (eds.), *Ammonothermal Synthesis and Crystal Growth of Nitrides*, Springer Series in Materials Science 304,
https://doi.org/10.1007/978-3-030-56305-9_11

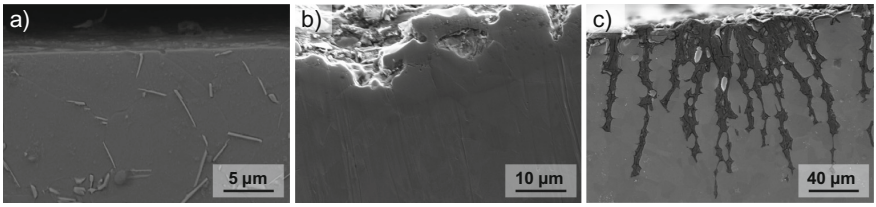

Fig. 11.1 Internal autoclave wall of an autoclave made of Alloy 718 **a** new autoclave after honing, **b** after about 50 ammonobasic experiments, **c** after about 50 ammonoacidic experiments [8]

grown crystals [3, 5]. However, detailed investigations on the corrosion behavior of autoclaves under ammonothermal conditions did not begin before the last five to ten years.

Hertweck et al. studied the differences of the corrosive attack on autoclaves made of Alloy 718 (Inconel® Alloy 718; 2.4668) in ammonoacidic (mainly sc-NH_3/NH_4Cl) and ammonobasic (mainly sc-NH_3/Na) environment [6, 7]. The intergranular attack during acidic ammonothermal syntheses combined with the high internal pressures lead to stress corrosion cracking besides general dissolution of the autoclave alloy, see Fig. 11.1c. During basic ammonothermal syntheses, the degradation is much less severe but still noticeable. A nitride layer is formed at the surface of Ni-base alloy autoclaves. However, this does not lead to passivation. The formation of a stable passivation layer is prevented by the difference in coefficients of thermal expansion between the nitride layer and the underlying alloy, which causes spalling of the nitride layer during the heating and cooling cycles, compare Fig. 11.1b.

Pimputkar et al. [9] as well observed severe corrosive attack of pure Ni and Ni-base alloys (Hastelloy C-276 and thermocouple junctions Chromel C/Alumel, Nicrosil/Nisil) in acidic environment and relatively good stability in pure sc-NH_3 and sc-NH_3/Na-solutions. A mass loss of about 50–60 wt% was observed in sc-NH_3/NH_4Cl (6 d/575 °C/100 MPa) compared to a mass gain below 0.5 wt% in pure sc-NH_3 (6 d/575 °C/103 MPa) and sc-NH_3/Na-solutions (6 d/575 °C/218 MPa). The authors used autoclaves made of René 41 in pure sc-NH_3 and sc-NH_3/Na-solutions, with relatively good stability. For use in sc-NH_3/NH_4Cl, autoclaves made of Alloy 625 (Inconel®Alloy 625; 2.4856) provided higher resistance than autoclaves made of René 41 (2.4973) but are still severely attacked and are therefore not recommended for long-term use. Details on the corrosion of Rene 41 and Alloy 625 are missing. Similar to Ni, pure Co showed a high mass loss of about 40 wt% in sc-NH_3/NH_4Cl (6 d/575 °C/100 MPa) [9]. However, the ternary Co-base alloy $Co_{80}W_{10.6}Al_{9.4}$ appeared stable in pure sc-NH_3 (6 d/575 °C/104 MPa), sc-NH_3/NH_4Cl (6 d/575 °C/100 MPa), and sc-NH_3/Na (6 d/575 °C/207 MPa), with a mass loss below 0.1 wt%.

Another study compares the different corrosion behavior of two Ni-base alloys (Alloy 718 and Alloy 282) and two Co-base alloys (CoWAlloy1 and CoWAlloy2 [10]) in acidic environment (sc-NH_3/NH_4Cl/24 h/550 °C/105 MPa) [11]. The investigated alloys are already in use or possess good potential for applications in ammonothermal autoclave design (compare Sect. 3.1). Similar to the above-mentioned publications,

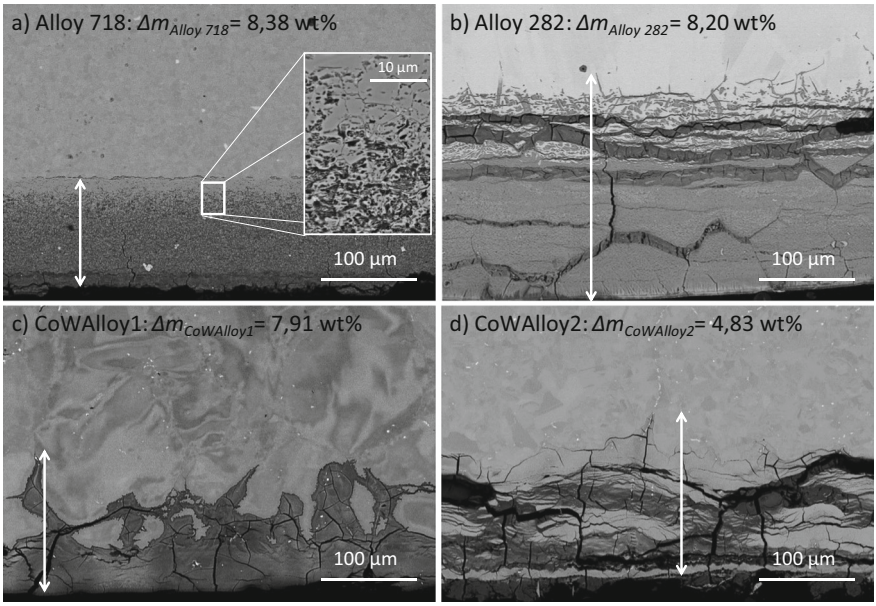

Fig. 11.2 BSE SEM images of corrosion layer of Alloy 718 (**a**), Alloy 282 (**b**), CoWAlloy1 (**c**) and CoWAlloy2 (**d**) after ammonothermal experiment in sc-NH_3/NH_4Cl ($t_{at\ Tmax}$ = 24 h, T_{max} = 550 °C, $p_{max} \approx$ 105 MPa, $\rho_{NH3} \approx$ 14.6 mol/l, $c_{mol,NH4Cl} \approx$ 0.7 mol/l). Δm_{Alloy} indicates the weight loss of the respecting alloy after the experiment. Arrows mark the maximum thickness of the area that is affected from corrosive attack. Reprinted and modified with permission from [11]

a strong corrosive degeneration of the Ni-base alloys was observed. In contrast to the findings on the ternary Co-base alloy ($Co_{80}W_{10.6}Al_{9.4}$) in [9] the higher alloyed Co-base superalloys CoWAlloy1 and CoWAlloy2 show as well high corrosive degradation after exposure to sc-NH_3/NH_4Cl, compare Fig. 11.2. The study verified the intergranular attack in the case of Alloy 718. For CoWAlloy1 and CoWAlloy2 as well, a propagation along the grain boundaries was visible. If present, Ni, Co, and Fe leach significantly from of the corrosion layers, matching the instability of the pure metals in [9]. One exception is CoWAlloy2 where a slight enrichment of Ni was observable in the corrosion layer. It is suggested that the higher W content of CoWAlloy2 might stabilize the alloy, resulting in the lowest mass loss (below 5 wt%) and therefore the biggest potential in acidic ammonothermal reactions of the investigated four alloys. Nonetheless, the corrosion resistance has to be further improved in acidic environment. Figure 11.2 shows scanning electron microscope (SEM) images of Alloy 718, Alloy 282, CoWAlloy1 and CoWAlloy2 after the described experiment. Weight loss and the maximum thickness of the area that is affected from corrosive attack are indicated. Mismatches between the two values are due to spalling or dissolution of the corrosion layer. A short-term experiment (1 d/550 °C/93 MPa) for reference showed good stability in sc-NH_3/Na: the weight change lays within the uncertainty of the measurement. Consequently, a first application could be to expand

the pressure/temperature-range to higher p and T compared to Alloy 718 or Alloy 282, in basic ammonothermal syntheses, see Sect. 3.1.

The Mo-base Ti-Zr-Mo alloy TZM shows good potential for ammonothermal reactor design: TZM possesses high strength and creep resistance at elevated temperature and good stability in NH_3-gas at up to 1000 °C [12], compare Sect. 3.1. Under ammonothermal conditions pure Mo and TZM have proven excellent resistance in sc-NH_3 (6 d/575 °C/100 MPa), sc-NH_3/Na (6 d/575 °C/213 MPa) and sc-NH_3/NH_4Cl (4 d/575 °C/86 MPa) [9]. Only a slight surface coloration was observable. Additional growth experiments of GaN in sc-NH_3/Na showed good long term (>2000 h) stability of a Mo-capsule below 500 °C. Above that temperature a black powder formed on the surfaces. Acidic growth with NH_4Cl mineralizer in an autoclave made of TZM could be performed without any sign of degradation [13]. Pure Mo is also suggested to be stable in sc-NH_3/NH_4F [14].

W and its alloys $W_{74.7}Ni_{15.6}Cu_{9.6}$, $W_{95}Re_5$ and $W_{74}Re_{26}$ show high stability in sc-NH_3, sc-NH_3/Na and medium to high stability in sc-NH_3/NH_4Cl [9]. Additionally W possesses excellent thermal stability and creep resistance [15]. Yet, their applicability as autoclave material under ammonothermal conditions has to be further evaluated.

Besides the mineralizers, also the used precursor materials have an influence on the autoclave alloys. The autoclave alloy is either exposed to the diluted precursors in the ammonothermal sc-NH_3/mineralizer/precursor-solution or directly in contact to the solid precursor prior to its dissolution. Precursors used vary from lower quality nitrides supposed to recrystallize (e.g. polycrystalline GaN), to bulk metals (e.g. pure Ga, In, Zn) or even alloys.

Ga, originating from dissolved GaN in sc-NH_3 and GaN in direct contact with the autoclave and internal setups was found up to 8 μm into the used Ni-alloys [16]. The authors supposed that this fact potentially falsifies the conducted solubility measurements, due to re-dissolution from migrated Ga inside the autoclave alloy and internal setups during subsequent experiments. The influence on the mechanical stability of the alloys has not been addressed so far. It is suggested that other precursor like In or Zn interact with the autoclave alloys as well [17, 18]. Further in-depth studies on that topic are in progress but have not been published yet.

Table 11.1 in Sect. 11.4 sums up the most promising alloy-solution-combinations already investigated for application in ammonothermal syntheses. Please refer to the individual studies for further details and additional alloy-solution combinations: [6, 7, 9, 11, 13, 16–18].

11.2 Stability of Materials for Internal Setups and Other Process Equipment Under Ammonothermal Conditions

A variety of different materials have been tested in different ammonothermal solutions, e.g. for use as internal setup, for additional pressure bearing parts like window

material enabling in situ measurements, or for corrosion protection. A brief summary of the most suitable candidates, not mentioned in Sect. 11.1, is given in the following.

The noble metals Au, Pt and Pd are stable in sc-NH_3 (6 d/575 °C/100 MPa) and sc-NH_3/NH_4Cl (4–6 d/>545 °C/>93 MPa or 14 d/600 °C/200 MPa) [9, 14]. All three have already been used as liner or coating material, compare Sect. 11.3. In sc-NH_3/Na (6 d/575 °C/>182 MPa) Au, Pd, and Pt suffer significant weight loss and/or embrittlement [9]. The Pt-alloy $Pt_{78}Rh_{22}$ was found stable in sc-NH_3 and sc-NH_3/NH_4Cl. $Pt_{91}Ru_9$ alloy additionally in sc-NH_3/Na, suggesting its use as universal but expensive liner material for both acidic and basic ammonothermal growth [9]. In sc-NH_3/NH_4F, the results on the stability of Pt are contradictory. A Pt-protective-coating system investigated in [14] was significantly dissolved in sc-NH_3/NH_4F (14 d/600 °C/200 MPa), suggesting that stability in acidic sc-NH_3 solutions is not a general feature but depending on the specific mineralizer. In contrast, a Pt-liner used in [19, 20] showed at least sufficient stability in sc-NH_3/NH_4F. However, no detailed information on the stability or degradation of the Pt-liner was given. Similar behavior could be observed for Ag. Ag was tested stable in sc-NH_3, sc-NH_3/Na, and sc-NH_3/NH_4F, whereas sc-NH_3/NH_4Cl leads to significant dissolution [9, 14]. Several corrosion protection systems made of Ag are already in use, compare Sect. 11.3.

All oxide ceramics tested in [9] where not stable in sc-NH_3/Na (6 d/>540 °C/>208 MPa) except for zirconia, which was also stable in sc-NH_3 (6 d/575 °C/101 MPa). Others were stable in both sc-NH_3 (6 d/575 °C/>98 MPa) and sc-NH_3/NH_4Cl (6 d/575 °C/>91 MPa): fused silica, quartz, sapphire, sintered alumina and yttria-stabilized zirconia. Quartz tubes have been used as sealed reaction chambers in the early ammonothermal research, e.g. in [21]. Sapphire is used in ammonothermal in situ monitoring technology as pressure loaded window material for optical access, due to its beneficial optical and mechanical properties [22].

The nitride ceramic Si_3N_4 shows good stability in both sc-NH_3 (6 d/575 °C/224 MPa) and sc-NH_3/NH_4Cl (>6 d/>450 °C/>100 MPa) [9, 23]. Application examples are a semi-hermetic capsule to reduce corrosive degeneration of Ni-base superalloys in ammonoacidic synthesis (see Sect. 11.3) or the use as ball material in a rolling ball viscometer, determining viscosity and density of ammonothermal solutions [24].

SiC and $(WC)_{90–94}Co_{6–10}Fe_{0–4}$ show good and universal potential for use in ammonothermal environment, as they are relatively stable in sc-NH_3/Na (6 d/>545 °C/>200 MPa), sc-NH_3 (6 d/575 °C/>104 MPa) as well as sc-NH_3/NH_4Cl (>3 d/>575 °C/>14 MPa) [9, 23, 25]. Only minor changes in surface quality or diameter are observable. SiC also appears relatively stable in sc-NH_3/NH_4F (>7d/>350 °C/>40 MPa) [25]. Polycrystalline SiC grown from physical vapor transport is used for crystal mounts inside the autoclave ([23], also see Sect. 10.4). Diamond, SiC und vitreous carbon (Sigradur G) have been identified as promising materials in ammonothermal in situ X-ray technology as they possess low X-ray absorption and good to excellent stability in sc-NH_3/NH_4Cl, sc-NH_3/NH_4F, and sc-NH_3/NaN_3 [25]. The application of diamond, with the best chemical stability in the mentioned supercritical solution, is however limited due to the extremely high investment costs and availability in the needed dimensions.

Table 11.1 in Sect. 11.4 sums up the most promising material-solution-combinations already investigated for application in ammonothermal syntheses. Please refer to the individual studies for further details and additionally material-solution combinations: [9, 14, 23, 25].

11.3 Protection Systems for Autoclaves and Internal Equipment During Ammonothermal Crystal Growth

To minimize corrosive degeneration and contamination of grown crystals, protection systems have been developed, especially in the ammonothermal syntheses using acidic mineralizers. Pt–liner on Ni-base alloy autoclaves during ammonoacidic crystal growth with NH_4Cl and NH_4F mineralizer improved crystal quality or purity during explorative ammonothermal syntheses [2, 4, 5, 19, 20, 26, 27]. However, the high cost of the noble metal limit its applications. To reduce the needed material amount and to overcome the mismatch in coefficient of thermal expansion of Pt and the Ni-base alloy, a three layer Au/Pd/Pt-coating system has been developed, showing good potential in sc-NH_3/NH_4Cl but not in sc-NH_3/NH_4F [14], compare Sect. 11.2. An Au-coating and an Au/Pd-coating-system showed good potential as well in sc-NH_3/NH_4Cl, additionally reducing the manufacturing and material costs. In sc-NH_3/NH_4F an Ag coating showed good stability [14]. The described coating systems have all been tested for 14 days at 600 °C and 200 MPa and enable to protect the autoclave body and periphery head parts (connection pipes, valves, etc.) at relatively low technological and financial effort.

In contrast to the satisfactorily stable noble metal coatings, ceramic coatings tested in [23] show no potential for use in acidic ammonothermal syntheses. Nitrided or borided Alloy 718 is not stable in sc-NH_3/NH_4Cl: complete dissolution or spalling of the coating prevents corrosion protection of the underlying alloy. The add-on coatings TiN and ZrO showed no sufficient adhesion or thermoshock resistance.

Some semi-hermetic capsule systems have been presented in the last decade, offering a good option to reduce corrosion at lower investment costs. In that case, adhesion and spalling problems of ceramics can be overcome, as the crucible is not fixed directly to the autoclave, tensile stresses on the crucible can be avoided. Another advantage is the easy removal for cleaning purposes or for replacement without the need of an entire new autoclave. Hertweck et al. developed a ceramic liner system (see Fig. 11.3) with a crucible made of BN or Si_3N_4 [23]. With its use, the corrosive degeneration of the autoclave decreased significantly in sc-NH_3/NH_4Cl. The described crucibles have been used during ammonothermal crystal growth of InN [28].

As already mentioned in Sect. 11.1, Mo, W and their tested alloys (TZM, $W_{74.7}Ni_{15.6}Cu_{9.6}$, $W_{95}Re_5$ and $W_{74}Re_{26}$) possess high stability in sc-NH_3/Na, sc-NH_3 and sc-NH_3/NH_4Cl and therefore show excellent potential as autoclave or liner

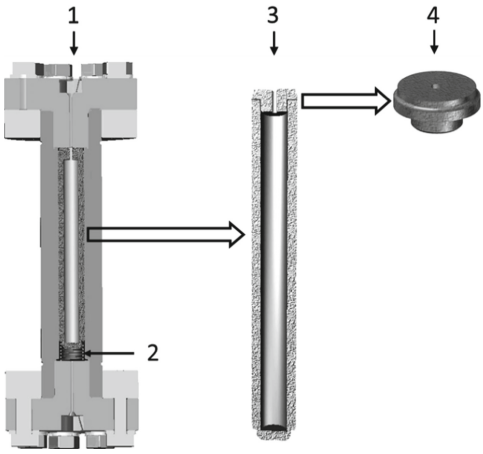

Fig. 11.3 Schematic view of the ceramic crucible presented in [23]. Pressure loaded autoclave (1) with spring (2) to fit tightly the capsule (3) to the lid (4) and autoclave (1). The lid and the area of the crucible in contact with the lid possess high surface quality (Ra ≈ 0.5 μm) to minimize leakage of the sc-NH_3/mineralizer solution. Reprinted and modified with permission from [17]

material. A Mo capsule used in [9] showed no degradation below 500 °C in sc-NH_3/Na, above that temperature a slight blackening was observable. A Mo-capsule (non-hermetically sealed) showed good potential as well, especially due to minimized oxygen concentrations found in the grown GaN crystals [29]. Mo or molybdenum nitrides allegedly act to getter oxygen under certain conditions. The use of an autoclave made of TZM completely eliminates the need of any corrosion protection when using the mineralizer NH_4Cl [13].

A non-hermetically sealed Ag capsule used in [30] resulted in a ultrahigh purity growth environment in basic (sc-NH_3/Na) ammonothermal growth, reducing the transition metal impurities in grown GaN crystals to less than 1×10^{17} cm^{-3}. Ag has been used as well to protect a Ni-base alloy in sc-NH_3 containing NH_4F mineralizer during the investigation of dissolved species during ammonothermal crystal growth of GaN [31].

11.4 Summary

Corrosion of process equipment, pressure bearing parts as well as internal setups, is still a big issue during ammonothermal crystal growth. Alloys suitable for reactor design have been discussed in Sect. 11.1. Most Ni-base and Co-base alloys investigated in ammonothermal environment are only stable in pure sc-NH_3 and sc-NH_3 containing basic mineralizers. If autoclaves made of those alloys are still to be used in acidic solutions, protection systems like liner, crucible and coatings have to be applied to minimize corrosive degeneration and contamination of grown crystals (Sect. 11.3). The high strength Ti-Zr-Mo alloy TZM, and pure Mo are also suitable for use in acidic ammonothermal growth using NH_4Cl mineralizer. Internal setups, capsules or corrosion protection are additional applications fields, due to their excellent chemical stability. A variety of materials for use as internal setups and corrosion

Table 11.1 Applicability of a variety of different materials for different sc-NH_3/mineralizer combinations at ammonothermal pressure/temperature-ranges

Material	sc-NH_3/Na	sc-NH_3	sc-NH_3/NH_4Cl	sc-NH_3/NH_4F
Ni	✓	✓	x	–
Alloy 718	✓	✓	x	(✓)
Alloy 625	✓	✓	x	–
Alloy 282	✓	✓	x	–
René 41	✓	✓	x	–
Co	✓	✓	x	–
$Co_{80}W_{10.6}Al_{9.4}$	✓	✓	✓	–
CoWAlloy1/CoWAlloy2	✓	✓	x	–
Mo	✓	✓	✓	✓
TZM	✓	✓	✓	–
W	✓	✓	o	–
$W_{74.7}Ni_{15.6}Cu_{9.6}$	✓	✓	o	–
$W_{95}Re_5$	✓	✓	✓	–
$W_{74}Re_{26}$	✓	✓	✓	–
Au	x	✓	✓	–
Pd	x	✓	✓	–
Pt	x	✓	✓	x
$Pt_{78}Rh_{22}$	x	✓	✓	–
$Pt_{91}Ru_9$	✓	✓	✓	–
Ag	✓	✓	x	✓
Aluminum silicate	x	o	✓	–
Fused silica	x	✓	✓	–
Quartz	x	✓	✓	–
Sapphire	x	✓	✓	–
Sintered alumina	x	✓	✓	–
Yttria-stabilized zirconia	o	✓	✓	–
Zirconia	✓	✓	o	–
Si_3N_4	x	✓	✓	–
BN	x	o	o	–
SiC	o	o/✓	o/✓	o/✓
$(WC)_{90–94}Co_{6–10}Fe_{0–4}$	✓	✓	✓	–
Diamond	✓	–	✓	✓
BC	✓	–	x	x
Vitreous carbon (Sigradur G)	o	–	o	o

Materials selected due to their good potential or as they are already in use in ammonothermal crystal growth. Please refer to the individual studies for further details and additionally material-solution combinations [6, 7, 9, 11, 13, 14, 23, 25]

(✓) good to excellent potential, (o) possible uses, (x) not recommended without protection system, (–) not investigated/reported so far

protection has been tested for application in ammonothermal solutions. The most promising are noble metals such as Pt, Pd, and Au in sc-NH_3, and sc-NH_3/NH_4Cl or Ag in sc-NH_3/Na and sc-NH_3/NH_4F. Pt liner as corrosion protection in acidic ammonothermal solutions containing NH_4Cl reduce corrosive attack on autoclaves, but at high investment costs. Au/Pd/Pt-coating systems are able to protect at lower investment costs. Ceramics such as Si_3N_4 can be used in sc-NH_3/NH_4Cl or SiC and WC in sc-NH_3, sc-NH_3/Na, and sc-NH_3/NH_4Cl. Semi-hermetic crucible systems made of ceramics (e.g. Si_3N_4) or metals (e.g. Ag, Mo, TZM) are a cheap alternative to Pt-liner or coatings combined with a good handling. To sum up, each specific synthesis route (different educt/mineralizer/process parameter) requires a specific review of potential autoclave materials and/or suitable protection system to reduce safety issues and contamination during the ammonothermal process.

Table 11.1 names the most promising material-solution-combinations already investigated or in use for application in ammonothermal syntheses. Please refer to the individual studies for further details and additionally material-solution combinations: [6, 7, 9, 11, 13, 14, 23, 25].

References

1. H. Jacobs, D. Schmidt, High-pressure ammonolysis in solid-state chemistry. Curr. Top. Mater. Sci. **8**, 383–427 (1982)
2. A.P. Purdy, R.J. Jouet, C.F. George, Ammonothermal recrystallization of gallium nitride with acidic mineralizers. Cryst. Growth Des. **2**, 141–145 (2002)
3. B. Wang, M.J. Callahan, Ammonothermal synthesis of III-nitride crystals. Cryst. Growth Des. **6**, 1227–1246 (2006)
4. D. Tomida, K. Kuroda, N. Hoshino, K. Suzuki, Y. Kagamitani, T. Ishiguro, T. Fukuda, C. Yokoyama, Solubility of GaN in supercritical ammonia with ammonium chloride as a mineralizer. J. Cryst. Growth **312**, 3161–3164 (2010)
5. D. Ehrentraut, Y. Kagamitani, T. Fukuda, F. Orito, S. Kawabata, K. Katano, S. Terada, Reviewing recent developments in the acid ammonothermal crystal growth of gallium nitride. J. Cryst. Growth **310**, 3902–3906 (2008)
6. B. Hertweck, T.G. Steigerwald, N.S.A. Alt, E. Schluecker, Corrosive degeneration of autoclaves for the ammonothermal synthesis: experimental approach and first results. Chem. Eng. Technol. **37**, 1903–1906 (2014)
7. B. Hertweck, T.G. Steigerwald, N.S.A. Alt, E. Schluecker, Different corrosion behaviour of autoclaves made of nickel base alloy 718 in ammonobasic and ammonoacidic environments. J. Supercrit. Fluids **95**, 158–166 (2014)
8. *Pictures provided with kindly permission by Benjamin Hertweck* (2020)
9. S. Pimputkar, T.F. Malkowski, S. Griffiths, A. Espenlaub, S. Suihkonen, J.S. Speck, S. Nakamura, Stability of materials in supercritical ammonia solutions. J. Supercrit. Fluids **110**, 193–229 (2016)
10. S. Neumeier, L.P. Freund, M. Göken, Novel wrought γ/γ' cobalt base superalloys with high strength and improved oxidation resistance. Scr. Mater. **109**, 104–107 (2015)

11. A.-C.L. Kimmel, T.F. Malkowski, S. Griffiths, T.G. Steigerwald, L.P. Freund, S. Neumeier, M. Göken, J.S. Speck, E. Schluecker, High-temperature corrosion of Inconel®Alloy 718, Haynes®282®Alloy and CoWAlloy1&2 in supercritical ammonia/ammonium chloride solution. J. Cryst. Growth **498**, 289–300 (2018)
12. Plansee, *Molybdenum* (2017). https://www.plansee.com/en/materials/molybdenum.html. Accessed 25 Oct 2017
13. T.F. Malkowski, S. Pimputkar, J.S. Speck, S.P. DenBaars, S. Nakamura, Acidic ammonothermal growth of gallium nitride in a liner-free molybdenum alloy autoclave. J. Cryst. Growth **456**, 21–26 (2016)
14. B. Hertweck, S. Zhang, T.G. Steigerwald, N.S.A. Alt, R. Niewa, E. Schluecker, Applicability of metals as liner materials for ammonoacidic crystal growth. Chem. Eng. Technol. **37**, 1835–1844 (2014)
15. Plansee, *Tungsten* (2020). https://www.plansee.com/en/materials/tungsten.html. Accessed 30 Jan 2020
16. S. Griffiths, S. Pimputkar, J.S. Speck, S. Nakamura, On the solubility of gallium nitride in supercritical ammonia–sodium solutions. J. Cryst. Growth **456**, 5–14 (2016)
17. B. Hertweck, *Dissertation: Chemische und physikalische Stabilität von technischen Materialien und Hochdruckapparaten für ammonothermale Systeme*, Friedrich-Alexander-Universität Erlangen-Nürnberg (2016)
18. S. Zhang, *Dissertation: Intermediates during the Formation of GaN under Ammonothermal Conditions*, Universität Stuttgart (2014)
19. Q. Bao, M. Saito, K. Hazu, K. Furusawa, Y. Kagamitani, R. Kayano, D. Tomida, K. Qiao, T. Ishiguro, C. Yokoyama, S.F. Chichibu, Ammonothermal crystal growth of GaN using an NH_4F mineralizer. Cryst. Growth Des **13**, 4158 (2013)
20. Q. Bao, M. Saito, K. Hazu, Y. Kagamitani, K. Kurimoto, D. Tomida, K. Qiao, T. Ishiguro, C. Yokoyama, S.F. Chichibu, Ammonothermal growth of GaN on a self-nucleated GaN seed crystal. J. Cryst. Growth **404**, 168–171 (2014)
21. A.P. Purdy, F.J.C. Mater, Ammonothermal synthesis of cubic gallium nitride. Chem. Mater. 1648–1651 (1999)
22. N.S.A. Alt, E. Meissner, E. Schlücker, L. Frey, In situ monitoring technologies for ammonthermal reactors. Phys. Status Solidi **9**, 436–439 (2012)
23. B. Hertweck, S. Schimmel, T.G. Steigerwald, N.S.A. Alt, P.J. Wellmann, E. Schluecker, Ceramic liner technology for ammonoacidic synthesis. J. Supercrit. Fluids **99**, 76–87 (2015)
24. T.G. Steigerwald, N.S.A. Alt, B. Hertweck, E. Schluecker, Feasibility of density and viscosity measurements under ammonothermal conditions. J. Cryst. Growth **403**, 59–65 (2014)
25. S. Schimmel, U. Künecke, M. Meisel, B. Hertweck, T.G. Steigerwald, C. Nebel, N.S.A. Alt, E. Schlücker, P. Wellmann, Chemical stability of carbon-based inorganic materials for in situ X-ray investigations of ammonothermal crystal growth of nitrides. J. Cryst. Growth **456**, 33–42 (2016)
26. T.M.M. Richter, S. Strobel, N.S.A. Alt, E. Schlücker, R. Niewa, Ammonothermal synthesis and crystal structures of diamminetriamidodizinc chloride $[Zn_2(NH_3)_2(NH_2)_3]Cl$ and Diamminemonoamidozinc Bromide $[Zn(NH_3)_2(NH_2)]Br$. Inorganics **4**, 41 (2016)
27. M. Saito, Q. Bao, K. Kurimoto, D. Tomida, K. Kojima, Y. Kagamitani, R. Kayano, T. Ishiguro, F.S. Chichibu, in *10th International Workshop on Bulk Nitride Semiconductors* (Espoo, Finland, 2017)
28. J. Hertrampf, P. Becker, M. Widenmeyer, A. Weidenkaff, E. Schlücker, R. Niewa, Ammonothermal crystal growth of indium nitride. Cryst. Growth Des. **18**, 2365–2369 (2018)
29. S. Pimputkar, J.S. Speck, S. Nakamura, Basic ammonothermal GaN growth in molybdenum capsules. J. Cryst. Growth **456**, 15–20 (2016)

30. S. Pimputkar, S. Kawabata, J.S. Speck, S. Nakamura, Improved growth rates and purity of basic ammonothermal GaN. J. Cryst. Growth **403**, 7–17 (2014)
31. P. Becker, T. Wonglakhon, D. Zahn, D. Gudat, R. Niewa, Approaching dissolved species in ammonoacidic GaN crystal growth: a combined solution NMR and computational study. Chem. Eur. J. **279**, chem.201904657 (2020)

Part III
Chemistry of Ammonothermal Synthesis

Chapter 12
Explorative Synthesis of Novel Nitride Compounds by Ammonothermal Synthesis

Mathias Mallmann, Niklas Cordes, and Wolfgang Schnick

Abstract This chapter provides a brief overview of the synthesis of nitrides and oxonitrides by the ammonothermal method. Numerous binary, ternary and multinary nitrides as well as oxonitrides are discussed. The synthesis conditions with regard to the temperatures, pressures, precursors and mineralizers are mentioned. In addition, the crystal structure of the respective compounds will be briefly described. Since most of these compounds possess interesting electronic and optical properties, the bandgaps of the compounds are discussed in more detail and are summarized at the end.

The ammonothermal method, as mentioned in Chap. 1, is suitable for the synthesis of a large range of different nitride materials. Because of the solution-based approach at relatively low temperatures, the ammonothermal process exhibits advantages in crystal growth compared to common solid-state reactions. For this reason, the ammonothermal process is particularly interesting for compounds with industrial application, such as semiconducting materials like GaN. Recently, this method was also used for the synthesis and study of other nitrides. The following chapter gives an overview of the development of ammonothermal synthesis of nitrides and oxonitrides and briefly summarizes the resulting properties and possible applications of these materials.

12.1 Binary Nitrides

In 1966 Juza and Jacobs reported on the ammonothermal synthesis of α-Be_3N_2, which was the first nitride synthesized by this innovative approach [1]. Thereby, the

M. Mallmann · N. Cordes · W. Schnick (✉)
Chair of Inorganic Solid-State Chemistry, Department of Chemistry, University of Munich (LMU), Butenandtstr. 5-13, 81377 Munich, Germany
e-mail: wolfgang.schnick@uni-muenchen.de

E. Meissner and R. Niewa (eds.), *Ammonothermal Synthesis and Crystal Growth of Nitrides*, Springer Series in Materials Science 304,
https://doi.org/10.1007/978-3-030-56305-9_12

reaction temperature could be lowered from 1270 to 870 K, reaching a pressure of 20 MPa, compared to conventional synthetic approaches like ammonolysis. At these reaction conditions α-Be_3N_2 was obtained as microcrystalline powder. So far, no other group II-nitrides could be synthesized ammonothermally. A few years later, the first single crystals were obtained during the ammonothermal process. The rare earth metal nitrides LaN and EuN were prepared at temperatures around 650 K and pressures up to 500 MPa starting from $K_3[La(NH_2)_6]$ or europium metal and KNH_2 as mineralizer (see Table 12.1) [2, 3]. Whether the crystallization process is based on a chemical transport of intermediates within the autoclave or in a melt of KNH_2 is not clarified. Other rare earth metal nitrides with general formula *Ln*N (*Ln* = Y, Ce, Sm and Gd) could only be synthesized as microcrystalline products. CeN and SmN were synthesized under ammonobasic conditions, starting from the rare earth metals and Cs or K which form the respective amides as mineralizers. In contrast, ammonoacidic conditions with NH_4I as mineralizer were employed for the synthesis of YN and GdN [4–7].

Besides the already mentioned compounds, probably the most prominent nitrides synthesized ammonothermally are group 13 nitrides, namely BN, AlN, GaN and InN. Most of today's research interest on the ammonothermal method is focused on the crystal growth of GaN, caused by the importance of GaN as semiconductor in laser diodes, field-effective transistors or light emitting diodes [8]. Therefore, large single crystals with high purity are required for homoepitaxial growth of GaN by HVPE (hydride vapor phase epitaxy) or MOVPE (metal organic vapor phase epitaxy) [8]. As mentioned above, the ammonothermal method has advantages in crystal growth compared to other solid-state reaction methods, making it specifically interesting for fabrication of GaN semiconductor devices. The growth process can be carried out under both, ammonobasic and -acidic, conditions. Alkali metal amides are used as mineralizer in the ammonobasic process. During the growth process, polycrystalline GaN reacts with the mineralizer forming soluble intermediates (see Chap. 13) in the cold zone of the autoclave. With respect to retrograde solubility of GaN, the intermediates are transported to the hot zone of the autoclave and decompose on crystal seeds, forming GaN single crystals with high purity. On the other hand, ammonium halides can be used for ammonoacidic crystal growth of GaN as well. Higher growth rates were detected under latter conditions, caused by a better solubility of GaN with ammonium halides instead of alkali metal amides. Extensive research efforts in the past years made it possible to achieve growth rates of 1000 μm per day and even more [9]. By this method crystals with sizes up to 50 mm in diameter have been prepared [10]. In contrast, the crystallization process of the other group 13 nitrides is more challenging, caused by the differing reactivity of liquid gallium in comparison to solid boron or aluminum, or due to the better solubility of GaN in ammonia compared to the other nitrides. Thereby, h-BN was only obtained as microcrystalline product from boron and lithium or potassium amide at 820 K and 100–500 MPa [11]. However, even after a reaction period of 21 days, elemental boron occurs as side phase in the reaction product, indicating a low reactivity or solubility of boron under ammonobasic conditions. AlN was synthesized

Table 12.1 Reaction conditions of ammonothermally synthesized (oxo)nitrides

Compound	Starting material	Mineralizer	Temperature (K)	Pressure (MPa)	Duration (h)	Reference
Binary nitrides						
α-Be_3N_2	Be	–	673	20.3	168	[1]
YN	Y	NH_4I	623	61	168	[6]
LaN	$K_3(La(NH)_2)_6$	KNH_2	650	500	240	[2]
EuN	Eu	K	673	500	168	[3]
CeN	Ce	Cs	490	200	288	[4]
SmN	Sm	K	433–453	500	240–720	[5]
GdN	Gd	NH_4I	523	507	552	[7]
BN	B	$LiNH_2/KNH_2$	820	100–500	504	[11]
AlN	Al	K/NH_4Cl	723–873	200	24–432	[12, 13]
GaN	Ga	$LiNH_2/K$	823	500	≥168	[61]
InN	$InCl_3$	KNH_2	630–770	190–280	10–100	[15]
η-Mn_3N_2	Mn	K/Rb	673–873	≥600	840	[17]
ε-Mn_4N	Mn	$GaN + ANH_2$	723–823	400–500	72–240	[19]
θ-Mn_6N_{5+x}	MnI_2	$NaNH_2$	673–723	600	1440–2880	[18]
Cu_3N	$[Cu(NH_3)_4]NO_3$	–	623–853	≥600	–	[21]
Ni_3N	$[Ni(NH_3)_6]Cl_2$	$NaNH_2$	523	200	168	[62]
γ′-Fe_4N	Fe	FeI_2	733–853	600–800	–	[20]
Ternary nitrides						
$Li_2Ta_3N_5$	Ta_3N_5	$LiNH_2$	823	600	120	[25]

(continued)

Table 12.1 (continued)

Compound	Starting material	Mineralizer	Temperature (K)	Pressure (MPa)	Duration (h)	Reference
$ATaN_2$ (A = Na, K, Rb, Cs)	Ta_3N_5, Ta_2O_5, $TaCl_5$ or NH_4TaF_6	MNH_2 (M = Na, K, Rb, Cs)	673–1073	≤600[a]	120–600	[22]
$NaSi_2N_3$	Si	$NaNH_2$	923	600	120	[26]
$LiSi_2N_3$	Si	LiN_3	970–1070	100–170	100	[28]
$LiGe_2N_3$	Ge_3N_4	Li	900	150–230	100	[28]
$MgSiN_2$	Mg + Si	KN_3	1070	100–170	125	[28]
$MgGeN_2$	Mg + Ge	NaN_3	870	150–230	120	[28]
$MnSiN_2$	Mn + Si	KN_3	1070	100–170	125	[28]
$MnGeN_2$	Mn + Ge	NaN_3	870	150–230	120	[28]
$ZnSiN_2$	Zn + Si	$LiN_3/NaN_3/KN_3$	870–1070	100–150	100	[29]
$ZnGeN_2$	Zn + Ge	$LiN_3/NaN_3/KN_3$	870	150–230	95	[29]
$K_3P_6N_{11}$	P_3N_5	KNH_2	773	600	168	[36]
Mg_2PN_3	Mg + P_3N_5	NaN_3	1070	140	72	[42]
Zn_2PN_3	Zn + P_3N_5	KN_3	800	200	96	[42]
Multinary nitrides						
$CaAlSiN_3:Eu^{2+}$	CaAlSi:Eu	$NaNH_2$	773–1073	0.1–100	20–92	[43–45]
$CaAlSiN_3:Eu^{2+}$	Ca, Al, Si, Eu	NaN_3	850	100–200	240–720	[46]
$CaAlSiN_3:Li^+/Ce^{3+}$	CaAlSi:(Li,Ce)	$NaNH_2$/Ca	1073	100	30–33	[63]
$SrAlSiN_3:Eu^{2+}$	SrAlSi:Eu	$NaNH_2$/Sr	1073	100	30	[47, 48]
$SrAlSiN_3:Na^+/Ce^{3+}$	SrAlSi:(Na,Ce)	Sr	1073	100	30	[64]
$CaGaSiN_3:Eu^{2+}$	CaGaSi:Eu	LiN_3/NaN_3	1070	50–150	140–270	[49]

(continued)

Table 12.1 (continued)

Compound	Starting material	Mineralizer	Temperature (K)	Pressure (MPa)	Duration (h)	Reference
$Ca_{1-x}Li_xAl_{1-x}Ge_{1+x}N_3$ ($x \approx 0.2$)	$Ca_3Al_2Ge_2$	Li	925	185	95	[52]
Oxonitrides						
$LaTaON_2$	LaTa	$NaNH_2$	773–1073	100	15–75	[54]
Ln$TaON_2$ (*Ln* = La, Ce, Pr, Nd, Sm, Gd)	La, Pr, Nd or Sm + Ta	NaN_3 + NaOH	870–1070	150–300	110	[23]
$LaNbON_2$	La_2Nb	$NaNH_2$ + NaOH	1073	100	33	[55]
$BaTaO_2N$	Ba_3N_2 + TaON	$NaNH_2$ + NaOH	823–973	100	20	[57]
EAMO_2N (*EA* = Sr, Ba; *M* = Nb, Ta)	Sr or Ba + Nb or Ta	NaN_3 + NaOH	900	100–300	80	[60]
$Eu_3Ta_2O_3N_4$	Eu + Ta	NaN_3 + NaOH	1070	170	80	[69]

with ammonobasic mineralizer KNH_2 as well as in ammonoacidic (NH_4Cl) environment [12, 13]. In addition to polycrystalline products, single crystalline AlN was grown on GaN seeds with KN_3 as mineralizer [14]. Recently, Niewa et al. succeeded in synthesis and crystal growth of InN. The authors used $InCl_3$ and KNH_2 as starting materials, with a molar ratio of 1:3, at temperatures between 630 and 770 K and pressures of 190–280 MPa, resulting in ammononeutral conditions. The shape of the obtained crystals differ from plate like morphology with diameters of up to 2 μm to rod-like crystals with length up to 5 μm (see Chap. 13, Fig. 13.2) [15]. These results can offer the possibility to synthesize single crystals of solid solutions of GaN and InN by the ammonothermal method as well, achieving a smaller bandgap compared to pure GaN. Bandgap values of InN in literature differ from 0.6 to 1.9 eV, resulting from different measuring methods, oxygen impurities or dopant concentration [16]. Photoluminescence measurements as well as XAS and XES measurements of ammonothermally synthesized InN indicated an optical and electronic bandgap of 1.7 eV [68].

Furthermore, Jacobs and coworkers were successful in synthesis of transition metal nitrides by the ammonothermal method with interesting properties such as high hardness, mechanical strength or semiconducting and magnetic properties. However, the number of such compounds is still small. Until now, three different manganese nitrides could be synthesized ammonothermally. While microcrystalline ε-Mn_4N was only observed during the synthesis of manganese doped GaN at 723–823 K in an ammonobasic milieu, single crystals of η-Mn_3N_2 and θ-Mn_6N_{5+x} grew during the ammonothermal process with temperature gradients between 673 and 873 K (see Table 12.1) [17–19]. In contrast, there is only one observed iron compound, namely γ′-Fe_4N which is isotypic to ε-Mn_4N and crystallizes in a perovskite-type structure. It was synthesized under ammonoacidic conditions starting from Fe and FeI_2 at 733–853 K and pressures of up to 800 MPa. Due to the corrosion of the autoclave under ammonoacidic conditions (see Chap. 3), γ′-Fe_4N contains traces of Ni, originated from the nickel-based alloy of the autoclave [20]. Pure Ni_3N was synthesized starting from $[Ni(NH_3)_6]Cl_2$ and $NaNH_2$ at 523 K and 200 MPa. It seems that ammonobasic and -acidic conditions can be used for the synthesis of early 3d-transition metal nitrides, while late transition metal nitrides are not accessible by this approach. This may be explained by the lower thermodynamic stability of the late transition metal nitrides. Therefore, Cu_3N could only be synthesized in neutral conditions starting from $[Cu(NH_3)_4](NO_3)_2$ and Cu metal at 620–850 K and 600 MPa [21]. During the reaction, $[Cu(NH_3)_4]NO_3$ is formed and decomposes in the hot zone of the autoclave to Cu_3N, water, ammonia and nitrogen. The formation of nitrogen prevents thermal decomposition of Cu_3N and therefore is essential for the synthesis.

12.2 Ternary Nitrides

Jacobs and co-workers also succeeded in synthesizing the first ternary nitrides using the ammonothermal process. In 1989 they obtained tantalum nitrides with general

formula $MTaN_2$ with M = Na, K, Rb and Cs. Microcrystalline products were obtained starting from Ta_3N_5, Ta_2O_5, $TaCl_5$ or NH_4TaF_6 and an excess of the corresponding alkali metal amide MNH_2 (M = Na, K, Rb, Cs) at temperatures between 673 and 1073 K and pressures up to 600 MPa. By washing with H_2O or liquid NH_3 at room temperature the pure compounds can be isolated, while no single crystals were obtained [22]. The first single crystals of $NaTaN_2$ with sizes up to 30 µm were prepared as side phase during synthesis of oxonitride perovskites [23]. Furthermore, crystals of the potassium and rubidium compounds could also be isolated as by-products. SEM images of $KTaN_2$ and $RbTaN_2$ are displayed in Fig. 12.1 [24]. The sodium compound crystallizes in the α-$NaFeO_2$ structure type, while the heavier homologues crystallize in a β-cristobalite type of structure.

There is no analogous lithium compound. Instead of that Li, Li_3N and $LiNH_2$ react with Ta_3N_5 to $Li_2Ta_3N_5$ at temperatures between 673 and 1073 K and pressure of 600 MPa within five days. An applied temperature gradient inside the autoclave causes separation of an excess of soluble $LiNH_2$ (cold zone) from less soluble $Li_2Ta_3N_5$ in supercritical ammonia. A pure product can be obtained by using a partly laterally perforated stainless steel ampoule. A large excess of lithium compounds leads to the formation of secondary phases, which cannot be separated. Tantalum nitrides other than Ta_3N_5, such as ε-TaN, ϑ-TaN or the use of $TaCl_5$ as starting material do not lead to the desired product [25].

Furthermore, the behavior of alkali metals with elements of the fourth main group, especially Si and Ge, were examined. Polycrystalline $NaSi_2N_3$ was synthesized by Jacobs et al. at temperatures between 823 and 873 K and pressures of 600 MPa starting from $NaNH_2$ and Si or Si_3N_4, respectively [26]. It crystallizes in a superstructure of the wurtzite-type in space group $Cmc2_1$ and the structure can be derived from that of hexagonal GaN (see Fig. 12.4). Attempts to grow macroscopic single crystals of this compound failed. Analogous reactions with KNH_2 did not yield in KSi_2N_3. Instead, different imidonitrides like $K_3Si_6N_5(NH)_6$ were formed [27]. Recently, Häusler et al. succeeded in the synthesis of isotypic $LiSi_2N_3$ and $LiGe_2N_3$. $LiSi_2N_3$ was prepared ammonothermally starting from Si and LiN_3 at 970 K and pressures between 100

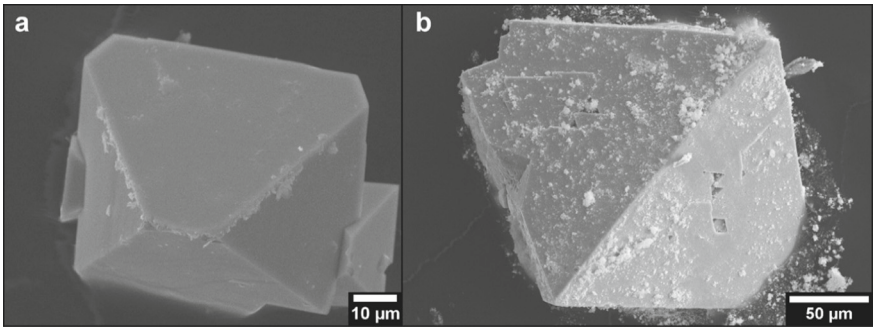

Fig. 12.1 SEM images of $MTaN_2$ crystals (**a** $KTaN_2$; **b** $RbTaN_2$). Reproduced by courtesy of Häusler [24]

and 170 MPa, while higher temperatures yielded Li_2SiN_2 as side phase. In addition $LiGe_2N_3$ was synthesized at 900 K and pressures of up to 230 MPa using Ge_3N_4 and Li as starting materials [28]. Due to the similarity of the structure and properties of these compounds to that of GaN, I-IV_2-N_3 compounds are of interest as potential semiconductor materials. Therefore, optical measurements were conducted to determine their bandgaps. Ammonothermally synthesized $LiSi_2N_3$ shows an optical bandgap of 4.4 eV, whereas $LiGe_2N_3$ shows a slightly smaller bandgap of 3.9 eV (see Fig. 12.9 in Sect. 12.5) [28].

Besides the just mentioned I-IV_2-N_3 compounds, II-IV-N_2 compounds are interesting as possible next-generation semiconductors as well. II-IV-N_2 nitrides also crystallize in a superstructure of hexagonal GaN in space group $Pna2_1$ (see Fig. 12.4). Recently, $ZnSiN_2$ and $ZnGeN_2$ were synthesized under ammonothermal conditions. While $ZnGeN_2$ was formed at 870 K and pressures up to 230 MPa, $ZnSiN_2$ requires higher temperatures of 1070 K to obtain crystalline products [29]. To improve crystallinity of the products, the syntheses was conducted with a second temperature step at lower temperatures (570 K), to guarantee a formation of intermediates for better solubility of the starting materials (see Chap. 13). Both compounds were achieved starting from the corresponding elements with alkali metal azides as ammonobasic mineralizers (NaN_3 or KN_3). After washing with 1 M HCl, phase pure products with well-shaped crystals with sizes up to several µm (see Fig. 12.2) were obtained. In situ X-ray imaging experiments illustrated the dissolution of $ZnGeN_2$ in ammonobasic conditions, pointing towards a possible dissolution-recrystallization process for

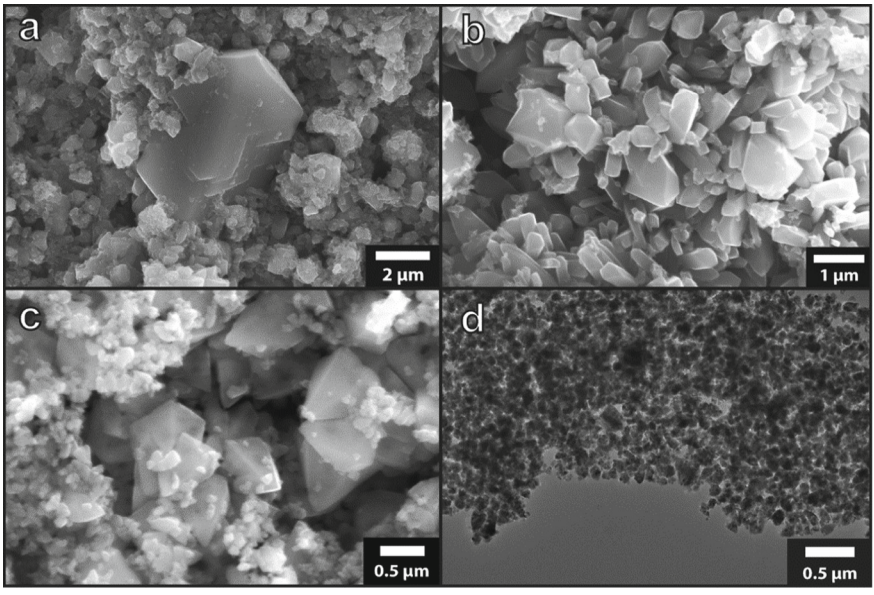

Fig. 12.2 SEM images of $ZnSiN_2$ (**a**/**b**) and SEM (**c**)/TEM (**d**) images of $ZnGeN_2$. Reproduced with permission from Wiley, Copyright 2017 [29]

crystal growth of such ternary nitrides (see Chap. 10). Furthermore, ammonoacidic conditions were tested for synthesis of $ZnGeN_2$, representing the first ammonoacidic synthesis of a ternary nitride. Si_3N_4 liners were used to prevent corrosion of the autoclave. Starting from NH_4F, Zn and Ge_3N_4 at temperatures around 870 K and 195 MPa resulted also in the desired product [24]. Recent studies showed, that fluoride ammoniates like $ZnF_2(NH_3)_2$ or $ZnF_2(NH_3)_3$ are formed during ammonothermal reaction starting from Zn and NH_4F and therefore are possible intermediates during synthesis of $ZnGeN_2$ [30].

As mentioned above, $ZnGeN_2$ was synthesized at lower reaction temperatures compared to $ZnSiN_2$, due to the lower thermal stability under ammonothermal conditions. A lower thermal stability of the respective ternary Ge nitride as compared with the isoelectronic Si nitride could be observed as a general trend in the synthesis of II-IV-N_2 and I-IV_2-N_3 compounds and is also the case for the following nitrides.

Besides the described ternary zinc nitrides Zn-IV-N_2, isotypic magnesium and manganese nitrides could be synthesized ammonothermally as well. $MgSiN_2$ and $MnSiN_2$ were obtained at 1070 K and pressures of 100–150 MPa, whereas $MgGeN_2$ and $MnGeN_2$ were synthesized at 870 K and pressures up to 230 MPa, starting from the elements with KN_3 as ammonobasic mineralizer. A second temperature step was inserted at 570 K (Si compounds) and 670 K (Ge compounds) to improve crystallinity of the products [28].

Due to their interesting optical and electronic properties, as well as the earth-abundance of the elements, the presented II-IV-N_2 compounds are, as already mentioned above, interesting candidates as next-generation semiconductors [31]. Additionally, similar lattice parameter make the growth of these materials on GaN substrates and therefore the formation of hybrid materials possible. Moreover, pure $MnSiN_2$ could be an attractive material in the field of spintronic applications and manganese doped $MgSiN_2$ shows interesting luminescence properties [32, 33]. Therefore, optical bandgaps of the six compounds were investigated by diffuse reflectance spectroscopy and Tauc-plots. The optical bandgaps are ranging from 2.5 to 4.8 eV ($MgSiN_2$: 4.8 eV, $MnSiN_2$: 3.5 eV, $ZnSiN_2$: 3.7 eV, $MgGeN_2$: 3.2, $MnGeN_2$: 2.5 eV and $ZnGeN_2$: 3.2 eV), covering a very large bandgap range comparable to AlN, GaN, InN and solid solutions thereof (see Fig. 12.9) [28, 29]. Additionally, XES and XAS measurements delivered 3.7 and 4.7 eV for electronic bandgap values of $ZnGeN_2$ and $ZnSiN_2$ [34]. Nevertheless, further physical studies have to be made, for which crystals of sufficient size would be needed, which could possibly be obtained by synthesis optimization and crystal growth experiments under ammonothermal conditions. Furthermore, the ammonothermal synthesis of $ZnSnN_2$ would be of great significance as a possible alternative of InN. However so far, bulk $ZnSnN_2$ was only synthesized by high-pressure metathesis methods leading to microcrystalline products [35]. Until now, neither microcrystalline nor single crystals of $ZnSnN_2$ were synthesized by the ammonothermal method.

Already in the 90s Jacobs and Nymwegen showed, that P-N compounds could also be synthesized via the ammonothermal method. They succeeded in synthesizing microcrystalline $K_3P_6N_{11}$ starting from P_3N_5 and KNH_2 at 773 K and 600 MPa NH_3 [36]. The crystal structure is composed of a highly

condensed framework of corner sharing PN_4-tetrahedrons. The nitrogen atoms can connect two ($N^{[2]}$) as well as three PN_4-neighboring tetrahedrons ($N^{[3]}$), resulting in the Niggli formula $P_6^{[4]}N_9^{[2]}N_2^{[3]}$ of the P-N network [37]. The potassium ions occupy the resulting voids in the network. Additionally to $K_3P_6N_{11}$, Jacobs et al. were able to synthesize other P-N-H compounds ammonothermally, namely HPN_2, DPN_2, $Na_{10}[P_4(NH)_6N_4](NH_2)_6{\cdot}0.5NH_3$, $Rb_8[P_4N_6(NH)_4](NH_2)_2$ and $Cs_5[P_4(NH)_4](NH_2)_2$ from P_3N_5 and the corresponding alkali metal amide at temperatures between 670 and 870 K [38–41]. More recently, the first ammonothermally synthesized alkaline earth and transition metal P-N compound was reported by Mallmann et al. Mg_2PN_3 and Zn_2PN_3 were synthesized starting from P_3N_5 and the corresponding metal (Mg or Zn) with NaN_3 or KN_3 as mineralizer [42]. Single crystals of Mg_2PN_3 with sizes up to 25 µm were obtained at 1070 K and pressures up to 140 MPa, while less stable Zn_2PN_3 decomposes at this reaction conditions in supercritical ammonia. Therefore, Zn_2PN_3 was only formed at 800 K and 200 MPa (see Fig. 12.3) with crystallites in the submicron range. Both compounds crystallize in a wurtzite superstructure in space group $Cmc2_1$. Infinite chains of corner sharing PN_4-tetrahedra running along the *c*-axis are probably the reason for the needle-shaped habitus of the Mg_2PN_3 and Zn_2PN_3 crystallites. The relation between the wurtzite structure and the herein mentioned superstructures are summarized in Fig. 12.4.

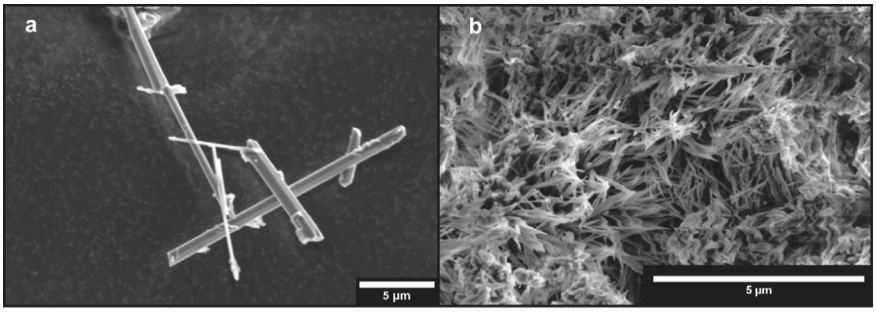

Fig. 12.3 SEM images of Mg_2PN_3 (**a**) and Zn_2PN_3 (**b**). Reproduced with permission from Wiley, Copyright 2018 [42]

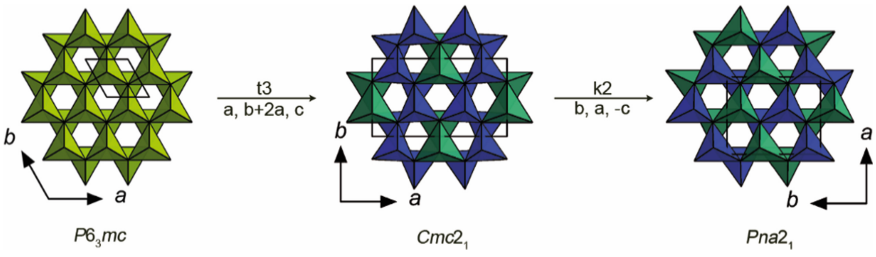

Fig. 12.4 Group-subgroup relations of wurtzite structure ($P6_3mc$) and corresponding superstructures ($Cmc2_1$ and $Pna2_1$)

Zn_2PN_3 has been discussed as a possible and promising semiconductor [31]. Therefore, the optical bandgaps of Mg_2PN_3 and Zn_2PN_3 were estimated by diffuse reflectance spectroscopy. Thus, the bandgaps for both compounds were determined to 3.7 eV for Zn_2PN_3 and 5 eV for Mg_2PN_3 [42].

12.3 Multinary Nitrides

In contrast to binary and ternary nitrides, there are just a few examples of quaternary and higher nitrides synthesized in supercritical ammonia. In 2007, Li et al. reported on the synthesis of europium doped $CaAlSiN_3$, which is a well known red phosphor material that found industrial application in pc-LEDs (see Chap. 2) [43]. Intermetallic CaAlSi:Eu and $NaNH_2$ were used as starting materials. It has been shown that both, temperature and pressure, as well as the concentration of the starting materials play an important role in the crystallization process and the luminescence properties of the samples [44, 45]. While $CaAlSiN_3$ is already formed at temperatures around 870 K, a temperature increase to 1070 K, with an additional temperature step at 670 K, where the starting materials were converted to reactive intermediates, leads to a significant improvement in crystallinity of the product. SEM images indicate, that needle shaped crystallites with several hundred nm in length can be observed. The photoluminescence of the product is also related to the pressure and the mineralizer ratio during reaction. The highest intensity was observed at pressures between 60 and 100 MPa [45].

The synthesis of $CaAlSiN_3$ starting from the elements and NaN_3 as mineralizer was reported as well [46]. Certainly, an increase in reaction time is required for the formation of the nitride, due to the insufficient mixing of the intermediates as compared to employment of an intermetallic precursors. $CaAlSiN_3$ crystallizes in orthorhombic space group $Cmc2_1$. Aluminum and silicon atoms are mixed occupied and coordinated tetrahedrally from nitrogen, whereas calcium is coordinated by five nitrogen atoms. The crystal structure is illustrated in Fig. 12.5 and can be regarded

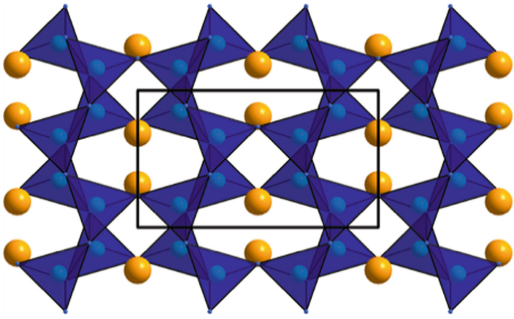

Fig. 12.5 Crystal structure of II-III-IV-N_3 along [001]. Group II metals in orange, group III and IV metals in gray and nitrogen in blue

as a strongly distorted superstructure of the wurtzite type structure (space group $P6_3mc$).

Isotypic $SrAlSiN_3:Eu^{2+}$ was synthesized in an analogous way, starting from SrAlSi:Eu and $NaNH_2$ or Sr as mineralizer at 1073 K and pressures around 100 MPa [47]. The reaction with Sr as mineralizer resulted in an increase in crystallinity and to a better photoluminescence efficiency, which can be attributed to lower strontium defect concentration. While needle-shaped crystals were obtained with $NaNH_2$ as mineralizer, bar- and platelike crystals occur with Sr [47, 48].

Recently, the first gallium containing nitridosilicate, namely $CaGaSiN_3:Eu^{2+}$, was synthesized by Häusler et al. in supercritical ammonia [49]. $CaGaSiN_3$ is isotypic to $CaAlSiN_3$ and $SrAlSiN_3$. The synthesis was conducted under ammonothermal conditions (1070 K and 150 MPa) starting from CaGaSi:Eu and NaN_3 as starting material. A second temperature step at 770 K was added for the formation of intermediates. Thereby crystals with up to 2 μm in length were obtained. Synthesis at lower temperatures or lower pressures resulted in products with poor crystallinity. They also showed that the choice of the mineralizer plays an important role in ammonothermal synthesis. While the use of LiN_3 and NaN_3 as mineralizer resulted in the desired product, KN_3 and CsN_3 resulted in formation of $Ca_{16}Si_{17}N_{34}$ and GaN. This indicates that $LiSi_2N_3$ and $NaSi_2N_3$ (see Sect. 12.2) may act as possible intermediates during synthesis. $CaGaSiN_3:Eu^{2+}$ exhibits red luminescence comparable to that of $SrAlSiN_3:Eu^{2+}$ with an emission maximum at 620 nm and FWHM (full width at half maximum) of 90 nm. Furthermore, the optical bandgap of $CaGaSiN_3$ was estimated to 3.2 eV (see Fig. 12.9) and therefore is considerably lower than the bandgap of $CaAlSiN_3$ with 4.9 eV [50, 51].

By substitution of Si by Ge, the new nitridogermanate $Ca_{1-x}Li_xAl_{1-x}Ge_{1+x}N_3$ with $x \approx 0.2$ was synthesized under ammonothermal conditions. $Ca_3Al_2Ge_2$ and lithium metal were used as starting materials. The synthesis was carried out in two temperature steps at 625 K (for the formation of intermediates) and 925 K, reaching a pressure of 185 MPa [52]. In contrast to the nitridosilicates, $Ca_{1-x}Li_xAl_{1-x}Ge_{1+x}N_3$ shows crystal sizes up to 15 μm in length (see Fig. 12.6), indicating a higher solubility of germanium or the corresponding intermediates in supercritical ammonia. $Ca_{1-x}Li_xAl_{1-x}Ge_{1+x}N_3$ crystallizes in space group $Cmc2_1$ and is isotypic to the three already mentioned quaternary nitrides (see Fig. 12.5). It can be considered as a solid solution of $LiGe_2N_3$ and not yet known $CaAlGeN_3$. The optical bandgap was estimated to be 4.3 eV (see Fig. 12.9) [52].

12.4 Oxonitrides

The hydrothermal synthesis of oxide perovskites is known for a considerable period of time [53]. The accessability of well formed crystals in this approach served as a starting point of recently reported ammonothermal growth of oxonitride perovskite crystals. The crystal structure of the oxonitride perovskites is illustrated in Fig. 12.7. Unfortunately, ammonia is a less efficient solvent for ionic substances (salts) than

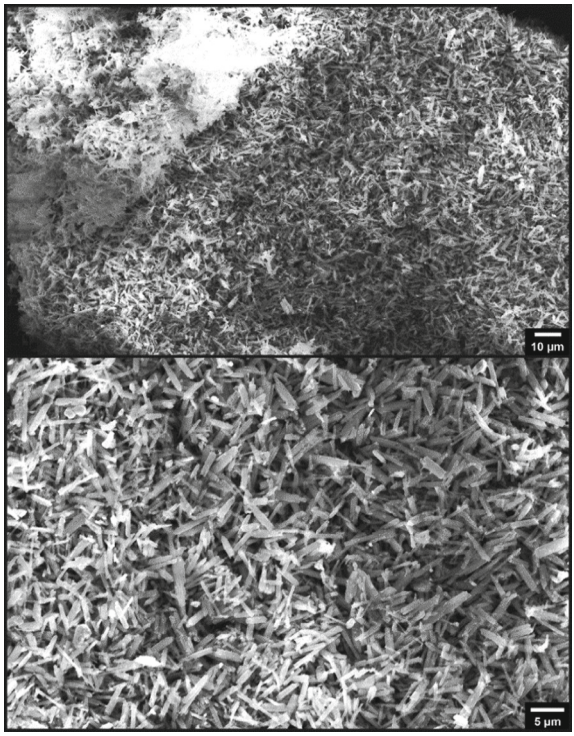

Fig. 12.6 SEM images of $Ca_{1-x}Li_xAl_{1-x}Ge_{1+x}N_3$ with $x \approx 0.2$. Reproduced with permission from Wiley, Copyright 2018 [52]

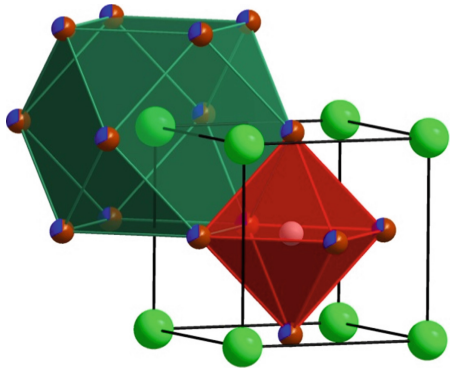

Fig. 12.7 Cubic perovskite structure ABX_3 with unit cell and coordination polyhedra of A (cuboctahedron, green), B (octahedron, red) and anions (red/blue)

water [54]. In 2011 Watanabe et al. described ammonothermal synthesis of $LaTaON_2$ in a high-pressure autoclave. A metallic alloy of La and Ta, which was previously arc melted, was used in combination with the mineralizer $NaNH_2$. The reaction temperature was 873 K, which is approximately 300 K lower than the temperature range necessary for solid-state synthesis of oxonitride perovskites in flowing ammonia (ammonolysis). The ammonia pressure within the autoclave was about 100 MPa and

the reaction period was 15–75 h. The obtained product showed better crystallinity if the reaction temperature was higher. At 773 K only the most intense powder X-ray reflection of the oxonitride perovskite could be detected. As major byproduct white $La(OH)_3$ occurred. At temperatures above 873 K, the black precursor alloy was transformed into red $LaTaON_2$. The reaction temperature, pressure and duration had no significant impact on the shape, size or lattice constant of the oxonitride. The addition of $NaNH_2$ as mineralizer is necessary for the successful formation of $LaTaON_2$ because no marked reaction between the LaTa alloy and ammonia occurs below 1073 K. The reason for that is that $NaNH_2$ increases the reaction rate by increasing the amount of anions in supercritical ammonia. It is worth to mention, that no explicit oxygen source was added, and thus the required oxygen-amount was introduced by uncontrolled hydrolysis of sodium amide. Further addition of mineralizers as oxygen-source raised the amount of $La(OH)_3$ as an undesired side product. The obtained cube like crystals showed a diameter of up to 1 μm. The intermediates formed during the ammonothermal reaction are not known. Because of the drastic change of the morphology of the alloy to the oxonitride perovskite a reaction proceeding in NH_3-$NaNH_2$ supercritical fluid solvent solution was assumed to occur [54].

For the ammonothermal synthesis of $LaNbON_2$ the previously described procedure has been modified. The starting alloy was used in an atomic ratio 2:1 (La:Nb) and milled under argon. For the synthesis of lower valence cation-doped $LaNbON_2$, the starting alloy (La:Sr:Nb = 1.9:0.1:1 or La:Nb:Ti = 2:0.95:0.05) was prepared through a similar process using Sr and Ti [55]. The alloy was loaded with $NaNH_2$ and NaOH in a bottom sealed nickel tube, which was then transferred vertically in a high-pressure vessel. The autoclave was filled with ammonia and heated to 573 K at a rate of 5 K/min for 20 h and then heated to 1073 K at a rate of 1 K/min for 5 h. The pressure raised to 100 MPa [55].

A more convenient ammonothermal synthesis of oxonitride perovskites abandoning the alloy precursor has been developed as well. By using custom-built high-pressure autoclaves the synthesis of $LnTaON_2$ with Ln = La, Ce, Pr, Nd, Sm, Gd became possible. The La, Pr, Nd, Sm oxonitride perovskites were accessible at temperatures of 870 K and maximum pressures of 300 MPa. Those with Ce and Gd were only obtained at higher temperatures of 1070 K and maximum pressure of 170 MPa. Starting from powdery metals Ta and Ln and employing the mineralizer NaN_3 and NaOH as defined oxygen source, highly crystalline products of the respective oxonitride perovskites were obtained. SEM images of the corresponding products are shown in Fig. 12.8. In supercritical ammonia NaN_3 reacts to $NaNH_2$ which was used in excess. The advantage of NaN_3 as a starting material compared to $NaNH_2$ is its stability against air and moisture. To prevent the autoclave from corrosion a Ta liner was used. Inside the liner the product was obtained as a crystalline powder. On the outside of the liner $NaTaN_2$ is often formed because of the excess of the mineralizer $NaNH_2$. There are several considerations of reaction intermediates, which might be relevant for the formation of oxonitride perovskites in supercritical ammonia. Under ammonothermal conditions NaN_3 reacts to $NaNH_2$ which probably reacts with the lanthanide metal to intermediate species of the assumed composition

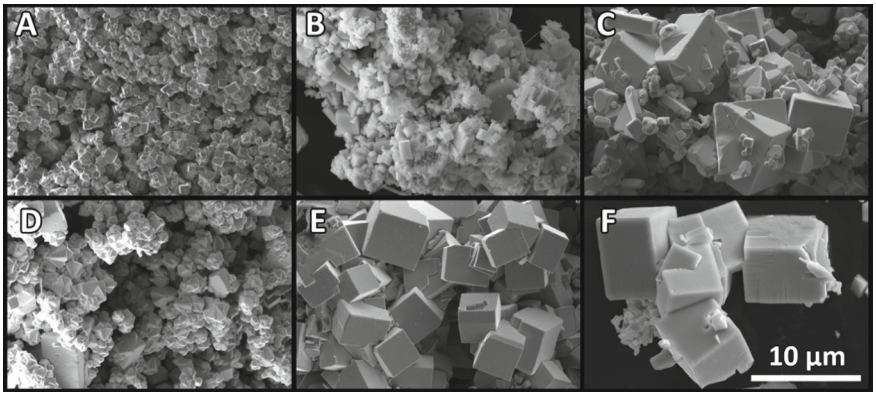

Fig. 12.8 SEM images of *Ln*$TaON_2$. **A** $LaTaON_2$, **B** $CeTaON_2$, **C** $PrTaON_2$, **D** $NdTaON_2$, **E** $SmTaON_2$, **F** $GdTaON_2$. Reproduced with permission from Willey, Copyright 2017 [23]

$Na_3Ln(NH)_6$ or $NaLn(NH)_4$ [56]. The single octahedral anion $Ta(O_{1-x},N_x)_6^{(7+6x)-}$ might as well be possible with Na^+ as counterion. Isoelectronic oxotantalate anions are well known from hydrothermal synthesis, in which a dissolution/precipitation process forms cube like crystals of oxide perovskites. The formed intermediates decompose during synthesis to reactive species at higher temperatures. Another possible reaction pathway is, that at the bottom of the liner a $NaNH_2$/NaOH melt is formed in which the starting materials dissolve. Druse like agglomerations grown at the bottom of the liner and can be found after the successful ammonothermal reaction. The obtained product was nearly phase pure and highly crystalline. Little amount of side-phases like $NaTaN_2$ and Ln_2O_3 could be eliminated by washing the product with HCl and water [23].

The ammonothermal synthesis of $BaTaO_2N$ was conducted in high pressure autoclaves. Ba_3N_2, TaON, NaOH were weighted as starting materials in a molar ratio of Ba:Ta:NaOH:$NaNH_2$ (1:1:1: $x = 1, 2, 5$). TaON was employed as a precursor, synthesized by heating Ta_2O_5 in flowing ammonia at 850 °C for 15 h. NaOH acted as oxygen source, while $NaNH_2$ was added as a basic mineralizer. The starting materials were placed in a bottom-sealed Ni tube, which was then transferred into the autoclave. The autoclave was subsequently filled with liquid ammonia and heated at 823–973 K for 20 h. The inner pressure of the autoclave was held at about 100 MPa. The obtained product was washed with deionized water and 1 M HNO_3 to remove excess sodium and other impurities. The authors also prepared a reaction with the starting materials (Ba, Ta, NaOH, $NaNH_2$) and a molar ratio of 1:1:1:1 but at lower pressures of 10.8 MPa and a temperature of 923 K. Comparing PXRD and SEM images the product at higher temperatures showed better crystallinity but larger amounts of side-phases like $NaTaN_2$ and other unknown impurities. At lower temperatures the starting material TaON was not completely transferred into the product. The reaction temperature for this ammonothermal approach is still 300 K lower than in conventional ammonolysis reactions. The synthesis mechanism herein is based on Ba and Ta

amides or imideamide intermediates. Presumably, oxygen is introduced as hydroxo- or oxo-ligand during the first reaction step. The detected impurities are formed via thermal decomposition of the Na–Ta-based intermediates according to the reaction $Na[Ta(NH_2)_6] \rightarrow NaTaN_2 + 4\,NH_3$. However, this reaction type under high pressures seems unlikely [57]. Furthermore, NH_3 is mandatory as a reaction medium. Using N_2 as the nitriding agent at high-pressure conditions instead of supercritical ammonia the particles were agglomerated and had indefinite shape. This results have also been observed at reaction temperatures in supercritical ammonia under 873 K. Cube like crystals were synthesized at temperatures above 923 K. The particle size increased with the reaction temperature as grain growth was promoted by a solution-deposition mechanism in supercritical ammonia. This ammonothermal synthesis results in particles with smooth surfaces and sharp edges, which is comparable to other solution processes. In contrast, the reaction of oxonitrides synthesized from oxide precursor results in porous particles [58]. Furthermore, the authors investigated the effect of the mineralizer. The best results were obtained with double molar ratio of Na [57].

The solubility of the alkali metals increases from Li to Cs, still all of the alkali metals are rather good soluble in liquid ammonia [59]. So far, sodium delivered the best results in the morphology of cube like crystals.

The ammonothermal reaction of $EAMO_2N$ with EA = Sr, Ba; M = Nb, Ta was conducted in high-pressure custom-built autoclaves. Metal powders of Nb or Ta and Sr or Ba as well as NaN_3 and NaOH were used as starting materials. NaOH is also the required oxygen source for the desired oxonitride perovskite. All of the starting materials were ground for better solubility, except for Sr and Ba. They were placed in Nb respectively Ta liners, to prevent the autoclave from corrosion and were used to facilitate isolation of the products from the autoclave. The four compounds were successfully synthesized at temperatures of about 900 K and pressures up to 300 MPa. The reaction duration was 80 h. The formation of side phases could be nearly eliminated by carefully optimizing experimental parameters. The use of complicated precursors which need to be pre-synthesized by arc melting was not necessary. Still, the Ca phases of the respective oxonitride perovskite could not be obtained which is probably due to the low solubility of Ca in supercritical ammonia [60].

In addition to oxonitride perovskites, Ruddlesden-Popper-phases could be synthesized by the ammonothermal approach, recently. The ammonothermal synthesis of $Eu_3Ta_2N_4O_3$, a Ruddlesden-Popper-phase with $n = 2$ was synthesized in supercritical ammonia at temperatures of 1070–920 K and pressures up to 170 MPa. Interestingly, $Eu_3Ta_2N_4O_3$ is a mixed valence phase containing both Eu^{2+} and Eu^{3+}. Besides $Eu_3Ta_2N_4O_3$, the perovskite phases $EuTaO_2N$ (cubic and tetragonal) were obtained as well under the same reaction conditions [69].

The manifold substitution possibilities of oxonitrides are also evident in the ammonothermal approach. We strongly believe that in addition to known compounds, a large number of new nitrides and oxonitrides, which are not accessible by conventional solid-state reactions, can also be synthesized using high-pressure custom-built autoclaves. On the other hand, the ammonothermal synthesis changes drastically the morphology of the products compared with for instance conventional ammonolysis

reactions. Since the ammonothermal reaction is a solution-based reaction, many products can be obtained in crystalline form. The smart use of mineralizers can further improve crystallization and is often mandatory for the successful reaction. Frequently, the alkali metals are used because they have good solubility and do not incorporate themselves into the product.

12.5 Summary

The results summarized in this overview clearly demonstrate that the ammonothermal approach is a powerful tool for synthesis of both nitrides and oxonitrides. Though Jacobs's pioneering work dates back to the 1960th, the full synthetic potential for synthesis of ternary, quaternary and multinary compounds has not been fully developed as yet. Table 12.1 summarizes the above mentioned, ammonothermally synthesized compounds and their reaction conditions. In the last years, the number of ammonothermally synthesized nitrides and oxonitrides was significantly increase, due to the establishment of the research group Ammono-FOR in Erlangen, Stuttgart and Munich. In the case of ternary nitrides, it turned out that especially compounds crystallizing in a wurtzite type superstructure (e.g. II-IV-N_2) are easily obtained under ammonothermal conditions. Crystal sizes of up to 25 µm for Mg_2PN_3 or several hundred µm for $RbTaN_2$ illustrate the high potential of the ammonothermal process for crystal growth.

Until now, all quaternary and multinary nitrides synthesized ammonothermally crystallize in a superstructure of the wurtzite type. However, it could be shown that this approach has a great potential to synthesize nitrides, which are difficult to synthesize by other methods (e.g. $CaGaSiN_3$ or $Ca_{1-x}Li_xAl_{1-x}Ge_{1+x}N_3$). Additionally, due to the high reactivity of supercritical ammonia, moderate reaction conditions are required. This is especially advantageous for compounds which have low thermal stability like nitridogermanates or -gallates. Furthermore, other structure types were observed for $K_3P_6N_{11}$ or at higher temperatures, resulting in the formation of Li_2SiN_2 or $Ca_{16}Si_{17}N_{34}$. This could also be interesting for quaternary or higher nitrides.

The synthesized ternary and quaternary nitrides with wurtzite superstructure are of interest as possible next-generation semiconductors. They have promising optical and electronic properties, perceptivity for bandgap engineering and are constructed of earth-abundant elements [28, 31, 65]. Furthermore, $ZnSiN_2$ and $ZnGeN_2$ exhibit significant smaller polarization differences compared to (Al,Ga,In)N, resulting in a suppression of polarization fields in polar growth directions [66]. Figure 12.9 summarizes the optical and electronic bandgaps of the herein described ammonothermally synthesized nitrides and oxonitrides. It can be seen, that almost the whole range from 1.7 to 5.0 eV is covered by these oxo(nitrides), offering a wide range of possible applications for these materials. Oxonitride perovskites for example are used as water splitting materials, whereas manganese doped $MgSiN_2$ exhibits interesting luminescent properties and Mn-IV nitrides are interesting for spintronic applications [32, 33, 67].

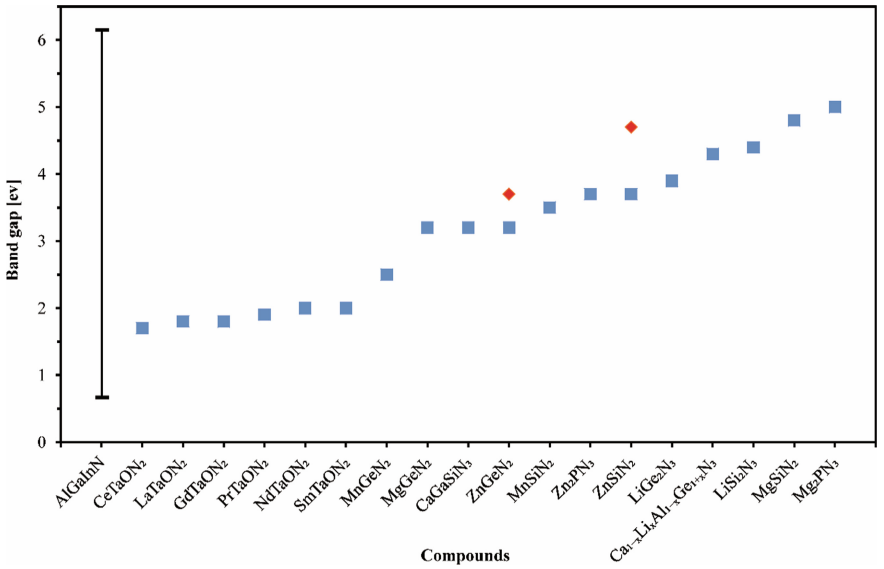

Fig. 12.9 Bandgaps of ammonothermally synthesized (oxo)nitride semiconductors. ■ symbols indicating optical bandgaps, ♦ symbols indicating electronic ones compared to the bandgap range of (Al,Ga,In)N [23, 28, 29, 34, 42, 49, 50, 52]

The class of the oxonitrides with perovskite structure type often possess bandgaps with 2 eV suitable for the solar watersplitting. Interestingly, the ammonothermal method provides a crystalline product and very pronounced morphology. The shape of the crystals are cube like and have a diameter of up to 15 μm. This makes the ammonothermal approach interesting for a wide range of oxonitride perovskites like $AB(O,N)_3$ with $A = EA, Ln$; $B = Nb, Ta$. Besides the perovskite structure, also oxonitrides crystallizing in distorted perovskite structure variants like the Ruddlesden-Popper-phases can be synthesized with the ammonothermal approach. Therefore, the ammonothermal synthesis seems to be a suitable method for the synthesis of new oxonitrides.

Literature

1. R. Juza, H. Jacobs, Ammonothermalsynthese von Magnesium- und Berylliumamid. Angew. Chem. **78**, 208 (1966). R. Juza, H. Jacobs, Ammonothermal synthesis of magnesium and beryllium amides. Angew. Chem. Int. Ed. **5**, 247 (1966)
2. H. Jacobs, D. Schmidt, High-pressure ammonolysis in solid-state chemistry. Curr. Top. Mater. Sci. **8**, 381 (1982)
3. H. Jacobs, U. Fink, Investigation of the system potassium/europium/ammonia. Z. Anorg. Allg. Chem. **438**, 151 (1978)

4. H. Jacobs, D. Schmidt, Struktur und Eigenschaften von perowskitartigen Cäsiumamidometallaten des Cers, Neodyms und Samariums $Cs_3Ln_2(NH_2)_9$. J. Less-Common Met. **76**, 227 (1980)
5. H. Jacobs, H. Kistrup, The system potassium/samarium/ammonia. Z. Anorg. Allg. Chem. **435**, 127 (1977)
6. A. Stuhr, H. Jocobs, R. Juza, Amide des Yttriums. Z. Anorg. Allg. Chem. **395**, 291 (1973)
7. G. Linde, R. Juza, Amidometallate von Lanthan und Gadolinium und Umsetzung von Lanthan, Gadolinium und Scandium mit Ammoniak. Z. Anorg. Allg. Chem. **409**, 191 (1974)
8. D. Ehrentraut, E. Meissner, M. Bockowski, *Technology of Gallium Nitride Crystal Growth* (Springer, Berlin, Heidelberg, 2010), p. 3
9. D. Ehrentraut, R.T. Pakalapati, D.S. Kamber, W. Jiang, D.W. Pocius, B.C. Downey, M. McLaurin, M.P. D'Evelyn, High quality, low cost ammonothermal bulk GaN substrates. Jpn. J. Appl. Phys. **52**, 08JA01 (2013)
10. W. Jiang, D. Ehrentraut, J. Cook, D.S. Kamber, R.T. Pakalapati, M.P. D'Evelyn, Transparent, conductive bulk GaN by high temperature ammonothermal growth. Phys. Status Solidi B **252**, 1069 (2015)
11. R. Dwilinski, R. Doradzinski, J. Garczynski, L. Sierzputowski, M. Palczewska, A. Wysmolek, M. Kaminska, AMMONO method of BN, AlN and GaN synthesis and crystal growth. MRS Internet J. Nitride Semicond. Res. **3**, e25 (1998)
12. D. Peters, Ammonothermal synthesis of aluminum nitride. J. Cryst. Growth **104**, 411 (1990)
13. Y.C. Lan, X.L. Chen, Y.G. Cao, Y.P. Xu, L.D. Xun, T. Xu, J.K. Liang, Low-temperature synthesis and photoluminescence of AlN. J. Cryst. Growth **207**, 247 (1999)
14. B.T. Adekore, K. Rakes, B. Wang, M.J. Callahan, S. Pendurti, Z. Sitar, Ammonothermal synthesis of aluminum nitride crystals on group III-nitride templates. J. Electron. Mater. **35**, 1104 (2006)
15. J. Hertrampf, P. Becker, M. Widenmeyer, A. Weidenkaff, E. Schlücker, R. Niewa, Ammonothermal crystal growth of indium nitride. Cryst. Growth Des. **18**, 2365 (2018)
16. K.S.A. Butcher, T.L. Tansley, InN, latest development and a review of the band-gap controversy. Superlattices Microstruct. **38**, 1 (2005)
17. H. Jacobs, C. Stüve, Hochdrucksynthese der η-Phase im system Mn-N: Mn_3N_2. J. Less-Common Met. **96**, 323 (1984)
18. G. Kreiner, H. Jacobs, Magnetische Struktur von η-Mn_3N_2. J. Alloys Compd. **183**, 345 (1992)
19. M. Zając, J. Gosk, E. Grzanka, S. Stelmakh, M. Palczewska, A. Wysmołek, K. Korona, M. Kamińska, A. Twardowski, Ammonothermal synthesis of GaN doped with transition metal ions (Mn, Fe, Cr). J. Alloys Compd. **456**, 324 (2008)
20. H. Jacobs, J. Bock, Einkristallzüchtung von γ′-Fe_4N in überkritischem Ammoniak. J. Less-Common Met. **134**, 215 (1987)
21. U. Zachwieja, H. Jacobs, Ammonothermalsynthese von Kupfernitrid, Cu_3N. J. Less-Common Met. **161**, 175 (1990)
22. H. Jacobs, E. von Pinkowski, Synthese ternärer Nitride von Alkalimetallen: Verbindungen mit Tantal, $MTaN_2$ mit M ≡ Na, K, Rb und Cs. J. Less-Common Met. **146**, 147 (1989)
23. N. Cordes, W. Schnick, Ammonothermal synthesis of crystalline oxonitride perovskites $LnTaON_2$ (Ln = La, Ce, Pr, Nd, Sm, Gd). Chem. Eur. J. **23**, 11410 (2017)
24. J. Häusler, Ammonothermal synthesis of functional ternary and multinary nitrides. Dissertation, LMU München (2018)
25. T. Brokamp, H. Jacobs, Synthese und Kristallstruktur eines gemischtvalenten Lithium-Tantalnitrids $Li_2Ta_3N_5$. J. Alloys Compd. **176**, 47 (1991)
26. H. Jacobs, H. Mengis, Preparation and crystal structure of a sodium silicon nitride, $NaSi_2N_3$. Eur. J. Solid State Inorg. Chem. **30**, 45 (1993)
27. D. Peters, E.F. Paulus, H. Jacobs, Preparation and crystal structure of a potassium imidenitridesilicate, $K_3Si_6N_5(NH)_6$. Z. Anorg. Allg. Chem. **584**, 129 (1990)
28. J. Häusler, R. Niklaus, J. Minár, W. Schnick, Ammonothermal synthesis and optical properties of ternary nitride semiconductors Mg-IV-N_2, Mn-IV-N_2 and Li-IV_2-N_3 (IV = Si, Ge). Chem. Eur. J. **24**, 1686 (2018)

29. J. Häusler, S. Schimmel, P. Wellmann, W. Schnick, Ammonothermal synthesis of earth-abundant nitride semiconductors $ZnSiN_2$ and $ZnGeN_2$ and dissolution monitoring by in situ X-ray imaging. Chem. Eur. J. **23**, 12275 (2017)
30. T.M.M. Richter, S. LeTonquesse, N.S.A. Alt, E. Schlücker, R. Niewa, Trigonal-bipyramidal coordination in first ammoniates of ZnF_2: $ZnF_2(NH_3)_3$ and $ZnF_2(NH_3)_2$. Inorg. Chem. **55**, 2488 (2016)
31. Y. Hinuma, T. Hatakeyama, Y. Kumagai, L.A. Burton, H. Sato, Y. Muraba, S. Iimura, H. Hiramatsu, I. Tanaka, H. Hosono, F. Oba, Discovery of earth-abundant nitride semiconductors by computational screening and high-pressure synthesis. Nat. Commun. **7**, 11962 (2016)
32. D. Naveh, L. Kronik, Spin-polarized electronic structure of Mn-IV-V_2 chalcopyrites. Phys. Status Solidi B **243**, 2159 (2006)
33. C.J. Duan, A.C.A. Delsing, H.T. Hintzen, Red emission from Mn^{2+} on a tetrahedral site in $MgSiN_2$. J. Lumin. **129**, 645 (2009)
34. T. de Boer, P. Strobel, J. Häusler, W. Schnick, A. Moewes, Band gap and electronic structure of $Zn(Ge,Si)N_2$: probing defects using XEOL, in *Advanced Light Source (ALS) User Meeting*, Berkeley, CA (2017)
35. F. Kawamura, N. Yamada, M. Imai, T. Taniguchi, Synthesis of $ZnSnN_2$ crystals via a high-pressure metathesis reaction. Cryst. Res. Technol. **51**, 220 (2016)
36. H. Jacobs, R. Nymwegen, Synthesis and crystal structure of a potassium nitridophosphate, $K_3P_6N_{11}$. Z. Anorg. Allg. Chem. **623**, 429 (1997)
37. U. Müller, *Anorganische Strukturchemie*, 6th edn. (Vieweg + Teubner, Wiesbaden, 2008), p. 246
38. H. Jacobs, R. Nymwegen, S. Doyle, T. Wroblewski, W. Kockelmann, Crystalline phosphorus(V) nitride imide, HPN_2 and DPN_2, respectively—structure determination with X-ray, synchrotron, and neutron radiation. Z. Anorg. Allg. Chem. **623**, 1467 (1997)
39. H. Jacobs, S. Pollok, F. Golinski, Synthesis and crystal structure of $Na_{10}[P_4(NH)_6N_4](NH_2)_6(NH_3)_{0.5}$ with an adamantane-like anion $[P_4(NH)_6N_4]^{4-}$. Z. Anorg. Allg. Chem. **620**, 1213 (1994)
40. F. Golinski, H. Jacobs, Synthesis and crystal structure of $Rb_8[P_4N_6(NH)_4](NH_2)_2$ with the adamantane-like anion $[P_4N_6(NH)_4]^{6-}$. Z. Anorg. Allg. Chem. **621**, 29 (1995)
41. H. Jacobs, F. Golinski, Synthesis and crystal structure of a cesium-tetraimidophosphate-diamide, $Cs_5[P(NH)_4](NH_2)_2 = Cs_3[P(NH)_4]{\cdot}2\ CsNH_2$. Z. Anorg. Allg. Chem. **620**, 531 (1994)
42. M. Mallmann, C. Maak, R. Niklaus, W. Schnick, Ammonothermal synthesis, optical properties and DFT calculations of Mg_2PN_3 and Zn_2PN_3. Chem. Eur. J. **24**, 13963 (2018)
43. J. Li, T. Watanabe, H. Wada, T. Setoyama, M. Yoshimura, Low-temperature crystallization of Eu-doped red-emitting $CaAlSiN_3$ from alloy-derived ammonometallates. Chem. Mater. **19**, 3592 (2007)
44. J. Li, T. Watanabe, N. Sakamoto, H. Wada, T. Setoyama, M. Yoshimura, Synthesis of a multinary nitride, Eu-doped $CaAlSiN_3$, from alloy at low temperatures. Chem. Mater. **20**, 2095 (2008)
45. J. Li, T. Watanabe, H. Wada, T. Setoyama, M. Yoshimura, Synthesis of Eu-doped $CaAlSiN_3$ from ammonometallates: effects of sodium content and pressure. J. Am. Ceram. Soc. **92**, 344 (2009)
46. J. Cho, B.K. Bang, S.J. Jeong, C.H. Kim, Synthesis of red-emitting nanocrystalline phosphor $CaAlSiN_3$:Eu^{2+} derived from elementary constituents. RSC Adv. **4**, 23218 (2014)
47. K. Nonaka, K. Kishida, C. Izawa, T. Watanabe, Low temperature ammonothermal synthesis of europium-doped $SrAlSiN_3$ effect of mineralizers. J. Ceram. Soc. Jpn. **122**, 17 (2014)
48. T. Watanabe, K. Nonaka, J. Li, K. Kishida, M. Yoshimura, Low temperature ammonothermal synthesis of europium-doped $SrAlSiN_3$ for a nitride red phosphor. J. Ceram. Soc. Jpn. **120**, 500 (2012)
49. J. Häusler, L. Neudert, M. Mallmann, R. Niklaus, A.C.L. Kimmel, N.S.A. Alt, E. Schlücker, O. Oeckler, W. Schnick, Ammonothermal synthesis of novel nitrides: case study on $CaGaSiN_3$. Chem. Eur. J. **23**, 2583 (2017)

50. R. Niklaus, J. Minar, J. Häusler, W. Schnick, First-principles and experimental characterization of the electronic properties of $CaGaSiN_3$ and $CaAlSiN_3$: the impact of chemical disorder. Phys. Chem. Chem. Phys. **19**, 9292 (2017)
51. L. Wang, R.-J. Xie, Y. Li, X. Wang, C.-G. Ma, D. Luo, T. Takeda, Y.-T. Tsai, R.-S. Liu, N. Hirosaki, $Ca_{1-x}Li_xAl_{1-x}Si_{1+x}N_3:Eu^{2+}$ solid solutions as broadband, color-tunable and thermally robust red phosphors for superior color rendition white light-emitting diodes. Light: Sci. Appl. **5**, e16155 (2016)
52. J. Häusler, L. Eisenburger, O. Oeckler, W. Schnick, Ammonothermal synthesis and crystal structure of the nitridoalumogermanate $Ca_{1-x}Li_xAl_{1-x}Ge_{1+x}N_3$ ($x \approx 0.2$). Eur. J. Inorg. Chem. **2018**, 759 (2018)
53. D.R. Modeshia, R.I. Walton, Solvothermal synthesis of perovskites and pyrochlores: crystallisation of functional oxides under mild conditions. Chem. Soc. Rev. **39**, 4303 (2010)
54. T. Watanabe, K. Tajima, J. Li, N. Matsushita, M. Yoshimura, Low-temperature ammonothermal synthesis of $LaTaON_2$. Chem. Lett. **40**, 1101 (2011)
55. C. Izawa, T. Kobayashi, K. Kishida, T. Watanabe, Ammonothermal synthesis and photocatalytic activity of lower valence cation-doped $LaNbON_2$. Adv. Mater. Sci. Eng. **2014**, 5 (2014)
56. H. Jacobs, H. Scholze, Investigation of the system Na/La/NH_3. Z. Anorg. Allg. Chem. **427**, 8 (1976)
57. T. Toshima, K. Kishida, Y. Maruyama, T. Watanabe, Low-temperature synthesis of $BaTaO_2N$ by an ammonothermal method. J. Ceram. Soc. Jpn. **125**, 643 (2017)
58. K. Ueda, T. Minegishi, J. Clune, M. Nakabayashi, T. Hisatomi, H. Nishiyama, M. Katayama, N. Shibata, J. Kubota, T. Yamada, K. Domen, Photoelectrochemical oxidation of water using $BaTaO_2N$ photoanodes prepared by particle transfer method. J. Am. Chem. Soc. **137**, 2227 (2015)
59. J. Jander, H. Spandau, C.C. Addison, *Anorganische und allgemeine Chemie in flüssigem Ammoniak* (Friedr. Vieweg & Sohn, Braunschweig, 1966)
60. N. Cordes, T. Bräuniger, W. Schnick, Ammonothermal synthesis of $EAMO_2N$ (EA = Sr, Ba; M = Nb, Ta) Perovskites and ^{14}N solid-state NMR investigations of $AM(O,N)_3$ (A = Ca, Sr, Ba, La). Eur. J. Inorg. Chem. **2018**, 5019 (2018)
61. R. Dwilinski, J.M. Baranowski, M. Kaminska, R. Doradzinski, J. Garczynski, L. Sierzputowski, On GaN crystallization by ammonothermal method. Acta Phys. Pol. A **90**, 763 (1996)
62. A. Leineweber, H. Jacobs, S. Hull, Ordering of nitrogen in nickel nitride Ni_3N determined by neutron diffraction. Inorg. Chem. **40**, 5818 (2001)
63. Y. Maruyama, T. Watanabe, Low-temperature synthesis of $CaAlSiN_3:Ce^{3+}$ using the ammonothermal method. J. Ceram. Soc. Jpn. **124**, 66 (2016)
64. Y. Maruyama, Y. Yanase, T. Watanabe, Ammonothermal synthesis of charge-compensated $SrAlSiN_3:Ce^{3+}$ phosphor. J. Ceram. Soc. Jpn. **125**, 399 (2017)
65. A.D. Martinez, A.N. Fioretti, E.S. Toberer, A.C. Tamboli, Synthesis, structure, and optoelectronic properties of II-IV-V_2 materials. J. Mater. Chem. A **5**, 11418 (2017)
66. T.R. Paudel, W.R.L. Lambrecht, First-principles calculations of elasticity, polarization-related properties, and nonlinear optical coefficients in Zn-IV-N_2 compounds. Phys. Rev. B **79**, 245205 (2009)
67. M. Ahmed, G. Xinxin, A review of metal oxynitrides for photocatalysis. Inorg. Chem. Front. **3**, 578 (2016)
68. M.R. Amin, T. de Boer, P. Becker, J. Hertrampf, R. Niewa, A. Moewes, Bandgap and electronic structure determination of oxygen-containing ammonothermal InN: experiment and theory. J. Phys. Chem. C **123**, 8943 (2019)
69. N. Cordes, M. Nentwig, L. Eisenburger, O. Oeckler, W. Schnick, Ammonothermal synthesis of the mixed-valence nitrogen-rich europium tantalum ruddlesden-popper phase $Eu^{II}Eu^{III}{}_2Ta_2N_4O_3$. Eur. J. Inorg. Chem. **2019**, 2304 (2019)

Chapter 13
Intermediates in Ammonothermal Synthesis and Crystal Growth

Rainer Niewa

Abstract Mineralizers possess a central relevance in ammonothermal synthesis and formation of soluble species for material transport and crystal growth in particular, governing the solubility, transport direction and deposition processes. In this chapter we review the knowledge on solubilities and chemical behavior of common mineralizers for ammonothermal synthesis. Additionally, we present the current knowledge on intermediates during ammonothermal gallium nitride crystal growth, depending on the nature of the applied mineralizer, as well as during a conceivable ammonothermal synthesis of zinc nitride. Additionally, crystal growth of indium nitride is discussed with focus on chemical processes within the ammonia medium.

13.1 Introduction

Since the first synthetic explorative pioneering work of *Herbert Jacobs* and *Robert Juza* synthesizing the binary beryllium and magnesium amides as well as cubic beryllium nitride [1] a plethora of inorganic compounds was produced under ammonothermal conditions. These materials comprise mostly metal ammoniates, amides, few imides and nitride imides, but also hydrides and nitride hydrides, hydroxides and hydrates thereof, (poly)sulfides, selenides and tellurides as well as cyanamides and frequently ammoniates of several such compounds [2–4]. Additionally, pure metals and intermetallic compounds were obtained under ammonothermal conditions [5]. However, the number of nitrides obtained under ammonothermal conditions appears surprisingly small, as there were reports on the synthesis of binary nitrides of beryllium [1], rare-earth metals [6–13] and the earth metals B, Al, Ga, and In [14–24] next to titanium, vanadium, molybdenum, manganese, iron, nickel and copper [13, 18, 25–28]. Even more rare are reports on ammonothermally obtained higher nitrides, like the substitution phase γ'-$(Fe,Ni)_4N$ [29–31], Cu_3Pd_xN

R. Niewa (✉)
Institute of Inorganic Chemistry, University of Stuttgart, Pfaffenwaldring 55, 70569 Stuttgart, Germany
e-mail: rainer.niewa@iac.uni-stuttgart.de

E. Meissner and R. Niewa (eds.), *Ammonothermal Synthesis and Crystal Growth of Nitrides*, Springer Series in Materials Science 304,
https://doi.org/10.1007/978-3-030-56305-9_13

($x = 0.020, 0.989$) [32], $CaAlSiN_3$, $CaGaSiN_3$, and $SrAlSiN_3$ [33–42], $MSiN_2$ and $MGeN_2$ (M=Mg, Mn, Zn) [42, 43], $LiSi_2N_3$, $LiGe_2N_3$ [43], and oxide nitrides like $BaTaO_2N$ [44], $LaNbON_2$ and $RTaON_2$ with R = La, Ce, Pr, Nd, Sm, Gd [45–47], although the ammonothermal synthesis of higher nitrides is an emerging and recently quickly developing field. Of all these nitrides, several were obtained only in microcrystalline form (for example the binary nitrides of Be, Ti, V, Mo, Ni, and most rare-earth metals with exception of lanthanum and europium, or $CaAlSiN_3$ and $SrAlSiN_3$), putting forward the idea of an ammonia-mediated solid state reaction for formation of some of these examples, rather than a homogeneous reaction in solution followed by nucleation or precipitation and crystallization. For those nitrides obtained as well-shaped crystals, ideally after spatial transport to a spot within the autoclave different from the source material location, it appears save to assume that they have been dissolved and recrystallized from solution in most cases.

Most nitrides are virtually insoluble in pure ammonia under the temperature and pressure conditions of ammonothermal synthesis (typical 2–4 kbar, 300–600 °C) and dissolution as well as effective mass transport is only observed in presence of a suitable mineralizer, which typically represents either an ammonoacid or an ammonobase. The mineralizers serve a number of purposes in solvothermal synthesis and crystal growth: Primarily, they increase the solubility of the source material via formation of dissolved and mobile species. These mobile species are usually referred to as intermediates. In a chemical kinetic sense, the mineralizer is expected to ease the cleavage and reformation of chemical bonds in the source material and the sink, which is represented by the surface of the growing crystal. In the growth zone, the mobile species needs to deposit at the seed surface, while reforming the mineralizer. Technologically, the choice of mineralizer additionally determines the corrosion processes within the autoclave interior. In this way, it also dictates the optimal design of the surfaces exposed to the solution, for example via application of new autoclave material alloys, protective surface layers on the autoclave inner surface, liner materials or closed ampoules, ideally suited if chemically inert against the solution [13, 48–54], and vice versa the nature of the impurities and the impurity concentrations incorporated in the product crystals [55]. Additionally, the choice of mineralizer may govern the formation of a specific product, particle size or modification. It was observed for GaN crystal growth that there is an increasing tendency to form the cubic Sphalerite-type modification rather than the typical hexagonal Wurtzite-type form upon use of ammonium halides in the order from the chloride, bromide to iodide [56–60]. Decreasing temperatures seem to promote this trend, while addition of so-called co-mineralizers, typically represented by soluble salts, may further aid the formation of cubic GaN for a given mineralizer.

The ammonium halides (most notably the fluoride and the chloride) serve as typical and most common ammonoacids, while typical ammonobases are the alkali metal amides, of which particularly those of sodium and, to a lesser extent, potassium currently gained a practical importance. These latter ammonobases may be added directly or produced in situ from reaction of the alkali metal or its azide with ammonia. Similarly, the ammonoacids can be produced in situ, for example by reaction of ammonia with the water-free hydrogen halide (for example hydrogen

fluoride, HF). The need to increase the solubility of the target nitride in supercritical ammonia via addition of a mineralizer and the fact that the transport direction within a (temperature) gradient depends on the chemical nature of the mineralizer—i.e. the nature of the dissolved species formed from reaction of the dissolved mineralizer with the feed material—give the mineralizer a central importance in the ammonothermal synthesis and particularly in the ammonothermal crystal growth. In this sense, in literature several approaches to determine the solubility of mostly GaN in ammonia with use of various mineralizers and depending on temperature, pressure and mineralizer concentration were reported, discussing the results typically as solubility of GaN per amount of mineralizer [56, 61–66]. However, little is known about the dissolved species formed and realizing the mass transport. Similar rare information can be found in literature on the solubility of the mineralizer itself, clearly limiting the solubility of the dissolved species of the target material via chemical solution equilibria. Generally, nitrates show a rather high solubility in ammonia at room temperature compared to many other salts [67, 68], while ammonium halides and alkali metal amides as typical mineralizers show significant higher solubilities for the heavy counter ions iodide or cesium than for the lighter ones, particularly fluoride and lithium, respectively.

13.2 Mineralizers

13.2.1 Ammonobasic Mineralizers

Ammonobasic conditions mean increase of the amide ion concentration on cost of the ammonium ion concentration within the frame of the autoprotolysis equilibrium of ammonia. The application of ammonobasic milieus as compared to ammonoacidic conditions in synthesis and crystal growth has the advantage of only reduced corrosion of the autoclave material. The autoclave alloy typically experiences some increase of nitrogen content at the surfaces exposed to the basic ammonia solution including formation of nitrides in a generally even protective layer, which, however, may eventually show blistering [48, 50].

Ammonobasic conditions may be obtained by dissolution of the amides of metals with low electronegativity in ammonia, typically the alkali metals. Alternatively, the amides may be produced by reaction of the alkali metals or their azides with ammonia reacting to form the corresponding amides in situ while forming hydrogen or nitrogen as by-products, respectively (see 13.1 and 13.2). Both, hydrogen and nitrogen add to the gas mixture inherently provided in decomposition of ammonia (13.3). The choice of the mineralizer source, for example sodium metal or sodium azide to produce sodium amide as effective mineralizer during early stages of a crystal growth experiment, or as-prepared sodium amide itself, may influence the final crystal quality of the target material, as was shown for the example of GaN [69]. The differences in obtained crystal qualities were traced back to different impurity contents of the

starting materials, connected to the unlike degrees of air and moisture sensitivities, purification and handling. Few studies address the addition of further halide salts as so-called co-mineralizers, which may alter the solubility of the mineralizer or reaction products (intermediates) or function in surface activation of the feedstock. The addition of KI to potassium amide mineralizer apparently aided ammonothermal GaN crystal growth to a somewhat larger extend than the addition of the respective chloride [16].

$$2NH_3 + 2A \rightarrow 2NH_2^- + 2A^+ + H_2 \tag{13.1}$$

$$2NH_3 + 3N_3^- \rightarrow 3NH_2^- + 4N_2 \tag{13.2}$$

$$2NH_3 \rightleftarrows N_2 + 3H_2 \tag{13.3}$$

Similar to the alkali metal amides, the alkaline-earth metals, their amides, or azides can be applied as mineralizers, for which an effective GaN production was reported for barium and strontium [70, 71]. Due to the very low solubility of $Sr(NH_2)_2$ in ammonia compared to $Ba(NH_2)_2$, elemental Ga is only oxidized to GaN above 873 K, independent if started from Sr, $Sr(NH_2)_2$, SrN_3, SrH_2 or $Sr(NO_3)_2$. GaN crystal growth or coarsening of powder was not observed [24, 70]. Similarly, no obvious change of elemental Ga under ammonothermal conditions was detected up to temperatures of 873 K if applying the amides of Mg, Ca, or Eu as mineralizers. One advantage of using alkaline-earth metal amides, specifically barium amide, appears to be the lower basicity of the resulting solution due to the low solubility of these amides and thus, less corrosive action on the autoclave material. However, while early ammonothermal syntheses mostly applied lithium or sodium amide, currently particularly sodium and, to a lesser extent, potassium amide has gained practical importance.

Ternary amides and amidometalates can be used as quasi pre-reacted ammonobasic mineralizers. For example $Na_2[Zn(NH_2)_4]\cdot 0.5NH_3$ was used as mineralizer to ammonothermally grow crystals of zinc amide, $Zn(NH_2)_2$, at 3.8 kbar and 250 °C starting from elemental zinc. In a similar reaction crystals of manganese amide, $Mn(NH_2)_2$, were obtained from Mn and $Na_2[Mn(NH_2)_4]$ serving as ammonobasic mineralizer in ammonia, although under milder conditions (100 bar, 130 °C) [72]. The applied ternary amidometalate mineralizers at the same time are suspected to represent effective dissolved species, both for the growth of the binary amides and for the ammonobasic growth of manganese nitrides [25].

Available information on solubilities of the binary amides acting as ammonobasic mineralizers is rare in general, rather old and mostly only for low temperatures around and below ambient. Table 13.1 gives some literature data on solubilities of alkali and alkaline-earth metal amides in ammonia. These numbers may indicate an increasing solubility with decreasing charge density of the cation, meaning that the amides of doubly charged alkaline-earth metal ions are less soluble than those of the single charged alkali metals and that the larger the cation the better the solubility of the

Table 13.1 Solubility data of alkali and alkaline-earth metal amides per amount of ammonia [67, 73, 78, 152]

T (°C)	$NaNH_2$	KNH_2	$RbNH_2$	$CsNH_2$
−33	3.9 g/100 mL 0.1 g/100 g	45 g/100 mL 65.8 g/100 g 61 g/100 g	413 g/100 g	145 g/100 g
20	0.15 g/100 g			
25	0.004 g/100 g	3.6 g/100 g		
	$LiNH_2$	$Ca(NH_2)_2$	$Sr(NH_2)_2$	$Ba(NH_2)_2$
	Hardly soluble	Badly soluble	Hardly soluble	Very little soluble

amide. In the temperature range below the boiling point of ammonia at ambient pressure the solubilities seem to drop with decreasing temperature [73], however, little is known about solubilities at higher temperatures.

13.2.2 Ammonoacidic Mineralizers

Ammonoacidic conditions are obtained by increase of the ammonium ion concentration with concomitant reduction of the amide ion concentration linked together by the autoprotolysis equilibrium of ammonia. The application of ammonoacidic milieus result in larger degrees of corrosion of most materials exposed to the ammonia-based solution. The particularly observed pit corrosion and formation of stress-corrosion cracks is apparently connected to dissolution of alloy components [49, 50]. In agreement, typically the intermediates in ammonoacidic nitride synthesis, obtained from plain autoclaves without application of liners or similar protection, presented colors due to typically chromium or nickel impurities originating from the autoclave wall [74, 75].

Typical ammonoacidic mineralizers are the ammonium halides, of which ammonium fluoride and chloride gained the most practical importance. These ammonium halides may be added in solid form, but normally contain large amounts of moisture and are only difficult to dry. Thus, one alternative is the addition of the binary water-free hydrofluoric or hydrochloric acid in order to produce the acidic mineralizer in situ via reaction with ammonia. Similarly, the alternative addition of hydrazine hydrochloride apparently produces ammonium chloride as effective mineralizer under process conditions [76]. Mixtures of ammonium halides were explored on their effect on crystallization of GaN [56]. Alternatively, metal halides were used to produce ammonoacidic conditions, most straightforward upon use of $GaCl_3$ for GaN synthesis. $ZnCl_2$ was discussed to not only aid the growth rate of GaN crystals, but additionally serve as oxygen sink due to formation of zinc oxide [77]. The manganese nitrides η-Mn_3N_2 and θ-Mn_6N_5 were crystallized using MnI_2 or I_2 as initial mineralizer. The elemental iodine is speculated to be reduced to iodide ions with contact

Table 13.2 Solubility data of ammonium halides per amount of ammonia [7, 67, 68, 153]

T (°C)	NH_4F	NH_4Cl	NH_4Br	NH_4I
−50		5.2 g/100 g	47.1 g/100 g	62.1 g/100 g
−42		7.0 g/100 g	49.0 g/100 g	66.7 g/100 g
−33	Not soluble	15 g/100 mL	90 g/100 mL	135 g/100 g
25		61.91 g/100 mL 102.5 g/100 g	143.69 g/100 mL 237.9 g/100 g	368.10 g/100 g

to the metallic autoclave wall and thus to provide the ammonoacidic conditions [25, 26]. Dissolved intermediates during growth of these manganese nitrides were discussed to be represented by $[Mn(NH_2)_6]I_2$. However, as already mentioned, the choice of mineralizer may influence the product crystallization fundamentally. With use of ammonium iodide cubic *c*-GaN rather than the hexagonal form was obtained, while with ammonium bromide and chloride the yield of hexagonal *h*-GaN increased on the cost of the amount of *c*-GaN [56–60]. Decreasing temperatures, as a second important parameter, seem to aid crystallization of *c*-GaN. The addition of further halide salts may alter the solubility of the mineralizer or reaction products (intermediates), but generally the role of so-called co-mineralizers is rather unexplored. The addition of LiCl to ammonium chloride mineralizer in ammonothermal *c*-GaN synthesis was reported to enhance the transport rate [57]. Addition of extra well soluble ammonoacids clearly increases the solubility of intermediates in ammonia near room temperature (see below).

The solubility of the ammonium halides at −33 °C, i.e. the boiling point of ammonia at ambient pressure, increases from the virtually insoluble fluoride towards the iodide (Table 13.2) [78]. Additionally, the solubility of those halides was reported to strongly increase with temperature in the range of −50 to +50 °C. An extraordinary high solubility of ammonium salts in ammonia as a general finding is attributed to the formation of strong H-bridge bonds between ammonium ions and solvating ammonia molecules [78]. The tendency of ammonium ions to form H-bonds in this sense is much higher than for amide ions, due to highly basic (proton acceptor) properties of NH_3. An increase of the heats of solution of the ammonium halides in ammonia from the chloride to the iodide might indicate a rising acidity [79].

13.2.3 Ammononeutral Conditions

For few ammonothermally synthesized nitrides, a rather ammononeutral milieu was successful for crystal growth, namely Cu_3N [28], Cu_3Pd_xN [32] and InN (see Sect. 13.4) [23, 24]. In case of the copper nitrides, the nitrates of the metals, which form ammoniates upon action of liquid ammonia at room temperature, are treated under ammonothermal conditions ($T \geq 350$ °C, $p \geq 5$ kbar) to form the nitrides.

Although not explicitly experimentally studied, the nitrate ions under these conditions may react with ammonia to form elemental nitrogen and water according to (13.4). Water and hydroxide ions (possibly providing some ammonobasic contribution according to 13.5) are expected to react with the autoclave wall surface to form metal oxides. Dissolved species at room temperature were discussed to be represented by di- and triammoniates of copper(I) nitrate, $[Cu(NH_3)_3]NO_3$ and $[Cu(NH_3)_2]NO_3$, and the tetraammoniate of palladium(II) nitrate, $[Pd(NH_3)_4](NO_3)_2$ [41], all used as precursors.

$$3NO_3^- + 5NH_3 \rightarrow 4N_2 + 3OH^- + 6H_2O \tag{13.4}$$

$$OH^- + NH_3 \rightleftarrows H_2O + NH_2^- \tag{13.5}$$

13.3 Gallium Nitride

13.3.1 Intermediates in Gallium Nitride Crystal Growth Under Ammonobasic Conditions

The first report on a successful ammonothermal GaN synthesis in 1995 employed $LiNH_2$ and KNH_2 as ammonobasic mineralizers, but the chemical and physical knowledge about processes in the autoclave under process conditions was scarce [80]. Initial high-quality GaN crystals were produced with $NaNH_2$ as mineralizer [81, 82], while similar results were obtained upon application of sodium metal [83]. With $CsNH_2$ as mineralizer the formation of nanocrystalline *h*-GaN was reported, showing a slight red-shift in the bandgap compared to bulk crystalline material [84]. Early investigations revealed $Na[Ga(NH_2)_4]$ as one ternary amidogallate, which was studied in detail [85–88]. Ever since, this compound was assumed to represent a possible soluble species formed during ammonobasic GaN crystal growth upon application of sodium amide as mineralizer. Further explorative studies mention $Na_2Ga(NH_2)_5$ as solid in this system [89], but only a low symmetry unit cell was given from powder X-ray diffraction, which was never confirmed. In analogy to the system with sodium amide as mineralizer the—at this time unknown—compound $Li[Ga(NH_2)_4]$ was suggested as possible intermediate upon use of lithium amide [90]. With potassium amide a viscous liquid was observed [91–93], however, based on the sodium system, frequently $K[Ga(NH_2)_4]$ was postulated to represent the soluble species with potassium amide mineralizer [94].

Recent explorative studies on the solid intermediates formed in experiments designed for ammonobasic GaN synthesis, but typically performed at slightly lower temperatures revealed several compounds to form depending on used alkali metal

amide mineralizer and the local conditions at the spot of crystallization in the autoclave. All solids transport towards higher temperature within a gradient indicating a retrograde solubility. Such retrograde solubility was also observed for GaN under ammonobasic conditions at elevated temperatures depending on the mineralizer: With $NaNH_2$ the solubility of GaN apparently changes from a positive temperature dependence below 600 °C to a negative (retrograde) one at higher temperatures. However, there are indications for variations in the temperature ranges of retrograde and normal solubility depending on concentrations, pressure and density of the solution [66]. With KNH_2 a retrograde temperature dependence of the solubility of GaN was detected down to 400 °C, below a positive dependence occurs [91, 95, 96].

With $LiNH_2$ as mineralizer two modifications of $Li[Ga(NH_2)_4]$ were obtained typically coexisting in the products, thus forming under very similar conditions [75]. One modification is an isotype of $Na[Ga(NH_2)_4]$ and $Na[Al(NH_2)_4]$ [86–88]. Both forms show tetrahedral coordination of lithium ions, while differing distinctly in the inter-linkage of the amidogallate complex ions by Li^+. Interestingly, for $Li[Al(NH_2)_4]$ a further different modification was reported earlier [97], indicating a rich polymorphism for both compounds depending on temperature and probably on pressure, not even speaking about formation of possible metastable forms. Such rich polymorphism appears to be common for ternary amidometalates, since it was reported for a multitude of related compounds composed of a variety of different metals [for example 70, 71, 93, 98–103]. In case of sodium amide mineralizer, $Na[Ga(NH_2)_4]$ was confirmed as solid intermediate upon application of higher process pressures (above 200 MPa) or lower temperatures (below 450 °C), while at lower pressures a tetraamidogallate amide $Na_2[Ga(NH_2)_4]NH_2$ was the dominant product [75]. This latter compound might be identical to the earlier reported $Na_2Ga(NH_2)_5$ [89], but diffraction data clearly differ, indicating at least the presence of a different polymorph. With barium or barium amide as mineralizer $Ba[Ga(NH_2)_4]_2$ was obtained in three different modifications depending on synthesis conditions [71]. All alkali metal amidogallates characterized in detail decompose upon heating in inert gases to eventually form *h*-GaN and the binary alkali metal amide. $Ba[Ga(NH_2)_4]_2$ in contrast decomposes via several intermediate steps to finally form the intermetallic compound $BaGa_2$ [71]. All these solid intermediates contain isolated tetraamidogallate ions $[Ga(NH_2)_4]^-$ as building blocks, stacked together with alkali or alkaline-earth metal ions in various coordination environments within different three-dimensional arrangements. These findings may already be taken as first indication for the presence of such complex ions in the basic solution for GaN crystal growth under ammonothermal conditions. Figure 13.1 gives an overview on all solid crystalline intermediates characterized so far.

NMR investigations of solutions of the badly soluble alkali metal amidogallates $Li[Ga(NH_2)_4]$ and $Na_2[Ga(NH_2)_4]NH_2$ reveal $[Ga(NH_2)_4]^-$ to represent the exclusive dissolved gallium containing species present at ambient temperature and autogenous pressures [104]. This result makes it likely that this species is dominating also at somewhat elevated temperatures and higher pressures, however, in situ investigations under the conditions of ammonothermal GaN crystal growth still have to be performed. Indeed complex ions $[Ga(NH_2)_4]^-$ result as the most stable species

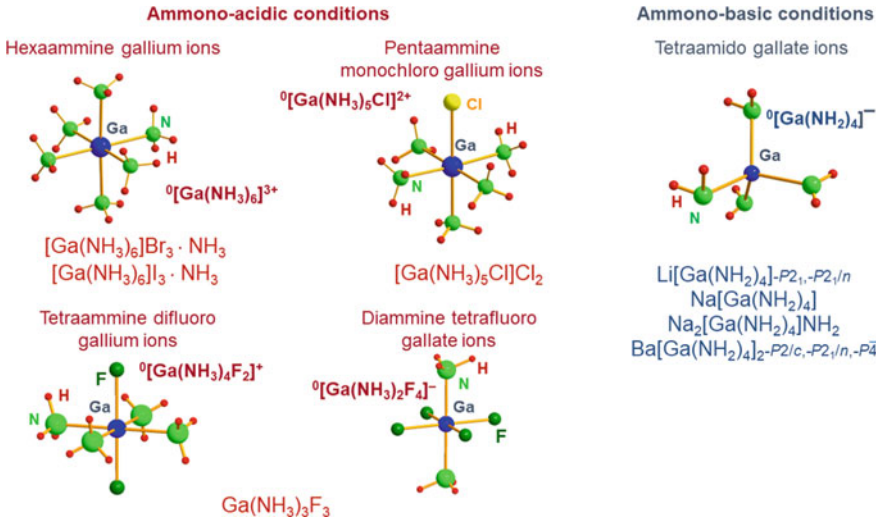

Fig. 13.1 Overview on solid crystalline intermediates in ammonothermal GaN synthesis. Gallium in octahedral coordination by ammine and halide ligands occurs in ammonoacidic milieus depending on the applied ammonoacid (left, red labels). In contrast, exclusively tetrahedral coordination by amide ions was observed in the solid compounds after ammonobasic treatment (right, blue labels)

in molecular dynamics studies, while rather drastic ammonoacidic conditions are necessary to stabilize an alternative charge neutral $[Ga(NH_2)_3(NH_3)_2]$ complex (see Chap. 15) [105]. Interestingly, aluminium ions result slightly less acidic in ammonia solutions than gallium ions according to these calculations, which would make the charge neutral complex more preferred even close to the ammononeutral milieu. Mildly basic conditions, however, appear to favor formation of negatively charged octahedral complexes $[Al(NH_3)_2(NH_2)_4]^-$, so far unseen in any solid crystallized intermediate containing alkali or alkaline-earth metal ions.

Upon turning to the heavier alkali metals potassium, rubidium or cesium, which all represent effective mineralizers for ammonobasic GaN synthesis, viscous liquids instead of crystalline solids are obtained after reacting Ga-containing precursors with these mineralizers under ammonothermal conditions and subsequent venting the excess ammonia at room temperature and ambient pressure. These oily liquids may eventually solidify, producing amorphous or badly crystallized solids after hours, days or even years, depending on alkali metal and purity of the sample. During aging and solidification, the sample does not necessarily show distinct changes in composition. The potassium containing liquid was described as "$KGa(NH)_n \cdot x\ NH_3$" according to acid base titration [91, 92], however, may lose some ammonia over time. Early tensimetric studies of the decomposition were taken as indication for the concomitant presence of amide and imide ions [93]. Earlier, the formation of a liquid during thermal decomposition of solid sodium tetraamidoaluminate, $Na[Al(NH_2)_4]$, under loss of about two equivalents of ammonia was reported, indicating the formation of a sodium diimidoaluminate [88]. Similarly, the presence of imide ions in

thermal decomposition products of alkaline-earth metal amidoaluminates was several times discussed [94, 106–108]. Recent studies indicate a stepwise condensation during the thermal decomposition of $Li[Al(NH_2)_4]$ to eventually form AlN and $Li_3[AlN_2]$ via intermediate phases with general composition $LiAl(NH_2)_x(NH)_yN_z$, [109] but follow-up investigations found no indication for the occurrence of imide species during this process [110].

All three liquids—containing potassium, rubidium or cesium—are fully miscible with ammonia at room temperature providing the possibility to study differently concentrated solutions as well as highly concentrated phases. Exemplarily, the liquid formed with cesium amide was studied in more detail [104]. Solution NMR investigations at ambient temperatures and under autogenous pressure (below 8 bars) reveal the exclusive presence of $[Ga(NH_2)_4]^-$ as gallium-containing species in diluted solutions. Upon reduction of the ammonia content in the liquid phase via application of vacuum and gentle heating, this species is in equilibrium with condensed μ-imide bridged complex ions $[(NH_2)_3Ga(NH)Ga(NH_2)_3]^{2-}$ and eventually $[(NH_2)_2Ga(NH)_2Ga(NH_2)_2]^{2-}$, which may be taken to represent first condensation steps towards GaN formation. Small oxygen impurities lead to the presence of the corresponding μ-oxide bridged dinuclear complex $[(H_2N)_3Ga(O)Ga(NH_2)_3]^{2-}$. These interrelations are visualized in Scheme 13.1. The Rb-containing liquid according to IR, Raman und NMR spectroscopy is very similar to the one obtained from reaction of $CsNH_2$ [24, 104]. A preliminary in situ ramanspectroscopic investigation of mixtures of the Cs-containing liquid with ammonia at elevated temperatures may indicate the presence of $[Ga(NH_2)_4]^-$ ions up to at least 545 K [24].

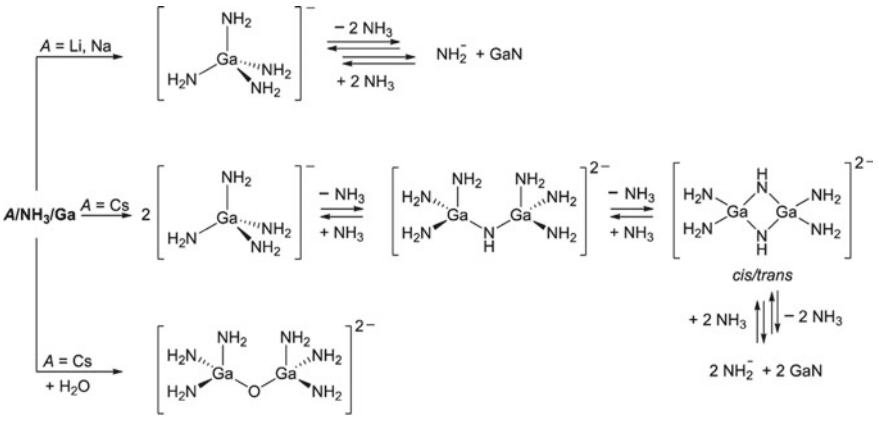

Scheme 13.1 Reactions of Ga-sources under ammonothermal conditions with different alkali metal amides serving as mineralizer and occurring equilibria of Ga-containing complex species. Reprinted with permission from J. Hertrampf, E. Schlücker, D. Gudat, R. Niewa, Cryst. Growth & Design Copyright 2017 American Chemical Society

13.3.2 Intermediates in Gallium Nitride Crystal Growth Under Ammonoacidic Conditions

Solid intermediates in ammonacidic solutions were typically obtained under reduced temperature and pressure conditions than usually applied for ammonothermal crystal growth of GaN. Upon use of the different ammonium halides or alternatively the gallium trihalides the following compounds could be unambiguously characterized so far: $[Ga(NH_3)_4F_2][Ga(NH_3)_2F_4]$ (=$GaF_3 \cdot 3NH_3$), $[Ga(NH_3)_5Cl]Cl_2$ (=$GaCl_3 \cdot 5NH_3$), $[Ga(NH_3)_6]Br_3 \cdot NH_3$ and $[Ga(NH_3)_6]I_3 \cdot NH_3$ (=$GaX_3 \cdot 7NH_3$). While the iodide and the bromide already crystallize at ambient temperature from solutions of the respective gallium trihalide in liquid ammonia, the chloride and the fluoride were obtained in the colder zone of the autoclave interior from ammothermal conditions [74]. The latter fact is in close agreement to the transport direction of GaN with use of ammonium chloride, bromide or iodide in the temperature range 200–550 °C [59, 111]. At higher temperatures above 923 K and 110 MPa the solubility of GaN with ammonium chloride mineralizer apparently changes to retrograde, meaning the GaN is transported to the hotter spot in the autoclave [112]. Similarly, a negative temperature dependence of the GaN solubility was observed for use of ammonium fluoride as mineralizer above 923 K [113].

The crystals of the chloride and the fluoride intermediates obtained from unlined autoclaves typically were colored violet or reddish, due to incorporation of nickel or chromium ions, respectively, originating from the autoclave material due to corrosion by the aggressive ammonoacidic medium [92]. Upon application of silver liners to minimize the contact of the medium and the autoclave alloy surface, the fluoride presents colorless [114]. The chloride was earlier synthesized via a different technique from organic solvent in glass ampoules and also presented colorless as expected [115]. At ambient pressure, the iodide and the bromide slowly loose ammonia, while both compounds as well as the chloride hydrolyze quickly in air. The fluoride in contrast is stable in air for longer periods of days to months. Upon heating in inert atmosphere, all four halides decompose under ammonia loss to eventually reform the gallium trihalide, however, small amounts of *h*-GaN are obtained as by-product.

In the crystal structures of the solid intermediates, gallium is exclusively octahedrally coordinated. Complex hexaamminegallium ions, $[Ga(NH_3)_6]^{3+}$, occur in case of the iodide and bromide as complex cations, while with chloride pentaamminemonochlorogallium ions, $[Ga(NH_3)_5Cl]^{2+}$, are present. In the fluoride compound both cation and anion are composed of gallium, fluoride and ammonia ligands, namely tetraamminedifluorogallium cations, $[Ga(NH_3)_4F_2]^{+}$, and diamminetetrafluorogallate anions, $[Ga(NH_3)_2F_4]^{-}$. From a chemical bonding point of view, the harder fluoride ion prefers to enter the first coordination sphere of gallium and partially supersedes ammonia. The larger chloride ion is still able to act in such way during crystallization of a solid compound from ammonoacidic solution, while this is not preferred for the even larger anions bromide and iodide. According to molecular dynamic simulations, under ambient conditions fluoride and gallium ions in liquid ammonia form both positive and negative charged ions, however with a

higher coordination numbers for gallium than found in the solid state: $[GaF_2(NH_3)_6]^+$ and $[GaF_4(NH_3)_4]^-$ ions with no apparent exchange of protons or ammonia ligands with the solvent were observed during the simulations [116], while the solubility of the isolated solid intermediate under this conditions is vanishing low, thus no experimental data are available up to date. The increased GaN growth rate for both the Ga- and the N-terminated face with ammonium fluoride as mineralizer may be taken as an indication for the presence of such ions of both charges even at elevated temperatures and pressures of ammonoacidic crystal growth [113]. However, upon increasing temperature the molecular dynamic simulations indicate the tendency to form ion pairs and multinuclear complexes due to decreasing polarity (i.e. permittivity) of ammonia under these conditions (see also Chap. 15) [116]. In case of ammonium chloride as mineralizer, a faster growth rate was reported for the nitrogen-terminated facet [111], while generally growth in both polar directions is observed, but only little growth on non-polar facets [14, 113]. Figure 13.1 gives an overview on all solid crystalline intermediates characterized so far.

Solution NMR studies of the dissolved intermediates as well as gallium trihalides in liquid ammonia at ambient temperatures and under autogenous pressures (<8 bar), reveal nearly no solubility of the fluoride compounds in agreement with the extremely low solubility of ammonium fluoride itself. For the iodide and the bromide, the exclusive presence of the hexaamminegallium ions was indicated, which are also present in the characterized solid intermediates [114].

13.4 Indium Nitride

While the crystal growth of GaN has seen significant advances in recent years and particularly the ammonothermal synthesis already presents high-quality substrate crystals, InN is still notoriously difficult to produce. One major problem in InN synthesis is the low thermal stability (decomposition ~ 500 °C) [117] of InN and the low heat of formation of -28.6 ± 9.2 kJ/mol. According to calorimetric measurements, indium nitride is metastable towards the decomposition into the elements above 258 K [118]. In InN layers and films obtained by CVD techniques at elevated temperatures the occurrence of In nanoparticles and four atom clusters is suspected. Such defects and impurities consequently would have significant influence on experimentally obtained physical properties like electron mobility and saturation velocity [119, 120]. A second obstacle is the lower reduction potential of rather noble indium, which facilitates the formation of metallic In from the feedstock material or dissolved intermediates upon contact with the metallic autoclave wall. Subsequent chemical reactions to intermetallic compounds like In_3Ni_2 along grain boundaries of Ni-based superalloy materials may lead to severe deterioration of the stability and thus destruction of the autoclave [92]. However, this effect can be minimized by use of ceramic liners fabricated from, for example, boron nitride or silicon nitride.

Triggered by the achievements in ammonothermal GaN crystal growth the successful ammonothermal InN synthesis was predicted in 1995 to be aided by

the stabilizing effect of ammonia and nitrogen pressures [80]. Indeed, Wang and Callahan indicated the formation of microcrystalline InN from metallic indium with KNH_2 as mineralizer at 450 °C under ammonothermal conditions, but gave no details [21]. In an independent study, the transport of elemental indium in a temperature gradient under ammonacidic conditions was observed [5]. Recently, the successful InN synthesis and growth of crystals in the micrometer range was presented [23]. Interestingly, the solely application of neither typical ammonoacidic nor ammonobasic mineralizers provided good products, eventually containing only small amounts of the desired nitride next to larger amounts of elemental indium. However, quantitative conversion into small InN crystals with sizes in the micrometer range were obtained from $InCl_3$ upon reaction with three equivalents KNH_2 in supercritical ammonia, expected to provide an essentially ammononeutral milieu after formation of well soluble KCl. After venting the ammonia the products thus consist of well crystallized InN next to significantly larger potassium chloride crystals. Size and morphology of the obtained InN crystals vary with process parameters like detailed heating program and maximum synthesis temperature, while the maximum pressure has little effect. Furthermore, even small indium oxide impurities during synthesis apparently provide preferred nucleation centers and lead to spherical aggregates of smaller crystals. Figure 13.2 presents selected micrographs of obtained samples under various synthesis conditions.

Only few studies address intermediates in such ammonothermal InN syntheses so far. This may be related to the above finding, in complete contrast to ammonothermal GaN crystal growth, that the InN formation in ammonoacidic as well as ammonobasic milieu appears not favored. Additionally, higher ammoniates of indium halides seem rather unstable against decomposition, still indications for formation of similar intermediates as found for the ammonoacidic GaN crystal growth were obtained [92]. Additionally, apparently air- and water-stable crystals of an indium fluoride imide ammoniate, $InF_2(NH_2)(NH_3)$, were grown from InN and ammonium fluoride in supercritical ammonia at 400 °C and a maximum pressure of 2.2 Kbar, suggesting the presence of soluble species in the ammonium fluoride acidic system [121]. In a different experiment starting from indium metal and ammonium chloride without ammonia serving as a solvent, the triammoniate $In(NH_3)_3Cl_3$ constituting of cationic $[In(NH_3)_4Cl_2]^+$ and anionic $[In(NH_3)_2Cl_4]^-$ building units was observed, in close correspondence to the Ga-containing intermediate $Ga(NH_3)_3F_3$ from ammonothermal GaN crystal growth applying ammonium fluoride as mineralizer [122].

Indium amide, $In(NH_2)_3$, apparently was obtained from InI_3 and three equivalents KNH_2 in liquid ammonia at room temperature [123]. The indium amide in turn was used for reactions with alkali metal amides likewise in liquid ammonia at room temperature to yield compounds denoted $Li_3In(NH_2)_6$, $Na_xIn(NH_2)_{3+x}$ ($x = 1$–3) and $K_xIn(NH_2)_{3+x}$ ($x = 2, 3$) according to chemical analysis and vibrational spectroscopy. Thermolysis of $In(NH_2)_3$, $Na_xIn(NH_2)_{3+x}$ and $K_xIn(NH_2)_{3+x}$ yields InN next to eventual amounts of metallic In, while $Li_3In(NH_2)_6$ thermally decomposes to a new compound designated to represent a ternary lithium indium nitride. In an independent study applying an excess of KNH_2 on $InCl_3$ under otherwise similar

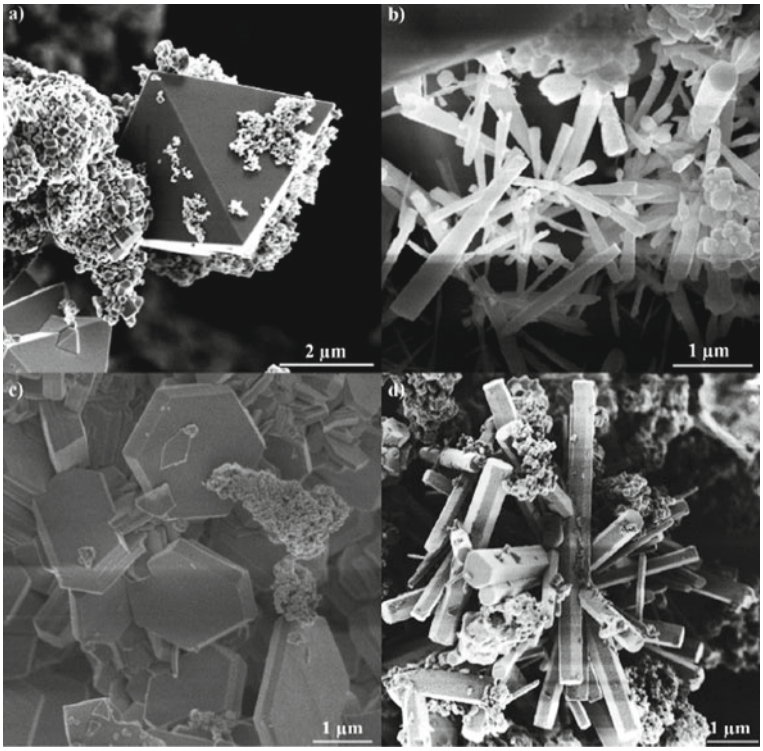

Fig. 13.2 REM images of ammonothermally obtained InN crystals with different morphologies depending on synthesis temperature: **a** 773 K, KCl octahedra and sphere-shaped aggregates of needle-like hexagonal InN crystals probably centered by an In_2O_3 impurity, **b** 773 K, hexagonal rods, **c** 633 K hexagonal plates, **d** 663 K followed by 773 K, hexagonal rods. Reprinted in part with permission from J. Hertrampf, P. Becker, M. Widenmeyer, A. Weidenkaff, E. Schlücker, R. Niewa, Cryst. Growth Design 2018 American Chemical Society

ammonobasic synthesis conditions a compound $KIn(NH_2)_4$ was obtained according to results of tensiometric decomposition investigations and vibrational spectroscopy, while the crystal structure could not be reliably determined [93].

13.5 Zinc Nitride

Zinc nitride recently gained considerable attention as promising n-type semiconductor with a narrow direct bandgap around 1 eV, a carrier concentration of $10^{19}-10^{20}$ cm^{-3} and an electron effective mass of about 0.3 m_0 (for Zn_3N_2 grown from rf-molecular beam epitaxy) [124–127]. While currently no crystal growth technique for Zn_3N_2 is known, ammonothermal conditions appear reasonable to be successful. Additionally, the study of intermediates and dissolved species containing zinc may

aid in a devoted ammonothermal synthesis of ternary materials like Zn*Tt*N_2 (*Tt* = Si, Ge, Sn) [42], which do not contain resource-critical elements like In or Ga and present direct optical band-gaps in the range of those of GaN and InN (see also Chaps. 2 and 12). Thus, such ternary nitrides and their mutual solid solutions are discussed to represent potential replacements for these III–V semiconductors in the future [128–131]. However, no successful ammonothermal synthesis or crystal growth of Zn_3N_2, neither ammonbasic nor ammonoacidic could be presented so far. Apparently, the decomposition of the dissolved intermediate species to Zn_3N_2 and subsequent solid precipitation requires higher temperatures above 1000 K, which were not accessible with the used autoclave materials so far. Still, a number of solid compounds were isolated from zinc-containing solutions under ammonothermal conditions, which represent the dissolved species or compounds formed from the dissolved material during precipitation and therefore are likely to be intermediates in a conceivable zinc nitride crystal growth. Figure 13.3 gives an overview on selected Zn-containing intermediates, depending on dimensionality in the amidozincate framework of the crystal structure, generally scaling with the synthesis temperature.

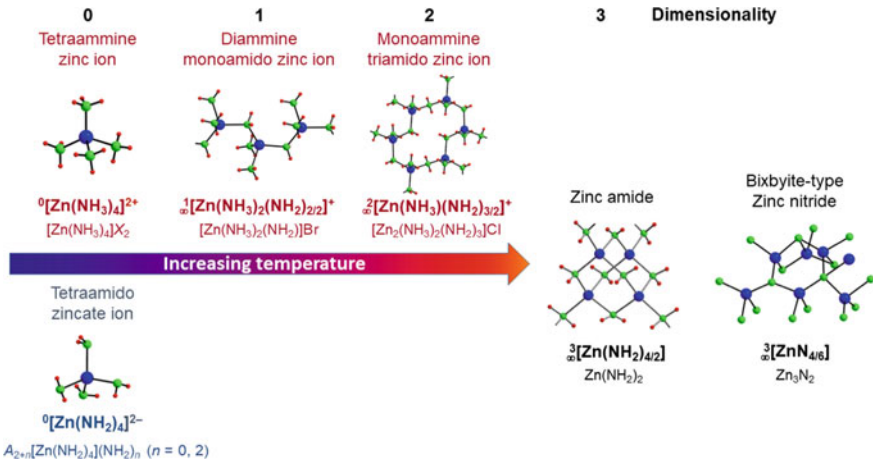

Fig. 13.3 Solid crystallized intermediates in conceivable ammonothermal growth of zinc nitride. At lower synthesis temperatures exclusively compounds containing isolated tetrahedral ions $[Zn(NH_2)_4]^{2-}$ in basic milieu (blue labels, A = alkali metal) and $[Zn(NH_3)_4]^{2+}$ in acidic (red labels, X = halide) were observed, if ammonium chloride, bromide or iodide were employed as ammonoacids. With ammonium fluoride as ammonoacid condensation over fluoride ligands occurs (not shown). While further condensation steps upon temperature increase under ammonobasic conditions still are enigmatic, in ammonoacidic solutions, compounds containing one and two dimensional amido-bridged building units were presented. Eventually increased temperatures led to formation of zinc amide with a three-dimensional amido-bridged network, however, zinc nitride with an even higher condensed framework was not obtained so far

13.5.1 Zn-Containing Intermediates Formed Under Ammonobasic Conditions

The study of alkali metal amidozincates has a long tradition. Early explorative work was mostly carried out in liquid ammonia [102, 132, 133]. $Li_4[Zn(NH_2)_4](NH_2)_2$ [134], $Na_2[Zn(NH_2)_4]\cdot 0.5NH_3$ [135], $K_2[Zn(NH_2)_4]$ in two modifications [100, 101, 103, 136], $Rb_2[Zn(NH_2)_4]$ [136], and $Cs_2[Zn(NH_2)_4]$ [137, 138] are established compounds within these systems. Additionally, $Na_3[Zn(NH_2)_4](NH_2)$ and $Na_3[Zn(NH_2)_3](NH_2)_2$ were obtained and characterized via X-ray diffraction, but vibrational spectroscopy reveals the presence of OH-groups in addition to the amide ions. Since X-ray diffraction is virtually unable to distinguish between oxygen and nitrogen atoms and it was currently not possible to quantify the oxide content. Thus, the exact nature these compounds, for examples as amide hydroxides, and the relevance of OH^-/H_2O-constituents for formation remains enigmatic [134]. The monoclinic modification of $K_2[Zn(NH_2)_4]$ as well as $Rb_2[Zn(NH_2)_4]$ and $Cs_2[Zn(NH_2)_4]$ crystallize as isotypes. In all unambiguously characterized alkali metal amidozincates, Zn^{2+} is tetrahedrally surrounded by four amide groups resulting in isolated $[Zn(NH_2)_4]^{2-}$ complex ions, while $Na_3[Zn(NH_2)_3](NH_2)_2$ shows infinite chains of such units connected via vertex-sharing.

Below 450 °C all these amidozincates were obtained in the colder zone of the autoclave, indicating a positive (normal) temperature dependence of the solubility. However, at higher temperatures crystals of monoclinic $K_2[Zn(NH_2)_4]$ grow at the highest temperature spot, demonstrating a change of the temperature dependence of the solubility to retrograde. Particularly the growth of large $Cs_2[Zn(NH_2)_4]$ crystals of up to several centimeters underlines its high solubility in ammonia under the applied ammonothermal conditions, which is in agreement with the concomitant high solubility of binary cesium amide itself. Figure 13.4 shows a photograph of one of the obtained crystal aggregates. All compounds comprising the heavier alkali metals Na–Cs can be synthesized from zinc powder and the binary alkali metal amides as reactant and mineralizer in supercritical ammonia. In contrast, $Li_4[Zn(NH_2)_4](NH_2)_2$ under these conditions was exclusively obtained from lithium metal instead of lithium

Fig. 13.4 Typical crystal aggregate of $Cs_2[Zn(NH_2)_4]$ together with a 10 €-ct. coin for size comparison. Photograph taken while sample was stored in inert gas. From T. M. M. Richter, N. S. A. Alt, E. Schlücker, R. Niewa, Z. Anorg. Allg. Chem. Copyright 2016 by John Wiley & Sohns, Inc. Reprinted with permission of John Wiley & Sohns, Inc.

amide, possibly reflecting the limited solubility of lithium amide once formed in combination with a rather high thermal and chemical stability of binary zinc amide [134, 139].

Frequently, binary zinc amide, $Zn(NH_2)_2$, was observed as by-product next to the described amidozincates, or at higher process temperatures as main product, while no binary zinc nitride was obtained under ammonobasic conditions so far. Still, microcrystalline Zn_3N_2 can be obtained from thermal decomposition of $Zn(NH_2)_2$ in inert atmosphere at 200 °C [140–142], indicating that the decomposition to the binary zinc nitride under ammonothermal conditions might be feasible at higher temperatures and concomitant low ammonia pressures. Unfortunately, the ternary solid alkali metal amidozincates do not decompose under formation of binary zinc nitride. The potassium and the cesium compounds rather decompose via intermetallic alkali metal zinc phases, while the lithium tetraamidozincate diamide produces the ternary nitride LiZnN [143] next to lithium amide. Recently, it was shown that crystals of $ZnSiN_2$ and $ZnGeN_2$ can be grown ammonothermally using potassium amide as mineralizer [42]. Furthermore, the magnesium and manganese analogues were synthesized under similar conditions [43].

Particularly the alkali metal amidozincates, as well as the respective alkali metal amidomanganates, in mixtures with LiH turned out to represent effective catalysts for superfast hydrogen absorption and desorption and thus may possibly find use in hydrogen storage materials [144–146]. Furthermore, such materials catalyze the equilibration of ammonia, hydrogen and nitrogen gas mixtures, thus have potential for ammonia synthesis and decomposition applications [99].

13.5.2 Zn-Containing Intermediates Formed Under Ammonoacidic Conditions

Until recently only few ammoniates of zinc halides were reported, namely $[Zn(NH_3)_2Cl_2]$ and $[Zn(NH_3)_2Br_2]$ [147], $[Zn(NH_3)_4]Br_2$ and $[Zn(NH_3)_4]I_2$ [148], all constituting tetrahedral coordination of zinc. With application of ammonium fluoride as ammonoacid, crystals of $ZnF_2(NH_3)_3$ and $ZnF_2(NH_3)_2$ were obtained under ammonothermal conditions (250 °C, 196 MPa and 500 °C, 136 MPa, respectively), with the triammoniate as major product at lower and the diammoniate at higher temperatures. The pressure has little influence on the products, as long as a minimum pressure for formation of the ammoniates is reached. For comparison, zinc difluoride does not react with gaseous ammonia of about 1 bar below temperatures of 250 °C. Upon thermal decomposition of both $ZnF_2(NH_3)_3$ and $ZnF_2(NH_3)_2$ a further intermediate $ZnF_2(NH_3)$ was obtained at about 150 °C prior formation of ZnF_2, which, however, was not observed from liquid ammonia solutions.

In $ZnF_2(NH_3)_3$ and $ZnF_2(NH_3)_2$ trigonal bipyramidal coordination environments of fluoride and NH_3 ligands around Zn^{2+} are realized [149]. The resulting isolated

units $ZnF_2(NH_3)_3$ constitute the respective triammoniate and are further interconnected via hydrogen bonding. In $ZnF_2(NH_3)_2$ the trigonal bipyramidal surrounding of Zn is realized by condensation at two of three fluoride ligands at the axial positions, resulting in infinite chains $^1_\infty[Zn(NH_3)_2F_{2/2}F]$. Again these chains are interconnected via hydrogen bonding.

The treatment of excess zinc in the presence of ammonium chloride or bromide under ammonothermal conditions leads to diamminetriamidodizinc chloride $[Zn_2(NH_3)_2(NH_2)_3]Cl$ (600 °C and 97 MPa) and diamminemonoamidozinc bromide $[Zn(NH_3)_2(NH_2)]Br$ (500 °C, 230 MPa), respectively. Both ammoniates of zinc amide halides were observed to crystallize in the colder zone of the autoclave, while additionally $Zn(NH_2)_2$ was obtained in the hotter zone. Although $Zn(NH_2)_2$ was reported to be insoluble in liquid ammonia at ambient conditions [150], we have frequently observed that it forms from Zn under various ammonoacidic and ammonobasic conditions in the colder zone of the autoclave in large crystals. This indicates an ammonoamphoteric character of Zn and an enhanced solubility at elevated temperatures and pressures. Furthermore, apparently the temperature dependence of the solubility can be adjusted by addition of halide ions and thus less soluble compounds crystallize in the lower temperature zone, while zinc amide may be found in zones of higher temperatures. $[Zn_2(NH_3)_2(NH_2)_3]Cl$ realizes a two-dimensionally μ-amido interconnected cationic substructure, while $[Zn(NH_3)_2(NH_2)]Br$ constitutes one-dimensional infinite μ-amido bridged cationic chains next to bromide ions [151].

References

1. R. Juza, H. Jacobs, Ammonothermal synthesis of magnesium and beryllium amides. Angew. Chem. Int. Ed. **5**, 247 (1966)
2. T.M.M. Richter, R. Niewa, Chemistry of ammonothermal synthesis. Inorganics **2**, 29–78 (2014)
3. S. Zhang, D.A. Zherebtsov, F.J. DiSalvo, R. Niewa, $Na_5[CN_2]_2[CN]$, $(Li, Na)_5[CN_2]_2[CN]$, and $K_2[CN_2]$: carbodiimides from high-pressure synthesis. Z. Anorg. Allg. Chem. **638**, 2111–2116 (2012)
4. M. Mallmann, J. Häusler, N. Cordes, W. Schnick, Ammonothermal synthesis of alkali-alkaline earth metal and akali-rare earth metal carbodiimides: $K_{5-x}M_x(CN_2)_{2+x}(HCN_2)_{1-x}$ (M=Sr, Eu) and $Na_{4.32}Sr_{0.68}(CN_2)_{2.68}(HCN_2)_{0.32}$. Z. Anorg. Allg. Chem. 643, 1956–1961 (2017)
5. A.P. Purdy, S. Case, C. George, Ammonothermal crystal growth of Germanium and its alloys: synthesis of a hollow metallic crystal. Cryst. Growth Design **3**, 121–124 (2003)
6. H. Jacobs, D. Schmidt, High-pressure ammonolysis in solid-state chemistry. Curr. Top. Mater. Sci. **8**, 387–427 (1982)
7. H. Jacobs, H. Kistrup, Über das System Kalium/Samarium/Ammoniak. Z. Anorg. Allg. Chem. **435**, 127–136 (1977)
8. H. Jacobs, U. Fink, Untersuchung des Systems Kalium/Europium/Ammoniak. Z. Anorg. Allg. Chem. **438**, 151–159 (1978)
9. G. Linde, R. Juza, Amidometallate von Lanthan und Gadolinium und Umsetzung von Lanthan, Gadolinium und Scandium mit Ammoniak. Z. Anorg. Allg. Chem. **409**, 191–198 (1974)
10. A. Stuhr, H. Jacobs, R. Juza, Amide des Yttriums. Z. Anorg. Allg. Chem. **395**, 291–300 (1973)

11. H. Jacobs, D. Schmidt, Struktur und Eigenschaften von perowskitartigen Caesiumamidometallaten des Cers, Neodyms und Samariums $Cs_3Ln_2(NH_2)_9$. J. Less-Common Met. **76**, 227–244 (1980)
12. B. Harbrecht, H. Jacobs, Hochdrucksynthese von Caesiumamidazid, $Cs_2(NH_2)N_3$ aus Caesiummetall und Ammoniak. Z. Anorg. Allg. Chem. **500**, 181–187 (1983)
13. S. Pimputkar, T.F. Malkowski, S. Griffiths, A. Espenlaub, S. Suihkonen, J.S. Speck, S. Nakamura, Stability of materials in supercritical solutions. J. Supercrit. Fluids **110**, 193–229 (2016)
14. K. Yoshida, K. Aoki, T. Fukuda, High-temperature acidic ammonothermal method for GaN crystal growth. J. Cryst. Growth **393**, 93–97 (2013)
15. R. Dwiliński, J.M. Baranowski, M. Kamińska, R. Doradziński, J. Garczyński, L. Sierzputowski, On GaN crystallization by ammonotherma method. Acta Phys. Pol., A **90**, 763–766 (1996)
16. D. Ketchum, J. Kolis, Crystal growth of gallium nitride in supercritical ammonia. J. Cryst. Growth **222**, 431–434 (2001)
17. R.J. Jouet, A.P. Purdy, R.L. Wells, J.F. Janik, Preparation of phase pure cubic gallium nitride, c-GaN, by ammonothermal conversion of gallium imide, $\{Ga(NH)_{3/2}\}_n$. J. Clust. Sci. **13**, 469–486 (2002)
18. M. Zając, J. Gosk, E. Grzanka, S. Stelmakh, M. Palczewska, A. Wysmołek, K. Korona, M. Kamińska, A. Twardowski, Ammonothermal synthesis of GaN doped with transition metal ions (Mn, Fe, Cr). J. Alloys Compd. **456**, 324–338 (2008)
19. D. Peters, Ammonothermal synthesis of aluminum nitride. J. Cryst. Growth **104**, 411–418 (1990)
20. Y.C. Lan, X.L. Chen, Y.G. Cao, Y.P. Xu, L. Xun, T. Xu, J.K. Liang, Low-temperature synthesis and photoluminescence of AlN. J. Cryst. Growth **207**, 247–250 (1999)
21. B. Wang, M. Callahan, Ammonothermal synthesis of III-nitride crystals. Cryst. Growth Des. **6**, 1227–1246 (2006)
22. R. Dwilinski, R. Doradzinski, J. Garcynski, L. Sierzputowski, M. Palczewska, A. Wysmolek, M. Kaminska, AMMONO method of BN, AlN and GaN synthesis and crystal growth. MRS Internet J. Nitride Semicond. Res. **3**, e25 (1998)
23. J. Hertrampf, P. Becker, M. Widenmeyer, A. Weidenkaff, E. Schlücker, R. Niewa, Ammonothermal crystal growth of indium nitride. Cryst. Growth Design **148**, 2365–2369 (2018)
24. J. Hertrampf, Intermediate in der ammonothermalen GaN-Kristallzucht durch Einsatz neuartiger Mineralisatoren und Synthesestrategie für Indiumnitrid. Doctoral Thesis, Universität Stuttgart, 2017
25. G. Kreiner, H. Jacobs, Magnetische Struktur von η-Mn_3N_2. J. Alloys Compd. **183**, 345–362 (1992)
26. H. Jacobs, C. Stüve, Hochdrucksynthese der η-Phase im system Mn–N: Mn_3N_2. J. Less-Common Met. **96**, 323–329 (1984)
27. A. Leineweber, H. Jacobs, S. Hull, Ordering of nitrogen in nickel nitride Ni_3N determined by neutron diffraction. Inorg. Chem. **40**, 5818–5822 (2001)
28. U. Zachwieja, H. Jacobs, Ammonothermalsynthese von Kupfernitrid, Cu_3N. J. Less-Common Met. **161**, 175–184 (1990)
29. H. Jacobs, D. Rechenbach, U. Zachwieja, Structure determination of γ-Fe_4N and ε-Fe_3N. J. Alloys Compd. **227**, 10–17 (1995)
30. H. Jacobs, D. Rechenbach, U. Zachwieja, Untersuchungen zur Struktur und zum Zerfall von Eisennitriden—γ′-Fe_4N und ε-Fe_3N. Härterei Techn. Mitt. **50**, 205–213 (1995)
31. H. Jacobs, J. Bock, Einkristallzüchtung von γ′-Fe_4N in überkritischem Ammoniak. J. Less-Common Met. **134**, 215–220 (1987)
32. H. Jacobs, U. Zachwieja, Kupferpalladiumnitride, Cu_3Pd_xN mit x = 0,020 und 0,989, Perowskite mit "bindender $3d^{10}$-$4d^{10}$-Wechselwirkung". J. Less-Common Met. **170**, 185–190 (1991)

33. J. Häusler, L. Neudert, M. Mallmann, R. Niklaus, A.-C. Kimmel, N.S.A. Alt, E. Schlücker, O. Oeckler, W. Schnick, Ammonothermal synthesis of novel nitrides: case study on $CaGaSiN_3$. Chem. Eur. J. **23**, 2583–2590 (2017)
34. J. Li, T. Watanabe, H. Wada, T. Setoyama, M. Yoshimura, Low-temperature crystallization of Eu-doped red-emmiting $CaAlSiN_3$ from alloy-derived ammonometallates. Chem. Mater. **19**, 3592–3594 (2007)
35. T. Watanabe, K. Nonaka, J. Li, K. Kishida, M. Yoshimura, Low temperature ammonothermal synthesis of europium-doped $SrAlSiN_3$ for a nitride red phosphor. J. Ceram. Soc. Jpn. **120**, 500–502 (2012)
36. Y. Maruyama, Y. Yanase, T. Watanabe, Ammonothermal synthesis of charge-compensated $SrAlSiN_3$:Ce^{3+} phosphor. J. Ceramic Soc. Jpn. **125**, 399–401 (2017)
37. Y. Maruyama, T. Watanabe, Low-temperature synthesis of $CaAlSiN_3$:Ce^{3+} using the ammonothermal method. J. Ceramic Soc. Jpn. **124**, 66–69 (2016)
38. J. Li, T. Watanabe, N. Sakamoto, H.S. Wada, T. Setoyama, M. Yoshimura, Synthesis of a multinary nitride, Eu-doped $CaAlSiN_3$ from alloy at low temperatures. Chem. Mater. **20**, 2095–2105 (2008)
39. J. Li, T. Watanabe, H. Wada, T. Setoyama, M. Yoshimura, Synthesis of Eu-doped $CaAlSiN_3$ from ammonometallates: effects of Sodium content and pressure. J. Amer. Ceram. Soc. **92**, 344–349 (2009)
40. K. Nonaka, K. Kishida, C. Izawa, T. Watanabe, Low Temperature ammonothermal synthesis of europium-doped $SrAlSiN_3$: effect of mineralizers. J. Ceram. Soc. Jpn. **122**, 17–20 (2014)
41. U. Zachwieja, H. Jacobs, Kollumnarstrukturen bei Tri- und Diamminnitraten, $[M(NH_3)_3]NO_3$ und $[M(NH_3)_2]NO_3$ des einwertigen Kupfers und Silbers. Z. Anorg. Allg. Chem. **571**, 37–50 (1989)
42. J. Häusler, S. Schimmel, P. Wellmann, W. Schnick, Ammonothermal synthesis of earth-abundant nitride semiconductors $ZnSiN_2$ and $ZnGeN_2$ and dissolution monitoring by in situ X-ray imaging. Chem. Eur. J. **23**, 1–9 (2017)
43. J. Häusler, R. Niklaus, J. Minár, W. Schnick, Ammonothermal synthesis and optical properties of ternary nitride semiconductors Mg-IV-N_2, Mn-IV-N_2 and Li-IV_2-N_3 (IV = Si, Ge). Chem. Eur. J. **24**, 1686–1693 (2018)
44. T. Toshima, K. Kishida, Y. Maruyama, T. Watanabe, Low-temperature synthesis of $BaTaO_2N$ by an ammonothermal method. J. Ceram. Soc. Jpn. **125**, 643–647 (2017)
45. C. Izawa, T. Kobayashi, K. Kishida, T. Watanabe, Ammonothermal synthesis and photocatalytic activity of lower valence cation-doped $LaNbON_2$. Adv. Mater. Sci. Eng. 465720 (2014)
46. T. Watanabe, L. Tajima, J.W. Li, N. Matsushita, M. Yoshimura, Low-temperature ammonothermal Synthesis of $LaTaO_2N$. Chem. Lett. **40**, 1101–1102 (2011)
47. N. Cordes, W. Schnick, Ammonothermal synthesis of crystalline oxonitride perovskites *Ln*$TaON_2$ (*Ln*=La, Ce, Pr, Nd, Sm, Gd). Chem. Eur. J. **23**, 11410–11415 (2017)
48. B. Hertweck, T.G. Steigerwald, N.S.A. Alt, E. Schluecker, Corrosive degeneration of autoclaves for the ammonothermal synthesis: experimental approach and first results. Chem. Eng. Technol. **37**, 1903–1906 (2014)
49. B. Hertweck, S. Zhang, T.G. Steigerwald, N.S.A. Alt, R. Niewa, E. Schluecker, Applicability of metals as liner materials for ammonoacidic crystal growth. Chem. Eng. Technol. **37**, 1835–1844 (2014)
50. B. Hertweck, T.G. Steigerwald, N.S.A. Alt, E. Schluecker, Different corrosion behavior of autoclaves made of nickel base alloy 718 in ammonobasic and ammonoacidic environments. J. Supercrit. Fluids **95**, 158–166 (2014)
51. B. Hertweck, S. Schimmel, T. G. Steigerwald, N.S.A. Alt, P. J. Wellmann E. Schluecker, Ceramic liner technology for ammonoacidic synthesis. J. Supercrit. Fluids. 99, 76–87 (2015)
52. S. Schimmel, U. Künecke, M. Meisel, B. Hertweck, T.G. Steigerwald, C. Nebel, N.S.A. Alt, E. Schluecker, P. Wellmann, Chemical stability of carbon-based inorganic materials for in situ x-ray investigations of ammonothermal crystal growth of nitrides. J. Cryst. Growth **456**, 33–42 (2016)

53. T.F. Malkowski, S. Pimputkar, J.S. Speck, S.P. DenBaars, S. Nakamura, Acidic ammonothermal growth of gallium nitride in a liner-free molybdenum alloy autoclave. J. Cryst. Growth **456**, 21–26 (2016)
54. S. Pimputkar, J.S. Speck, S. Nakamura, Basic ammonothermal GaN growth in molybdenum capsules. J. Cryst. Growth **456**, 15–20 (2016)
55. S. Suihkonen, S. Pimputkar, S. Sintonen, F. Tuomisto, Defects in single crystalline ammonothermal gallium nitride. Adv. Electron. Mater. **3**, 1600496 (2017)
56. D. Ehrentraut, N. Hoshino, Y. Kagamitani, A. Yoshikawa, T. Fukuda, H. Itoh, S. Kawabata, Temperature effect of ammonium halogenides as mineralizers on the phase stability of gallium nitride synthezised under ammonothermal conditions. J. Mater. Chem. **17**, 886–893 (2007)
57. A. Purdy, Growth of cubic GaN crystals from hexagonal GaN feedstock. J. Cryst. Growth **281**, 355–363 (2005)
58. A.P. Purdy, R.J. Jouet, C.F. George, Ammonothermal recrystallization of gallium nitride with acidic mineralizers. Cryst. Growth Design **2**, 141–145 (2002)
59. A.P. Purdy, Ammonothermal synthesis of cubic gallium nitride. Chem. Mater. **11**, 1648–1651 (1999)
60. J.A. Jegier, S. McKernan, A.P. Purdy, W.L. Gladfelter, Ammonothermal conversion of cyclotrigallazane to GaN: synthesis of nanocrystalline and Cubic GaN from $[H_2GaNH_2]_3$. Chem. Mater. **12**, 1003–1010 (2000)
61. S. Schimmel, M. Lindner, T.G. Steigerwald, B. Hertweck, T.M.M. Richter, U. Künecke, N.S.A. Alt, R. Niewa, E. Schlücker, P. Wellmann, Determination of GaN solubility in supercritical ammonia with NH_4F and NH_4Cl mineralizer by in situ x-ray imaging of crystal dissolution. J. Cryst. Growth **418**, 64–69 (2015)
62. D. Ehrentraut, T. Fukuda, Ammonothermal crystal growth of gallium nitride: a brief discussion of critical issues. J. Cryst. Growth **312**, 2514–2518 (2010)
63. S. Griffiths, S. Pimputkar, J.S. Speck, S. Nakamura, On the solubility of gallium nitride in supercritical ammonia-sodium solutions. J. Cryst. Growth **456**, 5–14 (2016)
64. D. Tomida, K. Kuroda, N. Hoshino, K. Suzuki, Y. Kagamitani, T. Ishiguro, T. Fukuda, C. Yokoyama, Solubility of GaN in supercritical ammonia with ammonium chloride as a mineralizer. J. Cryst. Growth **312**, 3161–3164 (2010)
65. D. Tomida, T. Kuribayashi, K. Suzuki, Y. Kagamitani, T. Ishiguro, T. Fukuda, C. Yokoyama, Effect of halogen species of acidic mineralizer on solubility of GaN in supercritical ammonia. J. Cryst. Growth **325**, 52–54 (2011)
66. S. Schimmel, M. Koch, P. Macher, A.-C.L. Kimmel, T.C. Steigerwald, N.S.A. Alt, E. Schlücker, P. Wellmann, Solubility and dissolution kinetics of GaN in supercritical ammonia in presence of ammonoacidic and ammonobasic mineralizers. J. Cryst. Growth **479**, 59–66 (2017)
67. H. Hunt, L. Boncyk, Liquid ammonia as a solvent. III. The solubility of inorganic salts at 25°. J. Amer. Chem. Soc. 55, 3528–3530 (1933)
68. H. Hunt, Liquid ammonia as a solvent. I. The solubility of inorganic salts at 25°. J. Am. Chem. Soc. 54, 3509–3512 (1932)
69. J.B. Shim, G.H. Kim, Y.K. Lee, Basic ammonothermal growth of bulk GaN single crystal using sodium mineralizers. J. Cryst. Growth **478**, 85–88 (2017)
70. J. Hertrampf, N.S.A. Alt, E. Schlücker, M. Knetzger, E. Meissner, R. Niewa, Ammonothermal synthesis of GaN using $Ba(NH_2)_2$ as mineralizer. J. Cryst. Growth **456**, 2–4 (2016)
71. J. Hertrampf, N. S. A. Alt, E. Schlücker, R. Niewa, Three solid modifications of $Ba[Ga(NH_2)_4]_2$: a soluble intermediate in ammonothermal GaN crystal growth. Eur. J. Inorg. Chem. 902–909 (2017)
72. B. Fröhling, G. Kreiner, H. Jacobs, Synthese und Kristallstruktur von Mangan(II)- und Zinkamid, $Mn(NH_2)_2$ und $Zn(NH_2)_2$. Z. Anorg. Allg. Chem. **625**, 211–216 (1999)
73. P.W. Schenk, H. Tulhoff, Zur Kenntnis von Lösungssystemen in tief siedenden Lösungsmitteln 2. Mitteilung: Die Systeme Alkaliamid/Ammonia. Ber. Bunsenges. 71, 210–214 (1967)
74. S. Zhang, F. Hintze, W. Schnick, R. Niewa, Intermediates in ammonothermal GaN crystal growth under ammonoacidic conditions. Eur. J. Inorg. Chem. 5387–5399 (2013)

75. S. Zhang, N.S.A. Alt, E. Schlücker, R. Niewa, Novel alkali metal amidogallates as intermediates in ammonothermal GaN crystal growth. J. Cryst. Growth **403**, 22–28 (2014)
76. G. Demazeau, G. Goglio, A. Denis, A. Largeteau, Solvothermal synthesis: a new route for preparing nitrides. J. Phys. Cond. Matter. **14**, 11085–11088 (2002)
77. C. Yokoyama, T. Hashimoto, Q. Bao, Y. Kagamitani, K. Qiao, Ammonothermal crystal growth of gallium nitride using $ZnCl_2$ as mineralizer. Cryst. Eng. Commun. **13**, 5306–5308 (2011)
78. J. Jander, Anorganische und allgemeine Chemie in flüssigem Ammoniak, in *Chemistry in Nonaqueos Ionizing Solvents*, vol. 1 *Chemistry in Anhydrous Liquid Ammonia*, ed. by G. Jander, H. Spandau, C. C. Addison (Vieweg & Sohn, Braunschweig, 1966), pp. 1–561
79. S.R. Gunn, L.G. Green, Heats of solution in liquid ammonia at 25 °C. J. Phys. Chem. **64**, 1066–1069 (1960)
80. R. Dwiliński, A. Wysmolek, J. Baranowski, A. Kamińska, R. Doradziński, J. Garczyński, L. Sierzputowski, GaN synthesis by ammonothermal method. Acta Phys. Pol., A **88**, 833–836 (1995)
81. T. Hashimoto, F. Wu, J.S. Speck, S. Nakamura, A GaN bulk crystal with improved structural quality grown by the ammonothermal method. Nat. Mater. **6**, 568–571 (2007)
82. T. Hashimoto, F. Wu, M. Saito, K. Fujito, J.S. Speck, S. Nakamura, Status and perspectives of the ammonothermal growth of GaN substrates. J. Cryst. Growth **310**, 876–880 (2008)
83. S. Pimputkar, S. Suihkonen, M. Imade, Y. Mori, J.S. Speck, S. Nakamura, Free electron concentration dependent sub-bandgap optical adsorption characterization of bulk GaN crystals. J. Cryst. Growth **432**, 49–53 (2015)
84. W. Lin, J. Huang, D. Chen, L. Zhang, J. Huang, F. Huang, Synthesis and characterization of nanocrystalline GaN by ammonothermal method using $CsNH_2$ as mineralizer. J. Nanosci. Nanotechnol. **10**, 5741–5745 (2010)
85. P. Molinie, R. Brec, J. Rouxel, P. Herpin, Structures des Amidoaluminates Alcalins $MAl(NH_2)_4$ (M = Na, K, Cs). Structure de l' Amidogallate de Sodium $NaGa(NH_2)_4$. Acta Crystallogr. B **29**, 925–934 (1973)
86. R. Guarino, J. Rouxel, L'amidogallate de sodium. C. R. Acad. Sci. Paris Série C **264**, 1488–1491 (1967)
87. G. Lucazeau, A. Novak, P. Molinie, J. Rouxel, Spectres de vibration et structure d'un cristal d'amidogallate de sodium. J. Mol. Struct. **20**, 303–311 (1974)
88. H. Jacobs, B. Nöcker, Redetermination of structure and properties of the isotypic sodium tetramide metallates of aluminium and gallium. Z. Anorg. Allg. Chem. **619**, 381–386 (1993)
89. P. Molinie, R. Brec, J. Rouxel, Le pentaamidogallate de sodium $Na_2Ga(NH)_5$. C. R. Acad. Sci. Paris Série C **274**, 1388–1391 (1972)
90. Y. Lan, X.L. Chen, Y. Xu, Y. Cao, F. Huang, Syntheses and structure of nanocrystalline gallium nitride obtained from ammonothermal method using lithium metal as mineralizator. Mater. Res. Bull. **35**, 2325–2330 (2000)
91. B. Wang, M.J. Callahan, Transport growth of GaN crystals by the ammonothermal technique using various nutrients. J. Cryst. Growth **291**, 455–460 (2006)
92. S. Zhang, Intermediates during the Formation of GaN under Ammonothermal Conditions. Doctoral Dissertation, Universität Stuttgart, 2014
93. A. Tenten, Amide und Nitride von Nickel, Palladium und Platin sowie von Aluminium, Gallium und Indium. Doctoral Dissertation, Universität Dortmund, 1991
94. R. Guarino, J. Rouxel, L'amidogallate de potassium $KGa(NH_2)_4$ et l'imidogallate $KGa(NH)_2$. L'obtention de l'amidure de gallium $Ga(NH_2)_3$. Bull. Soc. Chim. Fr. 7, 2284–2287 (1969)
95. B. Wang, M.J. Callahan, K.D. Rakes, L.O. Bouthillette, S.-Q. Wang, D.F. Bliss, J.W. Kolis, Ammonothermal growth of GaN crystals in alkaline solutions. J. Cryst. Growth **287**, 376–380 (2006)
96. T. Hashimoto, F. Wu, J.S. Speck, S. Nakamura, Growth of bulk GaN Crystals by the basic ammonothermal method. Jpn. J. Appl. Phys. **2**, 889–891 (2007)
97. H. Jacobs, K. Jänichen, C. Hadenfeldt, R. Juza, Lithiumaluminiumamid, $LiAl(NH_2)_4$, Darstellung, röntgenographische Untersuchung, Infrarotspektrum und thermische Zersetzung. Z. Anorg. Allg. Chem. **531**, 125–139 (1985)

98. A. Tenten, H. Jacobs, Strukturen und thermisches Verhalten von Kaliumtetraaluminat, α- und β-K[Al(NH_2)$_4$]. 28. Diskussionstagung der Arbeitsgemeinschaft Kristallographie, Hannover, Germany, 1989, pp. 289–290
99. H. Cao, J. Guo, F. Chang, C. Pistidda, W. Zhou, X. Zhang, A. Santoru, H. Wu, N. Schell, R. Niewa, P. Chen, T. Klassen, M. Dornheim, Transition and Alkali metal complex ternary amides for ammonia synthesis and decomposition. Chem. Eur. J. **23**, 9766–9771 (2017)
100. T.M.M. Richter, S. Zhang, R. Niewa, Ammonothermal synthesis of dimorphic $K_2[Zn(NH_2)_4]$. Z. Kristallogr. **228**, 351–358 (2013)
101. B. Fröhling, H. Jacobs, Positions of the protons in potassium tetraamidozincate, $K_2[Zn(NH_2)_4]$. Z. Anorg. Allg. Chem. **623**, 1103–1107 (1997)
102. L. Brisseau, J. Rouxel, Les amidozincates $Na_2Zn(NH_2)_4$ et $K_2Zn(NH_2)_4$. C. R. Acad. Sci. Paris Série C **268**, 2308–2311 (1969)
103. L. Guémas, P. Palvadeau, Étude structurale de l'amidozincate de potassium $K_2Zn(NH_2)_4$. Rev. Chim. Min. **14**, 381–386 (1977)
104. J. Hertrampf, E. Schlücker, D. Gudat, R. Niewa, Dissolved species in ammonothermal GaN crystal growth: stepwise condensation of $[Ga(NH_2)_4]^-$. Cryst. Growth Design **17**, 4855–4863 (2017)
105. D. Zahn, On the solvation of metal ions in liquid ammonia: a molecular simulation study of $M(NH_2)_x(NH_3)_y$ complexes as functions of pH. RSC Adv. **7**, 54063–54067 (2017)
106. J. Rouxel, P. Palvadeau, Les amidoaluminates $SrAl_2(NH_2)_8$ et $BaAl_2(NH_2)_8$. C. R. Acad. Sci. Paris Série C **272**, 63–66 (1971)
107. J. Rouxel, R. Brec, L'amidoaluminate et L'imidoaluminate de lithium. C. R. Acad. Sci. Paris Série C **262**, 1070–1074 (1966)
108. P. Palvadeau, M. Drew, G. Charlesworth, J. Rouxel, Structure de l'amidoaluminate $CaAl_2(NH_2)_8$, NH_3. C. R. Acad. Sci. Paris Série C **275**, 881–884 (1972)
109. T. Ono, K. Shimoda, M. Tsubota, S. Kohara, T. Ichikawa, K.-I. Kojima, M. Tansho, T. Shimizu, Y. Kojima, Ammonia desorption property and structural changes of $LiAl(NH_2)_4$ on thermal decomposition. J. Phys. Chem. C **115**, 10284–10291 (2011)
110. K. Ikeda, T. Otomo, H. Ohshita, N. Kaneko, M. Tsubota, K. Suzuya, F. Fujisaki, T. Ono, T. Yamanaka, K. Shimoda, Local structural analysis on decomposition process of $LiAl(ND_2)_4$. Mater. Trans. **55**, 1129–1133 (2014)
111. D. Ehrentraut, Y. Kagamitani, C. Yokoyama, T. Fukuda, Physico-chemical features of the ammonothermal growth of GaN. J. Cryst. Growth **310**, 891–895 (2008)
112. K. Yoshida, K. Aoki, T. Fukuda, High-temperature acidic ammonothermal method for GaN crystal growth. J. Cryst. Growth **393**, 93–97 (2014)
113. Q. Bao, M. Saito, K. Hazu, K. Furusawa, Y. Kagamitani, R. Kayano, D. Tomida, K. Qiao, T. Ishiguro, C. Yokoyama, S.F. Chichibu, Ammonothermal crystal growth of GaN using an NH_4F mineralizer. Cryst. Growth Design **13**, 4158–4161 (2013)
114. P. Becker, Chemie der ammonosauren GaN-Synthese. Master-Thesis, Universität Stuttgart, 2017
115. H. Yamane, Y. Mikawa, C. Yokoyama, Pentaamminechlorogallium(III) dichloride. Acta Crystallogr. E **63**, i59–i61 (2007)
116. S. Schimmel, P. Duchstein, T.G. Steigerwald, A.-C.L. Kimmel, E. Schlücker, D. Zahn, R. Niewa, P. Wellmann, In situ X-ray monitoring of transport and chemistry of Ga-containing intermediates under ammonothermal growth conditions of GaN. J. Cryst. Growth **498**, 214–223 (2018)
117. J.W. Trainor, K. Rose, Some properties of InN films prepared by reactive evaporation. J. Electron. Mater. **3**, 821–828 (1974)
118. M.R. Ranade, F. Tessier, A. Navrotsky, R. Marchand, Calorimetric determination of the enthalpy of formation of InN and comparison with AlN and GaN. J. Mater. Res. **16**, 2824–2831 (2001)
119. T.A. Komissarova, V.N. Jmerik, S.V. Ivanov, O. Drachenko, X. Wang, A. Yoshikawa, Calorimetric determination of the enthalpy of formation of InN and comparison with AlN and GaN. Phys. Rev. B **84**, 035205 (2011)

120. X.M. Duan, C. Stampfl, Nitrogen vacancies in InN: Vacancy clustering and metallic bonding from first principles. Phys. Rev. B **77**, 115207 (2008)
121. D.R. Ketchum, G.L. Schimek, W.T. Pennington, J.W. Kolis, Synthesis of new Group III fluoride–ammonia adducts in supercritical ammonia: structures of $AlF_3(NH_2)_2$ and $InF_2(NH_2)(NH_3)$. Inorg. Chim. Acta **294**, 200–206 (1999)
122. S. Bremm, G. Meyer, Triamminetrichloroindium(III), $[InCl_3(NH_3)_3]$. Acta Crystallogr. E **59**, i110–i111 (2003)
123. A.P. Purdy, Indium(III) amides and nitrides. Inorg. Chem. **33**, 282–286 (1994)
124. T. Suda, K. Kakishita, Band-gap energy and electron effective mass of polycrystalline Zn_3N_2. J. Appl. Phys. **99**, 076101 (2006)
125. S.-H. Yoo, A. Walsh, D.O. Scanlon, A. Soon, Electronic structure and band alignment of zinc nitride, Zn_3N_2. RSC Adv. **4**, 3306–3311 (2014)
126. M. Futsuhara, K. Yoshioka, O. Takai, Structural, electrical and optical properties of zinc nitride thin films prepared by reactive rf magnetron sputtering. Thin Solid Films **322**, 274–281 (1998)
127. G. Paniconi, Z. Stoeva, R.I. Smith, P.C. Dippo, B.L. Gallagher, D.H. Gregory, Synthesis, stoichiometry and thermal stability of Zn_3N_2 powders prepared by ammonolysis reactions. J. Solid State Chem. **181**, 158–165 (2008)
128. T. Endo, Y. Sato, H. Takizawa, M. Shimada, High-pressure synthesis of new compounds, $ZnSiN_2$ and $ZnGeN_2$ with distorted wurtzite structure. Mater. Sci. Lett. **11**, 424–426 (1992)
129. S. Chen, P. Narang, H.A. Atwater, L.-W. Wang, Phase stability and defect physics of a ternary $ZnSnN_2$ semiconductor: first principles insights. Adv. Mater. **26**, 311–315 (2014)
130. P.C. Quayle, K. He, J. Shan, K. Kash, Synthesis, lattice structure, and band gap of $ZnSnN_2$. MRS Commun. **3**, 135–138 (2013)
131. N. Feldberg, J.D. Aldous, W.M. Linhart, L.J. Phillips, K. Durose, P.A. Stampe, R.J. Kennedy, D.O. Scanlon, G. Vardar, R.L. Field, T.Y. Jen, R.S. Goldman, T.D. Veal, S.M. Durbin, Growth, disorder, and physical properties of $ZnSnN_2$. Appl. Phys. Lett. **103**, 042109 (2013)
132. F.F. Fitzgerald, Reactions in liquid ammonia (potassium ammonozincate, cuprous nitride and an ammonobasic mercuric bromide). J. Am. Chem. Soc. **29**, 656–665 (1907)
133. R. Juza, Concerning the amides of the 1 and 2 groups of the periodic system metal amides I announcement. Z. Anorg. Allg. Chem. **231**, 121–135 (1937)
134. T.M.M. Richter, N.S.A. Alt, E. Schlücker, R. Niewa, Ammonothermal synthesis and characterization of $Li_4[Zn(NH_2)_4](NH_2)_2$. Z. Anorg. Allg. Chem. **641**, 1016–1023 (2015)
135. B. Fröhling, H. Jacobs, Synthesis and crystal structure of a semiammoniate of sodium tetraamidozincate, $Na_2[Zn(NH_2)_4]\cdot 0.5NH_3$. Z. Anorg. Allg. Chem. 624, 1148–1153 (1997)
136. G. Lucazeau, L. Guemas, A. Novak, Vibrational spectra and structure of $K_2Zn(NH_2)_4$ and $Rb_2Zn(NH_2)_4$ amides. Inorg. Chim. Acta **20**, 11–18 (1976)
137. L. Brisseau, J. Rouxel, Préparation, caractérisation chimique at structural d'amidozincates alcalins. Rev. Chim. Min. **7**, 427–450 (1970)
138. T.M.M. Richter, N.S.A. Alt, E. Schlücker, R. Niewa, Ammonothermal synthesis and characterization of $Cs_2[Zn(NH_2)_4]$. Z. Anorg. Allg. Chem. **642**, 1207–1211 (2016)
139. T.M.M. Richter, Darstellung von Intermediaten in der ammonothermalen Zinknitridsynthese sowie Synthesestrategien für $Sc_xGa_{1-x}N$ ($0 \leq x \leq 1$). Doctoral Dissertation, Universität Stuttgart, 2016
140. E. Frankland, On a new series of compounds derived from ammonia and its analogues. Lond. Edinb. Dubl. Phil. Mag. Ser. **4**(15), 149–152 (1858)
141. R. Juza, A. Neuber, H. Hahn, Zur Kenntnis des Zinknitrides. Metallamide und Metallnitride, IV. Mitteilung. Z. Anorg. Allg. Chem 239, 273–281 (1938)
142. R. Juza, H. Hahn, Über die Kristallstrukturen von Zn_3N_2, Cd_3N_2 und Ge_3N_4. Metallamide und metallnitride, IX. Mitteilung. Z. Anorg. Allg. Chem. 244, 125–132 (1940)
143. R. Juza, F. Hund, Die Kristallstrukturen LiMgN, LiZnN, Li_3AlN_2 und Li_3GaN_2. Naturwissenschaften **33**, 121–122 (1946)
144. H. Cao, T.M.M. Richter, C. Pistidda, A.-L. Chaudhary, A. Santoru, G. Gizer, R. Niewa, P. Chen, T. Klassen, M. Dornheim, Alkali metal amidozincates for hydrogen storage. ChemSusChem **8**, 3777–3782 (2015)

145. H. Cao, A. Santoru, C. Pistidda, T.M.M. Richter, A.-L. Chaudhary, G. Gizer, R. Niewa, P. Chen, T. Klassen, M. Dornheim, New synthesis route for ternary transition metal amides as well as ultrafast amide-hydride hydrogen storage materials. Chem. Comm. **52**, 5100–5103 (2016)
146. H. Cao, C. Pistidda, T.M.M. Richter, A. Santoru, C. Milanese, S. Garroni, J. Bednarcik, A.-L. Chaudhary, G. Gizer, H.-P. Liermann, R. Niewa, P. Chen, T. Klassen, M. Dornheim, In situ X-ray diffraction study of the super-fast re-hydrogenation of $K_2[Zn(NH_2)_4]$-8LiH. J. Phys. Chem. C **121**, 1546–1551 (2017)
147. C. MacGillavry, J. Bijvoet, Die Kristallstruktur von $Zn(NH_3)_2Cl_2$ und $Zn(NH_3)_2Br_2$. Z. Kristallogr. **94**, 249–255 (1936)
148. R. Eßmann, Influence of coordination on N–H···X^- hydrogen-bonds. 1. $[Zn(NH_3)_4]Br_2$ and $[Zn(NH_3)_4]I_2$. J. Mol. Struct. **356**, 201–206 (1995)
149. T.M.M. Richter, S. Le Tonquesse, N.S.A. Alt, E. Schlücker, R. Niewa, Trigonal-bipyramidal coordination in first ammoniates of ZnF_2: $ZnF_2(NH_3)_3$ and $ZnF_2(NH_3)_2$. Inorg. Chem. **55**, 2488–2498 (2016)
150. J. Jander, V. Doetsch, G. Jander, *Anorganische und allgemeine Chemie in flüssigem Ammoniak* (Akademischer Verlag, Berlin, Germany, 1966)
151. T.M.M. Richter, S. Strobel, N.S.A. Alt, E. Schlücker, R. Niewa, Ammonothermal synthesis and crystal structures of diamminetriamidodizinc chloride $[Zn_2(NH_3)_2(NH_2)_3]Cl$ and diamminemonoamidozinc bromide $[Zn(NH_3)_2(NH_2)]Br$. Inorganics **4**, 41 (2016)
152. P.W. Schenk, H. Tulhoff, Das System Kaliumamid/Ammoniak. Angew. Chem. **74**, 943 (1962)
153. P.C. Scherer Jr., Solubility of salts in liquid ammonia. J. Am. Chem. Soc. **53**, 3694–3697 (1931)

Chapter 14
Equation of States and Ammonia Decomposition in Ammonothermal Systems

Siddha Pimputkar

Abstract Thermodynamic modeling of the ammonia decomposition under ammonothermal conditions (T > 600 K, P > 100 MPa) is presented given recent advances in developing a new, simple equation of state (EOS) describing ammonia, hydrogen, nitrogen and their mixtures under these conditions. The simplified EOS is based on the traditional form of the Beattie-Bridgeman (BB) EOS and expands relevant parameters to second order in density. As a consequence, a seven-parameter EOS is presented and compared to experimental data for ammonia up to 250 MPa and 810 K. Experimental data for ammonia, hydrogen and nitrogen are simulated using the reference multiparameter EOS for each individual gas. Gas mixtures are formed by applying mixing rules with separated contributions for polar and non-polar interactions. The accuracy of the expanded BB EOS is suggested to be 1–2% in pressure for temperatures greater than 700 K for ammonia, hydrogen, nitrogen and NH_3–N_2–H_2 mixtures. Additionally, a general thermodynamic expression for the equilibrium constant is presented and applied to the ammonia decomposition reaction by using non-ideal mixing contributions from the second virial coefficient using the expanded BB EOS. Comparison with experimental data (P <210 MPa, T <810 K) suggests an accuracy of ~2% in pressure.

14.1 Introduction

Nitride materials form an interesting class of materials with numerous technological applications due to the unique bonding characteristics yielding electronic structures that range from metallic to semiconducting [1–4]. Some current applications of interest include thermoelectrics [5, 6], photovoltaics [7, 8], solid-state optical emitters [9–11], superconductors [12, 13], photocatalysts [14], and power electronic devices [15].

S. Pimputkar (✉)
Materials Science and Engineering Department, Lehigh University, Bethlehem, PA 18015, USA
e-mail: siddha@lehigh.edu

E. Meissner and R. Niewa (eds.), *Ammonothermal Synthesis and Crystal Growth of Nitrides*, Springer Series in Materials Science 304,
https://doi.org/10.1007/978-3-030-56305-9_14

Synthesis of nitrides is challenging due to the great stability of the triple-bonded N_2 molecule resulting in relatively low decomposition temperatures and, in general, an inability to melt these materials. Growth of bulk, single crystal nitride materials therefore cannot readily be achieved from melts but typically is done from either the gas phase or from solution. One solution-based crystal growth technique, the ammonothermal method, is of particular interest due to the versatility of it and the ability to grow a large variety of nitride crystals [16].

The ammonothermal method forms a supercritical solution of ammonia and additional additives, also known as mineralizers, at elevated temperature (>700 K) and pressure (>100 MPa). These additives can enhance and lead to a temperature-dependent solubility of the desired element(s). By properly configuring an autoclave to contain a hot and cold temperature zone, dissolution and crystallization of desired compound can occur leading to bulk, single crystal growth of the desired nitride. Having a fundamental understanding of the chemical composition of the solvent and solutes during growth conditions is important towards tailoring and understanding the growth processes. In particular, a fundamental understanding of the solvent (supercritical ammonia) is needed to develop accurate thermodynamic and chemical models of the growth system at varying temperatures, pressures, densities, and chemical compositions.

While some information on the chemical and physical properties of ammonothermal systems can be found in literature [17–24], our current understanding of the system is incomplete. In particular, a lack of understanding revolves around how much ammonia is present in the autoclave under varying growth conditions and how much hydrogen and nitrogen is present due to decomposition of ammonia. Knowledge of these quantities would enable more accurate modeling of ammonothermal systems due to a more comprehensive view on the chemical equilibria present under ammonothermal conditions and would also improve models incorporating mass loss occurring during growth via outward diffusion of hydrogen through the autoclave walls.

Recent developments have provided new insight and experimental data on the chemical composition of equilibrium supercritical ammonia mixtures under ammonothermal conditions by developing an accurate thermodynamic model for the equilibrium constant for the ammonia decomposition reaction using a newly developed, practical equation of state (EOS) for supercritical ammonia mixtures with ammonia, hydrogen and nitrogen [25]. The chapter will summarize these advances by reviewing the development of the new EOSs and its substantiation via experimental data under ammonothermal conditions.

14.2 Theoretical Background

14.2.1 Equation of States

14.2.1.1 Pure Gases

An EOS is used to related state variables of a system (temperature T, pressure P and density ρ) thereby allowing for the determination of various thermodynamic properties of the system. The most accurate empirical EOS are typical based on a multiparameter approach unique to each gas or gas mixture resulting in a multiparameter equation of state (MEOS) for each individual gas or gas mixture. MEOSs are typically expressed in terms of their reduced Helmholtz free energy α. This energy is separated into a sum of ideal and residual terms, both of which are explicit in reduced temperature $\tau = T_c/T$ and density $\delta = \rho/\rho_c$, where c denotes its critical value, T absolute temperature and ρ its density. The ideal and real terms are parameterized and fit to large experimental data sets for the specific fluid providing a highly accurate expression.

$$\alpha(\tau, \delta) := \frac{a(T, \rho)}{RT} = \alpha^0(\tau, \delta) + \alpha^r(\tau, \delta) \tag{14.1}$$

Various thermodynamic properties can then be determined by proper derivations, including pressure, internal energy, entropy, enthalpy, heat capacities, speed of sound, Joule-Thomson coefficient, and isentropic temperature-pressure coefficient. Due to the significance of pressure to this particular application, the relationship is provided below:

$$P(\tau, \delta) = \rho RT\left[1 + \delta\left(\frac{\partial \alpha^r}{\partial \delta}\right)_\tau\right] \tag{14.2}$$

The National Institute of Standards and Technology (NIST) in the USA provides references properties for N_2, H_2, and NH_3. Current reference MEOS can be found for N_2 [26] (applicable for temperatures between 63.151 and 1000 K and pressures up to 2200 MPa), H_2 [27] (applicable up to 1000 K and 2000 MPa) and NH_3 [28] (applicable up to 700 K and 1000 MPa). Ammonia is amongst the most important MEOS, though has experimentally only been validated up to 700 K, while typical ammonothermal conditions occur beyond that. Figure 14.1 shows a P-T phase diagram for pure ammonia with overlaid contours of NH_3 densities and applicable stable phase for the given P-ρ-T condition.

Despite the high accuracy of these MEOSs, they are cumbersome to use for thermodynamic derivations due to the large number of terms (>20) with varying mathematical exponential forms. Additionally, quickly forming a new MEOS for a gas mixture from a pure gas MEOS is exceptionally hard due to dissimilar mathematical

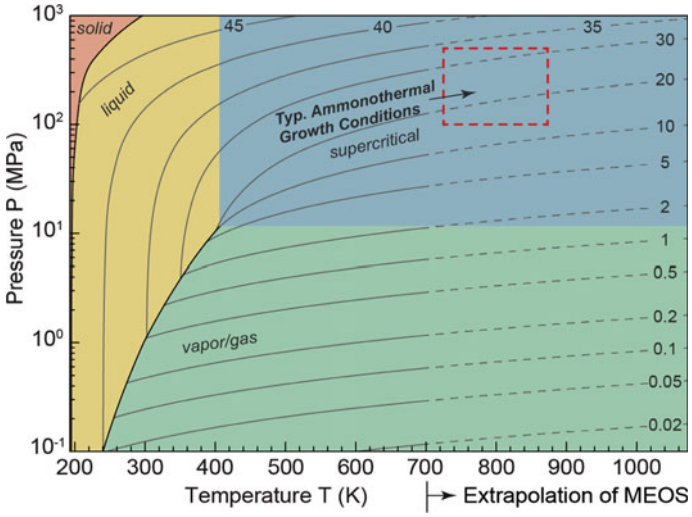

Fig. 14.1 *P-T* phase diagram of pure ammonia (NH_3) with contour lines of density ρ (mol/l) and superimposed phases present at equilibrium. Calculated and extrapolated beyond 700 K using the reference multiparameter equation of state (MEOS) as provided by the National Institute of Standards and Technology (NIST). Reprinted with permission from [25]

terms used in each MEOS. As such, a uniform, simple EOS is desired to enable rapid mathematical manipulation and development of new expressions for gas mixtures.

To that end, the Beattie-Bridgeman (BB) EOS was extended given its ability to accurately determine the equilibrium constant of ammonia decomposition at elevated pressures (<100 MPa) and temperatures (<775 K) [29]:

$$P = \frac{RT(1-\epsilon)}{v^2}(v+B) - \frac{A}{v^2} \tag{14.3}$$

where R is the universal gas constant, P is pressure, T is absolute temperature, and v the molar volume calculated by dividing the volume V by n moles of gas: V/n.

The three constants, A, B and ϵ, are used to include various molecular interactions as a result of deviations from ideal gas behavior. The constant A describes how the potential energy between molecules is related to the density of the fluid. Differentiating the potential energy with respect to volume provides the cohesive pressure. The constant B is related to the attraction and repulsion of molecules as a result of intermolecular forces leading to an overall increase in momentum transfer across any plane within the fluid, also referred to as kinetic pressure. Both of these terms depend on the density of the fluid and are expanded to second order to establish the expanded BB EOS specifically to accurately describe the behavior of ammonia under ammonothermal conditions. The traditional BB EOS expands them to first order only. The two terms written out in full form are as follows:

$$A = A_0\left(1 - \frac{a}{v} - \frac{a_1}{v^2}\right), \tag{14.4}$$

$$B = B_0\left(1 - \frac{b}{v} - \frac{b_1}{v^2}\right). \tag{14.5}$$

The ϵ term expresses temperature related effects on the intermolecular forces. Typically, as a system cools, molecules aggregate leading to the overall effect of an effective increase in average molecular weight while reducing the effective count of independent molecules. The correction term remains unmodified relative to the traditional BB EOS:

$$\epsilon = \frac{c}{vT^3} \tag{14.6}$$

Given these variables, a total of seven fitting parameters (A_0, B_0, a, a_1, b, b_1, c) are needed to fully express the expanded BB EOS.

For certain analyses, it is of value to reformulate the EOS as a virial expression. The expanded BB EOS therefore becomes:

$$P = \frac{RT}{v} + \frac{\beta}{v^2} + \frac{\gamma}{v^3} + \frac{\delta}{v^4} + \frac{\zeta}{v^5} \tag{14.7}$$

with

$$\beta = RTB_0 - A_0 - \frac{Rc}{T^2}$$

$$\gamma = -RTB_0b + A_0a - \frac{RcB_0}{T^2}$$

$$\delta = -RTB_0b_1 + A_0a_1 + \frac{RcB_0b}{T^2}$$

$$\zeta = \frac{RcB_0b_1}{T^2}$$

The traditional BB EOS ($a_1 = 0, b_1 = 0$) accurately represented the behavior of NH_3, H_2 and N_2 for moderate densities (<3 mol/l) and temperatures (<700 K). Table 14.1 provides accepted values for the traditional BB constants for NH_3, H_2 and N_2 along with the highest experimental data point in temperature and corresponding density used when creating the constants. Use of these parameters beyond the upper bounds leads to a significant loss in accuracy requiring the use of higher order terms in density (a_1, b_1).

14.2.1.2 Gas Mixtures

Given the same mathematical form for individual gases (i.e. the same EOS model with different parameter values), it is easy to arrive at an EOS describing a gas

Table 14.1 Standard values for the constants of the traditional Beattie-Bridgeman (BB) equation of state (EOS) for hydrogen (H_2), nitrogen (N_2) and ammonia (NH_3)

Gas	A_0	B_0 ($\times 10^5$)	a ($\times 10^5$)	b ($\times 10^5$)	c	Upper bound		Ref.
	(Pa m^6/mol^2)	(m^3/mol)	(m^3/mol)	(m^3/mol)	(K^3 m^3/mol)	T (K)	ρ (mol/l)	
NH_3	0.24247	3.4150	17.031	19.112	4768.7	598	2.9	[30]
H_2	0.02001	2.096	−0.5060	−4.359	0.5040	473	2.5	[29]
N_2	0.1362	5.046	2.617	−0.6910	42.00	673	1.5	[29]

Highest temperature and associated density data point used when fitting experimental data for determination of the constants is provided [25]

mixture made from two or more gases. Under the assumption that the form of the EOS does not change, it is a matter of properly mixing the various variables. For real gas mixtures, this can be done by analyzing the second virial coefficient β and derive appropriate mixing rules for the various constants according to statistical thermodynamic and analysis of the intermolecular potential energy.

As B_0 relates to the molecule diameter, the collision radii of two unlike molecules may be added to arrive at the collision diameter of the pair. Individual B_0 values are hence combined using a Lorentz combination.

Terms A_0 and c describe in part the intermolecular potential energy term. Theoretical predictions suggest that the dispersion term in the potential energy between two unlike pairs is close to the geometric mean of that for two similar pairs. This would suggest the use of a square-root combination.

An additional complication arises for ammonia due to its polar nature. The BB EOS is commonly used for non-polar gases and requires proper consideration when applied towards a polar gas, such as ammonia. As such, the terms A_0 and c need to be separated into a non-polar ($A_{0,np}$, c_{np}) and polar ($A_{0,p}$, c_p) term as the dipole-dipole forces vanish when one of the two molecules in the pair is non-polar, yielding the following relationship:

$$A_0 = A_{0,np} + A_{0,p}$$
$$c = c_{\text{np}} + c_p$$

The polar and non-polar contribution for a polar gas can be approximated by assuming a Stockmayer potential yielding the following relationships [31]:

$$A_{0,np} = \frac{1}{2}\left(A_0 + \left(A_0^2 - 7.56 \times 10^{-3}\mu^4\right)^2\right)$$
$$A_{0,p} = \frac{1}{2}\left(A_0 - \left(A_0^2 - 7.56 \times 10^{-3}\mu^4\right)^2\right)$$
$$c_{\text{np}} = c - c_p$$
$$c_p = 1.64 \times 10^{-6}\frac{\mu^4 A_{0,p}}{B_0^2}$$

where μ is the dipole moment of the gas in Debye units (1.471 for ammonia). The units for A_0 are Pa m^6/mol^2, B_0 m^3/mol and c K^3 m^3/mol. The mixing of the polar and non-polar terms can be performed individually by use of the square-root combination [32].

Higher order virial coefficients make increasingly smaller contributions to the final mixing terms for parameters a, a_1, b, and b_1. As such, linear combinations are selected.

The following equations summarize the applied mixing rules for which i denotes a gas species and x_i its mole fraction in the gas mixture:

$$\begin{aligned}
A_{0,m} &= \left(\sum_i x_i \sqrt{|A_{0,\mathrm{np},i}|}\right)^2 + \left(\sum_i x_i \sqrt{|A_{0,p,i}|}\right)^2 \\
a_m &= \sum_i x_i a_i \\
a_{1,m} &= \sum_i x_i a_{1,i} \\
B_{0,m} &= \frac{1}{8}\sum_i \sum_j x_i x_j \left(\sqrt[3]{B_{0,i}} + \sqrt[3]{B_{0,j}}\right)^3 \\
&= \frac{1}{4}\sum_i x_i B_{0,i} + \frac{3}{4}\left(\sum_i x_i B_{0,i}^{1/3}\right)\left(\sum_i x_i B_{0,i}^{2/3}\right) \\
b_m &= \sum_i x_i b_i \\
b_{1,m} &= \sum_i x_i b_{1,i} \\
c_{\mathrm{np},m} &= \left(\sum_i x_i \sqrt{c_{\mathrm{np},i}}\right)^2 + \left(\sum_i x_i \sqrt{c_{p,i}}\right)^2
\end{aligned} \tag{14.8}$$

In case of negative constants (as is the case for the A_0 value for H_2) the following rule can be applied:

$$\left(\sum_i x_i \sqrt{M}\right)^2 = \mathrm{Sign}\left[\sum_i x_i \mathrm{Sign}[M]\sqrt{|M|}\right]\left(\sum_i x_i \mathrm{Sign}[\mathrm{M}]\sqrt{|M|}\right)^2 \tag{14.9}$$

14.2.2 Decomposition of Ammonia

For ammonothermal systems, the solvent may decompose via the following reaction:

$$\frac{1}{2}\mathrm{N}_{2(g)} + \frac{3}{2}\mathrm{H}_{2(g)} \leftrightharpoons \mathrm{NH}_{3(g)} \tag{14.10}$$

The equilibrium constant, K_P, for this reaction under ammonothermal (real gas) conditions is dependent on the gas composition, total system pressure and temperature. The thermodynamic relationship relating these parameters and the equilibrium constant can be found to be:

$$\ln\left(\frac{K_P}{K_f}\right) = -\frac{1}{RT}\sum_i \left\{ \nu_i \int_0^P \left(\frac{\partial V}{\partial n_i} - \frac{RT}{P}\right) dP \right\} \tag{14.11}$$

while a detailed derivation, including assumptions used to derive this result, can be found in [25]. The term K_P is the equilibrium constant expressed in terms of partial pressures $\left(\sum_i \nu_i \ln(x_1 P) = \ln(K_P)\right)$, K_f is the equilibrium constant expressed in terms of fugacities $\left(\sum_i \nu_i \ln\left(f_i^e\right) = \ln\left(K_f\right)\right)$, R is the universal gas constant, T is the absolute temperature, P is the mixture pressure, i represents each gas species, n_i represent the number of moles of each gas, and ν_i is the stoichiometrical coefficient of each gas in chemical reaction.

Determination the value of K_P requires determination of the value of K_f and its dependence on temperature and the value of the integrand $\left(\frac{\partial V}{\partial n_i} - \frac{RT}{P}\right)$.

As K_f is only a function of temperature and not pressure, it can be determined at low pressure (i.e. within the approximate of the ideal gas law). One can therefore state that $K_f = K_P^*$. Using ideal gas approximations, it is possible to determine a value for K_P^* using the following expressions:

$$\ln\left(K_P^*\right) = \frac{\sum(\nu_i A_i) + \sum(\nu_i)R}{R}\ln(T) + \frac{\sum(\nu_i B_i)}{2R}T + \frac{\sum(\nu_i C_i)}{6R}T^2 - \frac{I}{RT} + J \tag{14.12}$$

The integration constants I and J are related to the specific heats, molar energy, $u_{0,i}$, and molar entropy, $s_{0,i}$, constants of the reacting gases at T_0 and infinitely low pressure [33].

$$I = \sum(\nu_i A_i)T_0 + \frac{1}{2}\sum(\nu_i B_i)T_0^2 + \frac{1}{3}\sum(\nu_i C_i)T_0^3 - \sum\left(\nu_i u_{0,i}\right) \tag{14.13}$$

$$J = \frac{1}{R}\left(-\left(\sum(\nu_i A_i) + \sum(\nu_i)R\right)(1 + \ln(T_0)) - \sum(\nu_i B_i)T_0 + \frac{1}{2}\sum(\nu_i C_i)T_0^2 + \sum\left(\nu_i s_{0,i}\right)\right) \tag{14.14}$$

The energy and entropy constants can be determined from the traditional BB EOS using following relationships [34]

$$u_0 = u + \frac{nA_0}{V}\left(1 - \frac{na}{2V}\right) + \frac{3nRc}{VT_0^2}\left(1 + \frac{nB_0}{2V} - \frac{n^2B_0b}{3V^2}\right) \tag{14.15}$$

$$s_0 = s - R\ln\left(\frac{V}{nRT_0}\right) + \frac{nRB_0}{V}\left(1 - \frac{nb}{2V}\right) + \frac{2nRc}{VT_0^3}\left(1 + \frac{nB_0}{2V} - \frac{n^2B_0b}{3V^2}\right) \tag{14.16}$$

The values for the reference molar energy, u, and molar entropy, s, of the gas at T_0 and the molar volume V/n are set to 0 for $T_0 = 273.13°$ C and using the applicable molar volume. The integration constants I and J can be experimentally determined and are to $I = -38319$ J /mol and $J = -5.33239$.

The integrand $\left(\frac{\partial V}{\partial n_i} - \frac{RT}{P}\right)$ can be determined using the expanded BB EOS in virial form resulting in:

$$\ln\left(\frac{K_P}{K_P^*}\right) = -\frac{1}{RT}\left\{\sum_i \nu_i \frac{PD_i}{RT} + \sum_i \nu_i\left(-RT\ln\frac{PV}{n_iRT} + \frac{2\beta_i n_i}{V} + \frac{3\gamma_i n_i^2}{V^2} + \frac{4\delta_i n_i^3}{V^3} + \frac{5\zeta_i n_i^4}{V^4}\right)\right\} \tag{14.17}$$

The value K_P needs to be determined using an iterative approach as it is composition dependent, though knowledge of the composition is what is sought. To determine an initial guess for the composition and hence determine an initial approximation for K_P, one can determine K_P^* using (14.12) and using a simplified, composition independent version of (14.17).

$$\ln\left(\frac{K_P}{K_P^*}\right) = -\frac{P}{RT}\sum_i\left[\nu_i\left(B_{0,i} - \frac{A_{0,i}}{RT} - \frac{c_i}{T^3}\right)\right] \tag{14.18}$$

Using this approximate K_P value (at the selected total system pressure P), the mole fraction of ammonia, α, can be determined using the following equation:

$$K_P = \frac{\alpha/(1+\alpha)^2}{\sqrt[2]{q - 3\alpha/2(1+\alpha)}\cdot\sqrt[3]{r - \alpha/2(1+\alpha)}}\cdot\frac{1}{P} \tag{14.19}$$

The values q and r correspond to the mole fractions of H_2 and N_2, respectively, in an equivalent system assuming all ammonia is converted to H_2 and N_2. For a stoichiometric mixture: $q = 3/4$ and $r = 1/4$.

Using the newly determined composition of the gas mixture, a new, more accurate value for K_P can then be determined using (14.17). This in turn would require a recalculation of the equilibrium mole fraction of ammonia in the system. This process can be repeated until the desired accuracy is achieved. The ultimate outcome of this calculation are the equilibrium concentrations of ammonia, hydrogen and nitrogen in the system.

14.3 Development of Expanded BB EOSs

14.3.1 P-v-T Relationship for Ammonia

Development of a new EOS requires extensive experimental datasets for varying values for temperature, pressure and density and then fitting the data to the prescribed model. To simplify the approach, an alternative may exist. In the case of ammonia, its current MEOS is highly accurate up to 700 K, yet the ability to extrapolate it is unknown. A smaller set of experimental data can hence be collected for pure ammonia at temperatures in excess of 700 K and provide information on the validity and accuracy of the MEOS for higher temperature values.

Figure 14.2 provides experimental data collected during the ramping of an autoclave containing pure ammonia preventing the decomposition of ammonia and hydrogen diffusion out of the autoclave. The temperature data collected is the fluid

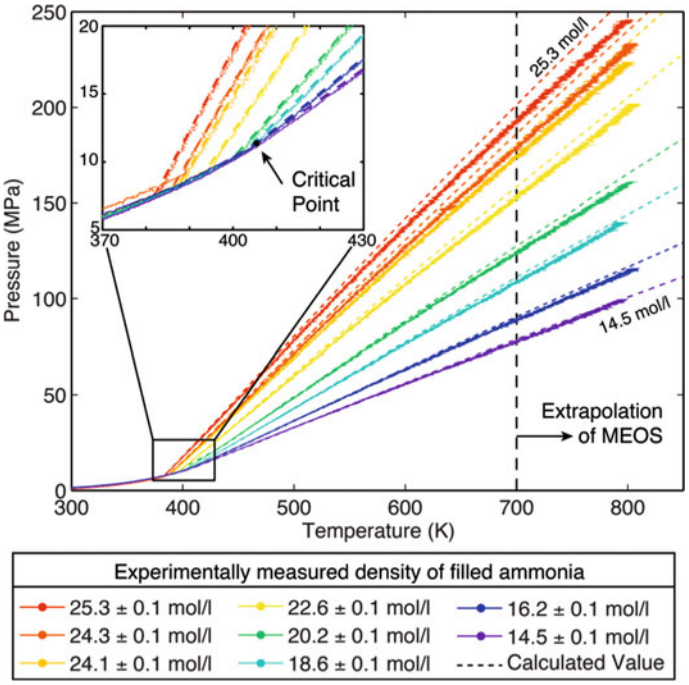

Fig. 14.2 Pressure versus temperature behavior for pure ammonia at different fill densities of ammonia compared with extrapolated multiparameter equation of state (MEOS) for ammonia as provided by the National Institute of Standards and Technology (NIST) with close up of the data in the vicinity of the critical point. Temperature values corresponds to internal fluid temperatures. Reprinted with permission from [25]

temperature measured internal to the autoclave. Dashed lines correspond to the anticipated trajectory using the MEOS of ammonia and its extrapolation beyond the validated 700 K temperature.

Deviations from the MEOS expression (dashed lines) at high temperature and pressure are a direct result from the thermal expansion of the autoclave at elevated temperatures resulting in the expansion of the internal free volume and hence a reduction in density of the fluid while higher pressures result in the expansion of the autoclave due to elastic expansion of the body leading to a reduction in density of the fluid. Adjusting the data for these effects, the deviation from the experimental data to the MEOS is summarized in Fig. 14.3.

Overall, the experimental data supports extrapolation of the MEOS to temperatures up to at least 800 K. Given the overall well-behaved trends of the extrapolation, is well suited to higher temperatures as well with minor losses to accuracy (<10%). Four traces in Fig. 14.3 noticeably deviate from the MEOS at elevated temperature, though are not due to a differing behavior of ammonia, but rather due to early onset of decomposition of ammonia due to a catalytic site within the autoclave volume.

Given the experimental data and the close agreement with the MEOS at temperatures below 700 K, around the critical point, and over a wide range of densities, the overall accuracy of the experimental data is deemed to be within 1% error or less. This suggests the ability to use the MEOS for ammonia to determine *P*-*v*-*T* data for determining the constants in the expanded BB EOS.

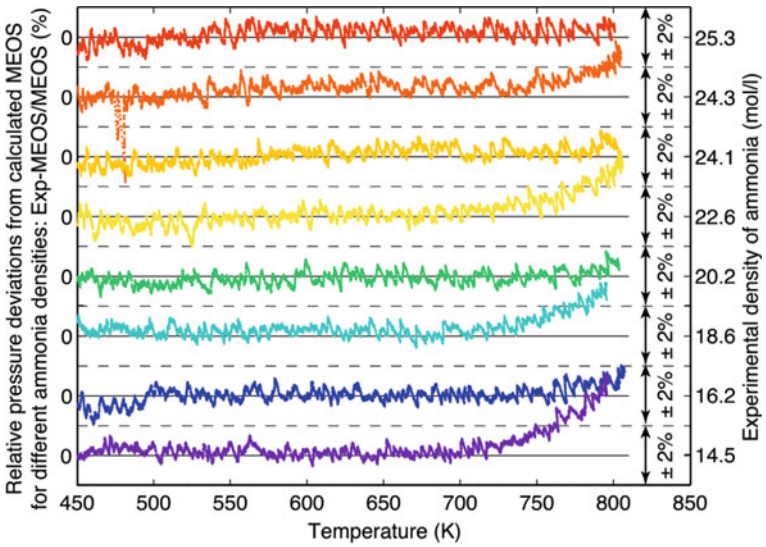

Fig. 14.3 Deviation in pressure from the corresponding calculated pressure using the reference multiparameter equation of state (MEOS) for ammonia as depicted in Fig. 14.2 at different fill densities of ammonia and adjusting for expansion in free volume due to temperature and internal pressure induced strain effects. Reprinted with permission from [25]

14.3.2 Determination of BB EOS Constants for Pure Gases

For a given dataset of *P*-*v*-*T* data for a pure gas, the following fitting procedure can be used on isochoric data to obtain the parameters in the expanded BB EOS.

$$P + \Gamma = \psi T - \phi \tag{14.20}$$

where

$$T^2\Gamma = \frac{\psi c}{v}$$
$$\psi = \frac{R(v + B)}{v^2}$$
$$\phi = \frac{A}{v^2}$$

with the molar volume v and the constants A, B, and c being those defined in BB EOS (3). A non-linear least square method can be used to determine the values of ψ, ϕ, and c for a given density. The slope, ψ, and intercept, ϕ, of a line fit through the pressure data corrected using the Γ term results in determination of the BB constants A and B.

The final value for c can then be found by averaging values determined for c at individual isochores over a specified density range. The density range can be selected as to reduce the relative errors from the expanded BB EOS with respect to the calculated values from the MEOS in the region of interest. Using this final value for c, a new round of non-linear least square fitting can be performed on the same dataset, thereby determining the final values of ψ and ϕ. The resulting values for A and B can be plot against their corresponding density $1/v$. A second order polynomial to the data yields values for A_0, B_0, a, a_1, b, and b_1.

Applying this procedure to the gases present in ammonothermal systems, H_2, N_2, NH_3, values for the expanded BB EOS are determined and presented in Table 14.2. The traditional BB EOS assumes first order expansions in density, while the expanded BB EOS used for ammonothermal systems expands them to second order. Figure 14.4

Table 14.2 Determined constants for the expanded Beattie-Bridgeman equation of state (BB EOS) as defined by (14.3), (14.4), (14.5), and (14.6) and depicted in Fig. 14.4 for ammonia, hydrogen, and nitrogen [25]

Gas	A_0 (Pa m^6/mol^2)	a ($\times 10^5$) (m^3/mol)	a_1 ($\times 10^{10}$) (m^6/mol^2)	B_0 ($\times 10^5$) (m^3/mol)	b ($\times 10^5$) (m^3/mol)	b_1 ($\times 10^{10}$) (m^6/mol^2)	c (K^3 m^3/mol)
NH_3	0.429	2.07	−1.44	5.51	1.58	−8.00	575
H_2	−0.0143	−5.19	−13.8	1.48	−0.724	−0.0667	220
N_2	0.0544	−6.89	78.7	3.70	−3.14	−0.311	487

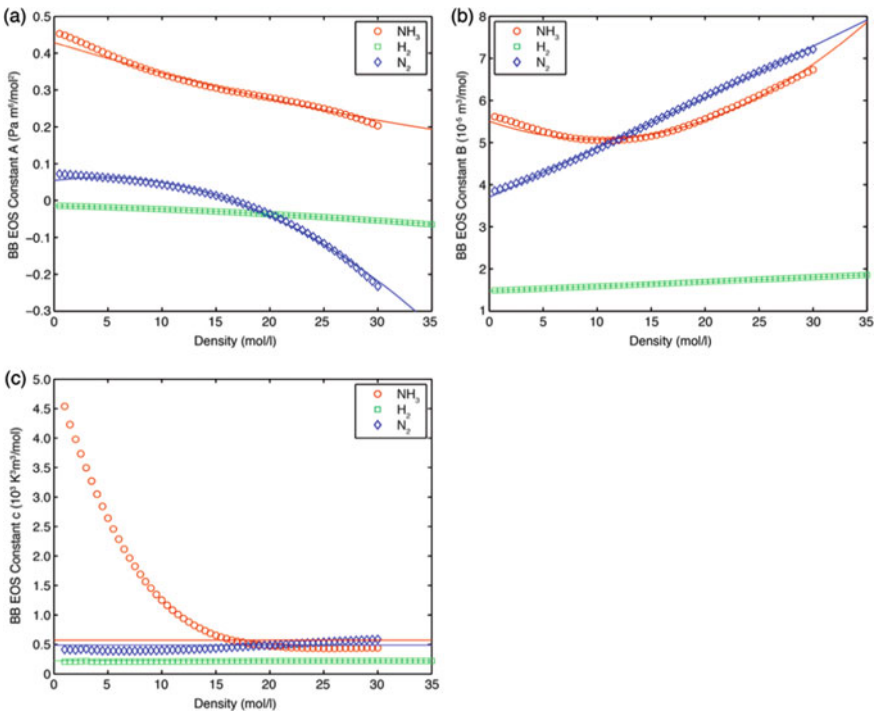

Fig. 14.4 Parameter values (**a**) A, (**b**) B, and (**c**) C as a function of density with superimposed second order polynomial fit for A and B calculated for the selected constant value of c](14.4), (14.5), and (14.6)]. Individual parameter values were calculated by fitting (14.20) the expanded Beattie-Bridgeman equation of state (BB EOS) as defined in (14.3) to isochoric data calculated using the reference multiparameter equation of state (MEOS) data provided by the Institute of Standards and Technology (NIST) for three gases: ○ Ammonia, □ Hydrogen, and ◊ Nitrogen. Reprinted with permission from [25]

provides the individual data points for values A, B and c clearly indicating the necessity and goodness of fit using a second order approximation for parameters A and B.

As the BB EOS is most applicable to non-polar gases, it lacks accuracy when describing polar gases, such as ammonia. This is most apparent when reviewing Fig. 14.4c as the strong variation in the parameter value c on the density of the polar gas ammonia as compared to the non-polar gases nitrogen and hydrogen. To improve on the expanded BB EOS, an exponential term could be used to capture the effect of clustering of molecules and on the intermolecular potentials given the strong dipole-dipole interactions that are possible in polar systems. For the desired window of utility of this expanded BB EOS for typical ammonothermal conditions (T > 600 K, P > 100 MPa), the level of accuracy is deemed sufficient thereby avoiding an increase in mathematical complexity when including an exponential term in the derivations to more accurately describe this phenomenon.

To assess the accuracy of the expanded BB EOS over a larger range, the total system pressure is calculated for each of the pure gases using the expanded BB EOS and compared to the corresponding MEOS. The deviation from the MEOS can be considered an error in accuracy of the expanded BB EOS and are provided in the form of relative deviations in color maps in Fig. 14.5 for ammonia, Fig. 14.6 for nitrogen, and Fig. 14.7 for hydrogen for which isobar contour lines are overlaid.

The expanded BB EOS for the non-polar hydrogen and nitrogen gases does well to accurately reproduce *P*-*v*-*T* relationship for ammonothermal conditions. Relative errors for nitrogen are typically below 0.5% and less than 0.25% for hydrogen in the region of interest.

The expanded BB EOS does a poor job representing ammonia near the critical point ($T = 405$ K, $P = 11.9$ MPa) leading to errors around 2–6% for densities ranging between 1–10 mol/l and when the liquid transitions to a supercritical fluid leading to deviations ranging from −2% for 12 mol/l density up to −16% at 30 mol/l and 450 K. In the region of interest ($T > 600$ K, $P > 100$ MPa) errors are around 1% or less. While no experimental data exists beyond 800 K, an approximate suggested error for the expanded BB EOS for ammonothermal conditions is suggested to be approximately 1%.

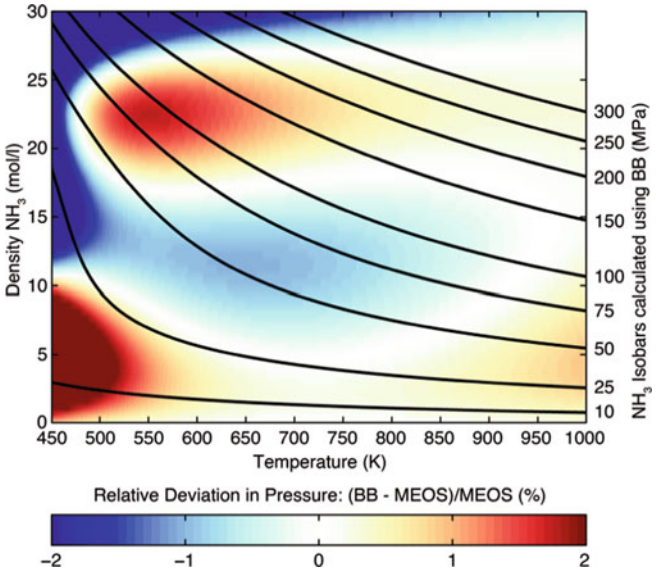

Fig. 14.5 Color map depicting relative deviation in pressure, as a function of density and temperature, for ammonia calculated using the expanded Beattie-Bridgeman equation of state (BB EOS) and parameters provided in Table 14.2 to the reference multiparameter equation of state (MEOS) as provided by the National Institute of Standards and Technology (NIST). Isobars are superimposed and were calculated using the BB EOS. Relative errors close to the critical temperature in the color saturated regions range from −2 to −16% for densities increasing from 12–30 mol/l, and 2–6% for densities ranging between 1–10 mol/l. Reprinted with permission from [25]

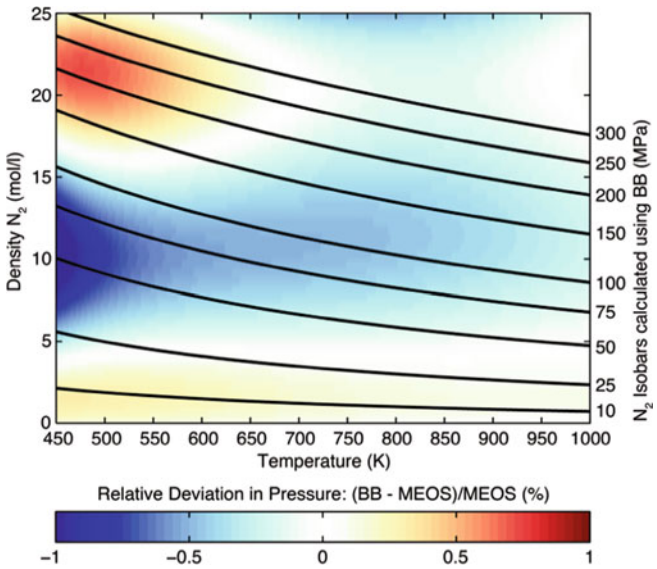

Fig. 14.6 Color map depicting relative deviation in pressure, as a function of density and temperature, for nitrogen calculated using the expanded Beattie-Bridgeman equation of state (BB EOS) and parameters provided in Table 14.2 to the reference multiparameter equation of state (MEOS) as provided by the National Institute of Standards and Technology (NIST). Isobars are superimposed and were calculated using the BB EOS. Reprinted with permission from [25]

14.4 Ammonia Decomposition

14.4.1 Equilibrium Constant

First determinations of the equilibrium constant for ammonia at elevated temperatures and pressures were done in 1930 using the traditional BB EOS by Gillespie and Beattie [35]. At pressures below 100 MPa good agreement was found to experimental data, though due to onset of divergence of their approximated BB EOS in virial high pressure systems could not be accurately calculated. Additionally, their derivation only included non-ideal mixing for the A_0 term (and not for B_0 and c) and no consideration was made to account for mixing of polar and non-polar gases to the terms A_0 and c.

Using the expanded BB EOS in its complete form during derivations without any approximations and using more sophisticated mixing rules to provide a more accurate representation of the EOS for NH_3–N_2–H_2 mixtures the equilibrium constant, K_p, for the ammonia decomposition as a function of pressure and temperature can be calculated using (14.17). The resulting values are shown in Fig. 14.8 for temperatures up to 1000 K and pressures up to 300 MPa. Decomposition of ammonia is

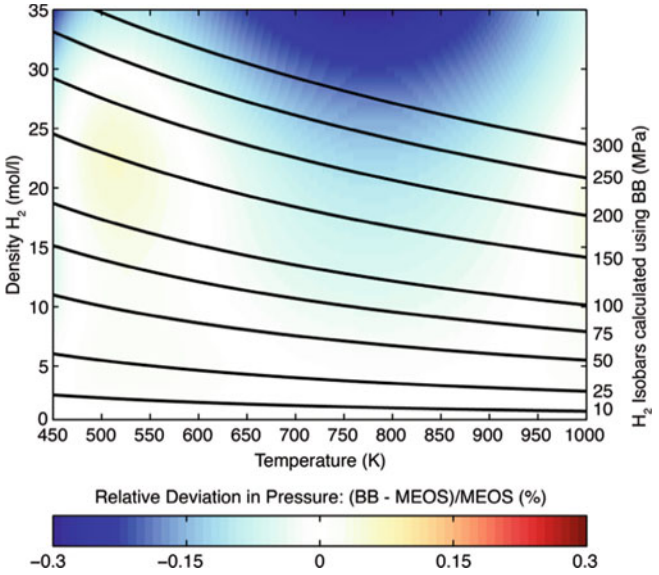

Fig. 14.7 Color map depicting relative deviation in pressure, as a function of density and temperature, for hydrogen calculated using the expanded Beattie-Bridgeman equation of state (BB EOS) and parameters provided in Table 14.2 to the reference multiparameter equation of state (MEOS) as provided by the National Institute of Standards and Technology (NIST). Isobars are superimposed and were calculated using the BB EOS. Reprinted with permission from [25]

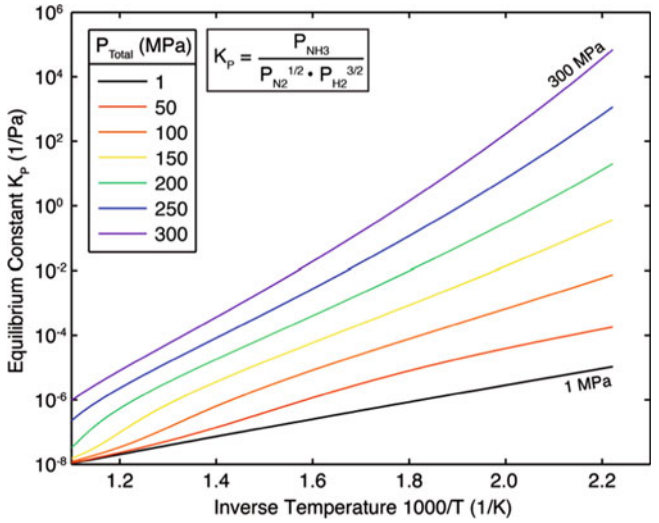

Fig. 14.8 Equilibrium constant, K_p, for the ammonia decomposition reaction defined by (14.10) as a function of inverse temperature calculated for various total system pressures ranging from 1 to 300 MPa. Reprinted with permission from [25]

greatly suppressed at elevated pressures. Note that for ideal gases there is no pressure dependence on the equilibrium constant K_p suggesting early deviation from ideal gas behavior after a few 10s of MPa of pressure.

14.4.2 Equilibrium Mole Fraction of Ammonia

Using the equilibrium constant, the equilibrium mole fraction of ammonia can be determined as a function of temperature and pressure and is shown in Fig. 14.9. To validate the accuracy of the derivation, computed values can be compared to data in literature for pressures below 100 MPa and temperatures below 500 °C [36, 37] and at higher pressures up to 210 MPa and temperatures up to 814 K [25]. For the three higher pressure and temperature points, mass loss of hydrogen from the autoclave was observed and was corrected for by determined the anticipated mole fraction of ammonia assuming a non-stoichiometric initial mixture, indicted as a dashed line in

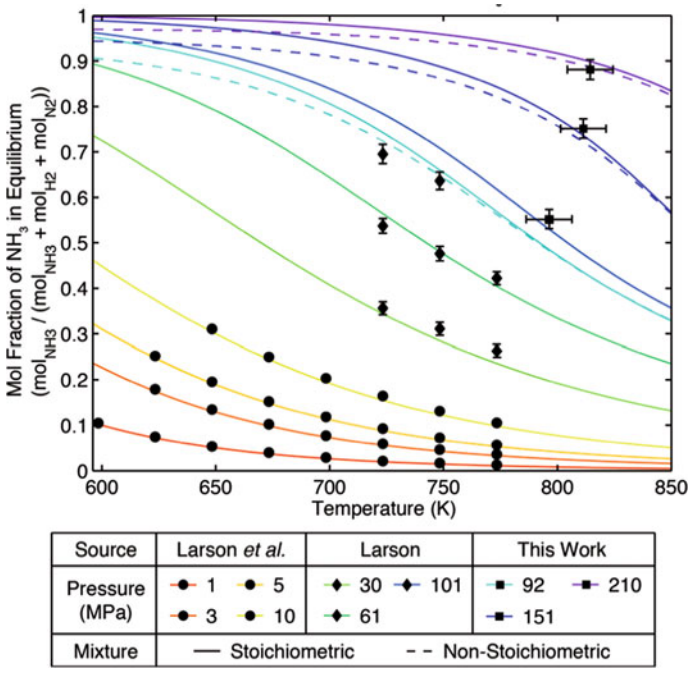

Fig. 14.9 Comparison of experimentally determined equilibrium mole fraction of ammonia from • Larson and Dodge [36], ◆ Larson [37], and ⋆ Pimputkar and Nakamura [25] with calculated equilibrium mole fraction of ammonia in stoichiometric mixtures (solid lines). Dashed lines correspond to calculated mole fractions of ammonia in equilibrium for non-stoichiometric mixtures taking into account the experimentally determined mass loss of hydrogen from the system. Modified and reprinted with permission from [25]

Fig. 14.9. Solid lines correspond to stoichiometric mixtures of hydrogen and nitrogen in the autoclave.

Overall, good agreement is found to the developed model using the expanded BB EOS with a notable exception for the highest-pressure value determined by Larson and the lowest pressure value determined by Pimputkar and Nakamura.

Deviation for the lowest pressure value was explained by an increase in error of the pressure readout due to hydrogen diffusing into the strain gauge causing an additional error in the readout as large as 10 MPa resulting in the actual pressure of the system potentially being at 102 MPa, i.e. at the same pressure as the highest-pressure value determined by Larson.

The deviation for the highest-pressure value determined by Laron is speculated to be due to an experimental error due to insufficient catalyst being present to accurately determine the ammonia mole fraction. Nevertheless, it cannot be ruled out that the performed derivations using the expanded BB EOS and mixing rules are insufficient and require the inclusion of the third virial coefficient for increased accuracy.

Given the overall excellent agreement of most experimental data points, it can nevertheless be concluded that the provided model and expanded BB EOS is a good approximation to describe supercritical ammonia under ammonothermal system in equilibrium to within a few percent error.

14.4.3 System Modeling

As a test for the ammonia decomposition model, it is desired to determine how predictive it is towards the behavior of an ammonothermal system solely provided with the initial, cold free volume, the initial fill of ammonia and a temperature at which point the system is in equilibrium. Figure 14.10 provides an overview of the measured and calculated total system pressure for four different quasi-isochores given different initial fills for ammonia. Figure 14.11 provides the corresponding mole fraction of ammonia for the last data point at the highest temperature, with the exception of the highest density fill.

To model the system, three different scenarios were calculated:

(a) $P_{\text{Pure NH}_3}$: assumes no ammonia decomposition, (solid lines in figures)
(b) $P^{\text{stoichiometric}}_{\text{Equil. NH}_3-\text{N}_2-\text{H}_2}$: couples the total system pressure to the equilibrium constant equation, while assuming a strictly stoichiometric mixture, (dashed lines in figures)
(c) $P^{\text{with H}_2\text{ Loss}}_{\text{Equil. NH}_3-\text{N}_2-\text{H}_2}$: permits ammonia decomposition while assuming an initially non-stoichiometric mixture consisting of ammonia and pure nitrogen based on measured hydrogen mass loss at end of run. (dash-dot lines in figures)

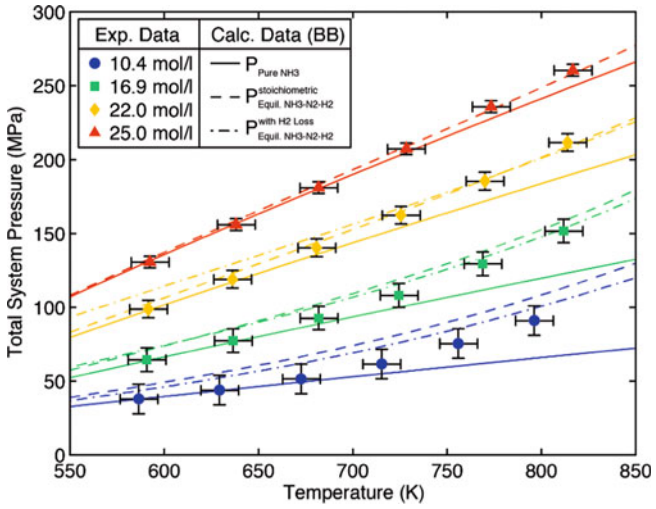

Fig. 14.10 Comparison of measured total system pressure at specified fluid temperatures for four different fill densities of ammonia after allowing the system to reach equilibrium to theoretically predicted values using the expanded Beattie-Bridgeman equation of state (BB EOS) with specified mixing rules assuming: (1) no decomposition of ammonia ($P_{\text{Pure NH}_3}$), (2) decomposition of ammonia and no hydrogen mass loss from the system ($P^{\text{stoichiometric}}_{\text{Equil.NH}_3-\text{N}_2-\text{H}_2}$), and (3) decomposition of ammonia with experimentally determined hydrogen mass loss at the end of the run, where available $\left(P^{\text{withH}_2\text{Loss}}_{\text{Equil.NH}_3-\text{N}_2-\text{H}_2}\right)$. Reprinted with permission from [25]

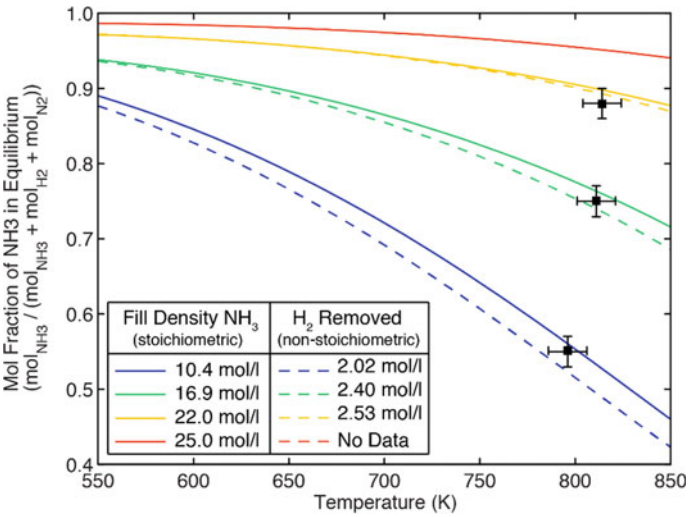

Fig. 14.11 Calculated equilibrium mole fraction of ammonia as a function of temperature and initial fill density corresponding to the four runs depicted in Fig. 14.10. Three experimentally determined mole fractions of ammonia corresponding to the highest temperature state for the three lower density runs in Fig. 14.10 are overlaid. Reprinted with permission from [25]

Overall, the total system pressure values are in good agreement with the predicted values for stoichiometric mixtures at lower temperatures and non-stoichiometric mixtures at higher temperatures when hydrogen mass loss becomes more pronounced. At temperatures below 650 K ammonia appears to be kinetically limited to decomposition leading to a non-thermodynamic equilibrium situation. Nevertheless, given the good agreement between modeled and experimental data, an error of 2% for temperatures below 850 K is proposed for the ammonia decomposition model based on the expanded BB EOS.

14.5 Summary

To aid in thermodynamic investigations of ammonothermal systems at elevated temperatures and pressures, a new EOS was developed which is based on the traditional Beattie-Bridgeman EOS leading to an expanded BB EOS. This new EOS was applied to three gases present in equilibrium in ammonothermal conditions: hydrogen, nitrogen and ammonia.

Deviations in pressure for the expanded BB EOS from established multi-parameter EOS in the region of interest ($T > 600$ K, $P > 100$ MPa) were found to be less than ~1%, with an unknown error for ammonia at temperatures beyond 800 K due to a lack of experimental data to support the extrapolation of the existing MEOS for ammonia. To build an EOS for mixtures of NH_3–N_2–H_2, proper mixing rules for the second virial coefficient were used, while linear mixing rules were applied to the third virial coefficient. Experimental validation of the EOS suggests it accurately represents data to within current experimental errors (around 1% or less).

Using a derived thermodynamic relationship for the dependence of the equilibrium constant on pressure, temperature and composition and combining it with the expanded BB EOS resulted in an expression that can determine the mole fraction of ammonia at equilibrium. Calculated values from this expression agree with experimental data at pressures up to 210 MPa.

Using the expanded BB EOS to predict the total system pressure and use this value in the developed expression of the mole fraction of ammonia at equilibrium allows for predicting the pressure trace and chemical make-up of a system, assuming thermodynamic equilibrium at every step. Comparison of this model with experimental data provided to be very well, suggesting the errors in the equilibrium constant to be around 2% for temperatures below 850 K.

References

1. N.E. Brese, M. O'Keeffe, in *Structure and Bonding* (1992), pp. 307–378
2. S.T. Oyama, *The Chemistry of Transition Metal Carbides and Nitrides* (Blackie Academic & Professional, 1996)

3. L. Toth, *Transition Metal Carbides and Nitrides* (Academic Press, 1971), pp. 1–296
4. W. Schnick, Angew. Chem. Int. Ed. Engl. **32**, 806 (1993)
5. I. Ohkubo, T. Mori, Chem. Mater. **26**, 2532 (2014)
6. C.X. Quintela, F. Rivadulla, J. Rivas, Appl. Phys. Lett. **94**, 152103 (2009)
7. A. Zakutayev, J. Mater. Chem. A **4**, 6742 (2016)
8. N. Lu, I. Ferguson, Semicond. Sci. Tech. **28**, 074023 (2013)
9. M. Kneissl, J. Rass (eds.), *III-Nitride Ultraviolet Emitters* (Springer, 2016)
10. F.A. Ponce, D.P. Bour, Nature **386**, 351 (1997)
11. M.T. Hardy, D.F. Feezell, S.P. DenBaars, S. Nakamura, Mater. Today **14**, 408 (2011)
12. X.-J. Chen, V.V. Struzhkin, Z. Wu, M. Somayazulu, J. Qian, S. Kung, A.N. Christensen, Y. Zhao, R.E. Cohen, H.-K. Mao, R.J. Hemley, Proc. Natl. Acad. Sci. U.S.A. **102**, 3198 (2005)
13. S. Yamanaka, K.-I. Hotehama, H. Kawaji, Nature **392**, 580 (1998)
14. Y. Moriya, T. Takata, K. Domen, Coord. Chem. Rev. **257**, 1957 (2013)
15. J.Y. Tsao, S. Chowdhury, M.A. Hollis, D. Jena, N.M. Johnson, K.A. Jones, R.J. Kaplar, S. Rajan, C.G. Van de Walle, E. Bellotti, C.L. Chua, R. Collazo, M.E. Coltrin, J.A. Cooper, K.R. Evans, S. Graham, T.A. Grotjohn, E.R. Heller, M. Higashiwaki, M.S. Islam, P.W. Juodawlkis, M.A. Khan, A.D. Koehler, J.H. Leach, U.K. Mishra, R.J. Nemanich, R.C.N.P. Podgurski, J.B. Shealy, Z. Sitar, M.J. Tadjer, A.F. Witulski, M. Wraback, J.A. Simmons, Adv. Electron. Mater. **4**, 1600501 (2018)
16. J. Häusler, W. Schnick, Chem. Eur. J. **24**, 11864 (2018)
17. M.P. D'Evelyn, H.C. Hong, D.-S. Park, H. LU, E. Kaminsky, R.R. Melkote, P. Perlin, M. Lesczynski, S. Porowski, R.J. Molnar, J. Cryst. Growth **300**, 11 (2007)
18. M.J. Callahan, B. Wang, K. Rakes, D.F. Bliss, L.O. Bouthilette, M. Suscavage, S.-Q. Wang, J. Mater. Sci. **41**, 1399 (2006)
19. B. Wang, M.J. Callahan, Cryst. Growth Des. **6**, 1227 (2006)
20. T.G. Steigerwald, N.S.A. Alt, B. Hertweck, E. Schluecker, J. Cryst. Growth **403**, 59 (2014)
21. N. Alt, E. Meissner, E. Schlücker, L. Frey, Phys. Status Solidi C **9**, 436 (2012)
22. Q.-S. Chen, J.-Y. Yan, Y.-N. Jiang, W. Li, Prog. Cryst. Growth Ch. **58**, 61 (2012)
23. Y. Masuda, A. Suzuki, T. Ishiguro, C. Yokoyama, Jpn. J. Appl. Phys. **52**, 08JA05 (2013)
24. I.M. Kakhki, M. Charmchi, H. Sun, in *ASME 2013 Heat Transfer Summer Conference Collocated with the ASME 2013 7th International Conference on Energy Sustainability and the ASME 2013 11th International Conference on Fuel Cell Science, Engineering and Technology* V003T09A001 (2013)
25. S. Pimputkar, S. Nakamura, J. Supercrit. Fluids **107**, 17 (2016)
26. R. Span, E.W. Lemmon, R.T. Jacobsen, W. Wagner, A. Yokozeki, J. Phys. Chem. Ref. Data **29**, 1361 (2000)
27. J.W. Leachman, R.T. Jacobsen, S.G. Penoncello, E.W. Lemmon, J. Phys. Chem. Ref. Data **38**, 721 (2009)
28. R. Tillner-Roth, F. Harms-Watzenberg, H. Baehr, DKV-Tagungsber. **20**, 167 (1993)
29. J.A. Beattie, O.C. Bridgeman, Proc. Am. Acad. Arts Sci. **63**, 229 (1928)
30. J.A. Beattie, C.K. Lawrence, J. Am. Chem. Soc. **52**, 6 (1930)
31. W.H. Stockmayer, J. Chem. Phys. **9**, 398 (1941)
32. W.H. Stockmayer, J. Chem. Phys. **9**, 863 (1941)
33. L. Gillespie, J.A. Beattie, Phys. Rev. **36**, 1008 (1930)
34. J.A. Beattie, Phys. Rev. **32**, 699 (1928)
35. L. Gillespie, J.A. Beattie, Phys. Rev. **36**, 743 (1930)
36. A.T. Larson, R.L. Dodge, J. Am. Chem. Soc. **45**, 2918 (1923)
37. A.T. Larson, J. Am. Chem. Soc. **46**, 367 (1924)

Chapter 15
Molecular Simulations as Guides to Ammonothermal Syntheses of Nitrides—State of the Art and Perspectives

Tanakorn Wonglakhon and Dirk Zahn

Abstract Molecular Simulations are increasingly entering the realm of materials syntheses. While pioneering studies were bound to simple models which could only address selected aspects of 'real chemistry' in the lab, recent advances in simulation methodology and computing hardware indeed paved the way to also modelling complex systems. Yet, we are hardly more than at the beginning of establishing molecular simulations as a routine tool for guiding syntheses. In the present contribution, we discuss the progress that has been made to understand ammonothermal syntheses of nitrides. This encompasses molecular dynamics simulations based on non-reactive force-fields—such as studies of liquid ammonia as a solvent, and its supercritical nature at high temperature and pressure. Moreover, we report on recent work on quantum and hybrid quantum/classical approaches for modelling the autoprotolysis of ammonia and ammonia protolyses in the course of metal ion solvation. This forms a basis for rationalizing the association of ion aggregates, size-induced proton transfer and the self-organization of amides, imides and nitrides from molecular simulations.

15.1 Introduction

Ammonothermal syntheses of materials are recently gaining increasing attention from both experiment and, more recently, theory [1]. While technically challenging, ammonothermal routes appear promising for producing amide semiconductors such as AlN and GaN as large single crystals—which are hard to get via conventional approaches [1–3]. The underlying processes that transform salt solutions in ammonia to amides, imides or nitrides are intrinsically complex because the 'solvent' is part of the formation reaction. Hence, the application of high temperature and pressure changes both, ammonia as a reactant and non-reacting ammonia that constitute the

T. Wonglakhon · D. Zahn (✉)
Lehrstuhl für Theoretische Chemie/Computer Chemie Centrum, Friedrich-Alexander Universität Erlangen-Nürnberg, Nägelsbachstraße 25, Erlangen 91052, Germany
e-mail: dirk.zahn@fau.de

E. Meissner and R. Niewa (eds.), *Ammonothermal Synthesis and Crystal Growth of Nitrides*, Springer Series in Materials Science 304,
https://doi.org/10.1007/978-3-030-56305-9_15

solvent. This results in a diversity of possible mechanisms and possible syntheses products, rendering ammonothermal syntheses hard to predict.

From the perspective of theory, it is therefore reasonable to closely interact with the experiment and to gradually increase our knowledge of ammonthermal syntheses by rationalizing selected aspects rather than challenging the whole complexity of possible reaction routes. It is the aim of this contribution to show such progress made by modelling and simulation. So far, theoretical studies related to the yet small field of ammonothermal syntheses are rather few and incremental. We shall therefore also describe modelling studies of ion dispersion/aggregation in aqueous solution, auto-protolyses of water and hydrothermal syntheses of metal oxides when needed. Without claiming completeness, we hence pick modelling techniques employed for characterizing water-based syntheses and take use of the analogy of ammonia and water to elaborate an extended perspective for the former.

To this end, molecular simulation methods and models may be filed in two categories, namely quantum approaches and molecular mechanics. The former solves the quantum mechanical problem of finding the wave functions (or densities in DFT calculations) of the electrons, and sometimes also the light-weighted nuclei (i.e. for proton transfer). The computational demand of these techniques prohibits the study of large systems and the sampling of large manifolds of ionic/molecular configurations. For this purpose, molecular mechanics approximate fundamental aspects of molecular interactions by simple potential energy functions (force-fields)—such as steric avoidance, electrostatics, bond vibrations etc. On this basis, much larger systems and much better sampling of structural diversity become accessible, though, typically at the price of pre-defining covalent bonds as permanent. To study bond breaking and formation in extended systems (such as reactions of ion aggregates embedded in ammonia solution) it is intuitive to combine quantum approaches and molecular mechanics. In what follows, we shall hence discuss all three types of simulation approaches and provide an overview of quantum mechanical (QM), molecular mechanical (MM) and combined QM/MM studies, respectively.

15.2 Quantum Mechanical Calculations of Ammonia and Amide Clusters

Already beginning in the 1950s quantum theory approaches were employed to ammonia and its ions and radicals [4–16]. At this time, calculations were limited to single molecules in vacuum. Fundamental insights include molecular geometry after structural relaxation, the distribution of charge, UV-Vis spectra and IR spectra. The latter requires characterization of the elastic constants of N-H bonds and for the bending of the H-N-H valence angle. Such data forms the basis for the creation of molecular mechanics models for intra-molecular force fields as discussed later.

Next, beginning in the 1970s, quantum calculations were used for the study of ammonia-ammonia interactions. To this end, the theoretical studies were still

addressing the gas phase, however now focusing on dimers, trimers etc. Along those lines, Dill et al. used Hartree-Fock calculations to investigate the structure and the energy of the ammonia dimer at reasonable agreement to the experiment [17]. Similarly, $(NH_3)_n$ ammonia clusters with $n = 3$–6 were modeled [18, 19] and compared to molecular beam experiments. In 1990, Dykstra and Andrews performed an in-depth characterization of the inter-molecular interactions in ammonia clusters [20]. On this basis, a molecular mechanics model was obtained, reproducing ab initio calculations of small ammonia cluster $(NH_3)_n$ with $n = 2$–4.

In analogy to the uncharged $(NH_3)_n$ ($n = 1$–5) clusters also ionic aggregates such as $NH_4^+(NH_3)_n$ ($n = 0$–5) were characterized [21–24]. This also included proton transfer processes, namely ammonia protolyses in small clusters, based on the structure and stability of $(NH_4^+\text{-}NH_2^-)$ $(NH_3)_{n-2}$ ($n = 3$–7) agglomerates [25]. Recently, simplified quantum approaches such as the density functional tight-binding method paved the ways to studying the dynamics of such clusters. On this basis, Fouqueau et al. used molecular dynamics simulations to study the structures and infrared spectra of the protonated ammonia clusters $NH_4^+(NH_3)_n$ with $n = 1$–8 as functions of temperature [26]. They found that the clusters with $n < 5$ are stable up to 100 K, whilst the clusters with $n \geq 5$ tend to isomerize.

Until today, quantum calculations at increasingly high level are used to characterize both charged and uncharged ammonia clusters. The wealth of experimental data provides robust benchmarks to theory—which by now can reliably predict structures, coordination numbers, hydrogen bond strength, UV-Vis and IR spectra [27–29].

15.3 Quantum Simulations of Liquid and Supercritical Ammonia

The analyses of molecular clusters in the gas phase are usually based on structures obtained from energy minimization. Such studies refer to zero Kelvin, and temperature effects remain unconsidered unless molecular dynamics or Monte-Carlo simulations are performed. The need for explicitly considering temperature becomes rather obvious when shifting focus from clusters to condensed phases, namely the liquid state. To describe molecular models of liquid or super-critical ammonia, we hence need Monte-Carlo or molecular dynamics simulations in combination with temperature and pressure controlling algorithms.

Both simulation methods explore the manifold of a system's configurations. In molecular dynamics (MD) simulations, Newton's equations of motion are solved iteratively in small time steps (typically around 1 fs, subject to the temperature). Molecular dynamics simulations follow the trajectory of all atoms and, provided that sufficiently long trajectories are computed, yield statistical sampling at a given temperature of the model system. On the other hand, Monte-Carlo simulations produce series of structural arrangements by initially attempting random modifications of a previous configuration, and then accepting/rejecting the new structure based on its energy. By

disfavoring any increase in energy ΔE via an acceptance rate of $\exp(-\Delta E/k_B T)$, the Monte-Carlo procedure also leads to a statistical sampling obeying Boltzmann distribution at a given temperature T (k_B is the Boltzmann constant). Both methods hence require the re-evaluation of interaction forces (for molecular dynamics) and energy (for Monte-Carlo) after implementing structural changes to the model system.

Such re-occurring calculations may be performed for quantum mechanically modelled systems, including ammonia. However, the computational demand calls for small model sizes and rather short trajectories or configuration sampling. So far, ab initio molecular dynamics simulations were subjected to liquid ammonia and to ammonia at high pressure (330 GPa) and high temperature (500–10000 K) [30, 31]. Therein, 5–25 ps runs were performed for models comprising up to 32 ammonia molecules subjected to cubic cells with periodic boundary conditions. While reflecting the forefront of high-performance computing, such dimensions are still very low in terms of sampling reliable statistics. Thus, the appealing accuracy in evaluating specific configurations and their interactions is traded for the risk of entirely missing configurations of potential importance. Indeed, sampling a liquid's pressure or the model density at constant pressure calls for longer molecular dynamics runs or sampling statistics from larger numbers of explicit molecules [31].

Diraison et al. compared three different methods to study the structural properties of liquid ammonia at 273 K [32]. This comprised path-integral molecular dynamics that treat both the electrons and the hydrogen atoms quantum mechanically, ab initio molecular dynamics (that describe the electrons quantum mechanically and all nuclei classically) and classical molecular dynamics (using force-fields instead of quantum calculations) methods. They found that the intermolecular structures obtained from both classical MD simulation and path-integral/ab initio MD simulations are in good agreement with the experiment [32]. Based on such benchmarking, we argue that classical molecular dynamics using force-fields adapted to quantum calculations appear most suited to studying ammonia solutions. In turn, quantum calculations can be limited to parameterization studies based on small test systems, whilst specific reaction events may be implemented by combined QM/MM approaches as discussed in the following.

15.4 Quantum/Classical Simulations of Ammonia Auto-Protolysis

In analogy to the hydrothermal syntheses of metal oxides, also ammonothermal syntheses of metal nitrides rely on the protic nature of the solvent. Theoretical investigations on auto-protolyses and acid/base reactions are abundantly available, however the overwhelming part is of course dedicated to water. It is therefore useful to compare H_2O and NH_3 auto-protolyses not only from a chemical viewpoint, but also from the perspective of method development.

In comparison to water, ammonia thus exhibits a much lower tendency to undergo spontaneous auto-protolysis - which motivates the use of autoclaves and high temperature in nitride syntheses:

$$2H_2O \rightarrow H_3O^+ + OH^- \quad \frac{c(H_3O^+)c(OH^-)}{c(H_2O)^2} = 10^{-14} \quad (1\ \text{atm, } 298\ \text{K})$$

$$2NH_3 \rightarrow NH_4^+ + NH_2^- \quad \frac{c(NH_4^+)c(NH_2^-)}{c(NH_3)^2} = 10^{-32} \quad (1\ \text{atm, } 239\ \text{K})$$

The prediction of the underlying equilibrium constants by means of molecular simulations is challenging [33]. On one hand, the accurate account of proton transfer reactions make quantum chemical approaches indispensable. However, reliable sampling of solvent effects, structural diversity etc. call for cost-effective classical mechanics models. Most approaches to estimating pK_S therefore combine both techniques [34–39]. The simplest QM/MM scheme uses quantum calculations for getting proton affinities of the donating and accepting molecules, respectively, whilst all other molecules (i.e. the non-reacting solvent molecules) are described by molecular mechanics simulations or even more approximate continuum models [40].

By means of Boltzmann statistics, we recently estimated the pK of NH_3 auto-protolysis from the change in free energy as obtained from QM/MM calculations via [40]:

$$\begin{aligned} K &= \frac{c(NH_4^+)c(NH_2^-)}{c(NH_3)^2} = \exp\left[-\frac{\Delta G}{k_B T}\right] \text{ with} \\ \Delta G &= G(NH_4^+ + NH_2^-) - G(2NH_3) \\ &\approx E_{\text{pot}}^{\text{vac}}(NH_4^+) + E_{\text{pot}}^{\text{vac}}(NH_2^-) - 2 \cdot E_{\text{pot}}^{\text{vac}}(NH_3) + G_{\text{solvation}} \end{aligned} \tag{15.1}$$

Here the first three terms refer to the gas phase and are obtained from inexpensive quantum calculations on isolated molecules/ions. The entire role of the (non-reacting part of the) solvent is sampled from molecular mechanics models. The underlying change of the free energy of solvation $\Delta G_{\text{solvation}}$ comprises changes in potential energy, volume work and entropy contributions.

$$\Delta G_{\text{solvation}} = \langle E_{\text{solv}}(NH_4^+)\rangle + \langle E_{\text{solv}}(NH_2^-)\rangle - 2 \cdot \langle E_{\text{solv}}(NH_3)\rangle + T \cdot \Delta S_{\text{solvation}} \tag{15.2}$$

For this, averages are obtained from statistical sampling of solvent structuring next to the ammonium/amide species and thus reflect average solvation effects that trigger the chemical equilibrium of the acid/base reactions.

While sampling the average change in potential energy $\Delta E_{\text{solvation}}$ upon ammonia auto-protolysis is comparably straight-forward, the calculation of the change in entropy $\Delta S_{\text{solvation}}$ requires thermodynamic integration. Such methods are in principle accurate, but actual sampling is limited by small simulation models. This is

problematic, because the proper account of the configuration entropy of the migration of just a single pair of NH_2^- and NH_4^+ in ammonia would require simulation systems of 10^{32} NH_3 molecules.

As this is far beyond the scope of molecular simulations, it is tempting to use smaller or implicit solvent models. This route was widely used for acid/base reactions in water and the typical error margins in estimating absolute pK values on such basis were found as 2 pK units, thus the equilibrium constants K vary by orders of magnitudes [34–39]. To circumvent this, we recently suggested a semi-empirical approach that only calculates $\Delta E_{\text{solvation}}$ from explicit simulations, whilst $\Delta S_{\text{solvation}}$ is deduced from experimental reference [40].

To this end, the pK of pure ammonia at 239 K and 1 atm is used as the reference point (using $pK_{\text{exp}}(239\text{ K}, 1\text{ atm}) = 32$). All deviations—be it different temperature T, pressure or the solvation of further solute species—lead to corrections of the reference pK using:

$$
\begin{aligned}
K &= \frac{K_A}{c(\mathrm{NH_3})} = \frac{c\left(\mathrm{NH_4^+}\right) c\left(\mathrm{NH_2^-}\right)}{c(\mathrm{NH_3})^2} = \exp\left[-\frac{\Delta G}{k_B T}\right] \\
\rightarrow \Delta G_{\text{ref}} &= \frac{k_B \cdot 239\text{ K}}{\log_{10}[e]} \cdot \left\{ \log_{10}\left[c(\mathrm{NH_3}) \cdot 1\,1\,\mathrm{mol}^{-1}\right] + pK_{\text{exp}}(239\text{ K}, 1\text{ atm}) \right\} \\
pK &= -\log_{10}\left[c(\mathrm{NH_3}) \cdot 1\,1\,\mathrm{mol}^{-1}\right] + \log_{10}[e] \cdot \frac{\Delta G_{\text{ref}}}{k_B T} + \log_{10}[e] \cdot \frac{\Delta\Delta E_{\text{solv}}}{k_B T}
\end{aligned}
\tag{15.3}
$$

Here, $\Delta\Delta E_{\text{solv}} = \Delta E_{\text{solv}}$ (actual system) $-\Delta E_{\text{solv}}$ (reference point) refers to difference of the energy change of ammonia dissociation observed for the system as compared to the reference model. In this notation, K and pK refer to the overall reaction involving two NH_3 molecules (one donor and one acceptor) and are thus dimensionless. This concept was first employed to model the temperature-dependence of the auto-protolyses of pure ammonia [40], and then transferred to studying ammonia dissociation next to metal ions in ammonia solutions as discussed in the next section [41].

15.5 Modelling Ion Solvation and Aggregation in Ammonia

Force-field based classical molecular dynamics simulations of liquid and super-critical ammonia demonstrated the proper treatment of the bulk solvent in terms of density, radial distribution functions and dielectric permittivity [40, 42]. Moreover, a number of studies showed the suitability of molecular mechanics for modelling ion solvation in liquid and super-critical ammonia. For an overview of modelling mono- and divalent metal ion—ammonia solutions without consideration of amide formation, we direct the reader to the review of Heinzinger [43]. In what follows, we focus on metal-amide complexes and their formation upon metal ion solvation in

ammonia. In other terms, we recall the QM/MM models of ammonia auto-protolyses from the previous section 15.315.3), to shift from spontaneous NH_3 dissociation to metal ion assisted amide formation:

$$\begin{aligned} NH_3 + NH_3 &\rightleftharpoons NH_2^- + NH_4^+ \quad ; pK = pK_A(\text{reference}) \\ &\Downarrow \\ [M(NH_2)_x(NH_3)_y]^q + z \cdot NH_3 &\rightleftharpoons [M(NH_2)_{x+1}(NH_3)_{y+z-2}]^{q-1} + NH_4^+ \\ pK &= pK_A(\text{reference}) + \log_{10}[e] \cdot \frac{\Delta\Delta E_{\text{solv}}}{k_B T} \end{aligned} \quad (15.4)$$

In equation 15.4, the upper panel refers to the auto-protolysis of the pure liquid, whilst the lower panel provides a 'local pK' stemming from ammonia/amide coordination to metal ions M. Here, q denotes the charge of $[M(NH_2)_x(NH_3)_y]^q$ complexes as resulting from the charge of the metal ion and the number x of amide ions in the complex. When protons are released from $[M(NH_2)_x(NH_3)_y]^q$ complexes, a NH_4^+ ion is migrated to the solution and a $[M(NH_2)_{x+1}(NH_3)_{y+z-2}]^{q-1}$ complex is obtained. For the proton transfer reaction, the accepting NH_3 may be an ammonia molecule of the coordination shell, or ammonia from the embedding liquid. Moreover, the metal ion may change its overall coordination number $x + y \rightarrow y + z - 2$ by associating ($z > 0$) or dissociating ($z < 0$) ammonia molecules to/from its coordination polyhedron.

Molecular dynamics simulations provide particularly detailed insights into atomic scale interactions accounting for ion solvation. In a recent study, we used the beforehand described QM/MM approach to elucidate metal ion solvation in ammonia [41]. The study encompasses mono-, di- and trivalent metal ions and the central focus of the analyses is the possibility of amide formation next to the metal ions. In other terms, we estimated the metal ion acidity within the respective solvent complexes. The resulting coordination complexes are illustrated in Fig. 15.1. For all metal ions, M··N(ammonia, amide) salt bridges lead to the association of a largely immobilized shell of nearest neighbors, whilst the second solvation shell is less structured and mobile. Apart from associating ammonia, the excess charge of the metal ion may also support amide formation. However, for the mono- and divalent metal ions investigated, we found that Coulomb repulsion does not suffice to make deprotonation exothermic, i.e. $\Delta\Delta E_{\text{solv}} < \Delta G_{\text{ref}}$ in equations 15.3 and 15.4. Accordingly, we identified $M^{I/II}(NH_3)_n^{+/++}$ complexes ($M = Na^+, K^+, Mg^{2+}$ with $n = 6$ and $M = Ca^{2+}$ with $n = 8$, respectively) as predominant species at ammono-neutral conditions.

Amide formation was however found to be favored by the trivalent Al^{3+} and Ga^{3+} species. For ammono-neutral conditions, $[Al(NH_2)_3(NH_3)_2]^0$ and $[Ga(NH_2)_4]^-$ complexes, respectively, were estimated as the thermodynamically preferred solvation structures. Interestingly, for Ga^{3+} solvation in ammonia an overcompensation of charge is observed, and negatively charged complexes dominate over a wide range of pH. This trend is also present for Al^{3+} solvation, however $[Al(NH_2)_4(NH_3)_2]^-$ complexes require moderately ammono-basic solutions.

The beforehand described simulations mimic an autoclave scenario. For this, the ammonia solution is first prepared at 239 K and 1 atm. We then keep it at constant

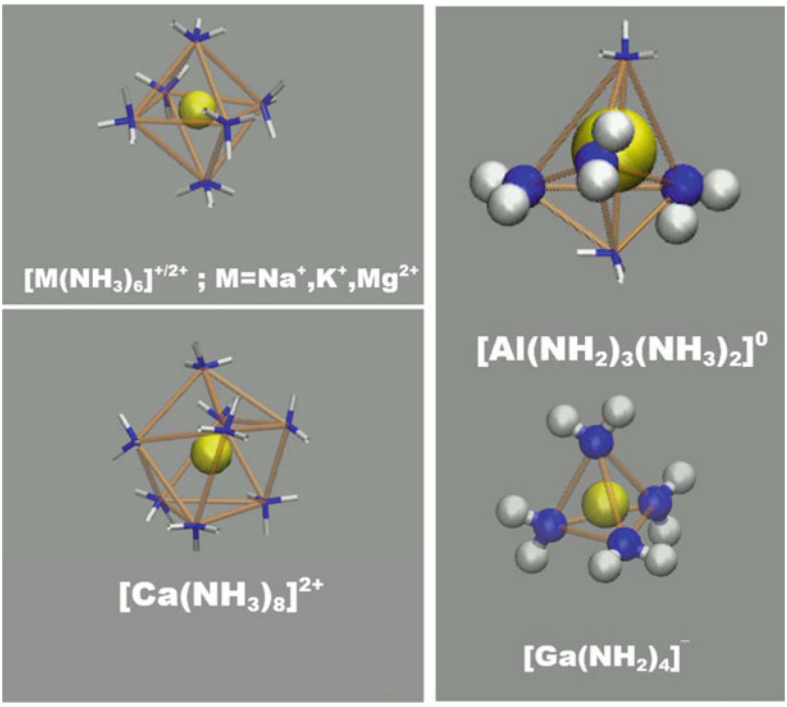

Fig. 15.1 Nearest neighbor coordination of different metal ion species in liquid ammonia. The investigated mono- and divalent ions ($M = Na^+$, K^+, Mg^{2+}, Ca^{2+}; shown in yellow) are coordinated by ammonia molecules (shown as sticks; N: blue, H: white), whilst the +3 charge of trivalent ions leads to amide formation (highlighted as ball-and-stick). For the case of $[Ga(NH_2)_4]^-$ complexes, tetrahedral coordination by amides implies an overcompensation of the positive charge and leads to −1 charged complexes

volume, whilst increasing temperature. This results in a reduction of the dielectric permittivity that changes the equilibrium of ammonium, amide and metal ion complexes considerably. Figure 15.2 illustrates the former by showing the *pK* of bulk ammonia in the autoclave setup as a function of temperature [40]. Moreover, the 'local *pK*' estimated for ammonia molecules that coordinate Al^{3+} and Ga^{3+} ions are calculated [41].

In the studies discussed so far, molecular dynamics simulations were used to model the ionic complexes and the embedding ammonia solution as functions of pressure and temperature [40, 41]. The method is however even more appealing for the investigation of dynamics, such as complex diffusion and aggregation processes. While there is still much work to be done to rationalize metal amide/imide or nitride formation from ammonia solution by molecular simulations, very recently we took some first steps in this direction. Inspired from the experiments of Schimmel et al. we compared the nature of GaF_3 dissolution in ammonia at different conditions [44]. Figure 15.3 illustrates snapshot from molecular dynamics simulations of gallium

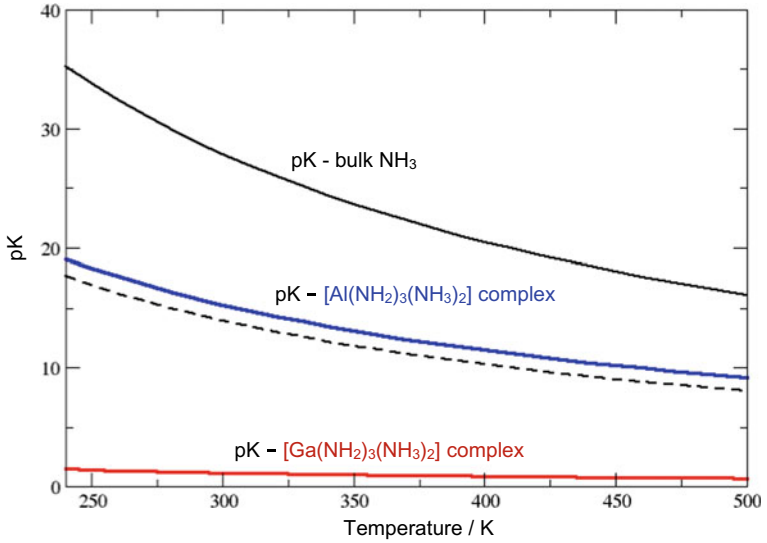

Fig. 15.2 Calculated values of pK in liquid ammonia as functions of temperature (volume fixed to that at 240 K to mimic an autoclave scenario). The pKs (solid curves) of NH_3 autoprotolysis for the bulk liquid are compared to $Al(NH_2)_3(NH_3)_2$ and $Ga(NH_2)_3(NH_3)_2$ complexes, as shown in black, blue and red, respectively. The dashed curve indicates ammono-neutral pH, that is $-\log_{10}[NH_4^+]$ for the pure liquid as a function of temperature. Figure and captions adopted with permission from [41]

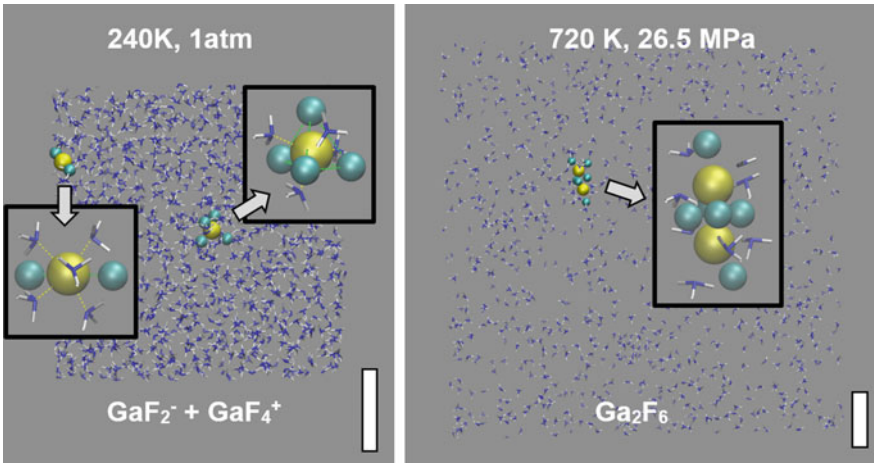

Fig. 15.3 Snapshot from molecular dynamics simulations of dispersed gallium fluoride complexes in ammonia. Left: liquid state at 240 K and 1 atm. Right: supercritical state at 720 K and 26.5 MPa. In the liquid state, the gallium ions were found to form octahedral $[GaF_2(NH_3)_6]^+$ and $[GaF_4(NH_3)_4]^-$ (GaF_4^- tetrahedra with an NH_3 molecule above each triangular face) complexes. While dispersed in the liquid, upon reducing solvent polarity in the supercritical state we find aggregation of these complexes within 100 ps. The scale bars refer to 1 nm. Colors: Ga (yellow), F (cyan), N (blue) and H (white). Figure and captions are adopted with permission from [44]

fluoride complexes in ammonia—in the liquid state (240 K and 1 atm) and in the supercritical state (720 K and 26.5 MPa). From this, ion dispersion was rationalized for the liquid state, in terms of separate $[GaF_2(NH_3)_6]^+$ and $[GaF_4(NH_3)_4]^-$ complexes, respectively. On the other hand, in the supercritical liquid, rapid aggregation was observed, hence hinting at GaF_3 precipitation. Indeed, at *low temperature* experiments indicate *fast Ga mobility* in accordance to nearest-neighbor clusters for the liquid state, whilst at *high temperature* drastically *slower migration* of precipitate particles is found for the superliquid state.

15.6 Conclusions and Perspectives

We are still in the infancy of developing a molecular understanding of ammonothermal syntheses. Molecular simulations can help, however a considerable amount of method development is required. In this contribution, we described a simple-to-implement and computationally efficient approach to calculate 'local *pK*' values. This concept allows the *pH*-dependent assessment of the preferred protonation state of ammonia, both in bulk solution and next to metal ion complexes. Using this simulation approach, parallel setups of classical molecular dynamics simulations are combined to identify the solvation of the reactants and the relaxation of possible products. Hence, a number of ionic species and different protonation states may be screened very effectively.

As a next step en route to metal amide, imide or nitride formation, such QM/MM approaches must be combined with efficient protocols to model aggregate formation. This calls for in-depth characterization of the structural evolution of forming aggregates—for which nanosecond-scale molecular dynamics simulations are nicely suited. On the other hand, the influx of solute species to the forming aggregate, dissociation of NH_4^+ and possibly other species, including fragments comes into play. The latter type of processes can be modelled by molecular dynamics, however at less efficiency compared to kinetic Monte-Carlo approaches. The Kawska-Zahn method therefore married both techniques—and the QM/MM formulation of proton transfer in the course of aggregate growth and relaxation [45, 46]. In some analogy to metal nitride formation, the nucleation of ZnO from $Zn^{2+}/2OH^-$ solutions was recently investigated by this approach [47]. In yet ongoing efforts, this will be transferred to the association of metal ions and metal amide complexes, and the size-dependent ripening that finally lead to stable structures. The ultimate goal of such modelling is to elaborate nucleation mechanisms including de-protonation and re-organization as functions of aggregate size—and hence provide guides to the syntheses of amides, imides and nitrides.

References

1. T.M.M. Richter, R. Niewa, Inorganics **2**, 29 (2014)
2. R. Dwiliński, A. Wysmołek, J. Baranowski, M. Kamińska, R. Doradziński, J. Garczyński, L. Sierzputowski, H. Jacobs, Acta Phys. Pol. A **88**, 833 (1995)
3. Y.C. Lan, X.L. Chen, Y.G. Cao, Y.P. Xu, L.D. Xun, T. Xu, J.K. Liang, J. Cryst. Growth **207**, 247 (1999)
4. J. Higuchi, J. Chem. Phys. **24**, 535 (1956)
5. H. Kaplan, J. Chem. Phys. **26**, 1704 (1957)
6. A.B.F. Duncan, J. Chem. Phys. **27**, 423 (1957)
7. D.M. Bishop, J.R. Hoyland, R.G. Parr, Mol. Phys. **6**, 467 (1963)
8. C.M. Reeves, M.C. Harrison, J. Chem. Phys. **39**, 1 (1963)
9. R. Moccia, J. Chem. Phys. **40**, 2176 (1964)
10. B.D. Joshi, J. Chem. Phys. **43**, S40 (1965)
11. P. Rajagopal, Z. Naturforsch. A 20, 1557 (1965)
12. R.M. Rutledge, A.F. Saturno, J. Chem. Phys. **44**, 977 (1966)
13. U. Kaldor, I. Shavitt, J. Chem. Phys. **45**, 888 (1966)
14. D.M. Bishop, J. Chem. Phys. **45**, 1787 (1966)
15. L.C. Snyder, J. Chem. Phys. **46**, 3602 (1967)
16. R.G. Body, D.S. McClure, E. Clementi, J. Chem. Phys. **49**, 4916 (1968)
17. J.D. Dill, L.C. Allen, W.C. Topp, J.A. Pople, J. Am. Chem. Soc. **97**, 7220 (1975)
18. O. Novaro, S. Cruz, S. Castillo, W. Kołos, A. Leś, J. Chem. Phys. **74**, 1118 (1981)
19. P.J. Turner, C.W. David, J. Phys. Chem. **85**, 3501 (1981)
20. C.E. Dykstra, L. Andrews, J. Chem. Phys. **92**, 6043 (1990)
21. K. Hirao, T. Fujikawa, H. Konishi, S. Yamabe, Chem. Phys. Lett. **104**, 184 (1984)
22. D.D. Nelson, G.T. Fraser, W. Klemperer, J. Chem. Phys. **83**, 6201 (1985)
23. D.D. Nelson, W. Klemperer, G.T. Fraser, F.J. Lovas, R.D. Suenram, J. Chem. Phys. **87**, 6364 (1987)
24. J.C. Greer, R. Ahlrichs, I.V. Hertel, Chem. Phys. **133**, 191 (1989)
25. J.K. Park, J. Phys. Chem. A **104**, 5093 (2000)
26. A. Fouqueau, M. Meuwly, J. Chem. Phys. **123**, 244308 (2005)
27. A. Malloum, J.J. Fifen, Z. Dhaouadi, S.G.N. Engo, N.E. Jaidane, Phys. Chem. Chem. Phys. **17**, 29226 (2015)
28. J. San Fabián, S. Omar, J.M. García de la Vega, Eur. Phys. J. B **91**, 124 (2018)
29. A. Malloum, J.J. Fifen, J. Conradie, J. Chem. Phys. **149**, 024304 (2018)
30. A.D. Boese, A. Chandra, J.M.L. Martin, D. Marx, J. Chem. Phys. **119**, 5965 (2003)
31. M. Bethkenhagen, M. French, R. Redmer, J. Chem. Phys. **138**, 234504 (2013)
32. M. Diraison, G.J. Martyna, M.E. Tuckerman, J. Chem. Phys. **111**, 1096 (1999)
33. J.H. Jensen, H. Li, in *Calculation of Reduction Potential and pKa. Encyclopedia of Inorganic Chemistry* (2009)
34. G. Li, Q. Cui, J. Phys. Chem. B **107**, 14521 (2003)
35. C.C.R. Sutton, G.V. Franks, G. Da Silva, J. Phys. Chem. B **116**, 11999 (2012)
36. J.R. Pliego, Chem. Phys. Lett. **367**, 145 (2003)
37. M.D. Liptak, G.C. Shields, J. Am. Chem. Soc. **123**, 7314 (2001)
38. M. Namazian, S. Halvani, J. Chem. Thermodyn. **38**, 1495 (2006)
39. N. Sadlej-Sosnowska, Theor. Chem. Acc. **118**, 281 (2007)
40. D. Zahn, Chem. Phys. Lett. **682**, 55 (2017)
41. D. Zahn, RSC Adv. **7**, 54063 (2017)
42. M. Albertí, A. Amat, L. Farrera, F. Pirani, J. Molec, Liquids **212**, 307 (2015)
43. K. Heinzinger, J. Molec, Liquids **88**, 77 (2000)
44. S. Schimmel, P. Duchstein, T.G. Steigerwald, A.-C.L. Kimmel, E. Schlücker, D. Zahn, R. Niewa, P. Wellmann, J. Cryst. Growth **498**, 214 (2018)
45. A. Kawska, J. Brickmann, R. Kniep, O. Hochrein, D. Zahn, J. Chem. Phys. **124**, 024513 (2006)

46. J. Anwar, D. Zahn, Angew. Chem. Int. Ed. **50**, 1996 (2011)
47. A. Kawska, P. Duchstein, O. Hochrein, D. Zahn, Nano Lett. **8**, 2336 (2008)

Chapter 16
Properties of Ammonothermal Crystals

Jaime A. Freitas Jr. and Marcin Zając

Abstract This chapter summarizes the present status of bulk GaN crystals grown by ammonothermal basic and acidic methods, and reviews their intrinsic physical properties. Crystals with low dislocation densities, typically well below 10^5 cm^{-2}, high crystal lattice flatness, and sharp X-ray rocking curves (typically below 20 arcsec) are reproducibly grown by both methods. High quality strain-free homoepitaxial films have been successfully deposited on both polar and non-polar ammonothermal substrates. Characteristics of testing devices produced using these epitaxial templates confirm the potential of ammonothermal substrates for fabrication of high performance and high yield devices.

16.1 Introduction

Gallium nitride semiconductor technological importance relies on their variety of applications covering optical, optoelectronic and electronic devices capable of operating under extreme values of current, voltage, temperature and in harsh environment. The major roadblock for full realization of potential applications of this semiconductor is still the availability of affordable large-area and high crystalline quality native substrates with controlled optical and electrical properties. Ammonothermal is the only successful method to grow high crystalline quality real bulk GaN. However, these crystals typically have high concentration of oxygen, resulting on high concentration of free-carriers at room temperature, which prevents full control of these material intrinsic physical properties. The luminescence spectra of such materials usually exhibit a broad and higher-energy shifted near-band-edge recombination emission

J. A. Freitas Jr. (✉)
Naval Research Laboratory, Washington, DC 20375, USA
e-mail: jaime.freitas@nrl.navy.mil

M. Zając
Institute of High Pressure Physics, Polish Academy of Sciences, 01-142 Warsaw, Poland
e-mail: zajac@unipress.waw.pl

E. Meissner and R. Niewa (eds.), *Ammonothermal Synthesis and Crystal Growth of Nitrides*, Springer Series in Materials Science 304,
https://doi.org/10.1007/978-3-030-56305-9_16

involving free-electrons from higher energy states in the conduction band, the so-called Burstein-Moss effect. It has been demonstrated, that the addition of oxygen getter in the feedstock yields one order of magnitude reduction in the concentration of oxygen. As a result, substrates with improved optical transmission, reduced free electron concentration, and low effective p-type electrical conductivity could be realized. Despite the non-optimized quality of epi-ready surface, high-crystalline quality homoepitaxial films have been accomplished, which allows the fabrication of optoelectronic testing devices. In addition, it has been demonstrated that homoepitaxial films conveniently reproduce the typically low concentration of extended defects observed in the ammonothermal substrates. However, considering the lower ammonothermal growth temperature and the relatively lower energy point-defects mobility, new defect may be introduced in the ammonothermal substrates during the epitaxial growth.

The limited access to GaN substrates of high crystalline quality produced by ammonothermal acidic- and basic-growth methods has averted the investigation of the intrinsic material properties and a detailed evaluation of its full potential application to the realization of new device concepts. Most of the studies of the intrinsic properties of GaN have been carried out on heteroepitaxial films or on homoepitaxial films deposited on thick freestanding films, which dislocation densities are in the range between 10^{11} and $10^{6}/cm^{2}$, respectively. In this chapter, we review the properties of the state of art ammonothermal grown GaN (ammono-GaN) crystals and wafers, and their utilization for epitaxial film deposition and device development.

16.2 Ammonothermal Growth: A Brief Overview

Ammonothermal technology, among HVPE and Na flux method, is regarded as the most promising method of bulk GaN manufacturing. It is a process based on solution growth, being an analogue of hydrothermal method, commonly used in industrial production of quartz [1]. The difference is the use of supercritical ammonia as nitrogen source instead of water as oxygen source. The scheme of ammonothermal process is the following: GaN feedstock is dissolved in highly reactive supercritical ammonia solution in one zone of a high-pressure autoclave (dissolution zone). The dissolved feedstock is then transported to the second zone (crystallization zone), where solution is supersaturated, enabling crystallization of GaN on GaN seeds [2]. An appropriate temperature gradient between these two zones induces the convection mass transport. An important aspect of the ammonothermal method is necessity of adding mineralizers to growth environment in order to accelerate its dissociation and enhance the solubility of GaN in ammonia solution. Exceptional structural properties, including threading dislocation density of 10^{4} cm^{-2}, doping feasibility and scalability, are the main advantages of this method. Main drawback of ammonothermal method is small growth rate (several tens of micrometers per day [2]) and time

consuming process required to obtain native seeds of sufficient size (minimum 2-inch) needed to fabricate substrates for commercial applications. However, once population of high quality seeds exceeds the critical mass, large production capacity can be achieved by growing many crystals simultaneously in one reactor at relatively low material cost.

Ammonothermal method is a well-controlled and reproducible process performed at relatively low temperature (a few hundred degrees Celsius) and pressure of a few hundred megapascals. The growth can be conducted under different environments: basic or acidic. The type of environment is determined by the choice of mineralizers. Ammonobasic growth makes use of alkali metals or their amides as mineralizers (NH_2^- ions are introduced into the supercritical solution) [3–5], while in ammonoacidic growth halide compounds are present (NH_4^+ ions are introduced into the supercritical solution) [6]. High-temperature ammonoacidic growth [7, 8] can also be realized by internal heating of the growth chamber (in opposite to external heating of the whole autoclave). This way higher growth temperature and pressure (about 750 °C and 0.6 GPa) than in conventional acidic (500–650 °C, 0.07–0.4 GPa) [6] and basic (400–600 °C, 0.1–0.4 GPa) ammonothermal approach [3] can be achieved by omitting the autoclave material limitations.

Characteristic feature of ammonobasic version of the method is a negative temperature solubility coefficient [3]. As a consequence of retrograde solubility the chemical transport of GaN is directed from the low-temperature solubility zone (with feedstock) to the high-temperature crystallization zone (with seeds). In acidic route the process configuration is reversed. The growth environment determines also the adopted autoclave material. In ammonobasic method the Ni-Cr-based superalloys are usually used as a material resistant to high pressure and harsh environment. In acidic route a use of liner made of precious metal is required to avoid contamination from autoclave walls and prevent autoclave corrosion. Lately, an ammonoacidic growth was realized in titanium-zirconium-molybdenum (TZM) alloy [9], while the acidic high temperature growth is carried out in sealed capsule, surrounded by internal heater, a ceramic shell providing mechanical support and thermal insulation, and steel outer shell that provides mechanical confinement [8].

Initial work on basic ammonothermal growth method was performed in the middle of the 1990s [10]. Synthesis of GaN was then realized in supercritical ammonia from metallic Ga at a temperature of 500 °C and pressure of 0.4–0.5 GPa. The first crystals were in the form of wurtzite-type microcrystalline powder of intense near band edge photoluminescence. Later reports describe synthesis of transparent GaN platelets or prismatic needles with dimensions up to 0.5 mm × 0.2 mm × 0.1 mm in ammonobasic solution [11] and needle-shaped GaN crystals (with diameter up to tens of micrometers and length of hundreds of micrometers) in ammonoacidic solution [12]. In the 2000s a few groups were engaged in ammonothermal method and took advantage of chemical transport in temperature gradient in both environments [13–21]. At present, there are several companies and academic institutions working on ammonothermal growth of GaN, such as Institute of High Pressure Physics, Polish Academy of Science (IHPP PAS), which lately acquired Ammono company (Poland; basic environment) [2–5], SixPoint Materials Inc. (United States; basic) [22, 23],

University of California at Santa Barbara (United States; acidic and basic) [24–26], University of Stuttgart (Germany; acidic and basic) [27], Mitsubishi Chemical Corp. (Japan; acidic) [6], Tohoku University (Japan; acidic) [28, 29], Asahi Kasei Corp. (Japan; acidic) [30], Soraa, Inc. (United States; high-temperature acidic) [7, 8]. Diameters of ammonothermal GaN crystal were of a few millimeters in 2006–2007 and reached 2 in. in 2010 [19]. Lately, a *c*-plane oriented seed crystal of 65 mm × 75 mm dimensions, that can be used for 3-inch crystal production after lateral expansion, was demonstrated in case of basic version of the ammonothermal method [2].

In general, the ammonobasic method can be carried out in *c*-direction. The highest growth rate in ammonothermal method takes place in the lateral *a*-direction ($\langle 11\bar{2}0\rangle$) (or in semipolar direction, like $\langle 11\bar{2}2\rangle$), while the lowest growth rate is in the *m*-direction ($\langle 10\bar{1}0\rangle$) [24, 25, 31]. Saito et al. published the following total growth rates: 11 μm/day in the *m*-direction, 79 μm/day in the *c*-direction and 87 μm/day in $\langle 11\bar{2}2\rangle$-direction [31]. When a silver capsule system is used (a non-hermetically sealed container placed in NiCr superalloy autoclave body), the growth rate can increase to 46 μm/day, 344 μm/day, and 550 μm/day in the *m*-direction, both *c*-directions, and $\langle 11\bar{2}2\rangle$-direction, respectively [24]. Later results show that molybdenum (Mo) capsules cause lower total growth rates: about 30 μm/day, 80 μm/day, 200 μm/day, and 250 μm/day in *m*-direction, both *c*-directions, *a*-directions and $\langle 11\bar{2}2\rangle$-direction, respectively [25]. It should be noted that the published growth rates include growth rates in two opposing directions, both in case of vertical (sum of growth rates in $+c$ and $-c$-directions) and planar growth. IHPP PAS uses an approach, in which the growth is conducted mainly in the $-c$-direction (N-face). Crystallization in the $+c$-direction is treated as parasitic with an unstable morphology and different composition of dopants (mainly oxygen) [17], leading to substantial stress in the crystal. Therefore, only the N-face surface is exposed for vertical growth. The tendency in relative growth rate in different directions remains similar, i.e. *m*-plane is the slowly growing face and *a*-plane is the fast growing face [2]. However, as soon as the lateral growth front meets the nearest *m*-plane, stable and slow growing *m*-plane faces form and further lateral growth is diminished. The acidic growth can be performed with the rate of few hundreds μm per day [29]. In particular, the choice of NH_4F mineralizer (instead of other halides) enables the growth in all directions with high speeds (410 μm/day and 465 μm/day in *c*-direction and *m*-directions, respectively) [29].

16.3 Structural Properties

GaN, together with AlN and InN, belongs to group-III-nitride family. It has three crystalline structures: the wurtzite, zincblende, and rocksalt. The thermodynamically stable wurtzite structure has a hexagonal cell with 6 atoms of each type and two lattice constants; *c* and *a*. This structure consists of two interpenetrating hexagonal close packed (HCP) sublattices, each with one type of atoms, offset along the *c*-axis by 5/8 of the cell height. The wurtzite structure belongs to the space group

$P6_3mc$ (C_{6v}^4). The zincblende structure has a cubic cell containing four Ga and four nitrogen atoms. This structure belongs to the space group $F\bar{4}3m$ (T_d^2) and has only been stabilized by chemical vapor or molecular beam epitaxial deposition processes on foreign substrates. The rocksalt structure can be induced only under very high-pressure conditions and it will not be discussed.

The basic unit of the wurtzite and the zincblende GaN structures consists of bonded tetrahedrons of Ga (or N) atoms with an N (or Ga) at the center (Fig. 16.1a). The identical polar layers of Ga_4N (or N_4Ga) are continuously stacked and the permutation of stacking sequences allows the different one-dimensional ordering or polytypes. The stacking sequence of these polytypes can be described by the "ABC" notation, where A, B and C represent the three sites available in one sublattice. In the zincblende structure, the stacking sequence of the (111) plane is (…ABCABC…) in the ⟨111⟩ direction. For the wurtzite structure, the sequence of the plane (0001) is (…ABABAB…) in the ⟨0001⟩ direction. Diagrams representing the wurtzite and zincblende stacking are show in Fig. 16.1b. These two structures also differ in the bond angle of the second-nearest neighbor. In the zincblende structure, differently from the wurtzite structure, there is a 60° rotation along the [111] direction that results in the stacking order of (…ABCABC…).

The lattice parameter semiconductors are affected by factors such as stoichiometry, excess of impurities, high concentration of point and extended defects. The wurtzite structure is characterized by lattice parameter ratio (c/a) and u-parameter value ($u = b/c$, where b is the bond-length in the c-direction) of 1.633 and 0.375, respectively [32]. The deviation from this ideal arrangement occurs with changing of c/a ratio and/or the u-parameter. Deviations from ideal arrangement are often observed in the wurtzite structure. Compounds characterized by larger deviation from ideal c/a show greater differences in the electron negativities [33, 34]. Only wurtzite crystals with c/a axial ratios close to the ideal value of 1.633 are stable. The c/a axial ratio for GaN is 1.627, and is very close to the ideal value [32].

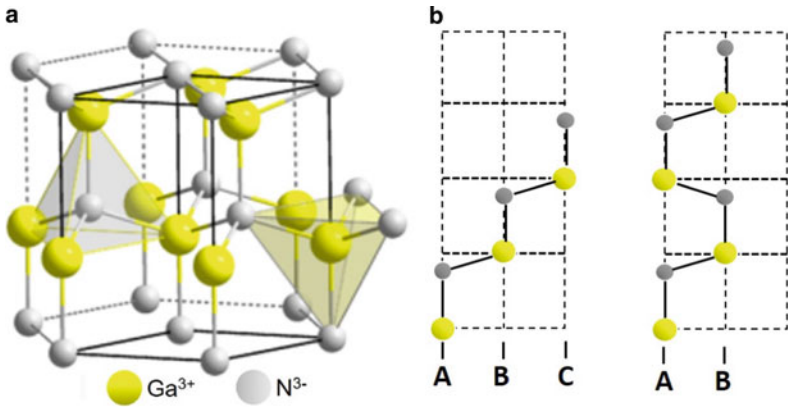

Fig. 16.1 **a** Wurtzite GaN structure formed by bonded tetrahedrons of Ga with N at the center. **b** Stacking sequence of the cubic (ABCABC…) and hexagonal (ABAB…) bi-layers

Sharp X-ray rocking curves were obtained for the symmetric reflections from *c*-, *a*-, and *m*-plane semi-insulating (SI) basic ammonothermal crystals (B-Ammono), as shown in Fig. 16.2a–c, with their FWHM values ~20 arcsec. Another significant observation is that the wafer curvature is less than 1.6×10^{-3} m^{-1} or radius of curvature is greater than 600 m from the size of the sample. Typical non-bulk GaN has a radius of curvature in the order of 0.5 m [35]. Multiple symmetric and asymmetric HR-XRD (High Resolution X-Ray Diffraction) scans of B-Ammono samples, depicted in Fig. 16.3, were used to obtain *a*, and *c*-lattice parameters using least squares fitting for all the samples as listed in Table 16.1. These values are the same as those reported for bulk GaN lattice constants [36], indicating almost no strain in the samples.

Yoshida et al., also reported sharp X-ray rocking curves for the symmetric reflections of *c*- and *m*-planes basic ammonothermal grown GaN crystals [30]. Acidic chemistry ammonothermal crystals grown on *m*-polar seeds also yields very sharp FWHM X-ray rocking curves, as reported by Mikawa and co-workers [6]. Bulk GaN with larger FWHM of X-ray rocking curves were obtained from crystals grown by a novel higher temperature acidic ammonothermal method, which uses an internally heated autoclave. These measurements were performed with a PANalytical MRD PRO high-resolution four-cycle diffractometer operating in a receiving mode (0.5° source slit, 1 mm vertical detector slit) using a Cu Kα radiation and a hybrid two-bounce Ge(220) monochromator [8].

Raman scattering (RS) spectroscopy is another well-established noninvasive technique commonly employed to study vibrational phenomena in solids. The inelastic

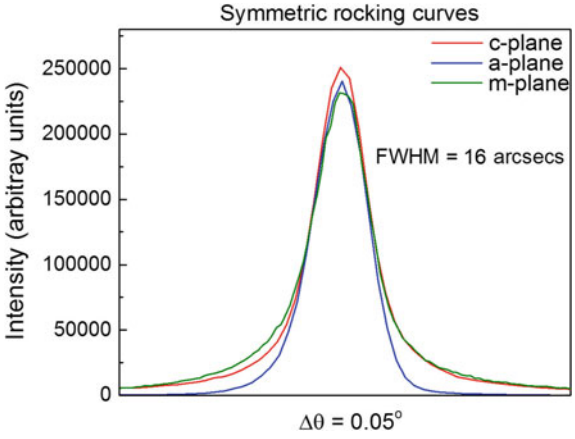

Fig. 16.2 High-resolution X-ray rocking curve of *c*-, *a*-, and *m*-plane SI B-Ammono samples. These measurements were acquired with a Rigaku Smartlab diffractometer, equipped with a 9 kW Cu rotating anode, a collimating mirror, and a four bounce Ge (220) channel cut monochromator. The slits widths were 1 mm on both the incident and analyzing sides in order not to artificially reduce the intrinsic sample FWHM (after [37])

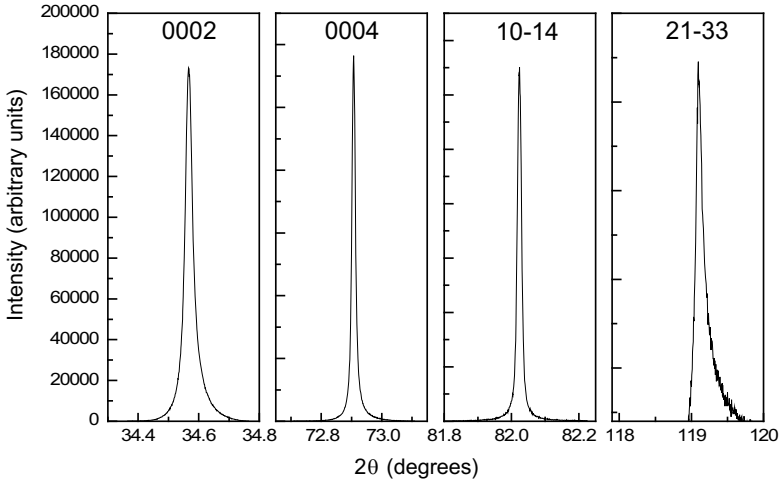

Fig. 16.3 Symmetric and asymmetric HR-XRD scans of *c*-plane B-Ammono GaN samples

Table 16.1 *a*- and *c*-lattice parameter obtained using least-square method from multiple symmetric and asymmetric HR-XRD scans of *c*-, *a*-, and *m*-plane B-Ammono SI samples (after [37])

Sample	*a* (Å)	*c* (Å)
c-plane	5.1856(1)	3.1890(5)
a-plane	5.1851(1)	3.1892(4)
m-plane	5.186(1)	3.1891(2)

scattered light is susceptible to selection rules originating from momentum conservation, which allows the detection of phonons (intrinsic material vibrational modes) near the center of the Brillouin zone (BZ, Γ-point). In case of semiconducting materials the laser light interacts with phonons or other excitation (e.g., plasma, spins) in the system, resulting in the energy shift of the photons, the Stokes (lower frequency/energy, phonon creation) and the anti-Stokes (higher frequency/energy, phonon annihilation). While light polarization (selection rules) measurements allow the identification of the crystal structure, measurements of the peak position and lines width of the phonons gives information about the material quality, stress, and sometimes impurity related phenomena. The number of atoms per unit cell (n_a) can be determined from the number of biplanes (n_b) in the polytype by: $n_a = n_b \times n$, where $n = 2$. Therefore, the zincblende polytype (ABC) will have two atoms (one molecule) per unit cell and the wurtzite polytype (ABAB) will have four atoms (two molecules) per unit cell. Group theory predicts for the wurtzite GaN structure eight Brillouin zone-center optical vibrational modes, namely $1A_1$(TO), $1A_1$(LO), $2B_1$, $1E_1$(TO), $1E_1$(LO), and $2E_2$. The two $2B_1$ modes are optically inactive, but all the allowed optical modes have been observed by RS [38]. The energy position of E_2 mode is very sensitive to stress present in the crystal.

The first order RS spectra of *a*- and *c*-plane SI and unintentionally doped (with high background concentration of free-electrons, n^+) B-Ammono samples, measured at room temperature, are represented in Fig. 16.4a and b, respectively. The Raman shifts for the allowed modes $1A_1(TO)$, $1A_1(LO)$, $1E_1(TO)$, $1E_1(LO)$, E_2 (low) and E_2 (high) are 530.7, 732.9, 558.2, 738.1, 141.6, and 567.1 cm^{-1}, respectively. Analyses of the peak positions and line widths of the observed first order phonons confirm the good crystalline quality and lower biaxial stress of the B-Ammono GaN wafers. Similar results were published by Gogova et al. [39] for *m*-plane non-intentionally doped (n^+-type) substrate with high oxygen concentration. High background concentration of free-electrons, introduced by high concentration of uncompensated shallow donors, results in the formation of free-carriers collective mode (plasmon) with low and high dispersion curves, ω^- and ω^+ respectively, depicted in Fig. 16.4b. The plasmon modes couple with the polar phonons ($A_1(LO)$ and $E_1(LO)$ phonons) introducing the new vibrational mode LPP (LO-phonon-plasmon couple mode), which peak position increases with increasing free-electron concentration. Spectral analysis of the LPP can be conveniently used to estimate the residual doping level of the samples [40, 41].

The spectra of SI wafers highlighted in Fig. 16.4a, which do not have the LPP modes, indicate that wafers with low effective free-carrier concentration may be obtained by doping with compensating acceptor impurities during the growth. However, the intrinsically high background concentration of shallow donors requires a higher concentration of compensating acceptors, which may affect the crystalline

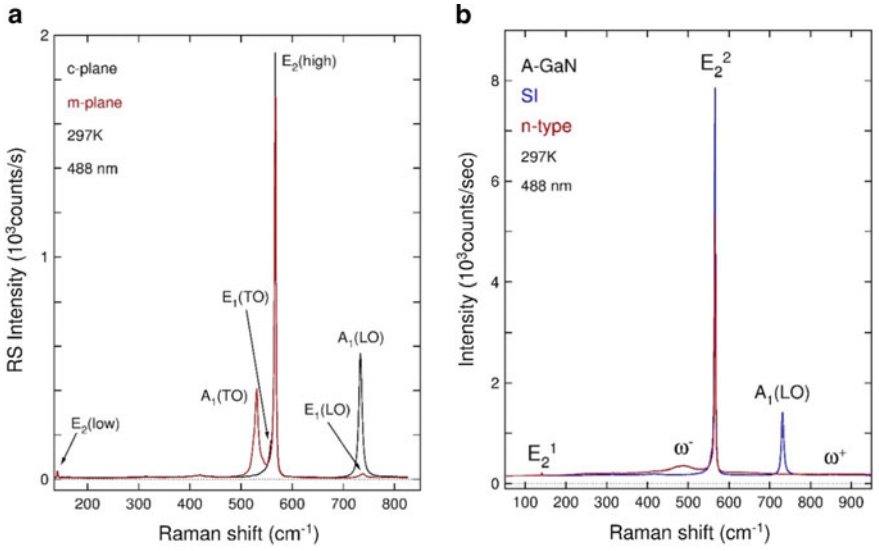

Fig. 16.4 **a** First order Raman spectra of *c*- and *m*-plane SI B-ammonothermal GaN. **b** First-order Raman spectra of SI and n^+ *c*-plane B-Ammono samples. The latter highlights the ω^- and ω^+ plasmon modes, commonly called LPP^- and LPP^+, respectively

quality and other properties of the substrates and limit their potential applications. Therefore, the ammonothermal growth processes must be improved to reduce orders of magnitude the pervasive high residual concentration of oxygen. Recently this high concentration of oxygen was reduced by the use of getter in ammonothermal growth [2].

16.4 Extended Defects

It has been well established that structural defects such as dislocations, low-angle grain boundaries, inclusions, growth sector boundaries, and twins present in the substrate and intersecting the growth interface will be replicated into the epitaxial layers. These defects may compromise the performance, lifetime, and yields of devices fabricated on these templates. Therefore, the identification of defect type and concentration must be carried out on the as-grown bulk single crystals, hoping that they may be eliminated or at least minimized. Techniques such as selective etching, transmission electron microscopy, and X-ray topography are commonly employed to evaluate the crystalline quality. The two first techniques are destructive and are adequate to investigate crystals with medium to high concentration of defects. X-ray topography (XRT) is a non-destructive method suitable to the characterization of structural defects in large crystals with relatively low defects densities [42]. Synchrotron white-beam X-ray topography (SWBXT) surmounts monochromatic XRT limitations and provides a rapid map of defects structures in large crystals [43].

The small FWHM of 16–18 arcsec, measured on B-Ammono GaN samples and listed in the previous section of this chapter, yields an upper limit of the average dislocation densities below to 10^5 cm^{-2} [44, 45]. However, a reliable value of dislocation density was only accessed by monochromatic HR-XRT (High-Resolution X-Ray Topography) imaging. Figure 16.5a shows the HR-XRT image of the (213) reflection from a *c*-plane GaN sample. In this image of the 1 cm^2 wafer, 16 threading dislocations (TD) were observed, indicating a dislocation density in the order of 20 cm^{-2}. The traces of chemical mechanical polishing (CMP) damage in the semi-insulating GaN *c*-plane sample are also observed. Another significant observation is that this image was taken in a single exposure, which is consistent with wafer curvature less than 1.6×10^{-3}/mm, or radius of curvature is greater than 600 m from the size of the sample. A single defect bounded by dislocations was observed on this HR-XRT image, which is a typical signature of stacking fault. This a singular case, as the HR-XRT imaging of other samples do not show this feature [37].

The HR-XRT image of a-plane wafer is depicted in Fig. 16.5b. The threading dislocation density is of the order of 10 cm^{-2}. Misfit dislocations are also observed emanating from the edge of the sample, tilted towards the surface. These are also of the order of 10 cm^{-2} [37]. The CMP process could have generated these misfit dislocations. Figure 16.5c shows the HR-XRT image of the *m*-plane wafer. The dislocation density is similar to the other basic ammonothermal wafers of the order

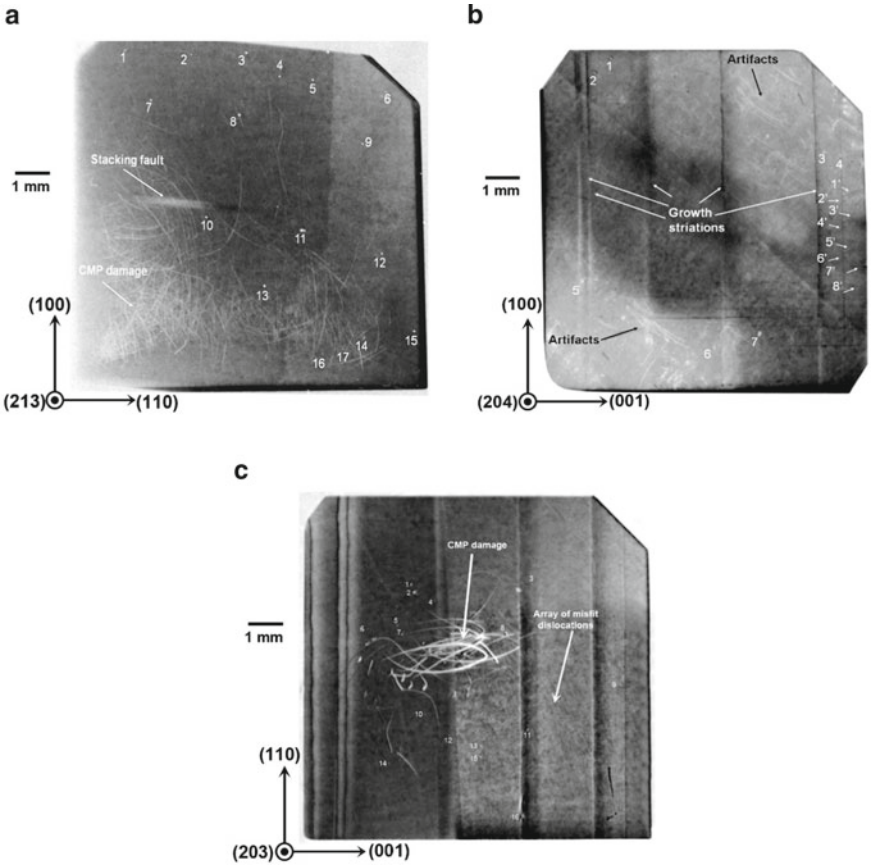

Fig. 16.5 HR-XRT (High-Resolution X-Ray Topography) imaging; **a** *c*-plane, **b** *a*-plane, and **c** *m*-plane (after [37])

of 20 cm^{-2}. Additionally, growth lamellas with clearly visible interfaces every 2–3 mm intervals are observed in non-polar samples. Here, the growth was performed in the *c*-axis direction in multiple growth runs and then the samples were cut in the *a*- and *m*-planes. Such GaN boules grown in subsequent runs have unintentional differences in impurity concentration at the interfaces resulting from different thermal conditions (cooling and heating) at the end of one process and start of the next one. At present thick boules are grown at higher growth rate regime in a single run [46]. Such approach leads to more homogeneous impurity incorporation.

Despite that contrast is strongly affected by numerous scratches present at the surface of the *c*-plane sample, highlighted in Fig. 16.5, the grazing incidence SWBXT topograph of these sample, depicted in Fig. 16.6, yields treading screw dislocation (TSD) and treading edge dislocation (TED) densities of 3.927×10^2 cm^{-2} and

Fig. 16.6 Grazing incidence SWBXT topograph of the SI *c*-plane sample depicted in Fig. 16.5a. After [47]

1.674×10^3 cm^{-2}, respectively. These results are in good agreements with the HR-XRT results.

Defect selective etching (DSE) performed on *c*-plane B-Ammono GaN wafer, using a KOH-NaOH eutectic etchant at 450 °C, verified the presence of treading screw and treading mixed dislocations with concentrations of ~3×10^4 and ~3×10^3 cm^{-2}, respectively. In contrast, no TED was observed across the studied areas, indicating that TED concentration was negligible. These results were in good agreement with SWBXT imaging acquired in the same sample regions [48]. Both SWBXT studies carried out on B-Ammono bulk crystals yield similar concentrations of dislocations. Etch pit density (formed during cooling period after the growth process in the autoclave) studies of acidic chemistry ammonothermal crystals grown on *m*-polar seeds was estimated at 2.5×10^2 cm^{-2} [6], which is similar to dislocation density observed on basic chemistry ammonothermal samples [3]. The DSE of the *c*-plane (0001) 2-inch wafers revealed by etching in sulfuric acid at 270 °C for 1 h was in the range 1×10^2 to 1×10^4 cm^{-2} [6].

Transmission electron microscopy (TEM) have been conveniently used during the initial development stage of ammonothermal growth method of bulk GaN. At that time, thread dislocation density were typically in the order of $\leq 1 \times 10^7$ cm^{-2}. In addition, microscopic misoriented crystal grains and basal plane stacking faults, the latter bounded to Shockley partial dislocations, were revealed by SWBXT and DSE [49, 50]. Presently, the concentration of TD in ammonothermal GaN has been drastically reduced to typical concentrations between 10^3 and 10^4 cm^{-2}, stacking faults have been eliminated, and single grain crystal growth has been accomplished.

Recent TEM studies of thermal annealed high crystalline quality ammonothermal GaN reveals that high concentration of vacancies, typical in ammonothermal GaN, can drive the conversion of thread dislocation to helical dislocation and the formation of voids [51].

16.5 Point Defects

It has been verified that point defects introduce localized states into the band gap of semiconductors. These defects may trap charge carriers, resulting in compensation and/or free carriers scattering, and may introduce bandgap absorption and emission bands. Therefore, the intrinsic electrical and optical properties of semiconductors can be strongly affected by the presence of point defects. The suppression of point defects, which is crucial to full control of the optical and electronic properties of GaN, will require the detection, identification, and characterization of their properties. Point defects in semiconductors have been traditionally investigated by electrical and optical techniques, such as Hall measurements, deep-level transient spectroscopy, and infrared absorption. Despite that the defects can be detected by these techniques, their atomic nature remains often unidentified. Electron paramagnetic resonance (EPR) is very sensitive to chemical nature and structure of defects, but due to the lack of hyperfine interactions, so far has provided very limited information about GaN defects. In the last two decades, positron annihilation spectroscopy (PAS) was widely used to investigate radiation damage in Si and Ge [52, 53]. In PAS technique, positrons produced by a radiative isotope (e.g., ^{22}Na; or by nuclear reactors and particle accelerators) impingent into a solid can get trapped in and localized at neutral, negative charged vacancies, and complexes. As a result, commensurable variation of the positron lifetime and the momentum distribution of the annihilating positron-electron pair (the two 511 keV photons, γ-rays) can be used to determine the vacancy concentration, distinguish between different vacancy types and their chemical environment [54].

PAS has been successfully employed to identify Ga vacancy in high-nitrogen-pressure GaN single crystals [55], which is now known to be the dominant intrinsic acceptor defect in both unintentionally and n-type doped GaN [56]. Preliminary PAS studies of B-Ammono GaN n-type samples verify the presence of relatively high concentration of Ga vacancy (V_{Ga}) related defects. However, no positron trapping at vacancy defects were observed in Mg-doped samples, which is consistent with Fermi level localization closer to the valence band and positively charged intrinsic defects [57]. Recent studies of n-type B-Ammono GaN with various concentration of oxygen, which has been directly correlated with free-carrier concentration, show that the V_{Ga} concentration increases with oxygen content. The measured positron lifetime of these samples indicates that V_{Ga} form complexes with hydrogen atoms. However, the number of hydrogen atoms in each vacancy decreases with increasing free electron concentration (oxygen doping level), as confirmed by Fourier Transformed Infrared Spectroscopy (FTIR) local vibrational modes [58]. Figure 16.7

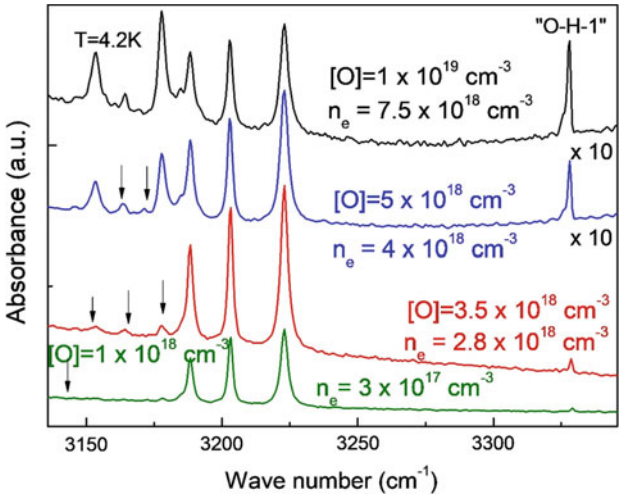

Fig. 16.7 FTIR absorption spectra of two basic ammonothermal GaN samples with different oxygen and free-electron concentrations, measured at 4.2 K with unpolarized light propagating along the *c*-axis. The arrows indicate gradually emerging lines attributed to $V_{Ga}H_{1,2}$ complex (after [2])

shows the local vibration modes between 3150 and 3230 cm^{-1} associated with V_{Ga}-multihydrogen complexes $V_{Ga}H_n$ with $n = \{1, 2, 3, 4\}$ [2, 16, 59]. Suihkonen et al., carried out a detailed polarization-dependent study of these lines on m-plane samples to obtain complete assignment of the $V_{Ga}H_n$ defects [60]. Similar results were observed on acidic ammonothermal grown bulk GaN, which reported that those defects were stable even after thermal annealing at 1000 °C [61]. More recently, Jiang and coworkers reported that complex point defects V_{Ga}-O-H and/or V_{Ga}-O-2H, are compensating acceptors in n-type acidic ammonothermal GaN. These hydrogenated Ga vacancies complexes are optically active with localization energy at about 0.5 eV above the valence band, and associated with increasing sub-band-gap absorption band at violet spectral region [62, 63].

16.6 Optical Characterization

The band structure of a semiconductor is of fundamental importance to determine its potential applications. Therefore, it is crucial to obtain an accurate band structure of GaN. The first wurtzite GaN band structure found through a pseudo-potential method yield a 3.5 eV direct bandgap. The conduction band wave function of wurtzite crystals are formed with atomic orbitals *s* and transform the Γ point congruent with the representation Γ_7 of the space group C_{6v}^4. The upper states of the valence band results from linear combination of p_x, p_y, and p_x-like orbitals. The crystal field and spin-orbit interactions, characteristic of the wurtzite structure, split the six-fold degenerated Γ_{15}

into Γ_9, and upper and lower Γ_7 levels. The hole effective mass of the three uppermost valence bands Γ_9, Γ_7, and Γ_7 have large k-dependency. These bands are labeled as HH (Heavy-Hole Γ_9; "A"), LH (Light-Hole, upper Γ_7, spin-orbit split—Δ_{SO}; "B"), and CH (Lower Γ_7, crystal-field split—Δ_{CF}; "C"). While the effective mass of Γ_9 is heavy in all k directions, both Γ_7 are relatively lighter in the k_x, k_y plane, but heavy in the k_z direction. A schematic representation of the wurtzite GaN electronic band structure near the Γ-point is represented in Fig. 16.8. A detailed review of the electronic band structure calculation employing various approximation methods, and optical and electronic parameters of III-V nitride semiconductors has been reported by Persson and da Silva [64]. It has been reported that the room temperature direct bandgap energy of wurtzite GaN polytype is 3.42 eV (the 4 K value is 3.505 eV), and the electron and hole effective masses are 0.22 m_o and >0.80 m_o [65], respectively.

It is well known that extended and point defects strongly affect the optical and electronic properties of semiconductors, limiting considerably the performance and yields of devices based on these material systems. The successful development of ammonothermal bulk GaN resulted on considerable reduction of the concentration of extended defects, such as dislocations and stacking faults, as discussed in previous section. Despite that, native point defects (mainly related to Ga vacancies and complexes) and impurities related defects (H, Si, O, C, Mn, Na, Mg, Zn), are still plaguing ammonothermal GaN substrates [2]. Table 16.2 shows current impurity concentrations of highly n-type and low n-type (high transparency) B-Ammono GaN

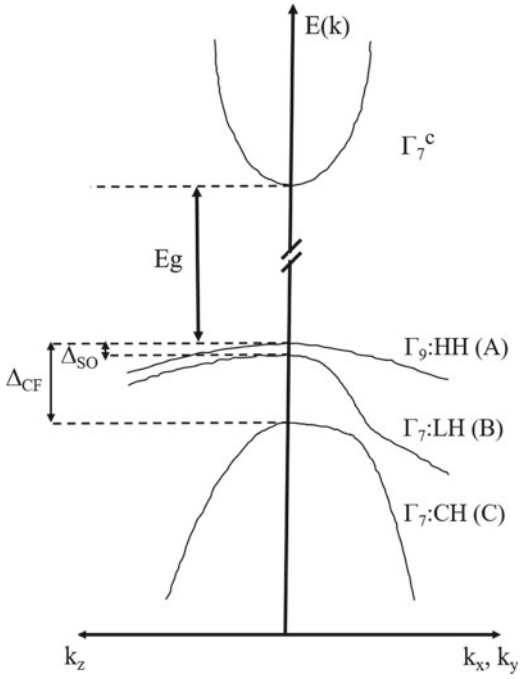

Fig. 16.8 Schematic representation of the wurtzite GaN electronic band structure

Table 16.2 SIMS concentration of various elements of highly n-type and low n-type (high-transparency) B-Ammono GaN substrate showing improvement in reduction of oxygen concentration

	H	SIMS concentration (cm^{-3})							
		O	Si	C	Mg	Zn	Mn	Fe	Na
Highly n-type	1×10^{19}	1.2×10^{19}	1.6×10^{17}	1×10^{17}	3.5×10^{16}	6.6×10^{16}	2.1×10^{16}	1.3×10^{15}	1×10^{16}
Low n-type	1.4×10^{18}	1×10^{18}	1.1×10^{17}	5.5×10^{16}	1.5×10^{16}	6.2×10^{16}	6.5×10^{15}	1.1×10^{15}	3.1×10^{15}

substrates. A reduction of oxygen concentration (and some other elements to some extent) by one order of magnitude in second sample is clearly observed. Native defects are always present in semiconductors, and they are often introduced as compensating centers if impurities (residual or intentional doping) are present. In the last two decades, due to a considerable improvement in computational power, ab initio calculation methods has significantly increased the accuracy of predicting the defect energy levels, formation energy, and range of concentrations [66–69]. More recently, first-principle calculation, based on self-consistent density-functional theory (DFT), usually within the local density approximation (LDA), general gradient approximation (GGA), or hybrid functional, enabled most accurate calculation of formation energy, position of the defect levels, binding energies, dissociation energy of complex defects, local vibration modes, and migration barriers [63].

Full identification of defects are very difficult to accomplish, therefore theoretical calculation predicting their energy positions, energy formations, and other properties are extremely helpful for experimental investigations. The formation energies for all native point defects in all stable charge states, as a function of the Fermi level, using advance computations employing large supercells have been reported [70–72]. It was found that, self-interstitial and antisite defects have very high formation energies and thus are less likely to be incorporated during the growth, at least in the n-type GaN. However, gallium and nitrogen vacancies can be abundant in n-type and p-type GaN, respectively.

There have been a number of calculations to estimate the energy levels of donors and acceptors in GaN. In general, it has been assumed that C, Ge, and Si substitutional to Ga (cation) sites and O, S, Se on the N (anion) sites are shallow donors, while Be, Ca, Cd, Mg, and Zn substitutional to Ga and C, Ge, and Si on the N sites could potentially give rise a relatively shallow acceptor levels. Effective mass approximation accounting for mass anisotropy and central cell corrections estimate donor ionization energies for C, Ge, and Si substitutional to Ga, and O, S, and Se on the N site between 29.0 and 34.0 eV [73]. However, first principle calculation indicates that differently from Si_{Ga} and Ge_{Ga}, C_{Ga} have much larger energy formation [69]. Presently, it is well accepted that oxygen is the dominant shallow donor in ammonothermal GaN responsible for the large free-carrier concentrations [2]. Mireles et al. and Wang et al. calculated the acceptor levels for Be, Mg, Zn, Ca on the cation sites and C and Si, and Ge in the anion sites [73, 74]. Despite that calculations predicted lowest ionization energies for Be_{Ga} and Mg_{Ga}, only Mg has resulted on effective hole concentration at room temperature [75].

Photoluminescence (PL) is a well-established, highly sensitive, non-invasive and non-destructive technique to detect and identify native and impurity related point defects and their complexes in semiconductors. Characterization by PL involves the measurement and interpretation of the spectral distribution of recombination radiation emitted by the samples. Photon-generated electrons and holes usually become localized or bound at an impurity or intrinsic defect before recombining, and the identity of the localized center that they were bound at can often be determined from the luminescence spectrum. Qualitative information about the crystal quality can be inferred from the efficiency and line width of near band edge emission spectra, and

impurities can sometimes be identified based on the binding energies inferred from the spectral positions and free-to-bound transitions. In general, due to the presence of various radiative and/or non-radiative recombination processes competing for the generated electron-hole pairs, luminescence process cannot be conveniently used as a reliable quantitative technique.

As high crystalline quality real bulk GaN crystals with low impurity background levels are still not available, thick freestanding films grown by hydride vapor phase epitaxy (HVPE) on foreign substrates has been used to investigate intrinsic material physical properties. These unintentionally doped (UID) samples are intrinsically n-type with typical carrier concentrations between low 10^{16} and high $10^{17}/cm^3$, due to uncompensated concentration of shallow silicon and oxygen donors. The low temperature PL spectra of HVPE GaN are dominated by an intense line around 3.47 eV, the near band edge (NBE) emission band, which are associated with the recombination processes involving the annihilation of free excitons and excitons bound to neutral donors and acceptors, if neutral Mg shallow acceptor impurity is present [76]. The spectra of samples with high concentration of uncompensated donors (typical for ammonothermal bulk GaN) exhibit a broad and high-energy shifted NBE free-carrier recombination emission due to the filing up of the states at the bottom of the conduction band, the so call Burstein-Moss effect [77]. These high-energy shifts of the NBE emission bands have been observed in the PL spectra of both the high-pressure nitrogen solution growth samples, and in the PL of both the B-Ammono and acidic ammonothermal GaN samples [61, 78]. Also, emission bands with peaks of around 2.2 and 3.2 eV are commonly observed. The former is the well-known yellow band, and the latter is assigned to the recombination processes involving the recombination of electrons bound to shallow-donors with holes bound to shallow-acceptors and its phonon replicas (DAP band) [79, 80].

Figure 16.9 shows the low temperature photoluminescence spectra of unintentionally doped (UID) *a*-, *c*-, and *m*-plane B-Ammono GaN wafers. The spectrum of the *m*-plane sample (the purple color line) is quite similar to that observed at HVPE samples, showing an intense sharp NBE emission band and a weaker contribution from the shallow Mg related DAP band. However, this spectrum also shows a relatively intense broad band with peak near 2.9 eV that has been observed in Zn-doped GaN films [81]. The spectrum of the *a*-plane samples (the red line spectrum), much weaker than that observed for the *m*-plane sample, shows a broader and high energy shifted NBE and a very weak contribution from Mg-related DAP emission band. SIMS analysis of B-Ammono GaN indicates that H and O are the main unintentional impurities, but Mg, Zn, and Mn acceptors are also incorporated at much lower levels [2], consistent with the observation of these DAP related emission bands. The spectra of the *c*- and −*c*-plane (Gallium and Nitrogen polar directions, respectively) are represented by the blue and green lines spectra, respectively. Dominant Mg related DAP emission bands are observed from both faces. Note that the Mg-DAP emission band of the N-polar face spectrum is over 6-fold more intense than that of the Ga-polar face, and the NBE intensity is substantially reduced. This observation is consistent with higher incorporation of Mg in the N-polar face, as previously reported by Freitas et al. [80]. Note that the intensity of the DAP emission band is much larger than the

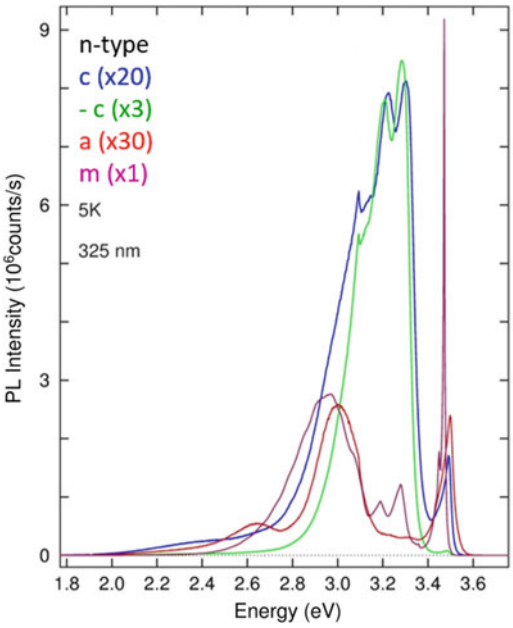

Fig. 16.9 Low temperature photoluminescence spectra of UID *a*-, *c*-, and *m*-plane wafers. Very intense Mg-related DAP emission bands observed in the spectra of the *c*-plane wafer are consistent with reactor doping memory

NBE emission band intensity in the *c*-plane sample spectra, while the opposite ratio is observed in the spectra of *m*- and *a*-plane samples. This suggests that this high concentration of unintentional Mg doping may result from reactor memory after the growth of Mg-doped boules.

Figure 16.10 shows the low temperature photoluminescence spectra of nominally semi-insulating *a*-, *c*-, and *m*-plane B-Ammono GaN wafers. These samples were grown by introducing oxygen getter to reduce the concentration of oxygen to 1–2 $\times$ 10^{18} cm^{-3} (from typically 2 $\times$ 10^{19} cm^{-3}), and adding Mg to achieve concentration of 1–2 $\times$ 10^{18} cm^{-3} in the crystal. Note the absence of any NBE emission related bands in all three spectra, indicating that the shallow donors have been fully compensated by the incorporation of Mg acceptors.

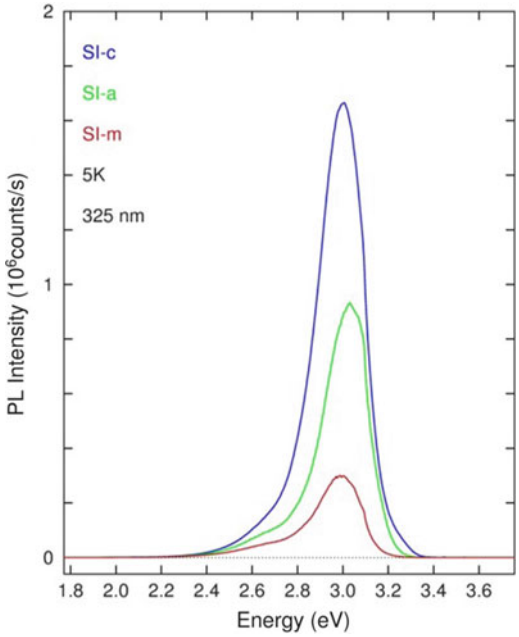

Fig. 16.10 Low temperature photoluminescence spectra of SI *a*-, *c*-, and *m*-plane wafers. Note the absence of any NBE emission bands

16.7 Electrical Properties

The combination of relatively high electron mobility (≅1800 cm^{-2} V s [82]) and saturation velocity ($v \leq 19 \times 10^6$ cm s^{-1}) with high breakdown voltage ($V_B = 26–33 \times 10^6$ V [83]) promotes wurtzite GaN as one of the most important wide bandgap semiconductor materials essential for modern optoelectronic and electronic device applications. However, the full-realization of GaN potential devices will require a full-control of the intrinsic and extrinsic material properties.

Despite the presence of relatively high concentration of compensating centers (cations, carbon, hydrogen, and V_{Ga}), both the UID basic and acidic ammonothermal GaN crystals are intrinsically n-type, mostly due to the very high concentration of oxygen, typically about $10^{19}/cm^3$ [2, 84]. The concentration of oxygen can be reduced by one order magnitude if oxygen-getter is added to the feedstock, resulting on improved transparency wafers [2, 85]. However, the electron mobility of such wafer showed only a minor improvement, as indicated in Table 16.3. Due to the excessive concentration of oxygen, it is difficult to achieve a full control of the electrical properties of ammonothermal GaN boules. Semi-insulating crystals were obtained with incorporation of Mg or Mn at concentrations of $2 \times 10^{18}/cm^3$ or $1 \times 10^{19}/cm^3$, respectively, which yielded wafer with resistivity over 10^{10} Ω cm at room temperature. If higher Mg doping level is employed to reach four fold higher concentration of Mg, the measured resistivity is reduced to ~10^6 Ω cm. These samples resistivity drops to 30 Ω cm after thermal annealing treatment. Such samples have

Table 16.3 Room temperature electrical properties of UID and doped B-Ammono GaN (after [2])

Material type	Conductivity type	Carrier concentration (cm^{-3})	Carrier mobility ($cm^2/V\ s$)	Resistivity (Ω cm)
High oxygen concentration	n-type	~10^{19}	~200	10^{-3}
Higher transparency	n-type	1–2 × 10^{18}	~250	10^{-2}
Low resistivity: Mg	p-type	~10^{16}	~6	~10
High resistivity: Mg	SI	–	–	≥10^{11}
High resistivity: Mn	SI	–	–	≥10^{11}

hole concentration of ~$10^{16}/cm^3$ and mobility of ~6 cm^2/V s. Measurements of the GaN:Mg samples resistivity as a function of the temperature, carried out with the van der Pauw configuration, yields an acceptor activation energy of 166 meV [2]. The large reduction of the resistivity after annealing reminds us of the thermal annealing activation process introduced by Nakamura et al., to activate hydrogen-passivated Mg in MOCVD heteroepitaxial films [86]. These adverse results provides a clear view of the difficult task to overcome to produce p-type ammonothermal GaN substrates.

Hall measurements of various *m*-plane acidic Ammono-GaN crystals showed n-type conductivity with carrier concentration from 9 × 10^{17} to 2 × 10^{19} cm^{-3}, resistivity from 2 × 10^{-2} to 2 × 10^{-3} Ω cm, and mobilities between 1 × 10^2 and 3 × 10^2 cm^2/V s. These values are similar to values obtained from B-Ammono GaN listed in Table 16.2. The low mobility results are obtained from samples with high free carrier concentration [6]. Similar results have been reported by Jiang and coworkers for high-temperature acidic ammonothermal wafers, with oxygen concentrations ranging from 1.5 × 10^{18} to 2.7 × 10^{19} cm^{-3}, which have free carrier concentration of 1.1 × 10^{18} cm^{-3} and mobility ~3 × 10^2 cm^2/V s [8]. They also have reported the growth of crystals with oxygen concentration as low as 3 × 10^{16} cm^{-3}, but no electrical transport was reported [62].

16.8 Thermal Properties

Among many others, an important potential application of GaN is the realization of devices operating at much higher power than that of the well-developed silicon-based power device technology. Operation at extreme condition of voltage and/or current will cause increasing of device junction temperature, reducing both device efficiency and lifetime, if the thermal conductivity is not sufficiently high. Therefore,

high thermal conductivity at device operating conditions is one of the fundamental material requirements for developing efficient high power devices.

Thermal energy transport in semiconductors occurs through phonons, which are scattered by other phonons or existing crystal defects. The former is referred as intrinsic scattering process while the latter is called extrinsic process. Thermal conductivity measurements as a function of temperature reveals the relative contribution of these processes at specific temperature ranges. Several publications have discussed the deleterious effects of various factors such as impurities, free carrier concentration, gallium vacancies, dislocation densities, grain boundaries, and impurities [87–94]. Mion et al., demonstrated that the GaN thermal conductivity, measured with 3-omega technique, is strongly dependent on dislocation density, but independent if dislocation densities are below 10^6 cm^{-2} [95]. Considering that ammonothermal GaN is single crystal with dislocation densities typically $\leq 10^5$ cm^{-2}, dislocations and grain boundaries should be disregarded as phonon scattering mechanisms in this type of crystal. Therefore, only intrinsic (vacancies, antisites, interstitials, isotopes) and extrinsic (impurities and complexes) point defects should be taken into account as major scattering mechanisms. High concentration of gallium vacancies and unintentional impurities (special oxygen and hydrogen) are the major point defects in ammonothermal GaN crystals. Recently, Rounds and co-workers demonstrated that extrinsic point defects dominate the scattering process between 30 and 295 K and that thermal conductivity has an inverse dependence on impurity concentrations [96]. Improved thermal conductivity values of about 230 W/mK have been reported for relatively low impurity background concentration crystals [94, 96]. However, this value is about one-half of the theoretical limit of 400 W/mK (for isotopically pure and undoped GaN) indicating that some material improvement may be possible, and would be beneficial for some device applications [97].

In addition to thermal conductivity, thermal expansion coefficients (α) of GaN are important parameters for the deposition of epitaxial layered device structures. A combination of thermal mechanical analysis and laser interferometric methods employed by Oshima and co-workers yielded values of α at room temperature of 5.3×10^{-6} K^{-1}, 4.2×10^{-6} K^{-1}, and 5.8×10^{-6} K^{-1}, along the $c[0001]$, $a[11\bar{2}0]$, and m [10], respectively, measured on freestanding low dislocation density HVPE samples [98]. These values are different from those reported by Grzegory et al., 2.80×10^{-6} K^{-1} ($c//$) and 3.1×10^{-6} K^{-1} ($c\perp$), using XRD technique of bulk GaN samples grown by high-pressure nitrogen solution (HPNS) method [99]. The growth HPNS method produce small crystals with very low dislocation density, but with very high concentration of oxygen. There are no detailed study of the dependence of the thermal expansion of GaN on point and extended defect concentrations. Presently, there are no reports discussing the thermal expansion coefficient of ammonothermal grown GaN crystals.

16.9 Homoepitaxial Deposition

The usefulness of a substrate is demonstrated if high crystalline quality epitaxial films can be reproducibly deposited on the substrate. In addition to the high crystalline substrate quality, well-controlled epi-growth surface finishing, and substrate miscut orientation, and reduced crystal lattice bowing are required.

Epitaxial GaN films were successfully deposited by metalorganic vapor phase epitaxy (MOVPE) with a RF-heated low-pressure horizontal reactor on the Ga-face of both n-type and SI B-ammono GaN substrates. The ammonia flow was kept constant during the heating and cooling process to prevent surface decomposition. The films deposition were carried out at 1170 °C at a total reactor pressure of 50 mbar [4, 100]. The FWHM of the X-ray rocking curves of these films, acquired on the (0002) planes, were between 22 and 24 arcsec, which are consistent with high crystalline quality films. Selective etching in eutectic mixture yielded etch pit density (EPD) of the order of 10^6 cm^{-2}, which is about two to three orders of magnitude larger than that observed in the B-ammono GaN substrates. It was observed that most of the pits in the epitaxial films agglomerated along the substrate scratches introduced during the substrates surface preparation. This indicates that surface preparation is critical and must be optimized to prevent the incorporation of additional dislocation in the epitaxial layer [4]. Sharp and intense recombination lines assigned to processes involving the annihilation of free-excitons and excitons bound to shallow donors and Mg-acceptors were observed in the low temperature PL spectra of these epitaxial films [4, 76]. The assignment of the free excitons was verified by low temperature reflectance measurements, which identified the excitons associated to holes from all three valence bands [4]. The high quality of the PL and reflectance spectra clearly indicates that the epitaxial layer have much lower concentration of background impurities, which is required for the deposition of films with electrical conductivity type control. Despite of this success, the small deposition rate of MOCVD presents a major roadblock for the fabrication of devices that requires thick epitaxial layers.

To address the small MOCVD growth rate, Sochacki and co-workers developed a method to deposit thick homoepitaxial GaN wafers by HVPE. Smooth 1 in. diameter wafers, crack and stress free, with dislocation density typically in the order of 5×10^4 cm^{-2} were deposited on B-ammono GaN substrate using a home-made HVPE horizontal reactor [101, 102]. SIMS analysis of these wafers reveal that only silicon with concentration of 3×10^{16} cm^{-3} exceeded the detection limit, while oxygen, carbon, hydrogen were below the detection limit. The room temperature free carrier concentration, as measured by van der Pauw method, were of 1.7×10^{16} cm^{-3}. The low temperature PL spectra of these HVPE films showed two dominant lines associated to the annihilation of excitons bound to neutral silicon and oxygen impurities, with FWHM under 170 μeV, which are consistent with low shallow donor concentrations and low sample inhomogeneity [76, 103]. The silicon and oxygen impurities are derived from the silica-based liners and susceptor, which would be reduced if they were made of Si and O free materials [104].

It has been established that UID B-ammono GaN crystals have typically Ga-vacancy concentrations in the order of 10^{17} cm^{-3} and vacancy-cluster concentrations at about 10^{16} cm^{-3}. However, annealing these substrates at temperatures well above the ammonothermal growth temperature of ~600 °C will change significantly the defect structure [57]. Therefore, considering that homoepitaxial film deposition by MOCVD or HVPE occurs at temperatures around 1200 °C, about double of the ammonothermal growth temperature, it is expected that the ammono-GaN substrate will be annealed during the deposition process. As result, the distribution of vacancies in the substrate will be affected. In fact, recently Horibuchi et al., reported that in ammono-GaN, with typically low concentration of dislocation and high concentration of vacancies, during the annealing or epitaxial processes, the vacancies migrate to the dislocation region to form helical dislocation [51]. They also observed that due to lower concentration of vacancies at the film-substrate interface, the helical dislocations stop at the interface region and only the TD propagates through the epitaxial film. In substrates with higher concentration of dislocations the number of vacancies per dislocation is low, avoiding helical dislocation formation.

16.10 Devices

The ultimate evaluation of substrate potentials is the performance and yields of testing devices based on epitaxial structures deposited on these substrates. Optoelectronic devices have been the major driving force for the development of GaN material system. The intrinsically high concentration of free carriers in Ammono-GaN is quite convenient for the fabrication of light emitting devices. A testing light emitting diode hetero-structure deposited by MBE on B-ammono GaN consisted of 3 nm single quantum well followed by 20 nm electron blocking layer (EBL), and 80 nm GaN:Mg, 0.35 nm AlGaN/GaN:Mg superlattice, and a 50 nm InGaN:Mg contacting layer. The Mg concentrations in the EBL and InGaN:Mg was about 5 $\times$ 10^{19} cm^{-3}, while for GaN:Mg it was about 2 $\times$ 10^{18} cm^{-3}. The electroluminescence emission band, extracted through the Ammono-GaN substrate, was peaked at 463 nm. The LED had an output power of 0.6 mW at 100 mA [5]. To further test optoelectronic application of this kind of substrates, a three stripes laser diode mini-bars heterostructure was deposited by MOVPE. The laser with the cavity length of 700 μm emitted in the range from 408 to 412 nm and had maximum output power of 2.5 W, which was mostly limited by cooling capability [105]. The output power was further improved to 4 W for 16-emitters laser diode array [106]. The ammonothermal GaN substrates enabled to overcome major limitation in performance of such device, lying in poor availability of bulk GaN substrates with sufficiently low and homogeneous dislocation density. These results demonstrate that ammono-GaN substrates have great potential for the development of high optical power density light emitting devices. The record high values of the intrinsic physical properties promoted GaN to one of the most suitable semiconductor material for high-power, high-frequency, and high-temperature operation devices. Despite the

lack of native substrates, lateral electronic devices fabricated on heteroepitaxial GaN templates have been commercialized. Their performance turned out to be superior to that of GaAs, Si, and SiC-based commercial devices. These heteroepitaxial device structures have typically dislocation densities in the range 10^9 to 10^{11} cm^{-3}, which is detrimental for higher performance devices. The fabrication of power devices on bulk GaN substrates will allow the realization of devices at the material limit potential including the true avalanche breakdown capability and open the possibility of creating vertical devices architectures. Vertical devices structures will improve the thermal management that limits lateral devices performance and will reduce the device cost by increasing the number of die per wafer. Due to low availability of bulk ammono-GaN, vertical devices concept were initially tested on freestanding HVPE-GaN, which has typical dislocation density around 10^6 cm^{-3}. Diodes with field-plate structure achieved a figure of merit over 3.0 GW/cm^2, reaching a breakdown over 1100 V, leakage current of 10^{-9} A, and on-resistance of 0.4 mΩ cm^2 mA [107]. Recently, Kizilyalli et al. demonstrated that 3.7 kV breakdown voltage and current density of 1 kA/cm^2 could be achieved in a p-n vertical diode fabricated on Ammono-GaN substrates by MOCVD deposition method. It is expected that further improvements of the edge termination should allow breakdown voltage near 5 kV [108]. It is also expected that reduction of the free carrier concentration and increasing of drift region thickness of the device will increase considerably the breakdown voltage [109].

16.11 Closing Remarks

The invention of the transistor and integrated circuit based on silicon semiconductor technology drove the twentieth century electronic revolution, which promoted silicon as the first generation electronic semiconductor. The development of the semiconductor lasers and microwave transistors based on gallium arsenide and indium phosphide, at the end of the twentieth century, ignited the wireless and communication revolution, promoting these materials to the second generation electronic semiconductors. The needs for semiconductor materials capable to perform at extreme conditions of voltage, current, temperature have sent the material scientists in an intensive quest for new wide bandgap semiconductors with the required intrinsic physical and chemical properties. Among the investigated wide bandgap semiconductors gallium nitride is prone to become the third generation electronic material leading a new semiconductor revolution. Despite the lack of high quality and electronic grade native substrates, efficient light emitters (near-UV, blue, green, and white LEDs, solid-state lightning, and laser diodes), solar-blind detectors, high-power solid-state switches and rectifiers, and high power/high frequency microwave transistors based on this material system have been realized. These devices excel the performance of devices based on the previous generation semiconductors, and open the opportunity to produce new kind devices.

Despite this unprecedented undeveloped semiconductor materials success, the realization of high-performance and high-yield devices will require native GaN substrates with well-controlled physical properties. Presently, acidic and basic ammonothermal methods are the only two growth approaches capable to produce real bulk GaN boules. *c*- and *m*-plane wafers are commercially available with some constrains. Wafers made from both the acidic and basic ammonothermal crystals have very low dislocation density and uniform lattice constant, consistent with very small X-ray full width diffraction peaks and curvatures. However, both kinds of crystals are plagued by high concentration of oxygen, hydrogen, point defects and complexes. These intrinsic growth defects play strong role on the optical and electronic properties of ammonothermal GaN, which seriously limit the utilization of these wafer for a number of important devices fabrication. Ammonothermal GaN wafer has been successfully used as seeds to grow hydride vapor phase crystals with low dislocation density, and orders of magnitude lower concentration of unintended impurities, or doped crystals. However, epitaxial growth only reproduce the dimension of the substrate, requiring larger ammonothermal substrates to produce larger HVPE wafers. There have been some success to reduce the background concentration of oxygen impurities, but more must be done to reach the level of well-developed commercial semiconductor wafers. Note that the fundamental parameters of GaN will be accessed only after ammonothermal substrates with improved physical properties become available.

Acknowledgements This research was supported by the Office of Naval Research.

References

1. K. Byrappa, M. Yoshimura, *Handbook of Hydrothermal Technology* (Noyes Publications, Norwich, 2001)
2. M. Zając, R. Kucharski, K. Grabianska, A. Gwardys-Bak, A. Puchalski, J.Z. Domagala, R. Piotrzkowski, E. Litwin-Staszewska, D. Wasik, M. Bockowski, Prog. Cryst. Growth Charact. Mater. **64**, 63 (2018)
3. R. Dwilinski, R. Doradzinski, J. Garczynski, L.P. Sierzputowski, A. Puchalski, Y. Kanbara, K. Yagi, H. Minakuchi, H. Hayashi, J. Cryst. Growth **310**, 3911 (2008)
4. R. Dwilinski, R. Doradzinski, J. Garczynski, L.P. Sierzputowski, M. Rudzinski, M. Zajac, J. Cryst. Growth **311**, 3058 (2009)
5. R. Dwilinski, R. Doradzinski, J. Garczynski, L. Sierzputowski, R. Kucharski, M. Zajac, M. Rudzinski, R. Kudrawiec, W. Strupinski, J. Misiewicz, Phys. Status Solidi (A) **208**, 1489 (2011)
6. Y. Mikawa, T. Ishinabe, S. Kawabata, T. Mochuzuki, A. Kojima, Y. Kagamitani, H. Fujisawa, Proc. SPIE **9363**, 936302-1 (2015). R. Kucharski, M. Zajac, M. Rudzinski, R. Kudrawiec, W. Strupinski, J. Misiewicz, Phys. Status Solidi (A) **208**, 1489 (2011)
7. D. Ehrentraut, R.T. Pakalapati, D.S. Kamber, W. Jiang, D.W. Pocius, B.C. Downey, M. McLaurin, M.P. D'Evelyn, Jpn. J. Appl. Phys. **52**, 08JA01 (2013)
8. W. Jiang, D. Ehrentraut, J. Cook, D.S. Kamber, R.T. Pakalapati, M.P. D'Evelyn, Phys. Status Solidi B **252**, 1069 (2015)
9. T. Malkowski, J.S. Speck, S.P. DenBaars, S. Nakamura, J. Cryst. Growth **499**, 85 (2018)

10. R. Dwilinski, A. Wysmolek, J. Baranowski, M. Kaminska, R. Doradzinski, J. Garczynski, L. Sierzputowski, Acta Phys. Pol. **88**(5), 833 (1995)
11. D.R. Ketchum, J.W. Kolis, J. Cryst. Growth **222**, 431 (2001)
12. A. Yoshikawa, E. Oshima, T. Fukuda, H. Tsuji, K. Oshima, J. Cryst. Growth **260**, 67 (2004)
13. B. Wang, M.J. Callahan, Cryst. Growth Des. **6**, 1227 (2006)
14. T. Hashimoto, K. Fujito, B.A. Haskell, P.T. Fini, J.S. Speck, S. Nakamura, J. Cryst. Growth **275**, e525 (2005)
15. T. Hashimoto, K. Fujito, R. Sharma, E.R. Letts, P.T. Fini, J.S. Speck, S. Nakamura, J. Cryst. Growth **291**, 100 (2006)
16. M.P. D'Evelyn, H.C. Hong, D.-S. Park, H. Lu, E. Kaminsky, R.R. Melkote, P. Perlin, M. Leszczynski, S. Porowski, R.J. Molnar, J. Cryst. Growth **300**, 11 (2007)
17. D. Bliss, B. Wang, M. Suscavage, R. Lancto, S. Swider, W. Eikenberry, C. Lynch, J. Cryst. Growth **312**, 1069 (2010)
18. T. Hashimoto, E. Letts, M. Ikari, Y. Nojima, J. Cryst. Growth **312**, 2503 (2010)
19. R. Dwilinski, R. Doradzinski, J. Garczynski, L. Sierzputowski, R. Kucharski, M. Zajac, M. Rudzinski, R. Kudrawiec, J. Serafinczuk, W. Strupinski, J. Cryst. Growth **312**, 2499 (2010)
20. K. Fujii, G. Fujimoto, T. Goto, T. Yao, Y. Kagamitani, N. Hoshino, D. Ehrentraut, T. Fukuda, J. Cryst. Growth **310**, 896–899 (2008)
21. Y. Kagamitani, D. Ehrentraut, A. Yoshikawa, N. Hoshino, T. Fukuda, H. Tsuji, K. Oshima, Jpn. J. Appl. Phys. **45**, 4018 (2006)
22. T. Hashimoto, S. Hoff, D. Key, K. Male, M. Michaels, J. Cryst. Growth **403**, 3 (2014)
23. E. Letts, D. Key, T. Hashimoto, J. Cryst. Growth **456**, 27 (2016)
24. S. Pimputkar, S. Kawabata, J.S. Speck, S. Nakamura, J. Cryst. Growth **403**, 7 (2014)
25. S. Pimputkar, J.S. Speck, S. Nakamura, J. Cryst. Growth **456**, 15 (2016)
26. T.F. Malkowski, S. Pimputkar, J.S. Speck, S.P. DenBaars, S. Nakamura, J. Cryst. Growth **456**, 21 (2016)
27. J. Hertrampf, N.S.A. Alt, E. Schlücker, M. Knetzger, E. Meissner, R. Niewa, J. Cryst. Growth **456**, 2 (2016)
28. D. Tomida, Y. Kagamitani, Q. Bao, K. Hazu, H. Sawayama, S.F. Chichibu, C. Yokoyama, T. Fukuda, T. Ishiguro, J. Cryst. Growth **353**, 59 (2012)
29. Q. Bao, M. Saito, K. Hazu, Y. Kagamitani, K. Kurimoto, D. Tomida, K. Qiao, T. Ishiguro, Ch. Yokoyama, S.F. Chichibu, J. Cryst. Growth **404**, 168 (2014)
30. K. Yoshida, K. Aoki, T. Fukuda, J. Cryst. Growth **393**, 93 (2014)
31. M. Saito, D.S. Kamber, T.J. Baker, K. Fujito, S.P. DenBaars, J.S. Speck, S. Nakamura, Appl. Phys. Express **1**, 121103 (2008)
32. R.G. Wyckoff, *Crystal Structures*, vol. 1 (Wiley, New York, 1995), pp. 111–113
33. H. Schulz, K.H. Thiemann, Solid State Commun. **23**, 815 (1977)
34. G.A. Jeffrey, G.S. Parry, R.L. Mozzi, J. Chem. Phys. **25**, 1024 (1956)
35. N.A. Mahadik, S.B. Qadri, M.V. Rao, Thin Solid Films **516**, 233 (2007)
36. M. Leszczynski, I. Grzegory, H. Teisseyre, T. Suski, M. Bockowski, J. Jun, J.M. Baranowski, S. Porowski, J.M. Domagala, Appl. Phys. Lett. **69**, 73 (1996)
37. N.A. Mahadik, S.B. Qadri, J.A. Freitas Jr., Cryst. Growth Des. **15**, 291 (2014)
38. L. Bergman, M. Dutta, R.J. Nemanich, *Raman Scattering in Materials Science*, Springer Series in Materials Science, vol. 42, ed. by W.H. Weber, R. Merlin (2000), p. 273
39. D. Gogova, P.P. Petrov, M. Buegler, M.R. Wagner, C. Nestiel, G. Callsen, M. Schmidbauert, R. Kucharski, M. Zajac, R. Dwilinski, M.R. Philips, A. Hoffmann, R. Fornari, J. Appl. Phys. **113**, 203513 (2013)
40. P. Perlin, J. Camassel, W. Knap, T. Talercio, J.C. Chervin, T. Suski, I. Grzegory, S. Porowski, Appl. Phys. Lett. **67**, 2524 (1995)
41. H.-Y. Kim, J.A. Freitas Jr., J. Kim, Electrochem. Solid State Lett. **14**, H5 (2011)
42. J.A. Freitas Jr., J.C. Culbertson, N.A. Mahadik, M.J. Tadjer, S. Wu, B. Raghothamachar, M. Dudley, T. Sochacki, M. Bockowski, J. Cryst. Growth **500**, 104 (2018)
43. M. Dudley, *Encyclopedia of Advanced Materials*, vol. 4 (Pergamon Press, NY, 1994), p. 2950
44. M.J. Hordon, B.L. Averbach, Acta Metall. **9**, 231 (1961)

45. P. Gay, P.B. Hirsch, A. Kelly, Acta Metall. **1**, 315 (1953)
46. R. Kucharski, K. Grabianska, A. Gwardys-Bak, M. Zajac, A. Puchalski, J.Z. Domagala, T. Sochacki, M. Bockowski, Presented at International Workshop on Nitride Semiconductors, Kanazawa, Japan, 11–16 Nov 2018
47. X. Bilaj, Dudley et al., to be published
48. S. Sintonen, M. Rudzinski, S. Suihkonen, H. Jussila, M. Knetzger, E. Meissner, A. Danilewsky, T.O. Tuomi, H. Lipsanen, J. Appl. Phys. **116**, 083504 (2014)
49. T. Hashimoto, F. Wu, M. Saito, K. Fujitu, J.S. Speck, S. Nakamura, J. Cryst. Growth **310**, 876 (2008)
50. J. Bai, M. Dudley, B. Raghothamachar, P. Gouma, B.J. Shromme, L. Chen, P.J. Hartileb, M. Michaels, J.W. Kolis, Appl. Phys. Lett. **84**, 17 (2004)
51. K. Horibuchi, S. Yamaguchi, Y. Kimoto, K. Nishikawa, T. Kachi, Semicond. Sci. Technol. **31**, 034002 (2016)
52. L.J. Cheng, C.K. Yet, Sol. State. Commun. **12**, 529 (1973)
53. P.U. Arifov, N.Y. Arutyunov, A.Z. Iliyasov, Sov. Phys. Semicond. **11**, 907 (1977)
54. F. Tuomisto, I. Makkonen, Rev. Mod. Phys. **85**, 1583 (2013)
55. K. Saarinen, T. Laine, S. Kuisma, J. Nissila, P. Hautojarvi, L. Dobrzynski, J.M. Baranowski, K. Pakula, R. Stepniewski, M. Wojdak, A. Wysmolek, T. Suski, M. Leszczynski, I. Grzegory, S. Porowski, Phys. Rev. Lett. **79**, 3030 (1997)
56. K. Saarinen, in *III-nitrides Semiconductors: Electrical, Structural and Defects Properties*, ed. by O. Manasreh (Elsevier, Amsterdam, 2000), pp. 109–149
57. F. Tuomisto, J.-M. Mäki, M. Zajac, J. Cryst. Growth **312**, 2620 (2010)
58. F. Tuomisto, T. Kuittinen, M. Zajac, R. Doradzinski, D. Wasik, J. Cryst. Growth **403**, 114 (2014)
59. C. Van de Walle, Phys. Rev. B **56**, R10020 (1997)
60. S. Suihkonen, S. Pimputkar, J.S. Speck, S. Nakamura, Appl. Phys. Lett. **108**, 202105 (2016)
61. A. Uedono, Y. Tsukada, Y. Mikawa, T. Mochizuki, H. Fujisawa, H. Ikeda, K. Kurihara, S. Terada, S. Ishibashi, S.F. Chichibu, J. Cryst. Growth **448**, 117 (2016)
62. W. Jiang, M. Nolan, D. Ehrentraut, M.P. D'Evelyn, Appl. Phys. Express **10**, 075506 (2017)
63. J.L. Lyons, A. Alkauskas, A. Janotti, C.G. Van de Walle, Phys. Status Solid **252**, 900 (2015)
64. C. Persson, A.F. da Silva, *Optoelectronic Devices: III-Nitrides*, ed. by M. Razeghi, M. Henini (Elsevier, Amsterdam, 2004), pp. 518–559
65. Authors and Editors of the LB Volumes III/17A-22A-41A1b, Gallium nitride (GaN), effective masses, g-factors, deformation potentials, in *Group IV Elements, IV-IV and III-V Compounds. Part B—Electronic, Transport, Optical and Other Properties*. Landolt-Börnstein—Group III Condensed Matter (Numerical Data and Functional Relationships in Science and Technology), vol. 41A1b, ed. by O. Madelung, U. Rössler, M. Schulz (Springer, Berlin, Heidelberg)
66. J. Neugebauer, C.G. Van de Walle, Phys. Rev. B **50**, 8067 (1994)
67. J. Neugebauer, C.G. Van de Walle, Appl. Phys. Lett. **68**, 1829 (1996)
68. J. Neugebauer, C.G. Van de Walle, Appl. Phys. Lett. **69**, 503 (1996)
69. P. Boguslawski, E.L. Briggs, J. Bernholc, Phys. Rev. B **51**, 17255 (1995)
70. T. Mattila, R.M. Nieminen, Phys. Rev. B **55**, 9571 (1997)
71. I. Gorczyca, A. Svane, N.E. Christensen, Phys. Rev. B **60**, 8147 (1999)
72. S. Limpijumnong, C.G. Van de Walle, Phys. Rev. B **69**, 035207 (2004)
73. H. Wan, A.-B. Chen, J. Appl. Phys. **87**, 7859 (2000)
74. F. Mireles, S.E. Ulloa, Phys. Rev. B **58**, 3879 (1998)
75. W. Gotz, N.M. Johnson, J. Walker, D.P. Bour, R.A. Street, Appl. Phys. Lett. **68**, 667 (1996)
76. J.A. Freitas Jr., W.J. Moore, B.V. Shanabrook, G.C.B. Braga, S.K. Lee, S.S. Park, J.Y. Han, Phys. Rev. B. **66**(2002), 233311 (2002)
77. E. Burstein, Phys. Rev. **93**, 632 (1954)
78. R. Doradzinski, R. Dwilinski, J. Garczynski, L.P. Sierzputowski, Y. Kanbara, in *Technology of Gallium Nitride Crystal Growth*, ed. by D. Ehrentraut, E. Meissener, M. Bockowski (Springer, Cham, 2010), pp. 137–159, Chapter 7
79. D.O. Demchenko, I.C. Diallo, M.A. Rashchikov, Phys. Rev. Lett. **110**, 087404 (2013)

80. J.A. Freitas Jr., B.N. Feigelson, T.J. Anderson, Appl. Phys. Express **6**, 111001 (2013)
81. M. Ilegems, R. Dingle, R.A. Logan, J. Appl. Phys. **43**, 3797 (1972)
82. M. Sakai, H. Ishikawa, T. Egawa, T. Jimbo, M. Umemo, T. Shibata, K. Asai, S. Sumiya, Y. Kuraoka, M. Tanaka, O. Oda, J. Cryst. Growth **244**, 6 (2002)
83. S. Addachi, *Properties of Group-IV, III-V and II-VI Semiconductors* (Wiley, Chichester, 2005)
84. D. Ehrentraut, T. Fukuda, Proc. IEEE **98**, 1316 (2010)
85. W. Jiang, D. Ehrentraut, B.C. Downey, D.S. Kamber, R.T. Pakalapati, H.D. Yoo, M.P. D'Evelyn, J. Cryst. Growth **403**, 18 (2014)
86. S. Nakamura, T. Mukai, M. Senoh, N. Iwasa, Jpn. J. Appl. Phys. **31**, L139 (1991)
87. D.I. Florescu, V.M. Asnin, F.H. Pollak, R.J. Molnar, C.E.C. Wood, J. Appl. Phys. **88**, 3295 (2000)
88. G.A. Slack, L.J. Schowalter, J.A. Freitas Jr., J. Cryst. Growth **246**, 287 (2002)
89. A. Jezowski, B.A. Denilchenko, M. Bockowski, I. Grzegory, S. Krukowski, T. Suski, T. Paszkiewicz, Solid State Commun. **128**, 69 (2003)
90. D.I. Florescu, V.M. Asnin, F.H. Pollak, A.M. Jones, M.J. Schurman, I. Fergunson, Appl. Phys. Lett. **77**, 1464 (2000)
91. J. Zou, D. Kotchetkov, A.A. Baladin, D.I. Florescu, F.H. Pollack, J. Appl. Phys. **92**, 2534 (2002)
92. W. Liu, A.A. Baladin, C. Lee, H. Lee, Phys. Status Solidi A **179**, R135 (2005)
93. D.I. Florescu, F.H. Pollak, T. Paskova, B. Monemar, Compound Semicond. **7**, 62 (2001)
94. R.B. Simon, J. Anaya, M. Kubal, Appl. Phys. Lett. **105**, 202105 (2014)
95. C. Mion, J.F. Muth, E.A. Preble, D. Hanser, Appl. Phys. Lett. **89**, 092123 (2006)
96. R. Rounds, B. Sarkar, T. Sochacki, M. Bockowski, M. Imanishi, Y. Mori, R. Collazo, Z. Sitar, J. Appl. Phys. **124**, 105106 (2018)
97. A. Witek, Diamond Relat. Mater. **7**, 962 (1998)
98. Y. Oshima, T. Suzuki, T. Eri, Y. Kawaguchi, K. Watanabe, M. Shibata, T. Mishima, J. Appl. Phys. **98**, 103509 (2005)
99. I. Grzegory, J. Jun, M. Bockowski, M. Wrobleski, B. Lucznik, S. Porowski, J. Phys. Chem. Solids **56**, 639 (1995)
100. D.D. Koleske, A.E. Wickenden, R.L. Henry, M.E. Twigg, J.C. Culbertson, R.J. Gorman, Appl. Phys. Lett. **73**, 2018 (1998). Erratum, Appl. Phys. Lett. **75**, 1646 (1999)
101. M. Amilusik, T. Sochacki, B. Lucznik, M. Bockowski, B. Sadovyi, A. Presz, I. Dziecielewski, I. Grzegory, J. Cryst. Growth **380**, 99 (2013)
102. T. Sochacki, M. Amilusik, B. Lucznik, M. Fijakowski, J.L. Weyher, B. Sadovyi, G. Kamler, G. Nowak, E. Litwin-Staszewska, A. Khachapuridze, I. Grzegory, R. Kucharski, M. Zajac, R. Doradzinski, M. Bockowski, Jpn. J. Appl. Phys. **53**, 05FA04 (2014)
103. T. Sochacki, Z. Bryan, M. Amilusik, R. Collazo, B. Lucznik, J.L. Weyher, G. Nowak, B. Sadovyi, R. Kucharski, M. Zajac, R. Doradzinski, R. Dwilinski, I. Grzegory, M. Bockowski, Z. Sitar, Appl. Phys. Express **6**, 075504 (2013)
104. H. Fujikura, T. Yoshida, M. Shibata, Y. Otoki, *Proceedings of SPIE*, vol. 10104, 1010403-1 (2017)
105. P. Perlin, L. Marona, K. Holc, P. Wisniewski, T. Suski, M. Leszczynski, R. Czarnecki, S. Najda, M. Zajac, R. Kucharski, Appl. Phys. Express **4**, 062103 (2011)
106. P. Perlin, S. Stanczyk, A. Kafar, A. Bojarska, L. Marona, R. Czarnecki, G. Targowski, G. Muziol, H. Turski, E. Grzanka, S. Grzanka, S. Najda, P. Wisniewski, T. Czyszanowski, M. Leszczynski, C. Skierbiszewski, M. Zajac, R. Kucharski, T. Suski, Photonics Lett. Pol. **6**, 32 (2014)
107. Y. Hatakeyama, K. Nomoto, N. Kaneda, T. Kawano, T. Mishima, T. Nakamura, IEEE Electron Device Lett. **32**, 1674 (2011)
108. I.C. Kizilyalli, A.P. Edward, H. Nie, D. Bour, T. Prunty, D. Disney, IEEE Electron Device Lett. **35**, 247 (2014)
109. B.S. Kang, F. Ren, Y. Irokawa, K.W. Baik, S.J. Pearton, C.-C. Pan, G.-T. Chen, J.-I. Chyi, H.-J. Ko, H.-Y. Lee, J. Vac. Sci. Technol. B: Microneelectron. Process. Phenom. **22**(2), 710 (2004)

Part IV
Future Aspects and Challenges

Chapter 17
Special Equipment for Ammonothermal Processes

Eberhard Schlücker, Benjamin Hertweck, Saskia Schimmel, and Peter Wellmann

Abstract As the ammonothermal method often requires technically challenging conditions such as high temperature, high pressure and reaction media that are rather corrosive towards most metals (see Chap. 11), the further development of ammonothermal process equipment is of vital importance for tapping the full potential of the ammonothermal method. Suitable high-pressure/high-temperature autoclaves are therefore the basic requirement for a successful process. Ammonothermal syntheses are conventionally carried out in autoclaves, which do not allow monitoring of the physical and chemical processes during the experiments. Therefore, in situ measurement techniques at process conditions are crucial for obtaining a holistic understanding of ammonothermal processes. The following chapter presents optical cells for in situ monitoring enabling UV/Vis and Raman spectroscopy, X-ray imaging and X-ray diffraction as well as ultrasonic measurements. Additionally, special equipment like a rotatable feedthrough and a ceramic-crucible-based systems for minimization of corrosion and contamination are described.

17.1 Optical Cells for In Situ Monitoring Technologies

Figure 17.1 shows three different apparatuses. The first one shows a uniaxial optical cell (Fig. 17.1a). It was designed for in situ monitoring of ammonothermal reactions. Due to its compact shape, its thick wall design, and the horizontal position of the reaction chamber it is particularly suited to establish a near-isothermal temperature

E. Schlücker (✉)
Chair of Process Machinery and Systems Engineering (IPAT), Friedrich-Alexander-University of Erlangen Nuremberg (FAU), Erlangen, Germany
e-mail: sl@ipat.uni-erlangen.de

B. Hertweck
Hugo Kern und Liebers GmbH & Co KG, Schramberg, Germany

S. Schimmel · P. Wellmann
Institute Materials for Electronics and Energy Technology (I-MEET), Friedrich-Alexander-University, Erlangen-Nuremberg, Germany

E. Meissner and R. Niewa (eds.), *Ammonothermal Synthesis and Crystal Growth of Nitrides*, Springer Series in Materials Science 304,
https://doi.org/10.1007/978-3-030-56305-9_17

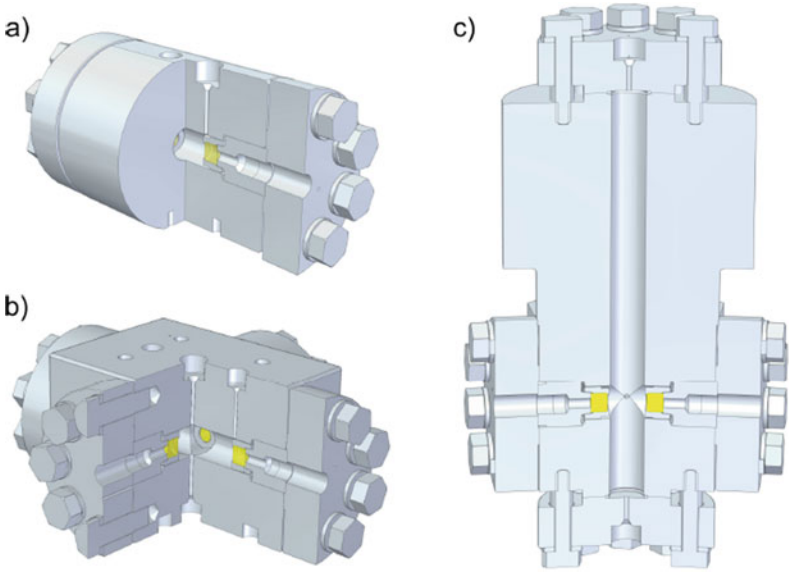

Fig. 17.1 Types of optical cells: **a** Uniaxial optical cell, **b** biaxial optical cell and **c** optical cell for in situ X-ray diffraction. The viewing windows are shown in yellow. Reprinted with permission from [1]

field for equilibrium studies, with minimized influence of both local thermal gradients and convection. Furthermore, it is transportable and thus allows to work under the same apparatus boundary conditions at different research stations. The construction was carried out according to the rules and proposals in Chap. 3. The viewing windows follow the Poulter principle and the sealing is realized with C-rings. A particular problem were the cross drillings, which produce a notch factor of up to three according to Chap. 3. However, a finite element analysis showed that a rounding of about 0.5 mm radius in combination with the ductility of the material Alloy 718, which still plastifies the notch somewhat, is sufficient to withstand the stresses.

Nevertheless, this problem was exacerbated in the biaxial optical cell (Fig. 17.1b). The biaxial optical cell has four windows for two paths of rays, which allows for simultaneous use of multiple in situ monitoring techniques. For instance, UV-VIS spectroscopy, Raman spectroscopy and X-ray imaging can be conducted simultaneously to extract complementary information under identical experimental conditions. The larger diameter of the main cross bore and the presence of several bores in the same region of the vessel, however, lead to more notching corners. Of course, this problem can only be solved with rounding of the corners, again with a radius of 0.5 mm, and good ductility of the autoclave alloy. Important in this context is that the maximum operating parameters had to be limited to 300 MPa and 600 °C. Moreover, a regulation had to be created that the full pressure may only be applied above approx. 200 °C in order to ensure the necessary ductility by softening due to the temperature.

Special challenges were posed by the apparatus shown in Fig. 17.1c, which was designed for in situ x-ray diffraction experiments during bulk GaN crystal growth. At this point the problem was caused neither by the material nor by notches. With the measures shown above this autoclave could also be realized as a functionally reliable component. In terms of high pressure technology, the special challenges associated with this type of experiments are threefold. Firstly, the optical channels equipped with windows need to stand at a certain angle to each other in order to allow entry of the incident beam and exit of the diffraction signal. The angle between incident beam and diffracted beam is calculated using the Bragg condition:

$$n \cdot \lambda = 2 \cdot d \cdot \sin(\Theta) \tag{17.1}$$

where

n Diffraction order (integer)
λ Wavelength of X-rays
d Distance of the lattice planes in the crystal.
Θ half diffraction angle (if the definition of the diffraction angle is two Θ).

Consequently, this angle depends on which reflection is to be recorded as well as on the X-ray wavelengths. Regarding the choice of reflection, it is important to consider both the obtainable information on the structural quality of the crystal as well as the relative intensity of different reflections [1], as the intensity of the diffraction signal affects what exposure times will be necessary. On this basis, a diffraction angle of 15.75° was obtained for the (0002) reflection of GaN, which was integrated into the autoclave. Due to the dimensions of the holes, however, a tolerance is automatically built in which can compensate for the effect of distortions and dislocations.

Secondly, it was necessary to use a window material with significantly improved transparency for X-rays of the selected photon energy (compared to sapphire as described in Chap. 3). Therefore, boron carbide was chosen (further information on potential materials for X-ray transparent windows can be found in Sect. 10.3). This material has an extreme hardness of 30–40 GPa and a modulus of elasticity of 390–400 GPa (about three times that of steel) and therefore improves mechanical strength parameters as well. The third challenge arises from the need to establish an appropriate thermal gradient between two temperature zones, which is necessary to facilitate growth on the seeds in the one zone and dissolution of the nutrient in the other zone. Therefore, thermal transport along the autoclave wall of the autoclave needed to be reduced compared to the full wall thickness which is necessary only in the window-containing part of the autoclave. For achieving a sufficiently large thermal gradient while keeping machining costs reasonable and while allowing for the use of windows, the wall thickness was reduced only in the middle section of the autoclave, which corresponds to the baffle region.

Figure 17.1c shows the angular arrangement of the windows. It is also evident from Fig. 17.1c that four bores meet in the center of the bottom part of the autoclave, which all influence each other negatively in terms of strength. The diffraction geometry with a simplified visualization of the diffraction signals of the GaN crystal as well

as the exit side B_4C window is shown in Fig. 17.4 (more detailed information on diffraction experiments can be found in the corresponding Sect. 17.3). The graphic in Fig. 17.5 represents the case of an ideal centric position of the primary beam in the center of the window with parallel alignment of the axes of the primary beam and window bore. Furthermore, it is assumed that the crystal surface is exactly in the center of the interior (i.e. on the center axis of the autoclave). In this case, the (0002) reflection of GaN passes exactly through the center of the exit window. Tolerances for practical deviations from this ideal diffraction geometry were created by using window assemblies with identical area of view (6 mm diameter) as for the other optical cells and by positioning the windows as closely to the vertical axis of the autoclave as possible.

17.2 Rotatable Feedthrough

The in situ diffraction experiments also motivated the development of a rotatable feedthrough. This is necessary for the alignment of the crystal to fulfil the Bragg condition as well for ensuring that all tilted domains can contribute to the diffraction signal. Since installing a motor inside the autoclave does not appear feasible, the rotation movement needs to be created outside and transferred into the autoclave However, since the autoclave is operated at around 300 MPa and 600 °C, the seal needs to withstand these parameters while allowing for a rotation movement.

Allowing rotary motion therefore means a grinding seal. For this requirement metals with good dry running properties have to be selected. Copper or beryllium would have good emergency running properties. However, these two materials cannot provide the necessary elasticity required for such a seal, even in alloyed form, and they are not resistant to ammonia. That is why we need to build a split gasket as follows. We install a clearance seal in the hot area, but it has a very narrow gap. Recommended would be about 0.02 mm. This seal should prevent mass and heat transfer to the next seal. At this location, we close a neck (tube) which carries another seal at the end. It can be assumed that after the realized distance of approx. 200 mm the temperature has dropped to the service temperature of plastics. This allows us to install a gland packing with plastics (e.g. PTFE) for 300 MPa. Figure 17.2 shows this arrangement in detail, whereby the clearance seal here is a lip seal with a defined gap, which is also slightly supported by the pressure, which then overcomes the stiffness of the seal and ensures very narrow gaps or even creates a certain sliding contact.

This feedthrough has been tested successfully at pressures up to 253 MPa and an internal temperature of the fluid in the growth zone of about 500 °C (higher pressures are also expected to be feasible but have not been tested).

The feasibility of transferring a torque into the reaction chamber may also be of interest for further applications, as it provides the option of creating forced convection through stirring of the solution. While it may find practical application in ammonothermal syntheses as well, the capability of introducing forced convection is certainly interesting with respect to fundamental studies of convection.

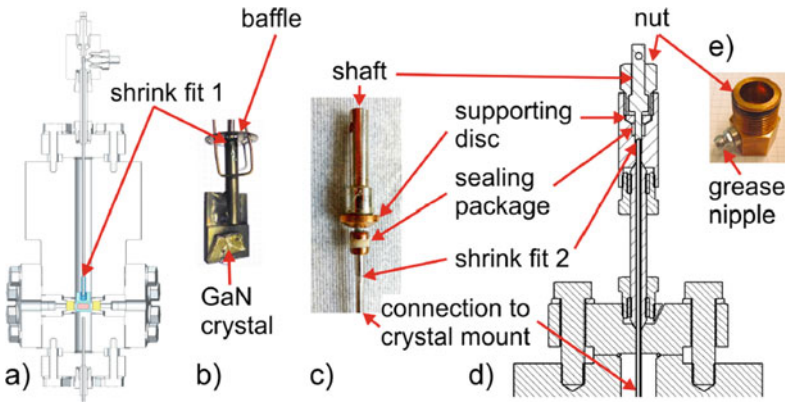

Fig. 17.2 Rotatable feedthrough: **a** Installation in the autoclave (blue: crystal holder, red: GaN seed crystal, yellow: window), **b** photo of a GaN crystal on the crystal holder with baffle and internal structure frame made of Inconel wire (cut), **c** photo of the sealing spindle with support disc, sealing packing and shrink fit to the Inconel shaft **d** cross-section of the feedthrough, mounted on the upper cover flange, **e** sealing nut with grease nipple (photo). Reprinted with permission from [1]

17.3 In Situ X-Ray Diffraction

Beyond these fundamental rules, technical solutions for the implementation and advancement of in situ monitoring techniques have proven to contribute significantly to the scientific understanding of ammonothermal processes. This is evident for the results of the in situ monitoring techniques. While tremendous technological progress has already been made, the development of in situ monitoring technologies has just begun and their further development is expected to pave the way to a much more comprehensive understanding of ammonothermal reactions.

In the area of spectroscopic and X-ray based in situ monitoring, integrating these measurement techniques with autoclaves designed for crystallization in an intentionally applied temperature gradient is expected to yield a variety of further insights. While spectroscopic and X-ray based techniques have so far been mostly applied to autoclaves that were designed for equilibrium studies, complementary results will become accessible through applying these techniques to autoclaves designed for temperature gradient based crystal growth. One intriguing future opportunity is thought to lie in the visualization of fluid flow in the autoclave by X-ray based and optical techniques since the results presented in Chap. 10 suggest that this will become possible. The development of suitable autoclaves for integrating in situ monitoring with temperature gradient based crystal growth has already begun in the course of the development of an experimental setup for in situ X-ray diffraction. In the following, the state of the development of this setup will be evaluated, including equipment-related aspects that are also relevant to other in situ monitoring techniques or other technological aspects of ammonothermal experimentation.

The autoclave for in situ X-ray diffraction during growth has been realized based on the window technology described in Chap. 10. In order to improve the X-ray transmission of the autoclave windows, in particular for reduced X-ray energies, boron carbide was established as a window material to substitute sapphire. For details on potential X-ray transparent window materials and their chemical stability under specific ammonothermal conditions, see Chap. 10.

The implementation of a thermal gradient together with autoclave windows presents conflicting requirements with respect to the construction of the autoclave. The basic issue is that the integration of windows is associated with an increased thickness of the autoclave walls, at least in proximity of the window flanges. In order to limit the conductive heat transfer occurring in the autoclave walls between growth and dissolution zone, the walls of the two-zone optical cell were thus thinned in the intersection area of growth and dissolution zone.

The optical cell windows are arranged in the diffraction angle of the (0002) reflection of GaN. It is noteworthy that the chosen geometry is also capable to be applied for studies of the (0002) reflection of the novel nitride semiconductor $ZnGeN_2$. An X-ray source with molybdenum anode is used. In order to minimize exposure times, an X-ray source yielding a very high photon flux was selected. For beam focusing and monochromatization, the X-ray source is equipped with a multilayer mirror optic.

In order to ease the alignment of the crystal to fulfil the Bragg condition as well as to ensure that all tilted domains can contribute to the diffraction signal, a rotatable feedthrough for rotating the crystal inside the autoclave under process conditions was developed.

A photograph of the setup for in situ X-ray diffraction including the autoclave is depicted in Fig. 17.3. The components shown in the photograph are mounted within an outer enclosure providing radiation protection. The purpose of the inner enclosure, which can be seen in the photograph, is to protect the operator as well as the X-ray equipment in case of failure of autoclave components, in particular accounting for the brittle nature of the X-ray transparent optical cell windows.

The resulting diffraction geometry is illustrated by Fig. 17.4. In order to achieve short exposure times in relation to the growth rates, an area detector based on phosphor image plates is used. As schematically shown in Fig. 17.4, the diffraction signal on the area detector comprises the (0002) reflection of the GaN crystal and ring-shaped diffraction signals from the microcrystalline boron carbide windows (in reality, only the ring segments that are not absorbed by metal autoclave parts, i.e. only the segment passing through the bore behind the window, is detectable). The diffraction signal originating from the windows is not an issue because it is rather weak and, in addition, it can be spatially separated from the GaN signal by appropriate adjustments of the alignment.

The experimentally obtained measurement signal is shown exemplary in Fig. 17.5 as an overview representing the entire area of the detector. Only the most intense diffraction signals of the window material contribute noticeably to the recorded signal and they are spatially well-separated from the reflection of the GaN seed crystal.

The primary parameter of interest is the intensity distribution within the (0002) reflection from the GaN seed crystal, as the width of the reflection contains information on the mosaicity of the crystal (more specifically, the tilt with respect to

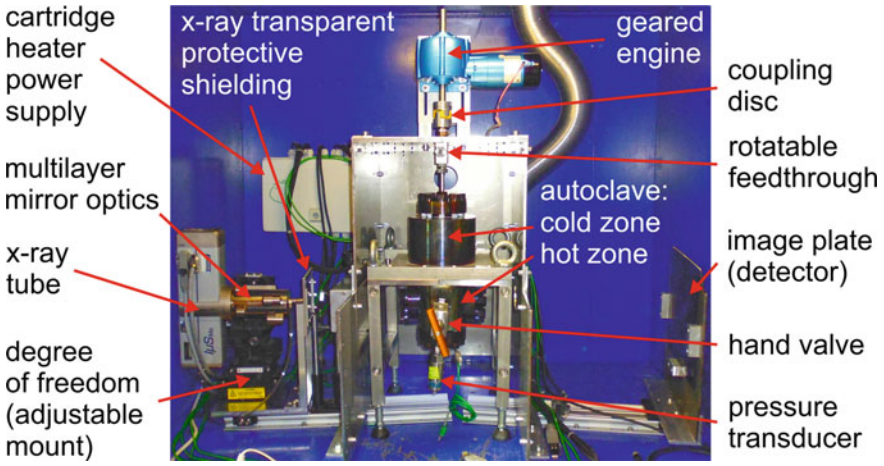

Fig. 17.3 Experimental setup for in situ X-ray diffraction during ammonothermal growth of GaN. The stainless steel enclosure in the center contains the autoclave and protects both the operator and the X-ray measurement equipment in case of failure of autoclave components (in the photograph, the front wall of the enclosure is not mounted because otherwise the autoclave could not be seen). The X-ray transparent protective shielding ensures that the damageable X-ray source is protected even during the measurements. The rotation of the crystal inside the autoclave is driven by a geared engine to ensure sufficient torque while minimizing wear on the feedthrough by utilizing a low rotational speed. Reprinted with permission from [1]

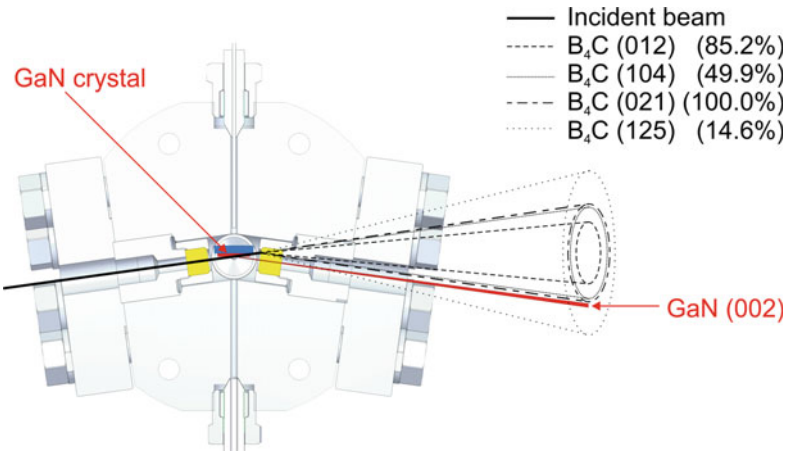

Fig. 17.4 Schematic visualization of the diffraction geometry, based on a horizontal section through the center of the crystallization zone of the autoclave. The X-ray transparent windows are shown in yellow, the GaN seed is shown in red, and the seed mount is displayed in blue color. The dashed lines represent the diffraction signals originating from the microcrystalline boron carbide windows. Due to the microcrystalline structure of the windows, their diffraction signal consists of cones. In the illustration, the absorption of part of the cone-shaped signal by metal components of the autoclave is neglected. The two screwed fittings are used for filling the autoclave and for measuring the inner wall temperature, respectively. Reprinted with permission from [1]

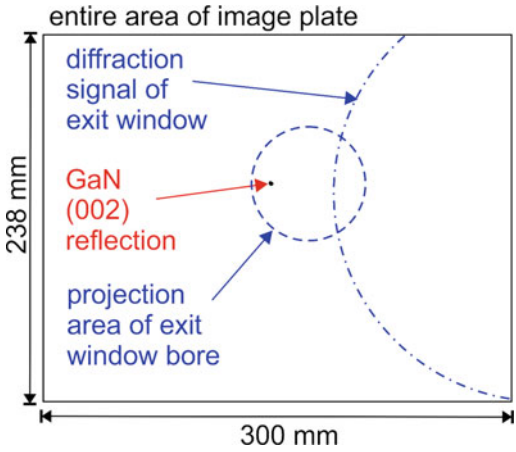

Fig. 17.5 Exemplary in situ X-ray diffraction measurement obtained at a pressure of 96.0 MPa and an internal temperature of 243 °C, which corresponds to an ammonia density suitable for ammonobasic growth of GaN. The overview of the entire area of the imaging plate shows the spatial separation of the diffraction signal originating from the GaN seed crystal and the diffraction signal originating from the microcrystalline autoclave window at the exit side. The exposure time was 10 min in total. Reprinted with permission from [1]

[0001]-direction). An example of the intensity distribution within the reflection is shown in Fig. 17.6.

Initial in situ diffraction measurements obtained at an ammonia density typical for ammonobasic crystal growth of GaN demonstrate that a significant signal of the (0002) reflection can already be accumulated within an exposure time of 5–10 min, which is in good agreement with expectations. The angular range of the swivel movement of the crystal has not been cut down to its minimum (which is determined by the angular range required to record the signal of all domains). Therefore, it is expected that through optimizing the angular range as well as detector readout settings, it will be possible to further improve the signal to noise ratio while keeping the exposure times short in relation to the rate of crystallization. Measuring the absolute value of the diffraction angle remains a technical challenge, which is due to the difficulty of determining the absolute position and rotation angle of the seed inside the autoclave with sufficient precision. The main target, however, is to monitor changes occurring during the experiment rather than a precise determination of absolute values. The current angular resolution for monitoring changes of the width of the (0002) reflection is about 0.02°. Considering the width of the diffraction peak of the crystal used in the presented measurements, which is about 0.32°, this is already a reasonably good resolution.

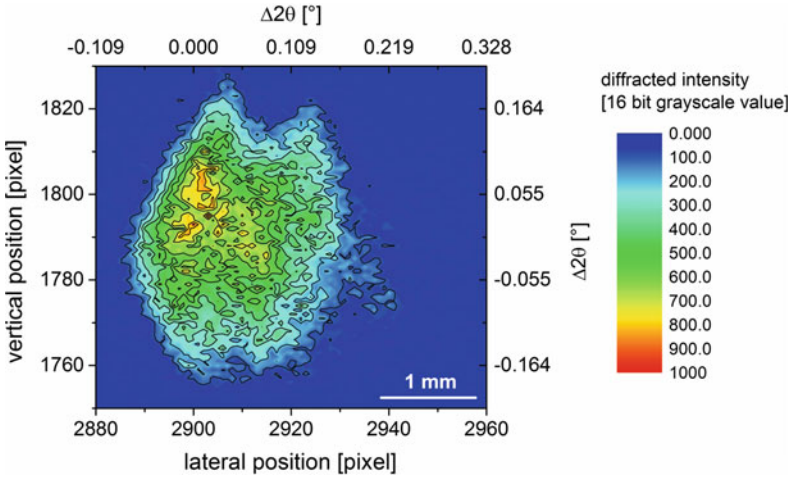

Fig. 17.6 Intensity distribution within the (0002) reflection of the GaN seed crystal, measured under ammonothermal process conditions (pressure: 253 MPa, fluid temperature in the growth zone: 503 °C). The lateral extension of the reflection contains information on the orientation distribution of the mosaic domains contributing to the signal (tilt with respect to [0001]-direction). Reprinted with permission from [1]

17.4 Liner-Concept Based on Ceramic Crucibles

The implementation of a crucible is an alternative to the realization of a concept based on a coating, in which the good resistance properties of ceramics can be exploited [2]. However, the strong difference in the coefficient of thermal expansion is also a critical factor for this variant of a liner concept. For this reason, it is not possible to implement a shrink construction for operating temperatures at $T_{\text{ammono}} = 600$ °C. On the one hand, the ceramics have only very poor elastic properties, which prohibit tensile loading of the material. On the other hand, the maximum shrinkage temperature is limited to $T_{\text{Schr.max}} = T_{\text{Alloy 718max 718}} = 650$ °C due to the thermal stability of the alloy (see Chap. 3). Subsequent heat treatment in the form of a second ageing without solution annealing would result in a modified microstructure. Solution annealing would have the advantage of producing a microstructural condition that is close to the original, but all intrinsic material stresses would then be relieved, including shrinkage stresses.

An alternative realization is based on a pressure balanced crucible, which is surrounded by two pressure chambers. It is not possible to create a hermetic seal between the chambers, but transport of the corrosive ammonoacidic or also ammonobasic species into the outer pressure chamber can be minimized, where contact with the metal would be possible. Vice versa, the transport of contaminant particles from outside the crucible into the inner chamber is also reduced. This technology also has further potential with regard to the realization of internal structures for convection control and positioning of solids, such as baffles or crystal mounts.

Since the microstructure and the resulting properties depend on the manufacturing process, especially for ceramics [3], the corresponding details must be considered ([2] or manufacturers). The chemical stability of ceramics and other materials in different ammonothermal reaction media has been discussed in detail in Chap. 11. In summary BN, Si_3N_4 have been found suitable for the described crucible concept. Compared to autoclave alloys (see Chap. 3), they show a significantly lower corrosion rate. In order to implement the novel liner concept (crucible), both materials are tested to determine their specific suitability. As can be seen from the descriptions above, the mechanical properties of the ceramics make different demands on the liner design.

(a) Stability of liner materials: Si_3N_4 as a hot pressed material is characterized by singular defects caused by the manufacturing process. Consequently, tensile stresses in the liner should be avoided, as they may lead to spontaneous failure. This also applies to BN, which manufactured by hot pressing as well and has poor mechanical properties. High compressive stresses are permissible for Si_3N_4. For BN, however, only minor stress is acceptable even if compressive.
(b) Closure of the capsule: Since the ceramics have only a vanishing elasticity, no hermetic sealing can be realized under the operating pressure of $P_{\text{ammono}} = 300$ MPa. For this reason, the lid and the area of the crucible in contact with the lid possess high surface quality (Ra ≈ 0.5 µm) to minimize leakage of the sc–NH_3/mineralizer solution to the outside of the crucible.
(c) The developed concept should also be applicable to the autoclaves already developed and described in Sect. 17.1.

The realization of a reactor concept with external heating based on two pressure chambers, which enable the pressure-balanced mounting of the liner, considers these requirements. Under optimized operating conditions, the heater generates a radial temperature gradient of $\Delta T \approx 2$ K [4] during the heating period. The use of the liner increases this gradient due to the relatively low heat conduction of the ceramics [3]. Thus, the fluid in the outer chamber always has a higher temperature than the fluid in the inner chamber, which results in a lower pressure load for the liner. Two separate filling nozzles, which necessitate a design with two lids, carry out the filling of the two chambers, compare Fig. 11.3 in Chap. 11. The liner is designed as a capsule with a matching lid. The lid is equipped with a radial bore. This bore allows the filling with ammonia through the filling line. The contact surfaces of the crucible lid are lapped to a roughness of $R_a \approx 0.5$ µm and low tolerance, thus, the fit enables a good sealing effect between crucible and lid. The sealing effect of the lid is produced by a spring, which is positioned at the bottom of the crucible. The spring exerts a force equal to twice the weight of the crucible. The spring is also made of a high-temperature nickel-based alloy (Alloy 600). These measures are intended to minimize the fluid exchange between the two pressure chambers. The outer pressure chamber is filled with ammonia through the second filling nozzle. Figure 17.1 shows the complete autoclave design.

The following aspects are considered when dimensioning the capsule:

(i) The length of the capsule and the spring need to be chosen so that the required spring force will be created.

(ii) The outer diameter of the crucible is limited by the inner diameter of the autoclave. To ensure easy handling, a difference in diameter of = 200 µm is selected. In this case the crucible can easily be inserted into the autoclave at room temperature. If a smaller outer diameter is selected, it can cause tilting during loading and unloading. Under process conditions, the diameter is increased due to the significant difference in the thermal expansion coefficients, but the internal pressure also expands the reactor.

The expansion of crucible and autoclave at temperature and the coefficients of thermal expansion of the reactor and liner materials were first determined by dilatometer measurement. It was found in good approximation that the coefficients for the materials used are constant. The values are: $\alpha_{BN} = -0.5 \times 10^{-6}\ K^{-1}$ and $\alpha_{Si3N4} = 3.4 \times 10^{-6}\ K^{-1}$. Both crucibles have a diameter of $d_{Si3N4\,ammono} = d_{BNammono} \approx 20.80$ mm under process conditions. The measured coefficient of expansion of alloy 718 is $\alpha_{alloy718} = 14.4 \times 10^{-6}\ K^{-1}$ and thus causes a thermal expansion of $\Delta r_{therm}\alpha(T;\ T_{room},\ p;\ p_{atmos})\Delta T = 0.18$ mm.

The liner is pressure balanced and therefore experiences almost no elongation due to the pressure load. The diameter of the autoclave, on the other hand, stretches by $\Delta r_p = 0.25$ mm due to the internal pressure. In total, the reactor diameter expands to 21.43 mm by the influence of temperature and pressure.

17.5 Liner Design Based on Shrink Constructions

Disadvantages of the crucible in Sect. 17.3 are the non-hermetical seal, which reduces but not inhibits corrosive attack of the autoclave and the requirement of pressureless mounting of the crucible to avoid tensile stresses on the ceramic. A shrink connection with a tight fit of a ceramic crucible to a metallic autoclave would reduce the free volume for corrosive attack. Simultaneously shrinking results in pressure stresses on the ceramic, enabling the high internal pressures under ammonothermal conditions. However, as mentioned in Sect. 17.3, shrinking of ceramics to Alloy 718 is not possible, due to the big difference in coefficients of thermal expansion. Additionally a shrinked ceramic crucible cannot be removed easily and the porosity of the ceramic has to be as low as possible to minimize infiltration. Therefore shrink connected ceramic crucibles would be only possible at low temperatures up to 400 °C (first stage for ammonothermal processes).

17.6 Summary

Building upon the uniaxial viewing cells (see Chap. 4) this chapter presented several autoclaves for different in situ monitoring techniques for the ammonothermal process. X-ray imaging, X-ray diffraction and ultrasonic measurements add to

UV/Vis- and *Raman*-spectroscopy described in Chap. 4 and therefore allow forming a holistic picture of the ammonothermal process.

Special equipment, such as the rotatable feedthrough enable to realize complex measurements under process conditions and therefore broaden the accessibility for new measurement techniques. The liner concept based on ceramic crucibles rounds up this chapter with an innovative corrosion protection possibility.

References

1. S. Schimmel, in *Dissertation: In situ Visualisierung des ammonothermalen Kristallisationsprozesses mittels Röntgenmesstechnik* (Friedrich-Alexander-Universität Erlangen-Nürnberg, Germany, 2018)
2. B. Hertweck, in *Dissertation: Chemische und physikalische Stabilität von technischen Materialien und Hochdruckapparaten für ammonothermale Systeme* (Friedrich-Alexander-Universität Erlangen-Nürnberg, Germany, 2016)
3. W. Kollenberg, *Technische Keramik: Grundlagen, Werkstoffe, Verfahrenstechnik* (Vulkan-Verlag, Essen, Germany, 2004)
4. N.S.A. Alt, E. Meissner, E. Schlücker, L. Frey, In situ monitoring technologies for ammonthermal reactors. Phys. Status Solidi **9**, 436–439 (2012)

Chapter 18
Ammonothermal Materials

Wolfgang Schnick, Niklas Cordes, Mathias Mallmann, Rainer Niewa, and Elke Meissner

Abstract Even more than fifty years after the first ammonothermal syntheses, the synthetic potential of this technique is still far from established. Even in the already commercialized crystal growth of GaN substrates, various technical obstacles remain, partly because of lack of materials for high pressure equipment sufficiently resistant against the aggressive medium and at the same time persistent at the process conditions, but clearly because of insufficient understanding of the chemical and physical processes in supercritical ammonia. Still, many novel nitrides already emerge from ammonothermal synthesis. This technique has already proven to hold great prospects in crystal growth of the other group III nitrides, AlN and InN, relevant from a technical point of view, and substitution variant among those nitrides with further trivalent ions. Huge potential was also demonstrated for synthesis of further hard to produce nitrides as nitridosilicates, nitridophosphates and similar compounds, or oxide nitride perovskites. With increasing understanding of the physiochemical background and concomitant extension of the accessible process parameters we definitely will see great advances in the ammonothermal synthesis of novel materials for future applications.

W. Schnick · N. Cordes · M. Mallmann
Chair of Inorganic Solid-State Chemistry, Department of Chemistry, University of Munich (LMU), Butenandtstr. 5-13, Munich 81377, Germany

R. Niewa (✉)
Institute of Inorganic Chemistry, University of Stuttgart, Pfaffenwaldring 55, Stuttgart 70569, Germany
e-mail: rainer.niewa@iac.uni-stuttgart.de

E. Meissner
Chair for Electron Devices, University of Erlangen-Nuremberg, Cauerstr. 6, Erlangen 91058, Germany

Fraunhofer Institute for Integrated Systems and Device Technology, Schottystr. 10, Erlangen 91058, Germany

E. Meissner and R. Niewa (eds.), *Ammonothermal Synthesis and Crystal Growth of Nitrides*, Springer Series in Materials Science 304,
https://doi.org/10.1007/978-3-030-56305-9_18

During recent years, the ammonothermal synthesis has proven to represent a powerful method with high scalability, thus suitable for small-scale fundamental research as well as for commercial large-scale materials production. Its advantages for commercial applications are obviously the synthesis of bulk material which is difficult to crystallize otherwise, for example large crystals of GaN. The essential benefit of the ammonothermal synthesis route is the fact that lower temperatures are needed for crystal growth (some hundreds of °C) compared to other techniques, where temperatures between 1000 and 2500 °C are usual. Due to the low temperatures, thermodynamically a minor concentration of intrinsic point defects and structural defects would be expected and the structural quality of such crystals is expected to be outstanding. Since the growth rates are very low, the crystallization in the sense of technological usage for the production of larger crystals must be performed batch wise in large autoclaves. This approach was already proven very successful by the hydrothermal method, whereby nowadays tons of quartz crystals are being produced per year. However, despite the great achievements over the years in the growth of larger GaN crystals, the chemistry of the ammonothermal method is complex and the crystal growth process itself as a technical process is not well understood, hard to control and the total number of impurities from the system is still too high for many applications.

Currently, the ammonothermal method appears particularly interesting for commercial GaN crystal growth, due to the good crystal quality and the principal opportunity of a larger scaled batch process. However, scalability has recently come into debate as ultra large pressure vessels, made from materials corrosion resistant enough under the given conditions with supercritical ammonia and for high pressures and temperatures (e.g. so far up to 300 MPa and 650 °C) have turned out to be a severe limitation. So new materials for autoclaves are needed and modified technical solutions like internally heated autoclaves have become a topic of research. Such studies are still comparatively rare and this lack may hinder to tap the full potential of the ammonothermal synthesis.

Irrespective of technical usage, for fundamental explorative research, the method offers stabilization of materials, which are generally difficultly to obtain including unusual modifications and metastable compounds, partly not accessible by other methods [1]. The facts which are often considered as drawback—the complex chemistry—may be turned into an advantage as it may be possible to mobilize compounds which are otherwise hard to transport, e.g. compounds with extremely low vapor pressure at process conditions that are nearly not accessible by means of physical vapor transport. Still, the method faces limitations in maximum temperature and pressure or combinations thereof, although some progress in extending the current boarders was recently achieved.

The development of fundamental comprehension of the physical and chemical processes inside the autoclave will be crucial for both the synthesis of novel materials and the improvement of crystal growth as well as respective apparatuses. A deeper understanding of the processes during dissolution, in solution and while precipitation on a molecular basis clearly will lead to improvements in the choice of feed stock substances and the mineralizer systems, which can then be specifically

designed for the desired product. For single ammonobasic and ammonoacidic mineralizers we already see a vivid advancement in knowledge about dissolved species and their chemistry during temperature and pressure changes from ex situ intermediate isolation and characterization, in situ spectroscopic investigations of solutions in ammonia as solvent and molecular dynamics studies. Particularly in situ and operando investigations under process conditions will in future doubtlessly boost understanding. This may lead to a knowledge driven adjustment of mineralizer concentration in ammonia, a suitable concentration design via addition of co-mineralizers of various kinds to regulate concentrations, appropriate acidity and ionic strengths and possibly to application of solvent admixtures to ammonia. The latter may modify the solvent properties of ammonia particularly at process conditions, for example to alter ion agglomeration at higher temperatures, apparently occurring due to diminishing permittivity of ammonia. This directly relates to the fundamental physical properties of ammonia-based solutions saturated with mineralizers, co-mineralizers and intermediates formed from the feedstock materials, which significantly deviate from those properties of pure ammonia, not only in terms of pressure-temperature relations. Currently, next to thermodynamical properties, all quantities relating to surface reactions, dissolution and transport seem to be most relevant, like, for example, acidity and basicity, dielectric properties or viscosity to name only few. Chemically, the solution system in ammonia must be viewed as a buffer system modifying the properties of the solvent with direct influence on the chemistry within the solution. Increasing information on physico-chemical properties of ammonia-based solutions and the complex chemistry in solution during the ammonothermal process, where we hardly scratched the surface of knowledge so far, will clearly lead to new directions of exploratory chemistry.

Finally, such anticipated improvements will doubtlessly lead to an improvement of the desired materials properties in synthesis. However, for the time being, many investigations focus on the crystal growth of hexagonal gallium nitride. In order to obtain a broader data basis, which would allow drawing conclusions on the processes, respectively the necessities for adjustments for different systems other than GaN, several promising material syntheses from ammonothermal conditions have to be studied in similar deep detail. Nitrides as a materials class are of great interest due to their wide variety of interesting properties. This can range from nowadays quite known semiconductors like gallium, aluminum or indium nitride to novel ternary compounds, which may be able to replace these group III nitrides in the future. Examples for promising compounds are Zn(Si, Ge, Sn)N_2, A_2ZnN_2 and AZn_2N_2(A = Ca, Sr, Ba), which offer similar properties and possibilities for band gap engineering as the binary compounds from the (Al, Ga, In)N system [2]. This could help to produce optoelectronic devices without consuming less earth-abundant or expensive raw materials. Thermoelectric materials or photocatalysts are also amongst the nitrides, for example Mo_3Co_3N or VN, which show higher catalytic activity in ammonia decomposition than the classical iron based catalyst [3]. Piezoelectric compounds like $(Ga, Al)_{1-x}(Sc, Y, Cr)_xN$ are extremely interesting for future applications due to the enhancement of polarization inside the structure by introduction of a larger ion [4]. On the other hand the classical physical vapor transport technique has shown to fail to sufficiently mobilize

scandium or yttrium, such that it can be incorporated into the host nitride structure to a larger extent than some small percentage [5]. So the ammonothermal synthesis with its special possibilities to chemically mobilize a species by an intermediate complex is seen as a powerful alternative. Many nitrides also exhibit superconducting properties like e.g. NbN or alike, which promise to be well suited superconducting materials for future applications in aviation technology. Moreover, other classes of materials like ternary or quaternary nitrides, oxide nitrides, amides, imides or fluoride nitrides have hardly been investigated due to difficulties in synthesis. For other compounds (e.g. photocatalysts) it was demonstrated that the degree of crystallinity can be much improved by the ammonothermal synthesis compared to classical high temperature processes, which opens the path to future applications.

Recent developments demonstrate aluminum nitride, indium nitride and partial substitution variants of these group III nitrides as well as various ternary and multinary nitridosilicates and nitridogermanates to be suitable new model systems to learn about fundamental properties of ammonia-based solutions and materials synthesis [6]. As mentioned in Chaps. 10 and 12 first preliminary studies (in situ X-ray monitoring) on the ternary system Zn–Ge–N have already been carried out, in order to obtain similar insights into the synthesis and crystallization process of ternary nitrides like $ZnGeN_2$ as there are already numerous for GaN [7]. Since ternary zinc nitrides (e.g. $ZnSiN_2$, $ZnGeN_2$ or Zn_2PN_3) are intriguing semiconductor materials with comparable physical properties as group III nitrides AlN, GaN and InN, further investigations of their properties and crystal growth are essential for possible applications [2]. It may be feasible to draw conclusions from the ammonothermal crystallization process of GaN (see Chap. 6) to the structurally related Grimm-Sommerfeld analogous compounds with wurtzite superstructures. Furthermore, especially those nitrides of formula type II-IV-N_2 offer the possibility for bandgap tuning by formation of solid solutions. Thus, it may be possible to cover a similar bandgap range both by substitution of Zn with other divalent metals, as well as by mixed Si-, Ge- and Sn-compounds, as it is possible within group III nitrides. As mentioned in Chap. 12, most ternary and higher nitrides produced by ammonothermal synthesis so far possess a wurtzite-type superstructure. However, exploratory experiments have shown that nitrides with other structure types are also accessible by the ammonothermal method and could be interesting for further research [6]. It turned out that high temperatures have a stronger influence on formation of nitrides from supercritical ammonia than high pressures. For instance, Li_2SiN_2 is formed at high temperatures (1070 K) as a side phase during the ammonothermal synthesis of wurtzite type $LiSi_2N_3$ [8]. While most of the nitrides mentioned in Chap. 12 were synthesized under ammonobasic conditions, ammononeutral or ammonoacidic conditions could lead to new compounds as well. The examples of Cu_3N and InN indicate that some compounds are solely accessible under ammononeutral conditions [9, 10]. In the case of $ZnGeN_2$, ammonoacidic conditions also resulted in the desired compound [11]. Next to nitridosilicates and nitridogermanates, nitridophosphates are interesting systems for ammonothermal synthesis. The lower thermal stability and decomposition temperature of P_3N_5 (as compared to Si_3N_4) are major challenges for synthesis of

nitridophosphates. Consequently, high-pressure synthesis techniques like the multi-anvil approach have been used for the preparation of most nitridophosphates [12, 13]. So far, $K_3P_6N_{11}$ and the wurtzite derivatives Mg_2PN_3 and Zn_2PN_3 have been obtained in supercritical ammonia [14, 15]. These findings already indicate that the ammonothermal method could be a promising route to other nitridophosphates as well.

With the purpose to gradually move to more distant systems and, concomitantly, to approach more complex processes and desired materials, a modification on the anionic part of the chemical compound may be taken into account, for example with the future focus on oxide nitrides or various chalcogenide-based materials. This approach is the next logical step after gaining a deeper understanding of the interaction of ammonia-based solutions with different types of metal ions, since the chemistry of non-metal anions in ammonia is likely to be rather different and probably even more complex.

The perovskite structure type is one of the most common and most extensively studied ones in inorganic solid state chemistry. With general formula ABX_3, the best known and most common representatives are oxides. A smaller number of fluorides, halides, selenides and sulfides are also known to crystallize in the perovskite structure type. Other, more complex structures with different anions can adopt the perovskite structure as well. Oxide nitride perovskites possess the same structure with oxygen being partially substituted by nitrogen. Typically, both anions share the same atomic site, forming solid solutions with atomic ratios that can be adjusted to some extent during the process of synthesis. In the past, it has been shown that the targeted use of mineralizers and precursors allows numerous oxide nitride perovskites to be synthesized using the ammonothermal approach. The compounds having the typical composition $AB(O, N)_3$ (A = alkaline earth or rare earth metals; B = transition metals) are obtained as crystalline products. SEM images show crystals with a size of several μm. So far, oxide nitride perovskites were mostly obtained in other synthesis methods like ammonolysis as crystalline powders, but without defined morphology. In contrast, crystals of oxide nitride perovskites obtained by the ammonothermal method exhibit a well-defined crystal habitus. Such oxide nitride perovskites show promising properties, e.g. for application in solar water splitting systems or as thermoelectric functional layers [16–18]. Ammonothermal synthesis may offer a pathway to overcome the lack of crystals of sufficient size for the fundamental exploration of physical properties.

Some of these compounds, e.g. $LaTaON_2$, were already obtained at 600 °C, whereas others, such as $GdTaON_2$, are only accessible at higher temperatures of 800 °C [19]. The replacement of some metals with others of similar ionic radius is obvious. By applying the Goldschmidt tolerance factor, the existence of some hitherto unknown oxide nitride perovskites has been predicted. Thus, $YTiO_2N$, $CdTaO_2N$ and $CdNbO_2N$ appear to be feasible. The smart use of reactive precursors could lead to other oxide nitride perovskites as well [20]. We could show that the ammonothermal approach is a powerful technique to synthesize new as well as known oxide nitride perovskites with an increased crystal size compared to conventional methods like ammonolysis.

The ammonothermal approach could be further developed for bulk crystal growth of oxide nitride perovskites. Although the crystals are only a few μm in size, initial experiments show that larger crystals are possible. One problem of thin film deposition for example is the lattice mismatch between the substrate and the heteroepitaxially grown crystal. Accordingly, further development of the ammonothermal approach could lead to larger crystals of oxide nitride perovskites that are grown in a homoepitaxial manner without a compositional change between substrate and crystal. This development will lead to an access of better understanding of intrinsic properties and extend application fields of oxide nitride perovskites. Single crystals obtained by this method will allow studying dielectric properties in insulating samples as well as charge carrier transport in conducting ones. Accordingly, the ammonothermal synthesis of oxide nitride perovskite crystals is very promising for the discovery of novel and innovative next generation semiconductors with suitable bandgaps.

Such oxide nitride perovskites have various interesting properties, like their varying colors as well as high chemical stability, which enable use as non-toxic pigments. Furthermore, some representatives show colossal magnetoresistance and ferromagnetism. In addition, these materials are semiconductors with a bandgap of about 2 eV [19]. With suitable bandgap values and positions, oxide nitride perovskites possess the property of using sunlight to split water into hydrogen and oxygen (photocatalysis). This is extremely important because of the scarcity of fossil resources, which can be substituted by hydrogen [21].

The synthesis at higher temperatures showed that also oxide nitride Ruddlesden-Popper phases can be synthesized. The latter can be interpreted as layered perovskite variants containing alternating slabs of NaCl and perovskite structure. Layered systems like $Li_2LaTa_2O_6N$ also have excellent photocatalytic activity properties and were examined as photocatalysts for visible CO_2 light reduction [22]. Such layered oxide nitride photocatalysts clearly demonstrate the high potential of 2D layered oxide nitrides as a visible-light-driven photocatalyst.

Taking a step further, pure nitride perovskites (ABN_3) were predicted to be thermodynamically stable as well. By assuming that nitrogen has oxidation number −III, highly charged transition metal cations are necessary to achieve charge neutrality. As a consequence the *B* cation would require an oxidation state between +V and +VII. Although there are transition metals with such high oxidation states, the synthesis of pure nitride perovskites is challenging, since nitrogen is less electronegative than oxygen, and with respect to a possible internal redox reaction the formation of such high oxidation states next to nitride ions seems less likely to be stabilized. Modern computational techniques offer an effective tool to screen possible materials in a fraction of time required by an equivalent experimental search. With the help of these findings and the synthetic possibilities of ammonothermal synthesis, nitride perovskites could be accessible in the future. In the past, compounds could be synthesized that were not accessible by other synthetic routes. This fact should also be transferable to new systems. The ammonothermal approach probably provides the required conditions for the synthesis of nitride perovskites $LaReN_3$, $YReN_3$ or $LaWN_3$ predicted to

be stable. It is precisely this substance class that promises unusual electronic properties. $LaWN_3$ for example has been calculated to be a semiconductor and could display a large ferroelectric polarization [23].

These examples impressively demonstrate the importance of extending the temperature and pressure range for the further development of the ammonothermal method. By increasing temperature and pressure, the synthesis of new compounds seems possible because of the better solubility at elevated conditions [24]. By further increasing the temperature it should be possible to grow crystals of even further compounds.

The synthetic potential of the ammonothermal technique, significantly more than fifty years after the initial start of the development [25], is nowadays still far from exhausted. As can be seen from the various contributions in this monograph, tasks and future directions are manifold. This does not only involve the growth of larger crystals but also the generation of layers, mass crystallization of functional materials or nanocrystals of completely novel compounds which were so far not demonstrated at all with other synthesis techniques due to difficulties in compound formation reactions.

In summary, we see great prospects for ammonothermal synthesis, crystal growth and novel materials production. The new developments will undoubtedly pave the way to improved materials as well as fully novel compound semiconductor materials.

References

1. T.M.M. Richter, R. Niewa, Chemistry of ammonothermal synthesis. Inorganics **2**, 29 (2014)
2. Y. Hinuma, T. Hatakeyama, Y. Kumagai, L.A. Burton, H. Sato, Y. Muraba, S. Iimura, H. Hiramatsu, I. Tanaka, H. Hosono, F. Oba, Discovery of earth-abundant nitride semiconductors by computational screening and high-pressure synthesis. Nat. Commun. **7**, 11962 (2016)
3. J.S.J. Hargreaves, Heterogeneous catalysis with metal nitrides. Coord. Chem. Rev. **257**, 2015 (2013)
4. M.A. Moram, S. Zhang, ScGaN and ScAlN: emerging nitride materials. J. Mater. Chem. A **2**, 6042 (2014)
5. A. Dittmar, J. Wollweber, M. Schmidbauer, D. Klimm, C. Hartmann, M. Bickermann, Physical vapor transport growth of bulk $Al_{1-x}Sc_xN$ single crystals. J. Cryst. Growth **500**, 74 (2018)
6. J. Häusler, W. Schnick, Ammonothermal synthesis of nitrides: recent developments and future perspectives. Chem. Eur. J. **24**, 11864 (2018)
7. J. Häusler, S. Schimmel, P. Wellmann, W. Schnick, Ammonothermal synthesis of earth-abundant nitride semiconductors $ZnSiN_2$ and $ZnGeN_2$ and dissolution monitoring by in situ X-ray imaging. Chem. Eur. J. **23**, 12275 (2017)
8. J. Häusler, R. Niklaus, J. Minár, W. Schnick, Ammonothermal synthesis and optical properties of ternary nitride semiconductors Mg-IV-N_2, Mn-IV-N_2 and Li-IV_2-N_3 (IV=Si, Ge). Chem. Eur. J. **24**, 1686 (2018)
9. U. Zachwieja, H. Jacobs, Ammonothermalsynthese von Kupfernitrid, Cu_3N. J. Less-Common Met. **161**, 175 (1990)
10. J. Hertrampf, P. Becker, M. Widenmeyer, A. Weidenkaff, E. Schlücker, R. Niewa, Ammonothermal crystal growth of indium nitride. Cryst. Growth Des. **18**, 2365 (2018)
11. J. Häusler, Ammonothermal synthesis of ternary nitride semiconductors and novel multinary nitrides. Dissertation, LMU München, Germany (2018)

12. F. Karau, W. Schnick, High-pressure synthesis and X-ray powder structure determination of the nitridophosphate BaP_2N_4. J. Solid State Chem. **178**, 135 (2005)
13. F.W. Karau, L. Seyfarth, O. Oeckler, J. Senker, K. Landskron, W. Schnick, The stuffed framework structure of SrP_2N_4: challenges to synthesis and crystal structure determination. Chem. Eur. J. **13**, 6841 (2007)
14. H. Jacobs, R. Nymwegen, Synthesis and crystal structure of a potassium nitridophosphate, $K_3P_6N_{11}$. Z. Anorg. Allg. Chem. **623**, 429 (1997)
15. M. Mallmann, C. Maak, R. Niklaus, W. Schnick, Ammonothermal synthesis, optical properties and DFT calculations of Mg_2PN_3 and Zn_2PN_3. Chem. Eur. J. **24**, 13963 (2018)
16. L. Sagarna, K.Z. Rushchanskii, A. Maegli, S. Yoon, S. Populoh, A. Shkabko, S. Pokrant, M. Ležaić, R. Waser, A. Weidenkaff, Structure and thermoelectric properties of $EuTi(O, N)_{(3 \pm \delta)}$. J. Appl. Phys. **114**, 033701 (2013)
17. A.E. Maegli, S. Pokrant, T. Hisatomi, M. Trottmann, K. Domen, A. Weidenkaff, Enhancement of photocatalytic water oxidation by the morphological control of $LaTiO_2N$ and cobalt oxide catalysts. J. Phys. Chem. C **118**, 16344 (2014)
18. S.G. Ebbinghaus, H.-P. Abicht, R. Dronskowski, T. Müller, A. Reller, A. Weidenkaff, Perovskite-related oxynitrides—recent developments in synthesis, characterisation and investigations of physical properties. Prog. Solid State Chem. **37**, 173 (2009)
19. N. Cordes, W. Schnick, Ammonothermal synthesis of crystalline oxonitride perovskites $LnTaON_2$ (Ln=La, Ce, Pr, Nd, Sm, Gd). Chem. Eur. J. **23**, 11410 (2017)
20. W. Li, E. Ionescu, R. Riedel, A. Gurlo, Can we predict the formability of perovskite oxynitrides from tolerance and octahedral factors? J. Mater. Chem. **1**, 12239 (2013)
21. A. Kudo, Y. Miseki, Heterogeneous photocatalyst materials for water splitting. Chem. Soc. Rev. **38**, 253 (2009)
22. T. Oshima, T. Ichibha, S.Q. Ken, K. Muraoka, J. J.M. Vequizo, K. Hibino, R. Kuriki, S. Yamashita, K. Hongo, T. Uchiyama, K. Fujii, D. Lu, R. Maezono, A. Yamakata, H. Kato, K. Kimoto, M. Yashima, Y. Uchimoto, M. Kakihana, O. Ishitani, H. Kageyama, K. Maeda, Undoped Layered Perovskite Oxynitride $Li_2LaTa_2O_6N$ for Photocatalytic CO_2 Reduction with Visible Light. Angew. Chem. **30**, 8286 (2018); Angew. Chem. Int. Ed. **57**, 8154 (2018)
23. R. Sarmiento-Pérez, T.F.T. Cerqueira, S. Körbel, S. Botti, M.A.L. Marques, Prediction of stable nitride perovskites. Chem. Mater. **27**, 5957 (2015)
24. S. Pimputkar, S. Nakamura, Decomposition of supercritical ammonia and modeling of supercritical ammonia–nitrogen–hydrogen solutions with applicability toward ammonothermal conditions. J. Supercrit. Fluids **107**, 17 (2016)
25. R. Juza, H. Jacobs, Ammonothermalsynthese von Magnesium- und Berylliumamid. Angew. Chem. **78**, 208 (1966); Ammonothermal synthesis of magnesium and beryllium amides. Angew. Chem. Int. Ed. **5**, 247 (1966)

Index

E. Meissner and R. Niewa (eds.), *Ammonothermal Synthesis and Crystal Growth of Nitrides*, Springer Series in Materials Science 304,
https://doi.org/10.1007/978-3-030-56305-9